

Sheffield Hallam University

Characterisation of minerals using evolved gas analysis and infrared spectroscopy.

FORSYTH, Jeffrey.

Available from the Sheffield Hallam University Research Archive (SHURA) at:

<http://shura.shu.ac.uk/19680/>

A Sheffield Hallam University thesis

This thesis is protected by copyright which belongs to the author.

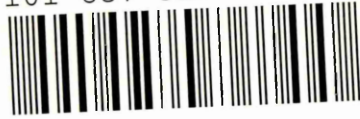
The content must not be changed in any way or sold commercially in any format or medium without the formal permission of the author.

When referring to this work, full bibliographic details including the author, title, awarding institution and date of the thesis must be given.

Please visit <http://shura.shu.ac.uk/19680/> and <http://shura.shu.ac.uk/information.html> for further details about copyright and re-use permissions.

LEARNING CENTRE
CITY CAMPUS, HOWARD STREET
SHEFFIELD S1 1WB

101 687 819 2



SHEFFIELD HALLAM UNIVERSITY
LEARNING CENTRE
CITY CAMPUS, HOWARD STREET
SHEFFIELD S1 1WB

REFERENCE

ProQuest Number: 10695720

All rights reserved

INFORMATION TO ALL USERS

The quality of this reproduction is dependent upon the quality of the copy submitted.

In the unlikely event that the author did not send a complete manuscript and there are missing pages, these will be noted. Also, if material had to be removed, a note will indicate the deletion.



ProQuest 10695720

Published by ProQuest LLC (2017). Copyright of the Dissertation is held by the Author.

All rights reserved.

This work is protected against unauthorized copying under Title 17, United States Code
Microform Edition © ProQuest LLC.

ProQuest LLC.
789 East Eisenhower Parkway
P.O. Box 1346
Ann Arbor, MI 48106 – 1346

**Characterisation of Minerals using Evolved Gas
Analysis and Infrared Spectroscopy**

Jeffrey Forsyth

**A thesis submitted in partial fulfilment of the requirement of
Sheffield Hallam University
For the degree of Doctor of Philosophy**

March 2001

Sheffield Hallam University
Department of Business Administration
Sheffield S1 1WB

1999

Sheffield Hallam University
Department of Business Administration
Sheffield S1 1WB

1999



ACKNOWLEDGEMENTS

I would like to take this opportunity to extend my thanks to several individuals who have contributed in some way or other to this research.

Firstly, I would like to thank my director of studies Prof. Jack Yarwood and supervisor Dr. Chris Breen for giving me the opportunity to complete this work, but also for their scientific input, enthusiasm and humour through the peaks and troughs of three years hard work.

A thank you also goes to Schlumberger for their financial support and encouragement, in particular Dr. Trevor Hughes.

Special thanks also goes to Terry Hudson for his help with all things computer related and the prevention of disasters there of. To Dr. Steve Habesch for his reliability, enthusiasm and speed. To Dr. Chris Sammon, for his support and amusing repartee. A big thank you also goes to Dr. Brian Lewis for his XRD support during times of need. Thank you to Margaret, Bob and Deeba for their help and support.

A particular note goes to Scott Taylor for his determination and hard work in helping me maintain the EGA system.

Especial thanks goes to my friends in the vibrational spectroscopy group, Chris Constable (soon to be Dr.-for his frankness), Paul Whelan (for his input to tackling software problems and understanding of all things gaseous), Nigel De Mello (for the retort) and Paul Hatton (for his appreciation of all things obscure and organic).

My sincere gratitude and love goes to my girlfriend Lesley Anne Wallace for her love, care, cooking, patience, full sympathy and ability to distract me with the tangible world of the veterinary surgeon. A great thank you also goes to her family for their interest, humour, support, and baking skills. To my family, the catalyst in driving me forward, in particular my mother for her tenacity, drive and durability.

**This work is dedicated to my girlfriend Lesley Anne Wallace and my
parents Elizabeth and Kevin Forsyth**

Abstract

Several methods have been used for the characterisation of minerals in powders and in rocks. Particular emphasis has been directed towards the use of chemical probes to elucidate the surface mineralogy in order to provide detection profiles suitable for both qualitative and quantitative chemometric analysis.

The first probe evaluated was cyclohexylamine (CHA). Ni²⁺- and Al²⁺-exchanged montmorillonite (SWy-2 -Wyoming, USA), were exposed to cyclohexylamine vapour (CHA). The samples were characterised by X-ray diffraction (XRD), thermogravimetric analysis (TGA) and evolved gas analysis (EGA), which included TGA, real time gas phase FTIR (RT-GP-FTIR), real time mass spectrometry (RT-MS) and organic trap module-gas chromatography-mass spectrometry (OTM-GC-MS). CHA decomposed along different routes via inter-related mechanisms that were cation dependent. Over Al³⁺-SWy-2 hydrodenitrogenation via the Hofmann degradation was the predominant route whereas ring dehydrogenation to aniline either directly from CHA or possibly via cyclohexylimine was significant over Ni²⁺-SWy-2. Very little unmodified cyclohexylamine was detected in the evolved gases which means that the desorption of CHA cannot be used as a quantitative measure of the acidity of cation-exchanged clays. Nonetheless, as a qualitative probe, CHA has the potential to distinguish the difference between Ni²⁺ and Al³⁺-SWy-2.

The second probe evaluated was 3-cyanopyridine (3CYP). TGA has shown that temperature programmed desorption (TPD) of 3CYP is capable of distinguishing between the Ni²⁺- and Al³⁺ exchanged forms of SWy-2. 3CYP was found to be unsuitable for a variety of reasons highlighted by its ability to condense within the EGA system and the long incubation times necessary to produce detectable thermal events.

The most suitable probe used so far is Dimethylformamide (DMF), being able to intercalate quickly and showing no evidence of modification. Principal component analysis (PCA) and partial least squares (PLS) modelling techniques were applied to the EGA DMF detection profiles of four clay mineral groups. Each group was successfully characterised and provided valuable information about intra and inter group relationships. The use of RT-MS detection profiles for ions $m/z = 18$ and 73 (DMF parent ion) were shown to have the most potential for more sensitive quantitative applications.

Application of quantitative PLS modelling to mixed mineral standards has shown that it is possible to estimate the clay mineral constituents in both powders and rocks. The use of the ion $m/z = 73$ provided an R^2 value of 0.98. Use of ion $m/z = 18$ (H₂O) has perhaps shown most potential, due to its ability to produce training sets with excellent correlation coefficients of 0.95 for SWy-2, 0.97 for KGa-2 and 0.95 for CCa-1. However, because SWy-2 and 1-Mt (illite) demonstrate overlapping detection of DMF (where uptake of DMF by 1-Mt is comparatively small), it is impossible to directly separate their relative contributions at the concentration levels under study. The use of mass spectrometry has shown that it is possible to detect to levels of 1% with considerable scope for detecting smaller levels.

Environmental scanning electron microscope (ESEM) and energy dispersive X-ray analysis (EDX) of cation exchanged SWy-2 and a sandstone rock exposed to 2-bromopyridine (2BPY) have shown the potential of using the bromine functional group as a tag to locate the presence of swelling minerals in rocks by EDX.

TABLE OF CONTENTS

Chapter 1 Introduction

1.0 Aims and objectives.....	1
1.1 Reservoir rocks.....	2
1.2 Sandstone rocks.....	3
1.3 The importance of surface mineralogy.....	6
1.4 Classification of minerals.....	9
1.5 Tectosilicates (Quartz, Feldspars).....	9
1.5.1 Quartz.....	9
1.5.2 Feldspar.....	10
1.6 Phyllosilicates (Clay minerals).....	12
1.7 Clay minerals examined in this thesis.....	17
1.7.1 The 1:1 Type minerals (kaolinite & halloysite).....	17
1.7.2 The 2:1 Type minerals (montmorillonite & saponite).....	18
1.7.3 The illite (or The clay-mica) group.....	22
1.7.4 Chlorite.....	23
1.8 Clay mineral active bonding sites.....	24
1.8.1 Neutral siloxane surface.....	28
1.8.2 Hydroxyl groups.....	28
1.8.3 Isomorphic substitution sites.....	30
1.8.4 Exchangeable Metal Cations & Undercoordinated Metal Atoms....	31
1.8.5 Polarized Water Molecules Surrounding Exchangeable Cations....	32
1.8.6 Hydrophobic sites.....	34
1.8.7 Broken edge sites.....	34

Chapter 2 Theory of Techniques used in this thesis

2.0 Introduction.....	36
2.1 Infrared.....	36
2.1.1 Adsorption of Infrared radiation.....	36
2.1.2 Vibrational Modes of polyatomic molecules.....	39
2.1.3 Factors affecting the intensity of infrared bands.....	42
2.1.4 Fourier transform infrared spectroscopy (FTIR).....	43
2.1.5 Potential Advantages of Interferometric measurements of vibrational spectra.....	47
2.1.5.1 Fellgett advantage.....	47
2.1.5.2 Connes advantage.....	47
2.1.5.2 Jacquinot advantage.....	48
2.1.6 Transmission Spectroscopy.....	48
2.1.7 Diffuse Reflectance Infrared Fourier Transform Spectroscopy (DRIFTS).	49
2.1.7.1 Refractive index.....	53
2.1.7.2 Particle size.....	54
2.1.7.3 Pressure.....	54
2.1.7.4 Sample Height.....	56
2.1.8 Variable Temperature-Diffuse Reflectance Infrared Fourier Transform Spectroscopy (VT-DRIFTS).....	57

2.1.8.1 Room temperature (RT) and VT-DRIFTS sample preparation.....	59
2.1.8.2 Effects of heat on VT DRIFTS spectra.....	60
2.2 Thermogravimetric Analysis (TGA).....	60
2.2.1 Experimental parameters.....	63
2.3 X-Ray Diffraction and Variable Temperature X-ray Diffraction (VT-XRD)	64
2.3.1 Experimental parameters.....	67
2.4 X-Ray Fluorescence Analysis (XRF).....	67
2.4.1 Experimental parameters.....	68
2.5 Environmental Scanning Electron Microscopy (ESEM).....	68
2.5.1 X-ray analysis in the ESEM.....	70
2.5.2 X-ray detector.....	73
2.5.3 Detection of X-rays.....	73
2.5.4 Qualitative analysis.....	74
2.6 Evolved gas Analysis (EGA) by Thermogravimetric- Fourier Transform Infrared Spectroscopy (TG-FTIR) and Thermogravimetric-Mass Spectrometry (TG-MS).....	76
2.6.1 (EGA) TG and FTIR.....	76
2.6.2 Mass spectrometer.....	77
2.6.2.1 Ion source.....	78
2.6.2.2 Ion analyser (quadrupole).....	81
2.6.2.3 Mass detector.....	81
2.6.2.4 Organic trap module (OTM).....	82
2.6.2.5 Gas Chromatography (GC).....	82
2.6.2.6 TGA/FTIR/MS interfaces.....	83
2.7 Statistical characterization methods.....	85
2.7.1 Multivariate Analysis –Principal Components Analysis (PCA)..	86
2.7.1.1 Data compression methods.....	90
2.7.1.2 Principal Component scores.....	92
2.7.1.3 Principal Component loadings.....	95
2.7.2 Partial Least Squares (PLS).....	96
2.7.2.1 Summary of PLS advantages.....	101
2.7.2.2 Summary of PLS disadvantages.....	101
2.7.3 Optimisation of PLS models.....	102
2.7.3.1 Self-Prediction.....	103
2.7.3.2 Cross Validation.....	105
2.7.3.3 Selecting the factors based on PRESS.....	107

Chapter 3 Traditional and Current Methods of Characterising Minerals

3.0 Introduction.....	108
3.1 X-ray Diffraction.....	108
3.2 Infrared Absorption Spectroscopy.....	110
3.3 Environmental Scanning Electron Microscopy.....	112
3.4 Chemical Analysis.....	113
3.5 Thermal Methods.....	114

Chapter 4 Literature Survey and Strategy

4.0 Introduction.....	121
4.1 The ‘Chemical Probe’ strategy.....	121
4.1.1 Chemical probe requirements.....	122
4.2 Method 1: Characterisation of EGA profiles by chemometrics.....	125
4.2.1 Review of chemometrics for qualitative and quantitative analysis	125
4.3 Review of organo-mineral interactions.....	129
4.3.1 Typical smectite-organic molecule interactions.....	130
4.3.2 Typical kaolinite-organic molecule interactions.....	137
4.4 Methods used to analyse organo-mineral interactions.....	146
4.4.1 Thermal methods TGA, DTA, DSC and EGA.....	146
4.4.2 Evolved gas analysis (EGA).....	147
4.4.3 X-ray diffraction (XRD).....	152
4.4.4 Infrared spectroscopy.....	152
4.4.5 Other techniques.....	154

Chapter 5 Application of chemical probes cyclohexylamine (CHA) and 3-cyanopyridine (3 CYP)

5.0 Introduction.....	157
5.1 Experimental.....	160
5.2 Materials.....	160
5.2.1 Preparation of a homoionic clay.....	160
5.2.2 Exposure/Intercalation procedures.....	161
5.2.3 Intercalation via the vapour phase.....	161
5.3 Characterisation of homoionic cation exchanged SWy-2 montmorillonite using cyclohexylamine (CHA).....	162
5.3.1 Introduction.....	162
5.3.2 Thermogravimetric analysis (TGA).....	166
5.3.2.1 Results.....	166
5.3.3 Variable temperature X-ray diffraction (VT-XRD).....	167
5.3.3.1 Results.....	168
5.3.4 Evolved gas analysis (RT-FTIR, RT-MS and OTM-GC-MS).	172
5.3.4.1 Results OTM-GC-MS.....	172
5.3.4.2 Results Real time TG-FTIR.....	175
5.3.4.3 Results Real-Time TG-MS.....	178
5.3.4.4 Results DRIFTS studies.....	181
5.3.4.5 Discussion.....	186
5.3.4.6 Summary.....	187
5.4 Characterisation of homoionic cation exchanged SWy-2 montmorillonite using the 3-cyanopyridine (3-CYP) probe	190
5.4.1 Results thermogravimetric studies.....	191
5.4.2 Results variable-temperature XRD (VT-XRD).....	192
5.4.3 Results OTM-GC-MS.....	195
5.4.4 Results Real-Time TG-MS.....	196
5.4.5 Results DRIFTS studies.....	202
5.4.6 Discussion.....	205
5.4.7 Summary.....	209
5.4.8 Other probes evaluated in this thesis.....	213

Chapter 6 The qualitative characterisation of minerals by chemometric analysis of EGA detection profiles produced during temperature programmed desorption (TPD)

6.0 Introduction.....	216
6.1 Transfer line and external heating zone experiments for the optimisation of DMF signal during EGA.....	220
6.2 Liquid DMF transfer line studies by gas phase FTIR (GP-FTIR) and RT-MS	222
6.3 Summary of transfer line studies	222
6.4 External heat zone (EHZ) studies.....	223
6.5 Summary of (EHZ) studies.....	224
6.6 The qualitative characterisation of minerals by chemometric analysis of EGA DMF and water detection profiles during temperature programmed desorption (TPD)	226
.....	226
6.6.1 Principal component analysis/partial least squares modelling..	226
6.6.2 Data output utilised for PCA/PLS modelling.....	226
6.6.3 Thermal reactions of untreated clay minerals.....	227
6.7 Samples.....	231
6.8 Results of RT-MS (TIC) for each clay mineral group (data overlays)....	234
6.9 Results model① data compression/discriminant rules.....	247
6.10 Results model① TGA (weight loss curve).....	250
6.11 Summary model①(a) using 2 PCA scores (mehalanobis distance metric)	256
6.12 Summary model①(a) using 3 PCA scores (mehalanobis distance metric)	260
6.13 Canonical variance analysis.....	261
6.14 Summary canonical variance analysis.....	265
6.15 Summary TGA model①(b) using 3 PLS scores (mehalanobis distance metric)	271
6.16 Results Model②GP-FTIR total infrared (TIR).....	271
6.17 Summary PLS Model② GP-FTIR (TIR) 3 scores.....	278
6.18 Summary Model② Canonical variance analysis.....	280
6.19 ResultsModel③(a) RT-MS (TIC).....	281
6.20 Summary PLS Model③(a) RT-MS (TIC).....	288
6.21 Results Model③(b) RT-MS using m/z = 18 (H ₂ O) and m/z =73 (DMF parent ion).....	290
6.22 Summary PLS Model③(b) using RT-MS ions m/z = 18 and 73.....	296
6.23 Conclusions.....	297

Chapter 7 The quantitative characterisation of minerals by chemometric analysis of EGA RT-MS detection profiles

7.0 Introduction.....	300
7.1 XRD and DRIFTS evaluation of the components of the mixed mineral standards for quantitative analysis.....	300
7.2 Results summary of XRD and DRIFTS analysis of the mixed mineral standards components used for quantitative analysis.....	303
7.3 MS component features of the data output of mixed mineral standards (1-21)	304
7.4 Untreated (no DMF) individual mineral components.....	305
7.4.1 Summary ion m/z = 18.....	305
7.4.2 Summary ion m/z = 44.....	307
7.4.3 Summary total ion current (TIC).....	308

7.5	Examination of untreated components in a quartz feldspar mixture (no DMF)	309
7.5.1	Summary of RT-MS reconstructed ion chromatograms for 10% chlorite (CCa-1), 80% Quartz (Seasand), 10% Feldspar (80% Orthoclase, 20% Albite)...	310
7.5.2	Summary of RT-MS reconstructed ion chromatograms for 10% illite (1-Mt), 80% quartz (Seasand), 10% feldspar (80% orthoclase, 20% albite).....	311
7.5.3	Summary of RT-MS reconstructed ion chromatograms for 10% kaolinite (KGa-2), 80% quartz (Seasand), 10% feldspar (of which 80% Orthoclase, 20% Albite).....	312
7.5.4	Summary of RT-MS reconstructed ion chromatograms for 10% montmorillonite (SWy-2), 80% quartz (seasand), 10% feldspar (of which 80% Orthoclase, 20% Albite).....	313
7.6	Examination of untreated (no DMF) mineral mixtures.....	314
7.6.1	Summary standard 1 (blank-no DMF) 70% Quartz, 10% SWy-2, 4% KGa-2, 4% 1-Mt-Illite, 8% CCa-1, 4% Feldspar.....	315
7.6.2	Summary (evaluation of source of m/z = 44).....	316
7.7	Quantitative characterization of mixed mineral standards by PLS multivariate analysis.....	318
7.7.1	Introduction.....	318
7.7.2	Sample Preparation (mixed mineral standards).....	318
7.7.3	Collection of RT-MS gas detection profiles.....	319
7.7.4	Evaluation of the linearity of DMF detection versus increasing montmorillonite concentration.....	319
7.7.5	Results of linearity of DMF detection versus increasing montmorillonite concentration.....	320
7.7.6	Summary of the linearity of DMF detection versus increasing montmorillonite concentration.....	321
7.7.7	Mixed mineral sample preparation.....	321
7.7.8	Evaluation of co-linearity between mixed mineral standard components	323
7.7.9	Summary of co-linearity between training set component concentrations	324
7.8	Model ① using RT-MS TIC (derivatised).....	324
7.8.1	Preprocessing.....	326
7.8.2	Results of model ① using RT-MS TIC (derivatised).....	328
7.8.3	Summary of Model ① RT-MS TIC (derivatised).....	335
7.9	Model ② using the RT-MS m/z = 73 (DMF parent ion).....	336
7.9.1	RT-MS m/z = 73 model ② test set.....	340
7.9.2	Summary of model ② m/z = 73 (DMF parent ion).....	341
7.10	Model ③ using the RT-MS ion m/z = 18 (H ₂ O).....	344
7.10.1	Introduction.....	344
7.10.2	Results of model ③ using the RT-MS ion m/z = 18 (H ₂ O).....	347
7.10.3	RT-MS m/z = 18 model ③ Test set.....	353
7.10.4	Summary of model ③ RT-MS ion m/z = 18 (H ₂ O).....	354
7.10.5	Conclusions.....	355

101
102
103
104
105
106
107
108
109
110
111
112
113
114
115
116
117
118
119
120
121
122
123
124
125
126
127
128
129
130
131
132
133
134
135
136
137
138
139
140
141
142
143
144
145
146
147
148
149
150
151
152
153
154
155
156
157
158
159
160
161
162
163
164
165
166
167
168
169
170
171
172
173
174
175
176
177
178
179
180
181
182
183
184
185
186
187
188
189
190
191
192
193
194
195
196
197
198
199
200
201
202
203
204
205
206
207
208
209
210
211
212
213
214
215
216
217
218
219
220
221
222
223
224
225
226
227
228
229
230
231
232
233
234
235
236
237
238
239
240
241
242
243
244
245
246
247
248
249
250
251
252
253
254
255
256
257
258
259
260
261
262
263
264
265
266
267
268
269
270
271
272
273
274
275
276
277
278
279
280
281
282
283
284
285
286
287
288
289
290
291
292
293
294
295
296
297
298
299
300
301
302
303
304
305
306
307
308
309
310
311
312
313
314
315
316
317
318
319
320
321
322
323
324
325
326
327
328
329
330
331
332
333
334
335
336
337
338
339
340
341
342
343
344
345
346
347
348
349
350
351
352
353
354
355
356
357
358
359
360
361
362
363
364
365
366
367
368
369
370
371
372
373
374
375
376
377
378
379
380
381
382
383
384
385
386
387
388
389
390
391
392
393
394
395
396
397
398
399
400
401
402
403
404
405
406
407
408
409
410
411
412
413
414
415
416
417
418
419
420
421
422
423
424
425
426
427
428
429
430
431
432
433
434
435
436
437
438
439
440
441
442
443
444
445
446
447
448
449
450
451
452
453
454
455
456
457
458
459
460
461
462
463
464
465
466
467
468
469
470
471
472
473
474
475
476
477
478
479
480
481
482
483
484
485
486
487
488
489
490
491
492
493
494
495
496
497
498
499
500
501
502
503
504
505
506
507
508
509
510
511
512
513
514
515
516
517
518
519
520
521
522
523
524
525
526
527
528
529
530
531
532
533
534
535
536
537
538
539
540
541
542
543
544
545
546
547
548
549
550
551
552
553
554
555
556
557
558
559
560
561
562
563
564
565
566
567
568
569
570
571
572
573
574
575
576
577
578
579
580
581
582
583
584
585
586
587
588
589
590
591
592
593
594
595
596
597
598
599
600
601
602
603
604
605
606
607
608
609
610
611
612
613
614
615
616
617
618
619
620
621
622
623
624
625
626
627
628
629
630
631
632
633
634
635
636
637
638
639
640
641
642
643
644
645
646
647
648
649
650
651
652
653
654
655
656
657
658
659
660
661
662
663
664
665
666
667
668
669
670
671
672
673
674
675
676
677
678
679
680
681
682
683
684
685
686
687
688
689
690
691
692
693
694
695
696
697
698
699
700
701
702
703
704
705
706
707
708
709
710
711
712
713
714
715
716
717
718
719
720
721
722
723
724
725
726
727
728
729
730
731
732
733
734
735
736
737
738
739
740
741
742
743
744
745
746
747
748
749
750
751
752
753
754
755
756
757
758
759
760
761
762
763
764
765
766
767
768
769
770
771
772
773
774
775
776
777
778
779
780
781
782
783
784
785
786
787
788
789
790
791
792
793
794
795
796
797
798
799
800
801
802
803
804
805
806
807
808
809
810
811
812
813
814
815
816
817
818
819
820
821
822
823
824
825
826
827
828
829
830
831
832
833
834
835
836
837
838
839
840
841
842
843
844
845
846
847
848
849
850
851
852
853
854
855
856
857
858
859
860
861
862
863
864
865
866
867
868
869
870
871
872
873
874
875
876
877
878
879
880
881
882
883
884
885
886
887
888
889
890
891
892
893
894
895
896
897
898
899
900
901
902
903
904
905
906
907
908
909
910
911
912
913
914
915
916
917
918
919
920
921
922
923
924
925
926
927
928
929
930
931
932
933
934
935
936
937
938
939
940
941
942
943
944
945
946
947
948
949
950
951
952
953
954
955
956
957
958
959
960
961
962
963
964
965
966
967
968
969
970
971
972
973
974
975
976
977
978
979
980
981
982
983
984
985
986
987
988
989
990
991
992
993
994
995
996
997
998
999
1000

Chapter 8 Characterization of swelling clay minerals using ESEM-EDX analysis of 2-Bromopyridine (2BPY)

8.0 Introduction.....	358
8.1 Experimental schedule.....	359
8.2 Results (thermogravimetric studies).....	360
8.3 Summary (thermogravimetric studies).....	361
8.4 RT-MS of Al ³⁺ -SWy-2-2BPY.....	362
8.4.1 Summary RT-MS of Al ³⁺ -SWy-2-2BPY.....	363
8.4.2 Summary RT-MS of <2um B4-2-BPY.....	364
8.4.3 Results VT (variable-temperature) XRD.....	365
8.4.4 Summary (XRD).....	367
8.4.5 ESEM-EDX analysis of untreated and treated (2BPY) Al ³⁺ and Ni ²⁺ -SWy-2.....	368
8.4.4.1 Experimental.....	368
8.4.6 EDX element mapping.....	373
8.4.7 Summary of ESEM-EDX analysis of untreated and treated (2BPY) Al ³⁺ and Ni ²⁺ -SWy-2.....	373
8.4.8 ESEM-EDX analysis of B4 rock and <2um B4-2BPY.....	374
8.4.9 Summary ESEM-EDX analysis of B4 rock and <2um B4-2BPY.....	378
8.5 ESEM and EDX analysis of a tripartite sample (Al ³⁺ -SWy-2, Na-Albite, Quartz(seasand)).....	379
8.5.1 Summary ESEM and EDX analysis of a tripartite sample (Al ³⁺ -SWy-2, Na-albite, Quartz-seasand)-2BPY.....	383
8.5.2 Conclusion.....	383

Chapter 9 Conclusions

9.1 Characterisation of swelling minerals using chemical probes.....	386
9.2 The qualitative characterisation of minerals by chemometric analysis of EGA detection profiles.....	389
9.3 The quantitative characterisation of minerals by chemometric analysis of EGA RT-MS detection profiles.....	391
9.4 Characterization of swelling clay minerals by ESEM-EDX analysis of 2-Bromopyridine	392

Chapter 10 Postgraduate study, Posters, Publications and References

10.1 Postgraduate study.....	393
10.2 Posters.....	393
10.3 Publications.....	394
10.4 References.....	394
10.5 Appendices.....	411

List of tables

Table 1.1 Typical mineral percentages in sandstones.....	3
Table 1.2 Silicate classification.....	9
Table 1.3 Main mineral groups according to structural type.....	16
Table 1.4 Classification of phyllosilicate clay minerals.....	20
Table 1.5 Principal smectite group members.....	21
Table 2.1 Instrumental parameters for collection of FTIR spectra.....	60
Table 5.1 Organic molecules used as potential probe molecules in this thesis	156
Table 5.2 Thermal desorption summary for Al ³⁺ -SWy-2-CHA and Ni ²⁺ -SWy-2-CHA	167
Table 5.3 VT-XRD summary for Al ³⁺ -SWy-2-CHA.....	168
Table 5.4 VT-XRD summary for Ni ²⁺ -SWy-2-CHA.....	169
Table 5.5 Experimental conditions for the GC-MS identification of probe molecules.....	172
Table 5.6 OTM-GC-MS desorption products and associated ions.....	173
Table 5.7 Physical properties of desorption products detected by OTM-GC-MS	173
Table 5.8 NH ₂ and NH ₃ stretching and bending frequencies (cm ⁻¹) for liquid cyclohexylamine, cyclohexylammonium-montmorillonite (AH ⁺) and montmorillonite containing Ni ²⁺ and Al ³⁺ interlayer cations at room temperature.....	184
Table 5.9 Thermal desorption summary for Al ³⁺ -SWy-2-3CYP and Ni ²⁺ -SWy-2- 3CYP.....	192
Table 5.10 VT-XRD summary for Ni ²⁺ -SWy-2-3CYP.....	193
Table 5.11 VT-XRD summary for Al ³⁺ -SWy-2-3CYP.....	194
Table 5.12 Comparison of IR frequencies of Ni ²⁺ -SWy-2-3CYP and uncoordinated 3-CYP.....	203
Table 5.13 Comparison of IR frequencies of Al ³⁺ -SWy-2-3CYP and uncoordinated 3-CYP.....	204
Table 6.1 Possible interactions between DMF and cation exchanged clay	218
Table 6.2 Relative intensities of the fragment ions of DMF and their possible molecular structure.....	220
Table 6.3 Low and high temperature transfer line experiment temperatures	221
Table 6.4 Summary of the characteristic maxima observed in the DTG traces of clay minerals.....	229
Table 6.5 Details of samples for qualitative analysis.....	236
Table 6.6 Detection maxima for m/z = 73 (DMF) and m/z = 18 (dehydroxylation) from montmorillonite-DMF complexes.....	234
Table 6.7 Detection maxima for m/z = 73 (DMF) and m/z = 18 (dehydroxylation) from montmorillonite/saponite-DMF complexes.....	235
Table 6.8 Detection maxima for m/z = 73 (DMF) and m/z = 18 (dehydroxylation) for- kaolinite-DMF complexes.....	237
Table 6.9 TGA Model ①(a) training and test groups samples.....	247
Table 6.10 Model ① data compression/discriminant analysis results.....	250
Table 6.11 Model ①(a) PCA score variance table.....	251
Table 6.12 PCA score plot key for model ①(a) training set.....	252
Table 6.13 Model ①(a) training group predictions using 2 PCA scores...	253
Table 6.14 Model ①(a) test group predictions using 2 PCA scores.....	256

Table 6.15 Model①(a) training group predictions using 3 PCA scores.....	259
Table 6.16 TGA Model①(a) 3 PCA scores applied to test samples.....	260
Table 6.17 TGA training group predictions based on 1 st and 2 nd canonical variates and 95% tolerance region using 2 scores.....	260
Table 6.18 TGA training set group predictions based on 1 st and 2 nd canonical variates and 95% tolerance region using three PCA scores.....	263
Table 6.19 TGA test set group predictions based on 1 st and 2 nd canonical variates and 95% tolerance region using three PCA scores.....	264
Table 6.20 TGA model①(b) PLS score variance table.....	266
Table 6.21 PLS score plot key for TGA model①(b) training set.....	267
Table 6.22 PLS TGA model①(b) training group predictions using 3 PLS scores	268
Table 6.23 PLS TGA model①(b) applied to test samples using 3 scores.....	270
Table 6.24 GP-FTIR (TIR) model② data compression/discriminant analysis.....	271
Table 6.25 GP-FTIR (TIR) model② PLS score variance table.....	272
Table 6.26 GP-FTIR (TIR) model② PLS training group and test group samples....	274
Table 6.27 GP-FTIR (TIR) model② training group predictions using 3 PLS scores	275
Table 6.28 GP-FTIR (TIR) model② applied to test samples using 3 PLS scores (mahalanobis distance).....	277
Table 6.29 RT-MS (TIC) model ③(a) data compression/discriminant analysis.....	281
Table 6.30 RT-MS (TIC) model③(a) training group predictions using 3 PLS scores (mahalanobis distance).....	282
Table 6.31 RT-MS (TIC) model③(a) PLS score variance table.....	283
Table 6.32 RT-MS (TIC) model③(a) applied to test samples using 3 PLS scores (mahalanobis distance).....	286
Table 6.33 Composition of test samples T6-T11.....	287
Table 6.34 RT-MS (m/z = 18) model③(b) data compression/discriminant analysis..	291
Table 6.35 RT-MS (m/z = 18) model③(b) training group predictions using 2 PLS scores (mahalanobis distance).....	292
Table 6.36 RT-MS (m/z = 18) model③(b) PLS score variance table.....	293
Table 6.37 RT-MS (m/z = 18) model③(b) applied to Test samples using 2 PLS scores (mahalanobis distance).....	294
Table 7.1 Characteristic IR bands for identification of mineral components	301
Table 7.2 Specific vibrational frequencies of layer silicates.....	302
Table 7.3 General vibrational frequencies of layer silicates.....	302
Table 7.4 Diagnostic d-spacings/Å (°2θ) for minerals in this study.....	303
Table 7.5 Component contaminants identified by XRD and IR.....	303
Table 7.6 Mixed mineral standards components.....	318
Table 7.7 Weight percent concentrations of the components in the mixed mineral standards.....	322
Table 7.8 Results of co-linearity between training set component concentrations	323
Table 7.9 Chemometric experimental details for RT-MS (TIC) model① training set.....	326
Table 7.10 RT-MS TIC model① actual V predicted concentration for SWy-2	329
Table 7.11 RT-MS TIC model① actual V predicted concentration for KGa-2..	330
Table 7.12 RT-MS TIC model① actual V predicted concentration for CCa-1..	333
Table 7.13 Chemometric experimental details for ion m/z = 73 training set	336
Table 7.14 RT-MS m/z = 73 model② actual V predicted concentration for SWy-2	339
Table 7.15 RT-MS m/z = 73 model② actual standard concentrations for 1-Mt	340
Table 7.16 RT-MS m/z = 73 model② test set actual V predicted concentrations (rocks).....	341

1. The first part of the document discusses the importance of maintaining accurate records of all transactions and activities. It emphasizes that proper record-keeping is essential for ensuring transparency and accountability in financial operations. This section also highlights the role of internal controls in preventing fraud and errors, and the need for regular audits to verify the accuracy of the data.

2. The second part of the document focuses on the implementation of a robust risk management framework. It outlines the process of identifying, assessing, and mitigating various risks that could impact the organization's performance. This includes the establishment of risk registers, the assignment of responsibilities, and the implementation of control measures to reduce the likelihood and impact of adverse events.

3. The third part of the document addresses the importance of effective communication and reporting. It stresses the need for clear, concise, and timely communication of financial information to all stakeholders. This involves the development of standardized reporting formats, the establishment of regular reporting cycles, and the use of appropriate channels for disseminating information.

4. The fourth part of the document discusses the role of technology in enhancing financial operations. It highlights the benefits of using modern accounting software and data analytics tools to streamline processes, improve accuracy, and gain valuable insights from the data. This section also touches upon the importance of data security and the need for robust IT infrastructure to support these operations.

5. The fifth part of the document concludes with a summary of the key findings and recommendations. It reiterates the importance of a holistic approach to financial management, one that integrates record-keeping, risk management, communication, and technology. The document also provides a list of actionable steps for the organization to implement these recommendations and achieve its financial goals.

Table 7.17 RT-MS m/z = 73 model [Ⓢ] test set actual V predicted concentrations (mixed mineral standards).....	341
Table 7.18 Chemometric experiment details of m/z = 18 model [Ⓢ] training set	346
Table 7.19 RT-MS m/z = 18 model [Ⓢ] actual V predicted concentrations for SWy-2.....	349
Table 7.20 RT-MS m/z = 18 model [Ⓢ] actual V predicted concentrations for KGa-2.....	351
Table 7.21 RT-MS m/z = 18 model [Ⓢ] actual V predicted concentrations for CCa-1.....	352
Table 7.22 RT-MS m/z = 18 model [Ⓢ] test samples actual V predicted concentrations (rocks).....	353
Table 7.23 RT-MS m/z = 18 model [Ⓢ] test set actual V predicted concentrations (mixed mineral standards).....	354
Table 8.1 Thermal desorption summary for Al ³⁺ - and Ni ²⁺ -SWy-2-2BPY..	360
Table 8.2 Thermal desorption summary for < 2 μ m B4-2BPY.....	361
Table 8.3 XRD d ₍₀₀₁₎ spacing for Ni ²⁺ -SWy-2-2BPY from RT-300°C.....	366
Table 8.4 XRD d ₍₀₀₁₎ spacing for Al ³⁺ -SWy-2-2BPY from RT-370°C.....	366
Table 8.5 XRD d ₍₀₀₁₎ spacing for < 2 μ m B4-2BPY from RT-300°C.....	367
Table 8.6 EDX standards.....	368
Table 8.7 EDX semi-quantitative analysis of untreated Ni ²⁺ -SWy-2.....	369
Table 8.8 EDX semi-quantitative analysis of Ni ²⁺ -SWy-2-2BPY.....	370
Table 8.9 EDX semi-quantitative analysis of untreated Al ³⁺ -SWy-2.....	371
Table 8.10 EDX semi-quantitative analysis of Al ³⁺ -SWy-2-2BPY.....	372
Table 8.11 EDX analysis of B4-3 (composite particle).....	376
Table 8.12 EDX analysis of 2BPY treated B4 rock.....	377
Table 8.13 EDX semi-quantitative analysis of < 2 μ m B4-2BPY.....	378
Table 8.14 Tripartite sample EDX bromine results.....	383

List of Figures

Figure 1.1 Discrete clay particles.....	4
Figure 1.2 Pore lining clays.....	5
Figure 1.3 Feldspar four member ring.....	10
Figure 1.4 Compositions of the feldspars.....	12
Figure 1.5 Silica tetrahedral sheet.....	13
Figure 1.6 Single octahedral sheet.....	14
Figure 1.7 The 1:1 structural layer.....	15
Figure 1.8 Sheet-like structures of clay minerals.....	16
Figure 1.9 The 2:1 structure of montmorillonite.....	19
Figure 1.10 Swelling state of smectite due to water vapour.....	26
Figure 1.11 Principal surface features on a clay.....	27
Figure 1.12 Isomorphous substitution in tetrahedral and octahedral sheets	30
Figure 1.13 Potential active sites in Kaolin stacks.....	35
Figure 2.1 The types of stretching and bending vibrations occurring in molecules	40
Figure 2.2 Vibrational motions of water (H ₂ O).....	41
Figure 2.3 Schematic of a Michelson interferometer.....	44
Figure 2.4 The three modes of reflection during a DRIFTS experiment...	50
Figure 2.5 TGA data output curves.....	61
Figure 2.6 The basic process of X-ray diffraction.....	65

Figure 2.7 Components of a typical energy dispersive microanalysis system	72
Figure 2.8 Diagrammatic representation of the SYNERGY EGA system	77
Figure 2.9 EI fragmentation pattern of Methanol.....	79
Figure 2.10 EI ion source	79
Figure 2.11 Sniffer interface.....	84
Figure 2.12 PCA data arrangement.....	87
Figure 2.13 Demonstration of RIC and TIC profiles.....	89
Figure 2.14 Matrix multiplication.....	91
Figure 2.15 Fifteenth bi-variate observations plotted (a) as spectral traces and (b) as points in a two dimensional coordinate system.....	93
Figure 2.16 First versus second PC scores.....	94
Figure 2.17 PLS modelling process.....	98
Figure 2.18 Relationship of spectral vectors to constituents.....	99
Figure 2.19 The PRESS plot.....	104
Figure 4.1 Chromatogram-type trace.....	122
Figure 4.2 Procedure of exposing samples to a probe.....	124
Figure 4.3 Possible clay-organic interactions.....	135
Figure 5.1 Derivative thermograms of Al ³⁺ -SWy-2-CHA and Ni ²⁺ -SWy-2-CHA	167
Figure 5.2 VT XRD traces of d ₍₀₀₁₎ spacing of Al ³⁺ -SWy-2-CHA from RT-450°C	168
Figure 5.3 VT XRD traces of d ₍₀₀₁₎ spacing of Ni ²⁺ -SWy-2-CHA from RT-450°C	169
Figure 5.4 Changes in d ₍₀₀₁₎ spacing of Al ³⁺ -SWy-2-CHA and Ni ²⁺ -SWy-2-CHA from room temperature to 450°C.....	170
Figure 5.5 Possible orientation of CHA within the interlayer space.....	171
Figure 5.6 RT-FTIR gas-phase FTIR for the desorption of saturated, unsaturated hydrocarbons and ammonia from Al ³⁺ -SWy-2-CHA.....	176
Figure 5.7 RT-FTIR gas-phase FTIR for the desorption of saturated,unsaturated hydrocarbons and ammonia from Ni-SWy-2-CHA.....	177
Figure 5.8 RT-MS ion chromatograms for the desorption of water (m/z =18), methylcyclopentene (m/z = 53), cyclohexene (m/z = 54), cyclohexylamine (m/z = 56), benzene (m/z = 78) and aniline (m/z = 93) from Al ³⁺ -SWy-2-CHA.....	178
Figure 5.9 RT-MS ion chromatograms for the desorption of water (m/z =18), methylcyclopentene (m/z = 53), cyclohexene (m/z = 54), cyclohexylamine (m/z = 56), benzene (m/z = 78) and aniline (m/z = 93) from Ni ²⁺ -SWy-2-CHA.....	179
Figure 5.10 Comparison of untreated Al ³⁺ and Ni ²⁺ -SWy-2 with CHA between 1200-2000 cm ⁻¹	181
Figure 5.11 Comparison of untreated Al ³⁺ and Ni ²⁺ -SWy-2 with CHA between 2000-4000 cm ⁻¹	182
Figure 5.12 VT DRIFTS spectra of (a) Al ³⁺ -SWy-2-CHA and Ni ²⁺ -SWy-2-CHA from 25-300°C as indicated.....	183
Figure 5.13 Derivative thermograms of Al ³⁺ -SWy-2-CHA and Ni ²⁺ -SWy-2-3CYP.....	192

Figure 5.14 VT XRD traces of $d_{(001)}$ spacing of Ni^{2+} -SWy-2-3CYP from RT-450°C.....	193
Figure 5.15 VT XRD traces of $d_{(001)}$ spacing of Al^{3+} -SWy-2-3CYP from RT-450°C.....	194
Figure 5.16 ATI-Cahn Mass spectrum of 3-CYP.....	195
Figure 5.17 EGA Total ion current (TIC) of 3-CYP (25-800°C).....	196
Figure 5.18 Representative mass spectrum 3-CYP.....	197
Figure 5.19 RT-MS ion chromatograms from Ni^{2+} -SWy-2-3-CYP TIC (total ion current) and 3CYP ions [$m/z=104, 77, 64, 50$]	197
Figure 5.20 RT-MS ion chromatograms from Ni^{2+} -SWy-2-3-CYP H_2O [$m/z = 18$], CO_2 [$m/z = 44$].....	198
Figure 5.21 RT-MS ion chromatograms obtained from Al^{3+} -SWy-2-3CYP TIC (total ion current) and 3CYP ions [$m/z =104, 77, 64, 50$].....	200
Figure 5.22 RT-MS ion chromatograms from Al^{3+} -SWy-2-3-CYP H_2O [$m/z = 18$], CO_2 [$m/z = 44$].....	200
Figure 5.23 VT DRIFTS spectra of Ni^{2+} -SWy-2-3-CYP from 25-350°C as indicated	202
Figure 5.24 VT DRIFTS spectra of Al^{3+} -SWy-2-3-CYP from 25-350°C as indicated	207
Figure 5.25 Derivative thermograms of Al^{3+} -SWy-2-2-CYP and Ni^{2+} -SWy-2-CYP.....	213
Figure 6.1 DMF mass spectrum.....	219
Figure 6.2 RT-MS TIC data overlays for montmorillonite-DMF complexes	234
Figure 6.3 RT-MS TIC data overlays for montmorillonite/saponite-DMF complexes.....	235
Figure 6.4 RT-MS TIC data overlays for illite-DMF complexes.....	236
Figure 6.5 Detection maxima for $m/z = 73$ (DMF) and $m/z = 18$ (dehydroxylation) for-illite-DMF complexes.....	233
Figure 6.6 TIC data overlays for kaolinite-DMF complexes.....	237
Figure 6.7 RT-MS reconstructed ion chromatograms of ion $m/z = 73$ (DMF parent ion) for kaolinite-DMF complexes.....	238
Figure 6.8 RT-MS reconstructed ion chromatograms of ion $m/z = 44$ for kaolinite-DMF complexes.....	235
Figure 6.9 GP-FTIR reconstructed chromatogram of H_2O ($3500\text{-}4000\text{cm}^{-1}$) for kaolinite-DMF complexes.....	239
Figure 6.10 GP-FTIR reconstructed chromatogram of CO_2 ($2200\text{-}2500\text{cm}^{-1}$) for kaolinite-DMF complexes.....	239
Figure 6.11 Room temperature DRIFTS spectra of untreated kaolinites...	240
Figure 6.12 RT-MS TIC data overlays for chlorite-DMF complexes.....	241
Figure 6.13 RT-MS TIC data overlays for Rock-DMF complexes.....	242
Figure 6.14 RT-MS TIC data overlays for < 2 μm rock fractions-DMF complexes	242
Figure 6.15 GP-FTIR TIR data overlays for montmorillonite/saponite-DMF complexes.....	243
Figure 6.16 GP-FTIR TIR data overlays for montmorillonite-DMF complexes	243
Figure 6.17 GP-FTIR TIR data overlays for kaolinite-DMF complexes...	244
Figure 6.18 GP-FTIR TIR data overlays for chlorite-DMF complexes....	244
Figure 6.19 TGA weight loss data overlays for montmorillonite-DMF complexes	245

Figure 6.20 TGA weight loss data overlays for montmorillonite/saponite-DMF complexes.....	245
Figure 6.21 TGA weight loss data overlays for Kaolinite-DMF complexes	246
Figure 6.22 TGA weight loss data overlays for chlorite-DMF complexes..	246
Figure 6.23 TGA Model①(a) PCA Scree test of percentage variance versus PCA score	251
Figure 6.24 PC score plot for TGA model①(a) PCA (correlation) using score 1 against score 2 (mehalanobis distance metric).....	252
Figure 6.25 TGA model①(a) PCA correlation method-loading 1.....	254
Figure 6.26 TGA model①(a) PCA correlation method-loading 2.....	255
Figure 6.27 TGA model①(a) PCA correlation method-loading 3.....	255
Figure 6.28 PC score plot for PCA TGA model①(a) using score 1 against score 3 (mehalanobis distance metric).....	258
Figure 6.29 Canonical variance analysis of TGA data using a 95% confidence interval and two PCA scores.....	261
Figure 6.30 TGA canonical variance analysis using a 95% confidence interval using three PCA scores.....	263
Figure 6.31 Application of canonical variance model to TGA test data using three scores.....	264
Figure 6.32 TGA model①(b) PLS Scree test of percentage variance versus PC score.....	266
Figure 6.33 PLS score plot for TGA model①(b) using score 1 against score 3 (mehalanobis distance metric).....	267
Figure 6.34 TGA model①(b) PLS-loading 1.....	269
Figure 6.35 TGA model①(b) PLS-loading 2.....	269
Figure 6.36 TGA model①(b) PLS-loading 3.....	270
Figure 6.37 GP-FTIR (TIR) model② PLS Scree test of percentage variance versus PLS score.....	272
Figure 6.38 PLS score plot for GP-FTIR (TIR) model② using score 1 against score 2 (mehalanobis distance metric).....	273
Figure 6.39 GP-FTIR (TIR) model② PLS-loading 1.....	276
Figure 6.40 GP-FTIR (TIR) model② PLS-loading 2.....	276
Figure 6.41 GP-FTIR (TIR) model② PLS-loading 3.....	277
Figure 6.42 GP-FTIR (TIR) model② applied to Test samples using 3 PLS scores (mehalanobis distance).....	278
Figure 6.43 GP-FTIR (TIR) model② Canonical variance analysis using a 95% confidence interval and three PLS scores.....	279
Figure 6.44 GP-FTIR (TIR) model② test set group predictions based on 1 st and 2 nd canonical variates and 95% tolerance region and three PLS scores.....	280
Figure 6.45 RT-MS (TIC) model③(a) PLS Scree test of percentage variance versus PLS score.....	283
Figure 6.46 PLS score plot for RT-MS (TIC) model③(a) using score 1 against score 2 (mehalanobis distance metric).....	284
Figure 6.47 RT-MS (TIC) model③(a) PLS-loading 1.....	285
Figure 6.48 RT-MS (TIC) model③(a) PLS-loading 2.....	285
Figure 6.49 RT-MS (TIC) model③(a) PLS-loading 3.....	286

Figure 6.50 RT-MS (TIC) model③(a) Canonical variance analysis using a 95% confidence interval and three PLS score.....	289
Figure 6.51 RT-MS (TIC) model③(test set group predictions based on 1 st and 2 nd canonical variates and 95% tolerance region and three PLS scores.....	290
Figure 6.52 RT-MS (m/z = 18) model③(b) PLS scree test of percentage variance versus PLS score number.....	293
Figure 6.53 PLS score plot for RT-MS (ion m/z = 18) model③(b) using score 1 against score 2 (mehalanobis distance).....	294
Figure 6.54 RT-MS (m/z = 18) model③(b) PLS-loading 1.....	295
Figure 6.55 RT-MS (m/z = 18) model③(b) PLS-loading 2.....	295
Figure 6.56 RT-MS (m/z = 18) model③(b) applied to Test samples using 2 PLS scores (mehalanobis distance).....	296
Figure 7.1 RT-MS (m/z = 18) for mineral component blanks analysed separately..	305
Figure 7.2 RT-MS (m/z = 18) for feldspar.....	306
Figure 7.3 RT-MS ion m/z = 44 for all mixed mineral component blanks analysed separately (no DMF).....	307
Figure 7.4 RT-MS TIC for all mixed mineral component blanks analysed separately (no DMF).....	308
Figure 7.5 RT-MS reconstructed ion chromatograms for 10% Chlorite (CCa-1), 80% Quartz (Seasand), 10% Feldspar (80% Orthoclase, 20% Albite).....	309
Figure 7.6 RT-MS reconstructed ion chromatograms for 10% Illite (1-Mt), 80% quartz (Seasand), 10% feldspar (80% orthoclase, 20% albite).....	311
Figure 7.7 RT-MS reconstructed ion chromatograms for 10% kaolinite (KGa-2), 80% quartz (Seasand), 10% feldspar (of which 80% Orthoclase, 20% Albite).....	312
Figure 7.8 RT-MS reconstructed ion chromatograms for 10% montmorillonite (SWy-2), 80% quartz (seasand), 10% feldspar (of which 80% Orthoclase, 20% Albite).....	313
Figure 7.9 RT-MS of standard 1 (blank-no DMF) 70% Quartz, 10% SWy-2, 4% KGa-2, 4% 1-Mt-Illite, 8% CCa-1, 4% Feldspar.....	314
Figure 7.10 RT-MS standard 7 (blank-no DMF) 87% Quartz, 0% SWy-2, 10% KGa-2, 2% 1-Mt-Illite, 0% CCa-1, 1% Feldspar.....	315
Figure 7.11 RT-MS standard 16 (blank-no DMF) 74% Quartz, 2% SWy-2, 6% KGa-2, 4% 1-Mt-Illite, 10% CCa-1, 4% Feldspar.....	316
Figure 7.12 Calibration plot for 1-8% Ca-SWy-2/Seasand (ground & mixed)	320
Figure 7.13 Calibration plot for 1-8% Ca-SWy-2/Seasand (un-ground & un-mixed).....	320
Figure 7.14 RT-MS TIC model④ training set concentration residuals for SWy-2	327
Figure 7.15 RT-MS TIC model④ cross validation PRESS plot for SWy-2.....	328
Figure 7.16 RT-MS TIC model④ calibration plot for SWy-2 using 3 PLS factors	328
Figure 7.17 RT-MS TIC model④ cross validation PRESS plot for KGa-2.....	329
Figure 7.18 RT-MS TIC model④ calibration plot for KGa-2 using 3 PLS factors	330
Figure 7.19 RT-MS TIC model④ cross validation PRESS plot for 1-Mt.....	331
Figure 7.20 RT-MS TIC model④ cross validation PRESS plot for CCa-1.....	332
Figure 7.21 RT-MS TIC model④ calibration plot for CCa-1 using 3 PLS factors	332
Figure 7.22 RT-MS TIC model④ cross validation PRESS plot for quartz.....	333
Figure 7.23 RT-MS TIC model④ calibration plot for quartz using 3 PLS factors...	334
Figure 7.24 RT-MS TIC model④cross validation PRESS plot for feldspar.....	334

Figure 7.25 RT-MS TIC model① calibration plot for feldspar using 3 PLS factors	335
Figure 7.26 RT-MS m/z = 73 model② cross validation PRESS plot for SWy-2...	337
Figure 7.27 RT-MS m/z = 73 model② training set concentration residuals for SWy-2.....	337
Figure 7.28 RT-MS m/z = 73 model② training set spectral residuals for SWy-2	338
Figure 7.29 RT-MS m/z = 73 model② calibration plot for SWy-2 using 2 PLS factors.....	339
Figure 7.30 Comparison of treated and untreated standard 1 for ion m/z = 18	345
Figure 7.31 Comparison of DMF treated standard 1 for ions m/z = 18 (H ₂ O) and 73 (DMF).....	346
Figure 7.32 RT-MS m/z = 18 model③ cross validation PRESS plot for SWy-2...	347
Figure 7.33 RT-MS m/z = 18 model③ training set concentration residuals for SWy-2.....	348
Figure 7.34 RT-MS m/z = 18 model③ spectral residuals for SWy-2.....	348
Figure 7.35 RT-MS m/z = 18 model③ calibration plot for SWy-2 using 5 PLS factors.....	349
Figure 7.36 RT-MS m/z = 18 model③ cross validation PRESS plot for KGa-2	350
Figure 7.37 RT-MS m/z = 18 model③ calibration plot for KGa-2 using 2 PLS factors.....	350
Figure 7.38 RT-MS m/z = 18 model③ cross validation PRESS plot for CCa-1	351
Figure 7.39 RT-MS m/z = 18 model③ calibration plot for CCa-1 using 2 PLS factors.....	352
Figure 8.1 Derivative thermograms of Al ³⁺ - and Ni ²⁺ -SWy-2-2BPY....	360
Figure 8.2 Derivative thermogram of < 2um B4-2BPY.....	361
Figure 8.3 RT-MS of Al ³⁺ -SWy-2-2BPY.....	363
Figure 8.4 RT-MS of <2um B4-2BPY.....	364
Figure 8.5 VT XRD traces of d ₍₀₀₁₎ spacing of Ni ²⁺ -SWy-2-2BPY from RT-300°C.....	365
Figure 8.6 VT XRD traces of d ₍₀₀₁₎ spacing of Al ³⁺ -SWy-2-2BPY from RT-370°C.....	366
Figure 8.7 VT XRD traces of d ₍₀₀₁₎ spacing of <2um B4-2BPY from RT-370°C.....	364
Figure 8.8 ESEM image of untreated Ni ²⁺ -SWy-2.....	369
Figure 8.9 ESEM image of Ni ²⁺ -SWy-2-2BPY.....	370
Figure 8.10 ESEM image of untreated Al ³⁺ -SWy-2.....	371
Figure 8.11 ESEM image of Al ³⁺ -SWy-2-2BPY.....	372
Figure 8.12 XDX element map of Al ³⁺ -SWy-2-2 BPY.....	373
Figure 8.13 B4-1 (high definition clay particle image).....	374
Figure 8.14 B4-2 (etched mineral).....	375
Figure 8.15 B4-3 (composite particle).....	376
Figure 8.16 ESEM image of 2BPY treated B4 rock.....	377
Figure 8.17 ESEM image of < 2um B4-2BPY.....	378
Figure 8.18 Tripartite sample (Al ³⁺ -SWy-2, Na-Albite and Quartz (seasand))	379
Figure 8.19 ESEM image of Al ³⁺ -SWy-2-2BPY (tripartite sample).....	380
Figure 8.20 EDX element map of Al ³⁺ -SWy-2-2BPY (tripartite sample)...	380
Figure 8.21 ESEM image of Na-feldspar-2BPY (tripartite sample).....	381
Figure 8.22 EDX element map of Na-feldspar-2BPY (tripartite sample)....	381
Figure 8.23 ESEM image of Quartz-2BYP (seasand)(tripartite sample).....	382
Figure 8.24 EDX element map of Quartz (seasand)-2BPY (tripartite sample)	382

Chapter 1 Introduction

1.0 Aims and objectives

The research in this PhD thesis has been undertaken in collaboration with Schlumberger Cambridge Research (SCR) and is concerned with the characterization of hydrocarbon reservoir rocks. When fluids or otherwise are forced through a rock the minerals they come in contact defines the surface mineralogy whereas the whole composition is known as the bulk mineralogy.

The work detailed in this thesis is concerned with the evaluation and development of non-destructive characterization methods that will be capable of determining surface mineralogy by virtue of the interactions and detection of organic chemical probe molecules. The aim behind the application of a chemical probe molecule is that it will associate itself with a particular constituent of a reservoir rock and at specified conditions its detection will be used to identify the presence of the constituent. The first objective therefore is to evaluate the suitability of a variety of probes.

Previously, bulk mineralogy has been characterized by X-Ray Diffraction (XRD) whereas Scanning Electron Microscopy (SEM) has distinguished between surface and bulk mineralogy.

The main programme of research has focused on two main characterization methods. The first method employs Evolved Gas Analysis (EGA) which aims to distinguish the clay constituents of a reservoir rock from differences in the evolved gas profiles of a desorbed probe molecule and/or the evolution of water during dehydroxylation. The intention is that the profiles obtained can be utilized to develop suitable chemometrics models for both qualitative and quantitative characterization.

The second method aims to use Environmental Scanning Electron Microscopy-Energy Dispersive X-Ray (ESEM – EDX) to elucidate the presence of swelling clay minerals in a sandstone rock by EDX detection of the presence of an inorganic functional group associated with a probe molecule of interest. In order to evaluate these methods, the research in this thesis has considered the following techniques.

- (i) Thermogravimetric Analysis (TGA)
- (ii) Evolved Gas Analysis – Fourier Transform Infrared Spectroscopy (TGA-FTIR)
- (iii) Evolved Gas Analysis – Mass Spectrometry (TGA-MS)
- (iv) Environmental Scanning Electron Microscopy (ESEM)

Corroborative evidence to support the chemical probe approach has come from Diffuse Reflectance Infrared Fourier Transform Spectroscopy (DRIFTS) and XRD.

1.1 Reservoir rocks

The term reservoir rock is used to describe any commercially viable rock that contains or yields oil, gas or both. The common types being either sandstone or carbonates and less common being shale. Knowledge of the composition and structural differences is therefore of vital importance for efficient and effective oil exploration. The focus of this thesis has been sandstone reservoir rocks.

1.2 Sandstone rocks

Sandstone rocks are classified into three principal types according to their composition

- (i) totally dominated by quartz grains
- (ii) containing high quantities of un-weathered feldspars
- (iii) high quantities of clay minerals

The typical percentage mineral composition within each sandstone type is shown in table 1.1.

Table 1.1 Typical mineral percentages in sandstones

Mineral	Type I (%)	Type II (%)	Type III (%)
Quartz	100	75-99	≈65
Feldspar	0	1-25	5-25
Clay minerals	0	0	1-20

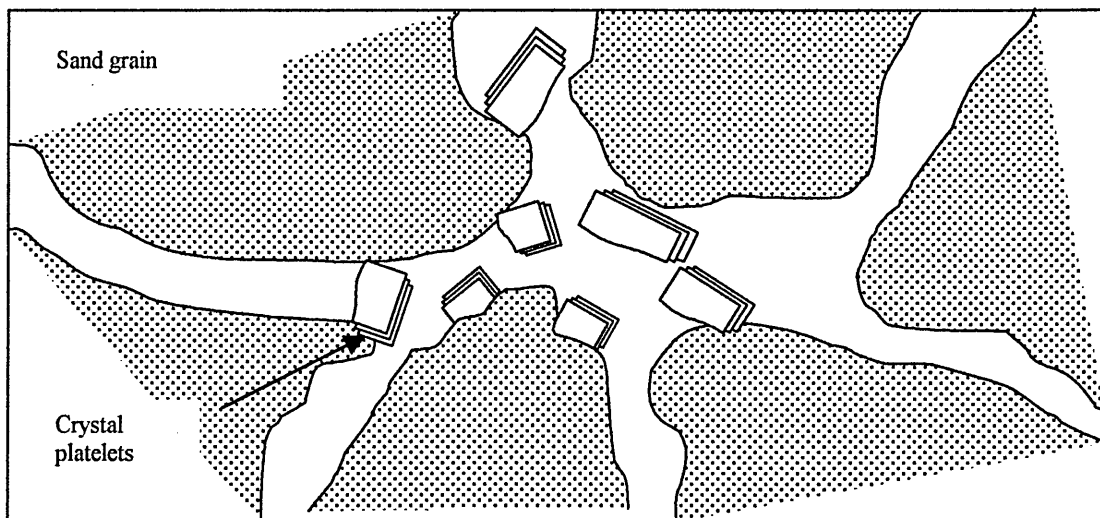
Table 1.1 shows that quartz grains are the major building blocks of sandstone rocks, which are considered to be a network of various structures that are subject to constant modification by diagenetic processes. This involves the addition or removal of constituents from the rock, which reduces or creates pore spaces. In addition, the presence of both clays and carbonates act like a cement by binding together quartz and feldspar grains. The most commonly occurring clay minerals found within sandstones are montmorillonite, illite, chlorite and kaolinite, which will be the focus of this thesis. A variety of other processes such as compaction, dissolution and

replacement affect network composition. In the case of compaction, the weight of overlying sediments can produce fracturing and grain re-shaping that can result in closer packing of grains. The dissolution of materials within these networks relies on several important factors. The chemical stability of these materials in the presence of water is important as the release of ions transported in solution may result in the formation of clay and carbonate minerals under favorable physical and chemical conditions. These processes may be both authigenic (occur within the sandstone) and allogenic (introduced into the sandstone from an external source). There are three basic types of dispersed clay minerals in sandstones [1].

(1) Discrete clay particles

These particle types reflect the occurrence of kaolinite in sandstones which usually develop as pseudo-hexagonal platy crystals which are attached as discrete particles to pore walls or occupying intergranular pores.

Figure 1.1 Discrete clay particles



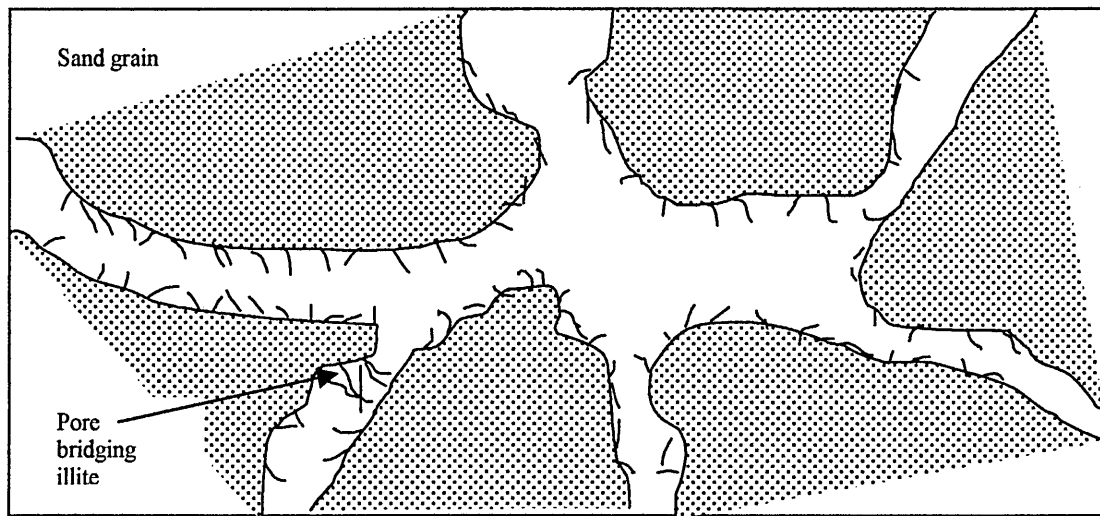
The crystal platelets may be stacked face to face forming long crystal aggregates or may occur singularly. They do not form intergrown crystal frameworks on pore walls

or within intergranular pores, they are characteristically scattered throughout the pore system. This may produce migrating fines within the pore network which reduces intergranular pore volume.

(2) Pore-lining clays

These are attached to pore walls to form a relatively continuous and thin ($\leq 12 \mu\text{m}$) coating which may be orientated parallel or perpendicular to the pore wall surface.

Figure 1.2 Pore-lining clays



Crystals attached perpendicularly to the pore wall surface are usually intergrown to form a continuous clay layer with abundant micropore space, with pore diameters in the 2 micron to sub-micron range. Illite, chlorite and montmorillonite clays have been observed with pore lining crystal morphologies.

(3) Pore-bridging clays

They are not only attached to pore wall surfaces but may extend far into or completely across a pore showing extensive development of intergrown and/or intertwined clay crystals within the pore network.

1.3 The importance of surface mineralogy

The aim of this thesis is to develop methods that can determine the surface mineralogy of a reservoir rock which are quick, accurate and have the ability to distinguish between surface and bulk mineralogy. It is assumed that surface mineralogy will differ from bulk mineralogy because direct observation by SEM shows that clay minerals cover quartz grains. When an oil reservoir is in decline, expensive multi-component fluids are needed to enhance the flow of oil. A major factor controlling the recovery of oil is permeability, which is affected by porosity. Porosity arises due to reservoir rock void spaces, which provide space for oil and gas to accumulate. Permeability is a measure of the ease with which fluid flows through a reservoir rock. Therefore an understanding of these factors is necessary because they are major factors controlling the recovery of hydrocarbons from sandstone reservoirs.

Changes in reservoir rock permeability are often due to the amount, location and type of clay minerals in the formation [2]. However the total amount of clay minerals predicted in the formation by total composition analysis, is a misleading indication of the potential changes in permeability. The primary causes of disagreement between calculated and measured mineral abundances are the presence of additional minerals beyond those included in the models and the variability in chemical composition of clay minerals due to ionic substitution and ionic adsorption

[3]. However, not all voids are accessible to fluids and this may be due to blocked pores which can arise from:

- (a) cement formation at a pore throat.
- (b) clay mineral growth blocking a pore throat.
- (c) clay mineral movement resulting in a blocked pore throat.

Therefore, a knowledge of the relative abundance of specific clay types and their distribution within pore spaces is very important. The primary objective of this thesis is to investigate the surface minerals with which a treatment fluid can come in contact. The development of a suitable method is part of a general strategy to understand fluid flow in reservoir rocks which may in turn become part of an investigation of the relationship between surface mineralogy and physiochemical properties (porosity, permeability, pore size distribution, pore fluid composition and rock structure). The application of this work is not confined to the oil industry, but may also contribute to the goal of determining the provenance of sedimentary rocks and clay diagenesis

Current laboratory techniques for evaluating the physiochemical properties of reservoir rocks include [4]:

- (a) Porosity: is determined by assuming grain density and then re-weighing the sample when saturated with a fluid of known density.
- (b) Permeability: cylindrical cores are solvent cleaned and air is forced longitudinally through the core. This method may overestimate permeability due to the fact that subsurface rocks when brought to the surface expand in all directions, thus changing permeability.

- (c) Grain size: determined by microscopy, sieve analysis or sedimentation.
- (d) Bulk mineralogy: methods include FTIR and XRD, which are discussed in chapter 2.
- (e) Pore lining mineralogy: qualitative analyses of rocks are made by Electron Microscopy.

However, all of these techniques may change or alter the rock composition by removal of fines or destruction of the rock pore network (grain size & bulk mineralogy).

- (f) Geochemical logging tool (GLT): measures the concentration of elements by measuring naturally radioactive and neutron activated elements. These concentrations are used to predict such properties as porosity, permeability, grain size and cation exchange capacity (CEC). The results are commonly used in conjunction with XRF and XRD. As a single method of analysis its routine use is hampered by the need for calibration from well to well.

1.4 Classification of minerals

The silicate class of minerals relevant to this thesis and found within the structure of sandstones are divided into two main subclasses. These subclasses are known as Tectosilicates (silica and feldspars) and Phyllosilicates (smectites, kaolinites, illites and chlorites). Table 1.2 shows this classification [5].

Table 1.2 Silicate classification

Class	Subclass	Group	Subgroup
Silicates	Tectosilicates	Silica	quartz
		feldspar	alkali series
			plagioclase series
	Phyllosilicates	smectites	
		kaolinites	
		illites	
chlorites			

1.5 Tectosilicates (Quartz, Feldspars)

1.5.1 Quartz

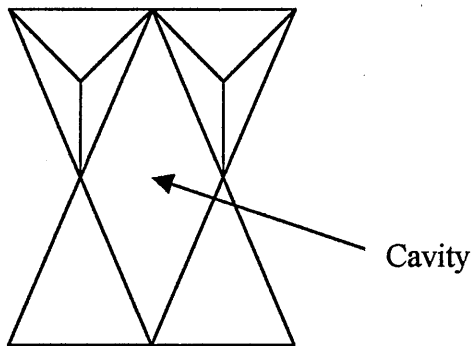
Quartz is the second most abundant mineral in the Earth's crust after feldspar. There are many varieties that consist primarily of silica or silicon dioxide (SiO_2), though impurities such as lithium, sodium, potassium and titanium may be present. It occurs in nearly all acid igneous, metamorphic and sedimentary rocks and is an essential mineral in rocks such as granites, which are resistant to weathering, tending to concentrate in sandstones and other detrital rocks. Quartz exists in two forms (a)

alpha- or low quartz which is trigonal and stable to 573°C and (b) beta- or high quartz which is hexagonal and is stable above 573°C .

1.5.2 Feldspar

Tectosilicates form a group known as the Feldspars, which constitute the major component in nearly all igneous rocks on the Earth, Moon and meteorites. They are also common in clastic and sedimentary rocks. The basic structural unit of feldspars is a tetrahedron composed of four oxygen ions surrounding either silicon or an aluminium atom. A three dimensional framework is constructed by each tetrahedron sharing an oxygen with another tetrahedron. However the rings are interconnected in a unique way that defines them. In the simple four-member ring two tetrahedra point upwards whilst two point downwards. This structure is shown below in figure 1.3 [6].

Figure 1.3 Feldspar four member ring

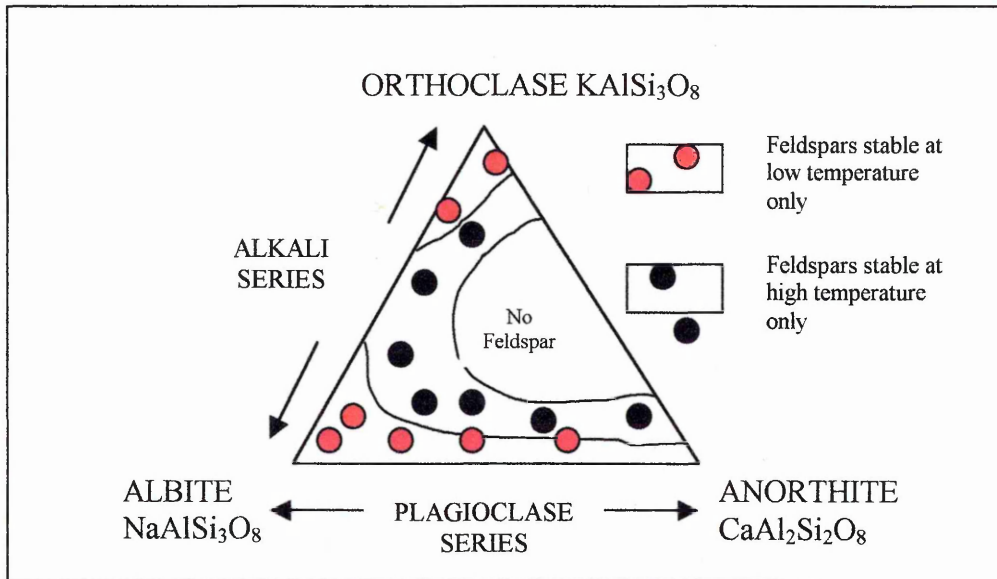


A neutral framework would be possible if each tetrahedron contained a silicon ion, however, one quarter to one half of the units contain aluminium, resulting in a net negative charge. This charge is balanced by monovalent sodium (Na) and potassium (K) or divalent calcium (Ca) located within the cavities. Natural feldspars are represented by two subgroups known as the alkali and plagioclase feldspars. The alkali feldspars show a continuous composition series between end members orthoclase (KAlSi_3O_8) and albite ($\text{NaAlSi}_3\text{O}_8$) intermediate members being homogenous mixtures of the pure end members. The structural chemistry of feldspars can be described by a simple chemical formula MT_4O_8 where $\text{M} = \text{K}, \text{Na}, \text{Ca}$ or some combination of all three and $\text{T} = \text{Si}$ and Al . They are very widespread in alkali and acidic igneous rocks, (syenites, granites) pegmatites and gneisses. Within this series distinct structural forms exist at both low and high temperature. At high temperatures this includes high-albite (Na), sanidine and high-sanidine (K) that have a random distribution of aluminium and silicon in their structure. At low temperature, albite (Na), orthoclase and microcline (K) are formed which have a more ordered distribution of aluminium and silicon.

The plagioclase series is continuous between end members albite ($\text{NaAlSi}_3\text{O}_8$) and anorthite ($\text{CaAl}_2\text{Si}_2\text{O}_8$) forming a chemical range called a solid solution series. However, only limited substitution occurs between potassium and calcium rich end members of the alkali and plagioclase series. Most of the crystals of this series exhibit on a microscopic scale, repeated lamellar twinning which produces fine parallel striations on some surfaces. This is the result of diffraction and/or diffusion of light by adjoining areas with different optical properties. Ordering in feldspars is of a complex nature due to the presence of silicon and aluminium atoms in nonequivalent tetrahedral sites. In low temperature feldspars the aluminium and silicon ions tend to

order into certain sites. The potassium feldspar sanidine orders to become microcline whereas the sodium feldspar, high albite, orders to become low albite. The composition of feldspars is shown in figure 1.4 [7].

Figure 1.4 Compositions of the feldspars



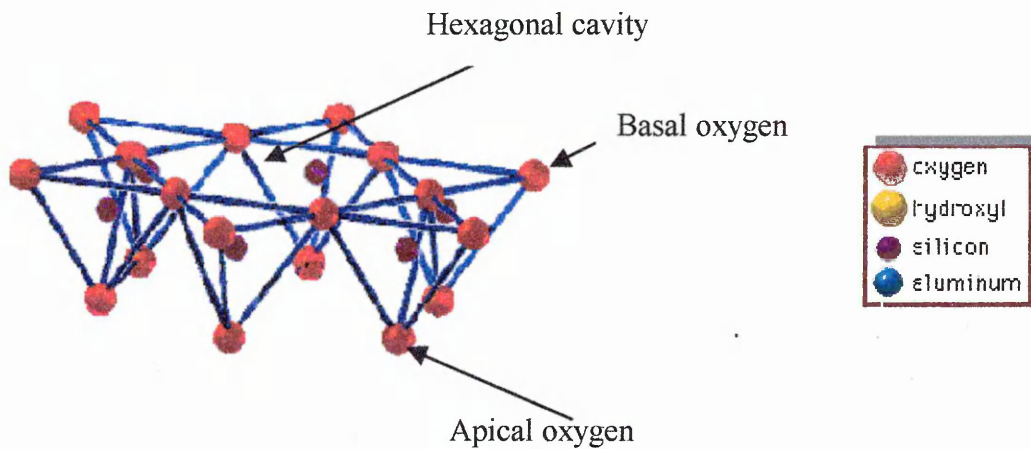
1.6 Phyllosilicates (Clay minerals)

In order to understand the importance of clay minerals, it is necessary to describe the compositional and molecular unit arrangements. The characteristic arrangement of constituent atoms in interlinked planes produces a structure called a sheet silicate or phyllosilicate [8]. In general, clay minerals may be considered as hydrous aluminosilicates where magnesium and iron substitute aluminium in varying degrees and where alkali and alkaline earth elements may also be constituents. Hydrogen is part of this structure as structural hydroxyls, as water between the layers or sorbed on the surface.

Two units are involved in the atomic lattices of most of the clay minerals. These are comprised of continuous two-dimensional sheets of linked tetrahedra (T_2O_5

T=tetrahedral cation, Si, Al or Fe^{3+}) with those of linked $\text{M}(\text{OH})_6$ octahedra (M= octahedral cation) . The tetrahedral unit of silicates is the (SiO_4) tetrahedron shaped anionic group with a charge of (4^-) . The central silicon ion has a charge of 4^+ while each oxygen has a charge of (2^-) resulting in a net negative charge. This condition leaves the oxygens with the option of bonding to another silicon ion and therefore linking one (SiO_4) tetrahedron to several others where the pattern is repeated indefinitely to form a sheet of composition $\text{Si}_4\text{O}_6(\text{OH})_4$ (fig.5). Thus the neighbouring tetrahedra are each linked by three corners (basal oxygens) to form a hexagonal cavity. The fourth corner (apical oxygen) is normal to the sheet whilst forming part of the octahedral sheet.

Figure 1.5 Silica tetrahedral sheet [9]



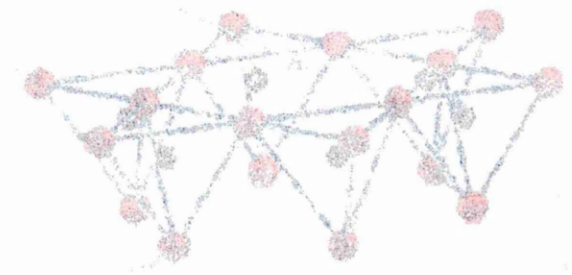
The octahedral sheet is constructed of two sheets of closely packed oxygens or hydroxyls and is linked laterally by shared octahedral edges. Octahedral cations are normally Mg, Al, Fe^{2+} , and Fe^{3+} , but may also contain Li, Ti, V, Mn, Cr, Co, Cu and Zn. These cations are octahedrally coordinated, being equidistant from six oxygens or hydroxyls. When magnesium is coordinated all the positions are filled to balance the

The first part of the paper discusses the general properties of the system under study. It is shown that the system exhibits a rich variety of phases, which are characterized by different symmetries and topological properties. The authors analyze the phase diagram in the parameter space of the coupling constants, showing the emergence of various phases as a function of the system size and the strength of the interactions.

The second part of the paper focuses on the numerical simulations of the system. The authors use a combination of exact diagonalization and Monte Carlo methods to study the ground state properties and the excitation spectrum of the system. The results show that the system exhibits a transition from a topological phase to a trivial phase as the coupling constants are varied.

The third part of the paper discusses the implications of the results for the understanding of topological quantum matter. The authors argue that the system under study provides a new platform for realizing topological quantum states, which are robust against local perturbations and have potential applications in quantum computing and quantum communication.

Figure 1: Schematic representation of the system under study.

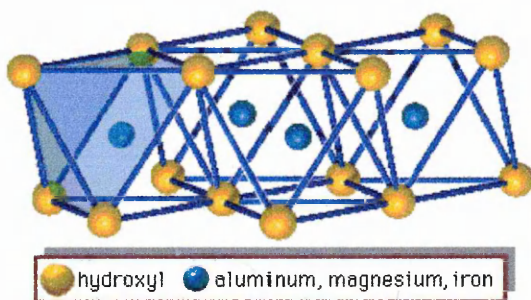


The authors conclude that the system under study exhibits a rich variety of phases, which are characterized by different symmetries and topological properties. The results show that the system exhibits a transition from a topological phase to a trivial phase as the coupling constants are varied. This transition is driven by the competition between the different interactions in the system, which leads to the emergence of different phases.

The authors also discuss the implications of the results for the understanding of topological quantum matter. They argue that the system under study provides a new platform for realizing topological quantum states, which are robust against local perturbations and have potential applications in quantum computing and quantum communication.

structure, which is known as the *brucite* sheet and has the formula $(Mg_3(OH)_6)$. When aluminium is coordinated, only two thirds of the positions need to be filled to balance the charge, which is the *gibbsite* sheet and has the formula $Al_2(OH)_6$. When all three octahedra have cations (Mg^{2+} and Fe^{2+}) at their centre the sheet is known as *trioctahedral* and *dioctahedral* (Al^{3+} and Fe^{3+}) when only two are occupied. Each major group is subdivided in this way.

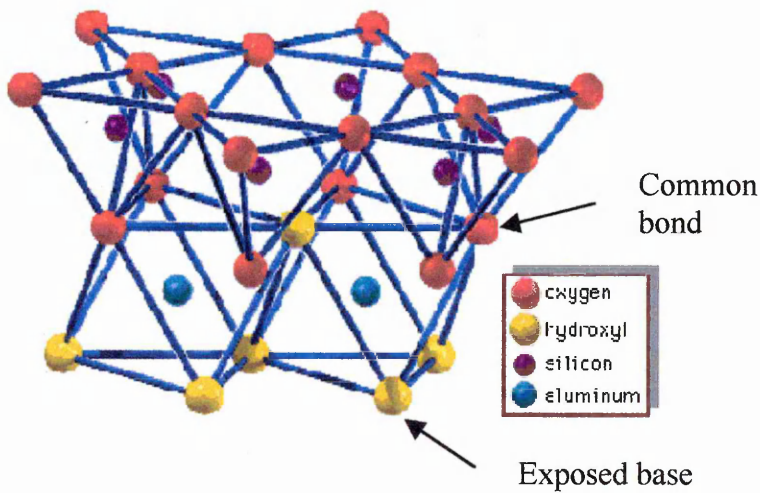
Figure 1.6 Single octahedral sheet



Due to the symmetry and dimensional similarities of the octahedral and tetrahedral sheets, they can be combined in a variety of different arrangements resulting in a collection of mineral sub-groups. The linkage of one tetrahedral sheet to one octahedral sheet is known as a 1:1 structural layer. At the bonds common to both octahedral and tetrahedral sheets, two thirds of the atoms are shared by silicon and aluminium and OH groups become oxygen. The effect of which places the remaining OH group of the octahedral sheet directly below the hexagonal cavity created by the tetrahedral sheet. Therefore in the 1:1 unit the exposed base of the octahedral sheet consists of hydroxyl groups.

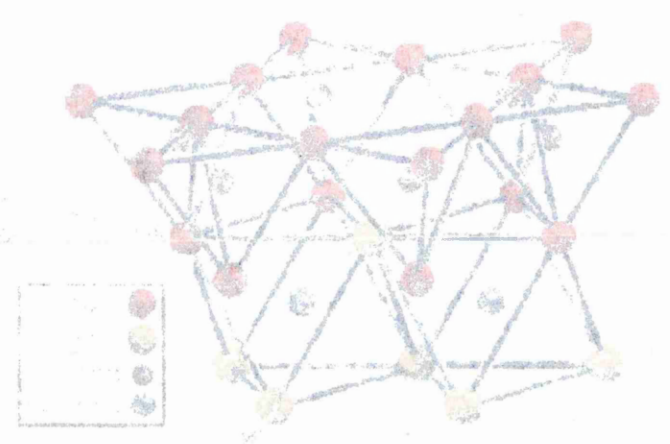
A 2:1 layer is constructed of an octahedral sheet sandwiched between two tetrahedral sheets. The space that is positioned between two stacked layers is known as the interlayer, interlamellar or gallery space. The term interlayer space will be used throughout this thesis. The complete assembly is known as a *structural layer* where the theoretical thickness of both sheets (assuming they are undistorted) is 5.05Å for the octahedral sheet and 4.65 Å for the tetrahedral sheet. The most basic of these structures the 1:1 layer is represented in figure 1.7.

Figure 1.7 The 1:1 structural layer



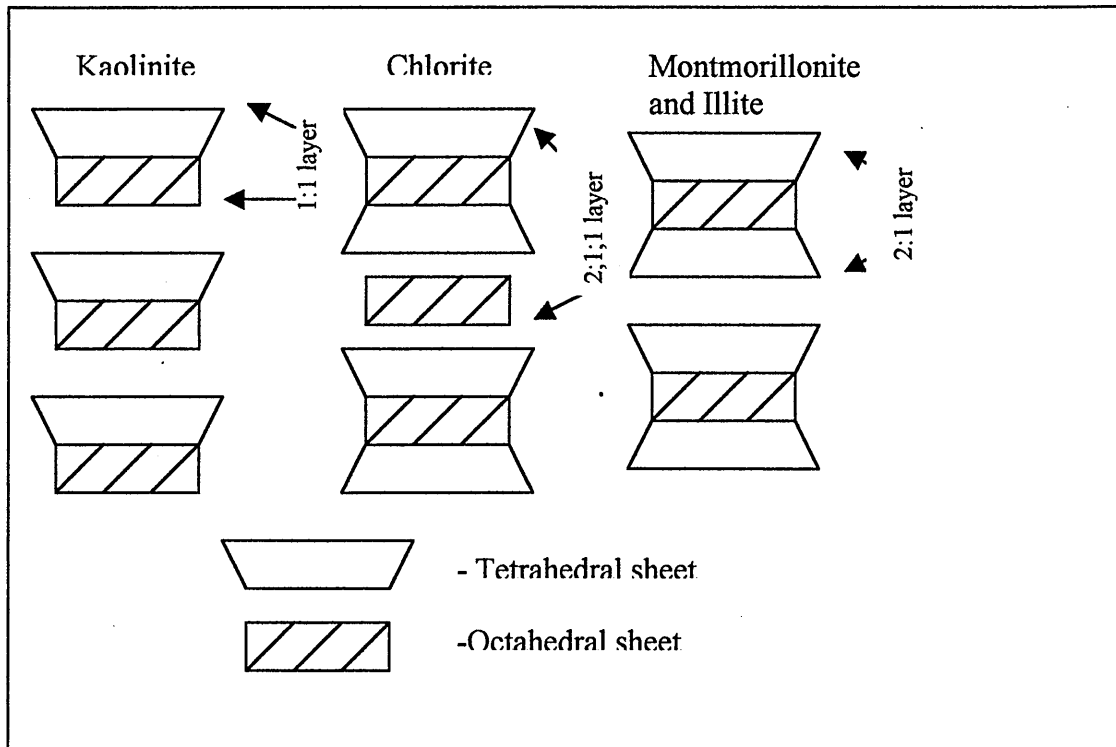
Clays are assigned to groups according to the ratio of tetrahedral to octahedral sheets and the type of cation coordinated within the sheets. The stacking arrangement of these sheet like structures are represented in figure 1.8.

The diagram illustrates the crystal structure of a material, showing the arrangement of atoms in a lattice. The structure is composed of several layers of atoms, with the top layer being a simple cubic lattice. The middle layer consists of atoms that are positioned in the gaps between the atoms of the top layer. The bottom layer is another simple cubic lattice, with atoms positioned directly below the atoms of the top layer. This arrangement is characteristic of a body-centered cubic (BCC) lattice.



The diagram illustrates the crystal structure of a material, showing the arrangement of atoms in a lattice. The structure is composed of several layers of atoms, with the top layer being a simple cubic lattice. The middle layer consists of atoms that are positioned in the gaps between the atoms of the top layer. The bottom layer is another simple cubic lattice, with atoms positioned directly below the atoms of the top layer. This arrangement is characteristic of a body-centered cubic (BCC) lattice.

Figure 1.8 Sheet-like structures of clay minerals



There are six main groups of minerals distinguished according to structural type, which are shown in table 1.3 [11].

Table 1.3 Main mineral groups according to structural type

Group	Structural summary
Kaolinite-Serpentine	Characterized by uncharged 1:1 layers and 7Å repeat layers no interlayer water and 10 Å containing interlayer water
Pyrophyllite-Talc	Characterized by uncharged 2:1 layers
Micas	Characterized by 10 Å layers of variable charge
Chlorites	Characterized by 14 Å layers of variable charge
Smectites - Vermiculites	With layers of variable thickness and charge
Fibrous Palygorskite-Sepiolites	Narrow ribbons of 2:1 type layers linked by their edges to produce a system of channels occupied by water

1.7 Clay minerals examined in this thesis

1.7.1 The 1:1 Type minerals (Kaolinite & Halloysite)

The minerals discussed here of importance to this project are the dioctahedral species Kaolinite and Halloysite. Kaolinite is a whitish-opaque, powdery mineral that was formed from the natural alteration products of feldspars, feldspathoids, and other silicates under extreme conditions of temperature and pressure. Kaolinite usually takes the form of individual crystals forming booklets from stacks of crystal sheets. This group has three members (kaolinite, dickite and nacrite) and a theoretical formula of $\text{Al}_2\text{Si}_2\text{O}_5(\text{OH})_4$. However, due to the variability in formation conditions, composition varies, due to the presence of other minerals such as mica and feldspar. The different members of this group are polymorphs, meaning that they have the same chemistry but different structures (polymorph = many forms). The general structure of the kaolinite group is composed of silicate sheets (Si_2O_5) bonded to aluminum oxide/hydroxide layers ($\text{Al}_2(\text{OH})_4$ (gibbsite layers)). Because there is no isomorphous substitution there is no unit layer charge deficiency and therefore no interlayer cations. This results in a strong, very difficult to separate hydrogen bonding network formed between the hydroxyls in the octahedral sheet and the basal oxygens in the tetrahedral sheet of the next layer. Therefore layer cleavage and subsequent intercalation is very difficult. Adsorption is therefore confined to external crystal surfaces. If exchangeable cations are present these are usually associated with broken bonds at crystal edges.

Halloysite another member of the 1:1 type minerals is considered to be composed of kaolinite 1:1 layers that are intercalated with a single layer of hydrogen bonded water molecules. However, in comparison to the flat hexagonal plates of

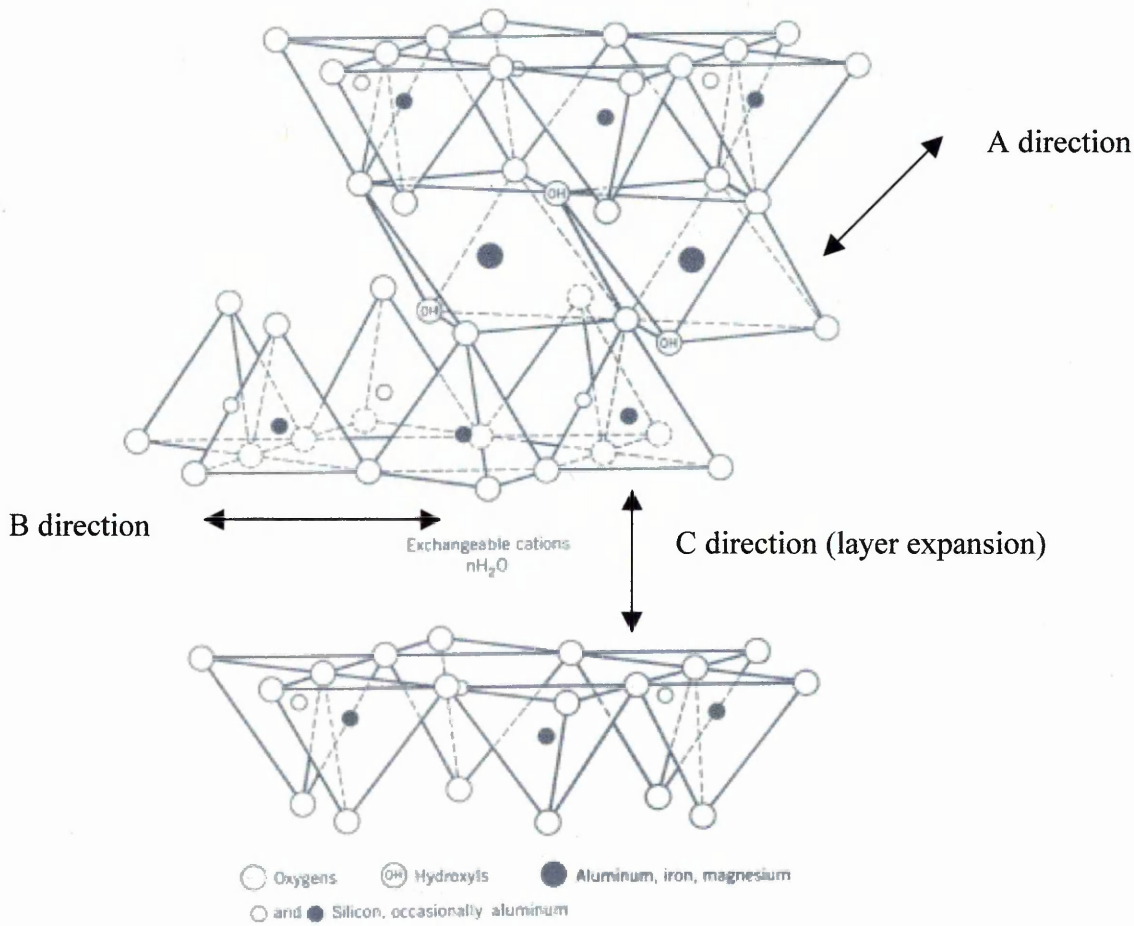
kaolinite, halloysite often appears as a tubular structure [12]. Although tubular forms are the most common, other morphological varieties are also known: prismatic, rolled, pseudospherical, and platy forms. The structure of halloysite is believed to be similar to that of kaolinite, but no precise structure has yet been revealed. Halloysite has a hydrated form with a composition of $\text{Al}_2\text{Si}_2\text{O}_5(\text{OH})_4 \cdot 2\text{H}_2\text{O}$. This hydrated form irreversibly changes to a dehydrated variety at relatively low temperatures (60°C) or upon being exposed to conditions of low relative humidity. The dehydrated form has a basal spacing about the thickness of a kaolinite layer (approximately 7.2 \AA), and the hydrated form has a basal spacing of about 10.1 \AA . The difference of 2.9 \AA is approximately the thickness of a sheet of water one molecule thick. Consequently, the layers of halloysite in the hydrated form are separated by monomolecular water layers that are lost during dehydration. The variety of morphologies are related to their chemical compositions [13] where differences in morphology seem to be related to iron content. High iron contents are found in halloysites (10 \AA) with spheroidal, crinkly film or crumpled lamellar morphology [14]. In comparison to kaolinites, halloysites appear to have a much wider range of $(\text{Al} + \text{Fe})/\text{Si}$ and others with excess of silica which probably reflects the conditions of formation.

1.7.2 The 2:1 Type minerals (montmorillonite & saponite)

Compositionally, montmorillonite always deviates from the ideal formula $\text{Al}_2\text{Si}_4\text{O}_{10}(\text{OH})_2 \cdot x\text{H}_2\text{O}$ [15,16] due to isomorphous substitution in both the tetrahedral and octahedral sheets which creates a unit layer charge deficiency. An idealized structural formula for montmorillonite is $\text{Na}_{0.3}(\text{Al}_{1.7}\text{Mg}_{0.3})\text{Si}_4\text{O}_{10}(\text{OH})_2$. The generally accepted structure (figure 1.9) was proposed by Hofmann, Endell and Wilm [17] and later modified by suggestions proposed by Maegdefrau and Hofmann [18], and

Hendricks [19] and Marshall [20]. Edelman and Favejee [21] proposed a radically different structure where every alternate silica tetrahedron is inverted.

Figure 1.9 The 2:1 structure of montmorillonite [22]



In general, the higher the unit layer charge, the more interlayer cations are required to balance the charge deficiency. In turn, increasing amounts of interlayer cations produce more strongly bonded layers. The typical crystal habit of this subclass is flat, platy and book-like. Most members display good basal cleavage and this is due to several reasons. Firstly, when stacked, the exposed oxygen surface of each unit layer is repulsed by the oxygen layers of neighbouring units. Secondly, isomorphous

substitutions in the tetrahedral and/or octahedral units creates a net negative charge which is satisfied by cations coordinated between the layers. These cations connect the 2:1 layer units to each other and are weakly bonded, often having water molecules and other neutral atoms or molecules trapped between the layers. Because of this weak bonding, water is readily adsorbed into the interlayer space, the amount being proportionate to the nature and number of interlayer cations. 2:1 layer structures are classified according to the net negative charge on the layer (table 1.4).

Table 1.4 Classification of phyllosilicate clay minerals [23]

Layer type	Group-charge per formula unit (x)	Sub-group	Species
1:1	(x ~ 0)	Serpentine- Kaolin	Chrysotile, amesite kaolinite, dickite, nacrite
2:1	(x ~ 0)	Talc Pyrophyllite	Talc, willemseite Pyrophyllite
2:1	(x ~ 0.2-0.6)	Montmorillonite Saponite	Montmorillonite, nontronite Saponite, hectorite
2:1	(x ~ 0.6-0.9)	Vermiculite	Tri & dioctahedral
2:1	(x ~ 1.0)	Mica	Phlogopite, biotite, lepidolite Muscovite, paragonite
	(x ~ 2.0)	Brittle mica	Clintonite, anadite
2:1:1	(x variable)	Chlorite	Clinochlore, chamosite, donbassite
2:1 ribbons	(x variable)	Sepiolite- Palygorskite	Sepiolite, palygorskite

It can often be difficult to distinguish between the 2:1 layer minerals as they share this common structure (mica, vermiculite, smectite and pyrophyllite-talc groups). However, differences in the charge characteristics of the interlayer cations and their behaviour towards water and organic compounds provide a basis for contrast. The principal members of the smectite group according to the origin of their layer charge are shown in table 1.5.

Table 1.5 Principal smectite group members

Origin of layer charge	Trioctahedral smectites	Diocahedral smectites
Octahedral	Hectorites $(Mg_{6-x}Li_x)(Si_8)O_{20}(OH)_4 \cdot xM^+$	Montmorillonites $(Al_{4-x}Mg_x)(Si_8)O_{20}(OH)_4 \cdot xM^+$
Tetrahedral	Saponite $(Mg_{6-x}Li_x)(Si_{8-y}Al_y)O_{20}(OH)_4 \cdot xM^+$	Nontronite $(Fe_4^{3+})(Si_{8-y}Al_y)O_{20}(OH)_4 \cdot xM^+$ Beidelite $(Al_4)(Si_{8-y}Al_y)O_{20}(OH)_4 \cdot xM^+$

Substitutions within the octahedral sheet of smectites may vary from partial to complete. Total replacement of aluminium by magnesium yields the mineral saponite; replacement by iron yields nontronite; by chromium volkhonskoite; by zinc, sauconite.

1.7.3 The illite (or The clay-mica) group

The basic structural unit of illite is the same as montmorillonite except that some of the silicon is replaced by aluminium producing a charge deficiency that is balanced by potassium ions in the interlayer space. Natural ammonium illites have been also described by Sterne et al. [24] substituting significantly for K^+ in the interlayer. Short range Van der Waals forces due to the small size of the potassium ions combined with electrostatic forces result in increased bonding between the layers, which makes illite both difficult to swell and exchange. The ideal structural formula for illite is $KAl_2(Si_3Al)O_{10}(OH)_2 - xH_2O$ where x represents the variable amount of water that this group can contain. The structure of illite differs from that of smectite in several important ways. The charge deficiency due to substitutions per unit cell layer is about 1.3 to 1.5 for illite and 0.65 for smectite. In illite, this occurs mainly in the silica sheet and therefore close to the surface of the unit layer, whereas in smectite it is chiefly in the octahedral layer and therefore at the centre of the unit. This means that in illite the charge deficiency is concentrated close to the surface attracting more interlayer cations, which results in more strongly bound layers. There is plenty of evidence in the literature that shows that various gradations exist between illites and smectites in mixed layer systems [25]. The classification of such material is difficult and therefore arbitrary, with expandable material being regarded as smectite and nonexpandable material regarded as illite. Newman describes illites as clay micas having a 10 Å repeat unit with no evidence of interstratification and with a total Fe content < 1 per four octahedral sites in comparison to glauconites and celadonites which have an Fe content of 1 per four octahedral sites.

1.7.4 Chlorite

The chlorite structural unit is comprised of a 2:1 layer with an interlayer consisting of an octahedral brucite sheet. Isomorphous substitution in chlorite occurs in the tetrahedral layer by iron and aluminium for silicon, the result of which generates a negatively charged surface which is neutralised by the interlayer brucite sheet $(\text{Mg Al})_6(\text{OH})_{12}$ where isomorphous substitution of aluminium ions for magnesium ions has occurred. Therefore there are two octahedral sheets in the structure, one in the 2:1 layer and the other between them. The ideal structural formula for chlorite is $(\text{Mg, Fe Al})_6 (\text{Al, Si})_4\text{O}_{10}(\text{OH})_8$ although appreciable amounts of chromium, nickel or manganese are present in some varieties. The bonding between the layers is partly a consequence of substitutions within the lattice and also due to adjacent sheets of oxygen (tetrahedral) and hydroxyl (brucite) ions similar to that found in kaolinite. Members of the chlorite group differ in several ways, such as:

- (a) type and number of substitutions within the brucite layer
- (b) type of isomorphous substitutions of the mica layer
- (c) orientation of successive octahedral and tetrahedral layers

which affects the relation of mica to brucite layers and therefore their stacking arrangements. In trioctahedral chlorites both octahedral sheets are trioctahedral, in dioctahedral chlorites both sheets are dioctahedral, whereas di/trioctahedral chlorites are dioctahedral in their 2:1 layers and trioctahedral in their interlayer sheets [26]. The octahedral layer of chlorite differs from that of montmorillonite, illite and kaolinite in that it has trioctahedral rather than dioctahedral arrangement from Mg_5Al (5:1) to Mg_4Al_2 (2:1) with Fe^{2+} and Mn^{2+} partially replacing Mg^{2+} and Fe^{3+} , or Cr^{3+}

partially replacing Al^{3+} . The Al^{3+} substitutions for Si^{4+} in the tetrahedral sheets expand sufficiently to accommodate the larger octahedral layer.

1.8 Clay mineral active bonding sites

In order to put clay organic interactions in the context of clay mineral structure, it is necessary to discuss the importance of active bonding sites. In general, clays can offer seven predominant active sites [27].

(1) Neutral siloxane surface (silica tetrahedra)

(2) Hydroxyl groups

(3) Isomorphous substitution sites

(4) Metal cations occupying exchange sites

(5) Water molecules surrounding exchangeable cations

(6) Hydrophobic sites

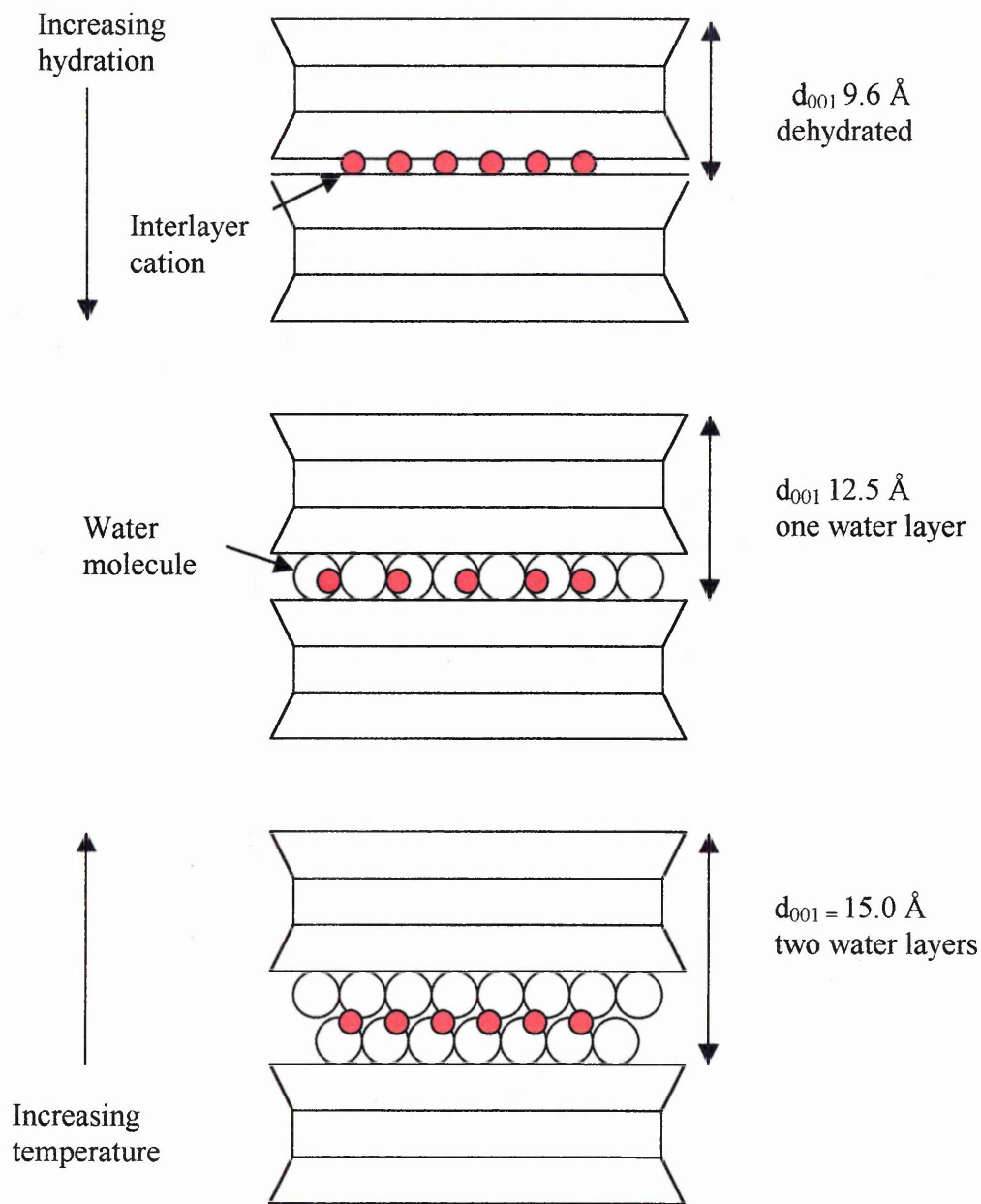
(7) Broken edge sites including exposed silanol and aluminol groups

However, before discussing the nature of these sites it is necessary to firstly discuss the nature of interlayer swelling as it is not only a diagnostic tool in clay mineral identification by X-ray diffraction, but the mechanism also enables suitable probe

molecules to successfully intercalate by bonding to many of these active sites. Many 2:1 layer silicates swell in water and a wide range of organic compounds. The control of swelling in these minerals is a balance between attractive and repulsive forces between adjacent layers. When the layers are in close contact such as in a collapsed state, there exists a Van der Waals attractive force between surface atoms of adjacent layers with the addition of electrostatic forces between charged ions. These forces are ultimately dependent on structure and therefore influence the degree of layer separation. Solvation of interlayer cations must be considered the most important contributor to layer repulsion and is further contributed to by the interaction of the solvate with the oxygens of the 2:1 layers. Other repulsive forces are exhibited by the hydrogens of hydroxyl groups which are linked to cations in the 2:1 layer and the interlayer cations. The magnitude of this force is proportionate to the proximity of the hydroxyl hydrogen to the charge in the interlayer. It is considered to be at its strongest when the OH dipole is normal to the plane of the 2:1 layer.

The ability of members of the smectite group to absorb water and other polar molecules produces an expansion of the interlayer spacing. This expansion causes the basal spacing to increase from approximately 10 Å when the layers are in direct contact (collapsed) to values in the order of 12.5-20 Å when fully expanded which depends on clay type and exchangeable cation (fig.1.10).

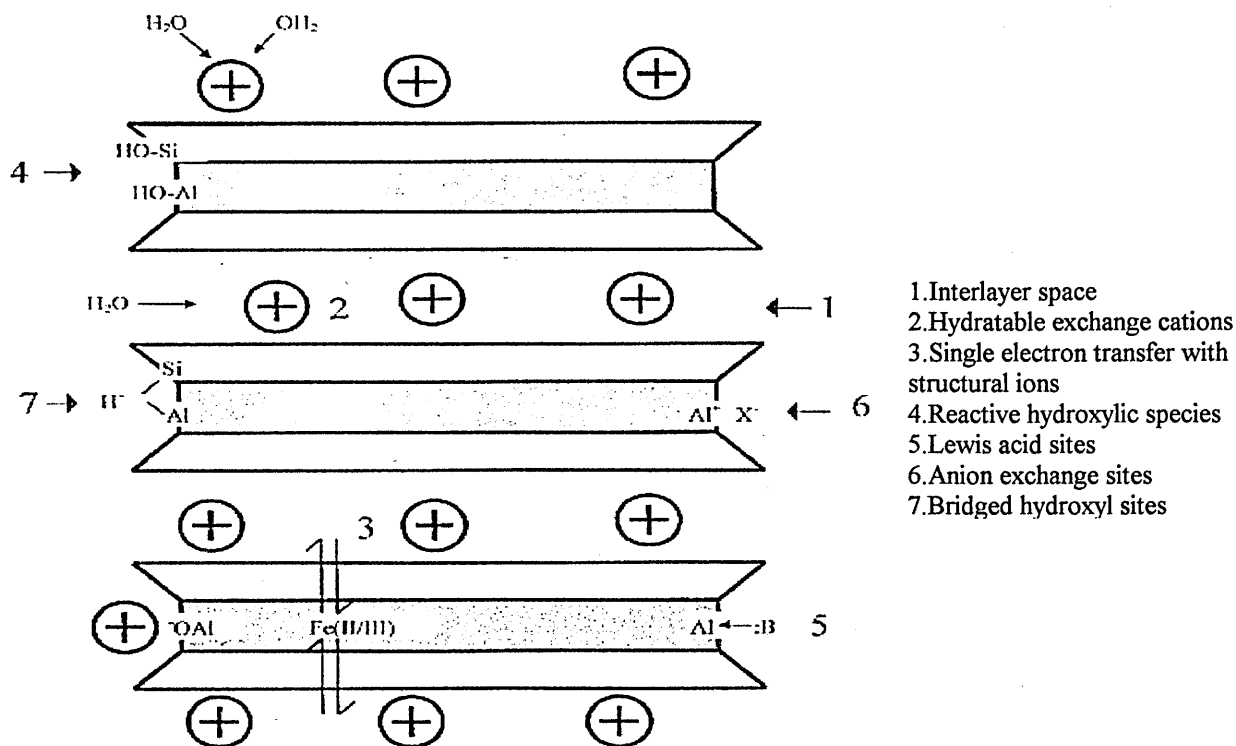
Figure 1.10 Swelling state of smectite due to water vapour



As seen in figure 1.10, the heating process affects the weight loss of clays. The temperatures at which weight losses are observed depends on the type of clay, interlayer cation, and the rate and time of heating. Pioneering work by Mooney et al

[28, 29] observed the behaviour of water molecules on smectite surfaces. With less than three molecular layers of water present in the interlayer region the sorbed water on smectites has been shown to be influenced predominantly by exchangeable cations [30,31,32]. According to Bradley and Grim [33], below 300° C, water and other molecules are adsorbed reversibly between the clay layers. Above 500° C the water of hydration is removed and the layers collapse irreversibly [28, 29]. After calcination of the clay at 600° C no water is adsorbed in the interlayer space. The principal surface features involved in these reactions are shown in figure 1.11.

Figure 1.11 Principal surface features on a clay



1.8.1 Neutral siloxane surface

For neutral 2:1 layer silicates the exposed siloxane surface is considered hydrophobic in character. These surfaces occur in 2:1 silicates where no isomorphous substitutions have occurred (talc and pyrophyllite) and the siloxane surface of 1:1 silicates e.g. kaolinite

These surfaces also occur on charged 2:1 silicates that have been exchanged with:

(a) Alkylammonium cations

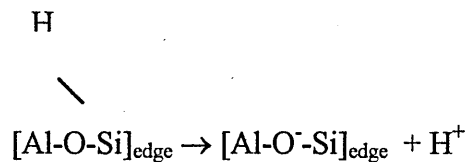
(b) Organic cations

Each of the surface oxygens are co-ordinated to two Si atoms and, as previously stated, the oxygen atoms are arranged in a hexagonal network. This type of surface has a low affinity for water and in terms of surface reactivity the siloxane surface in clay minerals is considered to be inert and unreactive due to the strong bond formed between Si and O atoms.

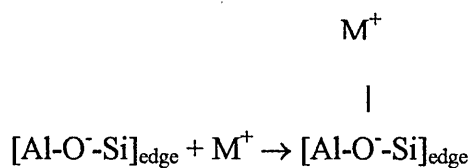
1.8.2 Hydroxyl groups

Hydroxyl groups located at external edge positions may be of two types, bridging and non-bridging, depending on the degree of hydration. These hydroxyl groups may in turn act as a source of Bronsted acidity (equation 1) or external binding sites for metal ions as illustrated in equation 2.

Equation 1(No. 7 Fig. 1.11)



Equation 2 (No. 6 Fig 1.11)

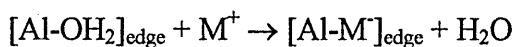


However, at higher levels of hydration terminal hydroxyl groups predominate at edge positions. These aquated sites are an additional source of Bronsted acidity (equation 4).

Equation 3 (can form at No 4. fig 1.11)

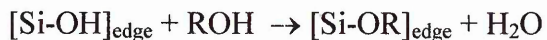


Equation 4



terminal hydroxyl groups can also engage in coupling reactions with organics containing functional groups as illustrated in equation 5.

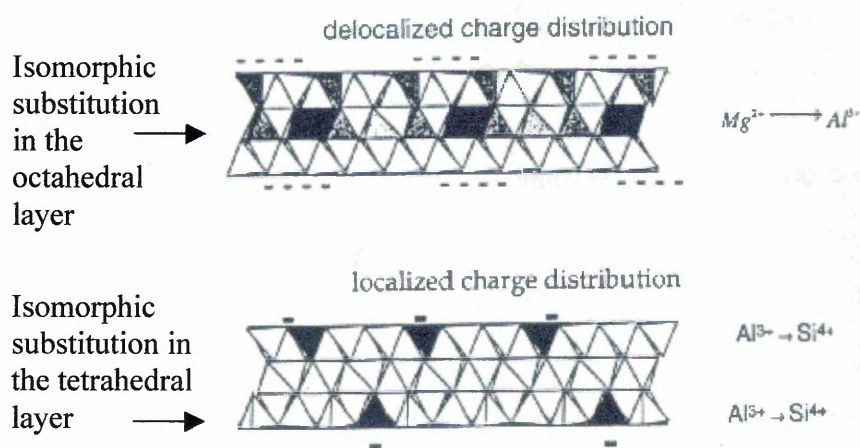
Equation 5



1.8.3 Isomorphous substitution sites

These sites are characterized by a permanent net negative charge and are referred to as “*constant charge sites*” This phenomenon occurs in both the octahedral and tetrahedral sheets of smectites. They are found on the basal surfaces of charged 2:1 clays (site separation of 1-2.0 nm). Mg^{2+} can substitute for Al^{3+} in the octahedral sheet. However the charge de-localizes in the sense that it is spread over 10 basal oxygen ions. In comparison, substitution in the tetrahedral sheets of Al for Si creates a more localised charge imbalance spread over three oxygens in the base of the tetrahedra. A diagrammatical representation of charge distribution in relation to isomorphous substitution is shown in figure 1.12.

Figure 1.12 Isomorphous substitution in tetrahedral and octahedral sheets [28]



All isomorphous substitution results in a net negative charge. In natural systems, this net negative charge is mostly satisfied by the presence of exchangeable cations that

occupy the interlayer space usually in the presence of water. However organic cations and protonated organic bases can participate. These are preferentially sorbed over most inorganic cations due to the combined attraction of electrostatic and non-coulombic forces.

1.8.4 Exchangeable Metal Cations & Exposed Undercoordinated Metal Atoms

Organic solutes do not replace the exchangeable metal cation rather they coordinate directly to the metal cation occupying the exchange sites. The degree of interaction depends on the ability of the organic solute to compete for coordination sites around the metal centre. The metal acts as a Lewis acid (Lewis acid is an electron pair acceptor) by accepting electrons from adjacent unsaturated organic solutes. This is affected by:

(a) reduction potential of the metal cation

(b) water content of the clay

A high water content creates an environment that leaves non polar organic solutes with limited ability to compete for coordination positions around the hydrated metal cation. At lower water content, unsaturated organic solutes can participate in electron transfer and polymerisation reactions may occur. This makes it possible to utilize organic molecules as potential diagnostic probes within the interlayer space.

1.8.5 Polarized Water Molecules Surrounding Exchangeable Cations (or uncoordinated metal cations at broken edges)

Johnston et al 1992 [36], showed that the molecular properties of water were strongly influenced by the water content of the clay-water complex. As previously stated the structure of sorbed water on smectites is influenced primarily by the nature of the exchangeable cations and it is suggested that there are two distinct types of sorbed water:

- (1) H₂O molecules coordinated directly to exchangeable cations
- (2) Physisorbed water molecules occupying interstitial pores, interlayer spaces between exchangeable cations or polar sites on external surfaces.

These sites function as sources of surface Bronsted acidity and are mainly concerned with site 1 fig. 11. The polarized water molecules surrounding *exchangeable cations* and *under coordinated surface atoms* can donate protons to adjacent organic solutes more readily than bulk water and therefore have the ability to promote a variety of chemical reactions. However, the extent of this ability depends strongly on the nature of:

- (1) Type of exchangeable cation - polarizing power (Al³⁺ greater than Ni²⁺ and therefore should be predominantly Bronsted in nature)
- (2) Amount of water present

In general, as the charge on the cation increases and the size decreases, surface Bronsted acidity increases because the cation's ability to polarize the water molecules also increases. The order of proton donation decreases as Al³⁺ > Mg²⁺ > Ca²⁺ > Na⁺.

However this is also strongly influenced by the basicity of the organic solute (i.e. pyridine (weak base) pK_b 8.8, cyclohexylamine (strong base) pK_b 3.3). The low water contents achieved by mild heat treatment or evacuation of the clay sample promotes acidity as the polarization power of the cation is acting on fewer water molecules (i.e. sample preparation, storage and experimental conditions will be influential), which in turn causes an increase in dissociation of the water molecule and an increase in the production of protons. A system described as the dry system (20% relative humidity), can be estimated by the sorption of either organic bases or ammonia where the corresponding protonated species can be observed using infrared spectroscopy (i.e. Anilinium 1578 cm^{-1}). In contrast a clay whose interlayer cations are exchanged with Cs is virtually dehydrated. Assuming that substitution is in the tetrahedral layer some of its water will be orientated with the positive ends of their dipoles directed towards the surface oxygens, hence this water has a basic character. Thus arises the term surface acidity that refers to the ability of layer silicates to act as Bronsted acids by donating protons to adsorbed bases.

Swoboda and Kunze [37] reported that weak organic bases i.e. pyridine & aniline were protonated more readily in minerals where the tetrahedral layer is the principal source of the negative charge. Thus protonation relies on several important factors

- (a) Nature of interlayer cation-acidity
- (b) The proportion of water in the system
- (c) The location of isomorphous substitution and charge density which controls the number of cations

The degree of protonation due to the location of isomorphous substitution has been demonstrated by Yariv & Heller [38] who compared Camp Berteau montmorillonite (where the charge resides chiefly in the octahedral layer) to Wyoming montmorillonite (where the charge is about equally distributed between the tetrahedral and octahedral layer). Camp Berteau was exhibited greater protonation than Wyoming due to the fact that isomorphous substitution occurs more readily in the tetrahedral layer.

1.8.6 Hydrophobic sites

Sorption of organic molecules on clay surfaces can impart a hydrophobic nature to the clay surface. For example, the exchange of alkyl-ammonium cations for inorganic cations on montmorillonite. It is known that smectite surfaces have a high selectivity for organic cations. These clays are referred to as organoclays and have significantly different surface properties to the original clay. This ion creates a hydrophobic surface and can be seen as molecular pillars to allow organic solutes to be adsorbed. A surface of this nature makes an efficient sorbent for non-polar compounds.

1.8.7 Broken edge sites (pH dependent active sites)

These are the surface hydroxyl groups located on the broken edges of clay minerals. Under coordinated Si^{4+} , Al^{3+} , Fe^{3+} ions which are located at broken edges, terraces, kinks or holes on the surface of clay minerals will react with water molecules forming OH groups to complete their coordination sphere. They can also form inner sphere complexation (OH groups formed) with metal species and can undergo hydrogen

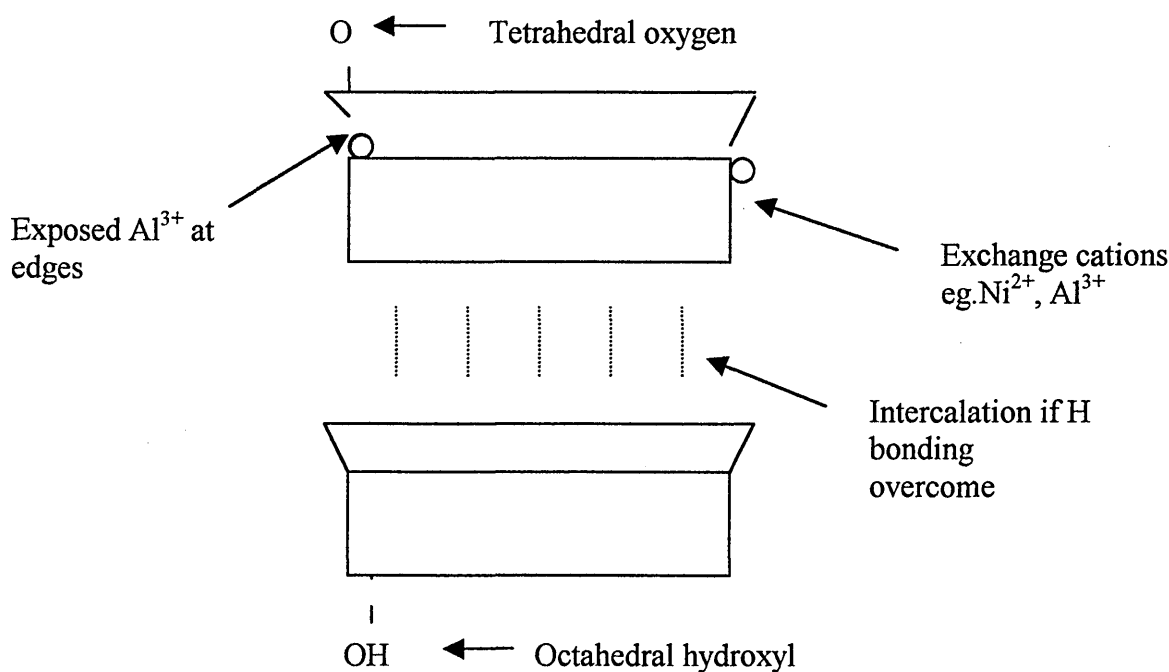
bonding. These active sites along with humic substances are responsible for the development of the pH dependent charge in soils and sediments. At low pH (high $[H^+]$) these sites develop a positive charge due to the adsorption of protons. Organic acids and oxyanions can interact strongly with these sites at low pH. As pH increases these sites become more neutral and ultimately acquire negative charge when the pH value is greater than the point of zero charge (PZC). The contribution of these sites to CEC depends on :

(1) particle size - as particle size decreases the contribution of edge sites becomes more appreciable

(2) Isomorphus substitution

Therefore for clays such as kaolinite, which exhibit little or no isomorphous substitution, pH dependent sites are the principle source of reactivity. The types of binding sites potentially available in kaolin stacks are shown in fig 1.13.

Figure 1.13 Potential active sites in Kaolin stacks



Chapter 2 Theory of Techniques used in this thesis

2.0 Introduction

Infrared radiation is electromagnetic radiation with a wavelength between 10^{-3} and 10^6 m approximately. Adsorption of particular frequencies of infrared radiation by polyatomic molecules gives rise to a characteristic infrared spectrum. A variety of techniques have been discussed in the past [39] for measuring the infrared spectra (IR) of powdered samples these include:

2.1 Infrared

- (1) Transmission spectroscopy
- (2) Diffuse reflectance spectroscopy
- (3) Emission spectroscopy
- (4) Photo acoustic spectroscopy

The first two techniques have been applied in this thesis and will be discussed further in this chapter.

2.1.1 Absorption of Infrared radiation

A summary of the theory of infrared spectroscopy is presented herein. For a more detailed account, the reader is directed towards more specialised texts [40, 41, 42]. For a molecule to produce absorption bands in the IR spectrum it is subject to certain rules. The simplest idealised model of an IR active vibrating molecule consists of two

atoms of differing mass (m_1 and m_2), which are joined by a weightless spring (i.e. a simple harmonic oscillator). The simplest of interpretations explains that if the atoms are pulled apart, attractive forces will pull them back together, whereas when forced together repulsive forces may push them apart again. Hookes Law as shown in equation 1 governs this system.

Equation 1

$$PE = -k(r-r_e)$$

Where f = restoring force,

k = the force constant

r = the internuclear distance

r_e = the internuclear distance at equilibrium or

bond length

If the bonds are pulled apart too far, then the bond (spring) will break. The energies associated with atoms during anharmonic compression and extensions are approximated by the Morse function.

Equation 2

$$PE = D_e [1 - \exp\{a(r_e - r)\}]^2$$

Where D_e = dissociation constant

a = constant for a particular molecule

r_e = equilibrium constant or bond length

r = internuclear distance

The above equation is used to solve the Schrödinger equation where the permitted energy levels are found to be

Equation 3

$$E_v = (v + 1/2) \omega_e - (v + 1/2)^2 \omega_e \chi_e$$

Where ω_e = oscillation frequency

χ_e = anharmonicity constant = $a^2/2\mu\omega_e$

$v = 0, 1, 2, \dots$

μ = reduced mass

Thus the selection rules for an anharmonic oscillator undergoing vibrational changes are $\Delta v = \pm 1, \pm 2, \pm 3, \dots$. The lowest energy level is when $v = 0$ and is called the ground state. At this point energy is not equal to zero, but is known as ‘zero point energy’ which is determined from equation 3 (approximated equation). To find the dissociation energy of a molecule a general equation has been derived which is used to fit experimental data (equation 4).

Equation 4

$$E_v = (v + 1/2) \omega_e - (v + 1/2)^2 \omega_e \chi_e + (v + 1/2)^3 \omega_e \chi_e \dots$$

Therefore if a molecule is to absorb infrared radiation it must undergo a net change in dipole moment due to its vibrational motion. A dipole moment can be described as the magnitude of the localised electrical charges within a molecule and the distance separating positive and negative components of these charges (i.e. atoms). As molecules vibrate changes in dipole moment may occur. Only those vibrations of a molecule which exhibit a strong change in dipole moment have strong infrared absorption bands. If the molecule is subjected to an incident infrared radiation beam and the frequency of the incident radiation is the same as that of the molecular vibration, a net transfer of energy can occur which results in a transition from one vibrational level to a higher level (i.e. a change in amplitude of the molecular

vibration) and adsorption of radiation occurs. It is important to note that bands in a spectrum arise from the adsorption of energy caused by chemical groups of two or more atoms, i.e. not individual atoms vibrating.

2.1.2 Vibrational Modes of polyatomic molecules

Predicting the principal IR absorption bands for small molecules is relatively simple.

The number of normal vibrations (B), which is related to the vibrational degrees of freedom, can be calculated from the formula:

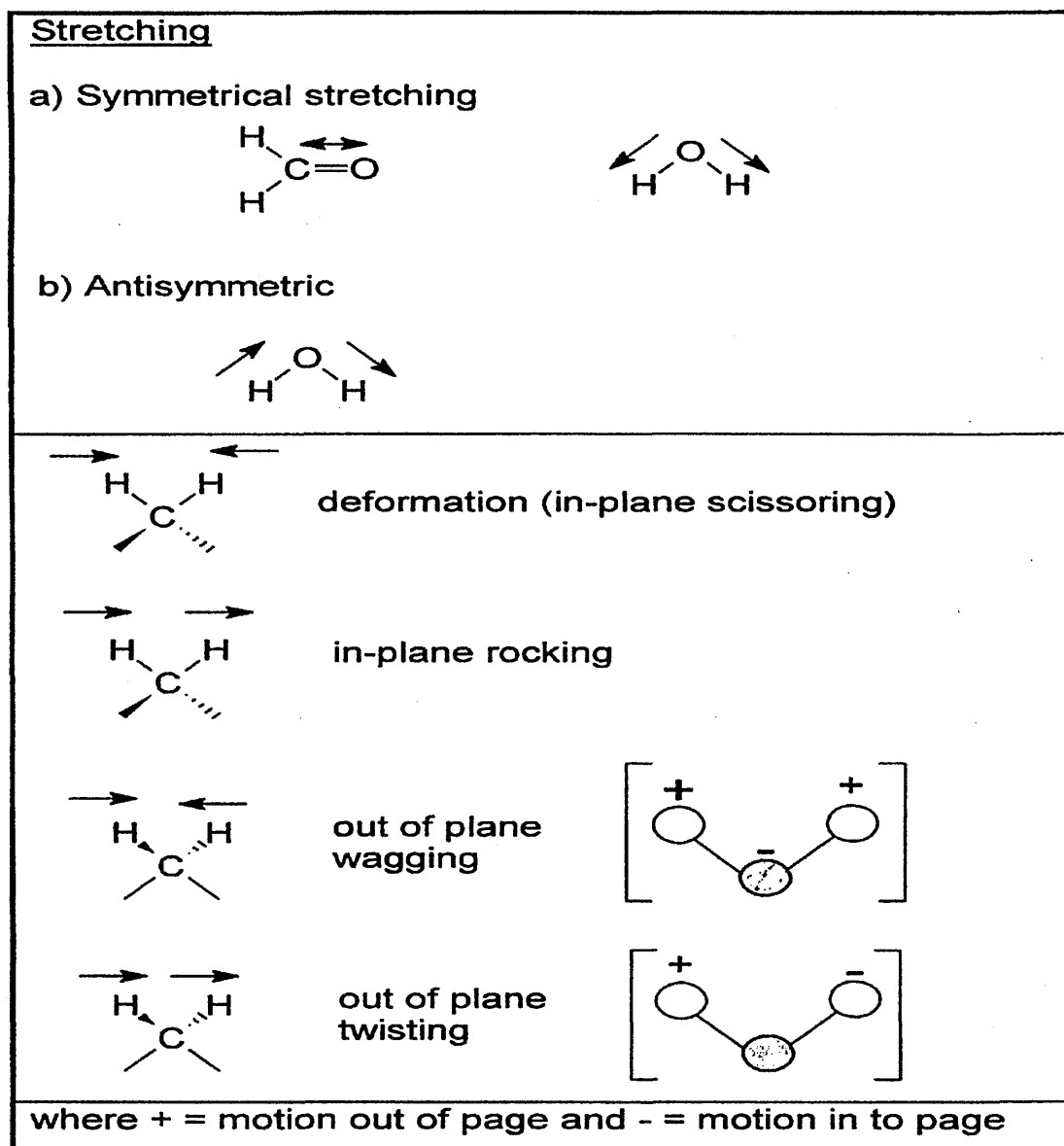
$$B = 3N - 6, \text{ or for a linear molecule, } B = 3N - 5,$$

where N is the number of atoms in the molecule.

In a polyatomic molecule, each atom has three degrees of motional freedom, that is, it can move independently in three different directions along the axes of a Cartesian coordinate system. Three of the degrees are translational (i.e. simultaneous movement of all atoms in the same direction parallel to the axes of a Cartesian coordinate system) and another three describe rotations about the principle axes. The remaining three $3N-6$ degrees are motions which change bond lengths and angles between atoms.

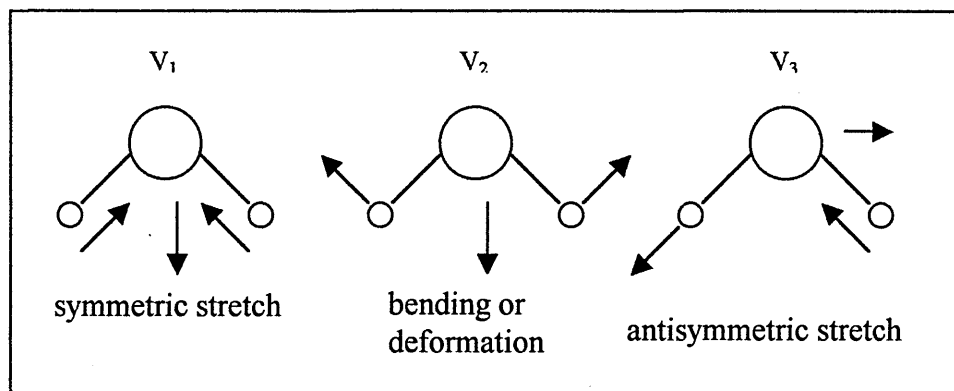
For large polyatomic molecules, the number of bands can be very large, and will also include overtone (multiple harmonics) and combination bands. These spectra contain a plethora of peaks and very difficulty to interpret. Vibrational band positions and shapes will be influenced by the overall shape of the molecule, molecular conformations and molecular packing (crystallinity, density). The types of stretching and bending vibrations that can occur in molecules is shown in figure 2.1.

Figure 2.1 The types of stretching and bending vibrations occurring in molecules



For a polyatomic molecule such as water the vibrational motions observed are as follows (fig 2.2).

Figure 2.2 Vibrational motions of water (H₂O)



The transitions that are normally observed for water are

$\nu = 1 \leftarrow 0$, which is a fundamental transition (i.e. the first harmonic)

$\nu = 2 \leftarrow 0$ or $\nu = 3 \leftarrow 0$, which are overtones and occur at near frequencies of $2\nu_1$ and $3\nu_1$, where ν_1 is the fundamental mode frequency. Water has four normal modes of vibration, two of which orthogonal bending motions are degenerate (i.e. of identical frequency). Other types of band, which may exist in infrared, include combination and difference bands. Combination bands arise from the addition of two or more fundamental frequencies or overtones and difference bands from the subtraction of two or more overtones or fundamental modes. The intensity of combination bands is generally smaller than fundamental vibrations.

2.1.3 Factors affecting the intensity of infrared bands

The intensity is dependent on two factors:

(a) Infrared selection rules

which determine whether the transition is 'forbidden' or 'allowed'

(b) The population of the initial state at thermal equilibrium (the difference in populations between initial and final states)

In general the ground state is most heavily populated at thermal equilibrium and transition intensities are proportional to the population of the initial vibrational state.

The population is described by the Boltzmann distribution shown in equation 5.

Equation 5

$$N_i/N_o = g_i/g_o \exp(-\Delta E/kT)$$

Where N_i = number of molecules in a particular state,

N_o = number of molecules in the ground state,

ΔE = difference in energy between the states

k = Boltzmann constant

T = temperature

g_i and g_o = degeneracies of the particular levels.

(c) The number of molecules in the beam (i.e. sample thickness or concentration)

The relationship between intensity of transmitted and incident radiation to the number of molecules is governed by the Beer-Lambert Law (eq. 6)

Equation 6

$$\text{Log}_e (I_0/I) = \epsilon cl.$$

Where I_0 = intensity of radiation falling on the sample (wavelength dependent)

I = transmitted radiation (wavelength dependent)

c = sample concentration

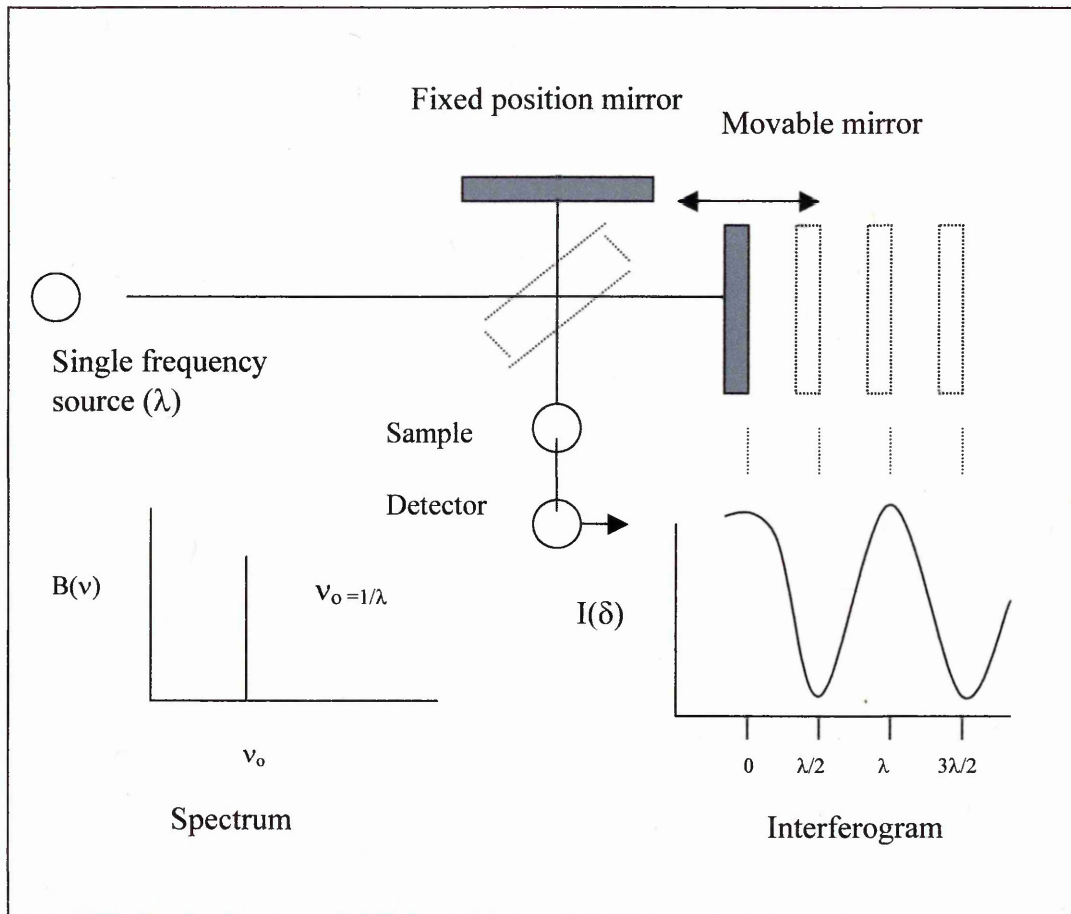
l = path length

ϵ = extinction coefficient at a given wavelength

2.1.4 Fourier transform infrared spectroscopy (FTIR)

The dominant infrared instrument now in commonplace use is the FTIR spectrometer. These instruments initially came to prominence as high performance research tools [43, 44] in industry in the late 1970s. A variety of instruments are now available from low cost bench spectrometers, to dedicated process analysers, through to systems interfaced as dedicated detectors to other analytical techniques (i.e. microscopy, TG-IR and GC-IR). FTIR spectrometers have largely replaced dispersive spectrometers for mid-infrared applications [45, 46]. In a dispersive instrument a prism or grating is used to resolve the radiation into its separate components for successive measurement whereas in an FTIR instrument a Michelson interferometer is used. An interferometer measures all the spectral radiation simultaneously reducing the measuring time of the instrument in proportion to the number of spectral elements (Fellgett advantage). The components of a Michelson interferometer are shown in figure 2.3.

Figure 2.3 Schematic of a Michelson interferometer



The principle behind its operation is best illustrated as seen above by the use of monochromatic light (i.e. single wavelength, λ). The components are comprised of a beam-splitter and two mirrors, one fixed in position, while the other is scanned back and forth. The collimated monochromatic radiation incident on an ideal beam-splitter will be divided into two equal beams, such that 50% is transmitted to one of the mirrors while 50% is reflected to the other mirror. These two beams are then reflected back and returned to the beam-splitter, where they are recombined and 50% is sent via the sample to the detector. The remaining 50% is essentially lost as it is sent back towards the source. Because the moving mirror is scanned, the optical path difference between the two recombined beams will be varied. When the path difference is an

integral number of wavelengths, then the beams will be in phase and constructive interference will occur between the re-combined beams. Destructive interference occurs when the path difference is $\lambda/2$, i.e. when the moving mirror has moved a distance equivalent to $\lambda/4$ from the in phase position. These differences in optical path are often referred to as optical retardation. If the moving mirror is scanned at constant velocity, the detector will measure a sinusoidally varying signal as the beams move in and out of phase. The intensity measured is therefore a function of the moving mirror displacement. As can be seen in figure 16, as the moving mirror travels away from the position of zero path difference between the two recombined beams, the intensity of radiation reaching the detector varies as a cosine function of the optical retardation [47], which is expressed as an equation of the form:

Equation 7

$$I(\delta) = B(\nu) \cos(2\pi\delta/\lambda) = B(\nu)\cos(2\pi\delta\nu)$$

Where $I(\delta)$ = the intensity of radiation at the detector

δ = the optical retardation

$B(\nu)$ = the single-beam spectrum intensity at wavenumber ν

The single beam spectrum is then calculated by computing the cosine Fourier transform of $I(\delta)$. The combination of the monochromatic source of wavelength λ (the spectrum) and the cosine function (its interferogram) are known as a Fourier transform pair (fig.16). For a polychromatic source (i.e. broad band infrared source) the interferogram represents the summation of all the individual cosine waves corresponding to each of the wavelengths in the source. These will only be in phase

at the position of zero path difference. Hence the strong interferogram centre-burst normally observed. For a continuum source equation 7 becomes:

Equation 8

$$I(\delta) = \int_{-\infty}^{+\infty} B(\nu) \cos(2\pi\delta\nu) d\nu$$

Where its spectrum can be calculated from equation 9,

Equation 9

$$B(\nu) = \int_{-\infty}^{+\infty} I(\delta) \cos(2\pi\delta\nu) d\delta$$

Because the moving mirror only moves a finite distance (i.e. cannot move from minus to plus infinity) during the collection procedure, an apodisation function is used to smoothly truncate the interferogram to remove spurious truncations. A variety of these functions are available, the effect of which convolutes the spectrum and introduces positive and negative side lobes to spectral bands. These lobes can be effectively minimised but at the expense of increased bandwidth and reduced intensity. High-resolution experiments may benefit from the use of an alternative apodisation function. The spectral resolution is directly related to how far the moving mirror has travelled. In order to resolve two bands, the mirror travel must equal or exceed one complete pattern generated between the two cosine waves in the interferogram, which represent two wavenumber positions of two bands. The approximate spectral resolution is given by (equation 10):

Equation 10

$$\Delta\nu = 1/\delta_{\max}$$

2.1.5 Potential advantages of Interferometric measurements of vibrational spectra

2.1.5.1 Fellgett advantage

In a monochromatic dispersive spectrometer, the single channel detector observes only one resolution element at a time and takes a long time to scan through each consecutive wavenumber in order to build a spectrum (typically 10-20 mins from 4000 -400 cm^{-1}). In an interferometer all the wavenumbers are detected simultaneously, for an equivalent wavenumber range spectrum (1 second or less) unlike a dispersive spectrometer, which spatially separates the spectral radiation into individual components for successive measurement. All other parameters being equal (source, detector, throughput etc.), there is a clear time advantage.

2.1.5.2 Connes advantage

In the past, the optical path difference was accurately determined using a cadmium or mercury lamp beam. In more modern instruments, a He-Ne reference laser monitors accurately the position of the moving mirror. This ensures accurate wavenumber positioning in the Fourier transformed spectrum and also triggers data acquisition. This precision allows comparative wavenumber calculation (usually quoted as better than 0.01cm^{-1}) and therefore accurate spectral superimposition, which are important

for spectral subtraction and spectral comparisons. However, it must be realised that sample preparation can be responsible for the change in position of spectral features.

2.1.5.4 Jacquinot advantage

Here the advantage is related to the signal throughput. The signal throughput in an interferometer is determined by the collimating area or the diameter of the circular entrance aperture, the so-called Jacquinot stop. The area of this aperture is generally considerably greater than the slits used within a monochromator system. The extent of this gain is resolution and wavenumber dependent, but improvements are in the order 50-100 times.

2.1.6 Transmission Spectroscopy

This classical method involves passing radiation through the sample and is known as transmission spectroscopy, a plot of difference in energy between the beams against wavelength/wavenumber is recorded. The amount of infrared radiation transmitted, T , by a sample is given by

Equation 11

$$T=I/I_0$$

Where, I_0 represents the intensity of infrared radiation incident on the sample, and I represents the amount of radiation transmitted by the sample. This standard plot is per cent transmission (%T) or transmittance (0-1T) against wavenumber (cm^{-1}).

A wide range of sampling techniques exist, which include mulls, potassium bromide (KBr) disks, free standing films and sodium chloride (NaCl) plates. Sodium chloride plates have been used in this thesis, the resulting transmission spectra are then converted to absorbance. Absorbance is logarithmically related to transmittance by the equation:

Equation 12

$$A = \log_{10}1/T$$

In order to produce quality spectra, good practice should include:

- (1) storage of NaCl plates in a dedicated dessicator to prevent contact with water.
- (2) Cleaning before and after use with pure acetone to remove organic residues and subsequently allowed to dry before use or storage.
- (3) Purging of the instrument with dry/scrubbed air in order to remove carbon dioxide and water.

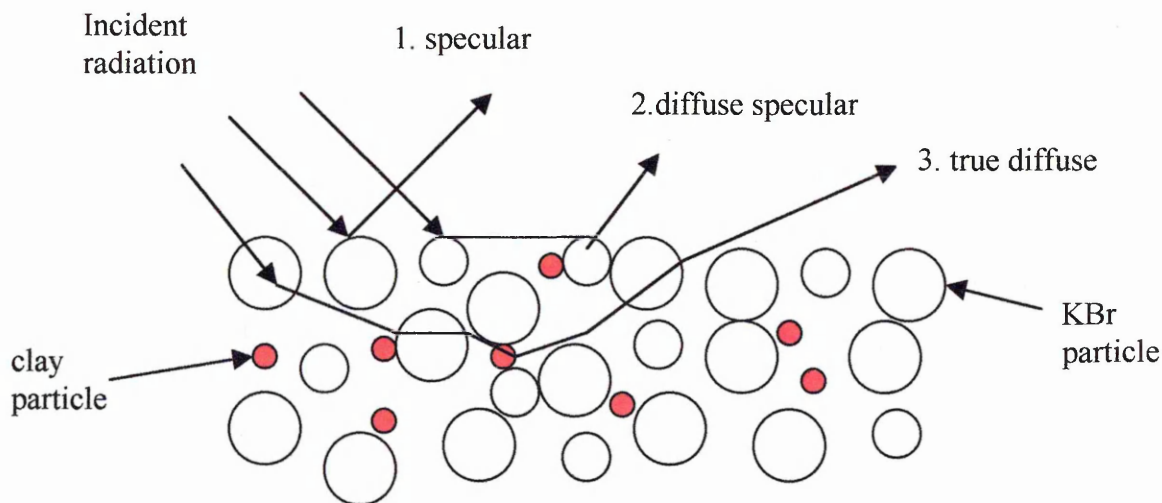
2.1.7 Diffuse Reflectance Infrared Fourier Transform Spectroscopy (DRIFTS)

Spectroscopic studies using special techniques of sample preparation have led to major breakthroughs in the investigation of clay organic complexes. Infrared spectra can provide characteristic information regarding the molecular orientation of organic probes in the interlayer space, mechanisms of interaction with the silicate surface, interlayer cations, residual water and interactions between the probes themselves. The infrared (IR) method has the ability to detect changes in chemical composition taking place in the interlayer space under the effect of heat, evacuation or changing humidity. Therefore Infrared is complementary to X-ray diffraction (XRD) which can

provide information regarding the modification of clay basal spacing in terms of probable packing and orientation. Infrared spectroscopy has contributed considerably to the understanding of the nature of clay-organic interactions by providing evidence that molecules are protonated in the interlayer space.

The most common infrared sampling technique used in this thesis is DRIFTS spectroscopy. In 1991 Mitchell [48] reviewed the literature for the mid-infrared region covering the fundamental theory and its applications to polymer powders, films and fibres. A more detailed review was written by Griffiths and Fuller [49] in 1982. There are three main modes in which the incident radiation can be reflected from a powdered sample in a DRIFTS experiment. These three modes are shown in Figure 2.4.

Figure 2.4 The three modes of reflection during a DRIFTS experiment



(1) Reflection mode 1 represents the *Fresnel specular component* [50], which is reflected from the first interface it encounters at the top of the sample. It also known as true specular reflectance, which is a function of [51]

(a) refractive index

(b) absorptivity of the sample

Here the angle of the incident radiation is equal to the angle of reflection from the sample. Because this type of reflection is not transmitted through any sample grains, it carries no analyte information and must be prevented from reaching the detector, to avoid a poor relationship between band intensity and sample concentration. This leads to much of the non-linearity associated with DRIFTS spectra. This type of radiation is removed by the rear ellipsoidal mirrors of the DRIFTS accessory [52]. The reflection from the top surface of the sample also retains the polarization of the incident beam. In general this radiation is easily prohibited from reaching the detector. One scheme is to collect radiation that excludes the plane of incidence of the incident radiation [53] whereas another scheme polarizes the incident radiation and collects radiation through an analysing polarizer orientated at 90° to the polarization of the incident field [54].

(2) Reflection mode 2 represents the *Fresnel diffuse component*. The beam undergoes multiple reflective interactions off particle surfaces without penetrating the surface and emerges from the sample at a random angle, which is a function of the refractive index. Therefore the incident angle of the IR beam is not equal to the reflected angle. This type of reflection does not carry any analyte information because it has not been absorbed. Unlike the Fresnel specular component this ray

may ultimately emerge at any angle relative to the incident radiation. For this reason it is optically indistinguishable from the true diffuse reflectance. However, neither of the methods to reduce Fresnel specular reflectance will reduce diffuse Fresnel reflectance. One method that will apparently decrease diffuse Fresnel reflectance is to grind the sample and diluent to very small particles. This decreases the fraction of incident radiation that is reflected out of the sample without being transmitted through a sample grain. The effect of using infrared absorbing materials as diluents was investigated by Brimmer and Griffiths [55]. In terms of clay materials, the use of KCl as a diluent is the source of certain potential problems as potassium and chloride ions can act as potential catalyst poisons which could clearly distort the effects of probe and interlayer cations reactions. Hence the use of KBr as a diluent. Other problems arising from using alkali halides include the presence of adsorbed water and organics at 3300 , 1640cm^{-1} , and 2950cm^{-1} respectively. Therefore, it is important that the alkali halide used should be very dry and clean.

(3) The reflected radiation that must reach the detector is reflection mode 3, which passes into the bulk of the material and undergoes reflection, refraction, scattering and absorption. This type of reflectance is known as true diffuse reflectance and satisfies the Kubelka-Munk function for intensity of absorption bands relative to concentration. This ray contains information about the absorptivity of the sample. However, there are several other factors, which can exert a significant influence over band shape and absorbance in DRIFTS spectra [56] these include:

- Refractive index of the sample
- Particle size considerations
- Sample homogeneity
- Concentration
- Use of pressure
- Sample height

2.1.7.1 Refractive index

The refractive index of a material can contribute to specular reflectance. In the case of organic samples, spectra can show pronounced changes in band shape and relative peak intensities, which in turn, contribute to the non-linear relationship between band intensity and sample concentration. With organic samples, the spectra display pronounced changes in band shape and peak intensities, resulting in the non-linearity associated with DRIFTS. For inorganic samples, strong specular reflection can result in complete band inversions (Reststrahlen bands). Reststrahlen effects occur as a result of a rapidly changing index of refraction near the dispersion frequency in highly absorbing (or ionic) materials and results in a broad band of reflection between the longitudinal and transverse optical phonon modes. This is the result of surface effects dominating over bulk effects, and specular, rather than diffuse reflectance, results [57]. Specular reflectance has been found to be reduced (in the mid-infrared) by grinding of the sample into very small particle sizes (less than the wavelength size) or by dilution in the appropriate matrix as previously mentioned.

2.1.7.2 Particle size

Another major consideration during DRIFTS is particle size. Studies of neat azobenzene have shown that band widths and relative intensities are dramatically altered as particle size decreases. In the case of highly absorbing inorganic materials with strongly varying refractive indices these effects are even more pronounced. For these samples the domination of specular contributions can be a problem if the particle size is too large. In their first paper, Fuller and Griffiths [58] investigated the effects of particle size and also found that small average particle sizes ($< 10\mu\text{m}$) gave better spectra and reduced peak widths compared to larger particle sizes ($> 90\mu\text{m}$). Therefore maximising DRIFTS spectra must involve some knowledge of the optimum grinding time for sample/diluent mixtures.

2.1.7.3 Pressure

The effects of pressure on KBr pellets are known to induce phase transitions as shown by a variety of workers [59,60]. Pressure applied to DRIFTS samples has been shown to have real effects on band intensity. Conventionally, a simplified equation, derived from Schuster [61] and the Kubelka-Munk [62] theory of light absorption is used to relate a chromophore concentration to the intensity of the samples diffuse reflectance:

Equation 13

$$f(R_{\infty}) \equiv (1 - R_{\infty})^2 / 2 R_{\infty} = K/S \propto c. [63]$$

In real terms the band intensity $f(R_\infty)$ in DRIFTS is equal to the ratio of the absorption coefficient (K) and the scattering coefficient (S). The assumption that both (K) and (S) are constant throughout the whole sample volume is unlikely, even in well mixed samples. The absorption coefficient is equal to $2.303 ac$, where a is the absorptivity of the absorption band of interest and c is its concentration. Because neither a or c is dependent on the pressure at which the sample is compressed, then provided the pressure is released before the spectra are taken, K should be independent of the pressure to which the powder is subjected. However the effect of pressure on scattering coefficient could be very large as shown by Yeboah et al [64]. The scattering coefficient in turn determines the magnitude of the interaction of the incident beam before it emerges from the sample. Therefore (S) to some degree determines the depth to which the beam penetrates the sample. The smaller the (S) value the greater the diffuse reflectance $f(R_\infty)$. In real terms there must exist a limiting particle size smaller than the wavelength of the radiation, below which the Kubelka-Munk equation is invalid. The use of pressure to overcome the non-reproducibility in spectra was observed by Yeboah et al [64], who found that two IR absorption bands in the caffeine spectrum increased by almost an order of magnitude between a sample prepared without pressure treatment and one subjected to 12,000 psi for 5 minutes. It was assumed that this resulted from the decrease in scattering coefficient an effect often seen when pressing pellets for IR analysis. However, this effect is particular to the sample type and Hembree and Smyrl [66] found that the reproducibility (std dev: $\pm 3\%$) found by Yeboah et al [64] could be replicated by careful sample preparation. Krivacsy and Hlavay [68] found that when applying pressure (a magnitude lower than Yeboah) to 1.1 Mpa the scattering coefficient, increases with applied pressure, which is in contrast to Yeboah et al. However,

pressure is necessary to obtain reproducible results (RSD = $\pm 3\%$) especially for the purpose of quantitative analysis.

In comparison to transmittance measurements, DRIFTS has an extremely broad sampling range. However, samples which have a high refractive index produce dramatic increases in specular reflectance and may indeed be uninterpretable without adequate dilution with a non absorbing matrix. Grinding is therefore recommended to minimize specular reflectance and sample scattering effects especially in terms of quantitative measurements. Generally DRIFTS spectra are qualitatively similar to those produced by transmittance or pellet methods, yet quantitatively they exhibit higher sensitivity and are less subject to scattering and sloping baselines than traditional KBr pellet measurements.

2.1.7.4 Sample height

It is necessary to optimise sample height in relation to the optics of the system in order to ensure that the point of contact of the IR radiation is at the focal point of the mirror arrangement. Murthy et al [69] showed that the effects of sample height on the intensity of the Si-O combination band at 1870cm^{-1} , Si-O stretch at 806cm^{-1} and the C-H stretch at 3000cm^{-1} were significant

There are several advantages to using DRIFTS for the study of the interactions between probe molecules and clay.

(1) There is minimal or little sample preparation in comparison to KBr disks, which through the application of preparation pressure, can change the absorption by clay.

functional groups, which are important to characterisation of minerals and probe interactions.

- (2) The ability to look at wide sample concentration ranges.
- (3) High sensitivity (low ppm levels).
- (4) Useful overtone and combination bands observed.
- (5) Band intensity enhancement at high wavenumbers
- (6) The ability to analyse irregular surfaces e.g. sandstone grains

2.1.8 Variable Temperature-Diffuse Reflectance Infrared Fourier Transform Spectroscopy (VT-DRIFTS)

VT DRIFTS allows diffuse reflectance spectra to be obtained at various temperatures and as previously mentioned, is complementary to other techniques used in this thesis. The information it provides on the changes of mineral/probe interactions can be correlated to other thermal techniques, for example, TGA, TG-MS, TG-FTIR and variable temperature XRD (VT-XRD) in order to elucidate the relationships between thermal properties and structural changes.

There are two types of experimental approach to VT DRIFTS [70]

(1) Stepped VT-DRIFTS [71]

Here the sample is allowed to equilibrate at the required temperature at which time a spectra is recorded. Or alternatively, the sample temperature is cooled to an arbitrarily selected temperature before recording a spectra.

(2) Ramped VT-DRIFTS

Here the sample is heated at a constant rate and each FTIR interferogram is collected over a temperature range [references 1,2,5,-8 in 70]. Stepped VT-DRIFTS requires more time than ramped VT-DRIFTS but generally yields fewer baseline distortions. Baseline distortions are typically broad features, which are imposed on DRIFTS spectra. VT-DRIFTS baseline errors can be minimised by measuring sample and reference interferograms at the same temperature. However, they cannot be eliminated by this procedure as they are the result of instrumental fluctuations (output variabilities in source, interferometer, detector and amplification electronics) occurring between reference and sample spectra [72, 73]. Due to the time constraints, collection of both sample and reference over a range of temperatures may span a couple of days. Inevitably changes in atmospheric water vapour spectra will result. The sample spectrum may therefore have a water vapour spectrum superimposed on it, and as a result, the bands of interest may become obscured. Taking steps to minimise the effects of water vapour will therefore consist of:

- (1) A good and reliable temperature controller to ascertain/compare dehydration temperatures
- (2) Dry sample storage
- (3) purging the instrument with dry air (CO_2 and H_2O are removed)
- (4) purging the sample holder with nitrogen
(to remove water vapour and other gaseous products evolved from the sample, which also speeds up the process of equilibrium).

Water vapour subtractions are then made using the software package. A spectra of water vapour is obtained by ratioing interferograms of two consecutive temperatures

from the stepping scheme, i.e. 100 and 125°C. The resulting spectra is then subtracted from the sample spectra recorded at 125°C. Due to the problems already discussed, complete subtraction is not possible. The Stepped VT-DRIFTS is the method used throughout this thesis.

2.1.8.1 Room temperature (RT) and VT-DRIFTS sample preparation

The KBr diluent as previously mentioned, may take up water and organics whilst containing inorganic impurities. Therefore to minimise these effects, the KBr was dried overnight at 400°C, then stored in an airtight dessicator. The instrument was then sealed and constantly purged with dry air to minimise carbon dioxide and water vapour contributions. Samples for RT and VT DRIFTS analysis were then diluted to 5% (by weight) in KBr and mixed for a period of 40 seconds in an agate pestle and mortar. For ST DRIFTS the sample is then placed on the sample holder, whereas in VT DRIFTS the sample is placed in an evacuable cell. All DRIFTS spectra in the following studies were produced using a Mattson Polaris FTIR spectrometer equipped with a Graseby Specac "Selector™" DRIFT accessory. The first VT DRIFTS spectrum was then obtained and the time recorded as time 0. The instrument was then left to purge overnight and the sealed environmental chamber (where the sample resides) , gently flushed with nitrogen and then sealed. The next morning nitrogen flow was resumed and spectra were collected at intervals of 25°C up to 200°C and of 50°C thereafter. Temperature within the environmental chamber was controlled by a Graseby Specac P/N 20130 series automatic temperature controller, which has a range of 0-500°C.

Table 2.1 Instrumental parameters for collection of FTIR spectra

Parameter	Setting	Parameter	Setting
Resolution	4.0cm ⁻¹	Start wavenumber	400cm ⁻¹
Sample scans	276	End wavenumber	4000cm ⁻¹
Background scans	276	Apodization function	Triangular
Iris	85%	Signal gain	1

2.1.8.2 Effects of heat on VT DRIFTS spectra

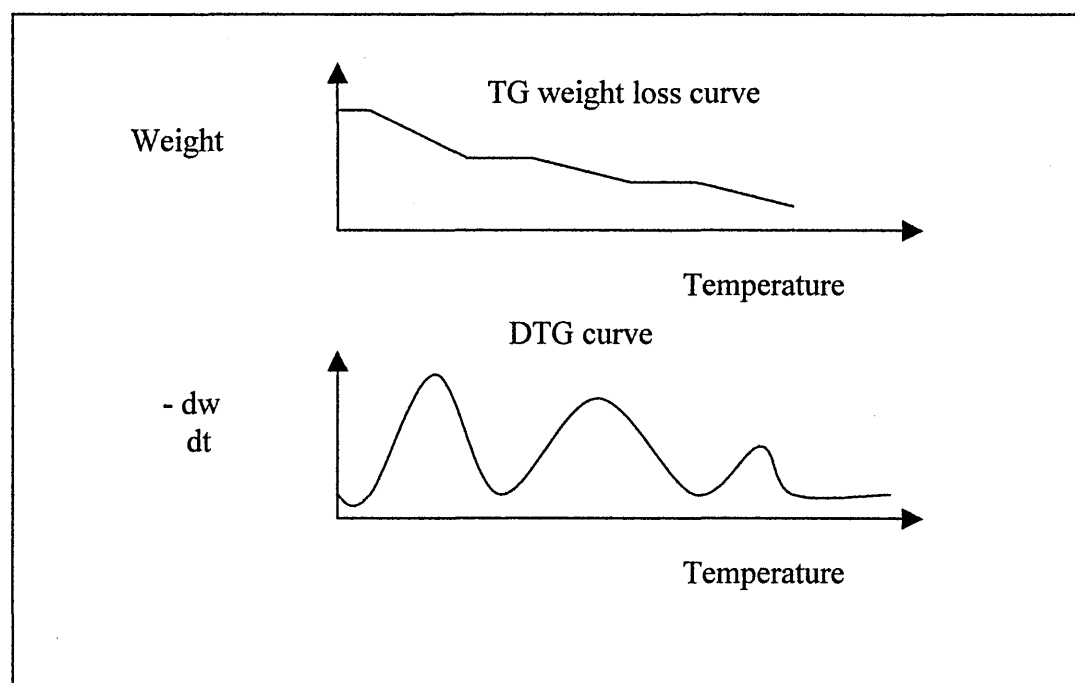
Hamadeh et al [74] have shown that the thermal emission from the heated cell effects the band intensity, because the d.c signal from the sample decreases the sensitivity of the MCT detector for unmodulated IR radiation. It has been further shown [75, 76] that thermal expansion of the sample post during a VT DRIFTS scan also effects band intensities as the sample is moving away from the optimum position. In ramped VT DRIFTS this is more of a problem, but it also highlights the importance of taking a spectra after it has equilibrated at a given temperature and the need to record reference materials under the same temperature conditions. This approach also reduces the occurrence of baseline offset.

2.2 Thermogravimetric Analysis (TGA)

The thermal stability of mineral complexes can be investigated using a variety of thermal techniques, including TGA, DTA (differential thermal analysis) and DSC (differential scanning calorimetry). The technique used throughout this thesis is

TGA. TGA involves the continual recording of sample weight when subjected to a precise temperature program [77]. Samples may be heated from room temperature to 1500°C. The TG curve plots weight decreasing downwards on the y axis and temperature increasing to the right on the x axis (fig. 2.5). This is known as a TG weight loss curve. However, in this format, subtle weight changes can be difficult to determine. Alternatively, the negative derivative curve ($-dw/dt$ -DTG) of the TG weight loss curve can be utilised, which shows the rate of change in mass in relation to the rate of change in temperature. These changes are shown as maxima, which are easier to relate to changes seen by other complementary thermal techniques i.e. TG-FTIR, TG-MS and VT DRIFTS.

Figure 2.5 TGA data output curves



The work was able to discern sample decompositional weight changes, however, TGA alone is unable to assign weight losses to specific components and must be used in conjunction with other thermal techniques, to provide corroborative evidence of the

association of specific weight losses with particular components. Paama et al [78], used TG-DTG, FTIR analysis of archaeological samples to determine the characteristic reactions associated during the course of heating. Similarly, Thornley and Primmer [79] utilised TG-evolved water analysis (EWA) to quantify clay minerals in whole rocks.

Several factors influence the shape of the TG curve, which are related to the sample, apparatus and experimental conditions [80].

(1) Sample size

Large samples can often produce poorer results in terms of resolution. This may be due to two factors

(a) a significant temperature gradient across within the sample

(b) the difficult evolution of volatile products escaping from the sample.

Therefore using a sample, which is consistent with the capabilities of the balance, is necessary. The samples analysed in this thesis were in the range 7-12mgs.

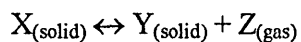
(2) Particle size distribution and packing density

These should vary as little as possible in order to optimise reproducibility

(3) The use of inert atmospheres/gas flow

Nitrogen was used to suppress the oxidation of organic material in clays in this thesis.

The effect of interaction of the sample and the gas involved with it is crucial. An atmosphere rich in decomposition product will delay the corresponding decomposition of the heated material until a higher temperature is reached. This principle is known as the Le Chatelier principle. Thus for the equilibrium



if we supply Z to the system we make it more difficult for X to decompose.

Therefore a nitrogen flow rate of $20 \text{ cm}^3 \text{ min}^{-1}$ was used.

(4) The sample holder

Obviously, the sample container must not react chemically with the sample as, e.g. silica containers do with certain carbonates. A refractory crucible was used in this thesis (4mm x 4mm). The depth of the container is also an important issue, as a shallow container will allow better exchange between the sample and its gaseous environment.

(5) Heating rate

Slow heating rates are the standard for a variety of reasons

Often with increased heating rates the resolution of the TG curve will decrease as the actual temperature between the sample and the recorded temperature increase.

Secondly maxima temperatures also increase with heating rate. Historically heating rates of $10^\circ\text{C min}^{-1}$ are standard. However, this will often depend on prior knowledge of the sample.

2.2.1 Experimental parameters

For samples where no evolved gas analysis was required, TGA was performed by a Mettler-Telodo TA8000 thermoanalyser. A nitrogen carrier gas flow of $20 \text{ cm}^3 \text{ min}^{-1}$ was maintained throughout. Samples were firstly conditioned at $35^\circ\text{C min}^{-1}$ for 15 minutes in order to remove physisorbed components and obtain a stable weight reading. Heating of the sample was then initialised at a rate of $20^\circ\text{C min}^{-1}$ up to 800°C .

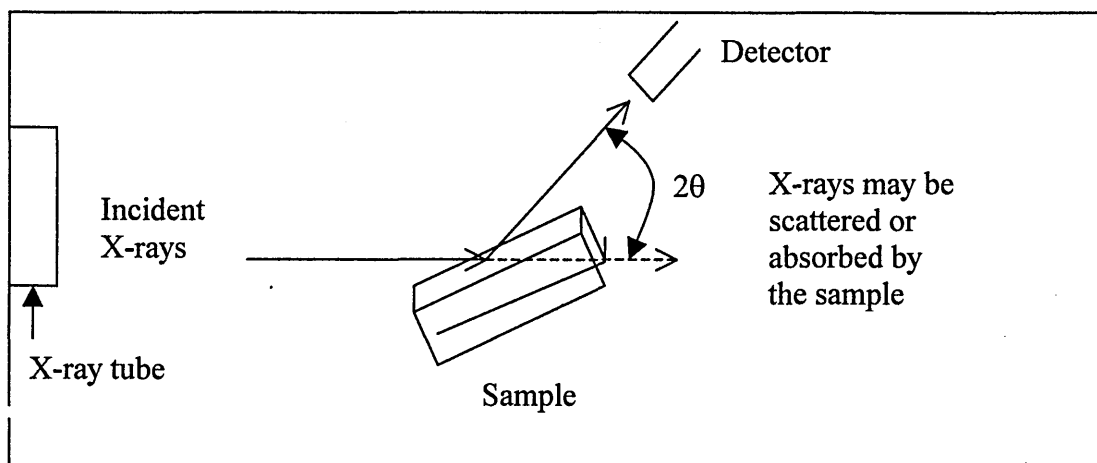
2.3 X-Ray Diffraction and Variable Temperature X-ray Diffraction (VT-XRD)

As far back as 1887 Le Chatelier had stated that clay sized material was composed of specific minerals. During the 1920's and the 1930's, very little distinction was made among fine grained materials, though petrographic microscope inferred that they were indeed crystalline. The same questions were being pursued by soil scientists, chemists and geologists. Were such materials crystalline or amorphous ?. XRD settled the controversy when Hendricks and Fry (1930) [81] and Kelley at al (1931) [82] provided evidence for these postulations. Subsequently, Hendricks and Teller [83] introduced the theoretical basis for XRD from a stack of clay mineral layers. It is a powerful technique used to identify crystalline phases present in materials [84,85, 86]. In the context of this thesis, XRD was used:

- (a) To evaluate the d_{001} spacing of swelling minerals to determine if potential probe molecules have successfully intercalated into the interlayer space.
- (b) To determine the molecular orientation of potential probe molecules in the interlayer space of the above swelling minerals
- (c) To identify crystalline phases of potentially interfering minerals in order to characterise the constituents of standards used for EGA
- (d) VT-XRD therefore provides evidence regarding the thermal stability and orientation of molecules in the interlayer space.

Although quantitative analysis is possible using XRD, there are various reasons why it is not used in this thesis (see: Traditional and Current Methods of Characterising Minerals). In general, from the point of view of reproducibility, XRD is dependent on many factors including sample length, thickness, position, alignment, sample homogeneity and the quality of the standards used. Hence, sample preparation can adversely compromise quantitative analysis. Secondly, quantitative XRD does not have the ability to determine the differences between surface and bulk mineralogy. Instead, it provides information about the bulk properties of whole populations, information averaging as many as perhaps 10^{11} - 10^{12} unit cells of billions of crystals [87]. The following section describes the XRD process.

Figure 2.6 The basic process of X-ray diffraction



The production of X-rays occurs when high speed electrons strike the atoms of any substance. The tube where the X-rays are produced is under vacuum. Inside this tube electrons are generated by a glowing tungsten filament (cathode). They are then accelerated by voltages (15-60Kv) in order to strike a metal target, (e.g. Cu) the anode. The accelerated electrons strike the inner more tightly bound electrons of the target and knock them out of their orbital positions, away from the influence of the

nucleus. This produces electron vacancies, which are filled by higher orbit electrons dropping inwards to fill the vacancy . The subsequent drop involves the production of an X-ray photon, the energy of which is proportional to the difference between the energy levels of the orbitals. This energy difference is dependent on the number of protons in the nucleus attracting the electrons.

In terms of clay minerals the spacing in the crystal structure may act as a diffraction grating for X-rays directed at the sample. The essential feature of the diffraction of waves of any wavelength is that the distance between scattering centres be about the same as the wavelength of the waves being scattered. The wavelength of X-rays and the structural spacing of crystals both have dimensions of about 10^{-8} cm ($\approx 1\text{\AA}$). The dimensions of X-rays and the spacing between atoms meet these conditions. The relationship between the wavelength of the radiation , the parallel lines of atoms causing the diffraction and the d spacing between these planes is called Bragg's law. If Bragg's Law is obeyed, diffraction will occur when a beam of X-rays falls on a series of atom-bearing planes, each a distance d apart at an angle θ , where:

$$n\lambda = 2d \sin \theta$$

(where λ is the wavelength of the rays and n is an integer). By rearranging this equation the d spacing may be calculated i.e.

$$d = n\lambda / \sin \theta$$

During an experiment, both the sample and detector are rotated by a goniometer in order to reach the required angle (2θ). For preliminary identifications of clay minerals, scanning from $2\theta = 2-33^\circ$ is usually considered adequate [88].

2.3.1 Experimental parameters

All samples were prepared by adding distilled water to maintain a dilute suspension, grinding for 30 seconds, followed by application of the suspension to a glass slide by a Pasteur pipette. The sample was then allowed to air dry under a protected cover. Untreated samples (i.e. no probe) were then analysed. Samples for probe applications were then put in a vapour saturator for fixed periods. For both room temperature and VT-XRD, samples were presented to the Phillips PW1830 X-ray diffractometer operating at 40kV and 40mA. A Cu K α radiation source was used, with a wavelength of 1.5418Å. The diffraction patterns were recorded with an angle range of 2-35° 2 θ at a scan rate of 2°2 θ per minute unless otherwise stated. VT-XRD traces were collected using the same instrumental parameters and subjected to a temperature ramp similar to that found in the VT DRIFTS experiments.

2.4 X-Ray Fluorescence Analysis (XRF)

XRF is a technique used to determine the quantity of elemental oxides present in a sample. X-rays are directed towards a sample and elements present in the sample produce characteristic fluorescence radiation at specific wavelengths. The amount of fluorescence at a specific wavelength is then related to the concentration of the element in the sample. XRF was utilised in this study to estimate the chemical composition of clays.

2.4.1 Experimental parameters

Each sample was ground into a powder and dried at 120°C. The dried material (1g) was then mixed with lithium-tetraborate ($\text{Li}_2\text{B}_4\text{O}_7$ -5g), put into a platinum crucible and heated at 125°C for 6 minutes (i.e.750°C). The mixture was then swirled to improve the mixing process, heated for a further 6 minutes, poured into a mould and allowed to solidify before analysis. The sample was then analysed by the staff in the XRF unit using a Phillips PW 2400 XRF spectrometer.

2.5 Environmental Scanning Electron Microscopy (ESEM)

The advent of scanning SEM in the late 1940's has facilitated the three dimensional visualisation of clay particles, however, the use of Scanning Electron Microscope (SEM) as a commercialised instrument did not occur until 1965. All samples at this time were observed and analysed under a vacuum. The ESEM may be seen as a natural extension of the SEM. The former incorporates all the conventional functions of the latter, and , in addition, it opens many new ways of examining any sample, wet or dry, insulating or conducting.

However, by eliminating most of the sample preparation and high vacuum constraints of the sample environment, the ESEM has opened up SEM to a host of applications. These include wet, oily, dirty, non-conductive samples, which may be examined in their natural state without modification or preparation. The result is high resolution imaging of samples of any composition in a gaseous environment, at pressures as high as 50 Torr, and temperatures as high as 1500°C. What makes this technique particularly useful is that the interaction of the electron beam with the

sample generates a variety of signals, some of which are X-rays, that are characteristic of the sample and inorganic atoms bound to its surface.

Examples of current uses of ESEM relating to surface chemistry are: corrosion studies of stainless steel where the various products formed can be monitored and analysed in-situ, or during and after formulation [90]. Crystal and plaque formation associated with bio-corrosion have been studied by observing the wetting properties and differential hygroscopicity on a microscale [91]. Energy dispersive spectroscopy and microanalysis in ESEM has demonstrated new uses and great promise [92, 93]. The study of clay minerals using ESEM has mainly been concerned with wettability, the effects of swelling in expanding clays due to water, in hydrocarbon reservoirs, water sensitive sandstones and mudrocks [94, 95, 96]. Or as new techniques to investigate phase interactions within reservoir rocks [97].

In terms of the work in this thesis, the conventional SEM (CSEM) could not be used for several reasons. Firstly, the requirement that samples must be clean, dry and electrically conductive would necessitate lengthy preparation. Secondly, the process of making a sample electrically conductive would entail coating in a conductive material such as carbon or gold, in turn interfering with the detection of clay probe interactions. Even if this were not the case, the necessity to maintain a high vacuum within the sample chamber would remove any potential probe molecule from the mineral surface.

The ESEM differs from the SEM in two fundamental ways:

- (1) The ability to operate a gaseous pressure in the sample chamber
- (2) A differential pumping system

An ESEM has been described as a SEM that can operate from high vacuum up to at least a pressure required to maintain fully wet samples [89]. The implications of this capability are enormous. In short, the ability to operate a gaseous pressure in the sample chamber defines the ESEM. The gas inside the chamber is ionised by the electron beam and becomes a good conductor, thus freeing the sample of the need for conductive coatings or chemical treatment. Apart from the gas pressure variation, temperature variation by use of cold and hot stages is also possible. The process of image generation can be found in greater detail in reference [98].

2.5.1 X-ray analysis in the ESEM

The interaction of the electron beam with the sample, produces X-rays. The lack of charging artefacts in the ESEM has direct benefits for X-ray analysis. Greater detail regarding characteristic x-rays can also be found in Vaughan [98, 100] and references there in.

Because of its poor spatial resolution, the X-ray signal is more often used for analysis than imaging. A qualitative analysis seeks to determine the presence or absence of characteristic peaks in the spectrum. A quantitative analysis tries to derive the relative abundances of elements in the sample from a comparison of their corresponding peak intensities, to each other, or to standards.

In the ESEM, the lack of charging artefacts has direct benefits for X-ray analysis. It eliminates the interference normally associated with sample coatings and it permits analysis at higher accelerating voltages on non-conductive samples.

Another important factor to make X-ray analysis easier and more accurate, is the necessity to consider what excitation energy is required to detect a particular

element line. Generally the simple well-separated peaks are the lowest order peaks, K lines are simpler than L lines, which are simpler than M lines. Efficient X-ray excitation, usually requires a beam voltage two to three times the energy of the line of interest. Low beam energies are often used in CSEM to reduce charging but also make X-ray analysis very difficult.

However ESEM is not without its problems, the presence of skirt electrons can further degrade X-ray spatial resolution. Skirt is formed by electrons scattered out of the beam by gas molecules. Displacement of a scattered electron from its original destination on the sample is a function of:

- (a) Scattering angle
- (b) Remaining distance to the sample from the scattering site

Each successive scattering event increases the potential range of displacement. The size of the resulting electron skirt depends on:

- (a) BGPL (beam gas path length-distance between last aperture and sample surface)
- (b) Sample Chamber pressure

These potential problems can be minimised by :

- (a) Minimising the path length reduces the likely displacement from any one scattering event. In ESEM, this is achieved by using an ESD that lowers the sample away from the pole piece while still maintaining a short gas path. In this configuration the X-ray detector can still be positioned close

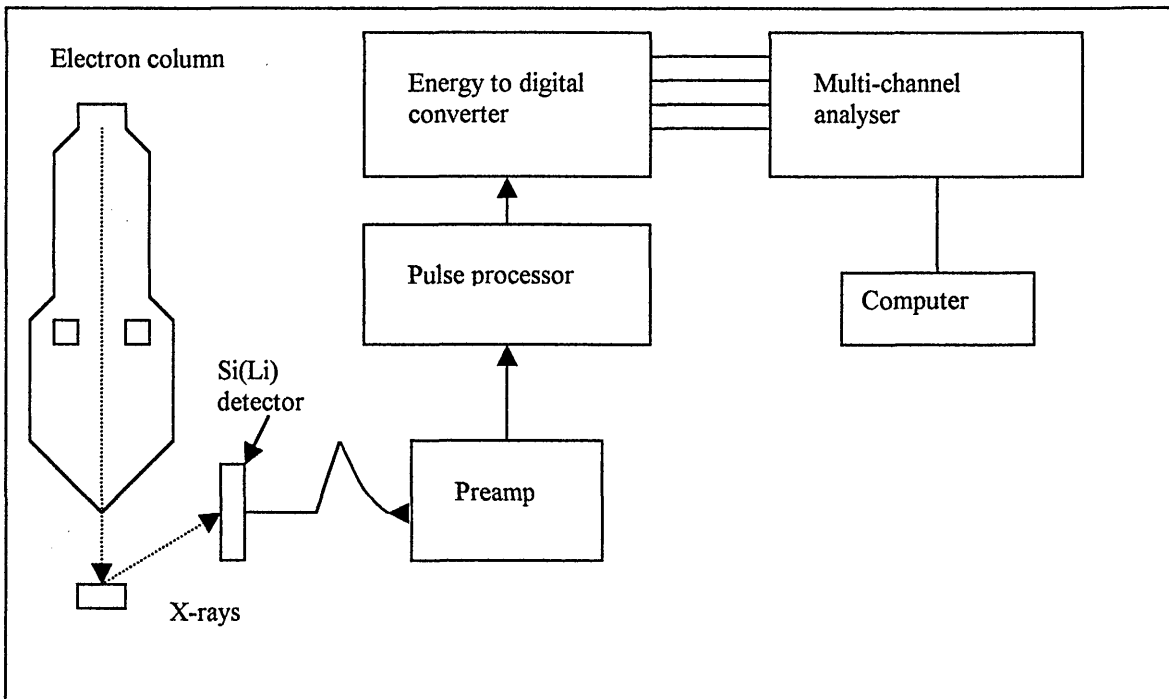
enough to collect X-rays at an efficient thirty degree take-off angle, while skirt is kept to a minimum by a gas path length of only 2mm.

(b) Minimising the chamber pressure also reduces the scattering probability

There is one other source of X-ray background of which the operator must be aware. Beam electrons can also excite X-ray from the chamber gas. These occur as a low level signal characteristic of the gas composition. Again, minimising gas path length and pressure reduces this signal. Therefore gas choice may be an issue, depending on the elements within the sample matrix.

The components of a typical energy-dispersive microanalysis system are shown schematically in Figure 2.7. The following paragraphs discuss the units of the system, starting with the detector.

Figure 2.7 Components of a typical energy dispersive microanalysis system



2.5.2 X-ray detector

All energy dispersive detectors have in common a solid-state detector, which is almost always manufactured from a single crystal of silicon. Appendix 1 shows a cross section of a typical lithium-drifted silicon detector.

2.5.3 Detection of X-rays

The process of x-ray detection is one of measuring the number of free charge carriers (electrons and holes) created in the crystal during the absorption of each X-ray. To allow this, the crystal is operated under a reverse-bias diode under an applied voltage of 100-1000 volts. Therefore, any free charge created within the diode leads to a temporary increase in its conductivity. If the resulting current is integrated with respect to time, the total charge conducted is found to be directly proportional to the energy of the absorbed X-ray.

Even in perfect semi-conductor crystals, some residual conductivity is expected, upon which X-ray absorption would be superimposed. This is known as leakage current and is caused by random thermal excitation of electrons across the gap between the valence and conductance bands. In order to minimize this current, detectors are operated at low temperatures by the inclusion of a liquid nitrogen cooling apparatus called a cryostat. A previously mentioned, crystalline imperfections and impurities can also contribute to conductivity. To overcome the problem of excess holes, caused by impurities and crystalline imperfections, a process called lithium drifting is applied, where lithium atoms are allowed to diffuse into the silicon crystal producing a lithium drifted silicon, or Si(Li), detector. Because of the

complexity of the interaction of X-rays with the Silicon lattice and competition between various energy processes, the magnitude of charge pulses may not be equivalent for identical X-rays. Instead, they vary statistically about some mean value in the form of a normal distribution. An indicator of the quality of a spectrometer (spectral resolution) is the width of this distribution relative to its height, measured as the full width at one-half its maximum height (FWHM). It is important to note that resolution is also a function of the energy of the X-ray measured (i.e. typically the 5.9-keV manganese $K\alpha$ line, at 1000 counts per second and an 8- μ sec pulse processor time constant).

2.5.4 Qualitative analysis

Qualitative analysis is the process of identifying which elements are present in a sample. An important statistical consideration in trace analysis is whether the element is present or not. At sufficiently low concentrations, it may only be possible to conclude that if element X is present, its concentration must be less than Z. This is known as the minimum detection limit (MDL). In microanalysis, we are concerned with the net peak intensity above the background signal. As previously mentioned, there is a counting error associated with any measurement of peak intensity. In practice MDL's are affected by experimental factors:

(1) Instrumental parameters

When making qualitative determinations based on relative line intensities, it is important to remember the significance of accelerating voltage. A perfect example is a comparison of copper at 10 and 20 keV. At 10 keV, the K lines at 8.04 and 8.91 are

not efficiently excited, in contrast to the L lines just below 1 keV. The line ratio changes dramatically as the accelerating voltage is increased to 20 keV. At least one set of X-ray lines can be observed below 10 keV for each element. Therefore energy dispersive spectra are acquired between 0 and 10 keV, though frequent use is made of higher voltages. The 0-10 keV acquisition range coincides nicely with the accelerating voltages available on modern SEM's (25-30 keV).

(2) Spectral peak overlaps

This is considered the greatest source of error in qualitative analysis. A notorious example is the overlap between barium and titanium. Titanium K lines appear at about 4.5 and 4.9 keV, whereas the strongest barium lines are at 4.5 and 4.8 keV respectively. Because of this overlap, information is required about relative emission intensities (peak height) to establish whether titanium emissions do or do not contribute to the two most intense peaks.

(1) Matrix effects

Since MDL's are a function of counts, it is also a function of counting time. Therefore there is a practical limit to increasing the acquisition time as a means of lowering the MDL. Nonetheless, MDL's as low as 0.01% are feasible under certain conditions. Refer to [101-102] for more extensive discussions of MDL's.

2.6 Evolved gas Analysis (EGA) by Thermogravimetric- Fourier Transform Infrared Spectroscopy (TG-FTIR) and Thermogravimetric-Mass Spectrometry (TG-MS)

The EGA in this thesis was performed on a Unicam-Synergic Chemical Analysis System (Synergy system). The TGA records the weight loss of a sample, whilst the FTIR and/or MS simultaneously detect the evolved gases corresponding to those weight losses in real time. This is known as real time analysis, where time/temperature related weight losses observed in TG are related to spectroscopic features seen in both FTIR and MS. For the purpose of this thesis, real time MS and FTIR will be known as (RT-FTIR) and (RT-MS).

FTIR uses characteristic functional group vibrations whereas MS produces a pattern consisting of a diagnostic pattern of charged particles and molecular fragments based on mass/charge (m/z). TG-FTIR, TG-MS and FTIR-OTM are linked via a series of transfer lines.

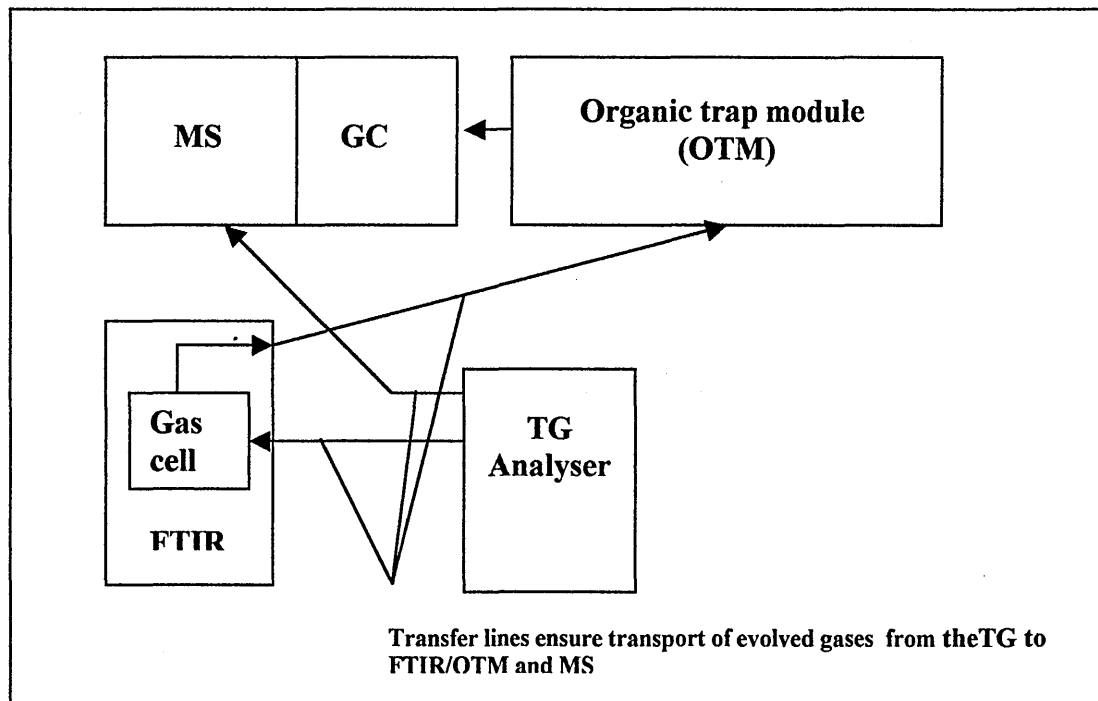
The function of the OTM is to trap evolved gases for future analysis by GC-MS (post run analysis).

2.6.1 (EGA)TG and FTIR

The basic principles of both TG and FTIR have already been outlined in sections 2.1-2.2. The reader should note that FTIR spectra collected by the Synergy system will be of the evolved gases. In comparison to the corresponding solid and liquid phase spectra, bands observed in gas phase spectra are generally sharper and positioned at

higher frequencies. For the purpose of this thesis gas-phase FTIR is known as GP-FTIR.

Figure 2.8 Diagrammatic representation of the SYNERGY EGA system



2.6.2 Mass spectrometer

The Synergy system Mass spectrometer is a (ATI Unicam Automass System 2) quadrupole mass spectrometer. In this thesis, the MS was operated in the Electron Impact (EI), positive ionisation mode. It is constructed of three main units:

- (1) Ion source
- (2) Ion analyser (quadrupole ion filter)
- (3) Mass detector

2.6.2.1 Ion Source

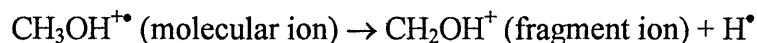
The ion source is where the sample is introduced into the MS. In RT-MS the TG-MS transfer line is directly interfaced with the ion source. The charged particles (ions) for mass analysis are formed by Electron Impact (EI) ionisation. The sample passes through an electron beam (70eV) and ionisation occurs when an electron strikes a molecule and imparts enough energy to remove another electron from that molecule.

Methanol, for example, would undergo the following reaction in the ion source:

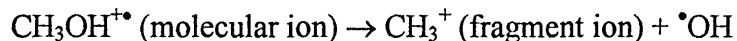


EI ionisation usually produces singly charged ions containing one unpaired electron. The charged ion, which remains intact, is called the molecular ion. Energy imparted by EI is more than that required to produce the molecular ion, this excess energy causes instability in the molecular ion, causing it to break into smaller fragments to give a characteristic mass spectrum. The methanol ion may fragment in various ways, with one fragment carrying the charge and one fragment remaining uncharged.

For example:

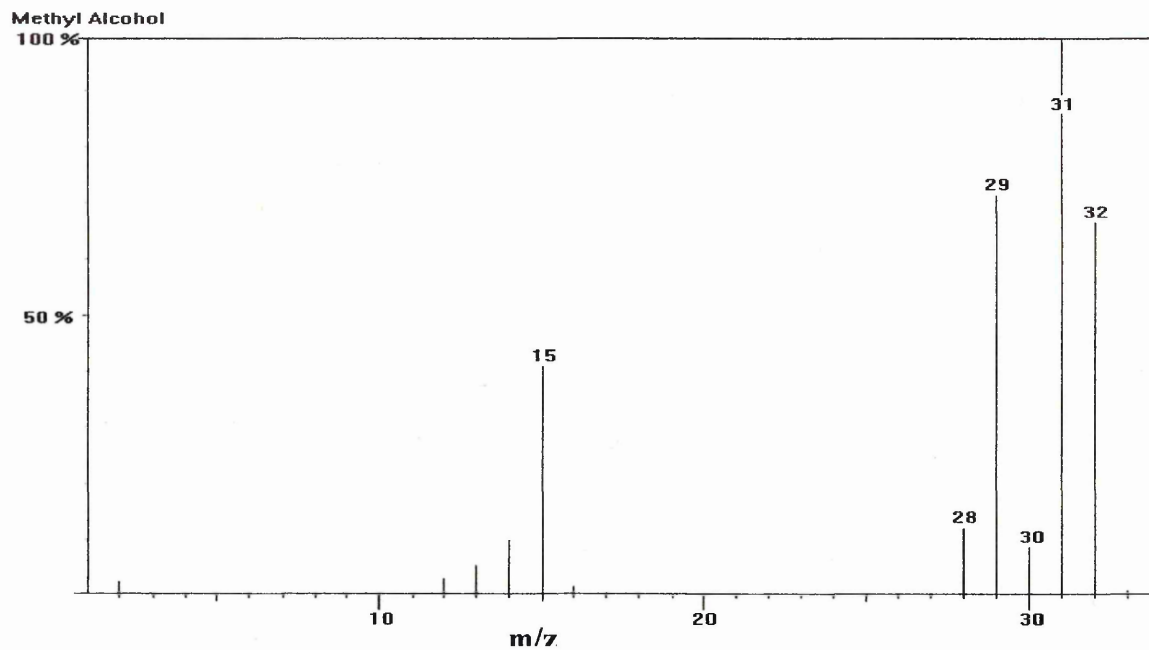


Or



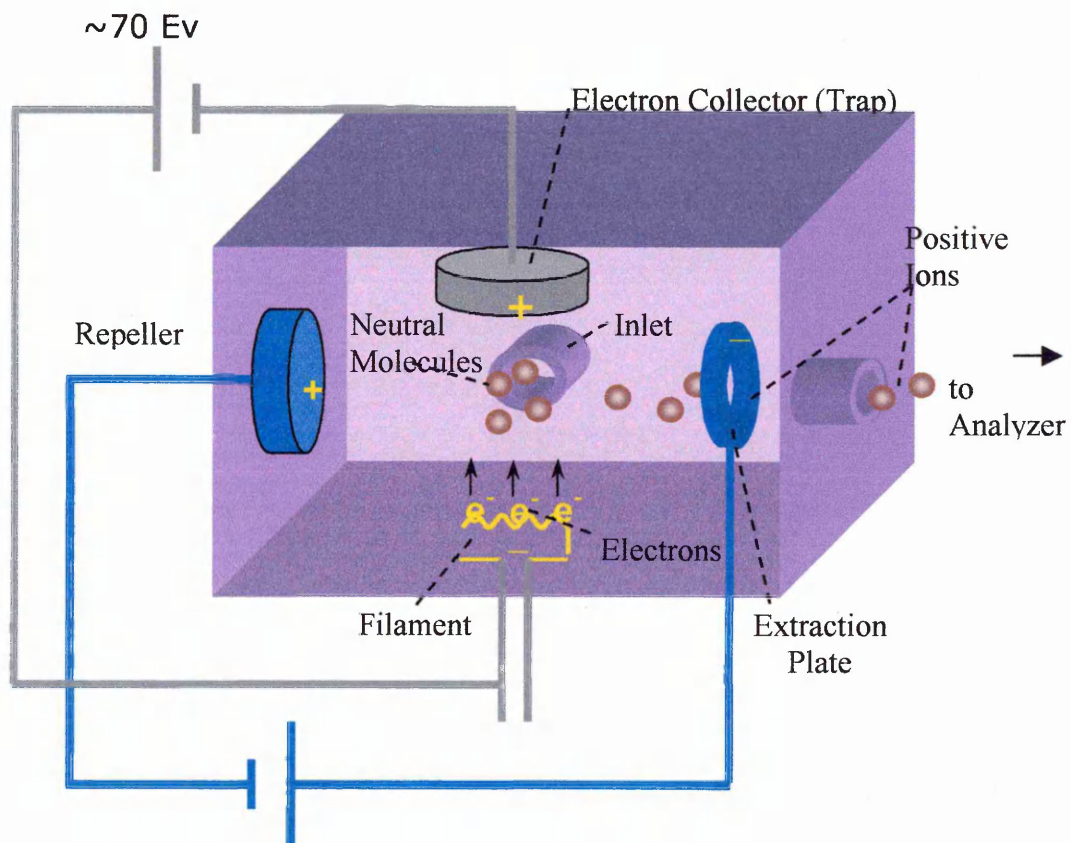
A typical EI fragmentation pattern of methanol is shown in figure 2.9.

Figure 2.9 EI fragmentation pattern of Methanol



A schematic of the EI ion source is shown in figure 2.10

Figure 2.10 EI ion source



From an analytical (qualitative) viewpoint, the important features of this type of spectrum are:

- (1) The ions produced are largely singly charged and the m/z ratio corresponds to the 'weight' of the elements involved. Not only is the elemental composition of each fragment ion accessible, but so are the molecular weight and molecular formula. These are probably the most important and discriminating pieces of information available to the analyst.
- (2) The ions produced may be related in most cases to the structure of the intact molecule using well-understood principles, which have a basis in theory.
- (3) The mass spectra so produced are reproducible. This is of crucial importance when libraries of reference spectra are used to aid structure determination.

However, there are two main disadvantages of EI, namely limitations in the range of compounds which may be successfully ionised and the utility of the resulting spectra. Samples must be volatile and thermally stable to yield an EI spectrum and this precludes the study of many unstable and thermally involatile analytes. However, this is also a prerequisite of choosing a suitable probe.

Fragmentation reactions may reduce the utility of EI spectrum by reducing the intensity of the molecular ion to a level that is not detectable. In these cases the molecular weight may not be determined and one of the single most valuable pieces of analytical information is lost. The optimisation of transfer line temperature and introduction of the sample into the MS source is therefore of utmost importance and will be discussed in section chapter 6.

2.6.2.2 Ion analyser (quadrupole)

Molecular ions and fragment ions produced during ionisation are accelerated by manipulation of the charged particles through the mass spectrometer. Uncharged particles and fragments are pumped away. The quadrupole ion filter uses positive and negative voltages to control the path of ions. Ions travel down the path based on their mass to charge ratio (m/z) and are made to oscillate in the x and y directions by the electric field. EI ionisation produces singly charged particles, so the charge (z) is one. Therefore, an ions path through the quadrupole will depend on its mass. A voltage consisting of a DC component and a radio frequency component is applied to adjacent rods with a 180° phase difference between the voltage applied to the two pairs. Therefore if the $+(U+V \cos\omega t)$ and $-(U+V \cos\omega t)$ rods shown in appendix 3 were fixed at a particular rf/dc voltage ratio, then one particular m/z would travel the successful path shown by the solid line to the detector. However, voltages are not fixed, but are scanned across a range of rf/dc voltages whilst maintaining a constant U/V ratio, so that ever increasing masses can find a successful path through the rods to the detector.

2.6.2.3 Mass detector

The MS detector works by producing an electronic signal when struck by an ion. A series of timing mechanisms integrates the signal abundance and associates it with a particular rf/dc voltage ratio (m/z). In doing so the associated mass and signal abundance are correlated.

Regular calibration is therefore necessary in order to maintain mass accuracy. Calibrations are performed by introducing a known compound into the instrument, and adjusting the circuits so that the compounds molecular and fragment ions are reported accurately.

2.6.2.4 Organic trap module (OTM)

The organic trap module is used for post run analysis in conjunction with GC-MS if components cannot be resolved by real time RT-FTIR or RT-MS, or as a confirmatory component check. The OTM consists of an adsorbent column (either Vocarb 4000 or Tenax), which receives its evolved gases from the FTIR gas cell through a silica lined stainless steel transfer line . The OTM is connected via a rigid quartz transfer line to the GC-MS system.

On completion of real time analysis, the contents of the trap can be thermally desorbed onto a GC column, separated, and subsequently analysed by the MS. To ensure cleanliness of the trap, it was baked overnight in a continuous helium flow, which was diverted away from the MS source. A blank (OTM-GC-MS) experiment was then performed to ensure the trap was free of adsorbed compounds.

2.6.2.5 Gas Chromatography (GC)

In conjunction with the OTM and MS, GC was utilised in this thesis for individual component identification. The GC column used was a capillary type of the following dimensions (DB-1, 30 m X 0.25 mm id X 0.25 μm film thickness). Thermal desorption of the OTM consisted of heating to 180°C while helium was passed

through the absorbent bed for 4 min during which time the GC was held at 35°C to allow components to deposit on its column. The GC column is then ramped at 5°C min⁻¹ to 250°C and the separated components are desorbed into the MS source where they are detected.

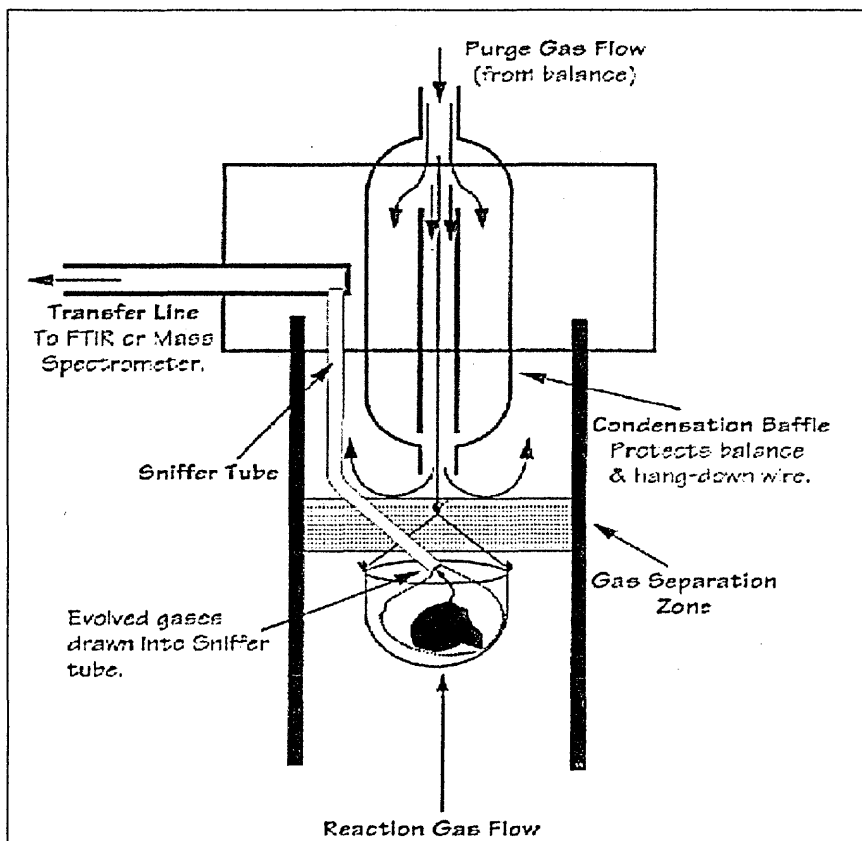
2.6.2.6 TGA/FTIR/MS interfaces

Traditionally, due to the differing flow requirements of the three instruments (TGA/FTIR/MS), there have been limitations on the quality of real-time data acquisition via the simultaneous use of all techniques. The Synergy system has a sniffer interface, which allows continuous operation of all acquisition techniques without any compromise in the quality of acquired data. The sniffer interface satisfies two primary objectives: Firstly, the interface must sample the evolved gases before they are allowed to diffuse through the entire volume of the TGA reaction cell. Secondly, it must be able to provide connection to both mass and FTIR spectrometers, providing optimum flow from the TGA without compromising the TGA, FTIR or MS performance [103].

The sniffer interface employs separate tubes for MS and FTIR sampling. They are constructed of a high temperature alloy and extend to a position just above the sampling cup. The tubes are positioned at an angle as not to interfere with the TGA hang-down wire. Evolved gases from FTIR analysis are pulled through the sniffer interface by a peristaltic pump, which is placed after the FTIR gas cell. In the case of the MS unit, the vacuum of operation serves to draw the evolved gas. To obtain the same flow rate, the vacuum and pump speed are adjusted for each

spectrometer [104]. A simplified schematic of the sniffer interface showing one transfer line is shown in figure 2.11.

Figure 2.11 Sniffer interface [105]



2.7 Statistical characterization methods

The strategy used in this work is two pronged. The first objective is to determine whether chemometric analysis of the desorption of a probe molecule and/or water by EGA can be utilised to qualitatively characterise a variety of mineral groups. In particular, swelling and non swelling clay minerals (i.e. montmorillonite, illite, chlorite and kaolinite). This will highlight whether the probe molecule approach can:

- (1) Determine the similarities within and between mineral groups by qualitative analysis
- (2) Quantitative analysis of mixed mineral mixtures

The first prong of this approach will identify fundamental problems with the method and therefore aid the choice of certain experimental parameters chosen for quantitative analysis.

The second objective is to use chemometric analysis of the desorption of a probe molecule and or water by EGA, to quantitatively determine the composition of mineral mixtures.

As previously mentioned, the statistical approach used in this thesis is chemometrics, which is commonly understood as the use of linear algebraic methods to make quantitative & qualitative measurements of chemical data measurements such as spectra. The following section draws the readers attention to the choice of methods, mechanics of operation and a comparative analysis of alternative approaches to justify their usage.

2.7.1 Multivariate Analysis –Principal Components Analysis (PCA)

Principal components analysis is a statistical approach to qualitative analysis. It has been applied in this thesis to the EGA of the DMF probe molecule, for the qualitative identification of a variety of mineral groups.

The application of this method is best understood if we consider the data output from the Synergy system to be a variety of profiles. A single experimental profile (i.e. reconstructed MS ion chromatogram) invariably comprises a large number of discrete data values. This usually means that fewer profiles are recorded in a complete experiment than there are data values in each profile. Sometimes, chemically different components give rise to visually similar profiles, and there may only be subtle differences among the measurements. For profiles that have many overlapping unresolved features, it may not be readily apparent which regions of the profile are most useful. All of these characteristics can make data analysis difficult.

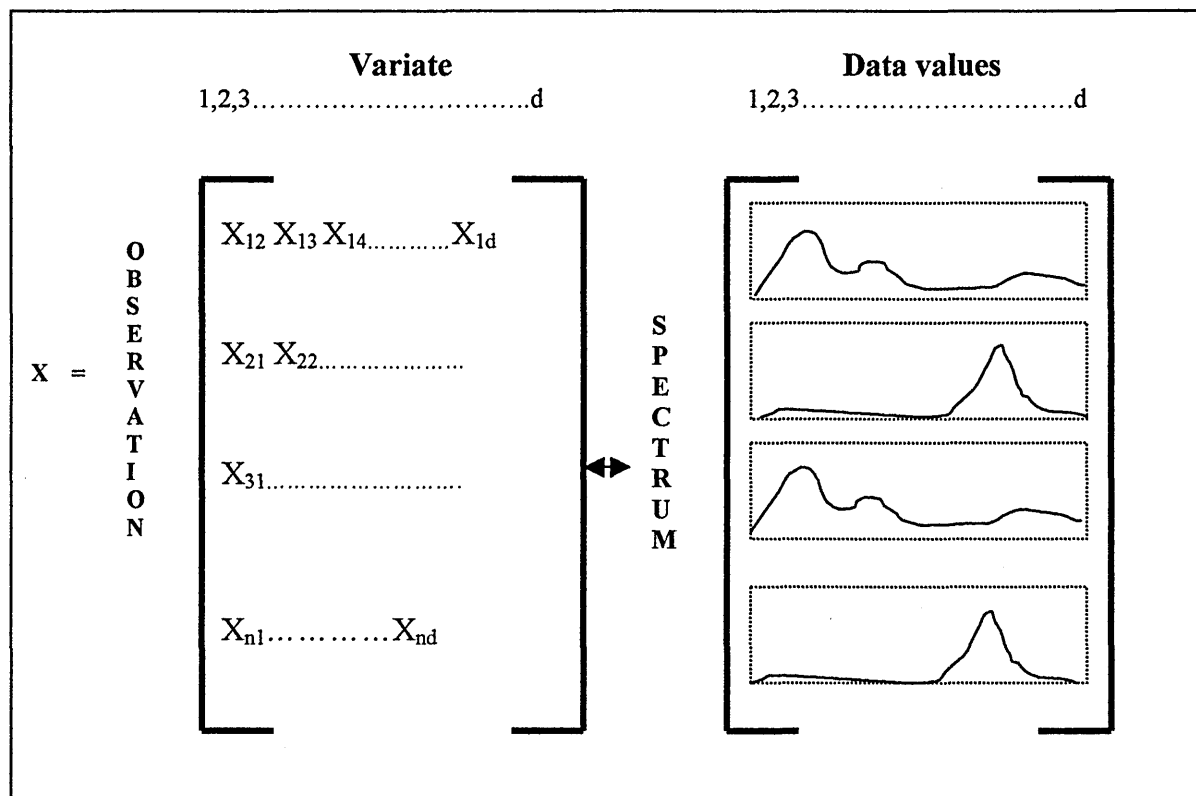
Fortunately, there are a variety of statistical techniques suitable for dealing with data of this kind: these have become collectively known as chemometrics.

PCA is a good method to use for data exploration, it arranges information in such a way that patterns may be revealed which, although present, were obscured in the original data. In fact PCA was first proposed as early as 1901 [107] and developed independently some years later [108].

In order to understand the data manipulation herein, it is necessary to understand how the data is presented and interpreted by the data analysis software. A measurement of a property or 'variate' (i.e. m/z) during a single specimen experiment is called an observation. A complete experiment generally comprises observations, which are multivariate (i.e. $m/z = 2-400$ or multiple frequencies $400-4000\text{cm}^{-1}$). This

type of data set can be arranged into a matrix in the following manner (figure 2.12). The first aim of PCA or PLS is to produce a training (calibration) and validation set by creating a model. Simply, prior to modelling, the matrices are split into a training and a validation sets. A PCA or PLS model is created using the calibration set and then the matrices in the validation set are used to choose the optimum number of factors/principal components required to model each analyte component (i.e. quartz, smectite, illite etc.).

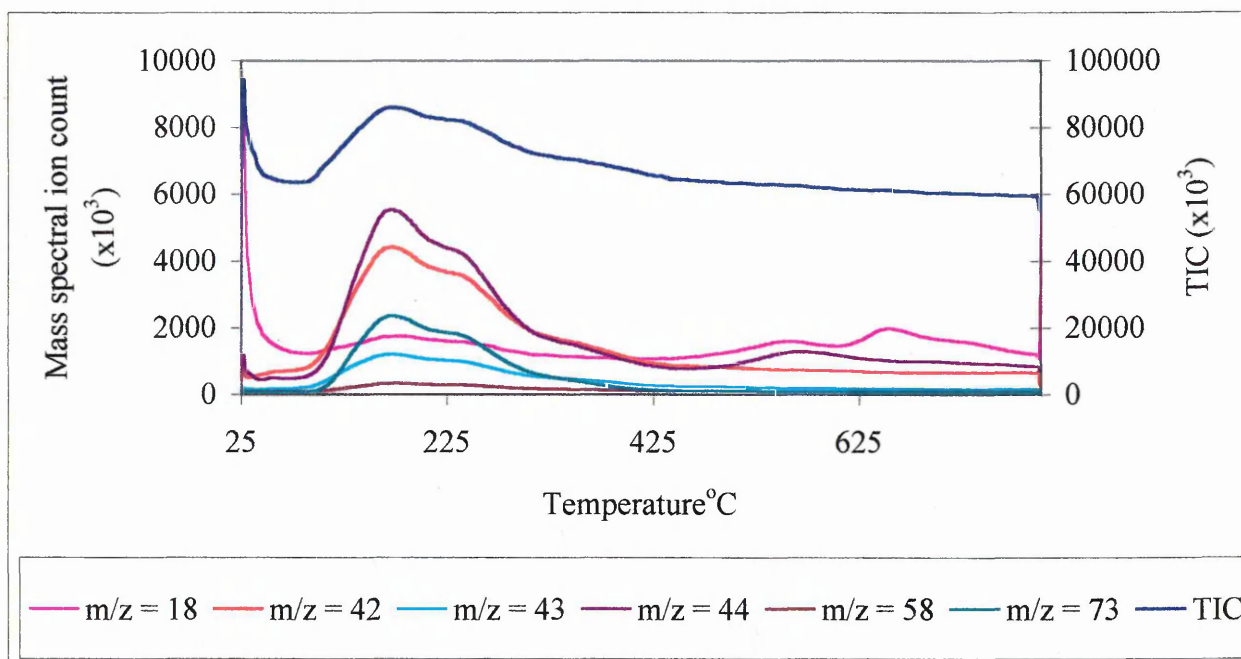
Figure 2.12 PCA data arrangement



Where n is the number of observations, and d the number of variates. Therefore each row of the matrix X contains a complete observation (spectrum, profile, trace etc.), and each column contains all the observed values of one of the d variates (m/z , frequency, weight loss etc.) A data set of this form is known as d -variate or d -dimensional, indicating the number of variates per observation. Data sets in which the number of variates is very large, and exceeds the number of observations are often described as 'high dimensional'. In such data sets, the variates will usually be intercorrelated to some extent. In other words, the correlation between any pair of variables is likely to be non-zero.

In this context, it would be appropriate to describe the nature of the data sets used from GPFTIR and RTMS. The RTMS output is comprised of total ion current (TIC) or reconstructed ion chromatogram (RIC). The TIC is a measure of the intensity of all ions detected across a temperature range, whereas a reconstructed ion chromatogram (RIC) is a measure of the intensity of a particular m/z (e.g. $m/z = 18$ - H_2O) detected across a temperature range during that same period. Both have the appearance of a smooth, continuous trace. The reconstructed ion chromatogram therefore contributes to the TIC. Figure 2.13 demonstrates this type of output.

Figure 2.13 Demonstration of RIC and TIC profiles



Therefore the dimensionality of both the RIC and TIC may be different. In this type of data, the variates (RIC or TIC) will be intercorrelated but the patterns are not as well defined as spectral frequencies observed in FTIR. However, the ion intercorrelations are more to do with the simultaneous detection of ion products caused by thermal chemical transformations and are just as complex, if not more so.

Many traditional methods of statistical analysis cannot be applied directly to data of this kind. However, there are chemometric approaches that are especially useful for dealing with high-dimensional data. These are known as data compression techniques (also known as data reduction or dimension reduction). The main goal of data compression is to transform the data set comprising a large number of inter-correlated variates into a new set of a more manageable size, whilst retaining crucial information. The aim is to produce a new data set, which is uncorrelated (or nearly so) and ordered, which contains most of the significant information that was spread across the original variates (frequencies, m/z etc.) The transformed variates are

known as scores. Because the data are now uncorrelated, patterns or groups of observations may be revealed which were not apparent from the original data.

2.7.1.1 Data compression methods

The data compression methods used in this thesis are PCA and PLS. PLS is particularly useful for treating grouped data. Both techniques can be summarised by the linear transformation

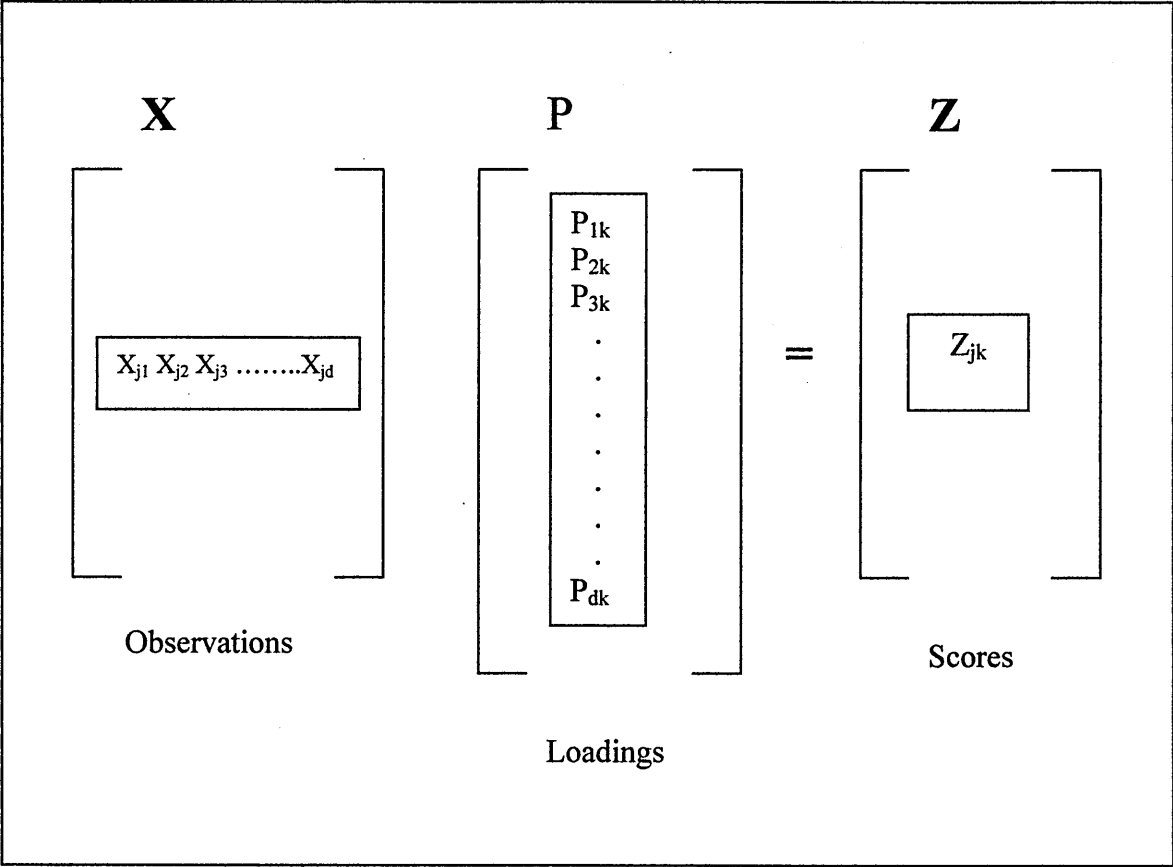
Equation 15

$$Z = XP$$

Z is an (n x q) matrix, each row of which contains a set of **q scores** for each of the n observations where X is now a mean centered data matrix (the mean observation has been subtracted from all observations) containing n observations, each of which is d variate; and P is a (d x q) matrix, the columns which are known as **loadings**. Loading plots provide detailed information about which spectral features are most associated with each constituent in pure and/or sample mixtures.

The mean centered step in this approach, simplifies certain aspects of data compression and it also assures that the scores obtained have zero means. Mean centered data may look different from the original data, but the total variability (or variance) of the data is not affected in this step. The process of matrix multiplication is shown in figure 2.14.

Figure 2.14 Matrix multiplication



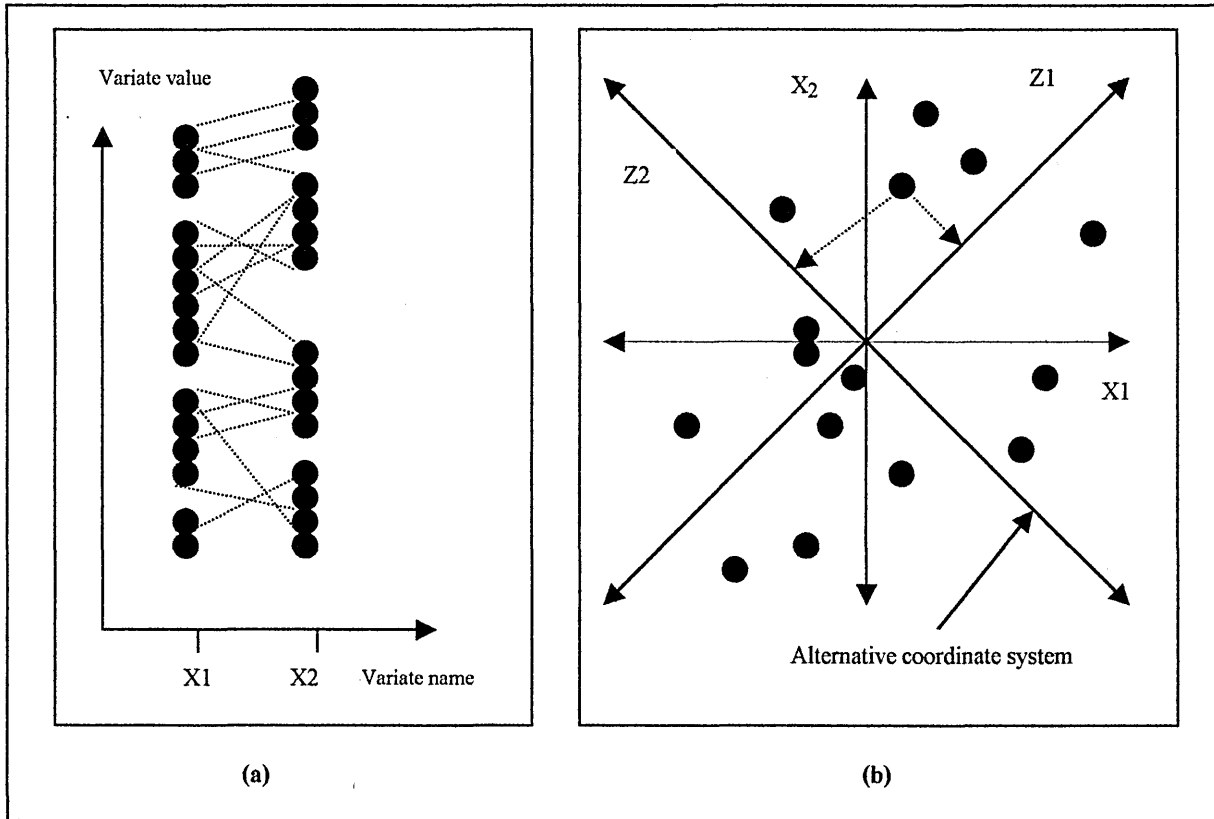
2.7.1.2 Principal Component Scores

Figure 2.14 shows the mechanics of matrix multiplication. To produce a single element in the Z matrix, the value of each variate (MS detection feature etc) in an observation in X is multiplied by a corresponding element in one of the loadings, and the sum of these products calculated. In effect, a score is a weighted sum of all the mean centered variates, whereas loadings can be seen as an applied weighting.

By multiplying all the observations in X in turn by one column of loadings, one column of scores is produced. By multiplying the observations by q columns of loadings, q columns of scores are produced (q transformed variates). In PCA, the product of a score X loading is called a 'principal component' (PC), whereas in PLS, it is often referred to as a factor. These terms will be used throughout this thesis. The number of q PC's or PLS factors is equal to whichever is the smallest out of $(n-1)$ or d , that is $q = \min((n-1), d)$. However, it is usually not necessary to calculate all the possible score-loading pairs, since in both techniques the scores are ordered so that the first few contain most of the variance that was shared amongst the original variates, and a primary aim of these techniques is to reduce the data set to a more manageable number of transformed variates.

It is helpful to think of the linear transformation ($Z = XP$) as a rotation. This can be illustrated graphically by use of a bivariate data set $d = 2$, as it would be impossible to represent a multidimensional coordinate system on a flat page. If the data is comprised of two variates X_1 and X_2 , made on $n = 15$ specimens (in a thermal desorption experiment, these could be measurements at two selected maxima) These observations can be plotted as traces (value versus variate name, fig. 2.15a), or they could be represented as fifteen points in a two dimensional coordinate system (fig. 2.15b).

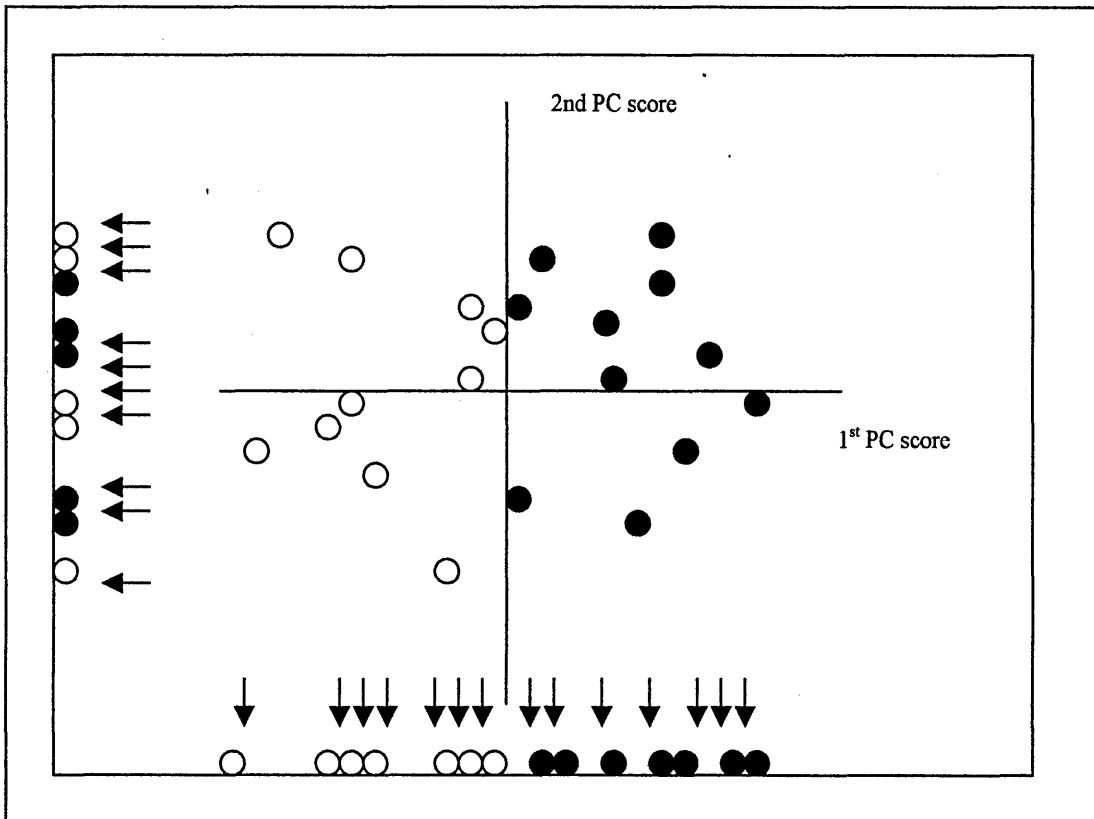
Figure 2.15 Fifteenth bi-variate observations plotted (a) as spectral traces and (b) as points in a two dimensional coordinate system



In figure 2.15 b there is a second pair of axes (Z1 & Z2) rotated with respect to the original coordinate system (X1 & X2). These axes are considered an alternative system, which by projecting each of the points onto the new axes as shown, we obtain values for two new variates Z1 and Z2. This operation of rotation and projection is precisely what is described in the equation $Z = XP$. The columns P (loadings) are d dimensional direction vectors, which define each of the new axes, and the rows in Z (scores) are the values obtained by projecting each of the original observations onto new axes. The differences between the various data compression techniques arise in the way in which the axes are rotated. In PCA, the rotation is such that the first loading produces scores with the maximum possible spread or variability, or in layman's terms, the score which retains the most important sample information that

can describe the spectra. Each consecutive score, contributes less and less variance and therefore less information. To demonstrate how data compression aids data exploration and analysis, it is necessary to consider a simplified example (figure 2.16).

Figure 2.16 First versus second PC scores



If we look at the bi-variate data set in figure 2.16, its corresponding spectral traces would contain overlapping bands, which would make separation into two separate groups difficult. However if both sets of data were plotted, we would need both set of variates and we would expect them to separate into two separate groups. But if we plot the two sets of PC scores against each other (fig 2.16), only one set of transformed variates are required, the first PC score. So the PC transformation has led

to a reduction in the number of dimensions needed to convey the information of interest, from two in the data set, to one in the PCA coordinate system.

2.7.1.3 Principal Component loadings

For PC loadings to be computed, the PC scores must have variance properties as previously described, the columns of P must be eigenvectors of a matrix given by:

Equation 16

$$S = \frac{X^T X}{(n-1)}$$

S is a square matrix of order (d x d) called the covariance matrix, since its elements are covariance's between all the possible pairs of variates. In general, the eigenvectors t_i of any square matrix M are vectors satisfying the equation:

Equation 17

$$M t_i = t_i \lambda_i$$

In which λ_i is the corresponding eigen value. The matrix S has $I = 1 \dots q$ non trivial eigenvalues, therefore there are q scores and loadings, where $q = \min((n-1), d)$. Various methods exist for finding eigen vectors. An alternative of PCA also exists, the correlation matrix. Here S is calculated using standardised data. Standardised data involves dividing each mean centered observation element-wise by a vector comprising the standard deviations of all the original variates. Therefore the loadings and scores will vary between covariance and correlation methods. The advantage for spectroscopic applications, is that the covariance method retains the same proportions

as the original data and therefore allow the analyst to ascribe physical meaning to individual loadings. However, in both variants PCA may be considered a rotation of the d dimensional coordinate system, chosen such that the projections of the observations onto the rotated axes have successively maximised variance.

When we have an idea about the way in which the data is structured, then a technique such as PLS is more preferable. PCA on the other hand does not conform to a pre-defined structure. No prior knowledge about concentration is needed; all that is needed is a single matrix of data. In other words PCA is not a modelling method. For a more comprehensive treatment of eigenvectors, eigenvalues and a full mathematical treatment of PCA, refer to Jolliffe [109].

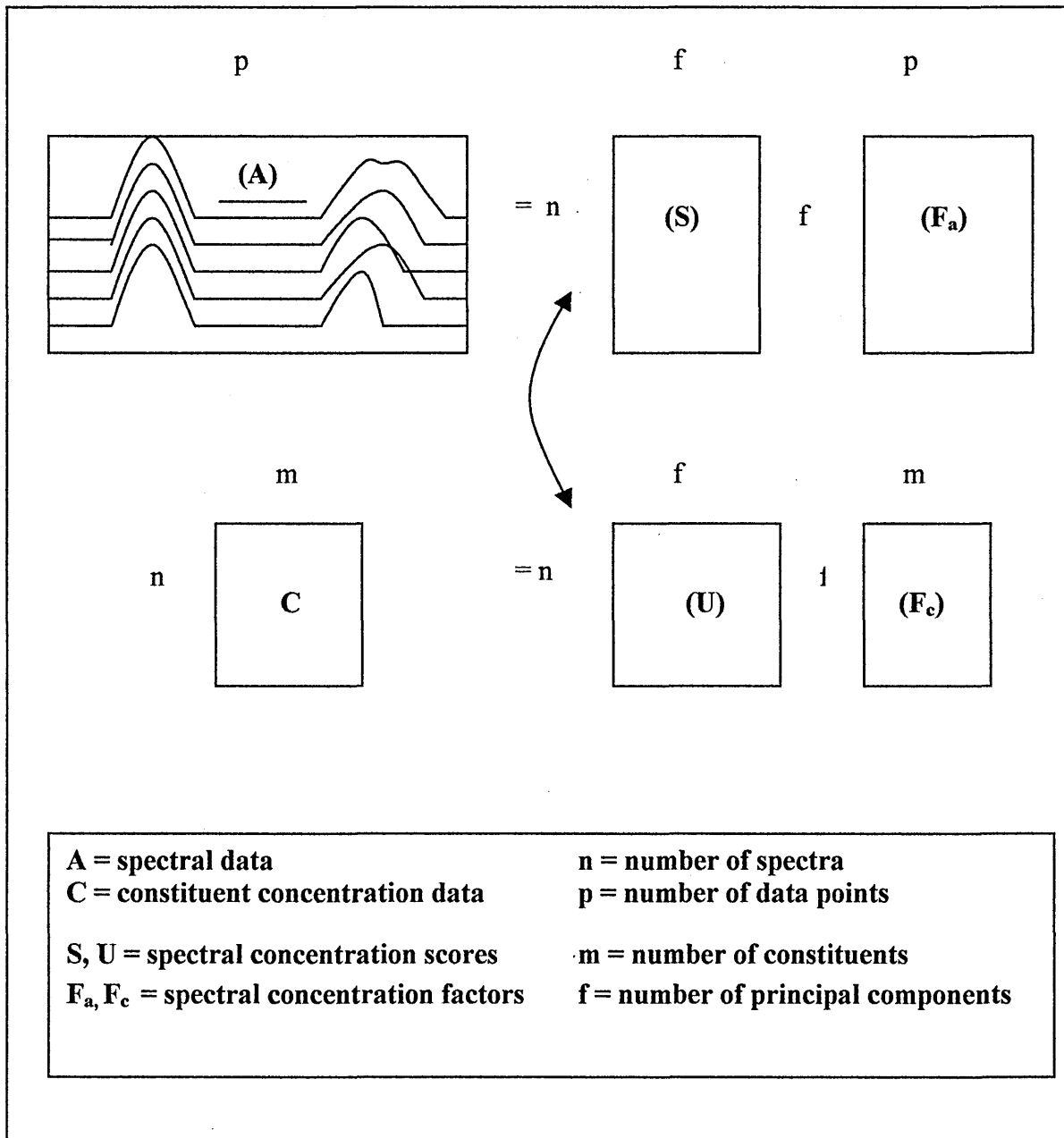
2.7.2 Partial Least Squares (PLS)

The aim of PLS, is to find a series of coefficients which relate concentration to spectroscopic data. PLS requires the analyst to supply a second matrix of information, which is utilised in the calculation of the PLS scores and loadings. PLS regression is well known as a calibration method. In terms of the work herein, the second matrix contains data pertaining to the concentration of individual minerals.

The suitability of the PLS method is shown in detail herein, for a comparison with more traditional techniques i.e. least squares and classical least squares, the reader is referred to a more detailed text [371].

Partial Least Squares (PLS) is a quantitative spectral decomposition technique that is closely related to Principal Component Regression (PCR). PCR is not discussed herein, but is mentioned for comparative purposes. PCR is an eigenvector modelling technique which bases concentration predictions on changes in the data, not absolute measurements. It is a two step process which combines principal components analysis (PCA) and inverse least squares regression (ILSR) to solve the calibration equation for the model. In PLS, the decomposition is performed in a slightly different fashion. Instead of first decomposing the spectral matrix into a set of eigenvectors and scores, and regressing them against the concentrations as a separate step, PLS actually uses the concentration information during the decomposition process. This causes spectra containing higher constituent concentrations to be weighted more heavily than those with low concentrations. Thus, the eigenvectors and scores calculated using PLS are quite different from those of PCR. The main idea of PLS is to get as much concentration information as possible into the first few loading vectors. PLS is simply taking advantage of the correlation relationship that already exists between the spectral data and the constituent concentrations. Since the spectral data can be decomposed into its most common variations, so can the concentration data. In effect, this generates two sets of vectors and two sets of corresponding scores; one set for the spectral data, and the other for the constituent concentrations. The two sets of scores are related to each other through some type of regression, and a calibration model is constructed. A schematic of this process is shown in figure 2.17.

Figure 2.17 PLS modelling process [adapted from 371]



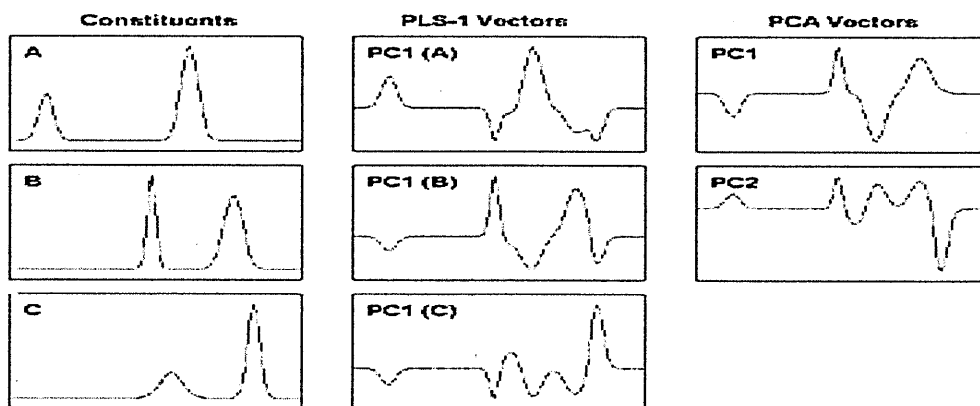
PLS is similar to PCA/PCR. However, in PLS the constituent concentration data is included in the decomposition process. In fact, both the spectral and concentration data are decomposed simultaneously, and the scores (S and U) are exchanged as each new factor is added to the model.

Unlike PCR, PLS is a one step process. In other words, there is no separate regression step. Instead, PLS performs the decomposition on both the spectral and

concentration data simultaneously. As each new factor is calculated for the model, the scores are swapped before the contribution of the factor is removed from the raw data. The newly reduced data matrices are then used to calculate the next factor, and the process is repeated until the desired number of factors is calculated. Unfortunately this makes the model equations for PLS significantly more complex than those of PCR.

As previously mentioned, one of the main advantages of PLS is that the resulting spectral vectors are directly related to the constituents of interest. This is entirely unlike PCR, where the vectors merely represent the most common spectral variations in the data, completely ignoring their relation to the constituents of interest until the final regression step. The vectors generated by PLS (especially PLS-1) are more directly related to the constituents of interest than those from PCA. This is demonstrated in figure 2.18, where the left column shows the spectra of the "pure" constituents used to construct the data set.

Figure 1.18 Relationship of spectral vectors to constituents [371]



The centre column shows the first PLS-1 vector for each constituent calculated from the data set, while the right column shows the first two PCA vectors for the same data.

There are actually two versions of the PLS algorithm; PLS-1 and PLS-2. PLS-1 is the algorithm used in this thesis. The differences between these methods are subtle but have very important effects on the results. Like the PCR method, PLS-2 calibrates for all constituents simultaneously. In other words, the results of the spectral decomposition for both of these techniques give one set of scores and one set of eigenvectors for calibration. Therefore, the calculated vectors are not optimised for each individual constituent. This may sacrifice some accuracy in the predictions of the constituent concentrations, especially for complex sample mixtures. In PLS-1, a separate set of scores and loading vectors is calculated for each constituent of interest. In this case, the separate sets of eigenvectors and scores are specifically tuned for each constituent, and therefore, should give more accurate predictions than PCR or PLS-2. Since a separate set of eigenvectors and scores must be generated for every constituent of interest, the calculations will take more time. However, even with training sets consisting of a large number of samples and constituents, the increased time of calculation with modern PC's would be insignificant. PLS-1 may have the largest advantage when analysing systems that have constituent concentrations that are widely varied, such as mineral mixtures. For example, a set of calibration spectra contains one constituent in the concentration range of 50 to 70% and a second constituent in the range of 0.1 to 0.5%. In this case, PLS-1 will almost certainly predict better than the other techniques.

2.7.2.1 Summary of PLS advantages

- (1) Combines the full spectral coverage of CLS with partial composition regression of LS.
- (2) Single step decomposition and regression; eigenvectors are directly related to constituents of interest rather than largest common spectral variations.
- (3) Calibrations are generally more robust provided that calibration set accurately reflects range of variability expected in unknown samples.
- (4) Can be used for very complex mixtures since only knowledge of constituents of interest is required.
- (5) Can sometimes be used to predict samples with constituents (contaminants) not present in the original calibration mixtures.

2.7.2.2 Summary of PLS disadvantages

- (1) Calculations are slower than most Classical methods, especially PLS-1.
- (2) Models are more abstract, thus more difficult to understand and interpret.
- (3) Generally, a large number of samples are required for accurate calibration.
- (4) Collecting calibration samples can be difficult; must avoid collinear constituent concentrations (i.e. there must be little or no linear relationship between the concentration of training set components).

2.7.3 Optimisation of PLS models

One of the most difficult tasks in using PLS is determining the correct number of loading vectors (factors) to use to model the data. As more and more vectors are calculated, they are ordered by the degree of importance to the model (either by variance in PCA or concentration weighted variance in PLS).

Eventually the loading vectors will begin to model the system noise. The earlier vectors in the model are most likely to be the ones related to the constituents of interest, while later vectors generally have less information that is useful for predicting concentration. In fact, if these vectors are included in the model, the predictions can actually be worse than if they were ignored altogether. Thus, decomposing spectra with these techniques and selecting the correct number of loading vectors is a very effective way of filtering out noise.

However, if too few vectors are used to construct the model, the prediction accuracy for unknown samples will suffer since not enough terms are being used to model all the spectral variations that compose the constituents of interest. Therefore, it is very important to define a model that contains enough vectors to properly model the components of interest without adding too much contribution from the noise.

Models that include noise vectors (factors) or more vectors than are actually necessary to predict the constituent concentrations are called **over fit**. Models that do not have enough vectors in them are known as under fit. Unfortunately, there is usually no clear indication of how many factors are required to move from "constituent" vectors into "noise" vectors and prevent both under fitting and over fitting. However, there are a variety of methods that can be used to aid in determining this value. One of the most effective is to calculate the PRESS (Prediction Residual

Error Sum of Squares) for every possible factor. This is calculated by building a calibration model with a number of factors, then predicting some samples of known concentration (usually the training set data itself) against the model. The sum of the squared difference between the predicted and known concentrations gives the PRESS value for that model.

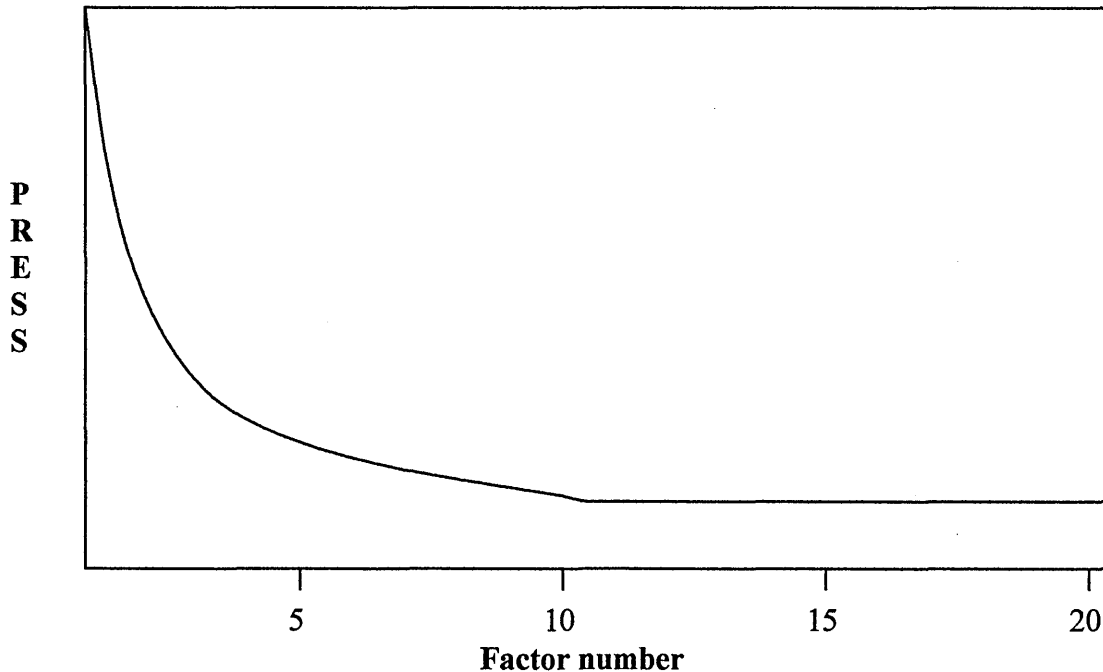
The smaller the PRESS value, the better the model is able to predict the concentrations of the calibrated constituents. By calculating the PRESS value for a model using all possible factors (i.e., first with 1 factor, then 2, 3, etc.) and plotting the results, a very clear trend should emerge (fig 2.19).

However, as with everything in chemometrics, there are a variety of methods that can be used to optimise a model. The main issue is what data to use during the prediction step before calculating the PRESS.

2.7.3.1 Self-Prediction

This is the simplest method for testing a calibration model, but unfortunately it is not very useful. In this method, the models are built using all the spectra in the training set, then the same spectra are predicted back against these models. The problem with this approach is that the model vectors are calculated from these same spectra. Therefore, All the vectors calculated exist in All the training spectra. The PRESS plot will continue to fall as new factors are added to the model and will never rise. In effect, this gives the impression that all the vectors are "constituent" vectors, and there are no "noise" vectors to eliminate, which is never the case with real data. An example of a Press plot is shown in figure 2.19 for a self prediction validation of a training set.

Figure 2.19 The PRESS plot



As new factors are added, the PRESS value continues to decrease. There is no clear indication of the optimum number of factors for this model. The only reason to use this method is that it is very fast. Since it only requires building the models once, predicting the samples can be done in one step. It may be possible to select the number of factors as the place where the plot starts to "flatten out". However this is an inexact measure, and gives no indication of the true optimum number of factors for the model when predicting unknown samples. In Figure 2.19, from 0 to 7 factors the prediction error (PRESS) decreases as each new factor is added to the model. This indicates that the model is **under fit** and there are not enough factors to completely account for the constituents of interest.

At some point the PRESS plot should reach a minimum and start to ascend again. At this point the model is beginning to add factors that contain uncorrelated noise which are not related to the constituents of interest. When these extra "noise"

vectors are included in the model, it is **over fit** and its predictive ability is diminished. However, there is a more robust approach to model validation known as cross-validation.

2.7.3.2 Cross Validation

There are two main advantages of cross-validation over all other methods:

The first advantage is in how it estimates the performance of the model. Since the predicted samples are not the same as the samples used to build the model, the calculated PRESS value is a very good indication of the error in the accuracy of the model when used to predict "unknown" samples in the future. The larger the training set and the smaller the groups of samples left out in each pass (optimally only one sample at a time, but this can be very time consuming), the better this estimate will be. In effect, the model is validated with a large number of "unknown" samples (since each training sample is left out at least once) without having to measure an entirely new set of data (see Validation set below).

The second benefit of cross-validation is better outlier detection. Cross-validation is the only validation method that can give complete outlier detection for the training set data. Since each sample is left out of the models during the cross-validation process, it is possible to calculate how well the spectrum matches the model by calculating the spectral reconstruction and comparing it to the original training spectrum (via the spectral residual). If the predicted concentrations for a single sample are very inaccurate and the spectrum does not match the model very well but the rest of the data works very well, the sample is possibly an outlier. Identifying and removing outlier samples from the training set should always improve

the predictive ability of the model. It is very difficult to perform outlier detection on the training set data without performing a complete Cross-Validation. The results of the other validation methods (Self-Prediction, Leverage and Validation Set) are generally not adequate since the predictions are based on a model built using every available sample. Any unique variations that are present in outlier sample(s) are therefore built into the model. Thus, when the validation spectra (either the training set or a separate validation set) are predicted back against the model, it can appear to be working well. The accuracy of the predictions is actually worse than if those training samples were removed and the model rebuilt. Unfortunately, cross-validation is a very time consuming process. It requires re-calculating the models for every sample left out. However, there are a few somewhat acceptable short cuts. If the number of samples in the training set is large enough, the number of samples rotated out in each pass can be more than one. This obviously does not give the best statistics for each sample, but it does speed the calculations and can be acceptable for determining the number of factors for the model. In fact, in some cases, leaving out groups of samples at a time can be preferable to leaving out only one at a time. In training sets that contain replicate spectra of the same sample, the rotation should be performed on each standard sample, not on each spectrum. For example, if a training set of 50 spectra contains two spectra each of 25 known samples, then each pair of replicates should be left out together. This completely removes the contribution of that sample from the model before prediction. Otherwise, if a rotation value of one is used, there will always be a similar spectrum of the removed sample in the set and the sample will never be predicted as a true unknown. Another approach is to use cross-validation to perform a pseudo-validation set prediction. If the training set is very large, setting the rotation to one-half the total number of samples effectively

accomplishes the same goal. By building a model with half the training set data and predicting it with the other half, similar trends will appear in the PRESS plot. The added advantage is that all the collected training samples can ultimately be used to build the final calibration, making it more robust.

2.7.3.3 Selecting the factors based on PRESS

To avoid building a model that is either over fit or under fit, the number of factors where the PRESS plot reaches a minimum would be the obvious choice for the best model (except in the case of Self-Prediction). While the minimum of the PRESS may be the best choice for predicting the particular set of samples, most likely it is not optimum for prediction of all unknown samples in the future. Since there are a finite number of samples in the set used for prediction, in many cases the number of factors that gives a minimum PRESS value can still be over fit for predicting unknown samples. In other words, there is a statistical possibility that some of the "noise" vectors from the spectral decomposition may be present in more than one sample. These vectors can appear to improve the calibration by a small amount when, by random correlation, they are added to the model. However, if these exact same noise vectors are not present in future unknown samples (and most likely they will not be), the predicted concentrations will have significantly larger prediction errors than if those additional vectors were left out of the model. A solution to this problem has been suggested in which the PRESS values for all previous factors are compared to the PRESS value at the minimum. The ratio between these values (also known as the F-ratio) can be calculated and assigned a statistical significance based on the number of samples used in the calibration set:

Chapter 3 Traditional and Current Methods of Characterising Minerals

3.0 Introduction

The characterisation techniques described in chapter 2 are chosen because they are complementary techniques. This traditional approach is revealed in the literature, for example Hudson-Edwards et al. [110] used XRD and EDX analysis to evaluate the geochemistry and mineralogy of alluvium contaminated by metal mining. Hillier [111] used chemical, XRD and SEM microprobe data to evaluate the possible origin of pore-lining chlorites in reservoir sandstones. Redfern and Bray [112] combined the techniques of TG, FTIR and XRD to determine the influence of exchange cation on the dehydroxylation of Ca^{2+} -, Mg^{2+} -, Na^+ - and K^+ -exchanged Wyoming montmorillonite.

3.1 X-ray Diffraction

Perhaps the most utilised and rewarding procedure for the identification of minerals is XRD. It is the instrumentation most commonly used to study clay-sized minerals and will almost certainly remain so [113].

It is one of the few procedures that can adequately evaluate complex mixtures of minerals as long as they are crystalline. However, XRD cannot detect non-crystalline materials. Quantitative analysis can be performed, but the accuracy depends on the complexity of the mixture and the availability of representative standards. This is a very difficult task, when we consider the structural, compositional and crystalline variations which lead to changes in intensities and

widths of diffraction peaks. Diffraction intensity also varies with particle size as demonstrated by Klug and Alexander [113], who showed that reducing the particle size of powdered quartz from 20-5 μ m reduced the deviation in peak intensity from \pm 18.2% to \pm 1.2%. This smaller particle size also has the distinct advantage of decreasing or eliminating preferential absorption of the X-ray beam by minerals (microabsorption) containing heavy metals in [114]. For any type of quantitative determination, precise, repeatable relative intensities are very important.

An inter-laboratory comparison of methods for quantitative clay analysis (mainly XRD) using different pre-treatment, preparation and analysis techniques, has revealed reasonable conformity for the associated minerals (quartz, calcite and dolomite), but on the other hand qualitative identification of clay minerals showed considerably stronger divergences, resulting in a greater deviation in quantitative analysis [118]. This highlights the temperamental behaviour of clay minerals when subjected to a variety of preparation techniques.

Ideally sample preparation requires a small particle size, which is well mixed and randomly orientated. If not completely randomly orientated, variations will occur from sample to sample. Variations in diffraction peaks can also occur due to aggressive dry grinding, causing changes of phase, and in extreme cases strains on the crystal structure that cause XRD line broadening or even the production of X-ray amorphous material. The X-ray diffraction tracing from a randomly ordered powder will estimate the proportion of clay to non-clay minerals. The presence of non-clay minerals, which is invariably the case in natural samples, may be of interest, but can also mask some of the 00l reflections of the clay minerals. Whole rock XRD gives only semi-quantitative estimates of clay mineral abundance, especially for sandstones in which the clay mineral contents are fairly low (<5-10%). This technique is

adequate for bulk analysis, but does not distinguish bulk from surface mineralogy, which is one of the aims of this thesis.

The intercalation of organic molecules into clays has been used as a method of identifying their presence and distinguishing between clay types. Churchman [115] used XRD to determine the presence of halloysite in kaolinite, by comparing the time taken for formamide to intercalate. This was necessary because without formamide intercalation the differences in the XRD traces were too subtle. Therefore a kaolinite XRD trace is taken before intercalation occurs, which enables the amount of the former to be determined. The total concentration of kaolinite and halloysite is determined by TGA, which can be used to determine the amount of kaolinite by simple subtraction. However, the error involved is $\pm 10\%$. Formamide intercalation appears to be the best method [115], as similar methods using Dimethylsulphoxide (DMSO) and Glycerol tended to intercalate as quickly into kaolinite as into halloysite. Calvert [116] devised a more involved method where DMSO intercalates kaolinite to give a $d(001)$ of 11.2\AA . Bohor and Triplehorn [117] have also reviewed the intercalation processes in relation to kaolinite in flint clays. The general approach revolves around analysis before and after probe treatment to allow estimates of the diffraction contribution of chlorite, halloysite, kaolinite and mixed layer clay minerals that produce possible interferences in the $12^\circ 2\theta$ region.

3.2 Infrared Absorption Spectroscopy

Infrared spectroscopy has been used since the late 1950's to identify mineral composition and their associated structures [118-120]. It is particularly suitable to study the effects of physical processes such as milling, interactions with organics and

water adsorption, since it is capable of representing not only interlayer sites, but also the bulk and surface of the mineral, and thus the vibrational modes of the clay structure and interacting molecules. However, it cannot distinguish between surface and interlayer sites and so is complimented by XRD. Advantages of infrared as a technique include:

- (1) Speed of handling
- (2) Applicable to crystalline and amorphous materials, hence it immediately complements the inability of XRD to characterise amorphous materials such as silicates [121]
- (3) Structural information is provided, enabling the broad classes of compound to be defined (carbonates, nitrates, sulphates etc..)
- (4) Accurate and precise identification of particular mineral species which enables group categorisation

However, as previously mentioned, the infrared technique, like XRD, produces analytical variations due to preparatory techniques, including variations in physical parameters such as particle size and shape [122]. Despite these limitations it is possible to quantify minerals. Notable first attempts to extract a rock composition from an infrared sample of a crushed and powdered sample were conducted by Hunt and Turner [123] in 1953 and Lyon et al. [124] in 1959. Further work by Lyon, with various collaborators, developed three important new hypotheses.

- (1) Spectral effects caused by preferential orientation of minerals are mainly a concern for foliated metamorphic rocks, as minerals in most igneous rocks are randomly orientated [125].

- (2) The wavelength positions of the fundamental absorption bands are not strongly affected by grain size [126].
- (3) The combined set of peaks and troughs composing a spectrum is diagnostic of the qualitative bulk composition of the rock rather than the surface mineralogy [127].

Walker and Graham recorded precision and accuracy results for quartz analysis by FTIR of less than 1.0% [128]. A comparative study of particle size dependency of IR and XRD methods for quartz analysis by Bhaskar et al. revealed some interesting relationships. It was found that both IR and XRD methods are size dependent but in an opposite sense. For the same quartz mass, as particle size increases, IR peak height decreases and XRD peak height increases. It is therefore important that both standard and samples have the same particle size distributions.

The FTIR technique is best suited to the qualitative identification of minerals rather than quantitative identification especially when investigating a mineral mixture. However, reasonable success in quantitative investigation of mineral mixtures has been achieved by chemometric analysis of DRIFTS spectra [129].

Matteson and Herron [130] have shown that it is possible to determine the type and quantity of feldspars in a mixture of feldspars by FTIR spectral analysis. Further to this, they have also determined the abundance of minerals in two carbonate rocks [130]. Kodama and Oinuma [132] used FTIR to identify the presence of kaolinite in sedimentary rocks; the results were comparable to those obtained by XRD (approximately 4.5%), without the harsh pre-treatments needed to remove other clay minerals for XRD.

3.3 Environmental Scanning Electron Microscopy

SEM is an established technique for the characterisation of reservoir rocks [133-137]. Clay minerals found within reservoir rocks have distinct morphologies that can be determined by SEM. However, the surface has to be altered before analysis and therefore cannot distinguish between blocked and unblocked sections [137]. In comparison, it is not necessary to coat samples for ESEM analysis, nor does it have to operate in a high vacuum environment. This has conferred upon several advantages to its use, which have enabled a variety of more informative studies. Baker et al. [138] have utilised this novel experimental environment to visualise osmotic swelling of constituent smectite in response to both fresh and salt water. These tests reveal significant microstructural reorganisation that under standard SEM operating conditions would remove the water of interest. An ESEM study of pore structure modification in sandstone after polymer treatment by Ali and Barrufet [139] has enhanced the understanding and visualization of the distribution of polymer in the pores of consolidated rocks, thus enabling a better understanding of the physical adsorption of the polymer at the pore level. When coupled with EDX it can provide pertinent data on the morphology of the samples together with elemental analysis.

3.4 Chemical Analysis

The chemical analysis of minerals involves accurately determining the elemental composition of a sample and subsequently comparing the elemental proportions to the type of minerals present. This analysis is usually carried out by wet chemical

techniques [140], though often include flame photometry, emission and atomic adsorption, colorimetric methods and XRF [141].

However, the calculations require a number of assumptions, one being that the minerals have been qualitatively determined by other methods. This involves complex calculations involving the use of a number of simultaneous equations. This technique is fraught with difficulties, which makes accurate analysis of complex mixtures very challenging.

3.5 Thermal Methods

Thermal methods used to characterise minerals include:

- (1) Thermogravimetric analysis (TGA)
- (2) Differential Thermal Analysis (DTA)
- (3) Differential Scanning Calorimetry (DSC)
- (4) Evolved Gas Analysis (EGA)

These techniques are rarely used in isolation and as previously stated provide complimentary data to enable confirmation of physical and chemical processes. In addition to TGA, which yields the sample mass as a function of time or temperature, a derivative mass-loss curve may also be computed for any TGA experiment. These derivative curves (DTG) can be reported as a function of either time or temperature. In this thesis they are expressed as a function of temperature. Barshad [142] has given a detailed and informative study of thermal analysis techniques for mineralogical identification and composition.

The basic principles and historical development of TGA/DTA can be found in Mackenzie [143]. Early studies by Brindley [144-147] and a variety of co-workers clearly demonstrate the dependence of dehydration and dehydroxylation reactions in hydrous minerals on the nature of the interlayer cation. They showed the dramatic effect of water vapour on the kinetics of dehydration and dehydroxylation reactions.

Thermal analyses by various workers demonstrate the thermal behaviour of different smectite specimens, in particular the effect of the exchangeable cation. Data from these papers highlights two points, the amount of water lost before dehydroxylation (interlayer water) is related to the hydration energy of the interlayer cation [148-149] and that dehydration is a two stage process at ambient and elevated pressures [150]. The work of Mackenzie and Bowden [151] elucidated the dehydroxylation thermal transformation (involving TGA, DTA and EGA) of amesite (1:1 phyllosilicate) at higher temperatures, clearly showing its two-stage nature.

DTA has also been used to distinguish kaolinite from other members of its group (halloysite, dickite and nacrite) and to detect their degree of disorder [152]. The temperature at which dehydroxylation occurs is strongly related to the mineral family and its degree of order and thus its history. A DTA study by Yariv, has been used to show the types of associations between water molecules, exchangeable cations, organic molecules and ions formed on clay surfaces. Curve comparisons recorded in the absence or presence of air show strong exothermic peaks under oxidative conditions, which are more sensitive for the identification of different associations [153]. Differential scanning calorimetry (DSC) has become very popular, being a much more precise technique than DTA with respect to measuring heat contents. Papers by Giese (1990)[154] and Dubrawski (1991) [155] show how DSC is currently used in clay and general mineralogical investigations.

EGA involves the analysis of gases when a mineral is heated with a particular temperature gradient. Changes taking place in the evolution of these gases, can be followed simultaneously by a variety of instruments (i.e. TGA, FTIR, DTG, DTA) and subsequently related to physical and chemical changes within a mineral including: dehydration, oxidation of organic matter, dehydroxylation, destruction of the crystalline structure, decomposition, sublimation, vaporisation, fusion and solid state transitions. Initial applications included characterising the combustion and pyrolysis products of materials related to the tobacco industry [156-158].

The application of DTA and TGA have been widely used to characterise geological materials and despite the analytical performance potential available from EGA, this technique has by no means achieved the same degree of use. The most common volatiles evolved on heating geological materials are water, carbon dioxide and sulphur dioxide. FTIR can be used to quantify these volatiles, however, other volatiles such as oxygen, hydrogen and carbon monoxide are often encountered and the analytical flexibility of a mass spectrometer is then required. Amounts of volatiles (and hence amounts of mineral phases) can be determined from peak areas either by empirical calculation [159] or by comparison of volatile evolution profiles from selected chemical compounds (i.e. sodium bicarbonate-H₂O and CO₂-sodium dithionate-H₂O and SO₂). Only rarely can XRD detect minerals below the 2-3% level accurately, whereas EGA has the potential for determining minerals well below these levels [160] (< 0.1 %). This has important implications for studies of oil-reservoir sandstones and argillaceous strata for low-level radioactive waste disposal, where the presence of small amounts of labile mineral phases may be significant in unravelling diagenetic events, such as their effect on porosity (clays), cementation (carbonates) and their buffering capacity under anaerobic conditions (sulphides). EGA profiles

have been used to characterise volcanic ashes [161] and have also been used to investigate the crystallation behaviour of volcanic glasses [162]. It has also been shown that hydroxyl water condensates from clays and shales contain trace amounts of elements such as F, Cl, B and Br, together with oxides of nitrogen and sulphur. Measurement of the temperature release patterns of these volatiles may link them to individual mineralogical phases and thus provide information on the geological history of these fine-grained materials [163].

EGA as a method of characterisation of clay minerals has over the last ten years attracted more and more attention, though at present is still very under-utilised, even though they produce distinctive patterns of volatile generation related to thermally induced reactions. In 1990, Bloodworth et al. [164] developed a system capable of running routine detection and estimation of kaolinite in synthetic and natural mixtures (kaolinitic sandstones), at concentrations as low as 0.25% (2500ppm). Their system was based on a DTA furnace linked to a non-dispersive infrared water vapour detector where kaolinite calculations were based on water vapour evolved during dehydroxylation. These low levels are often difficult to detect and/or quantify by conventional methods such as XRD and SEM. However this paper also touched upon the issue of calibration curvature at low analyte concentration (0.1%), a similar phenomenon identified by Milodowski and Morgan [165] was attributed to the rate of gas diffusion from the mineral mixture. They also highlighted the problems associated with resolving the dehydroxylation of kaolinite and chlorite, when if highly crystalline, kaolinite can dehydroxylate in the same region as chlorite. Unfortunately, mixtures of different clay minerals cannot be resolved by thermal methods alone.

Morgan [166] gives an overview of EGA applied to compositional determinations of clay raw materials and ceramics in order to highlight the importance and economic savings such analyses can potentially bring to industrial processes. Thornley and Primmer [167] extended the work of Bloodworth et al. [164], when they showed that combining the techniques of XRD and evolved water analysis (EWA) made possible the quantitative determination of illite and kaolinite in sandstone rocks. They studied mixtures of mineral standards whose compositions were similar to sandstones, where the lowest amount of kaolinite and illite was 2.3 and 1.4% respectively. The precision of repeat determinations for 20 analyses over a 12-month period was <5%. The technique was also applied to sandstones to accurately determine the illite abundance.

Cai [168] used a complicated EGA procedure to identify trace amounts of pyrite and siderite in dolomite and establish the thermal degradation mechanisms. The system consisted of a DTA coupled to a GC. The loss of H₂O at 550°C was due to kaolinite and a small exothermic effect at 580°C was due to quartz when the heated residue was programme cooled. Calcite could also be determined if the carrier flow gas was CO₂ and air (1:1) as opposed to N₂. However, the method was not quantitative and additional components would make interpretation difficult.

Heide et al. [169] have used EGA as a fingerprint to characterize minerals and rocks. The EGA system used consisted of TG-MS where gas release profiles were used as an effective tool for identification purposes. Detailed studies of the gas release profiles showed differences in the degassing rates and temperatures and also in the composition of the fluids released from the samples. Gas release profiles of rocks were comparable for H₂O, being characterised by three maxima and similar to those for the dehydration of clay minerals and silicates containing OH groups, such as

micas and amphiboles. The release of CO₂ demonstrated two degassing processes attributed to the decomposition of carbonates and the formation of CO₂ bubbles in the melt at temperatures > 1100°C. Another important point that has previously been overlooked in the literature was the release of hydrocarbon species (m/z = 15-CH₃⁺), which demonstrated that profile differences were significant from location to location. It was shown that the gas release profiles are governed by the physico-chemical conditions influencing the formation of and alterations in the solid sample.

Holdiness [170] reviewed EGA by MS in 1984 and paid particular attention to the instrumentation available at the time along with some selected applications. Gibson and Johnson [171] used TG-quadrupole MS for investigating the decomposition and identification of volatile components released from a meteorite sample. The gases released were related to previously identified mineral components. These included:

- (1) H₂O (150°C-200°C) associated with limonite (α -FeO₃.H₂O)
- (2) H₂O (300°C-500°C) associated with montmorillonite and chlorite
- (3) SO₂ (400°C-500°C) associated with epsomite (MgSO₄.7H₂O) and gypsum (CaSO₄.2H₂O), the loss of water was also observed in this region.
- (4) CO₂ (500°C-600°C) associated with siderite
- (5) CO₂ (600°C-700°C) associated with dolomite
- (6) CO (600°C-700°C) associated with carbonaceous matter

As with previous studies, the information provided by EGA cast light on the possible conditions that prevailed during meteor formation. Gibson [172] also studied shale and lunar soil samples by TG-quadrupole MS. MS confirmed that two weight loss events shown during TG analysis (to 1000°C) were due to loss of hydrocarbons followed by CO₂, which was due to decomposition of the former. This highlighted

the high sensitivity of MS even though TG weight losses were very low (0.35 ± 0.10 weight %) and uninformative.

Muller-Vonmoos et al. [173] developed a DTA/TG/MS EGA system. They investigated complex clay mineral samples and dealt with issues concerning calibration. Prior to clay analysis, standard materials (calcium oxalate hydrate $\text{CaC}_2\text{O}_4 \cdot \text{H}_2\text{O}$ and NaHCO_3 sodium hydrogen carbonate) were used to determine the MS response to H_2O , CO and CO_2 . Decomposition of NaHCO_3 showed that when H_2O and CO_2 are simultaneously desorbed, they have little effect on the quantitative ability of the MS. During decomposition of $\text{CaC}_2\text{O}_4 \cdot \text{H}_2\text{O}$, it was shown that amounts as low as 0.005mg of H_2O and CO_2 could be detected whilst still maintaining a straight-line calibration plot. The evolution of H_2O and CO_2 were then attributed to organic matter, dehydroxylation of clay minerals and siderite and calcite decomposition. However, their results were not compared to other techniques.

Chisem and co-workers (1997) [174] have also used TG-MS to investigate the thermal characteristics of a pillared acid activated smectite and characterise the types of acid site by monitoring cyclohexylamine desorption. They also investigated the thermal degradation of layered double hydroxides (LDH's-anionic clays), where MS confirmed for the first time the probable degradation mechanisms.

Chapter 4 Literature Survey and Strategy

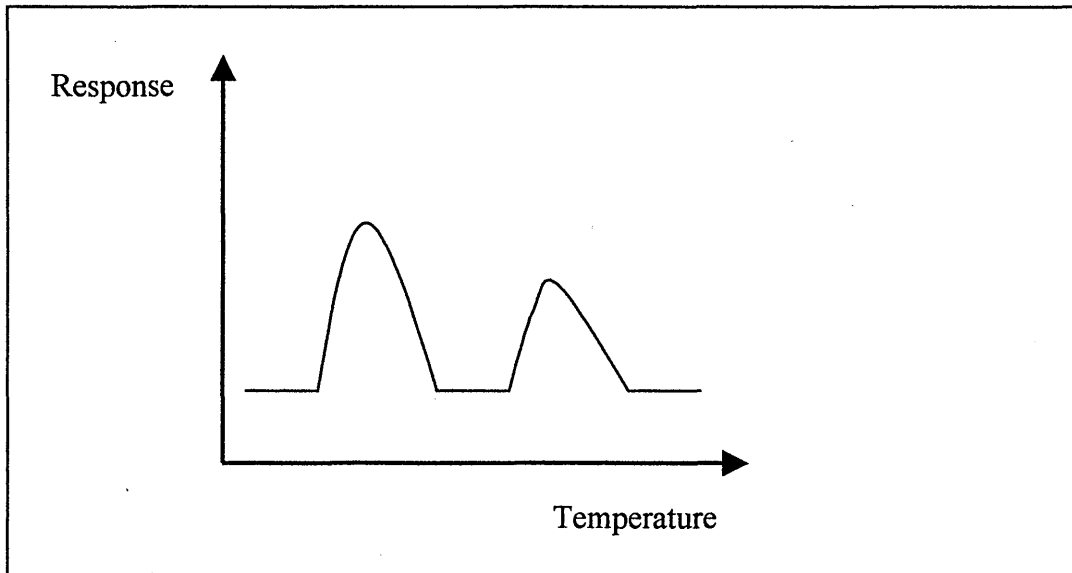
4.0 Introduction

The first objective of the research in this thesis is to identify a suitable probe molecule(s) for the characterisation of pore lining minerals in reservoir rocks.

4.1 The 'Chemical Probe' strategy

Ultimately this method aims to use organic molecules as chemical probes to elucidate the surface mineralogy of a rock. An organic molecule introduced, into a rock, will to some extent interact with the mineral constituents. Minerals differ in terms of structure and therefore the type, strength and extent of interaction with the probe should also differ. It is these differences the method attempts to exploit. If a treated rock is heated, the desorption temperature of the probe from each mineral should be different. Therefore, monitoring a characteristic desorption (weightloss, wavenumber(s), m/z) of the chemical probe as it desorbs from the rock as a function of increasing temperature should produce a chromatogram-type trace as shown in figure 4.1.

Figure 4.1 Chromatogram-type trace



It must also be noted, that clay minerals when heated without being subject to a probe, will produce distinct features due to the loss of water bound to its external surfaces, to the interlayer cations and as the result of dehydroxylation. These thermal events when combined with that of probe desorption, provide the analyst with a wealth of information. It is anticipated that chosen probes would bind strongly to swelling clays (montmorillonite), less strongly to kaolinite and not bind to quartz or feldspars. Therefore a knowledge of the desorption temperatures associated with individual minerals can be then used to characterise the rock.

4.1.1 Chemical probe requirements

As previously mentioned in chapter 1, the primary objective for using chemical probes is to overcome the disruption to the pore lining minerals of a rock. The principal reason for not using crushed rocks, is that minerals bound up in the rock

structure, may become exposed to the probe, which in turn exaggerates their contribution to surface mineralogy (i.e. the mineral surface which a fluid or gas may come in contact with in a whole rock). A chemical probe therefore needs to penetrate the pore structure and interact with pore lining minerals without disrupting them. The ideal method of exposing a rock to a probe is via the vapour phase, because it is known that changing or introducing a liquid in a pore can move fines, results in the blocking of pores and hence the true composition may not be evaluated. The choice of chemical probe will rely on the ability of the organic molecule to selectively react (because of the physical and chemical properties of both probe and mineral) to varying degrees with the different mineral constituents. Therefore, probe molecules need to demonstrate several key properties i.e.

- (a) a high vapour pressure so as to obtain a saturated environment
- (a) an ability to penetrate into the pore structure of rock cores
- (b) Be desorbed at a temperature characteristic of the interaction with different mineral components i.e. provide high specificity
- (c) They also need to provide a characteristic signal arising from :

- (i) Thermogravimetric Analysis (TGA)

- involves the mass loss from a sample under a linear temperature gradient thus enabling the monitoring of the desorption of a chemical probe. Large mass losses within a specific range may indicate the presence of a greater quantity of a particular constituent (i.e. if all the losses can be attributed to the probe alone). Therefore there is a need for confirmatory techniques such as FTIR and MS).

(ii) Fourier Transform Infrared spectroscopy (FTIR)

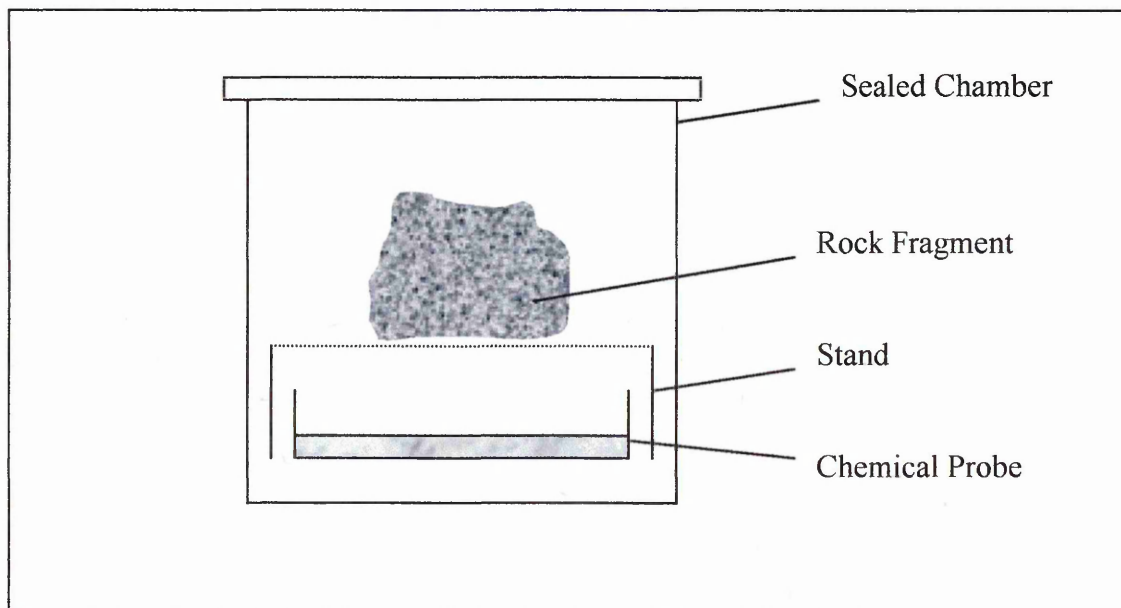
can be considered to be a more sensitive technique and is complimentary to TGA. Suitable probes must provide a strong characteristic absorption band with a high extinction coefficient (e.g. a carbonyl group). These absorption bands would perhaps experience cm^{-1} shifts due to temperature gradients.

(iii) Mass Spectrometry (MS)

Is also complimentary to both TG and FTIR, offering more sensitive detection by up to three orders of magnitude. It must be capable of identifying a unique fragment ion or a particular fragmentation pattern, which is characteristic of the probe.

The samples were exposed to the probe by simply placing the sample in a sealed chamber containing an atmosphere saturated with the probe, as seen in figure 4.2.

Figure 4.2 Procedure of exposing samples to a probe



During the development of the probe strategy, ideas for characterisation emerged, some of which will be discussed in the following chapters.

The main programme focused on developing two characterisation methods with the aid of several probe molecules. The first method aims to qualitatively distinguish between clay mineral groupings (i.e. smectites, kaolinites, chlorites and illites) by applying chemometric analysis (PCA) to the evolved gas analysis (EGA) profiles (i.e. DTG, FTIR and MS) after exposure to a probe molecule. This will demonstrate whether qualitative characterisation is possible and to what extent variability exists within the groupings.

The second part of the first method aims to demonstrate that it is possible to quantitatively identify minerals in mixtures by applying chemometrics to the evolved gas analysis (EGA) profiles of a set of known mineral standards after exposure to a probe molecule. The intention is that the EGA output obtained can be used to identify and quantify surface mineralogy.

The second method aims to use ESEM-EDX to elucidate the presence of a swelling clay mineral on the surface of sandstone rocks by the detection of a diagnostic functional group associated with a probe molecule.

4.2 Method 1: Characterisation of EGA profiles by chemometrics

4.2.1 Review of chemometrics for qualitative and quantitative analysis

Chemometrics has traditionally been used to identify the presence of minerals in infrared spectra i.e. FTIR. The partial least squares technique has been successfully applied in spectroscopy for the quantification of complex effluent mixtures from

sulphite pulp mills [175], in clinical chemistry [176], in research on the structural determination of pharmaceutical compounds [177], and the determination of crystalline and amorphous silica [178]. The study of silica was required because of almost complete spectral overlap of the main absorption bands of silica. This method proved to be more robust than the combined methods of infrared spectroscopy and XRD. Although quantitative analysis using DRIFTS spectra has its problems many publications report quantitative data. Moudgil et al [179] analysed a binary mixture of dolomite species, which differed only in their surface chemical groups. Conventional characterisation by X-ray diffraction could not be used because the dolomite species had the same diffraction patterns. Successful quantitative analysis was achieved using K-M transformations of DRIFTS spectra. Johnston and Hussey [180] have investigated the use of simultaneous linear equations based on chemical and physical properties (i.e. chlorite weight loss between 300-950°C) to quantitatively determine clay mineral composition. Determination of cement composition by Hughes et al [181], was made possible by the use of PLS and high quality DRIFTS spectra to provide some 14 items of compositional data with an accuracy that is adequate for many purposes. This allowed the composition of unknown cements to be determined quantitatively. Luinge et al. [182] compared PLS to artificial neural networks (ANN) as a quantitative tool for the automated interpretation of IR spectra. PLS was favourable, not only producing comparable results, but also was faster and more easily interpreted.

Pottel [183] used PLS to analyze gas phase FTIR spectra for the quantitative determination of gas concentrations from the smoke gases of burning textiles. Using PLS, it was shown that overlapping spectra could be evaluated without the need for spectral subtraction associated with more traditional techniques. In particular this

included overlapping spectral bands of H₂O/CO₂, but more importantly the overlap of H₂O/NO which is hindered by total H₂O overlap and the relatively small absorbance values associated with NO.

The use of chemometrics techniques in the food industry is commonplace. Spectroscopic methods are the attractive option, fulfilling many analytical requirements such as speed and ease of use. Of these, mid-infrared methods (Wilson & Goodfellow, 1994) [184] have been applied to the authentication of a range of materials, including fruit purees [185], jam [186], olive oil [187] and coffee [188]. In a number of cases, it has been shown that sample species can be determined, and multiple adulterants identified and quantified; in certain cases, adulterants not included during the development of the method can also be detected. Osama et al [189] in their study of the authenticity problems of selected meats showed that it was possible to distinguish between minced pork, chicken and turkey by PCA of the mid-infrared spectra. The method proved to be quick with the potential for authentication and quality control of meat products. Underlying this success is the fact that mid-infrared spectroscopy reports on a very large number of analytes simultaneously and that absorption bands are sensitive to the physical and chemical states of individual constituents.

A study of the literature reveals that little or no work has been published regarding the quantitative chemometric analysis of mineral mixtures using EGA spectral components. However there are cases cited which evaluate other component mixtures using a variety of related techniques. Nordmark [190] used PLS and PCA to quantitatively analyze the output of pyrolysis-gas chromatography in order to determine resin mixtures in the coating colours of paper. It was possible to predict unknown concentrations in mixed resins with errors ranging between 3.4-3.8%.

Gardner et al [191] illustrated the feasibility of quantitative analysis of mass spectral mixtures of chemically similar analytes by multivariate calibration in low-resolution mass spectrometers. They found that calibration performance improved slightly as the data used for calibration decreased from the full mass spectrum to only 12 or 18 judiciously chosen fragment ions. They also highlighted the effects on component detection as MS resolution was varied.

PCA has also been used to qualitatively determine carbonyl compounds in capillary gas chromatography utilizing their Kováts retention indices [192]. It was found that one principal component (boiling point and/or molecular mass) accounted for more than 94% of the total variance in the data. It was concluded that the retention behaviour of ketones and aldehydes are not fully distinguished although some characteristics of solute structure can be observed using PCA.

Wesolowski et al [193] used the chemometrically processed derivative thermogravimetric data for quality control of engine lubricating oils on the basis of chemical and thermal analyses. Relationships between chemical and thermal variables were evaluated by regression and PCA analysis. Good linear relationships were found between the majority of chemical and thermal variables. PCA results indicated that TG and DTG techniques were very useful in defining the degree of wear of used lubricating oils.

Elomaa et al., [194] using the EGA (MS) of inorganic salts and apatites, evaluated thermochromatograms by chemometrics (evolving factor analysis technique (EFA)) to provide information about individual thermal processes that occurred during sample heating. The data was decomposed into matrices of reconstructed chromatograms and thermal evolution curves, which connected each thermal decomposition step to the products evolved in a particular temperature region.

Within this the simple system all the evolved degradation components are known in advance as are their peak shapes. Therefore it was possible to reconstruct the TGA weight loss curves using evolution rate versus temperature data. This work demonstrated how abstract factor analysis of 2D objects makes it possible to determine a number of distinct thermal stages of decomposition which can be used as a fingerprint for a compound.

4.3 Review of organo-mineral interactions

The interactions between minerals and organic molecules have been studied by a great number of people in a variety of industries. Most interest in clay minerals has been shown because of their highly reactive nature. For example clay minerals (bentonite) are often used as barriers in landfills in order to prevent migration of pollutants. Clay minerals not only prevent migration, but in doing so, they give bacteria opportunities to degrade these pollutants to less harmful chemicals. Many industries take advantage of these favourable properties, resulting in widespread attention within a number of industrial sectors including waste treatment [195], catalysis [196], laundry powders [197] and many more. The smectite group receives the most attention because its members have a relatively high cation exchange capacity, which can be readily substituted by other cations causing significant changes in their properties. For example, the replacement of the naturally occurring inorganic cations by tetramethylammonium [198] or long chain alkyltrimethylammonium cations [199] can change the surface character from hydrophilic to organophilic thus making these organoclays very efficient scavengers of benzene, toluene and xylene from aqueous waste streams [200].

4.3.1 Typical Smectite-organic molecule interactions

Smectite clays are recognised widely for their ability to promote reactions involving organic molecules due to their Bronsted acidity [201]. The early work of Bradley [202] and MacEwan [203] on the adsorption of neutral organic molecules on phyllosilicates began an area of extensive study. Early studies attributed the predominant mineral/organic interaction to the binding of sorbate molecules to the silicate surfaces. However, as the use of spectroscopic techniques became more widespread, the relevance of a variety of other interactions involving cations, water and molecular sorbates were shown to play an important role. Organic molecules are adsorbed from the vapour phase, pure liquid or from solutions in water or other solvents. Molecules then compete for coordination sites around interlayer cations, and depending on the relative values of hydration and solvation, they will

- (a) replace water and become coordinated directly to the cation; or
- (b) occupy sites in a second coordination sphere around the cation being bonded by bridging water molecules ;or
- (c) accept a proton from the water of coordination around the cation or from the cation themselves if the clay is saturated with H^+ or NH_4 [204]

When organic molecules that have functional groups (with free electron pairs) penetrated the interlayer space of charged phyllosilicates, the possibility exists that coordination compounds may be formed with the exchangeable cations. This process is restricted by the electric field effects of the silicate layers combined with steric hindrance within the interlayer space. Corroborative evidence for coordination is

obtained from the shift in the IR bands for sorbed compounds compared with the pure molecule.

Each type of clay mineral may interact with an organic molecule differently since each clay surface and its interlayer space [205-206] have different types and populations of Bronsted and/or Lewis acidic and basic sites. The principal interactions observed between clays and organic molecules are of the acid-base type. Smectite clays [207] under appropriate conditions of dehydration have large negative acidity constants and have been compared to concentrated solutions of H_2SO_4 in their ability to protonate organic molecules. The association of organic molecules via water bridges was first demonstrated for pyridine adsorbed on montmorillonite [208]. The evidence consisted of a shift in both pyridine and water IR adsorption bands as a consequence of hydrogen bond formation. The linking water molecules are asymmetrically perturbed and their original symmetry is affected causing a downward shift in cm^{-1} . The IR absorption frequency of the OH bond is shifted to positions depending on the polarizing power of the exchangeable cation. Hydrogen bonding also displaces the position of the nitrile ($\text{C}\equiv\text{N}$) band but this frequency is not affected by the interlayer cation [209]. The strength of the hydrogen bonds depend on the basicity of the adsorbate.

The adsorption of pyridine on surfaces has been employed as a probe for acid sites by many people [210] and its interactions have received much interest [211]. Studies using pyridine (pK_b 8.8-weak base) as a probe molecule have shown that temperature programmed desorption cannot be interpreted in isolation and corroborative evidence must be sought from IR studies. IR studies of adsorbed pyridine by Breen et al [212] have shown that the DTG desorption maximum (360°C) from Ni^{2+} montmorillonite, usually associated with Bronsted acid sites, was indeed

diagnostic of Lewis-bound pyridine as confirmed by the intense bands near 1450 and 1607 cm^{-1} at 250°C. Therefore the TGA desorption maximum must be attributed to desorption of pyridine from Lewis acid centres. VT (variable temperature) IR (transmission) studies of pyridine sorbed to Ni^{2+} montmorillonite have shown the presence of a weak band at 1540 cm^{-1} attributed to Bronsted bound pyridine and strong bands at 1485, 1450 and 1606 cm^{-1} attributed to Lewis bound pyridine at 150°C. As the temperature was raised above 250°C the Bronsted band became indistinguishable. This is contrasted to the studies of Al^{3+} exchanged montmorillonite in which well resolved Bronsted bound pyridine bands at 1540 cm^{-1} were observed at 250°C.

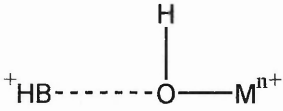
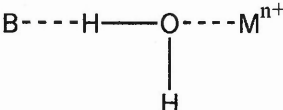
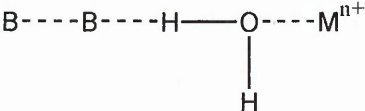
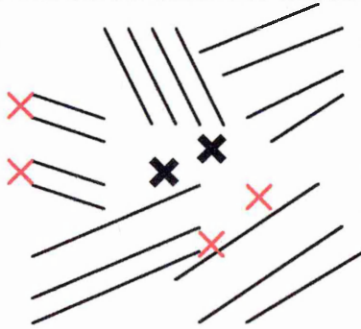
Haderlain and Schwarzenbach [213] have studied the sorption of a large number of nitro aromatic compounds on montmorillonite, illite and kaolinite surfaces in order to predict their movement through soil systems. The effects of pH was found to be very important in relation to sorption, degradation and mobility. There is an abundance of papers concerning the kinetics and effects of pH on clay organic interactions. Knözinger [214] in his investigation into infrared as a probe for surface acidity, laid out a selection of criteria for probe selection and reviewed the suitability of a variety of probe molecules (ammonia, pyridine, acetonitrile, benzene and carbon monoxide). The characterization of protonic sites is also discussed in terms of surface acidity and acid strength. Selected examples are described, but with special reference to simple binary oxides, supported oxides and zeolites. Shimazu et al. [215] the adsorption of pyridine and 4-vinylpyridine onto Li-hectorite by FTIR. The former forms a hydrogen bond with interlayer water (Bronsted acid site) whereas the latter forms a coordination bond with the exchangeable Li^+ (Lewis acid site). This was attributed to proton affinity, which is high in pyridine and lower in the vinyl

pyridine. Gonzalez et al. [216] determined surface acidity on Al- and Al/Ga- pillared montmorillonite using pyridine as the probe molecule and compared these surface acidities to that of Na- montmorillonite. The reference Na clay-pyridine complex heated at 200°C exhibits bands at 1445 and 1601 cm^{-1} due to Lewis sites, and very weak bands at 1546 and 1638 cm^{-1} due to Bronsted sites. At 400°C only bands attributable to Lewis acid sites are observed, but slightly shifted to lower frequencies. Al-pillared-montmorillonite pyridine complex heated to 200°C exhibits very intense bands at 1455 and 1620 cm^{-1} and a medium sized band at 1546 cm^{-1} indicating that the pillared clay contains mainly Lewis sites with fewer Bronsted sites at this temperature.

Montmorillonite can also be used in catalysis reactions because of its ability to retain and modify compounds after intercalation (process where guest molecules are introduced between the sheets of a layered silicate) has been achieved. Barrer [217] reviewed his work over a period of 40 years on non-porous sorbents and microporous shape-selective sorbents derived from palygorskite, smectite and vermiculite. He has shown the success of using modified clay minerals (shape selective, molecular sieves) as highly effective sorbents in the separation of mixtures. Lagaly and Beneke [218] have compared the process of intercalation of non-clay layer compounds to the exchange reactions of clay layer minerals. The general conclusion reached was that non-clay minerals in many ways behave like clay minerals, but that there was no doubt that the reactivity of clay minerals and the variety of their reactions cannot be exceeded by any other material. These properties can be modified as can the product yield by varying the exchangeable cation and fine tuning of selectivity of the relative concentrations, temperature and contact of the various species [219-221].

Lacher et al [222-224] performed a very detailed study on the interactions between cation exchanged montmorillonites and benzinine (a pesticide) and showed that numerous types of interactions were formed. Other examples of smectite complexes; include sufolane adsorbed on cation substituted montmorillonites [225] and interactions, the interactions of alachlor (a herbicide) with homoionic montmorillonite [226], and the adsorption of atrazine on smectites [227]. The different types of interaction are summarised in figure 4.3.

Figure 4.3 Possible clay-organic interactions

<p>(1)</p> 	<p>Protonation of Organic molecule Water that is coordinated to exchangeable metallic cations serves as a proton donor (Bronsted acid). This depends on two factors, firstly the polarising power of the metal (M^{n+}) and the basic strength of the organic molecule (B). The organic molecule may become protonated by accepting a proton from a H_2O molecule thus gaining a positive charge i.e.</p>
<p>(2)</p> 	<p>Water bridge The water molecule may act as a bridge between the cation and the organic molecule</p>
<p>(3)</p> 	<p>Lewis Acidity At room temperature or when subject to thermal dehydration, the exchangeable cations may serve as Lewis acids and adsorbed bases may become directly coordinated to the cations. If M is an alkali metal cation, then the bond between it and B is mainly electrostatic, ion dipole interaction.</p>
<p>(4)</p> 	<p>Water bridge associations Organic molecules may also be associated with molecules of type 2. The presence of these depends greatly on the size of the molecule.</p>
<p>(5)</p> 	<p>Other associations Organic molecules may also be associated with broken edges, external clay surfaces, with substitutions in the tetrahedral layer or clusters between stacks of clay layers.</p> <ul style="list-style-type: none"> ✕ Clusters ✕ Individual organic molecules

The bonding link between organic cations and the charged silicate surface is fundamentally electrostatic, but physical non-coulombic forces, contribute to adsorption. Fixation is favoured if the organic molecules contain functional groups capable of interacting by hydrogen bonding with the silicate surface oxygens of the tetrahedral layer. These tetrahedral layers are arranged in ditrigonal symmetry. Weiss et al. (1958) demonstrated that groups with trigonal symmetry i.e. NH_3^+ groups in alkylammonium or guanidinium ions, favoured reaction. It has been observed that when the charge on the silicate surface is tetrahedrally located, the combined effect of electrostatic and hydrogen bonding interactions determines the keying of the NH_3^+ groups of alkylammonium ions into the surface cavities. In addition to the five main types of interaction, it is possible for positively charged organic molecules to exchange with interlamellar cations [228]. However, the number and variety of organic compounds which can acquire a positive charge is limited. Many such compounds (e.g. alkylammonium ions) contain nitrogen, of which the amines form the largest class. The benefit of such cation- exchange is that a fixed internal porosity is achieved since the pore size and shape depend on the alkylammonium ion. Harper and Purnell [229] used this fact to create a novel absorbent system for organic vapour sampling which would overcome problems encountered by other absorbent systems (e.g. active carbons).

Polyamides have also been incorporated into drilling muds used for the exploration of oil [230] and a number of studies have investigated the interaction of smaller amides such as formamide [231], N-methylformamide [232] and N, N-dimethylacetamide [233] with kaolinite.

Other factors that determine the adsorption of organic molecules to smectites have been examined, such as the effect of molecular weight and basicity on

the adsorption and binding ability of amino acids to homoionic montmorillonites [234]. It was found that these factors were not as important in their adsorption as the type of exchangeable cation.

4.3.2 Typical kaolinite and organic molecule interactions

In comparison to smectites, the ability of kaolinite to intercalate organic molecules is limited, yet a range of compounds are known to do so. Molecules which were considered reactive were classified by Weiss et al [235] as follows

- (1) Compounds that would form strong hydrogen bonds to the silicate layers e.g. urea, formamide, acetamide and hydrazine
- (2) Compounds with pronounced betaine-like character with the possibility of strong dipole interactions with the silicate layers, e.g. dimethylsulphoxide
- (3) Alkali salts of short chain fatty acids, in particular acetic and propionic acid

Non-reacting guest compounds can be entrained between the layers by reactive guest molecules. The basic principles of intercalation reactions have been highlighted by Lagaly [236]. The reactive guest molecules enter the interlayer space and expand the kaolinite layers, essentially making the kaolinite into a single layered mineral. The intercalating molecule essentially breaks the hydrogen bonds between the hydroxyl groups and the adjacent siloxane layer. Hydrogen bonds are then formed with either the oxygen surface of the siloxane layer or the hydrophilic hydroxyl surface of the gibbsite like layer. The possibility also exists that the molecule may also interact with the end surfaces of the

kaolinite. However, it is more difficult to intercalate polar organic molecules because the strong hydrogen bonding between the kaolinite layers needs to be broken. Intercalation is strongly dependent on a variety of factors as highlighted by Olejnik et al [237]. The following factors may equally apply to swelling and non swelling minerals.

(1) Dipole moment-molecular size balance

To achieve direct intercalation, the organic compound should be small and possess a large dipole moment. However, in general high polarity is associated with large molecules. Obviously these characteristics may act in opposition to each other. The compounds pyridine N-oxide (PNO), hexamethylphosphortriamide (HMPT) and dimethyl sulphoxide (DMSO) were the most polar of compounds examined, each possessing a large dipole moment. Whilst PNO and DMSO intercalate quickly [238-239]. HMPT does not intercalate at all. This is not expected as HMPT is the most basic (i.e. dimethyl formamide (DMF) intercalates very slowly due to its low basicity).

(2) The effect of the extent of association in the liquid or solid

The concept is that the more 'free' solution molecules present the faster the intercalation. There appears to be a lower concentration limit of greater than 10 molar. It is suggested that at higher concentrations there is a larger proportion of molecules which are relatively free, that is not solvated by the solvent, compared to the situation in concentrations below 10M. However, there is an upper limit,

which is governed by the extent of association in the organic liquid itself. The addition of water or polar molecules such as methanol or ethanol may break up the extensive structure of the pure liquid into smaller aggregates which are more suitable for intercalation. Thus a large dipole moment can also slow the rate of intercalation. The degree and strength of hydrogen bonding in the liquid will determine the ease with which the structure is broken down. For example, strong hydrogen bonding exists between NMF molecules which accounts for its lower volatility when compared to formamide.

(3) Temperature

If the temperature of the liquid is raised, the greater thermal motion results in disruption of the structure. The temperature effect is more marked for DMSO than for formamide [240]. Equally, intercalated probes need to demonstrate selective thermal stability, where the detection of thermal events are well resolved and ideally do not desorb in the presence of other interfering components i.e. H₂O and CO₂. The reactivity of the probe molecule at applied temperatures should also be low to avoid surface reactions which might lead to decomposition and the evolution of other components other than the probe.

(4) Molecular dimensions

The size of the intercalating molecule is affected by the size and type of functional groups. The electron donating effect of methyl groups can enhance delocalisation of the charge in amides and increase the basicity of the carbonyl atom, resulting in

a marked variation in the intercalation of amides in kaolinite. Methyl substitution enhances complex formation and the stability of the complex (i.e. formamide and DMF). Therefore molecular size of the potential probe should be as small as possible for several reasons. Firstly, the most important adsorption sites are usually acid centres which may be located in narrow pores or in cavities which are only accessible through narrow openings or channels. Secondly, the acid site, in particular aprotic Lewis acid sites, may be exposed in an oxygen vacancy and therefore may be sterically hindered by neighbouring oxide ions of the probe (or the basic functional group of the probe). Thirdly, large probe molecules may adsorb on one site in turn blocking another potential site of close proximity (i.e. steric hindrance in 2, 6 disubstituted pyridines) [241]

(5) Orientation and packing of the intercalated molecules

Olejnik et al. [237] also found that the difference between the minimum dimensions of non-expanded kaolinite and the d-spacing of a variety of complexes, suggested that there was considerable keying of the molecules into the kaolinite surface. Considering the lack of exchangeable cations and the absence of multi-layers in the gallery (as seen in montmorillonite complexes), it suggested that the polarity of kaolinite plays a much more important role in swelling behaviour than montmorillonite. Molecular orientation of an intercalated probe can be determined by XRD (by virtue of the d-spacing) combined with IR dichroic studies, where the sample angle to the IR beam is altered and the intensity of chosen bands are seen to increase or decrease, which infers the orientation of the probe.

The intercalation of dimethyl sulphoxide (DMSO) has received considerable attention. Intercalation of DMSO into kaolinite provides a method for the incorporation of alkali and alkaline metal salts into the kaolin by the replacement of DMSO [242-243]. Due to strong dipole interactions with the silicate layers, DMSO is able to intercalate very efficiently. It was shown by Breen and Lynch [244] that 1.5 DMSO molecules were intercalated per unit cell of kaolinite. Due to the very strong interactions, DMSO was found to greatly distort the kaolin layer. After removal of DMSO, the structure did not return to the dimensions of its pre-intercalated state. It was suggested that this was due to introduction of severe stacking faults. Confirmation was provided by IR spectroscopy, which showed that DMSO oxygens with their basic electron donor characteristics, resulted in strong perturbations of the inner surface hydroxyls [245]. Complimentary studies by Frost et al. [246] (on the de-intercalation of DMSO from high and low defect kaolinite) showed clear changes in the 3660 cm^{-1} band which was attributable to inner surface hydroxyls hydrogen bonded to DMSO. Johnson [245] has shown that as DMSO intercalates into the interlayer space of kaolinite, causing it to expand. It was demonstrated that the DMSO molecules are orientated within the layers so that the oxygen of the DMSO molecule hydrogen bonds to the inner surface hydroxyls of the kaolinite.

A study by Sugahara et al.[247] showed that it was possible to intercalate pyridine into kaolinite to form a well ordered complex with a basal spacing of 12Å . This suggests that the pyridine molecule is intercalated in a perpendicular position as the thickness of the collapsed layer is of the order of 7.14Å . The subsequent IR spectroscopic studies, again reveal similar trends seen with other

intercalates. Because of the lack of interlayer cation, intercalated molecules may have direct access to both inner surface and inner hydroxyls, generally the effect of which is seen as reduction in relative intensities and shifts to lower frequency. Similar effects have been observed by Ledoux & White [248] during a study involving the intercalation of kaolinite with hydrazine, formamide and urea.

Other organo-mineral interactions

Illite is a non-expanding 2:1 layer silicate and adsorption of organic molecules is generally confined to crystal edges. However, some workers would allow a small amount of expandable layers (up to 10%); others would allow none. Srodori and Eberl [249] have determined the presence of expandable layers by comparing the ratio of the air dried XRD tracing to that of the glycolated tracing. A ratio of one indicates the complete absence of expandable layers.

Frissel and Bolt [250] compared the uptake capacity of non-ionic herbicides and found it was in the order montmorillonite > illite > kaolinite. This same pattern was also observed by Pinck et al [251]. when they studied the adsorption of a number of antibiotics. Tomlinson et al. [252] studied the uptake of paraquat and found that displacement increased in the order montmorillonite < illite < kaolinite. Grim et al. [253] determined the uptake of large organic cation (i.e. N-butyl ammonium) by potassium saturated samples of kaolinite, illite and montmorillonite. Uptake was shown to be accompanied by a stoichiometric replacement of potassium from the exchange sites. It was believed that illite reacted with the organic ions up to its exchange capacity. However, the ions were

thought to be limited to the exterior surface of the illite particles, i.e. they did not replace the interlayer potassium ions.

Faure and Landas [254] evaluated (by GC-MS), the low temperature oxidation (100°C) of n-alkanes to determine the effect of two different minerals, illite and calcite. Illite demonstrated both retention and catalytic properties underlined by the production of oxygenated compounds. They suggested that the compounds generated seemed to be formed through both the fixation of oxygen in different positions on the original n-alkane chains and the breakdown of the initial alkanes. In contrast calcite demonstrated none of these properties.

Whilst there is an abundance of examples of studies on chlorite in the literature, these are mainly concerned with the diagenetic processes leading to its formation and distribution. In comparison, the adsorption of organic molecules to chlorite has not been investigated in much detail due to the fact that it has a limited adsorption capacity. It is believed that if adsorption does occur, it will be confined to the external crystal edges [255]. Interestingly enough, studies by Sannino et al. [256] on the adsorption-desorption of simazine on montmorillonite (under buffered conditions) reveal that simazine was adsorbed in large quantities by montmorillonite surfaces, whereas adsorption was significantly decreased with increasing $\text{Al}(\text{OH})_x$ (chlorite-like complexes) species on montmorillonite surfaces. Another relevant study [257] involved the sorption interactions between trace metals (Cd and Ni) and phenolic substances on suspended clay minerals (chlorite, illite and kaolinite) [256] from an estuarine system. Adsorption isotherms for Cd, Ni and phenolic compounds (eugenol and vanillic acid) were investigated. It was found that chlorite was a better adsorbent for both Cd and Ni and that the presence of phenolic compounds increased the sorption of metallic cations.

Very little is found in the literature relating to the adsorption of organic molecules to carbonates. Ince et al., have studied the adsorption of oleic acid and oleate on apatite surfaces and dolomite. Under buffered conditions (pH 4) and addition of Na ions, flotation of dolomite was achieved. This occurred because of preferential adsorption of oleic acid, which was confirmed by FTIR spectroscopy.

Similarly literature demonstrating the adsorption of organic molecules to quartz and feldspar is also sparse. In comparison to clay minerals, the surface area of the minerals is both small and relatively unreactive. However, an infrared study of the adsorption of n-butylamine to SiO₂ and Al₂O₃ by Sokoll et al. [258] reveals that n-butylamine formed only weak hydrogen bonds with the surface hydroxyl groups of SiO₂, but stronger bonds between the nitrogen atom and the Al³⁺ cation of Al₂O₃ were formed. In comparison, Quartz does not possess such a large number of hydroxyls and therefore interaction would be less likely and more difficult to observe. Several other correlations between IR frequency shifts (OH) of silanol groups with various properties of basic probe molecules have been reported and were reviewed by Paukshtis and Yurchenko [259] and by Boehm and Knozinger [260]. Other studies by Titova and Koshleva [261] studied the interaction between triethylamine (TEA) and silica by IR spectroscopy. TEA is widely used as a probe for acid sites on silica. A variety of bonding types were identified ranging from hydrogen bonding to proton transfer from TEA to SiOH, which yielded a thermostable salt (Et₃HN)⁺(Si-O)⁻ to 500°C [262].

In short, the expected interactions between quartz, feldspar and organic molecules will be limited and ultimately will be confined to weak hydrogen bonding and possible proton transfer at edge sites. Analogies are generally drawn between the surface chemistry of alumina and feldspar. However, Korentsky et al.

[263] have shown that this is not a reliable guide when they demonstrated that isolated SiOH surface species such as those found on quartz and silica do occur on feldspar, but AlOH groups seen on alumina do not. The implication for these potential reactions, is that in the presence of clay minerals, both the low surface area and reactivity will make these interactions difficult to detect.

4.4 Methods used to analyse organo-mineral interactions

4.4.1 Thermal methods TGA, DTA, DSC and EGA

Thermal analysis refers to a group of methods in which some physical property of the sample is continuously measured as a function of temperature whilst the sample is subjected to a controlled temperature change [264]. Thermal methods have been used for a very long time to study organo-mineral interactions. TGA curves show when the sample is losing weight, while DTA or DSC show if that reaction is exothermic or endothermic, which can be associated with desorption, adsorption, sublimation, vaporisation fusion and solid state transitions [265]. DTA and TGA are often carried out in a variety of atmospheres, i.e. air, where organic material undergoes oxidation, although pyrolysis may also occur. In inert atmospheres such as N₂ or He, pyrolysis and liberation of the organic material occurs.

In this thesis, TGA is rarely used in isolation as it is not possible to assign particular weight losses without confirmatory techniques such as FTIR and/or EGA. TGA may have the potential to provide kinetic data, however the weight losses in many cases may be attributable to a variety of interrelated reactions, which in TGA may appear as one thermal event. More often than not, the output from TGA contains several un-resolved weight losses, where weight loss assignments are difficult if not impossible. Therefore, they provide no information which would elucidate the type of interaction(s) occurring between the clay and organic molecule. For example, modified TGA studies of the analysis of calcium montmorillonite treated with hexamethylene diisocyanate [266], have without

confirmatory evidence attempted to determine the amount of polymer produced between 20-1000°C. However the authors were unable to verify the nature of the products produced due to the restrictions of the technique used. Similarly, Yariv's DTA study of the adsorption/desorption of organic molecules [267] (aliphatic and aromatic amines) demonstrated the presence of a catalytic effect, but failed to recognize any correlation between the behaviour of non adsorbed, free, complexed, and adsorbed amine. In turn the authors recognised this problem with a view to utilising more sophisticated methods as seen below.

4.4.2 Evolved gas analysis (EGA)

On the most important techniques which compliments the information gained from TGA and DTA is Evolved Gas Analysis (EGA). There are many types of EGA systems and there are numerous examples in the literature. A review by Dollimore et al. [268] and more recent articles by Redfern [269] have set out the ideal requirements of any combined system. Relevant to this thesis are two excellent reviews which discuss the use of EGA with MS [270-271].

EGA has not been widely used in mineralogy or as a geochemical technique. However, Roche et al. [272] demonstrated the usefulness of pyrolysis-mass spectrometry during determination of NH_4 as a litho chemical indicator of mineralisation, whereas Shepherd et al [273] suggested EGA had the potential to detect subtle zones of hydrothermal alteration where trace element indicators would fail. Carbonate, sulphate, sulphide and clay minerals are all suitable for examination by this technique, as they produce distinctive profiles of volatile generation related to thermally-induced reactions such as decarbonation, oxidation

and dehydroxylation. Provided the stoichiometry is known, measurement of the amount of volatile generated gives the concentration of the host mineral phase in the rock.

In an early paper by Morgan [274], DTA-EGA were used simultaneously with a view to quantitative determination of the mineralogical composition of potential industrial raw materials (sulphides, alunite, pyrite in shale, impurities in fullers earth and ceramics). The DTA apparatus was linked to specific non-dispersive H₂O and CO₂ infrared detectors and an electrochemical SO₂ detector. For example, using known standards it was found that integration of the EGA H₂O profile for malachite was shown to be very close to the stoichiometric theoretical value of 8.40%. Close agreement was also achieved for CO₂. However, the author also highlighted problems related to the transport of evolved gases, which showed a time lag of 30 seconds, possibly due to temporary condensation between the furnace and analysis cell.

A study by Yariv [275] of organo-clay complexes (cationic dye-smectite complexes and amine-sepiolite/palygorskite complexes) by combined DTA-MS focused on the contribution of EGA to the interpretation of different DTA peaks. It was concluded that CO₂ and NO₂ curves were unequivocal, but H₂O curves could be misleading because dehydration and dehydroxylation of the clay may overlap the organic water evolution. However, it was suggested that this could be overcome by performing parallel runs under nitrogen and air. No attempt was made to relate gas evolution profiles with particular organic-mineral associations. Inglethorpe et al.[276] also used EGA (TG and non-dispersive infrared detectors) to quantitatively determine NH₄, H₂O and SO₂ in geological materials (i.e. feldspars, illite). The system was shown to be capable of detecting

NH₄ as low as 120 ppm. However, fully quantitative determination was less successful and was attributed to the partial oxidation of NH₃. In comparison NH₃ did show a positive linear correlation with NH₄ determined by a modified Kjeldahl method.

A review of the applications of evolved gas analysis in the earth sciences was assembled by Morgan et al [277]. They concluded, that in comparison to conventional methods, those employing MS, offer the versatility of several volatiles being investigated simultaneously and with greater sensitivity. It was also inferred, that volatile temperature release patterns may link them to individual mineralogical phases, which could provide information pertaining to their geological history.

Mullens et al [278] used TGA-FTIR EGA for detection of evolved gases from clay under a linear temperature ramp (25-1200°C). Initial assignments included the detection of two CO₂ maxima, which were attributed to the combustion of organic matter (200-600°C) and the decomposition of calcite (700°C). The detection of two H₂O maxima were attributed to the breakdown of organic matter (200-400°C) and the dehydroxylation of clay minerals (550°C). The preliminary results also identified different sulphur containing functional groups present in the clay. However, the clay mineral in question was not identified, but a dehydroxylation maxima present at 550°C suggests a member of the kaolinite group of minerals. This study encouraged the authors to further investigate the system using suitable model compounds.

Using a EGA system based on a non-dispersive infrared detector, Parsons et al. [282] were able to identify and quantify the principal volatiles produced by heating powdered brick samples. Results demonstrated, that water vapour

performs a critical role in the firing process where organic matter is only able to oxidise completely when the pore system is free of water vapour. It was also inferred that anhydrite formation takes place during pyrite oxidation by a sulphur dioxide-calcite displacement reaction. From mimicking the production heating process, atmospheric emissions from brick production could be predicted.

Bloodworth et al. [279] developed an evolved water analysis (EWA-DTA-FTIR) system which was used for the detection and estimation of low levels of kaolinite (0.25%) in mineral mixtures and kaolinite bearing sandstone rocks. The method described the analytical determination of kaolinite as a result of dehydroxylation. Linear regression was applied to peak area profiles from artificial mixtures of quartz and kaolinite (0-10%) and gave a statistically significant correlation coefficient of 0.997, but with curvature developing at low concentrations. Previous studies on the evolution of carbon dioxide from low concentrations of carbonate minerals [280] suggest this was an experimental artifact, being a function of the rate of gas diffusion. In comparison, the analysis of kaolinite in sandstone mixtures demonstrated a distinctive two-stage dehydroxylation. The authors suggested that the two-stage dehydroxylation may be due to the presence of chlorite, a low temperature event at 600°C attributable to the dehydroxylation of the brucite sheet and dehydroxylation of the talc sheet at about 800°C. To confirm this suggestion, the samples were acid treated to remove chlorite, followed by XRD analysis, which identified a minor chlorite presence. EGA analysis of acid treated samples also showed a slight reduction in the area of the water peak. However the authors eliminated the presence of chlorite without additional FTIR analysis, though they did suggest the possibility that a more

crystalline member of the kaolinite group may be responsible for the higher temperature peak.

Thornley and Primmer [281] used TG-MS combined with XRD for the quantitative whole-rock analysis of clay minerals in sandstones by evolved water analysis (EWA). Artificial sand/clay mineral mixtures were prepared with known amounts of different clay minerals (chlorite-CCa1, illite-1Mt and kaolinite-KGa2). Results showed that over a twelve month period, the precision of repeat determinations was < 5% for TG-EWA in comparison the accuracy of the combined methods (TG-EWA-XRD) which was higher and therefore more influenced by the XRD data. Unlike the methods used in this thesis, the authors calculated the total clay content from dehydroxylation alone. They did not attempt to calculate the weight percentages of the individual components, because of the inherent overlap of the individual dehydroxylation temperatures. No smectite was included in their studies.

Heide et al [282] showed that TG-MS gas release profiles are an effective tool for the identification and characterization of minerals and rocks extracted from a variety of depths. By examining whether the profiles were continually changing or subject to spikes, they were able to indicate the physico-chemical conditions influencing the formation and alterations in the samples. They observed that hydrocarbon release ($m/z = 15$) was different depending on the extraction depth, but more importantly, there existed a correlation between release of hydrocarbons and the water of dehydration.

4.4.3 X-ray diffraction (XRD)

Organic molecules which have been intercalated into the interlayer space of clay minerals can be observed by X-ray diffraction. The determination of the d_{001} spacing is used to establish whether intercalation has occurred. A knowledge of the molecular dimensions of the adsorbed molecules and interlayer space of the clay can help elucidate the orientation of the adsorbed molecule and number of adsorbed layers. However, XRD does not give direct evidence of adsorption mechanisms.

4.4.4 Infrared spectroscopy

In this thesis DRIFTS and VT DRIFTS have been chosen to study the interaction between the chemical probes and the clay minerals. Knozinger [214] has reviewed infrared spectroscopy for the study of acidic sites on oxides and zeolites using probe molecules. Several types of compound were evaluated for their suitability. Nitriles were considered to be less sterically hindered. In particular the C-N stretching mode is found to be sensitive to intermolecular interactions and typically shifts by 30-60 cm^{-1} to higher frequencies when coordination bonds are formed to aprotic (Lewis) sites via the nitrogen lone pair electrons, whilst hydrogen bonding leads to a shift of only 10-15 cm^{-1} . Hydrogen bonding is also noted for inducing a characteristic shift of the O-H stretching mode of surface hydroxyl groups. A similar review by Larcher et al. [283] examined IR spectroscopy of adsorbed molecules, some of which were organic (e.g. n-butylamine, pyridine, nitriles and benzene). The paper reviewed simple oxides and zeolites, however, these have similar structures to clay minerals

and therefore their spectroscopic absorbance bands will be of interest. Absorbance shifts examined included the N-H deformation band of ammonia, 1450 and 3300 cm^{-1} when present as the ammonium ion, and 1250, 1630 and 3330 cm^{-1} when it is coordinated.

Parker and Frost [283] have studied molecular adsorption and desorption reactions of volatile organic compounds on montmorillonite (dimethyl sulphide, propanoic acid and trimethylamine) as a mechanism of slow release odour generation for the application of attracting pest animals, in particular wild dogs. Multicomponent analysis of the DRIFTS spectra provided an effective means of measuring low concentrations ($\approx 10\text{mg.g}^{-1}$).

The thermal and DRIFTS characterisation of dimethyl formamide/Ca-, Mg- and Na- exchanged montmorillonite intercalates Breen et al [284] has shown that the derivative thermograms for the desorption of DMF from the M^{n+} -SWy-2 complexes can be used to distinguish between different exchange cations by the temperature at which the most strongly held DMF molecules were desorbed. Strongly held DMF molecules are directly coordinated to the exchangeable cations. VT DRIFTS has also shown that maxima observed in the DTG traces at lower temperatures are due to the desorption of DMF and water clusters.

Petit et al.[285] used DRIFTS spectroscopy to interpret the infrared NH_4^+ spectrum of ammonium saturated smectites. The study showed that K^+ from KBr can easily replace NH_4^+ in some clays, and that Ca^{2+} is able to replace even those NH_4^+ ions which are not replaceable by K^+ . The NH_4^+ band at 1440 cm^{-1} was assigned to the NH_4^+ ions compensating the negative charge of the clays. When KBr was used as a diluting matrix, the ν_4 band was located at 1400 and/or 1440 cm^{-1} . The band at 1400 cm^{-1} , related to the NH_4Br , originating from the replacement of NH_4 in the clay

by K^+ from the KBr. For swelling minerals the 1400 cm^{-1} band indicated that layers have permanent low charge density of variable charge only. The $\nu_4\text{ NH}_4^+$ band at 1440 cm^{-1} suggested that the NH_4^+ in the clay was not replaced by K^+ from KBr. Johnston et al. [286] used VT infrared spectroscopy to study the vapour phase sorption of p-xylene on Co and Cu-exchanged montmorillonite. The cell used incorporated TG and FTIR analysis. This is similar to VT-DRIFTS previously discussed, in addition the sample weight losses are recorded. Shifts in the infrared bands of p-xylene in the presence of Cu-montmorillonite, demonstrated chemical bonding, whereas p-xylene bands in the presence of Co-montmorillonite showed no shifts and therefore demonstrated chemisorption.

Other examples of the use of DRIFTS spectroscopy include, White [287] (polystyrene in diamond powder), Davies et al.[288] (fuel hydrazines adsorbed on silica, alumina and ferric oxide surfaces), Chalmers and Mackenzie [289] (foams), Martin and Zabransky (zeolites-ZSM-5, H-ZSM-5, Fe-ZSM-5 and Na-ZSM-5) [290].

4.4.5 Other Techniques

Other techniques have been used to study organo-clay reactions. Raman spectroscopy has been used with a host of other techniques (XRD and FTIR microscopy) to study the intercalation of kaolinite with formamide [291]. Comparisons with FTIR showed that Raman provided more favourable results in the hydroxyl region (i.e. not observed in the FTIR spectrum), resolving two additional bands at 3610 and 3627 cm^{-1} , which were attributed to inner surface hydroxyls hydrogen bonding to the carbonyl group (C=O).

Cenens and Schoonheydt [292] have used UV-VIS spectrophotometry to study the kinetics of the interactions of methylene blue and neutral red dyes on montmorillonite and hectorite. Adsorption bands were assigned to specific dye-clay complexes.

NMR has been used in the conformation of poly(ethylene oxide), PEO, intercalated in layered clays and MoS₂ has been characterized by double-quantum solid-state NMR [293]. NMR has also been used by Breen [294]. Here the interaction of polymers with clays is considered with particular emphasis on the adsorption of polycations of the type [CH₂CHOHCH₂N(CH₃)₂]_n^{nt+} onto a low iron Texas bentonite, Westone-L (WL). The information obtained from Cs⁺- and Na⁺-WL suspensions using ¹³³Cs and ²³Na solution phase NMR can provide quantitative information regarding the displacement of Cs⁺-ions from the exchange sites by polycation in suspension.

Currently the use of molecular modelling has become a popular technique for studying the interactions between solids and liquids. Furthermore, clay particles are reasonably well characterized and may be used in numerical simulations as a model of mineral surfaces. Boek et al, [295] have used Monte Carlo simulations in order to understand the role of potassium as a clay swelling inhibitor. Comparisons of simulation data with experimental swelling curves, found a striking level of agreement. When Na⁺ and Li⁺ were increasingly hydrated in simulation, they were found to become detached from the clay surface. In contrast, K⁺ ions migrated, and bind to the surface, in effect screening the negative charge of the mutually repelling clay surface, thus inhibiting layer expansion.

Teppen et al. [296] also used molecular modelling simulations to determine the sorption of trichloroethane to kaolinite and pyrophyllite at different levels of

hydration. In agreement with experimental trends, water was found to be more competitive than C_2HCl_3 for clay surface sites, demonstrating that at least three distinct mechanisms coexist for C_2HCl_3 on clay minerals in the environment. The most stable interaction was coplanar with full molecular contact to the basal surface, however this was suppressed by increasing water loads. The other remaining mechanisms in order of stability, were single atom contact through the Cl atom and contact through a water bridge.

Electron paramagnetic resonance (EPR) spectroscopy has been used to mainly study subtle changes in the structure of kaolinite layers and to study the kaolinite/organic complexes [297-298]. (EPR) spectroscopy has also been used to study the control of bioavailable xenobiotics in soils and sediments [299]. The fate and spatial distribution of two nitroxide spin probes (Tempol and Tempamine⁺) were monitored in batch experiments involving Ca-hectorite suspensions and pastes. In these systems, EPR was able to discriminate between probe molecules in different environments (e.g., adsorbed, in bulk solution or in large interstitial pores). Addition of sodium ascorbate causes the chemical degradation of the probes in the bulk solution and allowed the kinetic release of the probes from the clay aggregates and/or paste to be monitored in time. In all cases, the release proceeded to completion in less than a day, indicating that the probes were not durably sequestered by the hectorite.

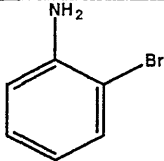
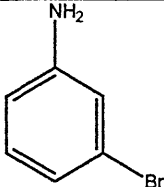
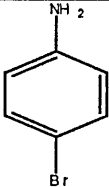
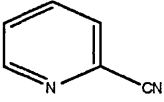
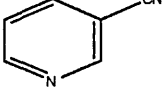
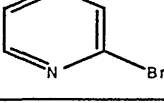
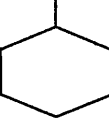
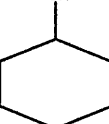
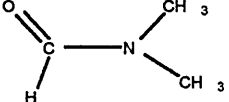
Chapter 5 Application of chemical probes cyclohexylamine (CHA) and 3-cyanopyridine (3 CYP)

5.0 Introduction

The chemical probe method may be in its development stage, but great progress has been made. The potential probes which have been studied so far are shown in Table 5.1. Most of these probes are liquid at room temperature, (except 3-Cyanopyridine) with sufficient volatility to interact with minerals via their vapour phase. Throughout the development of the method, probes were chosen progressively, i.e. when a probe proved to be limiting (i.e. failed to intercalate, long exposure time, catalytically altered), then another chemical probe was chosen in order to overcome the limiting factor.

Initial observations of probe mineral interactions are made by TGA/DTG analysis. This is the part of a 'first look' approach, the objective being to identify thermal weight losses which could be attributed to the probe molecule. For swelling minerals, more usually, EGA/FTIR analysis reveals the presence of other components such as CO₂ or H₂O and is therefore ideal for evaluating the components which contribute to particular weight losses. Ideally, weight losses should be sharp and well resolved, whilst not overlapping other areas of interest (i.e. dehydroxylation). Potential probes, because of certain chemical attributes are ideal on paper, often fail to bring about any weight losses after vapour saturation, or are so broad (lost at such a slow rate) and unresolved as to be unusable.

Table 5.1 Organic molecules used as potential probe molecules in this thesis

POTENTIAL PROBE MOLECULES	Molecular structure	RMM/bp.	Abbreviation used throughout this thesis
2-Bromoaniline C_6H_6BrN		172.02/229°C	2BA
3-Bromoaniline C_6H_6BrN		172.02/251°C	3BA
4-Bromoaniline C_6H_6BrN		172.02/62-64°C	4BA
2-Cyanopyridine $C_6H_4N_2$		104.11/212-215°C	2CYP
3-Cyanopyridine $C_6H_4N_2$		104.11/201°C	3CYP
2-Bromopyridine C_5H_4BrN		156.96/192-194°C	2BYP
Cyclohexylamine $C_6H_{13}N$		99.18/134°C	CHA
Benzonitrile C_7H_5N		103.12/191°C	BN
Dimethylformamide C_3H_7ON		73.10/153°C	DMF

Each mineral was exposed to the chemical probe separately and their derivative thermograms collected. The results show that some of the chemical probes were more suited to the requirements than others (i.e. desorption maxima due to the probe were present). However, it was not envisaged that the probe would interact with all mineral components. This does not rule out the use of a particular probe, it simply means that other detectable features of the mineral component must be utilized to enable successful qualitative/quantitative analysis (e.g. dehydroxylation). TGA alone was unable to determine whether the DTG maxima were due to the probe or residual water on or within the clay interlayer, or indeed both. This is particularly relevant to montmorillonite, as it is nearly always in a hydrated state. As expected, TGA was unable to detect low levels of the chemical probe. If TGA was successful (i.e. it was possible to detect desorption of the probe) then further studies were initiated. However, if the probe failed to produce any useful desorption events, then further studies were not carried out. If the probe provided a strong desorption maximum in TGA, then XRD studies were performed to examine whether intercalation had occurred (i.e. whether the probe occupied the interlayer space).

TG-FTIR and TG-MS were used to identify the components desorbed from thermal features observed during TGA analysis. Thus EGA helped determine not only the comparative sensitivity of TGA, but highlighted that lower quantities of the mineral could ultimately be detected. Consequently, the techniques used for chemometrics analysis was considerably easier.

VT-DRIFTS and VT-XRD were used to give a greater understanding of the types of interactions occurring. Firstly, VT-XRD could not only confirm intercalation, but could also be correlated to the changes in probe/clay interactions

observed spectroscopically using VT-DRIFTS, and desorbed gases detected during EGA. The majority of VT DRIFTS and XRD are discussed in this chapter.

5.1 Experimental

5.2 Materials

The chemical probes studied were obtained from Aldrich (>99% pure)

5.2.1 Preparation of a homoionic clay

Montmorillonite (SWy-2) containing nickel and aluminium-exchanged cations were prepared by dispersing SWy-2 in the nitrate salt of $\text{Al}(\text{NO}_3)_3 \cdot 9\text{H}_2\text{O}$ and $\text{Ni}(\text{NO}_3)_2 \cdot 6\text{H}_2\text{O}$, respectively. The samples were shaken overnight and repeatedly washed and centrifuged with deionised water until the conductivity of the supernatant was less than 50 μS .

In order to check that the clays were successfully exchanged, quantitative X-ray fluorescence (XRF) analysis was performed. Samples for XRF analysis were prepared using the $\text{Li}_2\text{B}_4\text{O}_7$ fusion method and the data was collected using a Phillips PW2400 XRF spectrometer.

5.2.2 Exposure/Intercalation procedures

Exposure of a sample to a chemical probe was achieved by exposing the probe to the vapour by the method described in chapter 4.

5.2.3 Intercalation via the vapour phase

50 mg of the sample was ground for a period of 1 minute using a pestle and mortar, was weighed into a small sample vial and transferred to a sealed gas jar which contained 5ml of the chemical probe for fixed periods of time.

5.3 Characterisation of homoionic cation exchanged SWy-2 montmorillonite using cyclohexylamine (CHA).

5.3.1 Introduction

Cyclohexylamine, the first potential chemical probe investigated in this thesis, was chosen because it demonstrates several important features which may help characterise pore lining minerals .i.e.

- (1) Cyclohexylamine should give sharp desorption events that would distinguish adsorption to various cation exchanged clays, which are easily identified by TGA, FTIR and MS.
- (2) A high vapour pressure and the ability to be absorbed very quickly into smectites [300].
- (3) The presence of nitrogen (NH_2 group) in the molecule where lone pair electrons would be available to bond to an interlayer cation centre. The presence of an NH_2 group, may in the presence of a polarizing interlayer cation and water, produce a protonated adduct which may be detected using infrared spectroscopy.

Ultimately, the use of chemical probes will be applied to whole rock samples obtained from working reservoirs. Before this can be done, a more basic understanding of the interactions with relatively pure mineral samples needs to be established. The interaction with homoionic swelling minerals, mixtures of mineral standards and whole and crushed rocks have been examined in this thesis.

The interaction of chemical probes was first studied with homoionic swelling smectite ($\text{M}^{\text{n}+}$ -SWy-2) for several reasons. Firstly, it is more likely to interact with a

swelling mineral due to the reasons previously discussed (i.e. greater surface area, more potential binding sites etc.). Secondly, SWy-2, is the smectite which is most representative of that found in working reservoirs. In addition, using different homoionic Ni^{2+} (Lewis acidity), Al^{3+} (Brönsted) SWy-2 provides the opportunity to determine whether the probe can distinguish both the swelling mineral and the type of interlayer cation (i.e. whether it produces a resolved thermal event for each type of cation). This distinction can provide the analysts with characterisation information to determine whether different swelling minerals with the same interlayer cation provide similar desorption patterns. Such information not only enhances the understanding of the smectite present, but it provides observable differences to enable the application of chemometrics. Indeed, Haderlein and Schwarzenbach [301] highlighted the need to quantify the type of cations on clay mineral surfaces in order to predict the fate of environmental pollutants in soils and sediments.

It is well established that clays can act as effective catalysts for a variety of organic reactions where they act as a source of protons. Al^{3+} -exchanged clays generally exhibit the highest activity and this is attributed to the polarisation of the water molecules in the coordination shell by the small highly charged Al^{3+} -cation [302-305]. The acidity of the catalytically active forms of clays and other acidic solids is often probed using the thermal desorption of sorbed nitrogen-containing, bases including ammonia [306-308] and butylamine [306, 307, 310, 311]. The desorption of cyclohexylamine (CHA) to determine the acidity of cation-exchanged [311], acid-treated [312-316] and pillared clays [317] has been extensively used since Ballantine et al. [318] first reported how the weight loss in the 300°C region of the desorption thermogram was well correlated with the yield from selected test reactions over Al^{3+} and Zr^{4+} -exchanged clays. The CHA desorption method is straightforward

and effective but is occasionally misleading, particularly when there are Ca^{2+} -cations on the exchange sites when the CHA method reports high acidities but there is zero conversion in the associated test reaction [315-319]

Yariv and Heller [320] first used IR spectroscopy to study the extent to which CHA was protonated on a range of cation-exchanged clays and reported that most interlayer cations, with the exception of Na^+ and Cs^+ , were able to produce at least some cyclohexylammonium ions at room temperature in degassed samples. Indeed IR spectroscopic investigation of adsorbed pyridine still remains the only way to unequivocally distinguish between Bronsted (proton-donating) and Lewis (electron pair accepting) sites on the surface of solid acid catalysts. Breen [310] showed that Ni^{2+} - and Co^{2+} -exchanged clays contained Lewis acid sites at all temperatures whereas Al^{3+} - and Fe^{3+} -exchanged forms offered only Bronsted acid sites whilst Cr^{3+} -exchanged clays offered a combination of both types [311]. These observations, which were obtained using samples treated with pyridine vapour, have recently been shown to be true in the presence of liquid solvents such as benzene and dioxan [321] and in test reactions which distinguish Bronsted from Lewis acidity [322]. The dominance of Lewis acid centres in Ni^{2+} - and Co^{2+} -exchanged clays has been attributed to the lower temperatures at which these two cations shed their coordination shell water [310, 323]. Indeed, Ni^{2+} -ions are known to migrate into the clay layer via the ditrigonal cavity in the silica sheet [324] as do Li^+ -ions in the well-established Hoffman-Klemen effect [325].

Evolved gas analysis (EGA) of the thermally desorbed products arising from adsorbed amines is well established and Jacobs and Uytterhoeven [306] were the first to report that sorbed alkylammonium-ions were likely to undergo Hofmann degradation during the heating process. This degradation mechanism results in

cleavage of the C-N bond to produce ammonia and the corresponding alkene, e.g. butylamine breaks down to yield ammonia and butene isomers. Indeed, Ghosh [307] demonstrated the need for caution when selecting a suitable base for the determination of acidity because the desorption of n-butylamine from mordenite exhibited two desorption maxima and mass spectral analysis revealed the presence of ammonia, and butene as well as butylamine and traces of propene and/or CO₂. Similar results were reported by Shuali et al. for the desorption of butylamine from sepiolite and palygorskite [326]

Huang and co-workers [327-328] have shown that CHA breaks down to form ammonia and benzene, which are indicative of C-N cleavage and dehydrogenation, and dehydrocyclisation on Ni (111) surfaces. In contrast, NEXAFS spectra of adsorbed CHA on the Ni (100) surface indicates the presence of both CHA and aniline. In general the interaction between CHA and metal surfaces appears to be dominated by electron pair donation from the amine to the nickel surface. Finally, Sokoll et al. [329] have shown that the main desorption products of CHA when interacting with strong Lewis acid centres on alumina are ammonia, cyclohexene and aniline.

Thus, it is clear that the desorption of bases more complex than ammonia may result in the observation of a number of decomposition products which depend upon the nature of the exchange cation in the interlayer space. Indeed Yiu et al. [309] have recently shown that secondary and tertiary amines more closely reflect the acidity values determined using ammonia than primary amines. Consequently, a detailed study of the desorption of CHA from Al³⁺- and Ni²⁺-exchanged SWy-2 has been undertaken because these cations offer Brønsted acidity or Lewis acidity, respectively. The major desorption products have been identified after trapping the gases evolved

throughout a complete desorption cycle and this information has been used to determine when the individual compounds were evolved using a combination of infrared and mass spectral analysis of the desorbed products.

5.3.2 Thermogravimetric analysis

The desorption of the chemical probe from an exposed sample was measured using a Mettler TA3000 Thermogravimetric Analyser. The sample (6-12mg) was transferred directly out of the vapour into an alumina crucible and placed directly on the thermobalance. The sample was pre-conditioned in a nitrogen gas flow ($20\text{cm}^3/\text{minute}$ for 15 minutes at 35°C). The sample was then heated to 800°C using a temperature ramp of $20^\circ\text{C}/\text{minute}$. The measurement was recorded as weight loss against temperature and then converted into the negative of the first derivative (i.e. $-dw/dt$).

5.3.2.1 Results

The derivative thermograms for the desorption of CHA from Ni^{2+} - and Al^{3+} -exchanged SWy-2 are shown in Fig.5.1. The desorption maxima at $630\text{-}640^\circ\text{C}$ has been attributed to structural dehydroxylation and the sharp maximum at 330°C for Al^{3+} -SWy-2 correlates well with that observed previously for CHA treated Al^{3+} -exchanged montmorillonite as does the shoulder at 370°C [311] However, the desorption maximum at 360°C for Ni^{2+} -SWy-2/CHA occurred 60°C above that previously reported for a Ni^{2+} -exchanged montmorillonite of different origin. The reason for this is not clear.

Figure 5.1 Derivative thermograms of Al³⁺-SWy-2-CHA and Ni²⁺-SWy-2-CHA

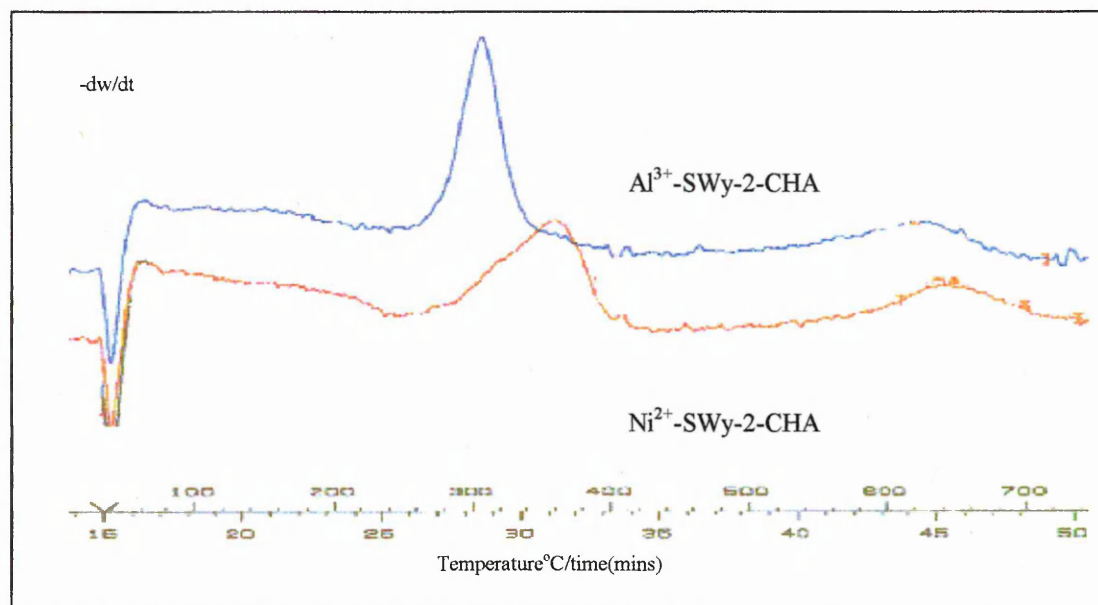


Table 5.2 Thermal desorption summary for Al³⁺-SWy-2-CHA and Ni²⁺-SWy-2-CHA

Sample	1 st weight loss maxima/°C	Dehydroxylation maxima/°C
Al ³⁺ -SWy-2	330 (sharp)/370 shoulder (broad)	630 (broad)
Ni ²⁺ -SWy-2	360 (broad)	620 (broad)

5.3.3 Variable temperature x-ray diffraction (VT-XRD)

Samples were coated on glass slides and exposed to the probe. Diffractograms were recorded at a specific temperature after a 15-minute equilibrium period. Above 300°C (max temperature), the sample was heated in a solvent free oven, then immediately replaced on the heating stage where the XRD trace was recorded. The confirmation and extent of intercalation was measured by noting the intensities and positions of their respective $d_{(001)}$ peaks. The VT XRD traces of both Al³⁺- and Ni²⁺-exchanged SWy-2-CHA (48 hrs) are shown in figures 5.2 and 5.3 respectively.

5.3.3.1 Results

Figure 5.2 VT XRD traces of $d_{(001)}$ spacing of Al^{3+} -SWy-2-CHA from RT-450°C

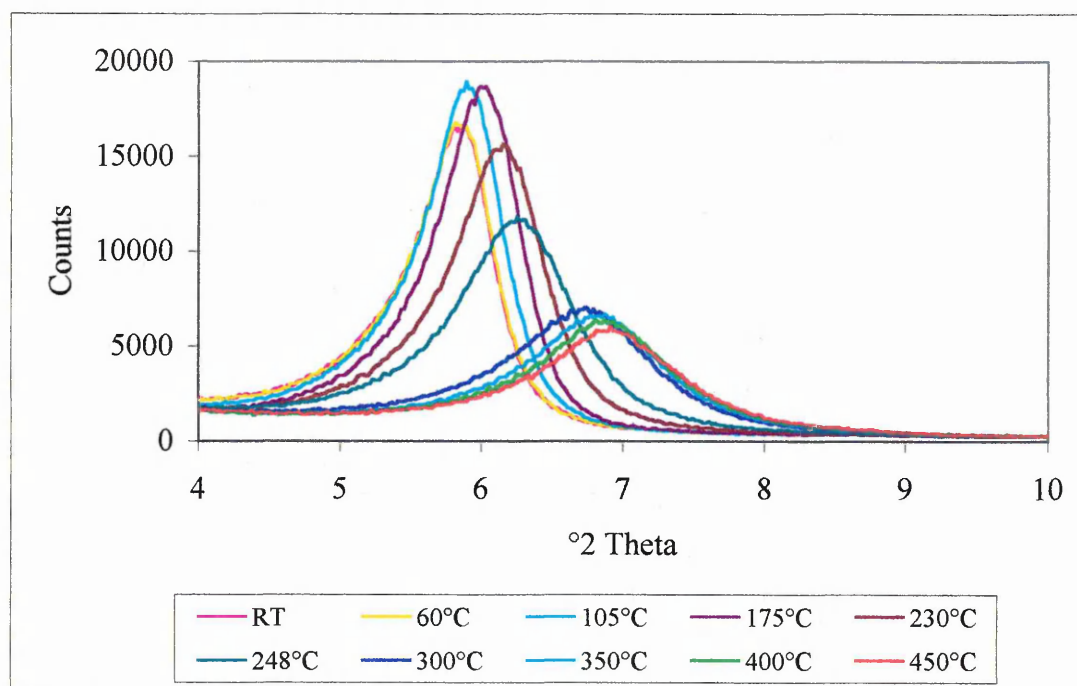


Table 5.3 VT-XRD summary for Al^{3+} -SWy-2-CHA

Temperature $^{\circ}C$	$d_{(001)}$ spacing	Temperature $^{\circ}C$	$d_{(001)}$ spacing
RT	15.13	248	14.12
60	15.10	300	13.10
105	14.95	350	12.93
175	14.69	400	12.88
230	14.38	450	12.80

Figure 5.3 VT XRD traces of $d_{(001)}$ spacing of Ni^{2+} -SWy-2-CHA from RT-450°C

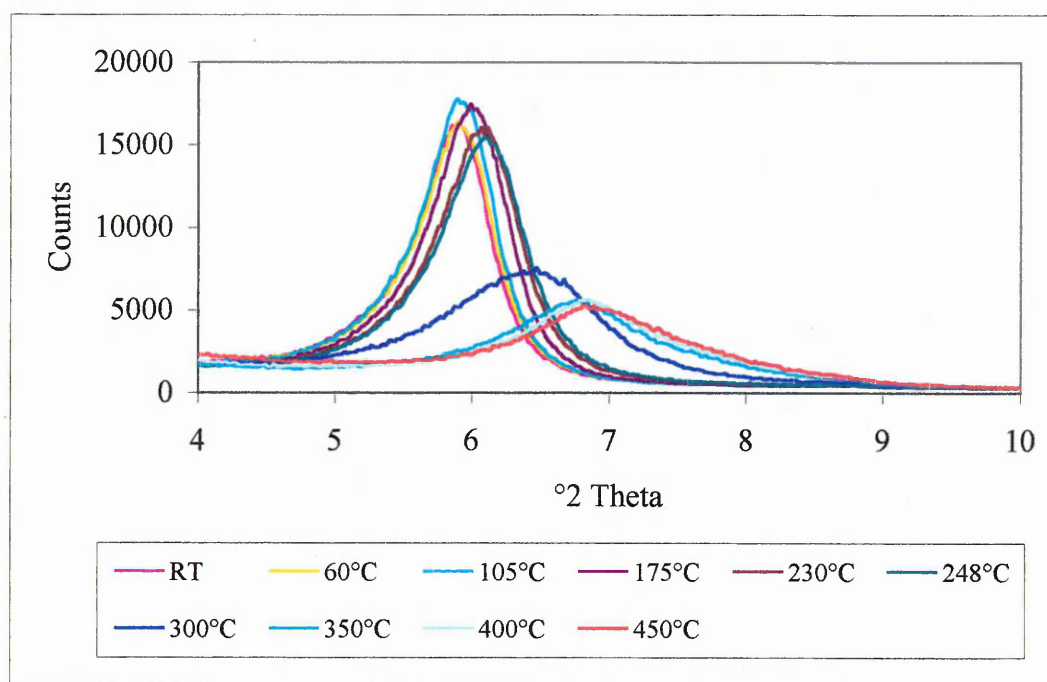
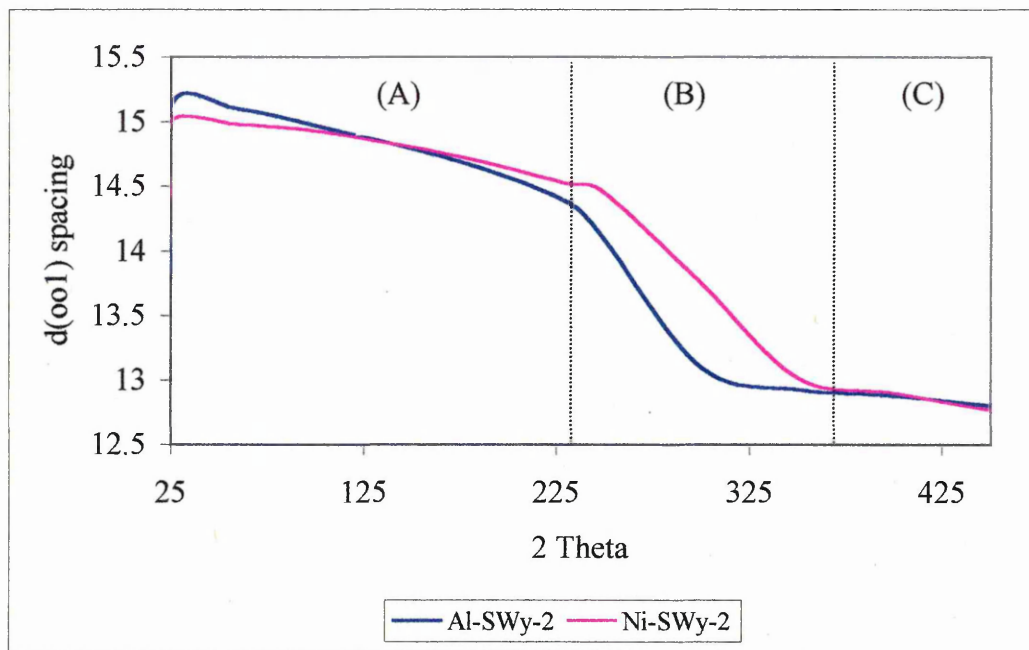


Table 5.4 VT-XRD summary for Ni^{2+} -SWy-2-CHA

Temperature °C	$d_{(001)}$ spacing	Temperature °C	$d_{(001)}$ spacing
RT	15.01	248	14.47
60	14.98	300	13.75
105	14.92	350	13.02
175	14.73	400	12.90
230	14.52	450	12.77

A comparison of the rate of change in $d_{(001)}$ spacing of Ni^{2+} - and Al^{3+} -SWy-2-CHA is shown below in figure 5.4. For convenience of interpretation, the plot has been split into three sections i.e. (A) between RT-250°C-corresponding to the low temperature detection events seen in TG-FTIR-MS, (B) 250-400°C-corresponding to the high temperature detection events seen in TG-FTIR-MS, and (C) 400-450°C where detection of desorption products is much lower.

Figure 5.4 Changes in $d_{(001)}$ spacing of Al^{3+} -SWy-2-CHA and Ni^{2+} -SWy-2-CHA from room temperature to 450°C



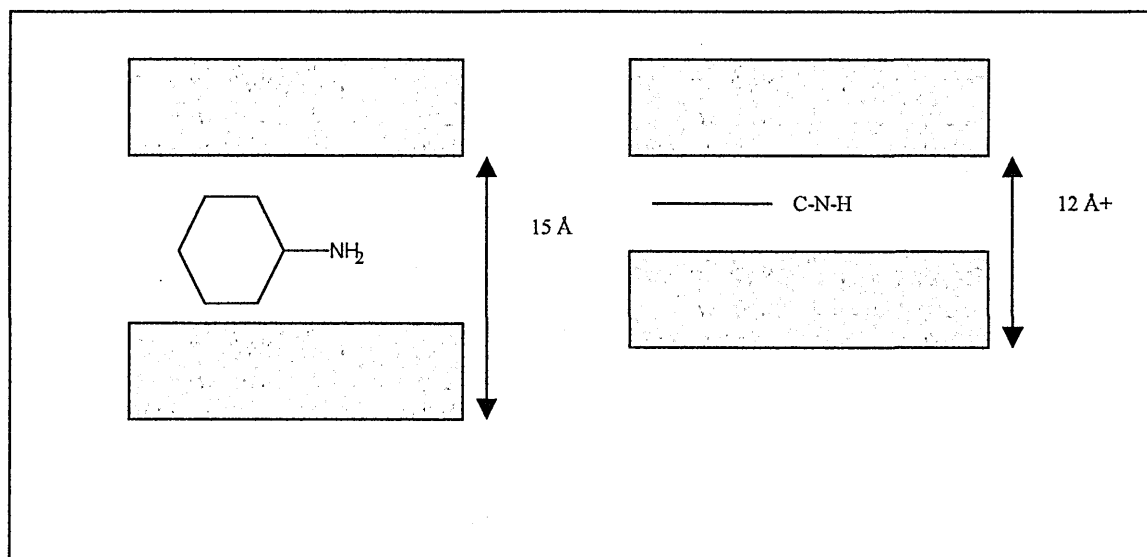
Examination of the change in $d_{(001)}$ with temperature has revealed several important points:

- VT XRD of Al-SWy-2-CHA shows that the interlayer space has expanded to 15.1Å after exposure to CHA vapour for 48hrs. This expansion corresponds to that seen by Yariv et al. [320] after 20hrs immersion in CHA. In a fully collapsed state the d spacing is of the order of 10Å and when hydrated under atmospheric conditions it is approximately 13.83Å. In addition, a d-spacing of 14.12Å at 230°C suggests that CHA remains in the interlayer space.
- For Al-SWy-2, section (A) shows that there is a gradual decrease in the d spacing between room temperature and 250°C whereas in section (B), 250-400°C, the rate at which the layers collapse increases, as seen by the increase in the d spacing slope. This change of slope corresponds to the detection of

the high temperature detection event in RT-FTIR-MS, where the detection of unchanged CHA begins at 250°C, reaches a maximum at 370°C concurring with the detection of alkenes and benzene.

- The interlayer space in Al-SWy-2 is not collapsed at 450°C (12.8 Å), though in RT-MS, aniline is still being detected at this temperature. This effect may also be due to coking between the layers.
- In comparison, VT XRD of Ni-SWy-2 shows that the interlayer space has expanded to 15.01Å after 48 hrs exposure. When hydrated under atmospheric conditions it is approximately 14.43Å. In addition, a d-spacing of 14.12Å at 230°C suggests that the interlayer space is occupied.
- The interlayer space in Ni-SWy-2 has not collapsed by 450°C which again may suggest coking.

Figure 5.5 Possible orientation of CHA within the interlayer space



5.3.4 Evolved gas analysis (RT-FTIR, RT-MS and OTM-GC-MS)

EGA was performed using a Unicam-Cahn Synergic chemical analysis system as discussed in chapter 2.

Table 5.5 Experimental conditions for the GC-MS identification of probe molecules

Interface temperature	250°C
Ionisation energy	70 eV
Source temperature	130°C
Detector gain	700 volts
Detector current	500 μ amps
Mass range scan	4-200 amu

5.3.4.1 Results OTM-GC-MS

OTM-GC-MS revealed that a variety of individual components (Table 5.6) were evolved during the thermal decomposition of the clay/CHA samples and these were identified using the ATI-Cahn mass spectral library, together with their major diagnostic ions.

Table 5.6 OTM-GC-MS desorption products and associated ions

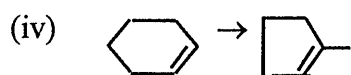
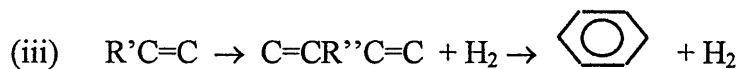
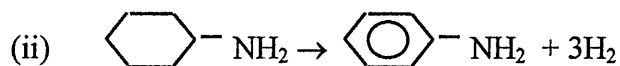
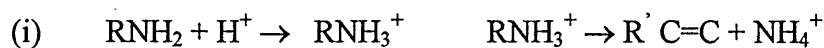
Desorption product	Parent ion (amu)	Base peak (amu)	Secondary ions (amu)	% Yield over Al ³⁺ -SWy-2	%Yield over Ni ²⁺ -SWy-2
Cyclohexylamine	99	56	43	11	15
Cyclohexene	82	67	54, 39, 27	36	46
Aniline	93	93	66, 39	2	27
Methylcyclopentene	82	67	53, 39, 27	50	4
Benzene	78	78	51, 39	1	8

Table 5.7 Physical properties of desorption products detected by OTM-GC-MS

Desorption product	Structure	Formula	Formula wt. (g)	Boiling pt. °C
Cyclohexylamine		C ₆ H ₁₁ NH ₂	99.18	134
Cyclohexene		C ₆ H ₁₀	82.15	83
Aniline		C ₆ H ₅ NH ₂	93.13	94
Methyl Cyclopentene		C ₆ H ₁₀	84.12	80
Benzene		C ₆ H ₆	78.11	80

These diagnostic ions (Table 5.6) were later used to determine the temperatures at which the individual components were evolved from Al³⁺- and Ni²⁺-exchanged SWy-2 during real time TG-MS. Table 5.6 shows that methylcyclopentene and cyclohexene share the same parent ion [82], and therefore the ions [53] and [54] were used for their detection. Table 1 also shows that the CHA thermally decomposed into different products over the different cation exchanged forms of SWy-2. The most abundant product for Ni²⁺-SWy-2 was cyclohexene but it also produced more aniline than the Al³⁺-form. Al³⁺-SWy-2 produced large quantities of methylcyclopentene and cyclohexene but very little aniline. A small quantity of benzene was produced over Ni²⁺-SWy-2. The production of aniline was unexpected but its formation has been observed over Lewis acid catalysts such as alumina [329] and cobalt oxide [331]. However, given that Ni²⁺-exchanged montmorillonite is known to exhibit Lewis acid character when interacting with sorbed pyridine [312] then aniline production is justified. Thus there are four main interrelated mechanisms for CHA transformation:

(i) deamination via the Hofmann degradation process resulting in the formation of ammonia and cyclohexene; (ii) ring dehydrogenation to form aniline; (iii) partial/complete dehydrogenation of the deaminated species leading first to cyclohexadiene (which was observed in quantities of < 1% over Ni²⁺-SWy-2) and ultimately to benzene; and also (iv) the acid catalysed isomerisation of cyclohexene to methylcyclopentene;



5.3.4.2 Results Real time TG-FTIR

The data is presented as total absorbance recorded in a selected spectral region as a function of temperature and illustrates the temperature intervals over which particular components were desorbed (Fig. 5.6-5.7). The spectral window 2800 - 3000 cm^{-1} is attributed to CH stretching vibrations in saturated and unsaturated species, whereas signal intensity in the CH stretching region (3000 - 3150 cm^{-1}) region arises only from molecules containing C=C double bonds such as cyclohexene and aromatics which in these samples are produced via the Hofmann degradation. Signal intensity in the 890-1000 cm^{-1} region is particularly useful herein because it provides direct spectral evidence for the evolution of ammonia in contrast to MS detection where the signal may be contaminated by mass ions originating from the fragmentation of organic species and water. It is important to note that the signal intensities recorded for saturated and unsaturated species are not directly comparable since the observed absorbance depends on the relative amounts of the saturated and unsaturated components passing through the FTIR cell at a given instant and the extinction coefficients of each of those components.

Figure 5.6 RT-FTIR gas-phase FTIR for the desorption of saturated, unsaturated hydrocarbons and ammonia from Al^{3+} -SWy-2-CHA

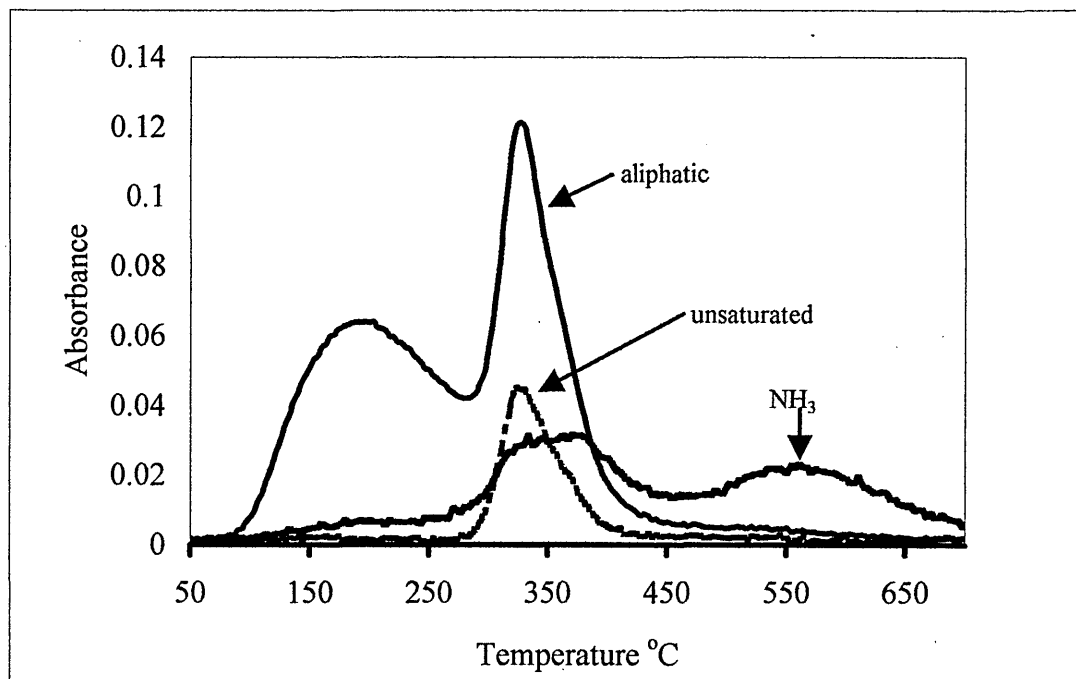
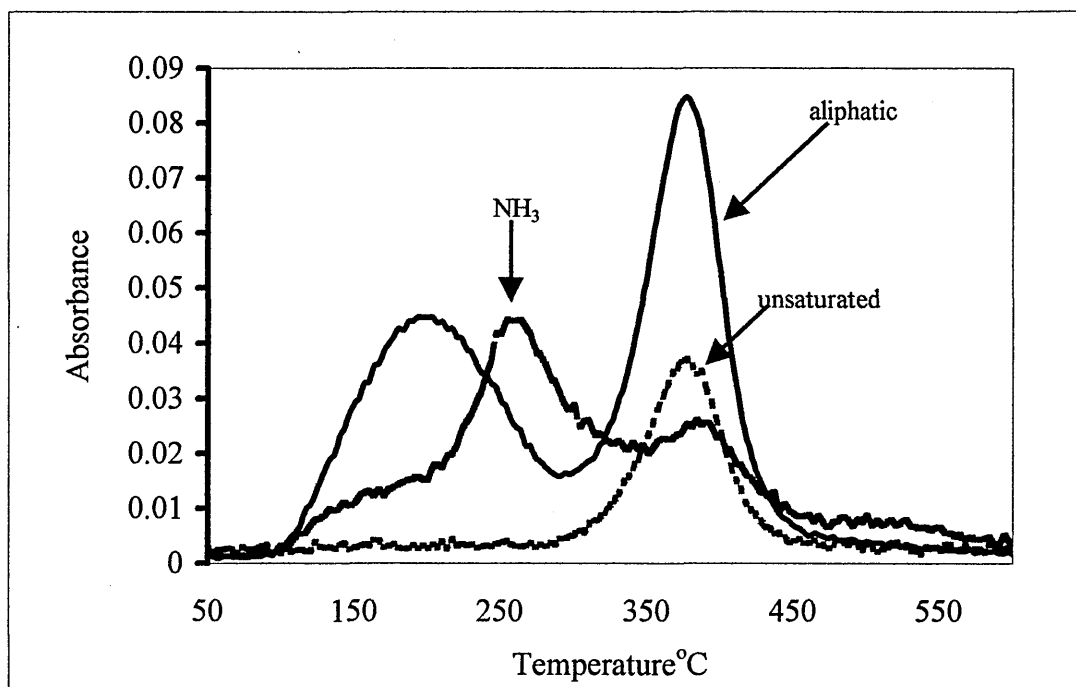


Figure 5.6 shows that there were two distinct maxima in the saturated C-H stretch region at 180 and 335°C, which correlate with the broad maximum below 240°C and the sharp maximum at 330°C in the derivative thermogram (fig. 5.1), as organic species were desorbed from Al^{3+} - SWy-2. The major desorption of species containing C=C bonds occurred under the 335°C maximum, whereas ammonia was evolved in three stages with maxima at 180, 365 and 560°C. The maximum at 560°C indicated that a proportion of the ammonia produced was very strongly bound to some acid sites as NH_4^+ .

Figure 5.7 RT-FTIR gas-phase FTIR for the desorption of saturated, unsaturated hydrocarbons and ammonia from Ni-SWy-2-CHA



The desorption of species containing saturated CH_2 groups from Ni^{2+} -SWy-2 (fig.5.7) also exhibited two maxima at 185 and 380°C, with the latter having the higher absorbance. Molecules containing $\text{C}=\text{C}$ bonds were only observed under the 380°C maximum. Ammonia was also desorbed under the 380°C maximum but the highest signal occurred at 260°C and there was a shoulder near 165°C. This suggests that ammonia was desorbed near the temperatures at which it was produced and was not retained to high temperatures as on Al^{3+} -SWy-2.

5.3.4.3 Results Real-Time TG-MS

Figure 5.8 RT-MS ion chromatograms for the desorption of water ($m/z=18$), methylcyclopentene ($m/z = 53$), cyclohexene ($m/z = 54$), cyclohexylamine ($m/z = 56$), benzene ($m/z = 78$) and aniline ($m/z = 93$) from Al^{3+} -SWy-2-CHA

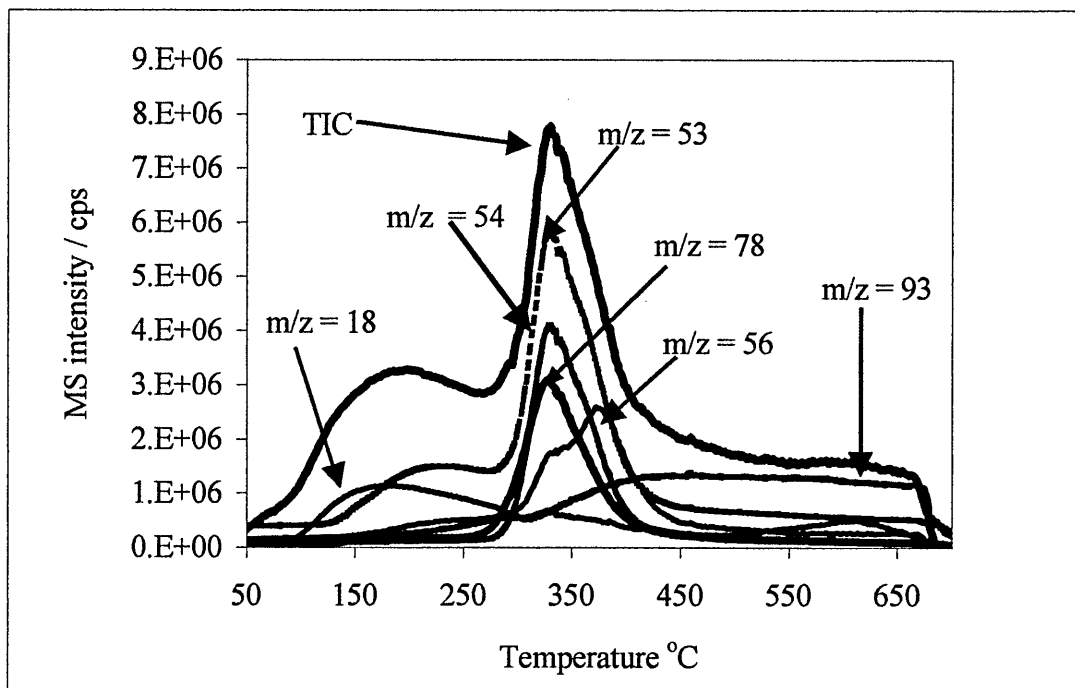
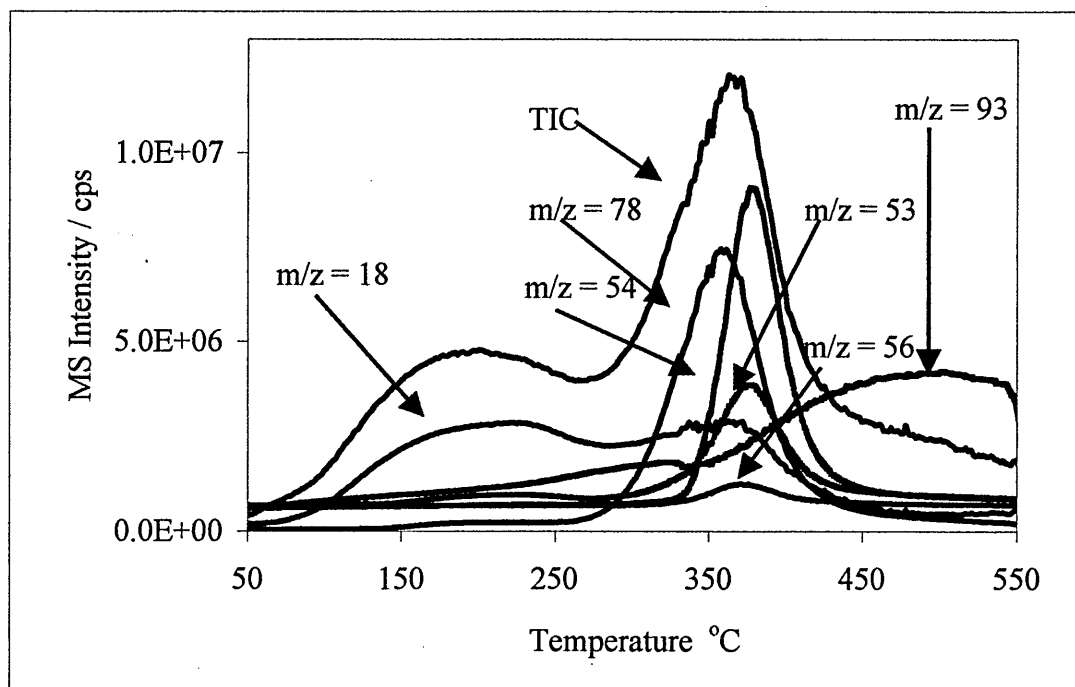


Figure 5.9 RT-MS ion chromatograms for the desorption of water ($m/z = 18$), methylcyclopentene ($m/z = 53$), cyclohexene ($m/z = 54$), cyclohexylamine ($m/z = 56$), benzene ($m/z = 78$) and aniline ($m/z = 93$) from Ni^{2+} -SWy-2-CHA



Comparison of real-time gas-phase FTIR and real-time MS data show several important correlations, even though the total ion currents, TIC, and specific ion chromatograms (fig. 5.8-5.9), exhibit minor differences in desorption temperatures when compared to TG-FTIR (fig. 5.6-5.7). Real-time TG-MS confirmed the earlier figures from TG-OTM-GC-MS in that the majority of the hydrocarbons ($m/z = 53$, methylcyclopentene; $m/z = 54$, cyclohexene; and $m/z = 78$, benzene) evolved under both maxima contained one or more double bonds. Surprisingly significant quantities of neat cyclohexylamine ($m/z = 56$) were only evolved under the high temperature maximum and there were two maxima at 344 and 390 $^{\circ}C$ for Al^{3+} - SWy-2 but only one maximum at 400 $^{\circ}C$ for the Ni^{2+} - form. Note also that the desorption profiles for benzene and the alkenes from Al^{3+} - SWy-2 were evolved over a broad temperature

interval (250 - 450°C). In contrast the major evolution of cycloalkenes from Ni²⁺-SWy-2 occurred over a much narrower temperature interval although the desorption of benzene was more extended.

The real-time FTIR data showed that approximately 60% of the ammonia produced was evolved from Al³⁺-SWy-2 at the same temperature as benzene and the cycloalkenes and the remaining 40% desorbed under the maximum at 560°C, i.e. much later than the alkenes which accompanied its formation. In contrast, the major production of ammonia over Ni²⁺-SWy-2 ($T_{\max} = 260^{\circ}\text{C}$) preceded the major evolution of benzene and the cycloalkenes (380 and 400°C, respectively). The evolution of ammonia prior to the increase in the diagnostic signal for unsaturated species suggests that at temperatures below 300°C a portion of the CHA decomposed via the Hoffman degradation process and the ammonia produced was desorbed and detected whereas the unsaturated by-products were retained and subsequently evolved under the desorption maximum at 380°C, with perhaps part of it being converted to coke. Apparently, the Ni²⁺-exchange cations interacted more strongly with the delocalised electrons in the C=C bond than with the lone pair of electrons on the nitrogen atom in ammonia, whereas the NH₄⁺ formed in the Al³⁺-exchanged SWy-2 was retained in preference to the alkenes. This most probably reflects the ability of the Ni²⁺-ions to coordinate the alkene double bond via its unfilled d-orbitals - an interaction which is well established in the use of Grignard reagents.

The derivative thermograms for the desorption of CHA from Al³⁺-exchanged SWy-2 had a high temperature shoulder (at 380°C) which correlated well with the desorption of unchanged CHA ($m/z = 56$) in the real-time TG-MS. Chisem et al. briefly reported MS data for the desorption of cyclohexylamine from a pillared acid activated clay in which unchanged CHA was desorbed at 260 and 370°C [232]. No data was given for

the desorption of any breakdown products of CHA. There is no doubt that the OTM-GC-MS facility played a significant role in identifying the range of decomposition products observed herein.

5.3.4.4 Results DRIFTS studies

Room temperature DRIFTS spectra (fig. 5.12) show bands associated with Al^{3+} -SWy-2 after exposure to CHA (48 hrs). These spectra focus on two spectral regions, 1200-2000 cm^{-1} (spectra (a)) and 2180-4000 cm^{-1} (spectra (b)).

Figure 5.10 Comparison of untreated Al^{3+} and Ni^{2+} -SWy-2 with CHA between 1200-2000 cm^{-1} .

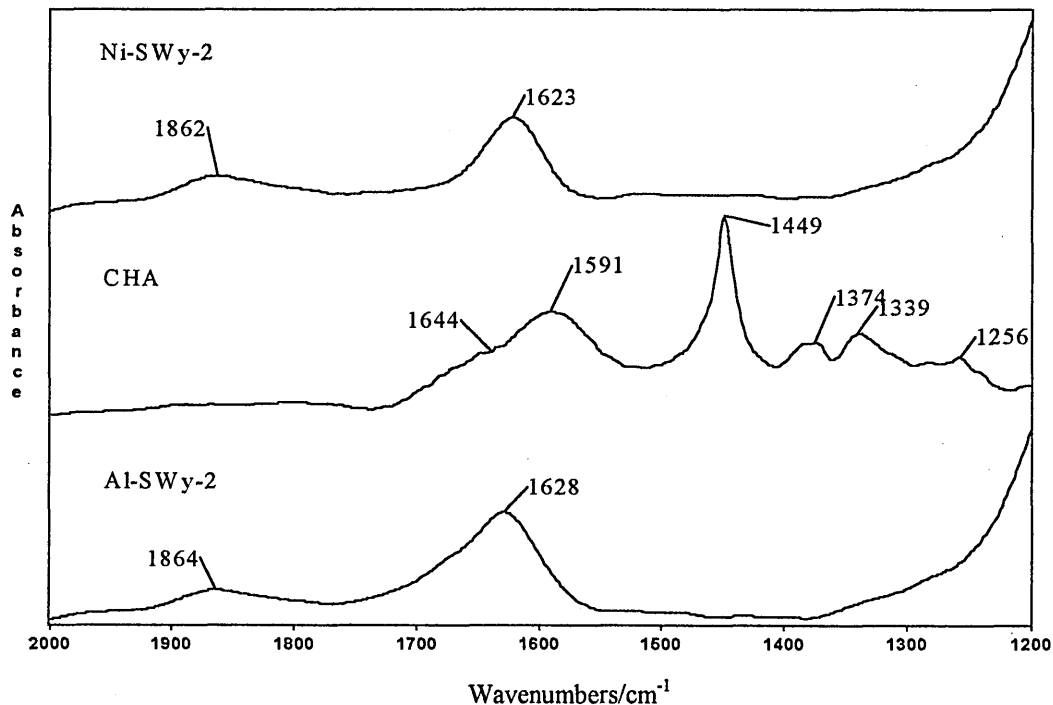
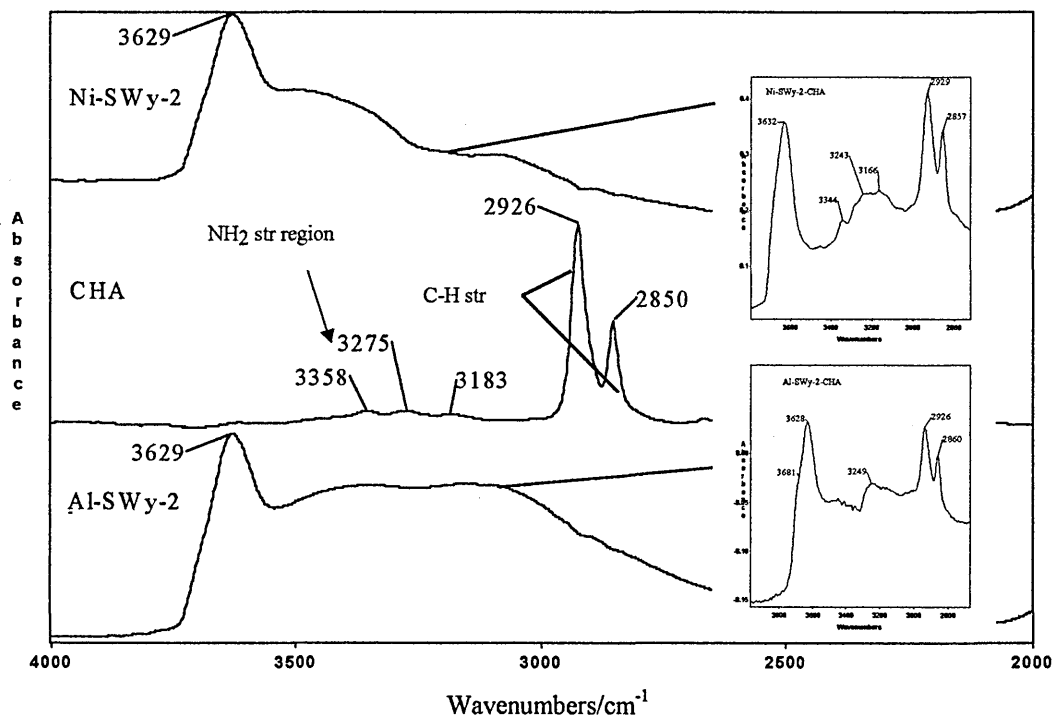


Figure 5.11 Comparison of untreated Al^{3+} and Ni^{2+} -SWy-2 with CHA between 2000-4000 cm^{-1} .



The spectral region 3200-3400 cm^{-1} , where further evidence of protonation (NH stretching modes) may be found is briefly shown for several reasons (fig 5.10-5.11 above). Firstly, these bands are known to be weak (as seen in the CHA spectra), but more importantly, this region overlaps the strong structural OH stretching modes of montmorillonite, and is badly resolved. However there is sufficient evidence of protonation between 1200-1800 cm^{-1} , and application of spectral deconvolution and/or curve fitting to further elucidate these bands (3200-3400 cm^{-1}) was shown to be a very subjective process. Complicating the issue further, VT DRIFTS is a method which applies a temperature ramp to the sample. When attempting to deconvolute these spectra, the deconvolution factor will differ between both temperatures and samples. However, alternative approaches may include Raman spectroscopy, which

is more sensitive to NH_2 stretching, but beyond the scope of this study. Table 5.8 lists the observed frequencies for the NH_2 and NH_3^+ stretching and bending modes of cyclohexylamine in the liquid state and when adsorbed as either neutral molecule or the cation or the cyclohexylammonium montmorillonite (AH^+) after immersion in liquid CHA [320]. These are compared to the work herein where CHA is adsorbed from the vapour phase.

Figure 5.12 VT DRIFTS spectra of (a) Al^{3+} -SWy-2-CHA and Ni^{2+} -SWy-2-CHA from 25-300°C as indicated

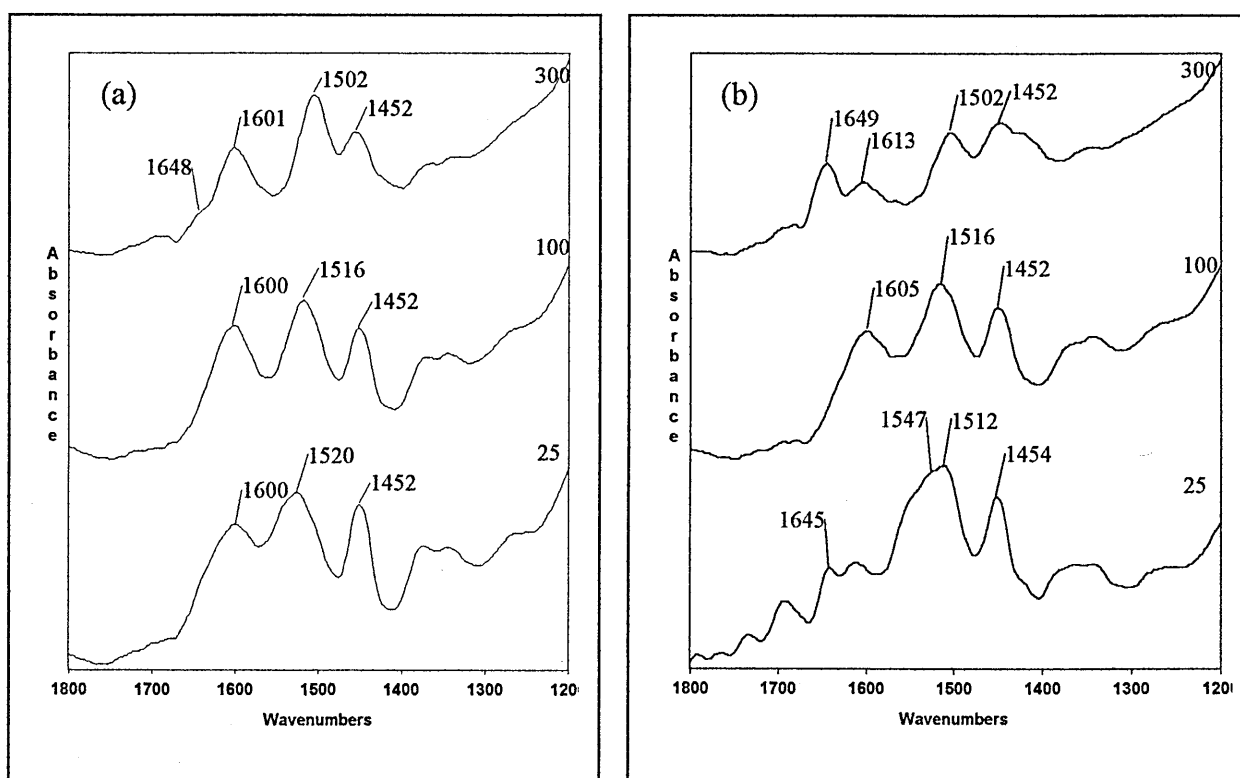


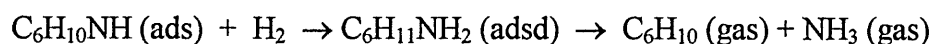
Table 5.8 NH₂ and NH₃ stretching and bending frequencies (cm⁻¹) for liquid cyclohexylamine, cyclohexylammonium-montmorillonite (AH⁺) and montmorillonite containing Ni²⁺ and Al³⁺ interlayer cations at room temperature

Vibrations	Liquid CHA	AH ⁺	Ni ²⁺ -	Observed Ni-SWy-2	Al ³⁺ -	Observed Al-SWy-2
NH ₂ stretching	3358	3340	3344 (VW)	N/A	3346(W)	N/A
NH ₃ ⁺ stretching	3278	3220	3244	N/A	3225(S)	N/A
NH ₃ ⁺ bending		1518/1630	1515	1512	1604/1525	1600/1520
NH ₂ bending	1610	1595	-		-	

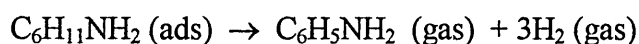
(W = weak) (VW = very weak) (S = strong) (B = broad)

The variable temperature DRIFTS study of CHA treated Al³⁺- and Ni²⁺- exchanged SWy-2 focussed on the spectral region 1200-1800 cm⁻¹ at 25, 100 and 300°C (fig 5.12 a-b). The absorbance of the CHA bands were relatively weak which made the complete subtraction of water vapour from the sample spectra difficult and accounts for the quality of the spectra in figure 5.12.

As seen in figure 5.12, all the spectra contain bands near 1510 and 1450 cm^{-1} which have been assigned, respectively, to the protonated amine groups (RNH_3^+ deformation mode) in a hydrated clay gallery and CH_2 deformation mode [320, 333]. There was also evidence for an RNH_3^+ bending mode near 1600 cm^{-1} in all the spectra for the Al^{3+} sample, but only at 100°C for the Ni^{2+} form. The RNH_3^+ deformation band has been reported at 1488 cm^{-1} in dehydrated smectites which suggests that the shift from 1510 cm^{-1} to 1502 cm^{-1} as the temperature reached 300°C correlates with water being lost from the gallery as shown in figure 5.9 ($m/z = 18$). The other important feature in the spectra at 300°C was the prominent band at 1648 cm^{-1} for the Ni^{2+} - SWy-2/CHA sample which has been attributed to the formation of the corresponding imine over n-butylamine-treated oxides including SiO_2 , Al_2O_3 and CaO [329, 334]. However, cyclohexylimine was not detected among the desorption products. Sokoll et al. suggested that the imine was rehydrogenated to cyclohexylamine before undergoing Hofmann degradation to cyclohexene and ammonia [329].



Indeed both the amine and imine species must be taken into consideration, as others have done, in the production of aniline which is definitely detected [335, 336].



There was never any evidence for the NH_2 deformation band of cyclohexylamine which occurs at 1614 cm^{-1} in the gas phase and is shifted downwards to 1575 cm^{-1} on alumina [329] and 1590 to 1604 cm^{-1} on cobalt oxides [331]. This indicated that no 'free' cyclohexylamine was retained after 15 min in dry N_2 . None of the anticipated bands for aniline were observed either which suggests that this compound was desorbed as it was formed. Finally, there was no spectral evidence for an NH_4^+ deformation band at 1428 cm^{-1} although it was not possible to record the spectra at temperatures $> 400^\circ\text{C}$ when the ammonia, strongly bound as NH_4^+ , should have been in evidence on Al^{3+} -SWy-2.

Thus, the picture that emerges is one in which the decomposition of CHA over Ni^{2+} - and Al^{3+} -SWy-2 differs considerably in detail. The decomposition over both exchange forms produces differing quantities of cyclohexene, methylcyclopentene and benzene which desorbed as they were produced over Al^{3+} -SWy-2 whereas they are retained in preference to ammonia over Ni^{2+} - SWy-2. The production of aniline is favoured over Ni^{2+} - SWy-2 and may proceed via the formation of cyclohexylimine, as shown by the presence of a 1648 cm^{-1} band at 300°C , as well as directly from cyclohexylamine. Ammonia is evolved from Al^{3+} - SWy-2 at temperatures 450 - 560°C , i.e. long after the corresponding alkene was evolved.

5.3.4.5 Discussion

CHA decomposed along different routes via inter-related mechanisms that were cation dependent. Over Al^{3+} -SWy-2 hydrodenitrogenation via the Hofmann degradation was the predominant route whereas ring dehydrogenation to aniline either directly from CHA or possibly via cyclohexylimine was significant over Ni^{2+} -SWy-2. A proportion of the ammonia produced over Al^{3+} -SWy-2 was retained to temperatures

in excess of 500°C. In contrast some ammonia was released from Ni²⁺-SWy-2 prior to the corresponding alkene which was probably held on the clay surface via the unfilled d-orbitals of the Ni²⁺-cation. Very little unmodified cyclohexylamine was detected in the evolved gases which means that the desorption of CHA cannot be used as a quantitative measure of the acidity of cation-exchanged clays. Nonetheless, because all the products which evolve during the diagnostic weight loss are derived from CHA the mass loss does give a semi-quantitative measure of the clay acidity. However, the acidity is likely to be underestimated because ammonia is lost before the diagnostic event in Ni²⁺-SWy-2 and at much higher temperatures from Al³⁺-SWy-2. It appears that this discrepancy may be compensated by the presence of evolved water which contributes to the weight loss under the diagnostic peak. This probably explains why values for the acidity of clays and related oxides derived from 'cyclohexylamine' desorption in the temperature range 250 to 400°C have been linearly related to their catalytic activity.

5.3.4.6 Summary

As a potential probe, CHA was not considered suitable for several reasons:

- EGA has shown that CHA is not a stable probe molecule i.e., the amount of CHA detected is not directly proportional to the amount of swelling mineral present. Instead, detection involved the detection of catalytically altered CHA as evolved products gases, which depended on the interlayer cation and varying amounts of water present. This is not to say that the catalytically altered product(s) could not be used.

- In the presence of hydrocarbon residues, this situation could potentially become more complex, where the advantages gained from the sensitivity of MS are negated due to the presence of interfering co-evolving species.
- The extinction coefficients of the infrared bands in CHA are relatively small and thus proved more difficult to detect by EGA-(gas-phase) FTIR.
- Nonetheless, as a qualitative probe, CHA has the potential to distinguish the difference between Ni^{2+} and Al^{3+} -SWy-2 due to the detection maxima of the observed evolved gas patterns .
- Though complex, the interrelated patterns of evolved gases helped to distinguish between Al^{3+} - and Ni^{2+} exchanged SWy-2 by virtue of the quantity and pattern of gas evolution patterns. In effect the combined techniques of EGA, XRD and DRIFTS could provide a basis for differentiation by chemometric analysis.
- From a quantitative point of view, the use of CHA highlights several problems. Interference from other co-evolving products makes it difficult to use the CHA parent ion and its detection varies considerably depending on the nature of the interlayer cation. In a mixed cation system, this may inhibit quantitation. The other important feature which may enable the detection of non swelling minerals is dehydroxylation. The thermal desorption of CHA and its products is known to have an adverse affect on the dehydroxylation region (broadening and lowering its detection range) which would complicate the determination of kaolinite, chlorite and illite by their characteristic dehydroxylation peaks. The study by Breen et al. [337] on the desorption of CHA from Ni, Co and Na acid treated montmorillonites by TGA, found that the dehydroxylation region between 650-800°C had doubled in size. Their

suggestion was that the additional loss was from products derived from CHA through pyrolytic or other processes (e.g. the desorption of CO₂ after coke was formed). In view of the results herein, it is evident from EGA, that the apparent earlier onset of dehydroxylation seen in TGA, is in part due to the evolution of gases, such as aniline in RT-MS and ammonia in RT-(gas-phase)-FTIR.

5.4 Characterisation of homoionic cation exchanged SWy-2 montmorillonite using the 3-cyanopyridine (3-CYP) probe

The second potential chemical probe investigated in this thesis was 3-cyanopyridine (3-CYP). There are two potential bonding sites for 3-CYP with the interlayer cations of swelling minerals:

- (a) The pyridine nitrogen, where there may be the possibility of producing a protonated adduct which could be detected by FTIR (DRIFTS).
- (b) The nitrile nitrogen.

However, there is no evidence in the literature of its use with clay minerals, probably because it is a solid at room temperature and therefore has a very low vapour pressure. Interest in the ligand properties of 2-, 3-, and 4-cyanopyridines has led to investigation due to the presence of two sites which raises the possibility of linkage isomerism whilst providing the opportunity for comparison of coordination bond strengths between metal ions and the nitrile or pyridine function of the same ligand. In general it has been observed that the four principal in-plane ring deformations (arising from the C-C and C-N stretching modes in the 1400-1600 cm^{-1} region are shifted to higher frequency on coordination of the pyridine nitrogen [338].

Early studies focused on the preferential coordination of metal ions by one group rather than the other, which depends on the relative ability of 3-CYP to form complexes with these metal ions which subsequently depends on polar, resonance and steric effects.

The clay/3-CYP interactions will be studied using RT-MS (unless otherwise stated)

because RT-MS offers:

- (a) its higher sensitivity (3 orders of magnitude)
- (b) the ability to provide molecular identification
- (c) the lack of interference from water

5.4.1 Thermogravimetric studies

The derivative thermograms for the desorption of 3-CYP from Ni²⁺- and Al³⁺-exchanged SWy-2 are shown in figure 5.13. The weight loss maximum at 620-640°C has been attributed to structural dehydroxylation and the broad maximum between 240°C and 500°C has been attributed to the desorption of 3-CYP. The high temperature maximum in Al³⁺-SWy-2-3-CYP at 700°C is probably due to coking.

Figure 5.13 Derivative thermograms of Al^{3+} -SWy-2 -CHA and Ni^{2+} -SWy-2-3-CYP (6days)

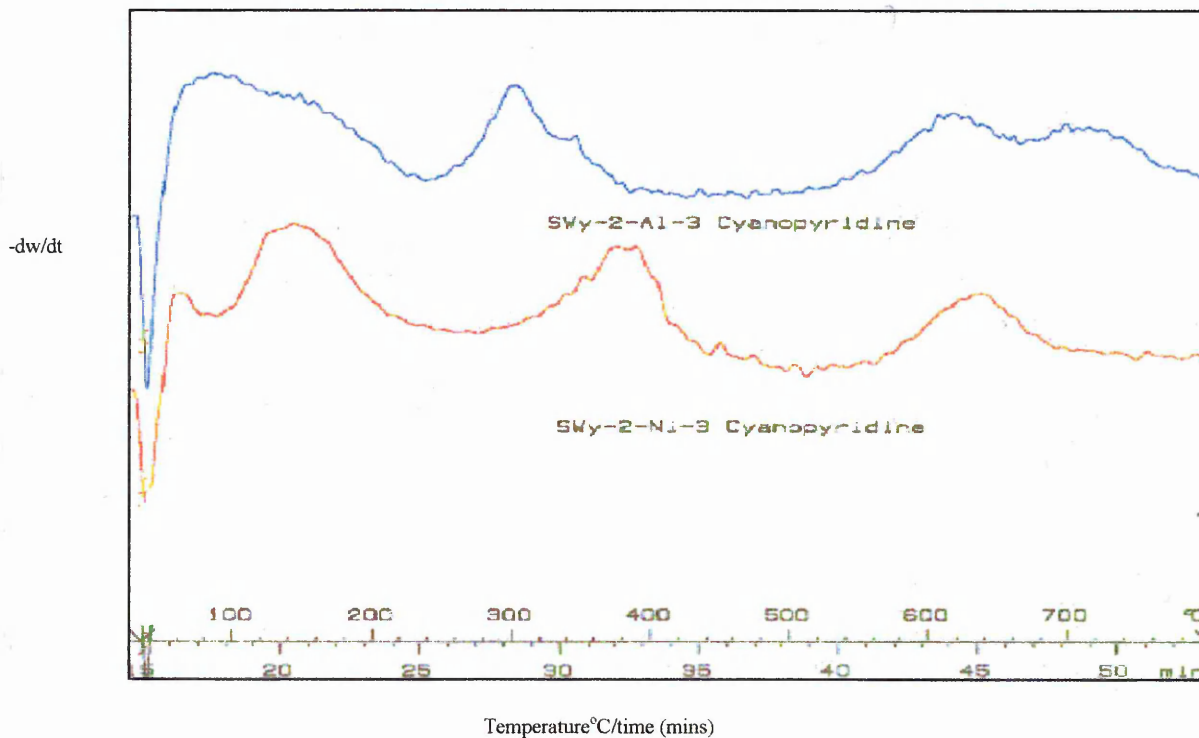


Table 5.9 Thermal desorption summary for Al^{3+} -SWy-2 -3CYP and Ni^{2+} -SWy-2-3CYP

Sample	Weight loss maxima °C / % wt loss	Dehydroxylation maxima/°C
Al^{3+} -SWy-2	300 (broad)/330-340 ≈(shoulder) /12.0	620/715
Ni^{2+} -SWy-2	380 (broad)/ 410 (shoulder)/13.23	640

5.4.2 Results VT (variable-temperature) XRD

Figure 5.14 VT XRD traces of $d_{(001)}$ spacing of Ni^{2+} -SWy-2-3CYP from RT-450°C

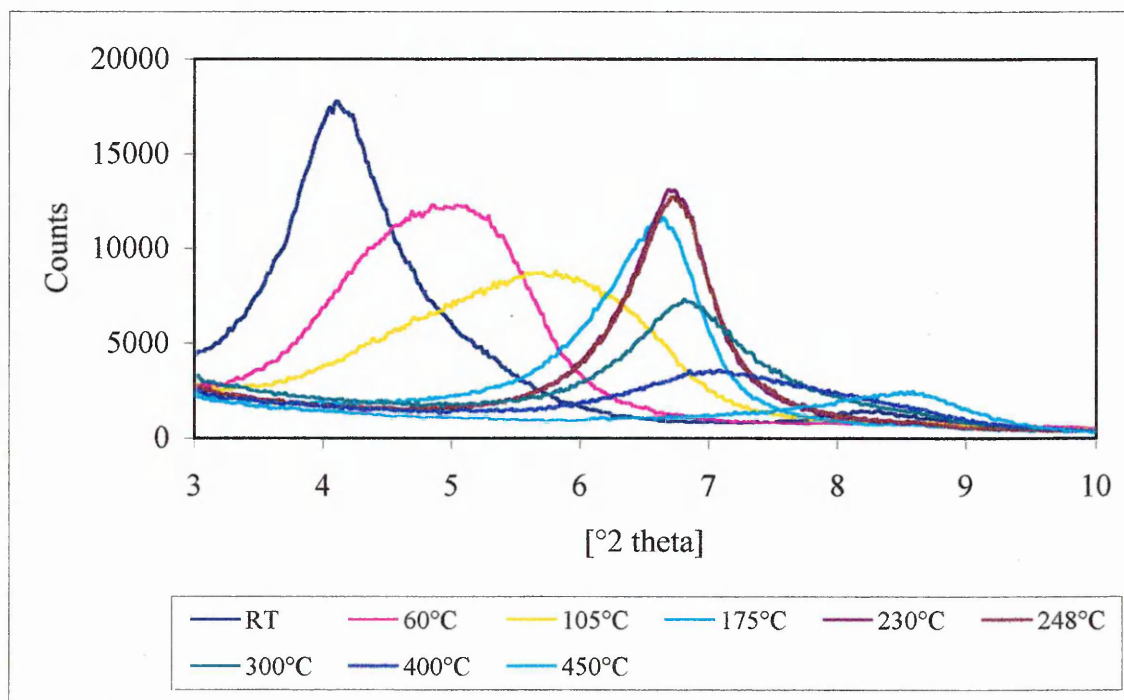


Table 5.10 VT-XRD summary for Ni^{2+} -SWy-2-3CYP

Temperature °C	$d_{(001)}$ spacing	Temperature °C	$d_{(001)}$ spacing
RT	21.45	248	13.13
60	17.5	300	12.94
105	13.88	400	12.90
175	13.33	450	10.34
230	13.17		

Figure 5.15 VT XRD traces of $d_{(001)}$ spacing of Al^{3+} -SWy-2-3CYP from RT-450°C

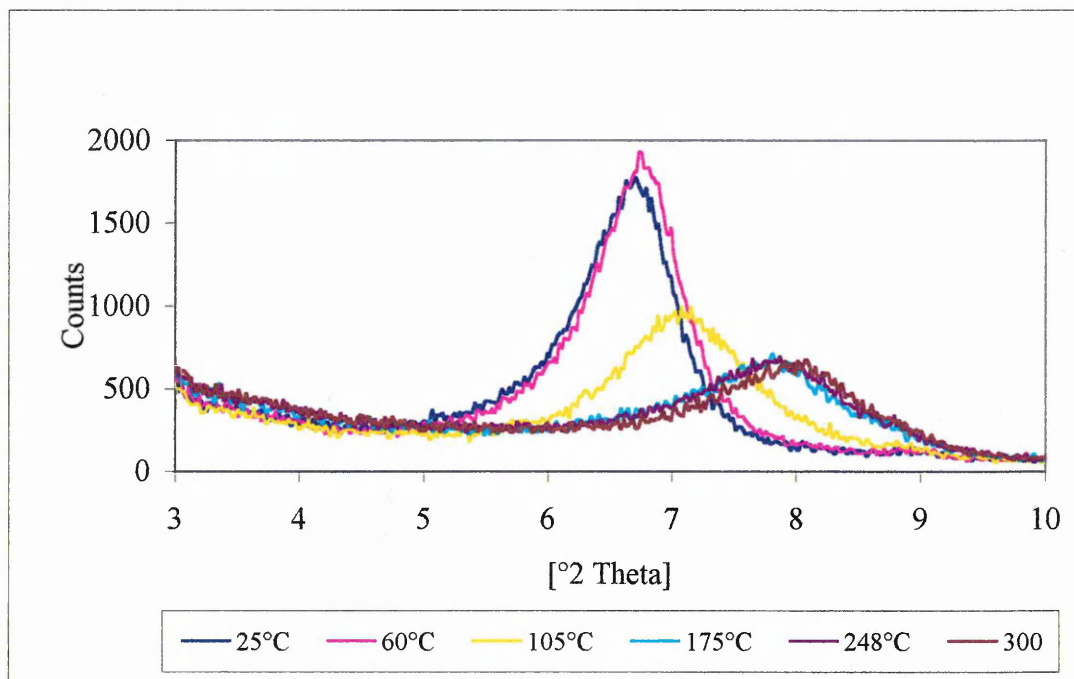


Table 5.11 VT-XRD summary for Al^{3+} -SWy-2-3CYP

Temperature °C	$d_{(001)}$ spacing
RT	13.18
60	13.05
105	12.45
175	11.33
248	11.28
300	11.0

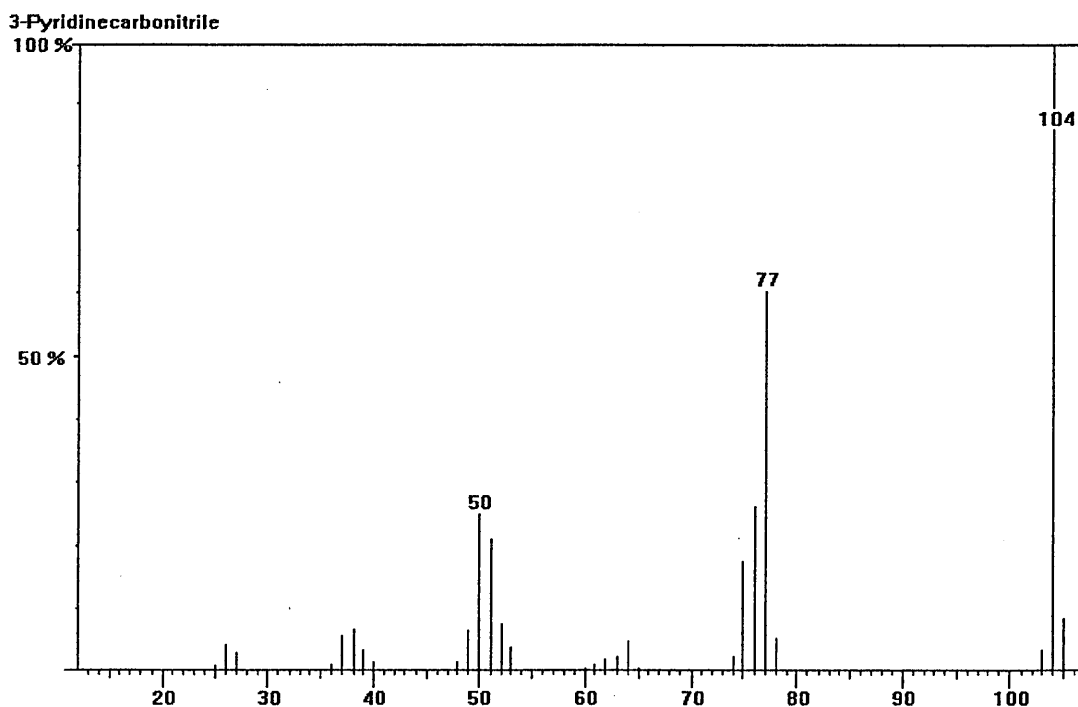
In general, the TGA desorption profiles for Al^{3+} - and Ni^{2+} -SWy-2-3CYP represent a weight loss between 12-13% respectively, which in conjunction with the summarised basal spacing data in tables 5.10-5.11, confirms that the 3CYP is intercalated and not

a surface moiety. VT XRD also confirms that the large differences in basal spacing after 6 days are due to differences in the orientation of 3CYP within the interlayer space, suggesting that at room temperature, the Ni^{2+} is perpendicular to the layers whilst the Al^{3+} is parallel. Raising the temperature to 100°C in the Ni^{2+} -sample, (d-spacing reduction of 7.5\AA) would seem to reorientate 3CYP to the parallel position.

5.4.3 Results OTM-GC-MS

OTM-GC-MS revealed that 3-CYP was the only product detected during the thermal decomposition of the clay/3-CYP samples and was identified using the ATI-Cahn mass spectral library, together with its major diagnostic ions as shown in figure 5.16.

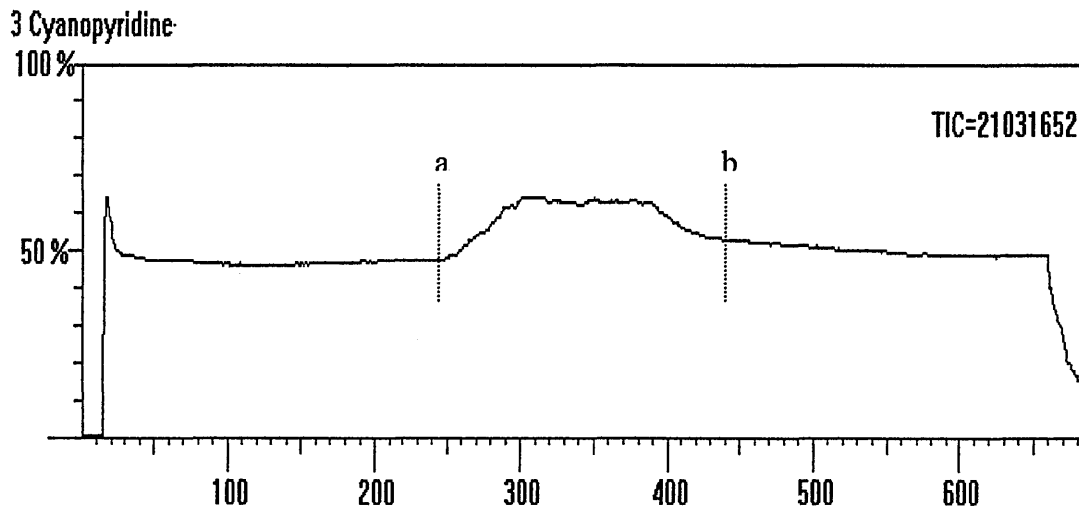
Figure 5.16 ATI-Cahn Mass spectrum of 3-CYP



5.4.4 Results Real-Time TG-MS

RT-MS analysis considered Ni²⁺- and Al³⁺- SWy-2-3-CYP. The EGA of 3CYP under the same conditions (minus the clay) is also shown in order to highlight any significant desorption changes after interaction with the clay sample.

Figure 5.17 EGA Total ion current (TIC) of 3-CYP (25-800°C)



The detection area between a-b represents the detection of 3-CYP. A mass spectrum containing the nitrogen carrier gas ($m/z = 28$) and 3-CYP ($m/z = 104, 77, 50$) from this area are shown below and represent the only components detected throughout the experiment.

Figure 5.18 Representative mass spectrum 3-CYP

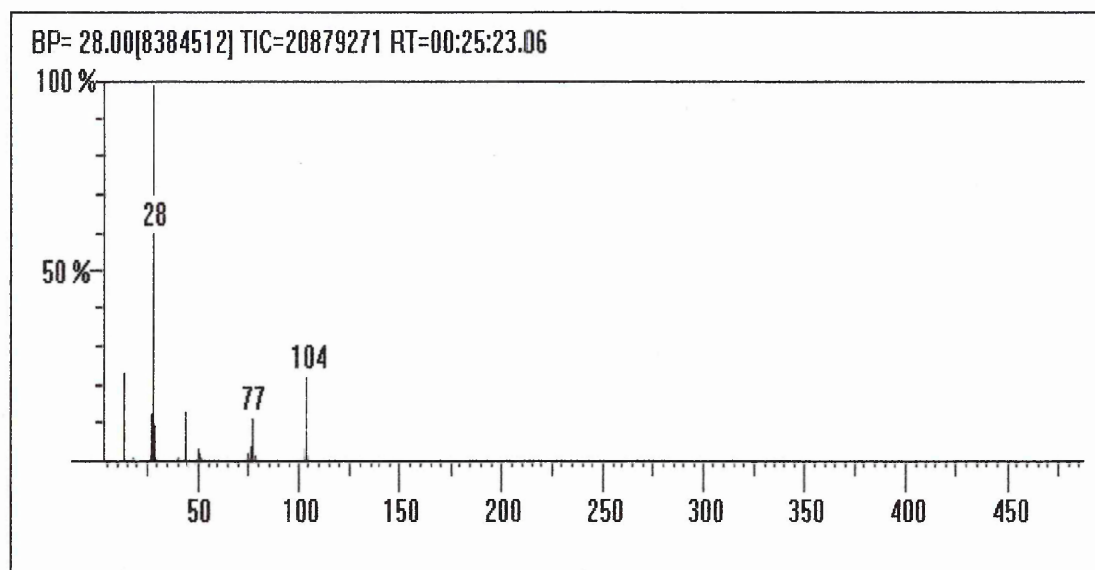
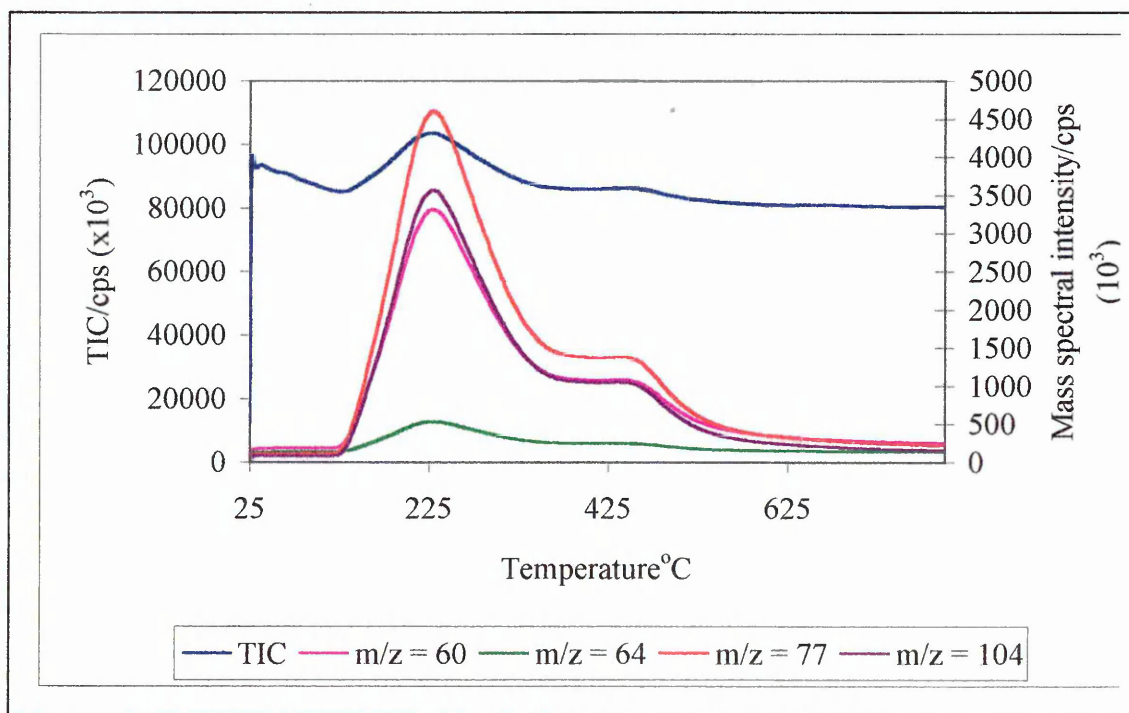


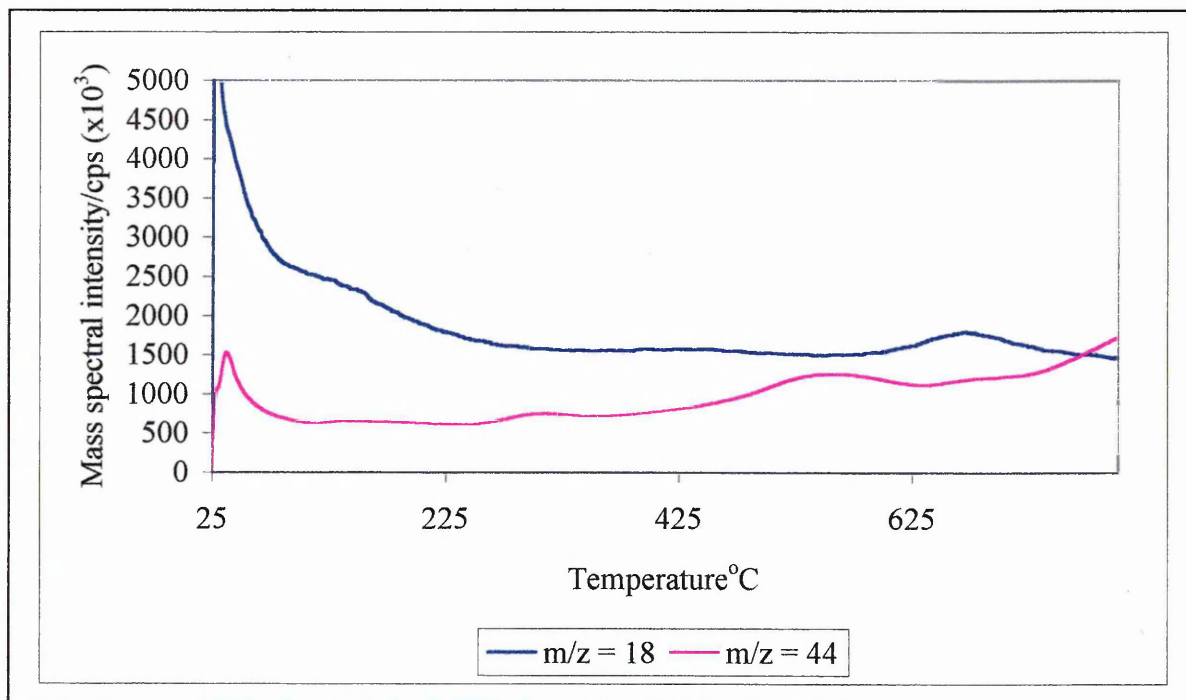
Figure 5.19 RT-MS ion chromatograms from Ni²⁺-SWy-2-3-CYP TIC (total ion current) and 3CYP ions [m/z =104, 77, 64, 50]



For emphasis the ions [m/z = 18-H₂O] and [m/z = 44-CO₂] are shown together.

Figure 5.20 RT-MS ion chromatograms from Ni²⁺-SWy-2-3-CY H₂O [m/z = 18],

CO₂ [m/z = 44]



The first weight loss maxima observed in the DTG trace of Ni²⁺-SWy-2-3CYP, have been assigned in MS to the loss of physisorbed water (m/z = 18/140°C), CO₂ (m/z = 44/150°C) and the beginning of the loss of 3CYP at 130°C. The desorption of 3CYP from Ni²⁺-SWy-2 is a relatively simple event in comparison to CHA, where it is detected by MS at 240°C and 415°C_≈ (shoulder) respectively. However, the corresponding DTG trace, shows a maxima at 300°C and a shoulder at 415°C, which highlights a difference between the first maxima (240°C) of approximately 60°C. The detection of 3CYP (m/z = 104, 77, 64, 50) is clearly responsible for the second detection maxima observed in the TIC, in comparison the breath of the DTG suggests contribution from other ions. There are several possible reasons for this. Firstly, it is important to remember that RT-MS is a highly sensitive technique capable of

resolving co-evolving mass changes, whereas DTG represents the rate of change of weight loss for all co-evolving species. Secondly, the detection of water ($m/z = 18$), though decreasing, is (5000×10^3 cps) comparable to that of 3CYP, being detected between 25 and 330°C. In addition the overlap of CO_2 ($m/z = 44$) between 240 to 340°C may contribute to the 60°C difference observed in the DTG trace, as they contribute to weight losses in the same temperature range. However, another probable explanation for these differences is the interaction of 3CYP with the transfer lines (250°C-3CYP Bp = 220°C). Considering the problems associated with the cleansing of the system (post-run). It is not improbable that 3CYP has been subject to diffusional broadening. This may occur due to temporary fluctuations in transfer line temperature which correct themselves at higher temperature. This would seem to be the case, as the second maxima at 415°C is positioned correctly. However, it immediately highlights the need to optimise transfer line temperature for each individual probe.

Further highlighting the sensitivity of MS, is the detection of water between 320-540 not observed in the DTG trace. The high temperature detection maxima for water ($m/z = 18/680^\circ\text{C}$) is attributed to dehydroxylation, the broadness observed in the corresponding DTG maxima is attributed to co-evolving CO_2 ($m/z = 44-380/570^\circ\text{C}$) and 3CYP detection to higher temperatures (625°C) (fig. 5.19).

Figure 5.21 RT-MS ion chromatograms obtained from Al³⁺-SWy-2-3CYP TIC (total ion current) and 3CYP ions [m/z =104, 77, 64, 50]

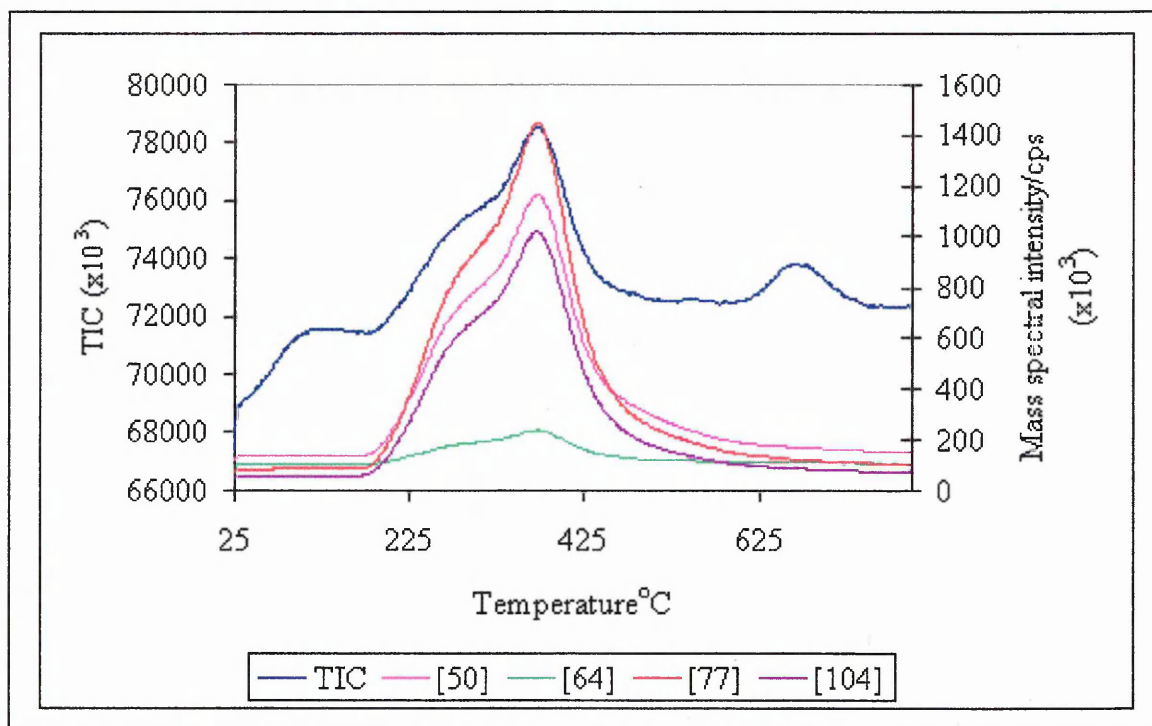
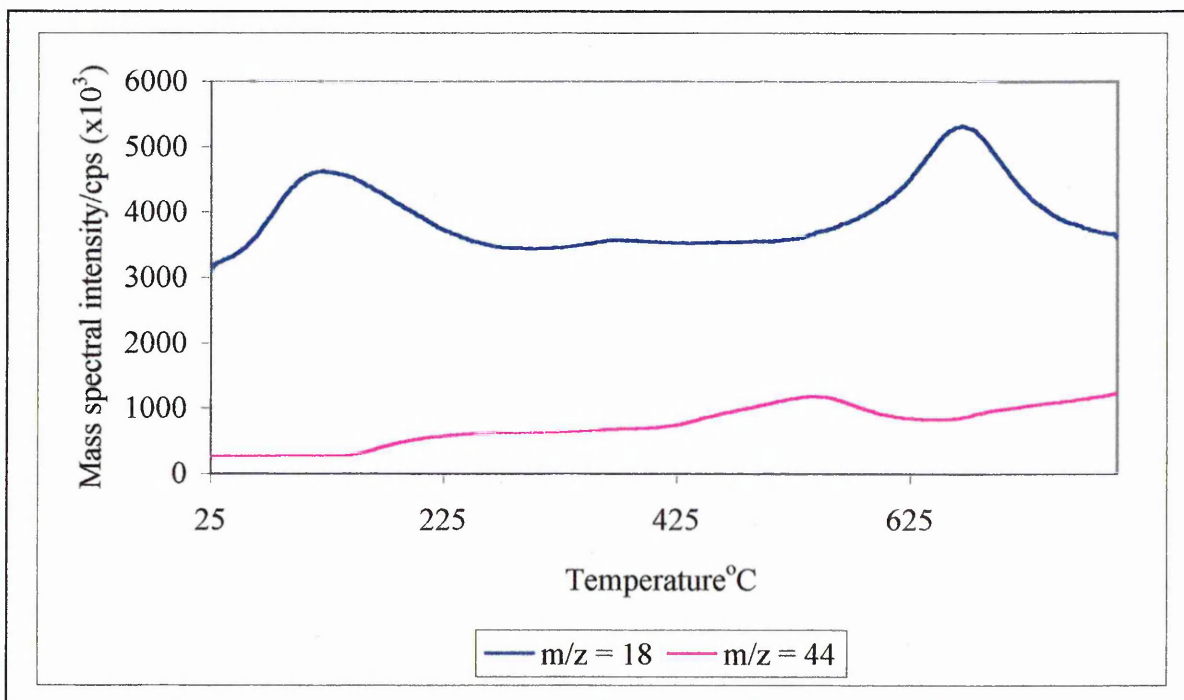


Figure 5.22 RT-MS ion chromatograms from Al³⁺-SWy-2-3-CYP H₂O [m/z = 18], CO₂ [m/z = 44]



Similarly, the first two overlapping weight loss maxima observed in the DTG trace of Al³⁺-SWy-2-3CYP, have been assigned in MS to the loss of physisorbed water CO₂ (m/z = 44/150°C) and the beginning of the loss of 3CYP at 180°C. The detection of 3CYP (m/z = 104, 77, 64, 50) occurs at 300 and 360°C ≈ and is clearly responsible for the second detection maxima observed in the TIC, but the breath of the TIC suggests contribution from other ions. Unlike nickel this coincides well with its corresponding DTG maxima. These other ions consist of water from 340-430°C (m/z = 18) and CO₂ (m/z = 44) from 340-550°C. Dehydroxylation (m/z = 18) is seen to start at 510°C with its maxima at 680°C. The co-evolving species H₂O, CO₂ and 3CYP would seem to be responsible for the two unresolved maxima observed in the DTG at higher temperature.

5.4.5 Results DRIFTS studies

Room temperature DRIFTS spectra (fig. 5.23) show bands associated with Ni²⁺-SWy-2 after exposure to 3-CYP (6 days). These spectra focus on two spectral regions, 2100-2300 cm⁻¹ (spectra (a)) and 1300-1750 cm⁻¹ (spectra (b)).

Figure 5.23 VT DRIFTS spectra of Ni²⁺-SWy-2-3-CYP from 25-400°C as indicated

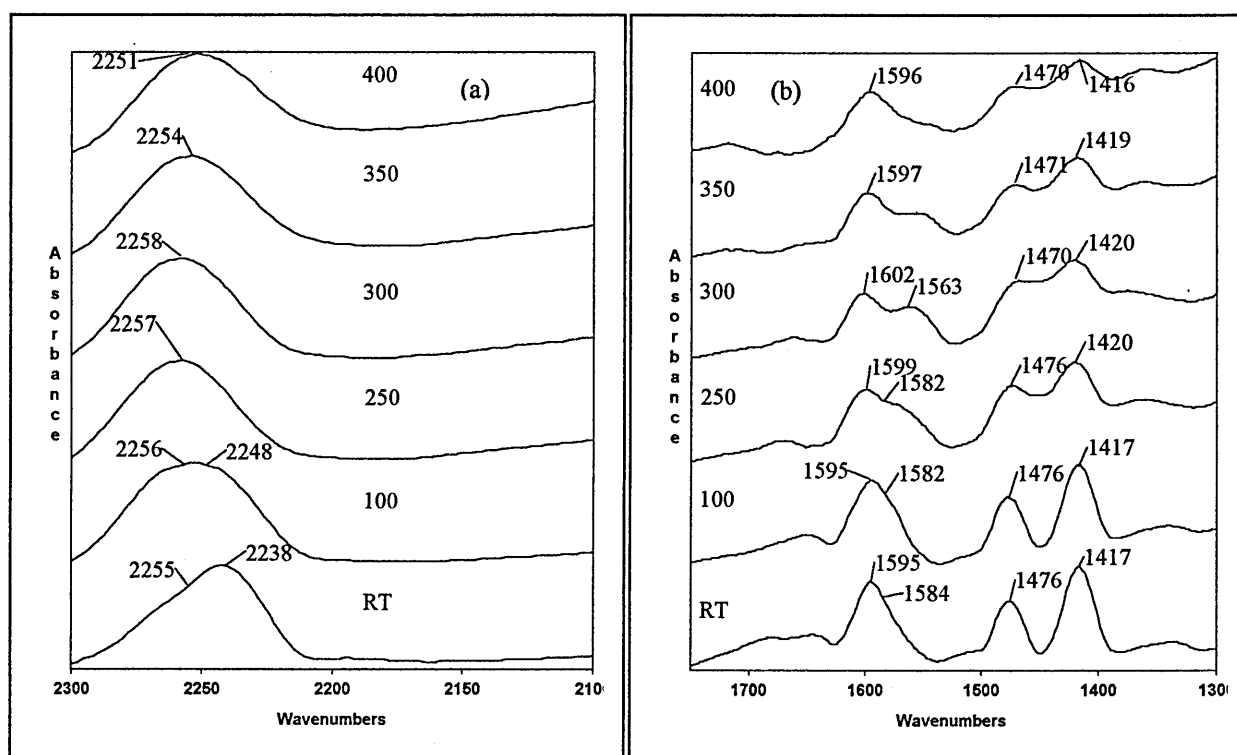


Table 5.12 Comparison of IR frequencies of Ni²⁺-SWy-2-3CYP and uncoordinated 3-CYP

Frequencies(cm ⁻¹) of uncoordinated 3-CYP	Assignment	Frequencies (cm ⁻¹) of coordinated Ni ²⁺ -SWy-2-3-CYP at 25°C
2229	v(C-CN) stretch	2238/2250 (two unresolved peaks)
1582	v(C-C) ring stretch	1595
1552	v(C-C) ring stretch	1584 (unresolved)
1460	v(C-C, CN) ring stretch	1476
1410	v(C-C, CN) ring stretch	1417

Figure 5.24 VT DRIFTS spectra of Al³⁺-SWy-2-3-CYP from 25-350°C as indicated

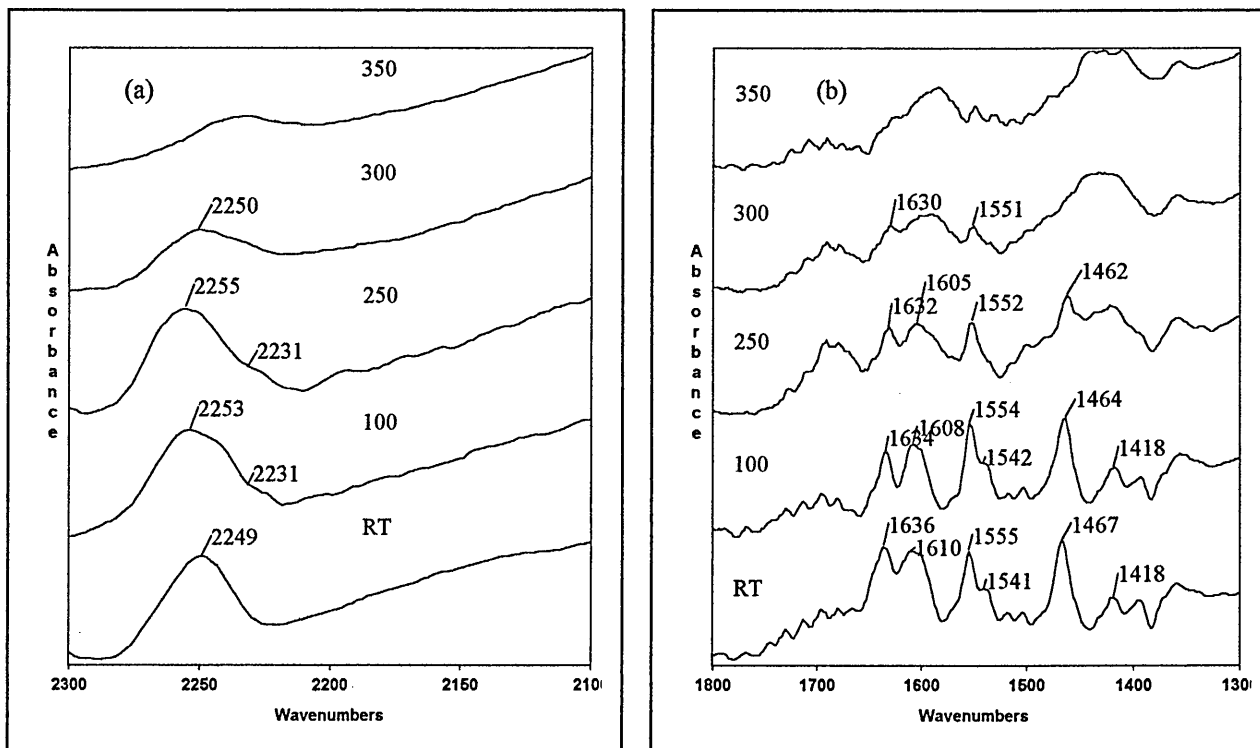


Table 5.13 Comparison of IR frequencies of Al³⁺-SWy-2-3CYP and uncoordinated 3-CYP

Frequencies(cm ⁻¹) of uncoordinated 3-CYP	Assignment	Frequencies (cm ⁻¹) of coordinated Ni ²⁺ -SWy-2-3-CYP at 25°C
2229	$\nu(\text{C-CN})$ stretch	2238/2250 (two unresolved peaks)
1582	$\nu(\text{C-C})$ ring stretch	Not present
1552	$\nu(\text{C-C})$ ring stretch	1554/1541 (shoulder)
1460	$\nu(\text{C-C, CN})$ ring stretch	1467
1410	$\nu(\text{C-C, CN})$ ring stretch	1418

The positions of the C-C and C-N vibrations shown in table 5.12-5.13 are characteristic of the aromatic ring and have previously been used to assign the coordination site of cyanopyridine-metal complexes [338-339]. In general it has been observed that the four principal in-plane ring deformations arising from the C-C and C-N stretching modes and occurring in the 1400-1600 cm⁻¹ region, are shifted to higher frequency on coordination of the pyridine nitrogen [340]. In addition, when the free pair of electrons on the nitrogen of a nitrile is involved in coordination, the stretching frequency of the nitrile group is shifted to a higher value than that of the free nitrile [341-342]. It has been shown that organic nitriles can coordinate metal ions, doing so with an upward shift (20-50 cm⁻¹) of the C-N stretching frequency. The nitrile stretching frequencies of cyanopyridines and complexes formed with interlayer cations (i.e. Ni²⁺-, Al³⁺), would provide valuable information concerning which nitrogen(s), that of pyridine or that of the nitrile, is coordinated in the interlayer space of the clay mineral. In addition Gill et al [343] have pointed out that the ring

breathing frequencies and C-H in plane deformations ($985\text{-}1250\text{ cm}^{-1}$) shift to higher frequencies on coordination. Unfortunately, for clay minerals, this region is heavily masked by the intense O-Si-O stretching vibrations of the clay mineral structure, making definitive assignments very difficult.

5.4.6 Discussion

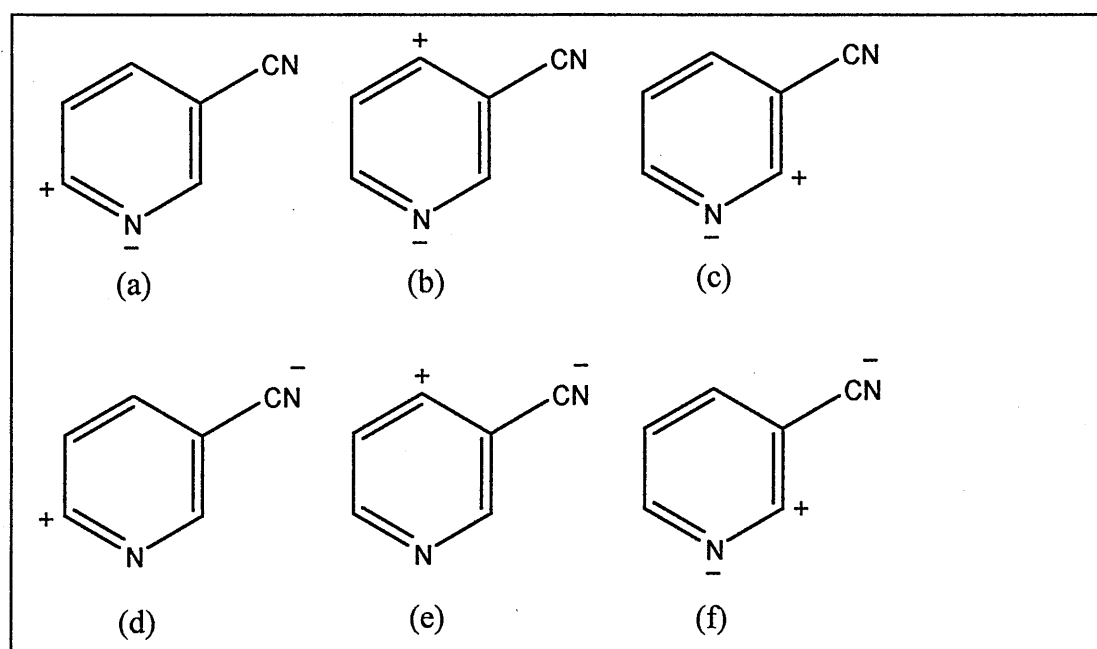
As previously mentioned, there is no evidence in the literature of the interaction of 3CYP with clay minerals. However, there is evidence for the interaction with compounds containing the nitrile group, such as acetonitrile and benzonitrile. Tarasevich et al. [344] have examined the IR spectra of acetonitrile adsorbed by homoionic montmorillonite films with a variety of interlayer cations (Li^+ , Na^+ , K^+ , Ca^{2+} , Co^{2+} and Cu^{2+}). It was shown that acetonitrile interacted through the $\text{-C}\equiv\text{N}$ group as indicated by the following frequency shifts, Na^+ (13 cm^{-1}) < Ca^{2+} (24 cm^{-1}) < Co^{2+} (64 cm^{-1}) < Cu (76 cm^{-1}). The upward band shifts for copper were comparable to those of acetonitrile bound to AlCl_3 and SnCl_4 (strong Lewis acceptors- 80 cm^{-1}). The magnitude of the $\text{C}\equiv\text{N}$ infrared band shift has been attributed to an increase in the force constant when directly coordinated to the interlayer cation. In comparison, Serratosa [345] studied the interaction of benzonitrile containing different interlayer cations (Mg^{2+} , Ca^{2+} and Ba^{2+}) by IR spectroscopy. He concluded that benzonitrile was hydrogen bonded through its $\text{C}\equiv\text{N}$ group to the magnesium ion by way of a water bridge, as intercalation caused a decrease of the O-H stretching frequencies of water before evacuation, leading to an increase in the water deformation frequency (1623 cm^{-1}). In further support of these conclusions, the $\text{C}\equiv\text{N}$ stretching frequency at 2225 cm^{-1} (uncoordinated) was shifted to 2240 cm^{-1} in the adsorbed state. On evacuating

the system, some of the cation coordinated water was removed, allowing direct coordination to the interlayer cation, which was shown by the development of the 2261 cm^{-1} band. However, using the shifts of both the structural O-H stretching frequencies and the $\delta(\text{HOH})$ mode of water as an indicator of reduced/increased hydrogen bonding is not necessarily so straightforward, because at low water contents the decrease in hydrogen bonding is consistent with isolated hydrated metal clusters of metal cations at the surface which are polarized by close proximity to the exchangeable cation [346]. Therefore separating these interactions in the presence of a probe molecule at higher temperature would be very difficult. As might be expected, the amount of displacement of the $\text{C}\equiv\text{N}$ stretching frequency from the uncoordinated state is influenced by the nature of the polarizing power of the cation, being greater for the highly polarizing type i.e. Ba^{2+} (12 cm^{-1}), Ca^{2+} (21 cm^{-1}) and Mg^{2+} (33 cm^{-1}).

The DRIFTS spectra of both Ni^{2+} - and Al^{3+} - exchanged SWy-2 previously shown demonstrate the differences between the different interlayer cations. As seen in figure 5.23 (a), the spectra of Ni^{2+} -SWy-2-3CYP at room temperature shows two unresolved nitrile bands at 2238 cm^{-1} and 2250 cm^{-1} , which suggests the presence of two different coordination environments. The band at 2238 cm^{-1} demonstrates a shift of 14 cm^{-1} ~ from uncoordinated 3CYP (2225 cm^{-1}), which suggests the presence of cation coordination (hydrogen bonding) through a water bridge as observed by with benzonitrile [345] at low temperature, or the free ligand in a more restricted environment. The band at 2250 cm^{-1} has experienced a shift of 20 cm^{-1} ~ from that of uncoordinated 3CYP, which suggests direct nitrile coordination through the Ni^{2+} cation. However, at 250°C, there is only evidence for direct coordination of the nickel cation, indicated by the one broad band at 2257 cm^{-1} , which would agree with the dehydration temperature of the nickel cation. From 340-400°C, there is a slight

downwards shift to 2251 cm^{-1} , indicative of a restricted environment due to the collapse of the interlayer space. Similarly a band of 2240 cm^{-1} has previously been observed in the spectra of $\text{Ni}(\text{3CYP})(\text{NCO})_2$ [347]. In addition, Nelson et al. [348] in their study of cobalt halide and thiocyanate complexes, have reported that the $\nu\text{C-N}$ stretching mode occurs as a weak to medium band at $2230\text{-}2250$ and is sometimes split. In many cases there is only a small upward shift in the in the $\nu\text{C-N}$ mode of $5\text{-}15\text{ cm}^{-1}$. Other workers [349] have reported small shifts of this order in complexes of 3CYP where the nitrile group is uncoordinated, being attributed to resonance effects. Explanation of these resonance effects are as follows [346].

Figure 5.24 Possible resonance effects for 3CYP



In 3CYP, the electron density localized at the ring nitrogen by the contribution of resonance forms (a-c) and delocalised by resonance forms (d-f). Coordination of the ring nitrogen to the metal ions relocalizes the electron density at the ring nitrogen and, therefore decreases the contribution of (d-f) to the electronic structure. The result of which causes the nitrile stretching frequency to shift to a higher value, which makes it appear as though the nitrile group was bonded to the metal atoms.

At room temperature, a comparison with Al^{3+} - shows a broad band located at 2249 cm^{-1} (a band shift of 24 cm^{-1} from uncoordinated 3CYP at 2225 cm^{-1}), which suggests direct coordination of the nitrile. However, between RT-100, there is the suggestion of an additional unresolved band at 2231 cm^{-1} (possibly higher), which is present to 250°C . This additional band which appears at 100°C is most probably related to the detection of water seen in MS between RT- 290°C , its maxima positioned at 120°C , being directly related to the relative increase in protonation (associated with water loss) within this temperature range.

In the lower wavenumber region ($1300\text{-}1800\text{ cm}^{-1}$), the Ni^{2+} - sample also shows evidence of direct coordination of the pyridine nitrogen ($1400\text{-}1600$ in-plane ring deformations) which is demonstrated by the upward shift of up to 16 cm^{-1} (i.e. $1582\text{-}1595\text{ cm}^{-1}$, $1552\rightarrow 1584\text{ cm}^{-1}$, $1460\rightarrow 1476\text{ cm}^{-1}$, $1410\rightarrow 1417\text{ cm}^{-1}$) and indicative of Lewis bound pyridine. This suggests that the observed upward shift of the nitrile stretch, may in fact be due to resonance effects. There is also some evidence of protonation due to a weak band at 1630 cm^{-1} evident to 300°C . In comparison, the Al^{3+} - sample shows much smaller shifts of the order of $7\text{-}8\text{ cm}^{-1}$ ($1460\rightarrow 1467\text{ cm}^{-1}$, $1410\rightarrow 1418\text{ cm}^{-1}$) which is similar to that seen due to weak hydrogen bonding through a water bridging molecule. In addition bands at 1552 and 1582 cm^{-1} seen in uncoordinated 3CYP demonstrate downward shifts to 1541 and

1555 cm^{-1} respectively. However, this effect could be due to protonation of the pyridine nitrogen, evidence for which, are bands at 1610 and 1636 cm^{-1} (Brønsted bound pyridine). As the temperature is raised from RT-250°C there is little change in the band positions (1300-1800) for the Al^{3+} - sample other than that attributed to a collapsing interlayer space. However, intensity changes show an increase in the band at 1610 cm^{-1} relative to bands at 1555 and 1467 cm^{-1} and this may be attributed to an increase in protonation at higher temperature as the solvent water layers surrounding the cation are reduced in number, the remaining layers being more easily polarized by the highly charged cation. These strong acid sites are present up to 250°C and decrease significantly by 300°C, especially bands at 1552, 1467 and 1418, the latter two becoming one broad peak, which agrees well with the dehydration temperature of the cation. Similarly, Occelli et al. [8] have shown that heating pillared clays to these temperatures converts the Bronsted sites to Lewis sites which results in the band broadening.

5.4.7 Summary

The study of 3CYP as a suitable probe has shown highlighted several important points:

- (a) TGA has shown that temperature programmed desorption (TPD) is capable of distinguishing between the Ni^{2+} - and Al^{3+} exchanged forms of SWy-2. Though the unresolved maxima attributed to 3CYP desorption, indicates that the different adsorption sites had similar desorption energies. However, 3CYP is a solid with a low vapour pressure, which is not ideal for its use as a probe

molecule. Therefore the six-day incubation period necessary to produce reasonable weight loss maxima (12-13 %) is expected, but too long in comparison to CHA. However, under conditions of increased temperature and pressure, this incubation period could be reduced to a shorter, more acceptable period. Future work for the purpose of publication would entail a full incubation study to monitor both uptake, desorption and 3CYP.

(b) VT DRIFTS indicates that the Al^{3+} -sample protonates 3CYP through the pyridine nitrogen suggesting its acidity is predominantly Brønsted in nature, with some evidence of Lewis acidity at higher temperatures. In relation to the corresponding DTG maxima, this would suggest that the main desorption (240°C-MS) may be attributed to the cyanopyridinium ion and the small shoulder at 340°C attributed to Lewis bound pyridine. There is also evidence to suggest that 3CYP is also coordinated through its nitrile group. The main nitrile band between 100-250°C shows a shoulder which changes from 2238-2248 cm^{-1} coinciding with increased protonation and alteration to Lewis bound pyridine above 300°C. Moreover, the disappearance of the shoulder at 2248 cm^{-1} and the appearance of one nitrile absorbance at 300°C (2250 cm^{-1}) is very similar to that seen in the Ni^{2+} sample at these temperatures. Contrastingly, the Ni^{2+} - sample shows direct evidence of Lewis bound pyridine and suggests protonation due to a weak band at 1630 cm^{-1} (to 300°C). This corresponds to a weak shoulder on its DTG maxima at 300°C, indicating the possible presence of Brønsted bound pyridine. However, the suggestion of resonance effects makes it difficult to determine whether the nitrile group is involved in bonding in the Ni^{2+} or Al^{3+} sample. However the fact that the Bronsted bound pyridine of the Al^{3+} sample desorbs at 80°C less, suggests that

the combination of protonation and nitrile coordination, effects not only coordination, but has the effect of lowering the desorption temperature of the Al^{3+} sample.

- (c) Complimentary evidence from VT XRD and TGA has shown that after 6 days incubation, the room temperature trace is representative of two different interlayer orientations (Ni^{2+} -perpendicular-21.45Å/ Al^{3+} -parallel-13.13Å) of 3CYP. Considering one of the probe pre-requisites is the ability to quickly intercalate, it is not possible to determine whether both samples were fully intercalated, hence studies of this nature were not pursued. However intercalation studies would be necessary for the purpose of publication. Heating from room temperature-105°C quickly reverts the Ni^{2+} - sample to a spacing of 13.88 Å, similar to that of the Al^{3+} -sample at room temperature. The broadness of the changing d_{001} peak between 60-105°C and its sharpening near at 175°C, indicate that 3CYP undergoes rearrangement of its orientation within the interlayer space. Brindley and Hoffmann [350] have suggested that aliphatic chain molecules adsorbed with their shortest axis perpendicular to the silicate surface, may adopt two kinds of orientation. The first type, designated α_i , refers to an interlayer arrangement in which the plane of the carbon is perpendicular to the silicate layer (complexes d_{001} range 13.25-13.65 Å). In the second type α_{ii} , this plane is parallel to the silicate layer (complexes d_{001} range 13.00-13.10 Å). An analogous situation occurs with aromatic ring compounds, where the α_i orientation is observed when the compound is saturated and α_{ii} when unsaturated. In fact Seratossa [351] confirmed the existence for both types of orientation when studying pyridine-montmorillonite complexes, by measuring the change in intensity of certain

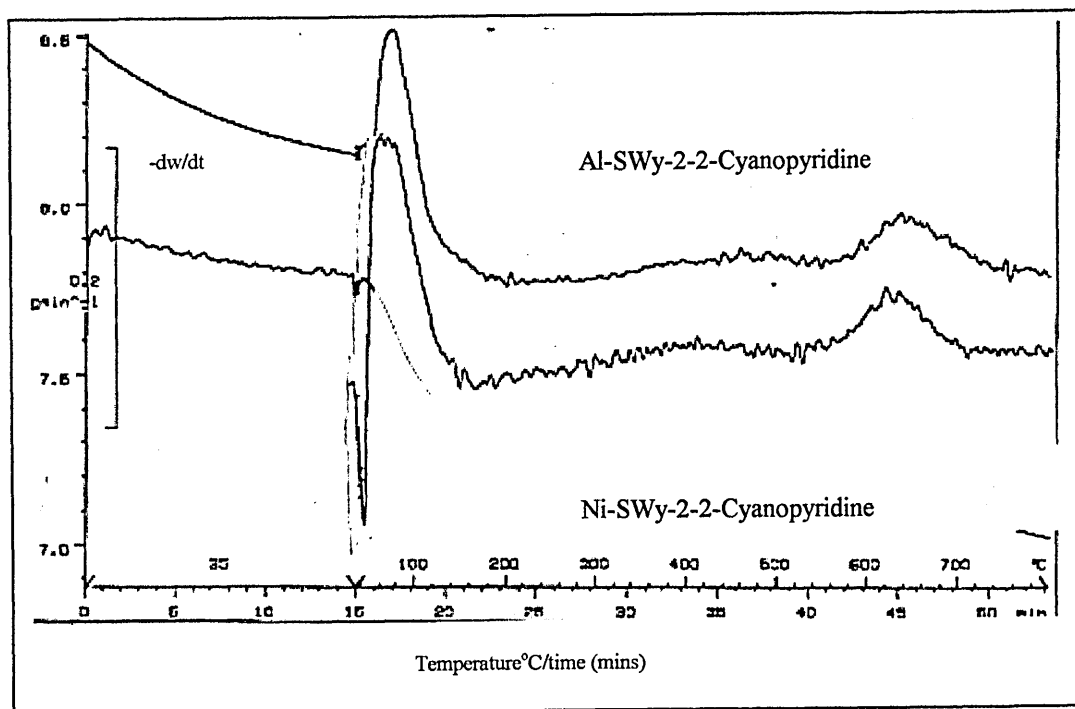
absorption bands ($700\text{-}1500\text{ cm}^{-1}$) in the infra-red spectrum of the complexes as the angle of incident beam makes normal to the sample was varied. However, as shown by Olphen and Deeds [352], the d-spacing of a Na^+ -montmorillonite/pyridine/water system can range from $29.3\text{-}14.8\text{ \AA}$ depending on the pyridine:water ratio. This suggests that the large hydration shell of the Al^{3+} cation draws the pyridine nitrogen into preferential coordination, in effect controlling both the acidity and subsequent orientation.

- (d) The unsuitability of 3CYP as a probe molecule is also highlighted by its ability to condense within the EGA system (Bp 202°C), demonstrated by the detection of 3CYP within the system after a routine post run blank. In particular, contamination occurred within the OTM trap and GC column, taking several days to clean the system. Any future EGA work would therefore have to consider optimising the transfer line temperatures to prevent condensation and diffusional broadening of MS peaks due to slow gas transfer.
- (e) Another problem seen in the DTG of Al^{3+} is overlap of the dehydroxylation maxima with a peak centered at 715°C . This is a problem if one wants to characterize the data using chemometrics, because the desorption due to the probe and dehydroxylation are fingerprint regions for the recognition of swelling minerals. In addition, the higher temperature peak could mislead the software into believing that the clay mineral illite was present (its dehydroxylation is 2 unresolved peaks at 570 and 640°C), when in fact it is due to the evolution of H_2O and CO_2 , produced when dehydroxylation provides oxygen to the coking residues formed by 3CYP. Evidence of which is provided by MS, by the detection of $m/z = [44\text{-CO}_2]$ under both peaks.

5.4.8 Other probes evaluated in this thesis

As previously shown, a variety of other probes have been evaluated in this thesis but with rather less success. 2-cyanopyridine (2CYP-a solid below 26°C) was also investigated, but failed to show any resolved weight losses after 6 days-maximum 11 days, other than usually associated with untreated M^n -SWy-2 samples, as shown by its DTG trace (figure). This was after three approaches, direct application of liquid 2CYP to an undried sample (shown). Drying overnight and immediately putting into a saturation vessel at 50°C and the application of liquid 2CYP to undried samples.

Figure 5.25 Derivative thermograms of Al^{3+} -SWy-2-2CYP and Ni^{2+} -SWy-2-2CYP



In figure 5.25 there is a weight loss between 150-500°C, but this is very gradual as observed in the corresponding weight loss curve (not shown). The lack of any well defined maxima is more than likely not only due to its low volatility, but caused by steric hindrance produced by close proximity of the pyridine nitrogen and nitrile groups in ring positions 1 and 2 respectively.

The probes 2, 3 and 4-Bromoaniline were evaluated because of the potentially strong bromine signal observed by mass spectroscopy. However, none of these probes produced any weight losses other than that normally associated with Mⁿ-SWy-2 samples.

The probe benzonitrile (BN) was evaluated because of its high volatility and ability to produce a strong signal in IR (C≡N stretch). However, its success was not hindered by its ability to produce well resolved peaks. Rather, the problem surrounded its inability to overcome water surrounding the interlayer cation, hence bonding was very weak and weight losses were only significant after 8 days vapour saturation and showed considerable overlap. As understood from Serratosa [345], BN has great difficulty in displacing water within the interlayer space. TGA/DTG studies (not shown) have shown that the time taken to intercalate benzonitrile is considerably longer than either CHA or 3CYP. Drifts spectra at room temperature suggest that benzonitrile may be coordinated. However the bands are rather weak and only slightly shifted from their positions in liquid BN. The strongest signal in the spectra was attributed to the C≡N stretching bands, which were similar in frequency for all samples, ranging from 2248 (room temperature)-2251cm⁻¹ (250 °C), suggesting direct coordination to the interlayer cation. Gas phase FTIR infrared also showed that over a three-month period, the absorbance intensity is only a fraction of that seen with

CHA or 3CYP. Therefore benzonitrile would be not be considered to be a suitable probe due to the time taken to intercalate, the weakness of the absorption bands seen in the infrared and the lack of separation of thermal events seen in the TGA.

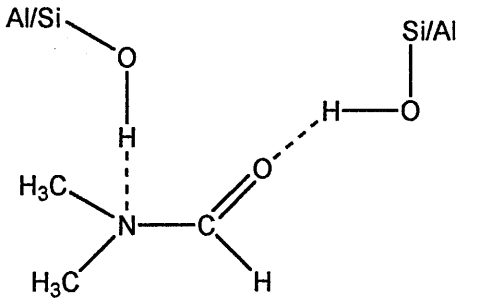
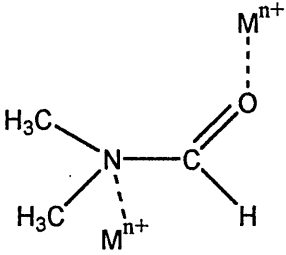
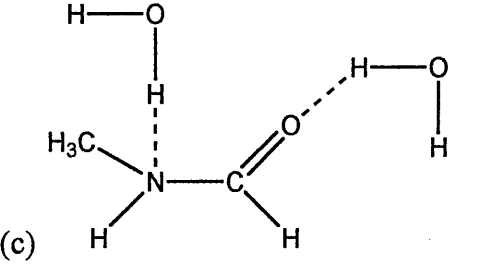
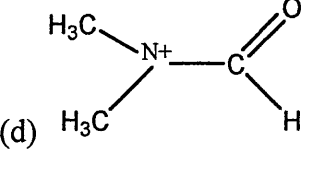
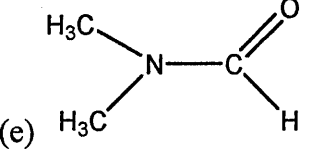
Chapter 6 The qualitative characterisation of minerals by chemometric analysis of EGA detection profiles during temperature programmed desorption (TPD)

6.0 Introduction

As previously shown in chapter 5, the potential of both CHA and 3CYP as probe molecules has highlighted a variety of complex interpretational problems, including slow intercalation, thermal degradation and diffusional broadening within the EGA system. However, the suitability of DMF as a chemical probe molecule has been highlighted in previous work [353] DMF was able to determine the presence of swelling clays in the presence of non-expanding minerals (i.e. kaolinite and SiO₂). DMF had a fast adsorption/intercalation rate, and distinctive maxima were seen in the DTG traces for montmorillonite and illite after only 5 and 17 hours respectively. The possible interactions between DMF and cation exchanged clays is shown in table 6.1. Very few of the results herein have been compared to literature. This is simple because no such data involving the EGA detection of DMF from minerals has been found. However, Olejnik et al. [354] studied the intercalation of DMF into Ca, Mg and Na-exchanged montmorillonites and found that their $d_{(001)}$ – spacings to be similar. Clegg [353] showed similar that intercalation occurred in steps and that different exchange cations within montmorillonites could readily be distinguished simply by the temperature at which the DMF molecules desorbed during TGA studies. The same author showed that illite exposed to DMF did not swell ($d_{(001)}$ – spacing 10.1Å) but did show comparatively weak EGA-DMF detection from (115-395°C) which is similar to that observed in the Mg-SWy-2-DMF complex. Differentiation between illite and Na and K-exchanged montmorillonites may be

difficult because DMF desorption occurs in the same temperature region. DMF-kaolinite complexes have also received little attention because the intercalation rate is slow and only a very small portion of the kaolinite expands to 12.2 Å [355] due to the inability of DMF to overcome the strong hydrogen bonding between the layers. Churchman and Theng [356] have shown that both NMF and DMF intercalate into halloysite (expanding kaolinite:H₂O complex). However, the strong dehydroxylation maxima observed in DTG may be used to highlight the presence of kaolinite. This may also be the case for chlorite.

Table 6. 1 Possible interactions between DMF and cation exchanged clay

<p>(a)</p> 	<p>(i) Hydrogen bonding of $(\text{CH}_3)_2\text{N-R}$ to hydroxyl on clay surface (ii) H-bonded via the carbonyl group to hydroxyl of clay surface (note: very few of these sites are available in a smectite clay)</p>
<p>(b)</p> 	<p>(i) Coordination to exchangeable cations (M^{n+}) via (a) carbonyl or (b) nitrogen. Cations could be positioned in the interlayer or on external surfaces</p>
<p>(c)</p> 	<p>Hydrogen bonding of water to (i) carbonyl (ii) lone pair electrons on N (note : the water could be bridges to exchange cations)</p>
<p>(d)</p> 	<p>Protonated species Hydrogen could come from either water present in the interlayer or from dehydroxylation of the clay structure</p>
<p>(e)</p> 	<p>DMF-though hydrogen bonding between DMF molecules is relatively weak.</p>

*note bonding angles are not correct

In comparison to N-methyl formamide (NMF), the high vapour pressure exhibited by DMF can be attributed to the replacement of the N-H bond of NMF with N-CH₃ bond, thus reducing the possibility of hydrogen bonding between DMF molecules. DMF

also demonstrates higher temperature weight loss maxima than NMF, indicating that DMF binds more strongly to M^{n+} -SWy-2. The rate of adsorption could possibly be influenced by the low energy state of bonded DMF molecules. Moreover, these studies have revealed that different cation exchanged cations forms of montmorillonite can readily be distinguished simply by the temperature at which the most strongly held DMF molecules are desorbed during thermogravimetric analysis. The time taken for uptake is considerably faster than the 3 and 6 days for both CHA and 3CYP. Therefore DMF represents the most ideal chemical probe to date, since it interacts rapidly, producing distinct detection maxima for each cation-exchanged montmorillonite. In contrast to the variety of complex thermal degradation products demonstrated by CHA, EGA-OTM analysis (not shown) reveals that DMF is the only thermal degradation product of the data output for chemometric analysis. Figure 6.1 shows a typical mass spectrum of DMF whilst table 6.2 shows its ion abundances.

Figure 6.1 DMF mass spectrum

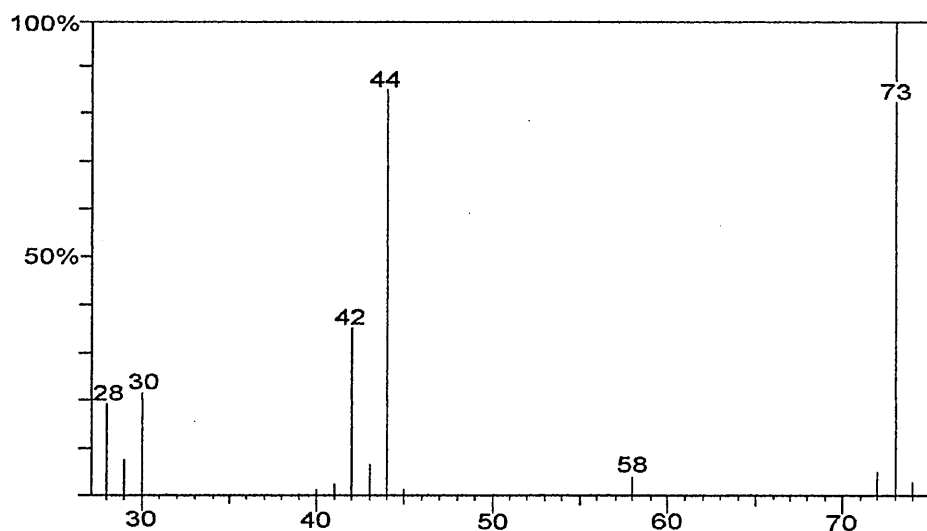


Table 6. 2 Relative intensities of the fragment ions of DMF and their possible molecular structure [353].

Ion mass	Possible fragment ions	Relative % intensity
73		100%
72		6%
58		4.8%
44		86%
43		7.2%
42		36%
30	currently unknown	22%
29	$\text{CH}_3\text{-N}^+$ H-C=O^+	8%
28	CO^+	20%
15	CH_3^+	no data

6.1 Transfer line and external heating zone experiments for the optimisation of DMF signal during EGA

However DMF is not without its potential problems. As previously mentioned (chapter 5), it is important, that when a suitable probe is chosen for further investigation, that it's detection signal is optimised. That is the fate of the probe is determined under different thermal experimental conditions as it is evolved and detected by EGA. Because, the method requires well-resolved thermal events, the

linear temperature ramp between 35-800°C was deemed satisfactory. However, the evolved gases detected during temperature programmed desorption (TPD) travel to the relevant detectors via a pair of sniffer tubes (which are housed in an external heating zone) along a set of transfer lines (chapter 2). In particular the transfer line temperatures need to be optimised because they are usually maintained at high temperatures during EGA to minimise the adsorption of evolved gases, which may result in the broadening of maxima in the resulting chromatographs and in a reduction in resolution of DMF thermal detection events. This effect is known as diffusional broadening. Previous work [353] considered two experiments that have prompted more detailed work herein. In these experiments liquid DMF was heated in the crucible from 35-800°C at 20°C/min after an initial 15 minutes at 35°C. This consisted of two experiments, a low temperature (145°C) and a high temperature (250°C) study, the details of which are seen in table 6.3.

Table 6. 3 Low and high temperature transfer line experiment temperatures

	Low temperature experiment°C	High temperature experiment°C
External Heat zone	145	235
Transfer line (FTIR)	145	240
Transfer line (MS)	145	250

The low temperature (145°C) experiment was carried out below the boiling point of DMF (153°C), thus DMF was less likely to break down within the transfer lines, but was also more thermally stable prior to ionisation in the MS and therefore less likely to effect the fragmentation pattern. Thus at 145°C DMF did not encounter a temperature higher than its boiling point until 20.9 minutes. In the low temperature

experiment DMF was detected over a longer period, 33 as opposed to 28 minutes (diffusional broadening). Moreover, the ions ($m/z = 73$ and 58) were more prominent at low temperature (higher intensity/cps), indicating more DMF was detected in the low temperature experiment. This not only effects resolution (i.e. when more than one interlayer cation is present), but could also impinge on the chemometric interpretation of the dehydroxylation region. In comparison, the high temperature experiment revealed more DMF breakdown, indicated by a decrease in detection of ions $m/z = 73$ and 58 , being concurrent with an increase in ion ($m/z = 44$ -DMF fragment ion and/or CO_2).

6.2 Liquid DMF transfer line studies by gas phase FTIR (GP-FTIR) and RT-MS

In order to optimise DMF detection, the experiments concentrated on four transfer line temperatures 250, 220, 190 and 175°C, which were observed by gas phase-FTIR (GP-FTIR) and RT-MS. The GP-FTIR studies focused on two IR absorbance bands representative of DMF at 2937 cm^{-1} (C-H stretch) and 1720 cm^{-1} (C=O stretch). A brief study of the ratios of these two bands may be also be indicative of DMF breakdown through oxidation of the carbonyl group. A higher ratio is indicative of greater DMF breakdown. A summary of these results is shown in section 6.3, greater detail can be found in the appendices.

6.3 Summary of transfer line studies

Each run at a particular transfer line temperature had one replicate and the integrated areas for replicates were shown to be consistent (not shown). In order to get a balance between diffusional broadening and DMF thermal degradation, 190°C was chosen as

the operational transfer line temperature for future work. Therefore for high precision work there is a need to monitor the actual transfer line temperature and its stability. Moreover there is a need to clean the source after an allotted time when using DMF due to deposition which effects consistency. Carryover of DMF from run to run was also monitored at the optimum temperature of 190°C but none was detected. Therefore this must be an integral part of TG-MS method development.

6.4 External heat zone (EHZ) studies

As previously mentioned, the external heating zone may also need optimisation as it provides heat to the sniffer tube housing. This will prevent cold spots where DMF may condense en route to the transfer lines, yet too high or too low a temperature may contribute to saturation, degradation or diffusional broadening. The manufacturers maximum operating temperature for this region is 200°C (Cahn-Thermo-Unicam). This is presumably kept below the maximum operating temperature of the transfer lines (250°C) so as to prevent analyte condensation and breakdown during the low temperature stage of a temperature ramp. When this zone dropped to room temperature due to an electronic fault, DMF condensation occurred. This produced a broad slug of DMF across the whole MS spectrum from 35-800°C (not shown) and saturated the detector. To optimise the temperature of the external heating zone, a series of experiments were conducted from 100-200°C in 20°C increments (including a repeat experiment at each temperature interval) whilst maintaining the transfer lines at 190°C. Greater detail of these experiments can be found in the appendices. In retrospect, both the external heating zone and the transfer

The first part of the paper discusses the importance of the
second part of the paper discusses the importance of the
third part of the paper discusses the importance of the
fourth part of the paper discusses the importance of the
fifth part of the paper discusses the importance of the
sixth part of the paper discusses the importance of the
seventh part of the paper discusses the importance of the
eighth part of the paper discusses the importance of the
ninth part of the paper discusses the importance of the
tenth part of the paper discusses the importance of the

Conclusion

The first part of the paper discusses the importance of the
second part of the paper discusses the importance of the
third part of the paper discusses the importance of the
fourth part of the paper discusses the importance of the
fifth part of the paper discusses the importance of the
sixth part of the paper discusses the importance of the
seventh part of the paper discusses the importance of the
eighth part of the paper discusses the importance of the
ninth part of the paper discusses the importance of the
tenth part of the paper discusses the importance of the
eleventh part of the paper discusses the importance of the
twelfth part of the paper discusses the importance of the
thirteenth part of the paper discusses the importance of the
fourteenth part of the paper discusses the importance of the
fifteenth part of the paper discusses the importance of the
sixteenth part of the paper discusses the importance of the
seventeenth part of the paper discusses the importance of the
eighteenth part of the paper discusses the importance of the
nineteenth part of the paper discusses the importance of the
twentieth part of the paper discusses the importance of the

line temperatures would need to be altered simultaneously and therefore this may need to be dealt with in future studies.

6.5 Summary of EHZ studies

The work herein suggests that the EHZ in combination with the transfer line temperature regulates the amount of DMF reaching the EGA detectors. At too low a temperature, diffusional broadening occurs, which can cause overlap of detection maxima and may reduce the effectiveness of chemometric analysis. At too high a temperature, the signal is not optimised due to DMF breakdown. The combined optimum operating temperature for liquid DMF subject to TPD (25-800°C) for both transfer lines and external heat zones was found to be 190 and 180°C respectively.

The results show that the breakdown of DMF does occur along the transfer lines, although it is not clear how. Breakdown of DMF on the clay is unlikely but may occur as it immediately leaves the clay [353]. This is more probable as the sample is heated and DMF is beginning to evolve. If DMF leaves the clay at a lower temperature and enters the sniffer tubes (a much smaller diameter opening) at a higher temperature, this sudden temperature change may cause instability of the molecule. In addition DMF may take up to 2 minutes to reach the detector, having to travel a distance of 5 ft, which is clearly too long, adding to thermal instability and possible increase in lower weight fragment ions. If the transfer lines were sufficiently short, a more effective approach would be to apply controlled rate thermal analysis (CRTA) as developed by Rouquerol [357] and Paulik [358]. It has been suggested that the optimum length for transfer lines are between 2-4 inches [359-360] aiming for a transfer time of 1 second. The aim of CRTA is to maintain a thermally induced

physiochemical process (e.g. mass loss, gas evolution etc) at a constant, pre-determined reaction rate. Increasing or decreasing the sample temperature as necessary, means that the heating rate is generally low through a process and fast between processes [361]. CRTA has been demonstrated to achieve high resolution. Another factor which should not be overlooked for future work is the application of lower (MS) ionisation energies (10-30 eV-) as they enhance the relative intensity of molecular ion peaks and reduce the number and relative abundances of the lower molecular weight fragment ions, as well as fragmentation, ionically induced rearrangements or ion molecule collisions. The operating ionisation energy of 70eV is very high (compared to the ionisation potential of atoms or molecules) though it has the advantage of producing a stable ion current.

Because DMF detection can overload the more sensitive quadrupole detector, additional experiments were performed to ascertain (not shown) what weight (mg) of fully loaded (DMF) swelling mineral (e.g. SWy-2-as DTG losses were greatest) could be used without saturating the detector at these temperatures. Repeat experiments were conducted between 8-16mg. It was found that a 12 mg caused saturation of the detector. Therefore the weight used in both qualitative and quantitative studies was confined to 10 mg for swelling minerals.

6.6 The qualitative characterisation of minerals by chemometric analysis of EGA DMF and water detection profiles during temperature programmed desorption (TPD)

6.6.1 Principal component analysis(PCA)/partial least squares modelling(PLS)

Chapter 2 describes the basic principles of PCA/PLS modelling.

6.6.2 Data output utilised for PCA/PLS modelling

This section attempts to qualitatively characterise minerals after exposure to DMF vapour. The clay minerals described were divided into four groups. For example, expanding minerals such as montmorillonite-saponite, illite and non-expanding such as kaolinite and chlorite. EGA detection profiles (i.e. TGA, GP-FTIR and RT-MS) obtained during TPD were analysed by Win-das chemometric classification software [359] to produce qualitative characterisation models with a view to determining the presence of these minerals in samples of unknown composition.

These profiles were dominated by both DMF desorption and dehydroxylation of the clay. Six simple chemometric models are described herein, that utilise different EGA profiles, which were obtained simultaneously from the same samples. Models (a and b) used the TGA weight loss profile, model (c) the total infrared (TIR) and model (d) the RT-MS total ion current (TIC) and ions $m/z = 73$ and 18 .

These models would provide important information regarding the variability within mineral groupings (i.e. the level of spread required to fully describe a group), in particular the swelling mineral montmorillonite. This is especially important when

choosing appropriate mineral standards for quantitative analysis which are representative of the type of mineral under study (i.e. a rock core from a different location may require different clay mineral calibration component(s). This is also important if a particular model is to be applied to a sample of unknown composition (i.e. interlayer cation can be identified by a knowledge of the particular DMF detection temperatures). These studies will also highlight the method(s) most suitable for quantitative analysis.

In short, qualitative chemometrics analysis will give a mathematical measure of the dimensional proportions of a particular group and show the similarities and dissimilarities within and between groups. This may also highlight samples which contain clay minerals from any number of the groups.

6.6.3 Thermal reactions of untreated clay minerals

A brief description of the principal thermal reactions of clay minerals are given to demonstrate to the reader the nature of the profiles produced during EGA. The temperatures described relate to the DTG. Confirmation of the nature of these losses is confirmed by RT-MS.

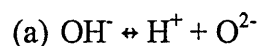
(1) below 400°C

For un-treated expanding clay mineral samples, the major weight losses/detection profiles are dominated by the loss of molecular water from the interlayer space. Much of this is related to the hydrated interlayer cations and is preceded and overlapped by physisorbed water bound to the exterior surfaces and broken edges.

However, in halloysite (polymorph of kaolinite), sheets of water molecules exist between the layers, which are probably hydrogen bonded to the surfaces.

(2) 400-750°C

This region in untreated minerals is concerned with dehydroxylation. The dehydroxylation of clay minerals has been studied by several techniques [360 and references therein] and is believed to result from the interaction of two hydroxyl groups in a two-step process to form a water molecule. The first step (a) involves hydroxyl deprotonation, which leaves a chemically bonded oxygen as a superoxide anion in the lattice. The proton then diffuses (proton hopping) to another hydroxyl resulting in the formation of water (b).



The DTG maxima of both untreated and DMF treated minerals used herein can be found in the appendices. The samples studied were initially purged for 15 minutes and then heated from 35-800°C at 20°C/minute in a nitrogen atmosphere. It should be noted that between these two events (i.e. after 15 minutes) a negative minimum followed by a small positive maximum occurs. The cause of this is not known. But could be caused by a sudden change in pressure of the carrier gas in a small chamber as the temperature is suddenly increased or an electrical interference from the instrument. Whatever the reason, it is not due to the sample as it occurs when a

control is performed i.e. no sample in the chamber [353]. A summary of the characteristic maxima observed in the DTG herein are shown in table 6.4.

Table 6.4 Summary of the characteristic maxima observed in the DTG traces of clay minerals

Mineral	Characteristic DTG maxima, °C (% wt. loss)
Montmorillonite M ⁿ⁺ -SWy-2	90 & 130°C (2-11%) ← 700°C (≈5%)→
Illite	70°C (0.7%) ← 570 & 650°C (4.7%) →
Kaolinite (KGa-2)	← 550°C (13-14%) →
Chlorite	← 600°C (8.7%) & 780°C (1.1%) →

DTG traces of untreated cation-exchanged montmorillonite (Mⁿ⁺-SWy-2) are denoted by two maxima, the low temperature maxima due to the loss of physisorbed water and dehydroxylation of the clay structure, respectively. The percentage weight loss of dehydroxylation centred at approximately 700°C should always remain constant and can be used as a qualitative internal reference standard to the size and position of other maxima present. It must be noted that cations with high hydration energies (Mg²⁺ and Al³⁺) exhibit two stages in the loss of physisorbed water in two stages, whereas cations with low hydration energies (i.e. Na⁺) lose water in one stage. The extent of dehydration depends on the exchangeable cation, temperature and moisture in the atmosphere. These results are typical of those presented in other papers [361-365].

Van der Gaast [366] proposed that dehydroxylation of kaolinite occurs in two steps. The first involves the hydroxyls of the upper un-shared plane in the octahedral sheet followed by the inner shared plane in the octahedral sheet (see Ch 1-Clay mineral structure). The temperature at which these occur are linked to the degree of ordering and crystal size. Most kaolinites lose their hydroxyls between 450-600°C, but it is well known for some well ordered kaolinites to give dehydroxylation temperatures as high as 690°C, though these are less common (Keokuk kaolinite from Iowa) [365]. The structural water for kaolinite composition $(\text{OH})_8\text{Si}_4\text{Al}_4\text{O}_{10}$ amounts to 13.96%, depending on the level of ordering. Continued heating after dehydroxylation produces metakaolinite and at higher temperatures (>1010°C) mullite crystallisation occurs [366].

Chlorite is recognised by its two-stage dehydroxylation, a low temperature event at 600°C is associated with the dehydroxylation of the brucite sheet, followed by dehydroxylation of the talc sheet at 800°C. Significantly more water is evolved in the first event (e.g. 8.7 as opposed to 1.1%) [367]. DTG traces of sea sand and feldspar produced no weight loss maxima (components in quantitative studies later in this chapter). Though the weight loss from quartz and feldspar were 0.5% and 1.7% respectively [368].

6.7 Samples

All samples were exposed to DMF vapour for a period of 3 weeks to ensure maximum saturation [353]. This time period is in excess of the time required to demonstrate maximum weight loss for swelling mineral components exposed to DMF so as to ensure maximum uptake and detection. Samples for qualitative analysis are shown in table (6.5).

Table 6.5 Details of samples for qualitative analysis

Montmorillonite/Saponite	Illite	Kaolinite	Chlorite
STx-1 (Ca -Montmorillonite) Source: Texas-USA	1-Mt Source: Silver Hills-USA	KGa-2 (kaolinite)	CCa-1
SAz-1 (Ca – Montmorillonite) Source: Arizona-USA	Illite	Jkaol Source: Jordan	CCa-2
SAP-Ca (Ca-Saponite) Source: Ballarat-California-USA		Kaol Source: Cornwall-UK	Pennitite
SCa-1 (Ca-Hectorite) Source: California-USA		Na-KGa-2 (Na-exchanged)	Mg-Chlorite
SWy-1 (Montmorillonite) Source: Wyoming-USA			
SWa-1(Fe exchanged) Nontrite Source: Washington-USA			
SWy-2 (Na, Ca ,Mg exchanged)			
Cr-SWy-2 (Cr exchanged SWy-2)			
Mg-SWy-2(Mg exchanged SWy-2)			
Ni-SWy-2 (Ni exchanged SWy-2)			
Al-SWy-2 (Al-exchanged SWy-2)			
Ca-SWy-2 (Ca-exchanged SWy-2)			
Test samples			
Hollington red: contains Illite , kaolinite			
B4 rock: Saponite, Talc, Actinolite Source: Trinity College Dublin			
Yorkstone rock: contains Illite, kaolinite Source: Schlumberger Cambridge Research			

It is necessary to understand that this is a feasibility study. The reader must note that all cation exchanged SWy-2 has been prepared by the procedure discussed in Chapter 5. The montmorillonite/saponite group has a greater number of samples than other groups. This is because this group of minerals is of most importance in oil well applications and is considered to demonstrate the greatest variability i.e. desorption temperature of DMF depends upon the interlayer cation present. Ideally the illite, kaolinite and chlorite groups should contain more samples, though this can be accommodated when deciding how many factors are sufficient to describe the variability within the data (see 'underfit' and 'overfit' Ch 2). However, a general rule states that the number of factors chosen to describe a particular group should never exceed the number of samples used to describe that group. When constructing a calibration model these points must be taken into consideration and the results described herein will therefore be interpreted with this in mind.

To inform the reader of the characteristic features which describe each group, it is necessary to show how the samples for each model are presented to the Windas programme. In this feasibility study, the RT-MS TIC (total ion current) and GP-FTIR (total infra-red) are chosen because they are representative of the summation of all the evolved gases detected, and therefore contain detection events (DMF, dehydroxylation) that will provide evidence for the presence of swelling and non-swelling minerals (i.e. kaolinite). Because this was a broad approach the method became more focused as it developed. In addition to the characteristic maxima observed in the DTG of untreated minerals, the following RT-MS TIC, RT-GP-FTIR TIR and TGA weight loss overlays highlight the detection features representative of these mineral groupings when exposed to DMF. It is clear that for expanding minerals, DMF detection dominates the TIC and for non-expanding minerals

dehydroxylation dominates. As the method developed it focused on particular m/z ions. Because this is a preliminary study, it is important to note that the MS is programmed to scan from 2-400 atomic mass units (amu). Therefore each scan (every 5 secs) counts the proportion of ions between 2-400 amu. Future work may include selective ion monitoring (e.g. $m/z = 18$ H_2O and/or $m/z = 73$ DMF parent ion) over a much smaller range. This makes the MS more sensitive to a particular ion as it spends less time scanning for other ions.

6.8 Results of RT-MS (TIC) for each clay mineral group (data overlays)

Figure 6.2 RT-MS TIC data overlays for montmorillonite-DMF complexes

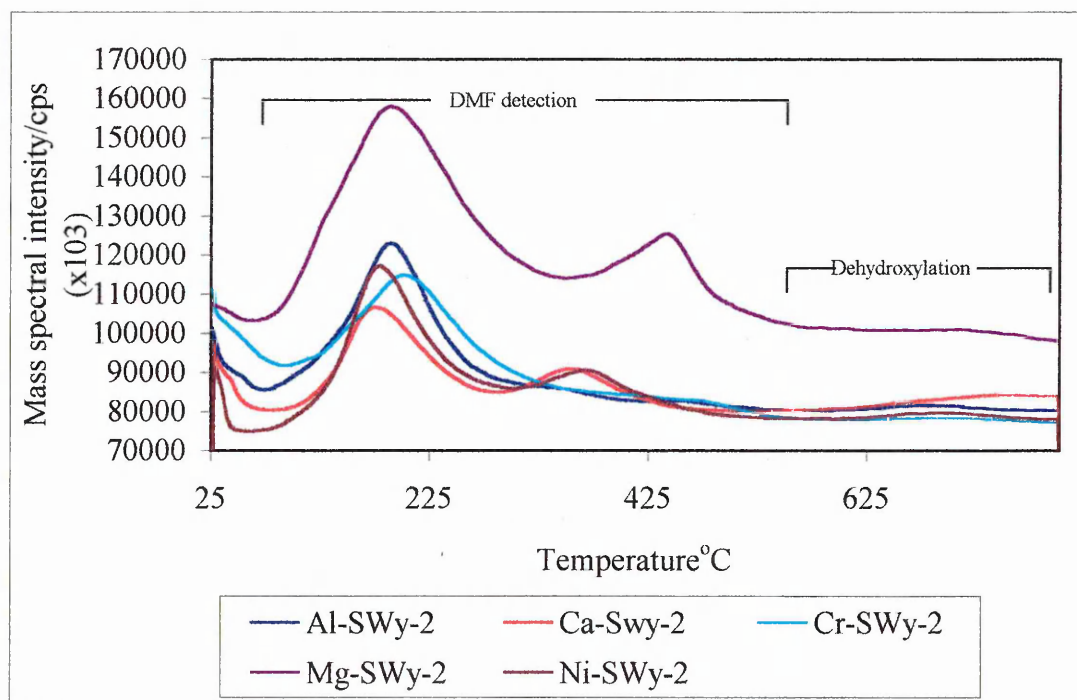


Table 6.6 Detection maxima for $m/z = 73$ (DMF) and $m/z = 18$ (dehydroxylation) from montmorillonite-DMF complexes

Sample	$m/z = 73$ (DMF) detection maxima (onset-maximum-end) $^{\circ}\text{C}$	$m/z = 18$ detection maxima (H_2O) $^{\circ}\text{C}$
Al-SWy-2	117-192-407	590-680-780
Ca-SWy-2	(1 st max) 114-185-286 (2 nd max) 308-363-451	570-745-800
Ni-SWy-2	130-178-317	540-700-800
Cr-SWy-2	116-211-460	612-700-800
Mg-SWy-2	(1 st max) 85-196-390 (2 nd max) 390-435-603	590-720-800

Fig 6.3 RT-MS TIC data overlays for montmorillonite/saponite-DMF complexes

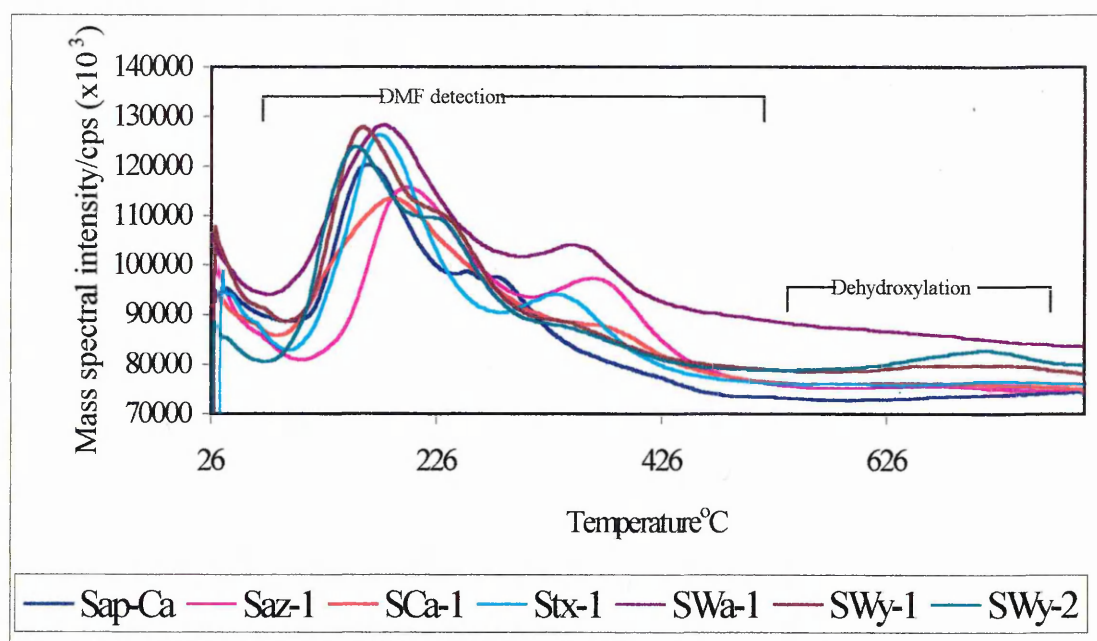


Table 6.7 Detection maxima for $m/z = 73$ (DMF) and $m/z = 18$ (dehydroxylation) from montmorillonite/saponite-DMF complexes

Sample	$m/z = 73$ (DMF) maxima (onset-maximum-end) $^{\circ}\text{C}$	$m/z = 18$ maxima (H_2O) $^{\circ}\text{C}$
Sap-Ca	1 st 108-173 2 nd 247-260 (very small) 3 rd 260-288	590-800 (no discernable maxima)
Saz-1	1 st 140-207-309 2 nd 332-260-460	565-683-800
SCa-1	1 st 102-200-345 2 nd 350 (shoulder)	595-714-800
STx-1	1 st 100-172-282 2 nd 282-330-514	570-720-800
SWa-1	1 st 110-188-313 2 nd 328-350-436 (small)	
SWy-1	1 st 103-161 2 nd 210-332 (shoulder) 3 rd 330-468	590-655 681-750-800
SWy-2	1 st 110-160 2 nd 210-407	560-720-800

Figure 6.4 RT-MS TIC data overlays for illite-DMF complexes

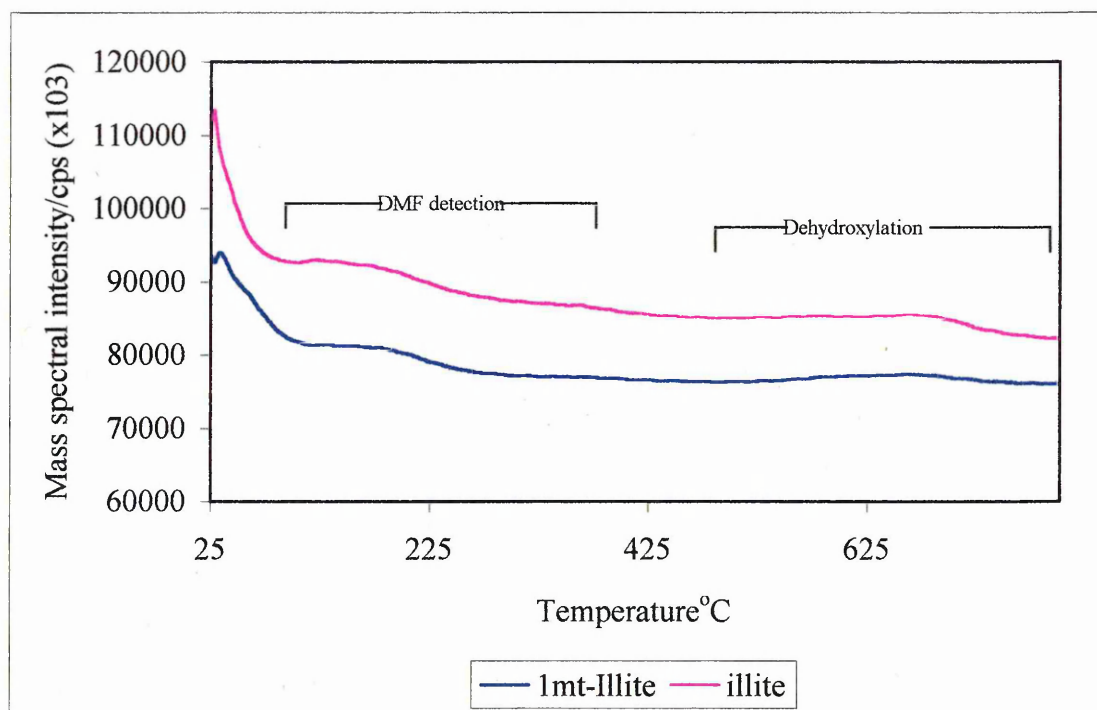


Table 6.5 Detection maxima for $m/z = 73$ (DMF) and $m/z = 18$ (dehydroxylation) for-illite-DMF complexes

Sample	$m/z = 73$ (DMF) detection maxima (onset-maximum-end) $^{\circ}\text{C}$	$m/z = 18$ detection maxima (H_2O) $^{\circ}\text{C}$
1-Mt-Illite	122-216-377	458-620-790 (broad)
Illite	114-214-320	280-615-800 (broad)

Fig 6.6 TIC data overlays for kaolinite-DMF complexes

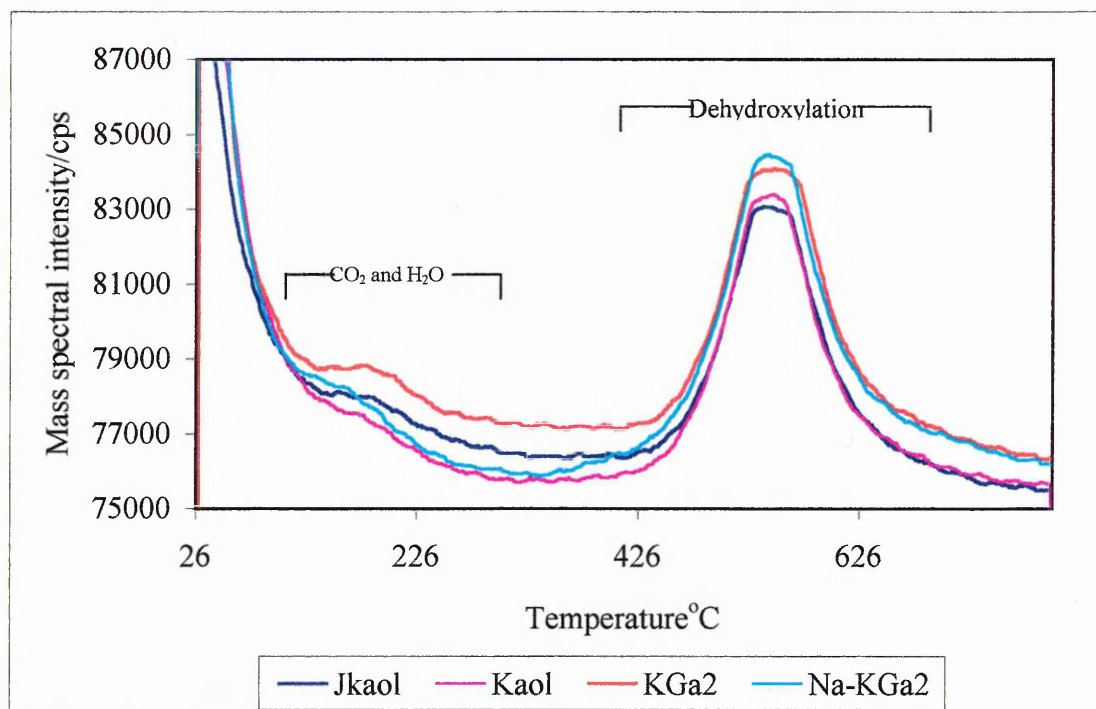


Table 6.8⁹ Detection maxima for $m/z = 73$ (DMF) and $m/z = 18$ (dehydroxylation) for-kaolinite-DMF complexes

Sample	$m/z = 73$ (DMF) maxima (onset-maximum-end)°C	$m/z = 18$ maxima (H ₂ O) °C
Jkaol	None*	403-560-790
Kaol	None*	373-553-800
KGa-2	None*	400-558-790
Na-KGa-2	None*	As above

Figure 6.7 RT-MS reconstructed ion chromatograms of ion $m/z = 73$ (DMF parent ion) for kaolinite-DMF complexes

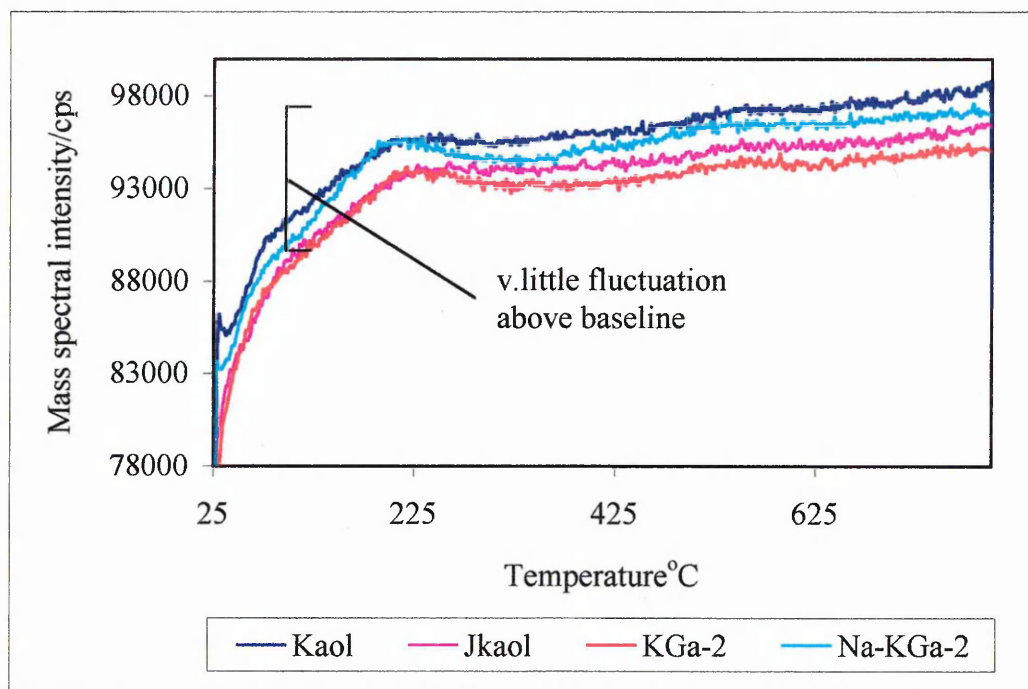


Figure 6.8 RT-MS reconstructed ion chromatograms of ion $m/z = 44$ for kaolinite-DMF complexes

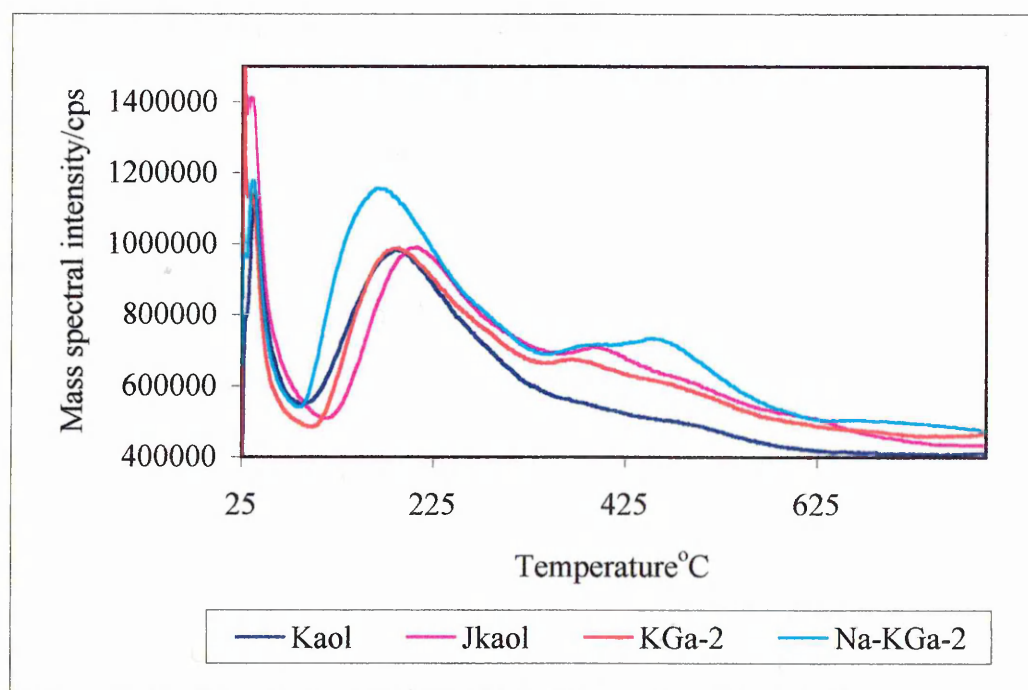


Figure 6.9 GP-FTIR reconstructed chromatogram of H₂O (3500-4000cm⁻¹) for kaolinite-DMF complexes

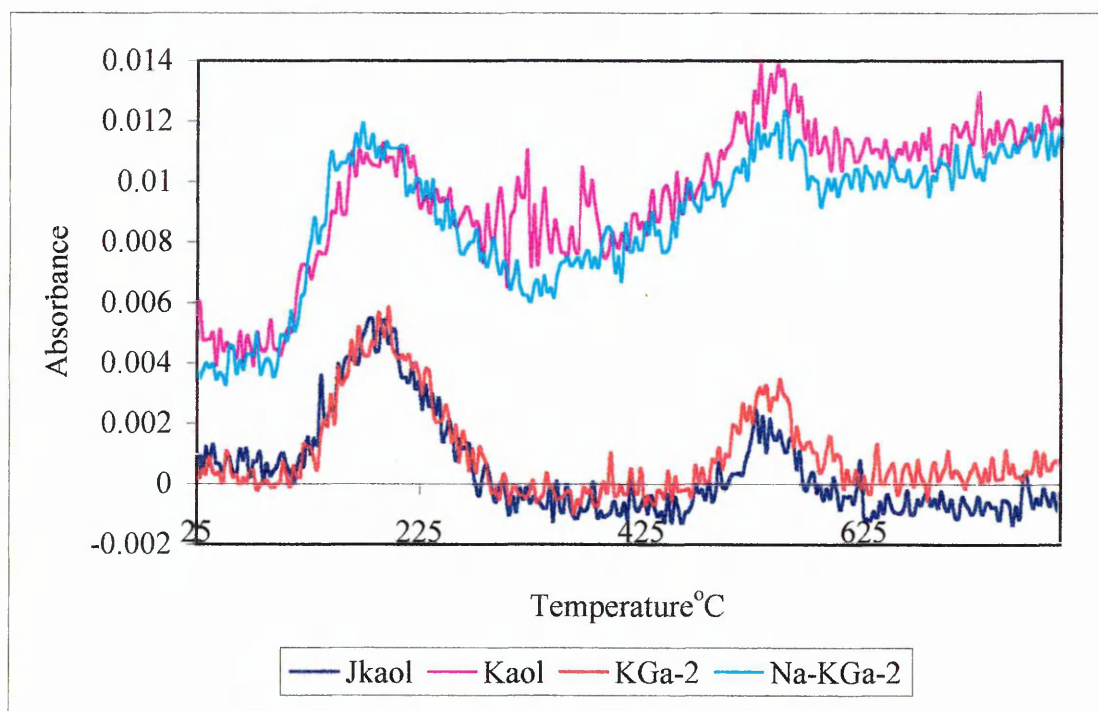


Fig 6.10 GP-FTIR reconstructed chromatogram of CO₂ (2200-2500cm⁻¹) for kaolinite-DMF complexes

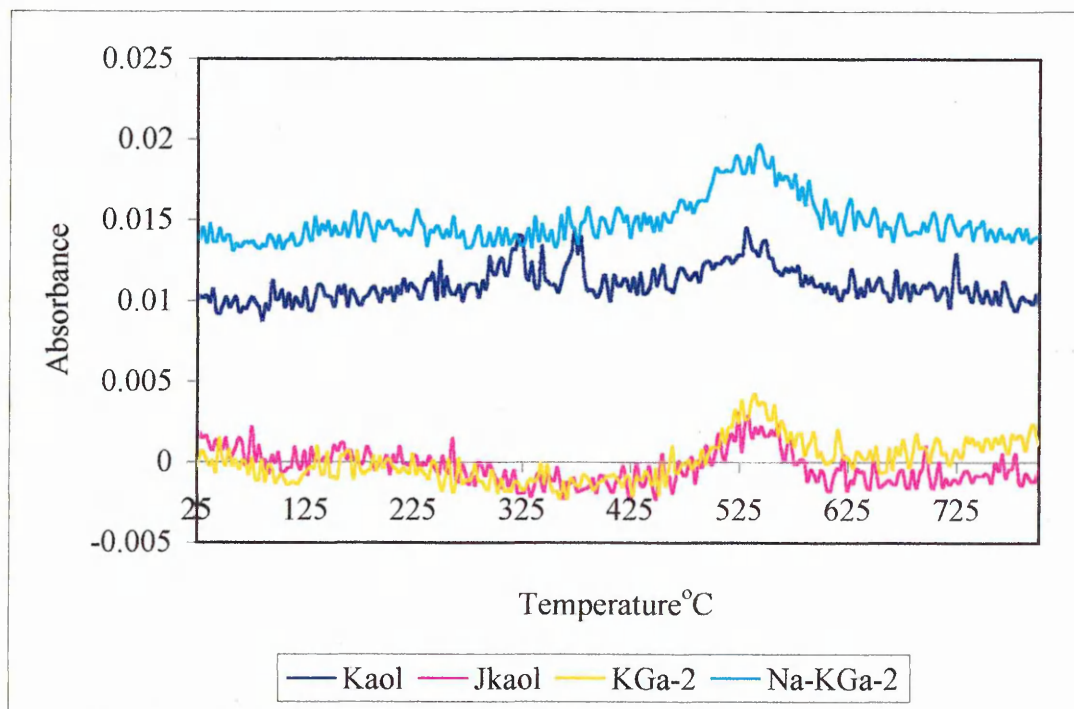


Figure 1: Comparison of the experimental results with the theoretical predictions for the first set of data.

Figure 1 (continued)

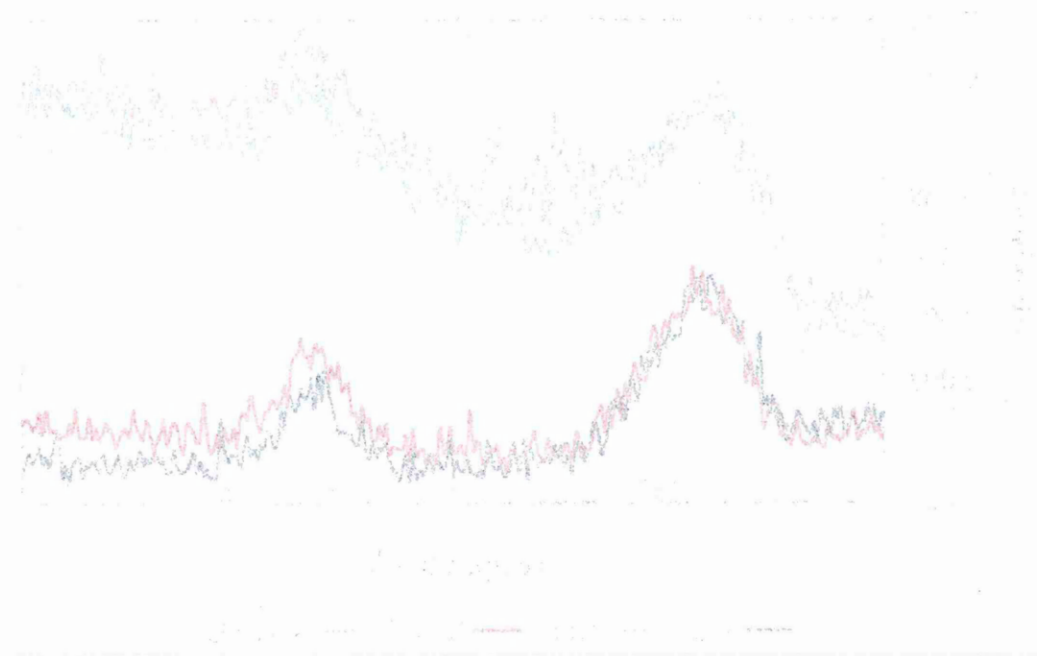
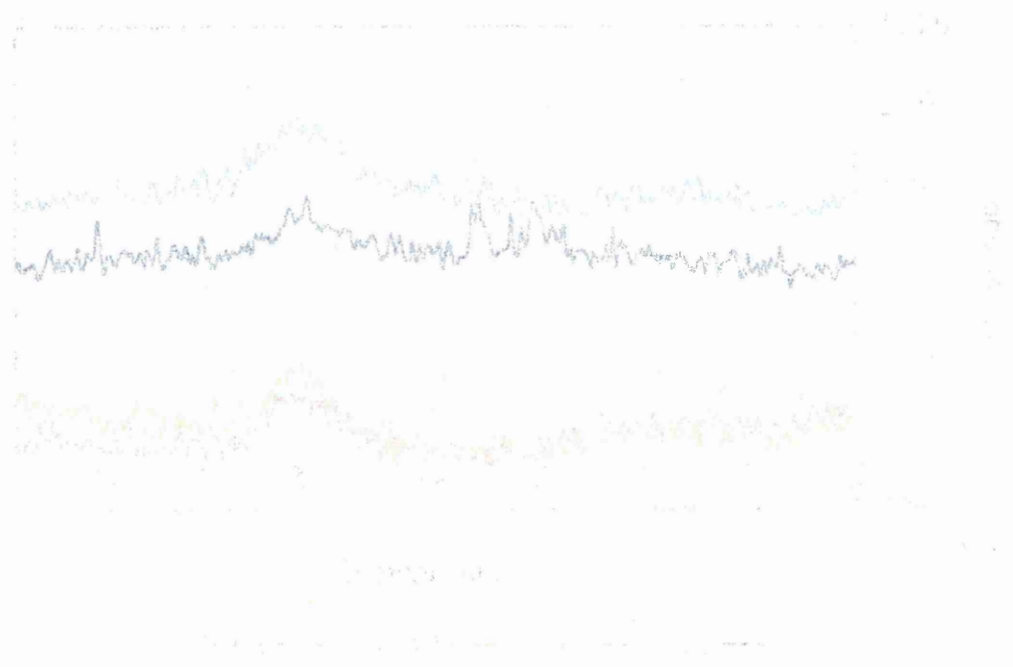


Figure 2: Comparison of the experimental results with the theoretical predictions for the second set of data.

Figure 2 (continued)



* GP-FTIR reconstructed absorbance chromatograms (figs. 6.9 and 6.10) confirm that the broad unresolved detection maxima in the overlaid TIC kaolinite samples (between 140-300°C) may be attributed to release of physisorbed water ($m/z = 18$ figure) and CO_2 on/in the powdered sample or trapped in the system. It is important to note that CO_2 and water are not quantitatively comparable as the extinction coefficient for CO_2 is greater than that of water. Whereas the TIC high temperature maxima between 300-800°C may be attributed to the thermal degradation of carbonates, CO_2 trapped in the structure and dehydroxylation (figs. 6.7 and 6.8). This assumption is based on the fact that neither the DMF parent ion nor associated fragment ions are detected throughout the kaolinite experiments. There is also evidence in the DRIFTS spectra of the untreated kaolinites for the presence of carbonates, indicated by shoulders at $878 \text{ cm}^{-1} \approx$ and weak bands at 1420 cm^{-1} (fig. 6.11). The band at 714 cm^{-1} was hard to identify due to overlap with clay structural bands

Figure 6.11 Room temperature DRIFTS spectra of untreated Kaolinites

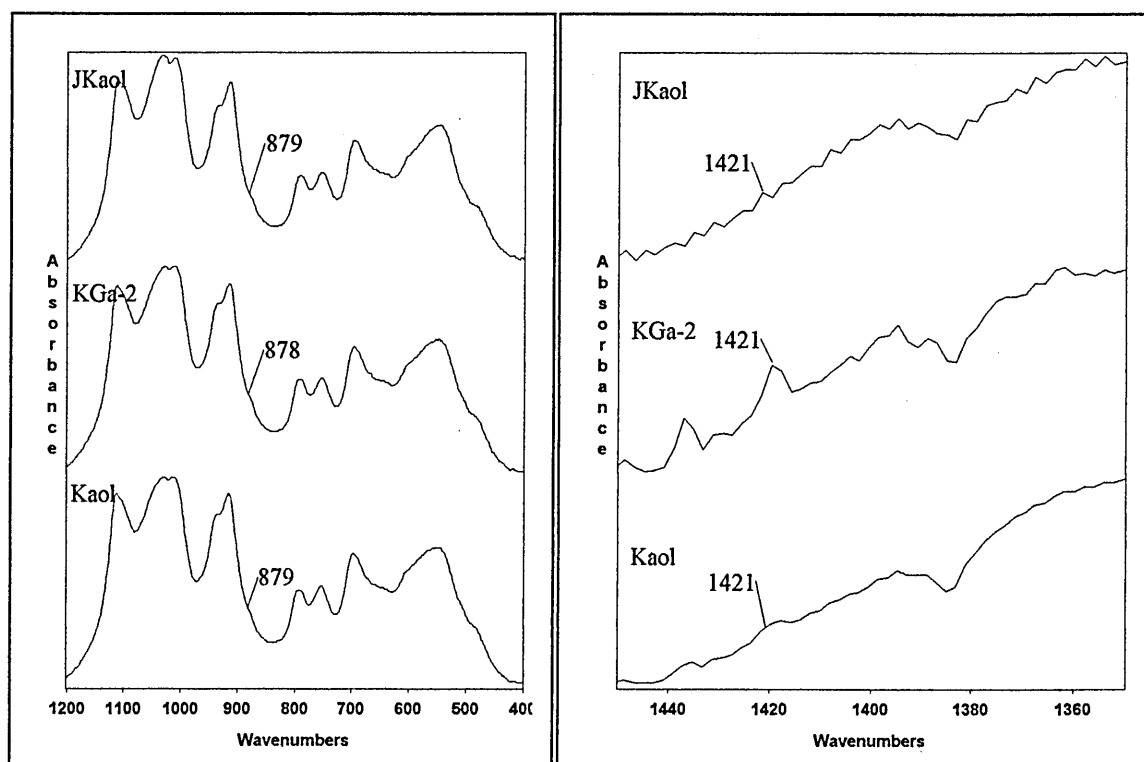


Figure 6.12 RT-MS TIC data overlays for chlorite-DMF complexes

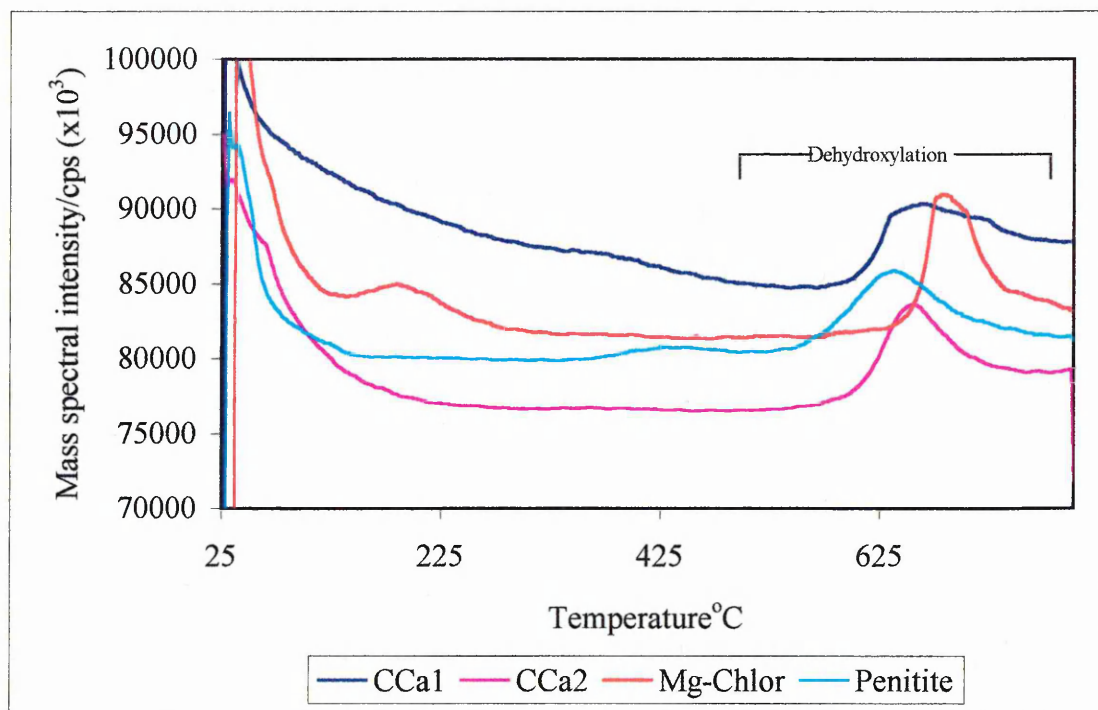


Figure 6.13 RT-MS TIC data overlays for Rock-DMF complexes

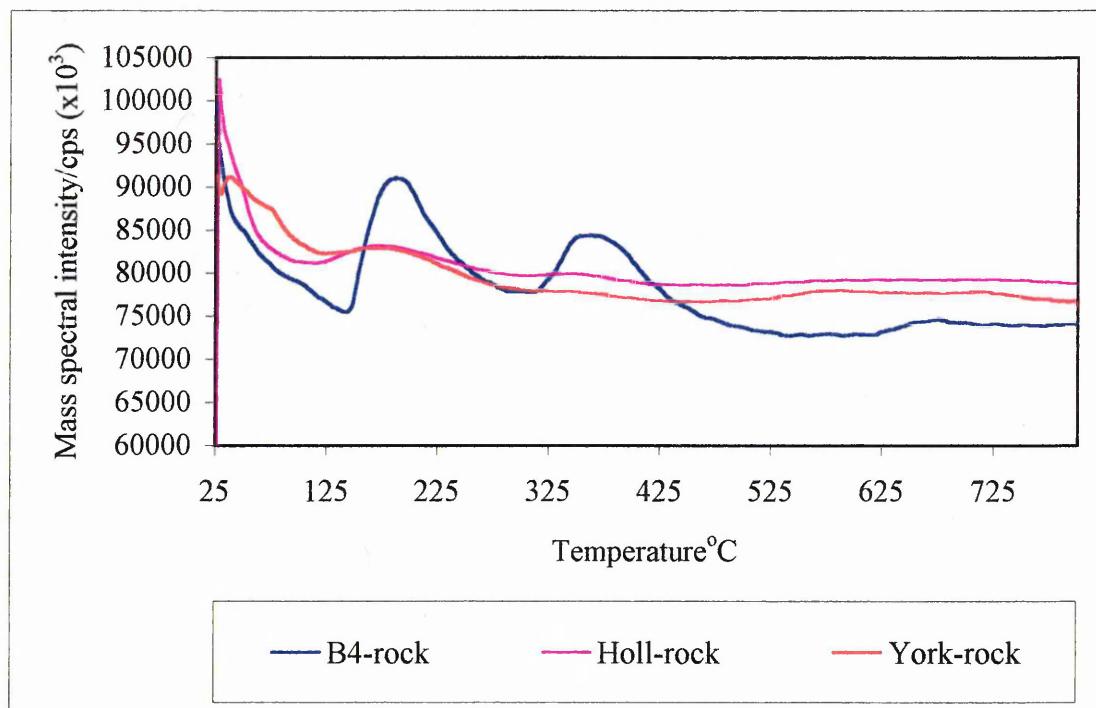


Figure 6.14 RT-MS TIC data overlays for < 2um rock fractions-DMF complexes

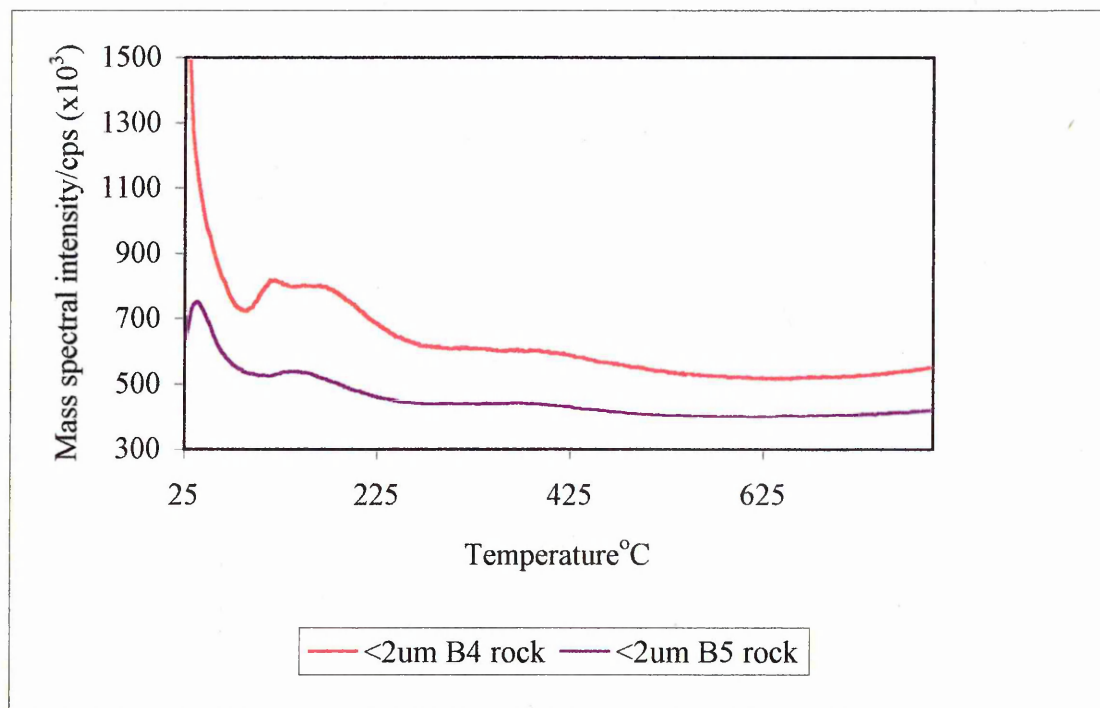


Figure 6.15 GP-FTIR TIR data overlays for montmorillonite/saponite-DMF complexes

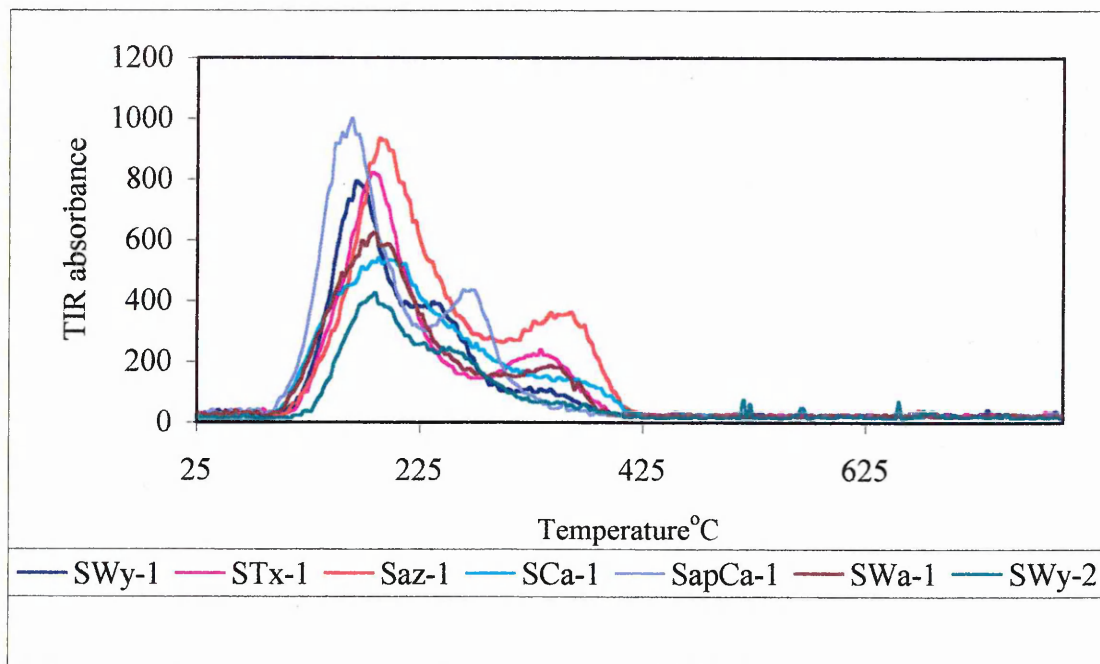


Figure 6.16 GP-FTIR TIR data overlays for montmorillonite-DMF complexes

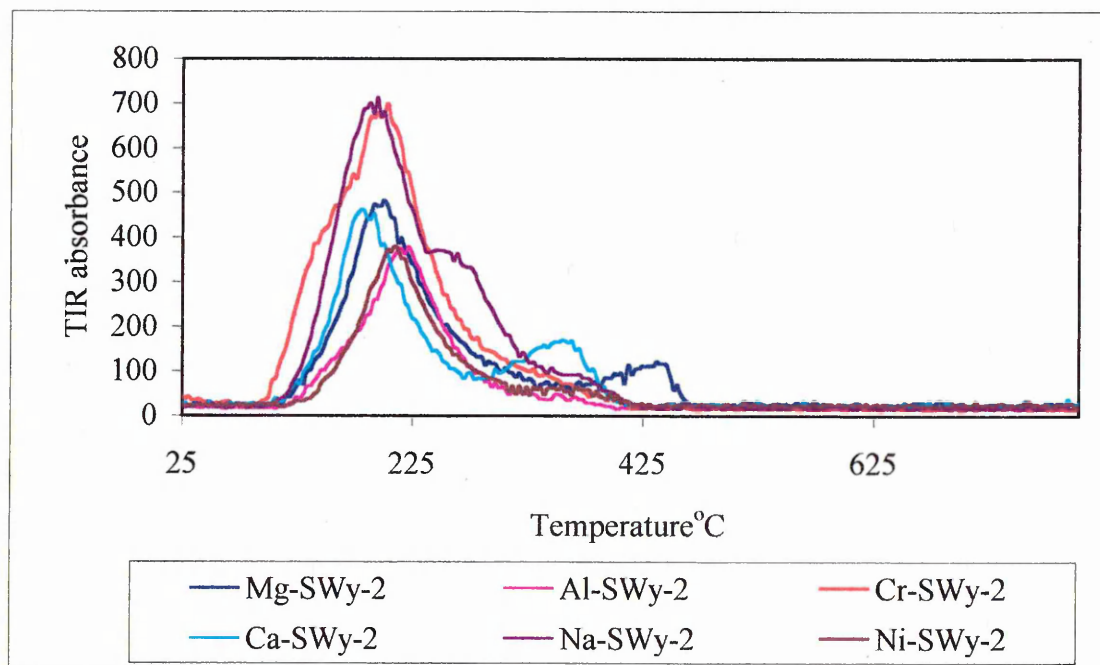


Figure 6.17 GP-FTIR TIR data overlays for kaolinite-DMF complexes

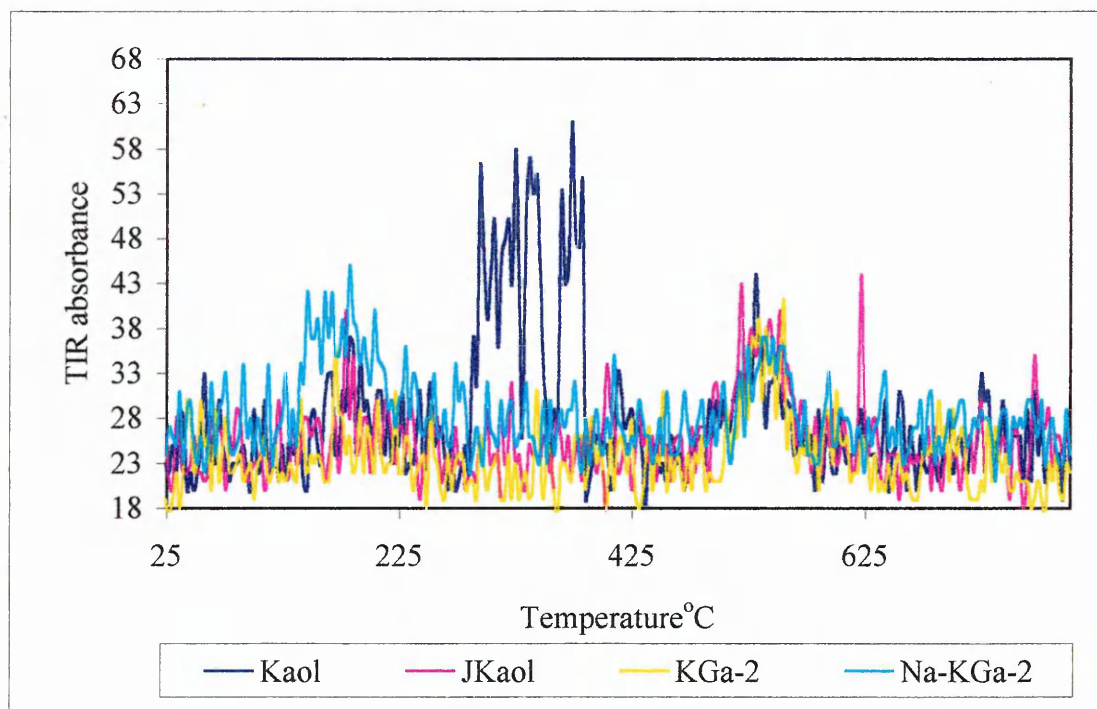
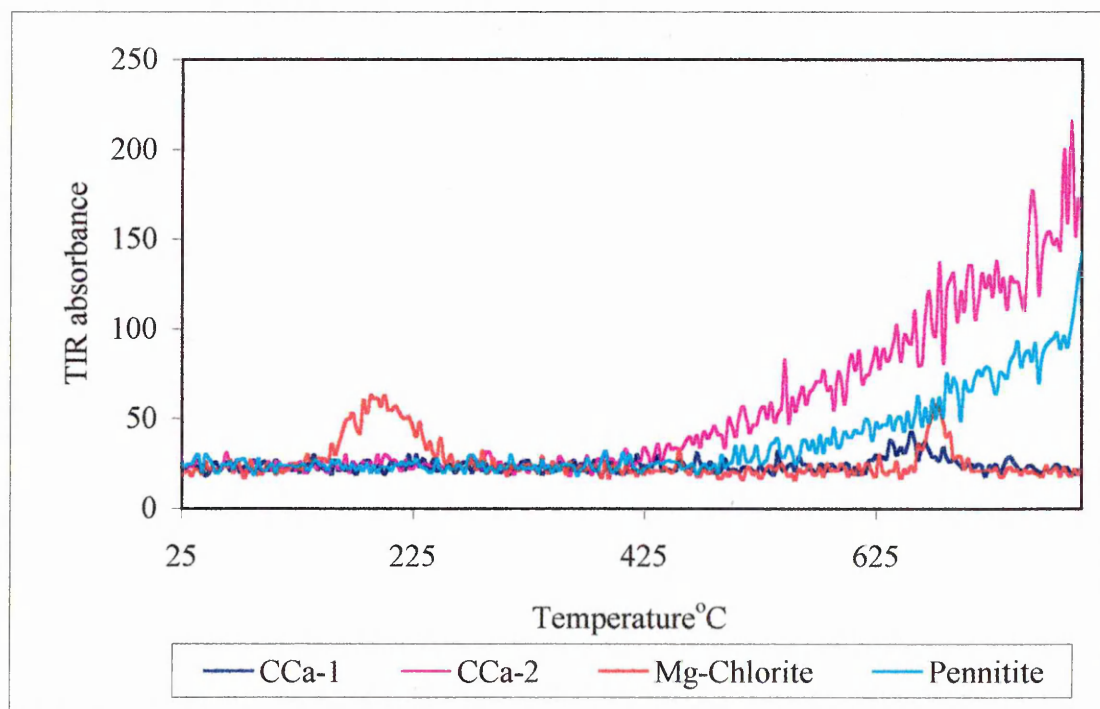


Figure 6.18 GP-FTIR TIR data overlays for chlorite-DMF complexes



*Illite is not included as its detection maximum is in the same region as montmorillonite.

Handwritten header text, possibly a title or date, located at the top of the page.



Handwritten text block located in the middle section of the page.



Handwritten text block located at the bottom of the page.

Handwritten text at the bottom right corner of the page.

Figure 6.19 TGA weight loss data overlays for montmorillonite-DMF complexes

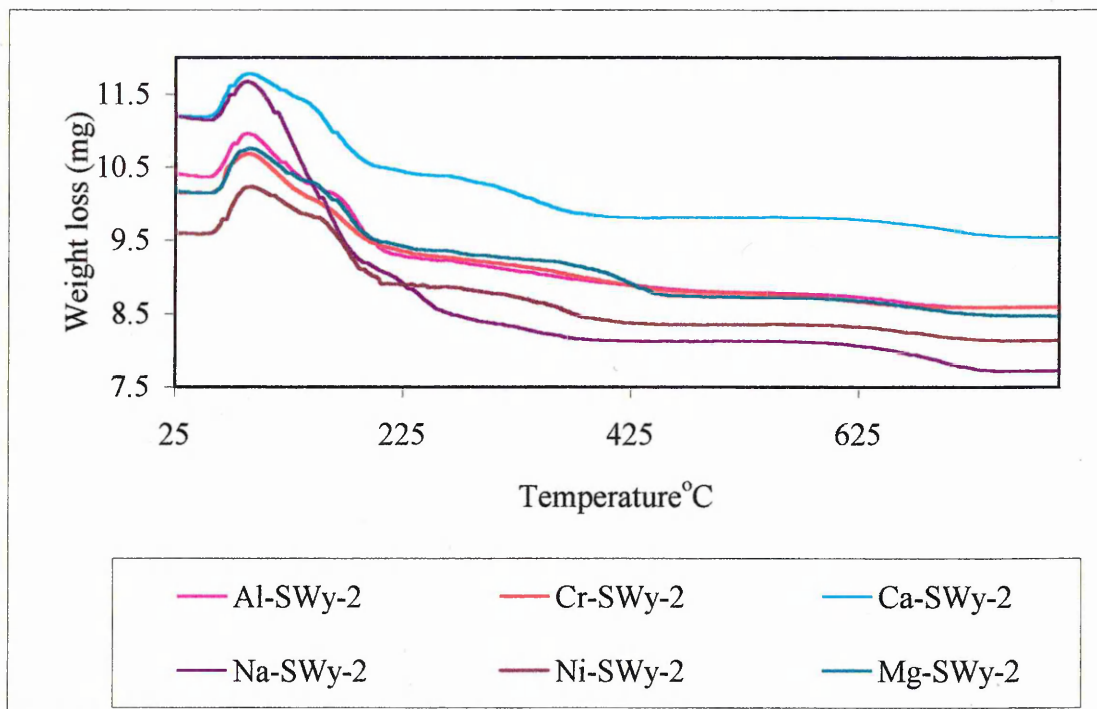


Figure 6.20 TGA weight loss data overlays for montmorillonite/saponite-DMF complexes

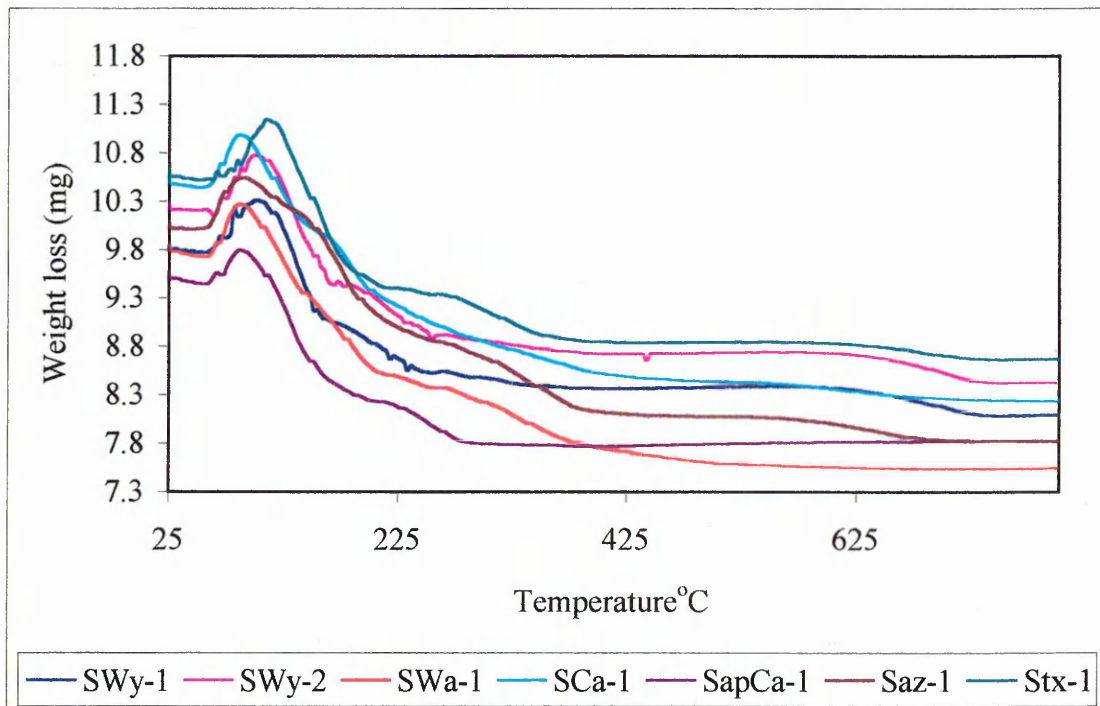


Figure 6.21 TGA weight loss data overlays for Kaolinite-DMF complexes

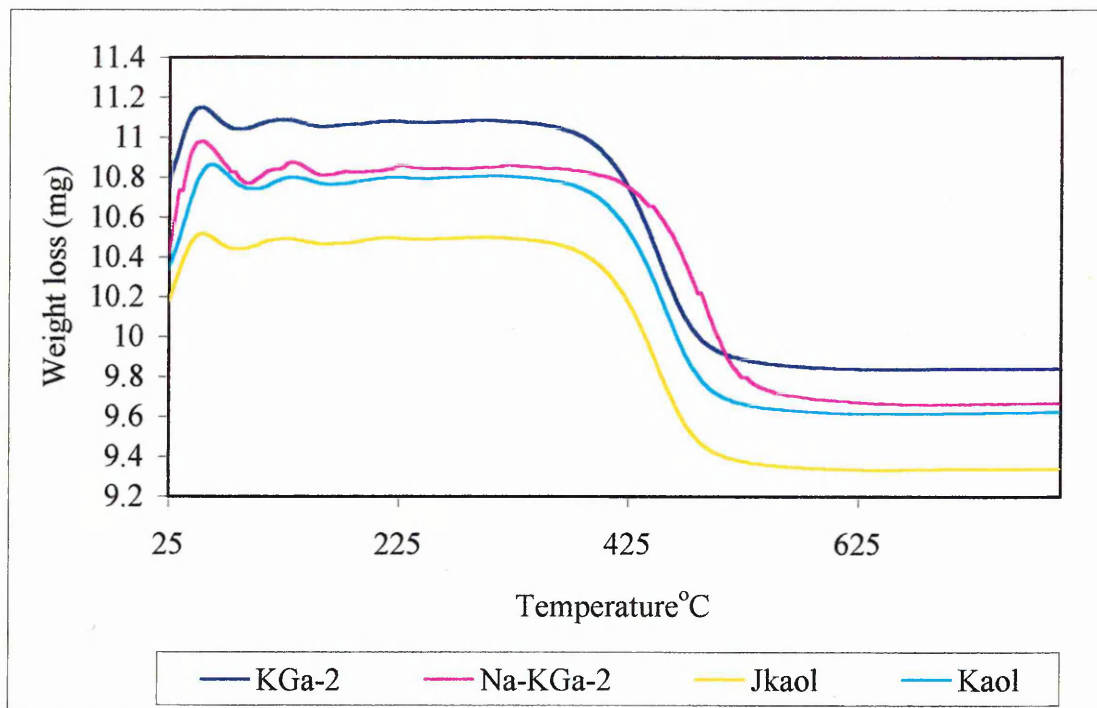
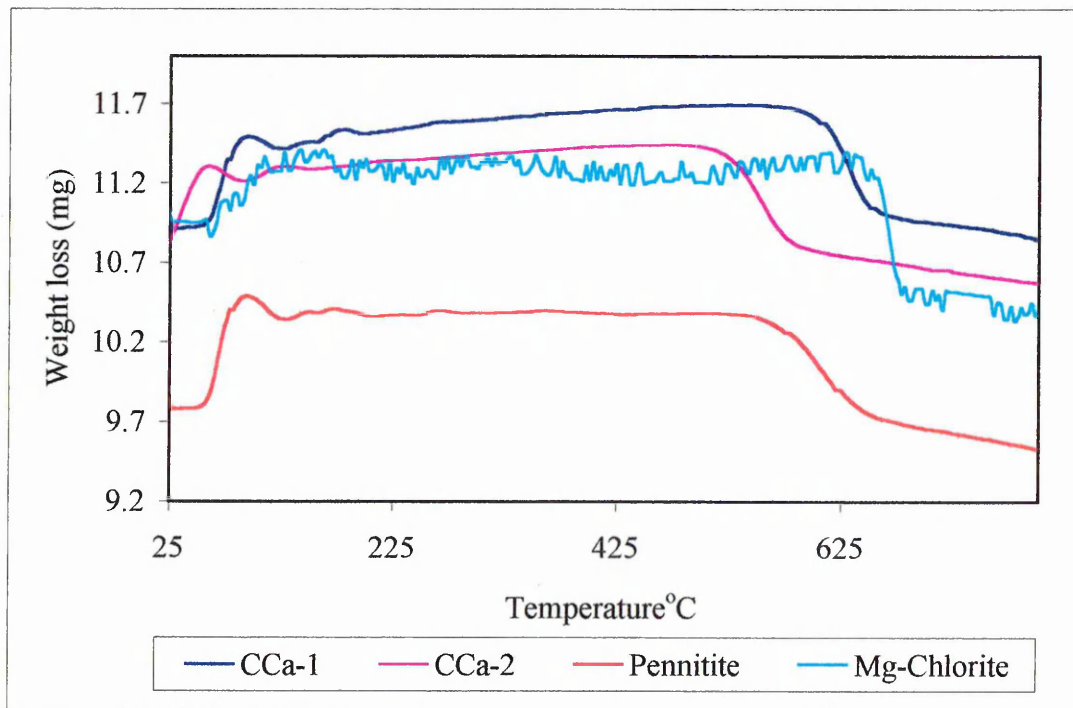


Figure 6.22 TGA weight loss data overlays for chlorite-DMF complexes



6.9 Results model ① data compression/discriminant rules

Model① (a) and (b) were applied to the whole TGA weight loss profiles as shown in figures (6.19-6.22). The clay mineral training groups are shown in table 6.9. All experiments used the same training and test groups for comparative purposes.

Table 6.9 TGA Model ① training and test groups samples

Group1	Group 2	Group 3	Group 4	Test group
Illite	Smectites/Saponite	Kaolinites	Chlorites	
Illite	Al-SWy-2	KGa-2	CCa-1	Yorkstone
1-Mt-Illite	Ca-SWy-2	Na-KGa-2	CCa-2	Hollington
	Cr-SWy-2	JKaol	MgChlor	B4 rock
	Mg-SWy-2			Kaol
	Ni-SWy-2			SWy-2
	Na-SWy-2			
	SAPCa-1			
	SAz-1			
	SCa-1			
	STx-1			
	SWa-1			

The data was presented to the Windas software as shown in the data overlays. The data was pre-processed by normalisation. This was achieved within the Windas

software and was necessary to correct for small non-linearities in the responses of the data to the constituent sample size. This worked well as the range of sample sizes was small, early studies using this technique yielded more precise group discrimination (not shown). Three data compression methods were then applied for comparison purposes. These compression methods arise from the way in which the matrix axes are rotated. In PCA, the rotation is made such that the first loading produced scores with the maximum possible spread or variability. The second loading is that producing the next possible largest variance and so on. Therefore PCA rearranged the data set, and in so doing ordered the scores in terms of decreasing variance (importance). Large variance may be commensurate with large information content, but this does not necessarily mean that the information is relevant or useful i.e. noise. On the other hand PLS is usually utilised as a calibration method, where there is a second matrix containing data pertaining to concentrations of the individual constituents. The aim as will be seen in the section on quantitative analysis, is to find a series of coefficients which relate the concentration and spectroscopic data by multiple linear regression (MLR) onto the PLS scores. In Win-das, PLS is not used for calibration, but solely for data compression and more specifically when data sets are believed to be structured in groups. This is known as discriminant PLS [369]. In order to classify individual observations to its nearest group some rule must be used. To decide on the similarity of samples the distance measures commonly applied in pattern recognition are used. The shorter the distance between samples the more similar they are. Ideally close knit group clusters are formed when there are sufficient samples to describe a group. The choice of metric rule can have quite an effect on the performance of the discriminant model. Three rules were used for comparative purposes:

(a) Euclidean distances

This is the simplest and most intuitive to understand. These distances are measured in the same way we measure distances in the real world. In all cases the axes have the same scale and the distances are measured by simple trigonometry.

(b) Manhattan City Block

This computes the sum of the absolute values of the differences.

(c) Mahalanobis distance

Essentially, the Mahalanobis distance is equal to the Euclidean distance with the additional factor taken into consideration being correlation or covariance of group members. In effect it considers the direction of the axis going through the group.

Out of a total of 20 samples the following results show how each metric performs as additional scores are calculated. The fractions noted, relate to the proportion of samples correctly allocated to each of the four groups seen in table 6.10. The chosen model(s) were then applied to test samples to evaluate their predictive properties.

Results Model① TGA (weight loss curve)

Table 6.10 Model① data compression/discriminant analysis results

Compression method	Metric:score 1	Metric: score 2	Metric: score 3
PCA (correlation)	Euc: 18/20	Euc: 20/20	Euc: 20/20
	Man:18/20	Man: 20/20	Man: 20/20
	Meh:18/20	Meh: 20/20	Meh: 20/20
PCA (covariance)	Euc: 19/20	Euc: 18/20	Euc: 18/20
	Man:19/20	Man:19/20	Man:18/20
	Meh:19/20	Meh:19/20	Meh:18/20
PLS (variance scaled)	Euc: 19/20	Euc: 20/20	Euc: 20/20
	Man:19/20	Man: 20/20	Man: 20/20
	Meh:19/20	Meh: 20/20	Meh: 20/20

Where Euc: = Euclidian distance metric

Man: =Manhattan block distance metric

Meh: =Mehalonobis distance metric

The data compression metric rules shown in table suggest that the PCA correlation method or the PLS method could be used to model the data using two scores with any of the three metric rules. The PCA covariance method was unable to fully allocate the samples to their appropriate groups and gave inconsistent results when the number of PCA scores used was increased. Model①(a) PCA (correlation) and Model①(b) PLS were examined in turn using 2 and 3 scores.

The score plots shown depict the linear projection of objects representing the main part of the total variance of the data. Because a large fraction of variance can be described by means of one, two or three PCA scores, the data can be visualised by

plotting the PCAs against each other. The Scree test is based on the observation that residual variance levels off when the correct number of principal components is obtained. The component number is then derived from the levelling-off of this dependence. In Figure 6.23 the slope can be seen to drop off between 3 and 4 components suggesting this is the optimum number of components to use.

Figure 6.23 TGA Model[ⓐ](a) PCA Scree test of percentage variance versus PCA score

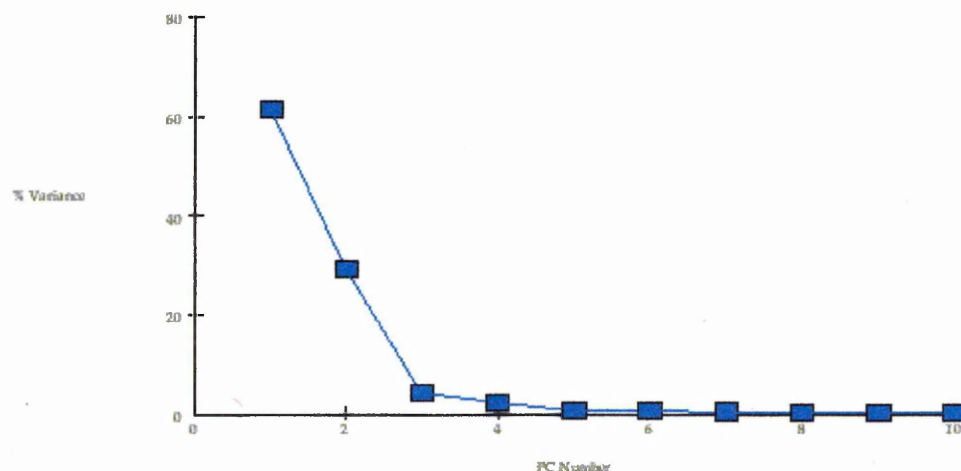
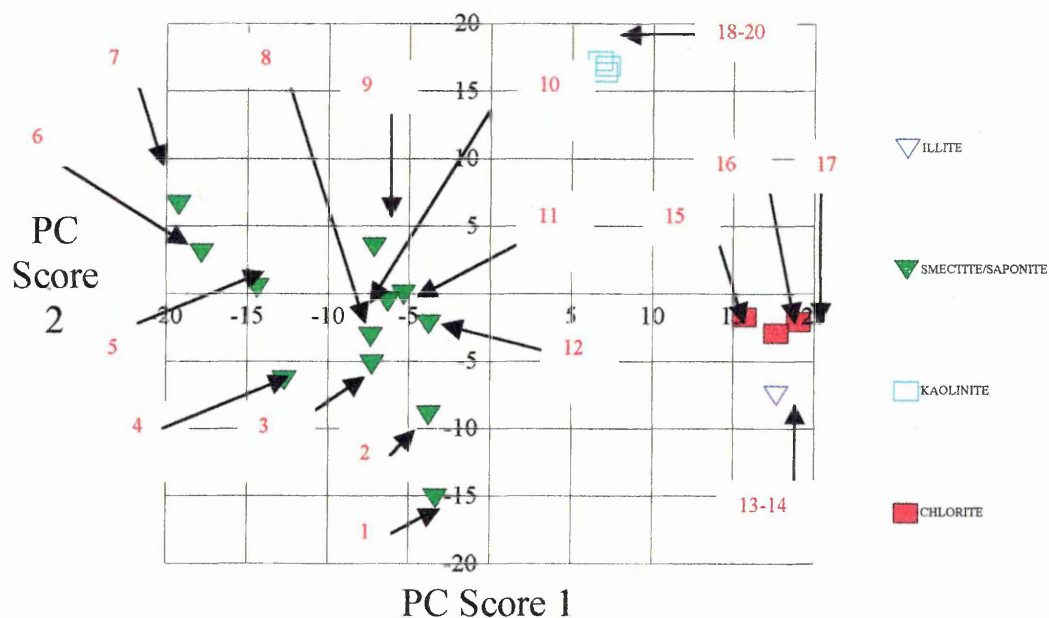


Table 6.11 TGA Model[ⓐ](a) PCA score variance table

PCA Score	Variance	% Variance	Cumulative variance
1	1.5871E+02	61.52	61.52
2	7.5810E+01	29.38	90.90
3	1.0806E+01	4.19	95.09
4	5.8410E+00	2.26	97.35
5	2.0070E+00	0.78	98.13
6	1.5477E+00	0.60	98.73
7	9.7290E-01	0.38	99.11
8	6.9921E-01	0.27	99.38
9	6.0009E-01	0.23	99.61
10	3.5632E-01	0.14	99.75

Figure 6.24 PC score plot for TGA Model[ⓐ] PCA (correlation) using score 1 against score 2 (mehalanobis distance metric)



Individual group samples in the PC score plot are identified by red numbers, which correspond to the numbered samples in the table below. The test group samples are also coloured red and identified as T1-T5 (table 6.12).

Table 6.12 PC score plot key for TGA Model[ⓐ] training set

Group 1 Illite	Group 2 Smectites	Group 3 Kaolinites	Group 4 Chlorites	Test group
Illite 13	Al-SWy-2 8	KGa-2 18	CCa-1 16	Yorkstone T1
1-Mt-Illite 14	Ca-SWy-2 12	Na-KGa-2 19	CCa-2 17	Hollington T2
	Cr-SWy-2 11	Jkaol 20	MgChlor 15	B4 rock T3
	Mg-SWy-2 9			Kaol T4
	Ni-SWy-2 10			SWy-2 T5
	Na-SWy-2 4			
	SAPCa-1 1			
	SAz-1 7			
	SCa-1 5			
	STx-1 3			
	SWa-1 6			
	SWy-1 2			

Each of the 20 observations has been allocated to a group on the basis of the following mehalanobis metric distance shown in table 6.13.

Table 6.13 TGA Model[ⓐ](a) training group predictions using 2 PCA scores

Observation	Distance From group 1 (Illite)	Distance From group 2 (Smectite)	Distance From group 3 (Kaolinite)	Distance From group 4 (Chlorite)	Group allocation	Correct or incorrect
1-Mt illite	0.00E+00	4.31E+01	2.52E+01	1.76E+00	1	Correct
Illite	0.00E+00	4.31E+01	2.52E+01	1.76E+00	1	Correct
Al-SWy-2	3.87E+01	1.34E-01	6.71E+01	4.82E+01	2	Correct
Ca-SWy-2	2.64E+01	2.13E+00	5.08E+01	3.38E+01	2	Correct
Cr-SWy-2	2.83E+01	2.13E+00	4.84E+01	3.48E+01	2	Correct
Mg-SWy-2	3.03E+01	3.45E+00	4.34E+01	3.53E+01	2	Correct
Na-SWy-2	6.60E+01	3.34E+00	1.05E+02	8.01E+01	2	Correct
Ni-SWy-2	3.18E+01	1.18E+00	5.36E+01	3.91E+01	2	Correct
SAp-Ca	5.09E+01	6.88E+00	1.05E+02	6.69E+01	2	Correct
SAz-1	6.97E+01	5.12E+00	8.19E+01	7.77E+01	2	Correct
SCa-1	5.89E+01	1.35E+00	8.26E+01	6.89E+01	2	Correct
STx-1	4.20E+01	3.41E-01	7.51E+01	5.30E+01	2	Correct
SWa-1	6.90E+01	3.56E+00	8.87E+01	7.88E+01	2	Correct
SWy-1	3.73E+01	1.94E+00	7.71E+01	4.92E+01	2	Correct
Jkaol	2.53E+01	7.15E+01	3.91E-03	1.49E+01	3	Correct
KGa-2	2.60E+01	7.10E+01	6.59E-03	1.55E+01	3	Correct
Na-KGa-2	2.43E+01	6.91E+01	9.92E-03	1.42E+01	3	Correct
CCa-1	2.78E+00	5.97E+01	1.47E+01	2.12E-01	4	Correct
CCa-2	1.40E+00	5.20E+01	1.60E+01	2.26E-02	4	Correct
MgChlor	1.52E+00	4.72E+01	1.44E+01	1.71E-01	4	Correct

The first three loading plots shown in figures 6.25-6.27 provides the projection of the profile features onto the principal components (scores). The information from this plot shows how the feature variables are correlated with the scores (fig.6.23-6.24). PC loadings represent factors that can be used to reconstruct the mean-centered data set. Looking at PCA loadings 1 and 3, this can be interpreted largely as the presence water of dehydroxylation, whereas the loading 2 is primarily related to DMF desorption. In combination, these three loadings are responsible for over 95% of the variability in the mean-centered data set, which is consistent with what we might expect from the nature of the samples.

Figure 6.25 TGA model (a) PCA correlation method-loading 1

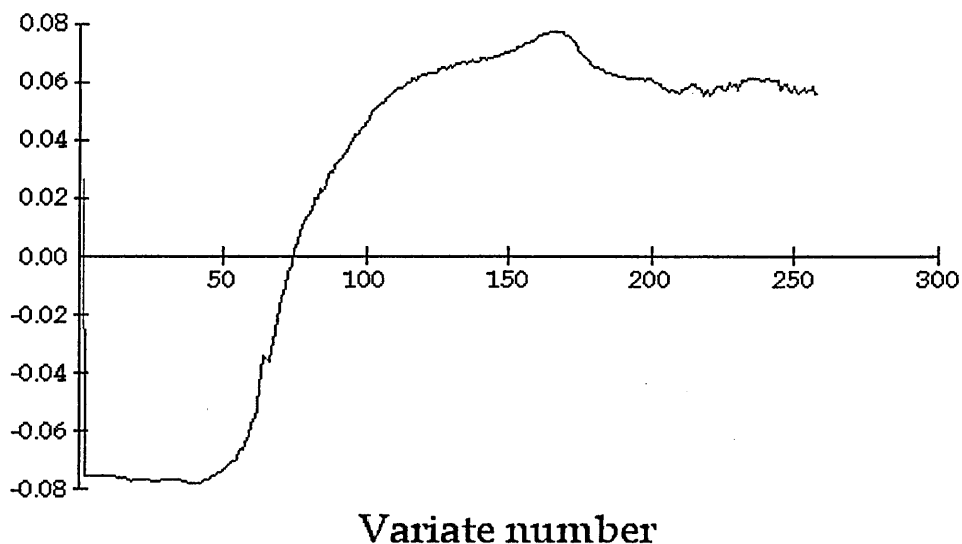


Figure 6.26 TGA modelⓐ)PCA correlation method-loading 2

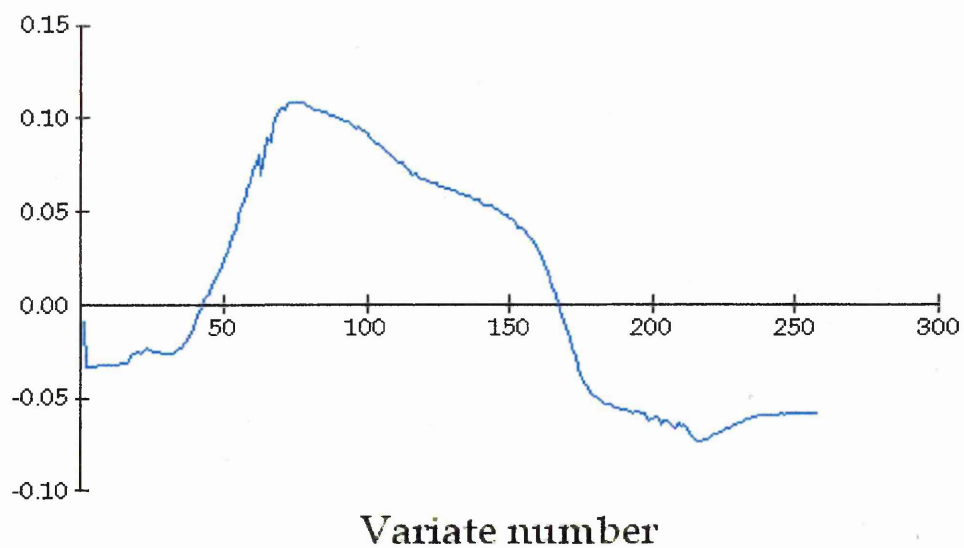


Figure 6.27 TGA modelⓐ)PCA correlation method-loading 3

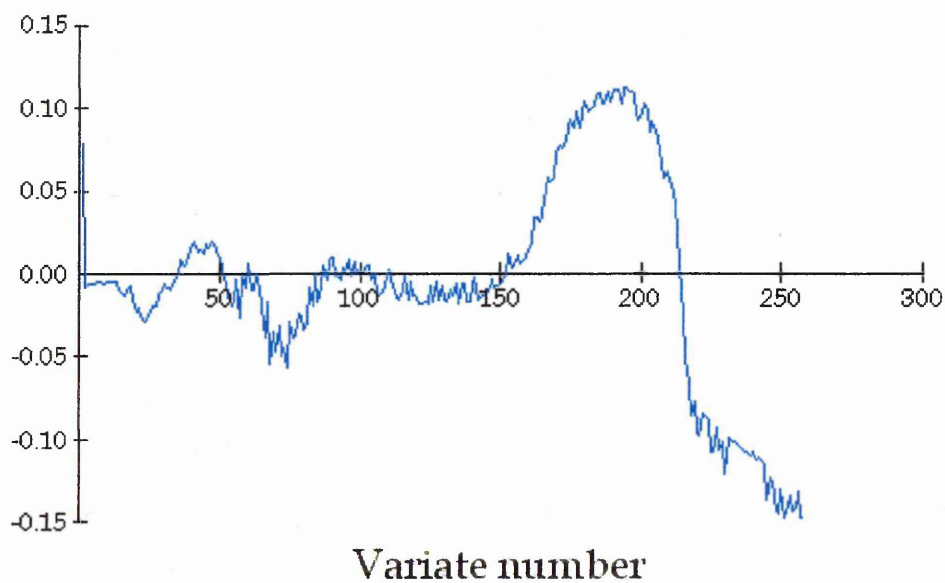


Table 6.14 TGA model[ⓐ] test group predictions using 2 PCA scores

Test Observation	Distance	Distance	Distance	Distance	Actual group	Predicted group
	From group 1 (Illite)	From group 2 (Smectite)	From group 3 (Kaolinite)	From group 4 (Chlorite)		
T1-Yorkstone	1.68E+00	5.13E+01	4.13E+01	5.24E+01	1 + 3	1
T2-Hollington (red rock)	2.61E+00	5.44E+01	4.43E+01	5.68E+01	1 + 3	1
T3-B4 (rock)	4.26E+00	5.76E+01	4.95E+01	6.29E+01	2	1
T4-Kaol (powder)	2.74E+01	7.12E+01	3.82E-01	4.64E+01	3	3
T5-SWy-2 (powder)	4.93E+01	3.63E+00	9.31E+01	5.71E+01	2	2

6.11 Summary TGA model[ⓐ] using 2 scores (mehalanobis distance metric)

The scree variance plot has shown that 90.90 % of the variance is contained in the first two PCA scores and loading 1 and loading 2 (figs.6.25-6.26) have successfully identified DMF desorption and dehydroxylation as the two main descriptive components contained within the weight loss profile. The PC training plot (fig.6.24) shows a large spread in the smectite/saponite group but predictable clustering due to Mⁿ⁺-exchanged SWy-2. This also shows that the illite and chlorite group seem to be very close together which may be due their overlapping dehydroxylation regions. This also implies that in the TG weight loss curve the small amount of DMF loss associated with illite may not be adequately described with two PCA scores. However, the training group distance scores show that all samples are well separated.

The test group has shown that the pure powder samples of SWy-2 and kaolinite were correctly predicted. Application of Model①(a) to the rock samples showed correct prediction for the presence of illite content in samples T1 and T2. However in both cases, the kaolinite content was inferred by the being the next closest group. T3 was predicted as being part of group 1 illite in contrast to its allocation within group 2 (smectite/saponite). However, it must be remembered that unlike quantitative analysis, the training sets herein only contain pure samples being incapable of supporting the evaluation of mixed mineral standards and therefore the models are trained to identify a test sample on the basis that it is closest to one particular training group. This implies that the distances to other groups other than the allocated group only suggest that these other minerals may be present or that there is little to distinguish group membership between the nearest groups. This may be due to concentration factor or overlapping detection events.

Table 6.15 TGA model[ⓐ](a) training group predictions using 3 PCA scores

Observation	Distance From group 1 (Illite)	Distance From group 2 (Smectite)	Distance From group 3 (Kaolinite)	Distance From group 4 (Chlorite)	Group allocation	Correct or incorrect
1-Mt-Illite	0.00E+00	4.65E+01	2.52E+01	2.98E+01	1	Correct
Illite	0.00E+00	4.65E+01	2.52E+01	2.98E+01	1	Correct
Al-SWy-2	4.28E+01	1.69E-01	7.12E+01	5.89E+01	2	Correct
Ca-SWy-2	2.96E+01	2.13E+00	5.40E+01	4.61E+01	2	Correct
Cr-SWy-2	3.07E+01	2.22E+00	5.08E+01	4.89E+01	2	Correct
Mg-SWy-2	3.43E+01	3.48E+00	4.74E+01	4.62E+01	2	Correct
Na-SWy-2	7.79E+01	5.93E+00	1.17E+02	8.35E+01	2	Correct
Ni-SWy-2	3.57E+01	1.21E+00	5.76E+01	5.00E+01	2	Correct
SapCa-1	5.09E+01	9.90E+00	1.05E+02	9.38E+01	2	Correct
SAz-1	7.42E+01	5.20E+00	8.65E+01	8.77E+01	2	Correct
SCa-1	6.12E+01	1.45E+00	8.50E+01	8.32E+01	2	Correct
STx-1	4.53E+01	3.42E-01	7.84E+01	6.51E+01	2	Correct
SWa-1	6.91E+01	6.04E+00	8.87E+01	1.04E+02	2	Correct
SWy-1	4.92E+01	4.53E+00	8.90E+01	5.27E+01	2	Correct
Jkaol	2.53E+01	7.49E+01	3.98E-03	4.31E+01	3	Correct
KGa-2	2.60E+01	7.43E+01	9.66E-03	4.31E+01	3	Correct
Na-KGa-2	2.43E+01	7.27E+01	1.22E-02	4.29E+01	3	Correct
CCa-1	2.11E+01	6.57E+01	3.30E+01	1.25E+00	4	Correct
CCa-2	2.16E+01	5.91E+01	3.63E+01	6.59E-01	4	Correct
Mg-Chlor	5.21E+01	7.50E+01	6.51E+01	3.47E+00	4	Correct

Model[ⓐ](a) (PCA-correlation method-mehalanobis distance metric-3 PCA scores)

was chosen and applied to the data test set. The results of these predictions are shown in table 6.16.

Table 6.16 TGA modelⓐ) 3 PCA scores applied to test samples

Test Observation	Distance From group 1 (Illite)	Distance From group 2 (Smectite)	Distance From group 3 (Kaolinite)	Distance From group 4 (Chlorite)	Actual group	Predicted group
T1 -Yorkstone	1.43E+00	5.06E+01	3.53E+01	4.20E+01	1 + 3	1
T2 -Hollington (red rock)	2.22E+00	5.35E+01	3.79E+01	4.56E+01	1 + 3	1
T3 -B4 (rock)	3.61E+00	5.65E+01	4.23E+01	5.05E+01	2	1
T4 -Kaol (powder)	2.31E+01	6.59E+01	2.47E-01	3.98E+01	3	3
T5 -SWy-2 (powder)	4.91E+01	3.60E+00	8.66E+01	5.31E+01	2	2

6.12 Summary TGA modelⓐ) using 3 scores (mehalanobis distance metric)

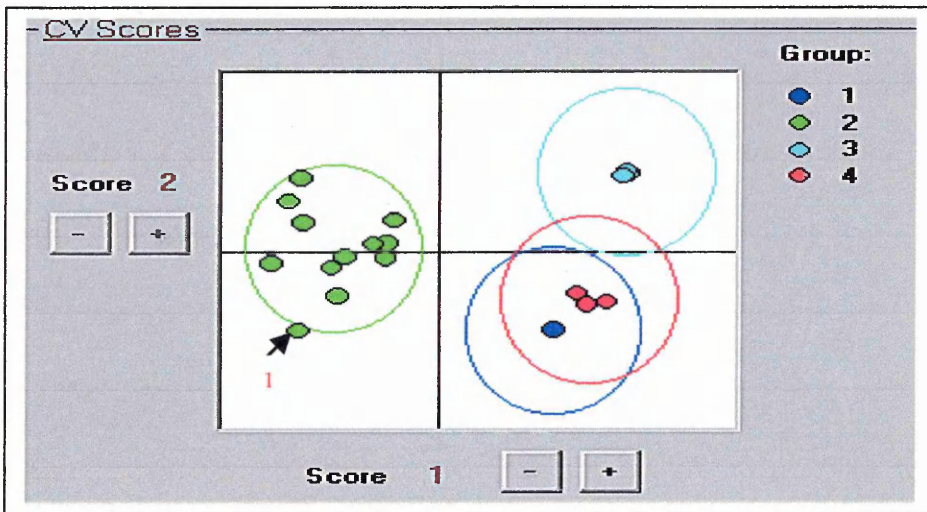
In comparison to Modelⓐ)(2 scores), the use of an additional score (95.09% variance) produced better separation between illite and chlorite groups. This is noticeable in the training set group distance scores, where the chlorite figures are higher. This shows that the third PCA score has descriptive data pertaining to illite and/or chlorite characterization. When loading 3 is evaluated the area associated with DMF desorption in illite is visualized as is the area of chlorite/illite dehydroxylation.

Application of modelⓐ)(b) to the test set has again shown that samples T1 and T2 have predicted illite correctly. In contrast to modelⓐ)(a), the group distance predictions are slightly better for kaolinite.

6.13 Canonical variance analysis

This method is used as the best approach of showing two-dimensional representations for highlighting differences between groups. The danger in this method is that simultaneous group membership or outlier detection will be categorized. However if different group centres exist and the data is normally distributed, a fixed variance range can be applied i.e. 95% confidence, whereby an object outside of the chosen range will not be categorized e.g. outside the coloured circle.

Figure 6.29 Canonical variance analysis of TGA data using a 95% confidence interval and two PCA scores



*1= SApCa-1

Table 6.17 TGA training group predictions based on 1st and 2nd canonical variates and 95% tolerance region using 2 scores

CV group assignment Illite	CV group assignment Smectites/saponite	CV group assignment Kaolinites	CV group assignment Chlorites
Illite (1 + 4)	Al-SWy-2 (2)	KGa-2 (3)	CCa-1 (1 + 4)
1-Mt-Illite (1 + 4)	Ca-SWy-2 (2)	Na-KGa-2 (3)	CCa-1 (1 + 4)
	Cr-SWy-2 (2)	Jkaol (3)	MgChlor (1 + 4)
	Mg-SWy-2 (2)		
	Ni-SWy-2 (2)		
	Na-SWy-2 (2)		
	SAPCa-1 (None)		
	SAz-1 (2)		
	SCa-1 (2)		
	STx-1 (2)		
	SWa-1 (2)		
	SWy-1 (2)		

Figure 6.30 TGA canonical variance analysis using a 95% confidence interval and three PCA scores

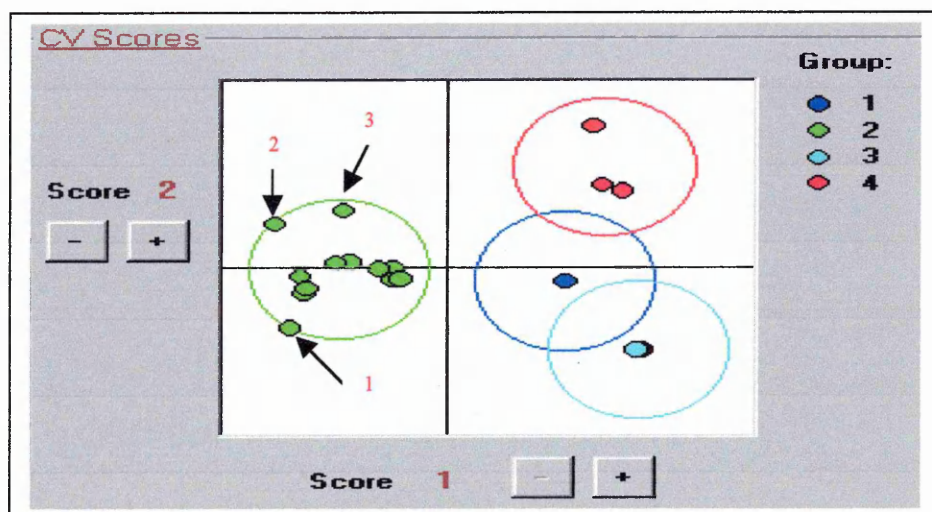


Table 6.18 TGA training group predictions based on 1st and 2nd canonical variates and 95% tolerance region using 3 scores

CV group assignment Illite	CV group assignment Smectites	CV group assignment Kaolinites	CV group assignment Chlorites
Illite (1)	Al-SWy-2 (2)	KGa-2 (3)	CCa-1 (1)
1-Mt-Illite (1)	Ca-SWy-2 (2)	Na-KGa-2 (3)	CCa-1 (1)
	Cr-SWy-2 (2)	Jkaol (3)	MgChlor (1)
	Mg-SWy-2 (2)		
	Ni-SWy-2 (2)		
	Na-SWy-2 (2)		
	SAPCa-1 (2) *1		
	SAz-1 (2)		
	SCa-1 (2)		
	STx-1 (2)		
	SWa-1 (2) *2		
	SWy-1 (2) *3		

* Numbers in red relate to the corresponding number in the canonical variance plot.

Figure 6.31 Application of canonical variance model to TGA test data using three scores

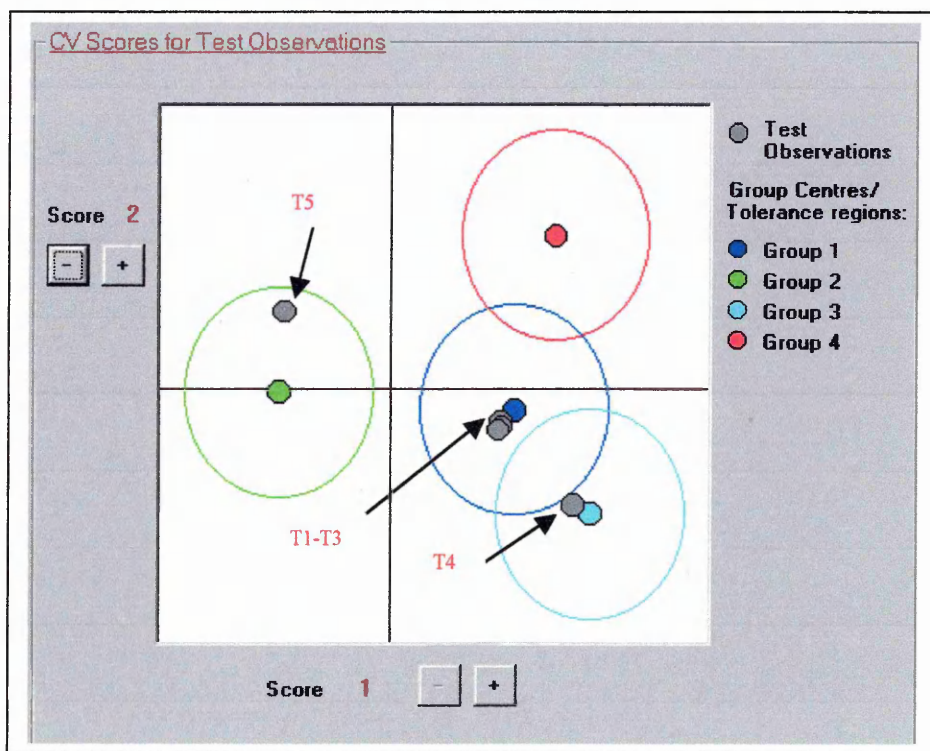


Table 6.19 TGA test set group predictions based on 1st and 2nd canonical variates and 95% tolerance region using three PCA scores

Test Observation	Actual group	Predicted group
T1-Yorkstone	1 + 3	1
T2-Hollington red	1 + 3	1
T3-B4 (rock)	2	1
T4-Kaolinite (powder)	3	3
T5-SWy-2	2	2

6.14 Summary of TGA canonical variance analysis

The use of CV analysis as a graphical tool highlights the importance of using the third PCA score. In addition it has successfully highlighted saponite (SapCa-1) as being possibly from another group because it lay outside the 95% confidence limit when using 2 PCA scores. The TIC for SApCa-1 reveals that its dehydroxylation region is quite dissimilar to the smectites even though weight loss due to DMF is located in the same area and this is the most probable reason for its exclusion. However, when using 3 PCA scores, SApCa-1 moves a little closer inside the 95% confidence line. SapCA-1 could technically be considered an outlier and removed from future training groups, therefore forming a group in its own right. This suggests that a greater number of samples would be required for future work to verify its group placement.

The application of the CV model to the test group has revealed a familiar picture again failing to predict the kaolinite content of T1 and T2 and allocating T3 to group 1 instead of group 2.

The PLS compression method using three PLS scores was then evaluated.

Figure 6.32 TGA Model①(b) PLS Scree test of percentage variance versus PC score

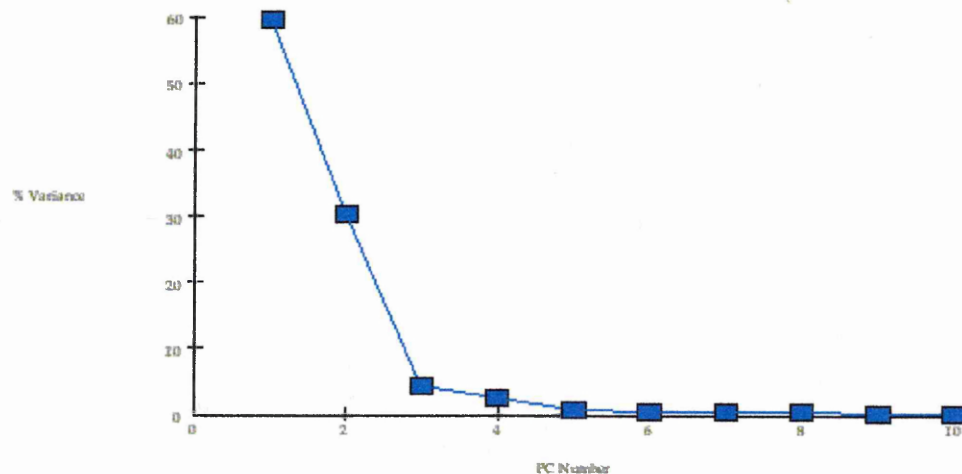
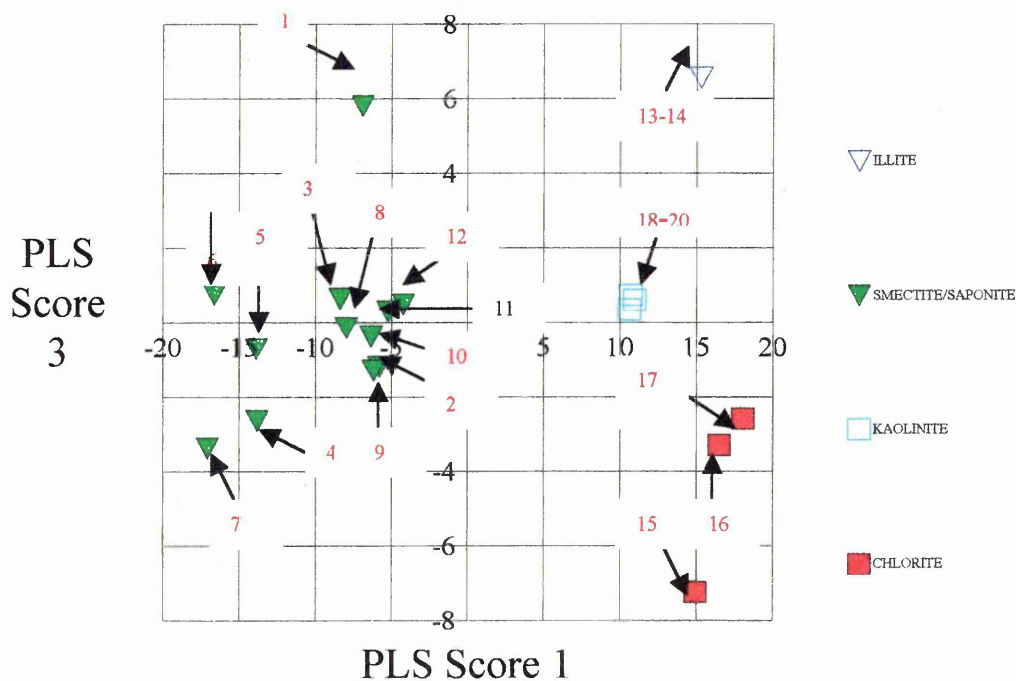


Table 6.20 TGA Model①(b) PLS score variance table

PLS Score	Variance	% Variance	% Cumulative variance
1	1.5394E+02	59.67	59.67
2	7.8473E+01	30.42	90.08
3	1.1278E+01	4.37	94.45
4	6.9269E+00	2.68	97.13
5	1.9022E+00	0.74	97.87
6	1.4065E+00	0.55	98.42
7	1.0219E+00	0.40	98.82
8	9.9447E-01	0.39	99.21
9	3.7438E-01	0.15	99.36
10	3.0064E-01	0.12	99.48

Figure 6.33 PLS score plot for TGA Model[ⓑ] using score 1 against score 3
(mehalanobis distance metric)



Individual training group samples in the PC score plot are identified by numbers coloured red, which correspond to the numbered samples in the table 6.19.

Table 6.21 PLS score plot key for TGA model[ⓑ] training set

Group1 Illite	Group 2 Smectites	Group 3 Kaolinites	Group 4 Chlorites	Test group
Illite 13	Al-SWy-2 8	KGa-2 18	CCa-1 17	Yorkstone T1
1-Mt-Illite 14	Ca-SWy-2 12	Na-KGa-2 19	CCa-2 16	Hollington T2
	Cr-SWy-2 11	Jkaol 20	MgChlor 15	B4 rock T3
	Mg-SWy-2 9			Kaol T5
	Ni-SWy-2 10			SWy-2 T6
	Na-SWy-2 4			
	SAPCa-1 1			
	SAz-1 7			
	SCa-1 5			
	STx-1 3			
	SWa-1 6			
	SWy-1 2			

Table 6.22 PLS TGA Model©(b) training group predictions using 3 PLS scores

Observation	Distance From group 1 (Illite)	Distance From group 2 (Smectite)	Distance From group 3 (Kaolinite)	Distance From group 4 (Chlorite)	Group allocation	Correct or incorrect
1-Mt-Illite	0.00E+00	4.68E+01	2.96E+01	3.74E+01	1	Correct
Illite	0.00E+00	4.68E+01	2.96E+01	3.74E+01	1	Correct
Al-SWy-2	4.31E+01	1.63E-01	7.74E+01	6.51E+01	2	Correct
Ca-SWy-2	2.99E+01	2.09E+00	6.02E+01	5.23E+01	2	Correct
Cr-SWy-2	3.08E+01	2.33E+00	5.56E+01	5.54E+01	2	Correct
Mg-SWy-2	3.45E+01	3.60E+00	5.17E+01	5.20E+01	2	Correct
Na-SWy-2	7.85E+01	6.08E+00	1.24E+02	8.72E+01	2	Correct
Ni-SWy-2	3.61E+01	1.12E+00	6.38E+01	5.64E+01	2	Correct
SapCa-1	5.14E+01	1.03E+01	1.14E+02	1.04E+02	2	Correct
SAz-1	7.48E+01	5.16E+00	9.24E+01	9.32E+01	2	Correct
SCa-1	6.15E+01	1.44E+00	9.10E+01	8.98E+01	2	Correct
STx-1	4.58E+01	3.80E-01	8.57E+01	7.19E+01	2	Correct
SWa-1	6.96E+01	6.37E+00	9.52E+01	1.14E+02	2	Correct
SWy-1	4.96E+01	4.66E+00	9.59E+01	5.64E+01	2	Correct
Jkaol	2.98E+01	8.12E+01	4.05E-03	5.27E+01	3	Correct
KGa-2	3.06E+01	8.07E+01	1.14E-02	5.25E+01	3	Correct
Na-KGa-2	2.86E+01	7.88E+01	1.37E-02	5.24E+01	3	Correct
CCa-1	2.76E+01	7.10E+01	4.10E+01	1.24E+00	4	Correct
CCa-2	3.05E+01	6.60E+01	4.69E+01	3.53E-01	4	Correct
Mg-Chlor	5.85E+01	8.08E+01	7.39E+01	2.71E+00	4	Correct

Figure 6.34 TGA ModelⓅ(b) PLS-loading 1

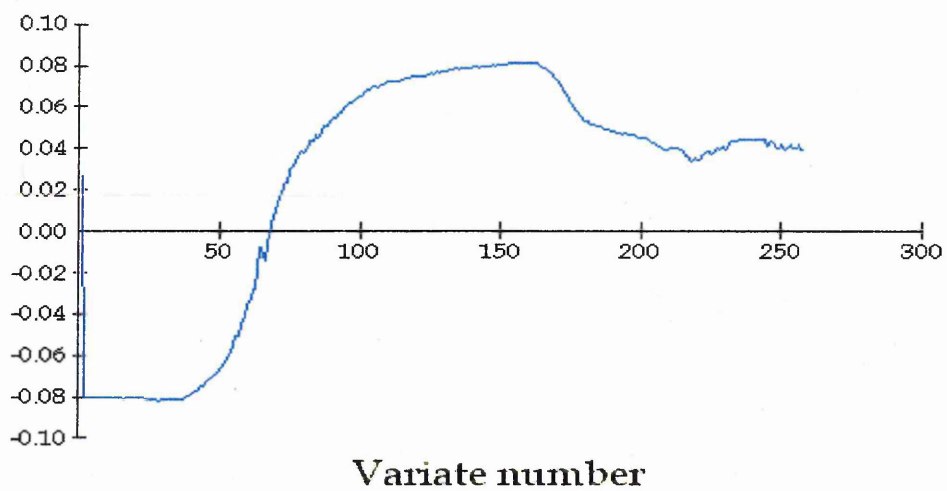


Figure 6.35 TGA ModelⓅ(b) PLS-loading 2

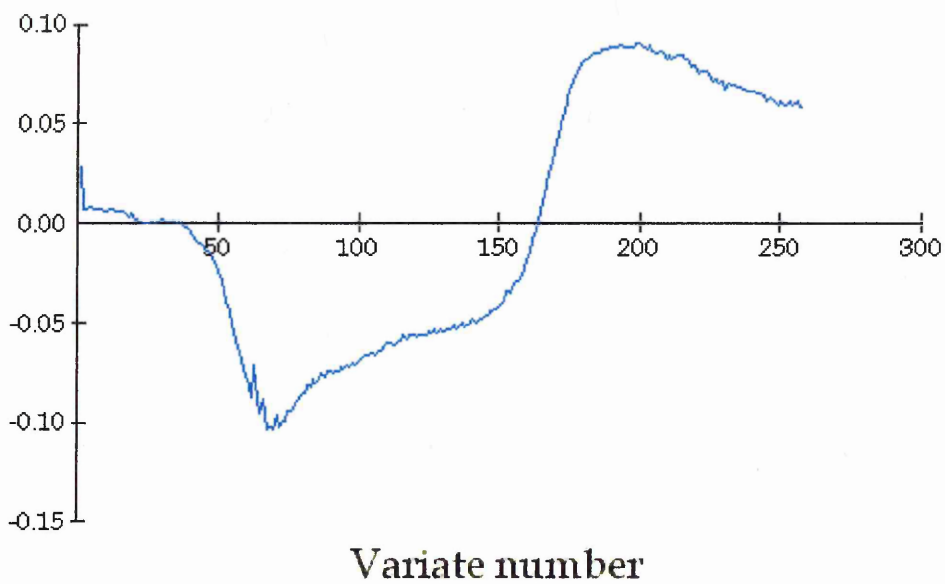


Figure 6.36 TGA Model①(b) PLS-loading 3

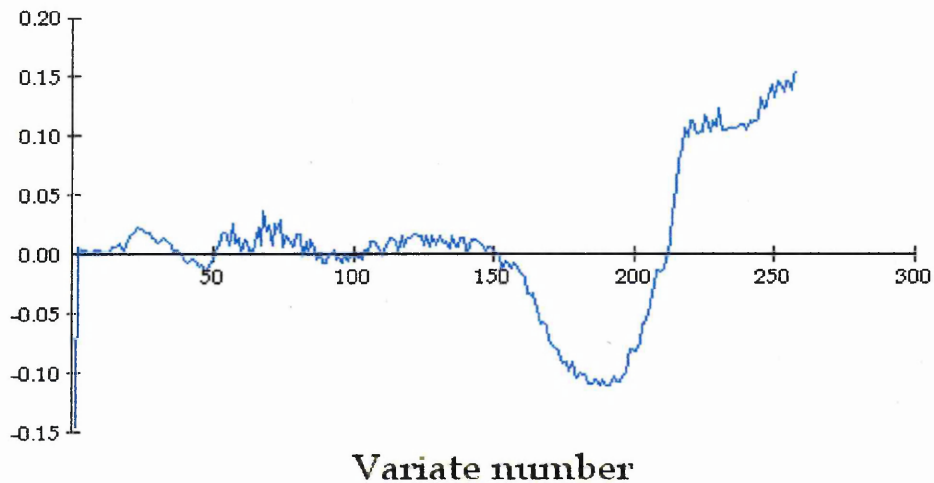


Table 6.23 PLS TGA Model①(b) applied to Test samples using 3 scores

Test Observation	Distance From group 1 (Illite)	Distance From group 2 (Smectite)	Distance From group 3 (Kaolinite)	Distance From group 4 (Chlorite)	Actual group	Predicted group
T1-Yorkstone (Rock)	1.68E+00	5.13E+01	4.13E+01	5.24E+01	1 + 3	1
T2-Hollington red	2.61E+00	5.44E+01	4.43E+01	5.68E+01	1 + 3	1
T3-B4 (Rock)	4.26E+00	5.76E+01	4.95E+01	6.29E+01	2	1
T4-Kaolinite (powder)	2.74E+01	7.12E+01	3.82E-01	4.64E+01	3	3
T5-SWy-2 (powder)	4.93E+01	3.63E+00	9.31E+01	5.71E+01	2	2

6.15 Summary TGA Model[ⓐ](b) using 3 PLS scores (mehalanobis distance metric)

The first three scores used in the PLS model contained 94.45% of the variance, the highest percentage of all models tested so far. This implies that for TGA weight loss curve PLS is the most appropriate compression technique when combined with mehalanobis distance. Again all groups showed good separation and SApCa-1 and Mg-Chlorite samples were highlighted as possible outliers. Mg-Chlorite may need further investigation (not investigated here) as the TGA weight loss curve (fig. 6.22) is noisy and its RT-MS TIC (fig. 6.12) reveals a detection maxima in a region normally associated with a smectite mineral. In addition dehydroxylation is also much sharper than the other two chlorites. These points would obviously preclude it from future quantitative studies. Prediction of test samples T1-T3 showed no improvement on model[ⓐ](a).

6.16 Results Model[ⓐ]GP-FTIR total infrared (TIR)

Table 6.24 GP-FTIR (TIR) Model[ⓐ]data compression/discriminant analysis

Compression method	Metric: score 1	Metric: score 2	Metric: score 3
PCA (correlation)	Euc: 17/20	Euc: 18/20	Euc: 18/20
	Man:17/20	Man: 18/20	Man: 18/20
	Meh:17/20	Meh: 18/20	Meh: 18/20
PCA (covariance)	Euc: 19/20	Euc: 19/20	Euc: 19/20
	Man:19/20	Man:19/20	Man:19/20
	Meh:19/20	Meh:19/20	Meh:19/20
PLS (variance scaled)	Euc: 17/20	Euc: 18/20	Euc: 18/20
	Man:17/20	Man: 18/20	Man: 18/20
	Meh:17/20	Meh: 18/20	Meh: 20/20 *

The PLS variance compression method was chosen for investigation using 3 scores and mehalanobis distance metric.

Figure 6.37 Model② PLS scree test of percentage variance versus PLS score

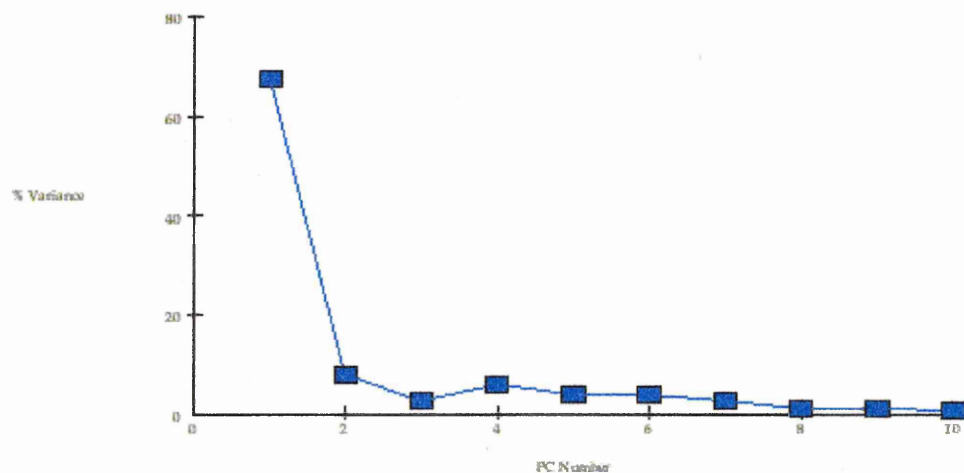
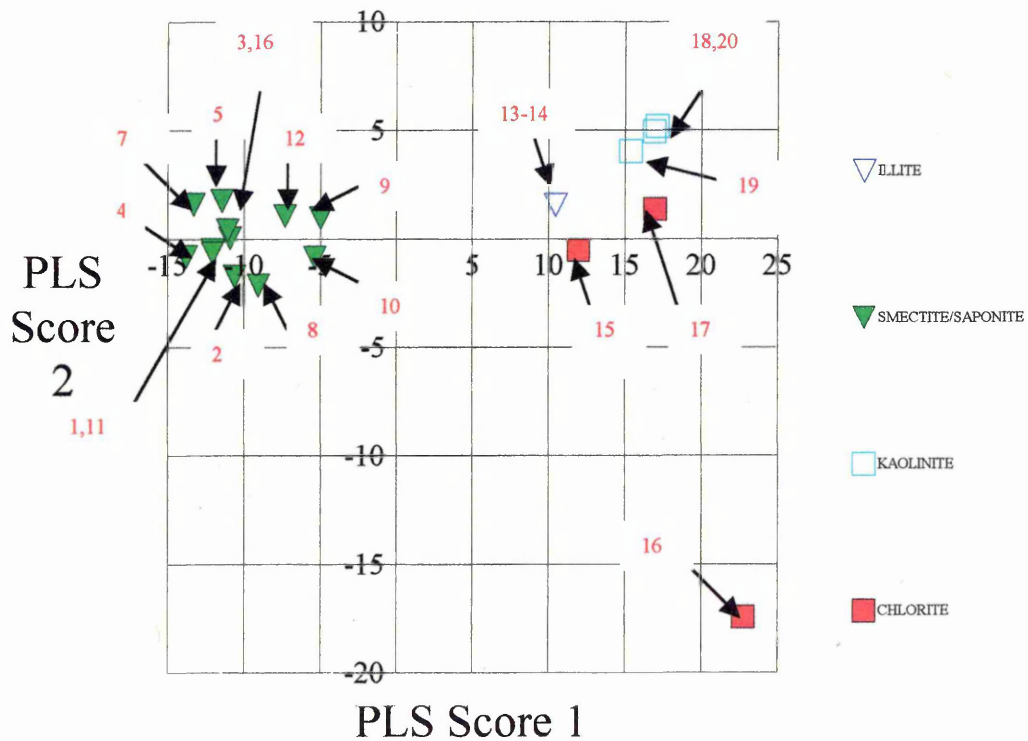


Table 6.25 GP-FTIR(TIR) Model② PLS score variance table

PLS Score	Variance	% Variance	% Cumulative variance
1	1.7444E+02	67.61	67.61
2	2.0816E+01	8.07	75.68
3	6.5477E+00	2.54	78.22
4	1.5015E+01	5.82	84.04
5	1.0108E+01	3.92	87.96
6	1.0226E+01	3.96	91.92
7	6.4305E+00	2.49	94.41
8	2.2311E+00	0.86	95.28
9	2.5192E+00	0.98	96.25
10	1.5336E+00	0.59	96.85

Figure 6.38 PLS score plot for GP-FTIR(TIR) model² using score 1 against score 2 (mehalanobis distance metric)



Individual training group samples in the PLS score plot are identified by numbers coloured red which correspond to the numbered samples in the table 6.24.

Table 6.26 GP-FTIR(TIR) model© PLS training group and test group samples

Group1 Illite	Group 2 Smectites	Group 3 Kaolinites	Group 4 Chlorites	Test group
Illite 13	Al-SWy-2 8	KGa-2 18	CCa-1 17	Yorkstone T1
1-Mt-Illite 14	Ca-SWy-2 12	Na-KGa-2 19	CCa-2 16	Hollington T2
	Cr-SWy-2 11	Jkaol 20	MgChlor 15	B4 rock T3
	Mg-SWy-2 9			Kaol T5
	Ni-SWy-2 10			SWy-2 T6
	Na-SWy-2 4			
	SAPCa-1 1			
	SAz-1 7			
	SCa-1 5			
	STx-1 3			
	SWa-1 6			
	SWy-1 2			

Table 6.27 GP-FTIR(TIR) model[©] training group predictions using 3 PLS

scores

Observation	Distance From group 1 (Illite)	Distance From group 2 (Smectite)	Distance From group 1 (Kaolinite)	Distance From group 1 (Chlorite)	Group allocation	Correct or incorrect
1-Mt-Illite	0.00E+00	6.29E+01	4.14E+01	1.97E+01	1	Correct
Illite	0.00E+00	6.29E+01	4.14E+01	1.97E+01	1	Correct
Al-SWy-2	6.41E+01	1.54E+00	1.32E+02	1.15E+02	2	Correct
Ca-SWy-2	4.66E+01	4.96E+00	1.41E+02	7.47E+01	2	Correct
Cr-SWy-2	7.55E+01	6.58E-01	1.63E+02	1.20E+02	2	Correct
Mg-SWy-2	3.41E+01	4.40E+00	1.03E+02	7.29E+01	2	Correct
Na-SWy-2	9.10E+01	3.76E+00	1.65E+02	1.48E+02	2	Correct
Ni-SWy-2	4.09E+01	3.48E+00	1.03E+02	8.57E+01	2	Correct
SapCa-1	7.85E+01	1.99E+00	1.50E+02	1.33E+02	2	Correct
SAz-1	7.85E+01	2.63E+00	1.78E+02	1.18E+02	2	Correct
SCa-1	6.64E+01	4.56E-01	1.42E+02	1.16E+02	2	Correct
STx-1	6.73E+01	1.23E+00	1.61E+02	1.04E+02	2	Correct
SWa-1	6.70E+01	8.09E-01	1.58E+02	1.06E+02	2	Correct
SWy-1	7.10E+01	6.79E-01	1.48E+02	1.19E+02	2	Correct
Jkaol	5.23E+01	1.56E+02	6.57E-01	1.16E+02	3	Correct
KGa-2	5.06E+01	1.57E+02	4.64E-01	1.13E+02	3	Correct
Na-KGa-2	2.46E+01	1.19E+02	2.19E+00	7.33E+01	3	Correct
CCa-1	1.46E+01	1.18E+02	7.75E+01	4.75E+00	4	Correct
CCa-2	4.50E+01	1.35E+02	1.33E+02	9.98E+00	4	Correct
Mg-Chlor	1.75E+01	8.72E+01	1.06E+02	3.36E+00	4	Correct

The first three loadings for model[©] (GP-FTIR (TIR)) are shown in figures 6.39-6.41.

Figure 6.39 GP-FTIR(TIR) model© PLS-loading 1

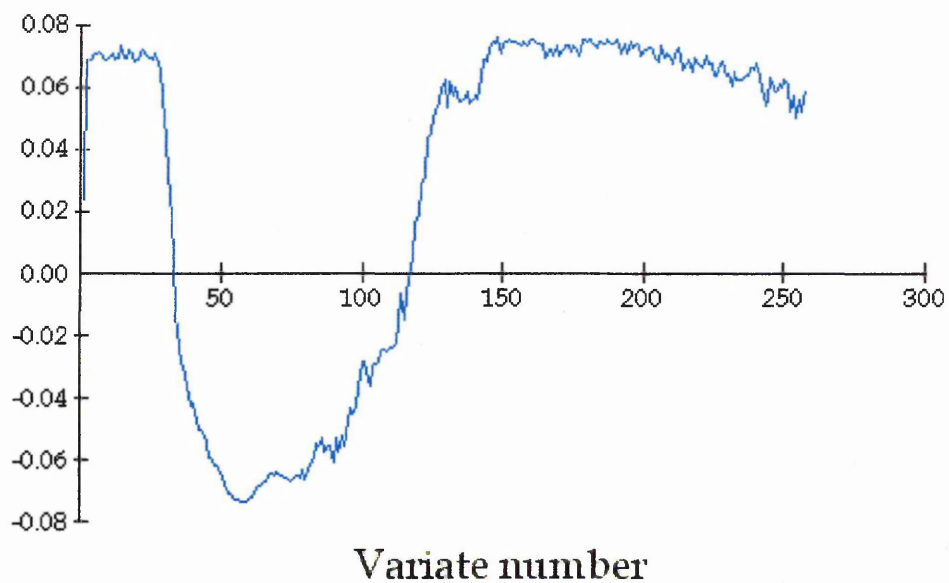


Figure 6.40 GP-FTIR(TIR) model© PLS-loading 2

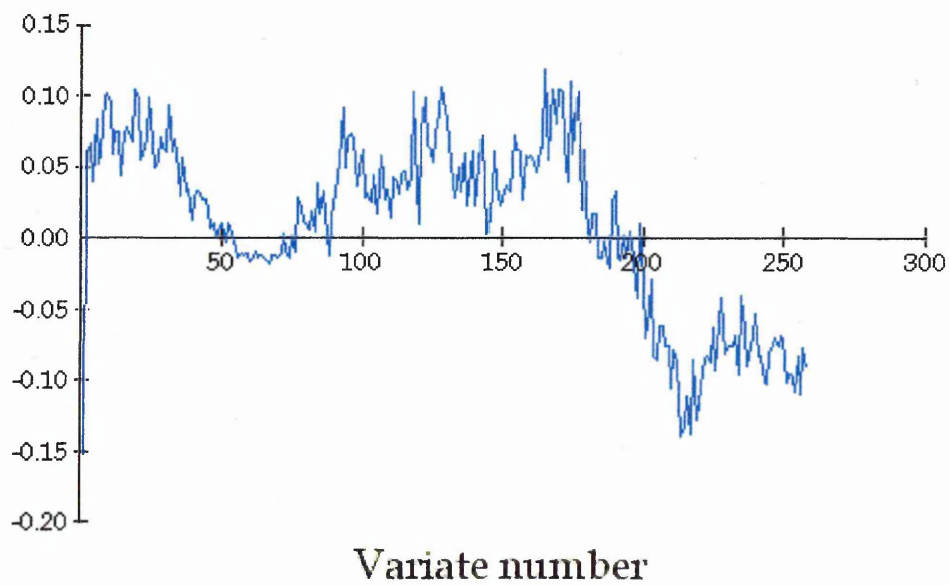


Figure 6.41 GP-FTIR(TIR) model[®] PLS-loading 3

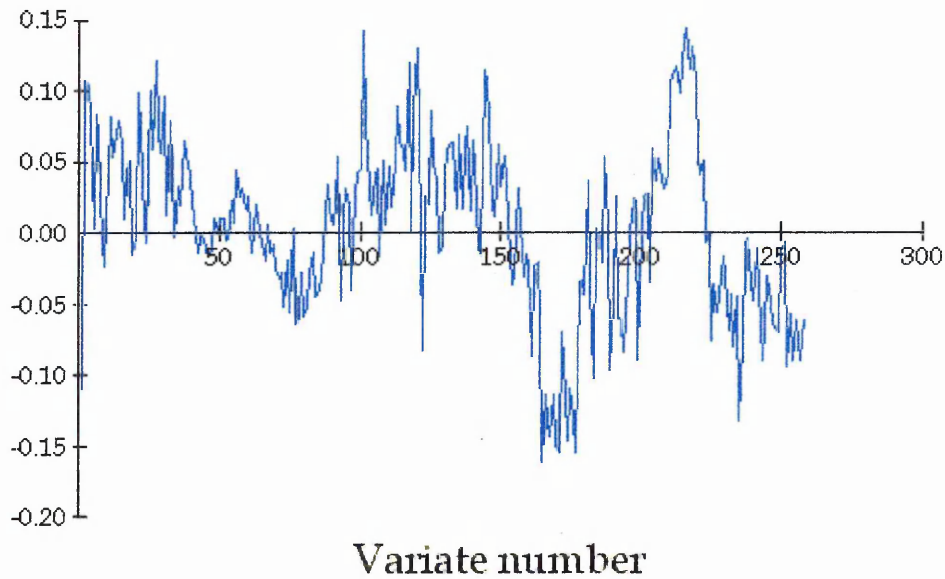
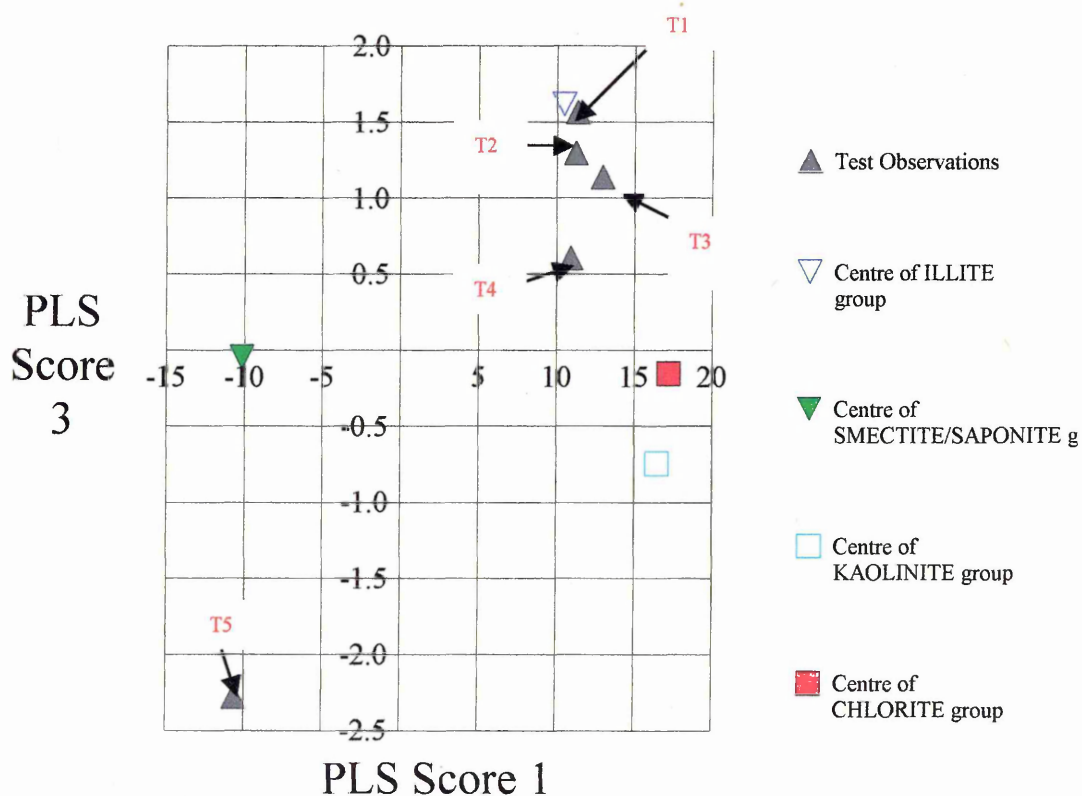


Table 6.28 GP-FTIR(TIR) model[®] applied to test samples using 3 PLS scores
(mehalanobis distance)

Test Observation	Distance From group 1 (Illite)	Distance From group 2 (Smectite)	Distance From group 3 (Kaolinite)	Distance From group 4 (Chlorite)	Actual group	Predicted group
T1-Yorkstone	7.47E-01	7.02E+01	3.12E+01	2.52E+01	1 + 3	1
T2-Hollington red	2.55E+00	6.77E+01	2.44E+01	3.37E+01	1 + 3	1
T3-B4 (Rock)	3.09E+00	7.28E+01	2.22E+01	3.50E+01	2	1
T4-Kaolinite (powder)	1.60E+01	9.96E+01	6.27E+00	6.19E+01	3	3
T5-SWy-2 (powder)	7.32E+01	2.22E+00	1.41E+02	1.27E+02	2	2

A graphical representation of these test results is shown in figure 6.42.

Figure 6.42 GP-FTIR(TIR) model² applied to test samples using 3 PLS scores (mehalanobis distance)



6.17 Summary of GP-FTIR (TIR) PLS model² using 3 scores

Model² was not as successful as model¹ (a) and (b). In fact it would take 6 PCA scores to describe 91.92% of the variance within the data. Using 3 PCA scores only describes 78.22% of the variance and therefore this model can be considered as 'underfit' i.e. the scores used for this model do not describe all the component features

within the training set. Using 3 scores is already slightly overfitting the illite data (2 samples). The profiles are generally noisier than both the RT-MS TIC and TGA weight loss profile. Further perusal of the first three loadings also shows that they become progressively noisier and only loading 1 and 2 seem to represent features of the reconstructed TIR (total infrared). Perhaps the most important issue with using GP-FTIR profile is the reliability of the detector response over time and ultimately its sensitivity.

Figure 6.43 GP-FTIR (TIR) model canonical variance analysis using a 95% confidence interval and three PLS scores

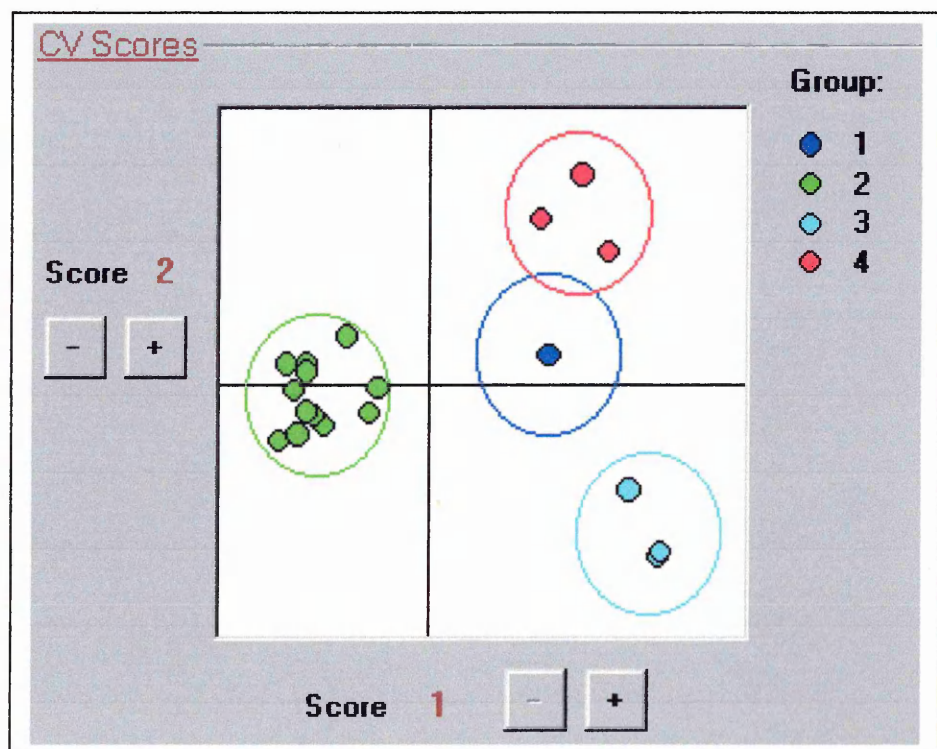
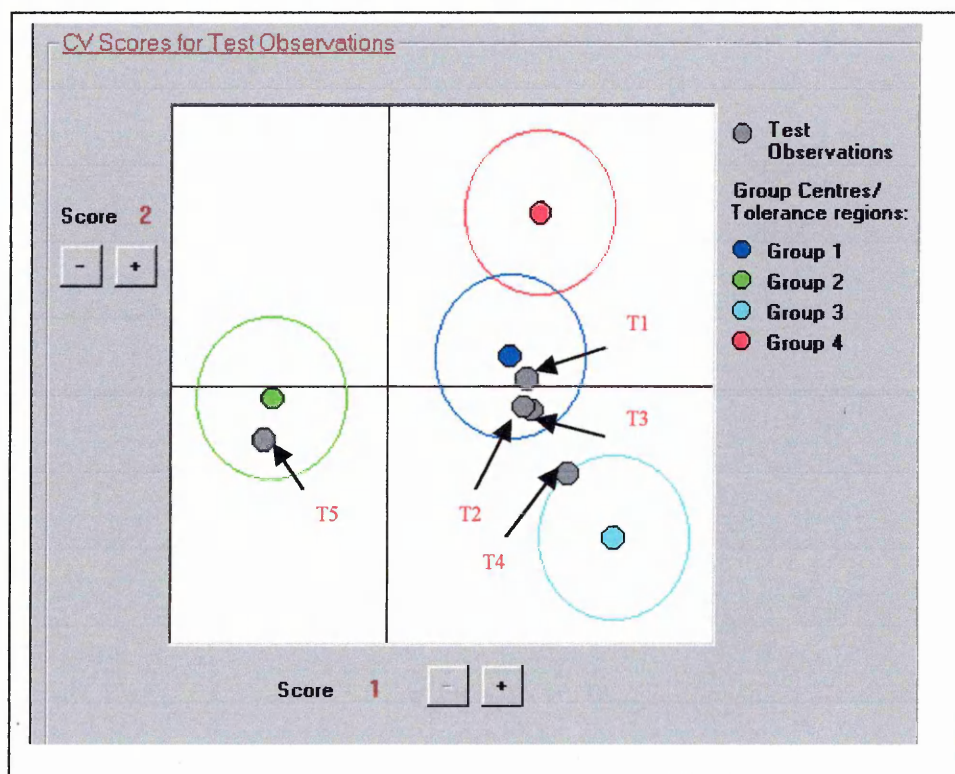


Figure 6.44 GP-FTIR (TIR) model[®] test set group predictions based on 1st and 2nd canonical variates and 95% tolerance region and three PLS scores



6.18 Summary of GP-FTIR (TIR) model[®] canonical variance analysis

Canonical variance analysis shows that even with 3 PLS scores the training set sample are well allocated within their respective groups. Considering the quality of the data output, GP-FTIR shows potential, though would need further investigation regarding issues of stability and signal optimisation. For future quantitative work GP-FTIR will not be considered further at this stage.

6.19 Results Model③(a) RT-MS (TIC)

Table 6.29 RT-MS (TIC) model ③(a) data compression/discriminant analysis

Compression method	Metric:score 1	Metric: score 2	Metric: score 3
PCA (correlation)	Euc: 15/20	Euc: 18/20	Euc: 20/20
	Man:15/20	Man: 18/20	Man: 20/20
	Meh:15/20	Meh: 18/20	Meh: 20/20
PCA (covariance)	Euc: 18/20	Euc: 18/20	Euc: 18/20
	Man:18/20	Man:17/20	Man:18/20
	Meh:18/20	Meh:18/20	Meh:18/20
PLS (variance scaled)	Euc: 15/20	Euc: 19/20	Euc: 20/20
	Man:15/20	Man: 19/20	Man: 20/20
	Meh:15/20	Meh: 20/20	Meh: 20/20

The PLS variance compression method was chosen for investigation using 3 scores and mehalanobis distance metric.

Table 6.30 RT-MS (TIC) model[ⓐ](a) training group predictions using 3 PLS scores (mehalanobis distance)

Observation	Distance From group 1 (Illite)	Distance From group 2 (Smectite)	Distance From group 1 (Kaolinite)	Distance From group 1 (Chlorite)	Group allocation	Correct or incorrect
1-Mt-Illite	2.32E-01	2.78E+01	3.93E+01	1.51E+01	1	Correct
Illite	2.32E-01	2.23E+01	3.33E+01	2.22E+01	1	Correct
Al-SWy-2	1.18E+01	3.23E+00	5.67E+01	3.80E+01	2	Correct
Ca-SWy-2	1.30E+01	8.81E+00	8.27E+01	1.66E+01	2	Correct
Cr-SWy-2	1.68E+01	2.18E+00	6.43E+01	4.40E+01	2	Correct
Mg-SWy-2	3.92E+01	6.49E+00	8.53E+01	7.22E+01	2	Correct
Ni-SWy-2	2.29E+01	3.13E+00	8.08E+01	4.16E+01	2	Correct
SapCa-1	3.80E+01	4.72E+00	1.10E+02	5.54E+01	2	Correct
SAz-1	5.22E+01	6.68E+00	1.32E+02	6.55E+01	2	Correct
SCa-1	3.26E+01	7.59E-01	9.79E+01	5.30E+01	2	Correct
STx-1	3.47E+01	1.30E+00	1.06E+02	5.15E+01	2	Correct
SWa-1	2.84E+01	3.57E+00	6.74E+01	6.57E+01	2	Correct
SWy-1	2.65E+01	1.84E+00	8.27E+01	5.18E+01	2	Correct
Na-SWy-2	2.58E+01	1.02E+00	9.45E+01	4.09E+01	2	Correct
Jkaol	3.23E+01	7.82E+01	1.33E-01	9.43E+01	3	Correct
KGa-2	3.60E+01	8.44E+01	3.13E-04	9.98E+01	3	Correct
Na-KGa-2	4.02E+01	9.17E+01	1.45E-01	1.06E+02	3	Correct
CCa-1	1.47E+01	3.67E+01	9.39E+01	5.30E-01	4	Correct
CCa-2	1.19E+01	4.44E+01	8.11E+01	1.08E+00	4	Correct
Mg-Chlorite	3.22E+01	6.05E+01	1.28E+02	1.91E+00	4	Correct

Figure 6.45 RT-MS (TIC) model③(a) PLS Scree test of percentage variance

versus PLS score

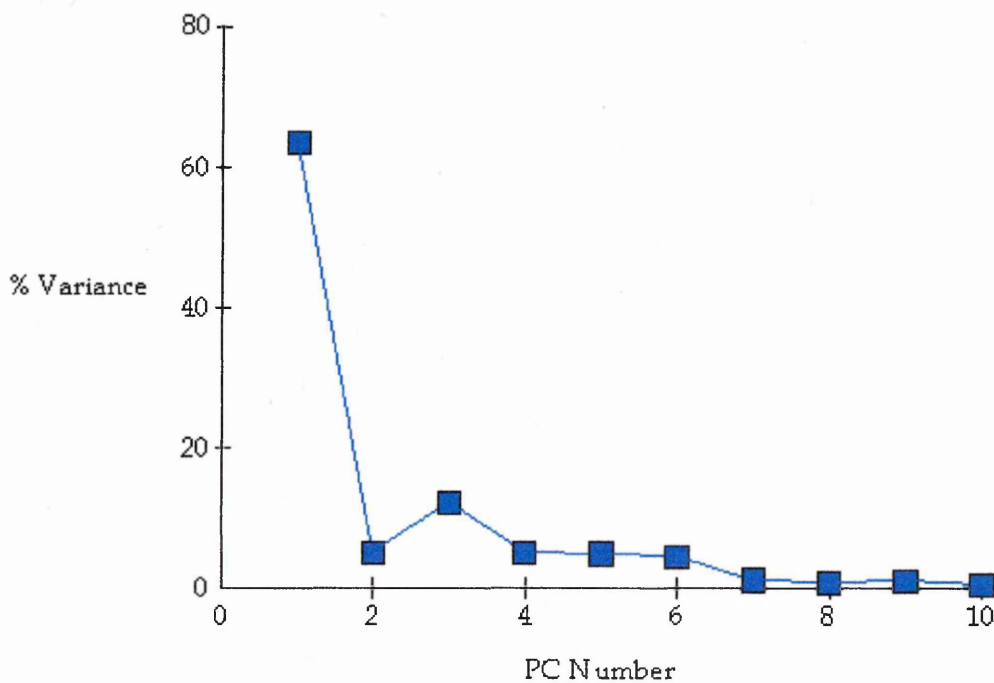


Table 6.31 RT-MS (TIC)model③(a) PLS score variance table

PCA Score	Variance	% Variance	Cumulative variance
1	2.8758E+02	63.48	63.48
2	2.3166E+01	5.11	68.60
3	5.5369E+01	12.22	80.82
4	2.2925E+01	5.06	85.88
5	2.2105E+01	4.88	90.76
6	2.0321E+01	4.49	95.25
7	5.2743E+00	1.16	96.41
8	3.4736E+00	0.77	97.18
9	4.7592E+00	1.05	98.23
10	2.4158E+00	0.53	98.76

Figure 6.46 PLS score plot for RT-MS (TIC) model[ⓐ] using score 1 against score 2 (mehalanobis distance metric)

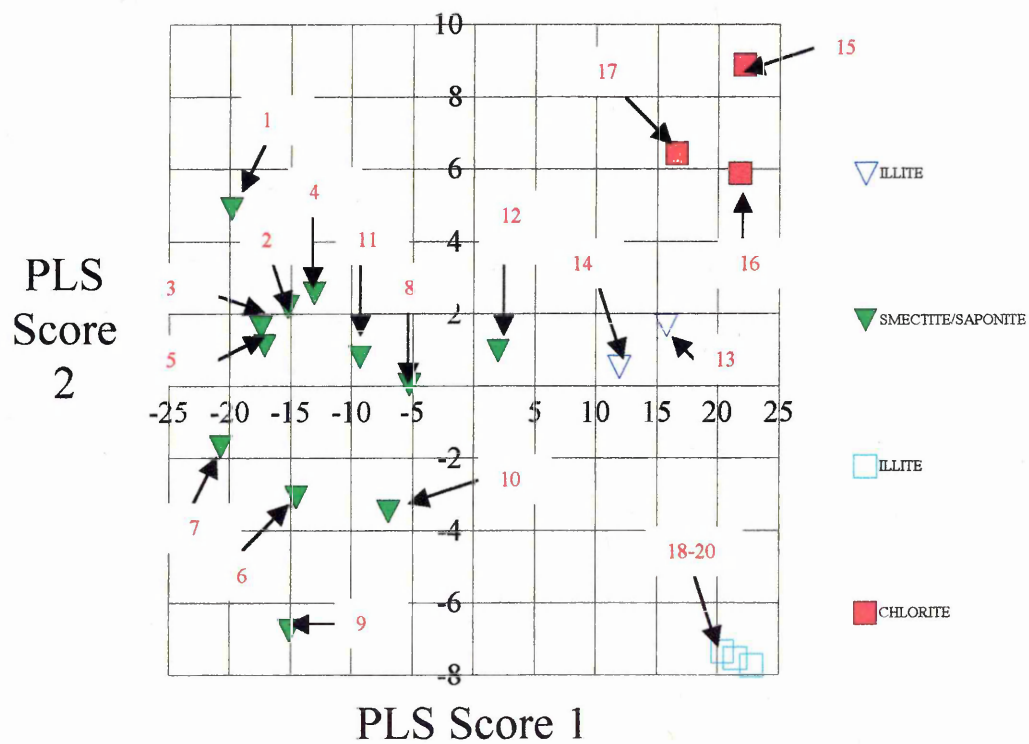


Figure 6.47 RT-MS (TIC)model③(a) PLS loading 1

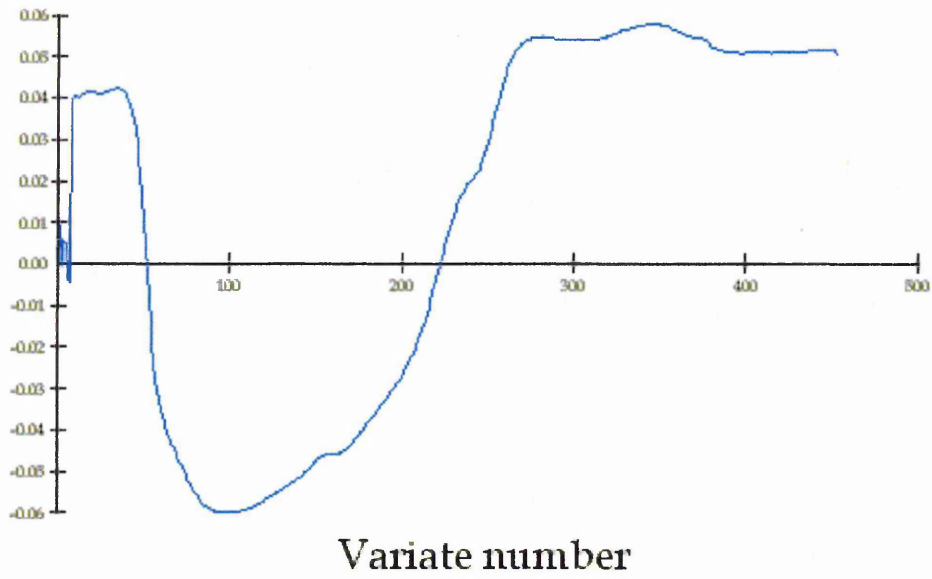


Figure 6.48 RT-MS (TIC)model③(a) PLS-loading 2

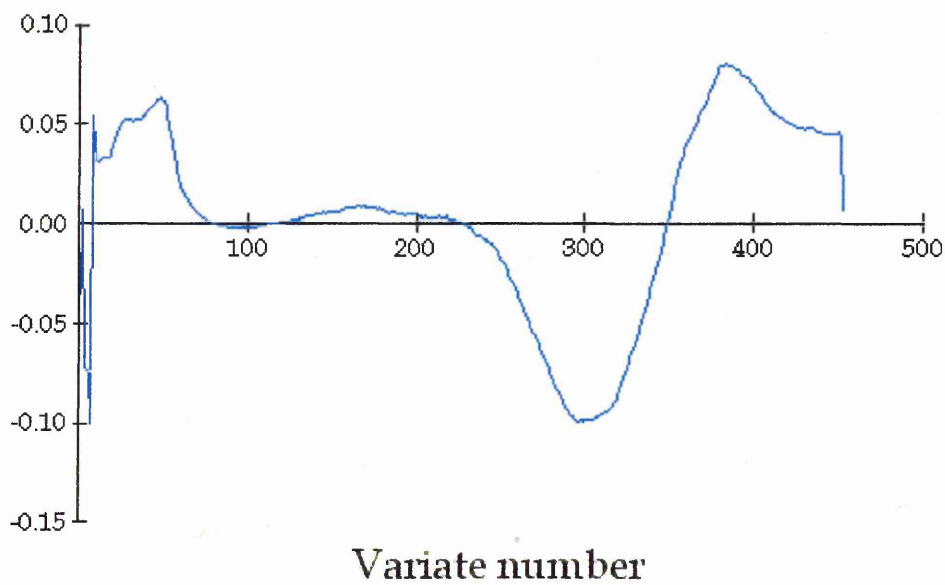


Figure 6.49 RT-MS (TIC)model③(a) PLS-loading 3

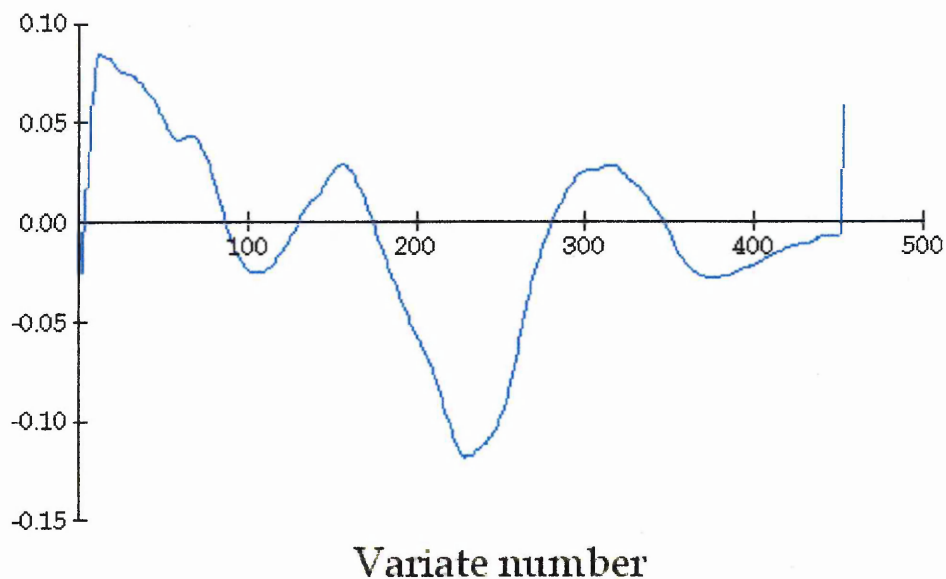


Table 6.32 RT-MS (TIC) model③(a) applied to test samples using 3 PLS scores (mehalanobis distance)

Test Observation	Distance From group 1 (Illite)	Distance From group 2 (Smectite)	Distance From group 3 (Kaolinite)	Distance From group 4 (Chlorite)	Actual group	Predicted group
T1-Yorkstone	2.05E-01	2.71E+01	3.96E+01	1.53E+01	1+3	1
T2-Hollington red	2.57E-01	2.65E+01	3.54E+01	1.83E+01	1+3	1
T3-B4 (Rock)	1.41E+01	1.17E+01	8.75E+01	1.39E+01	2	2
T4-Kaolinite	3.42E+01	8.32E+01	4.89E-02	9.65E+01	3	3
T5-SWy-2	2.58E+01	1.02E+00	9.45E+01	4.09E+01	2	2
T6-Std-1	3.07E+01	7.75E+00	5.90E+01	7.54E+01	1+2+3+4	2
T7-Std-2	4.52E+01	3.56E+00	1.05E+02	7.32E+01	1+2+4	2
T8-Std-4	3.03E+01	4.09E+00	6.89E+01	6.78E+01	1+3+4	2
T9-Std-15	7.07E-01	2.89E+01	2.75E+01	2.45E+01	1+3	1
T10-Std-20	3.83E+01	5.63E+00	7.71E+01	7.90E+01	1+2+3+4	2
T11-<2um B4	2.62E+01	1.34E+01	9.48E+01	3.91E+01	2	2

As seen in table 6.32, several new test samples have been added to the analysis suite (T6-T11). These samples are mixed clay mineral standards, which were used for quantitative characterisation (Chapter 7). Therefore these samples have known compositions and will test the ability of the more sensitive MS models^③ (a) and (b) to detect one mineral in the presence of the other. The test sample T11 is the extracted 2µm powder fraction from B4 rock. This was analysed to evaluate whether there were significant differences between DMF detection from the rock or the extracted form as this may have important implications for sample preparation of future test samples. B4 rock has been previously been characterised by traditional methods such as XRD and the predominant clay mineral found was the swelling clay mineral saponite [370].

The clay mineral composition of test samples T6-T10 is shown in table 6.31.

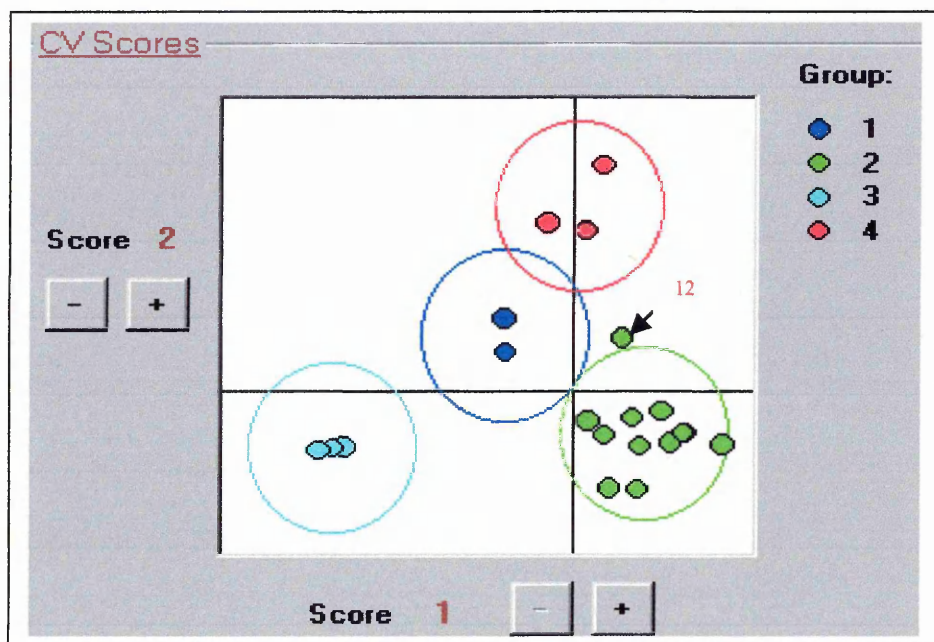
Table 6.33 Composition of test samples T6-T11

Test sample	Wt.% Illite (1-Mt-Illite)	Wt.% Montmorillonite (SWy-2)	Wt.% Kaolinite (KGa-2)	Wt.% Chlorite (CCa-1)
T6-Std1	4	10	4	8
T7-Std2	7	10	0	8
T8-Std4	0	9	10	3
T9-Std15	6	0	5	0
T10-Std20	6	9	10	7

6.20 Summary of PLS Model[ⓐ](a) RT-MS (TIC)

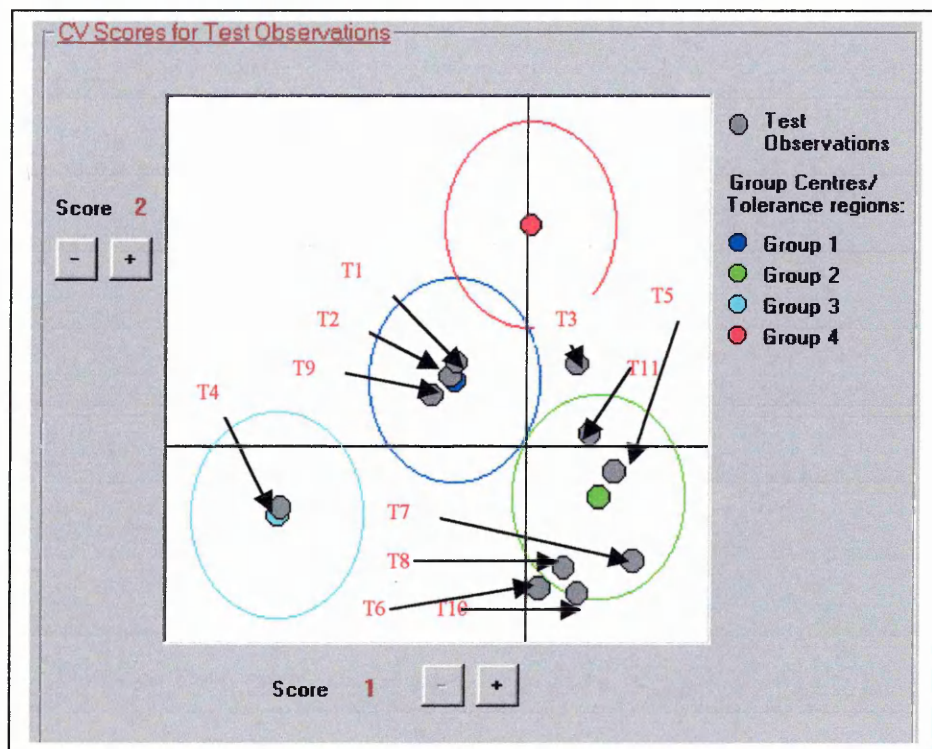
As with previous models, the most successful compression technique was PLS combined with Mahalanobis distance discrimination. However, the scree plot is quite unusual in that the variance contribution from score 2 is higher than score three, the first three scores providing only 77.38% of the variance within the data which suggests that the model is having difficulty discriminating between all of the components. As previously mentioned, application of the model to the test set has shown that in general the model assigns the test sample to the component of highest concentration though the test distances suggest the presence of other components. This is most probably caused by DMF detection dominating the TIC and therefore the main detection features associated with non-swelling minerals are suppressed (i.e. dehydroxylation). A possible solution would be the use of particular ions for each component or further pre-processing such as derivatisation to enhance the contribution of dehydroxylation and aid separation of the detection events.

Figure 6.50 RT-MS (TIC)model③(a) Canonical variance analysis using a 95% confidence interval using three PLS scores



The sample highlighted (12) outside the 95% confidence circle is Ca-SWy-2. Application of canonical variance model shown in figure 6.50 allocated the test samples as shown in figure 6.51.

Figure 6.51 RT-MS (TIC) model③(a) test set group predictions based on 1st and 2nd canonical variates and a 95% tolerance region using three PLS scores



6.21 Results Model③(b) RT-MS using $m/z = 18$ (H_2O) and $m/z = 73$ (DMF parent ion)

The output from RT-MS allows the operator to use a greater combination of detection features. In order to refine model③(a) further (where the RT-MS TIC was used) model③(b) utilized ions $m/z = 18$ and 73 . It is clear that smectite could be detected using DMF detection ($m/z = 73$). However, smectite/saponite and illite group analysis detected DMF in the same temperature region. Therefore quantitative studies of smectite/illite samples using $m/z = 73$ could produce an enhanced signal due to the presence of illite. However, as previously seen the determination of group distances can also reveal the presence of another mineral by examining the distance to the next

nearest group. Therefore an attempt was made to enhance kaolinite, illite and chlorite detection by utilizing ion $m/z = 18$ (dehydroxylation).

Table 6.34 RT-MS ($m/z = 18$) model[ⓐ](b) data compression/discriminant analysis

Compression method	Metric:score 1	Metric: score 2	Metric: score 3
PCA (correlation)	Euc: 17/20	Euc: 18/20	Euc: 20/20
	Man:17/20	Man: 18/20	Man: 20/20
	Meh:17/20	Meh: 18/20	Meh: 20/20
PCA (covariance)	Euc: 18/20	Euc: 18/20	Euc: 18/20
	Man:18/20	Man:18/20	Man:18/20
	Meh:18/20	Meh:18/20	Meh:18/20
PLS (variance scaled)	Euc: 18/20	Euc: 20/20	Euc: 20/20
	Man:18/20	Man: 20/20	Man: 20/20
	Meh:18/20	Meh: 20/20	Meh: 20/20

The PLS variance compression method was chosen for investigation using 2 scores and mehalanobis distance metric.

Table 6.35 RT-MS (m/z = 18) model③(b) training group predictions using 2 PLS scores (mehalanobis distance)

Observation	Distance From group 1 (Illite)	Distance From group 2 (Smectite)	Distance From group 1 (Kaolinite)	Distance From group 1 (Chlorite)	Group allocation	Correct or incorrect
1-Mt-Illite	2.27E-02	5.07E+01	1.31E+02	1.15E+02	1	Correct
Illite	2.27E-02	4.96E+01	1.38E+02	1.10E+02	1	Correct
Al-SWy-2	5.42E+01	1.36E-01	1.75E+02	1.96E+02	2	Correct
Ca-SWy-2	2.75E+01	3.40E+00	1.53E+02	1.60E+02	2	Correct
Cr-SWy-2	6.39E+01	8.44E-01	1.89E+02	2.03E+02	2	Correct
Mg-SWy-2	4.99E+01	1.24E+00	1.51E+02	2.09E+02	2	Correct
Ni-SWy-2	5.02E+01	1.04E-01	1.69E+02	1.93E+02	2	Correct
Na-SWy-2	5.94E+01	5.24E-01	1.94E+02	1.89E+02	2	Correct
SAPCa-1	1.66E+01	9.14E+00	1.53E+02	1.37E+02	2	Correct
SAz-1	5.65E+01	1.95E-01	1.81E+02	1.95E+02	2	Correct
SCa-1	6.04E+01	6.87E-01	1.97E+02	1.89E+02	2	Correct
STx-1	6.07E+01	5.72E-01	1.93E+02	1.93E+02	2	Correct
SWa-1	5.63E+01	2.94E-01	1.90E+02	1.86E+02	2	Correct
SWy-1	6.36E+01	8.26E-01	1.92E+02	1.99E+02	2	Correct
JKaol	1.10E+02	1.52E+02	1.25E+00	4.44E+02	3	Correct
KGa-2	1.18E+02	1.61E+02	5.40E-01	4.60E+02	3	Correct
Na-KGa-2	1.81E+02	2.22E+02	3.43E+00	5.77E+02	3	Correct
CCa-1	7.90E+01	1.49E+02	4.18E+02	2.95E+00	4	Correct
CCa-2	1.01E+02	1.77E+02	4.66E+02	4.24E-01	4	Correct
Mg-Chlor	1.67E+02	2.40E+02	6.00E+02	5.41E+00	4	Correct

Figure 6.52 RT-MS (ion m/z = 18) model③(b) PLS scree test of percentage variance versus PLS score number

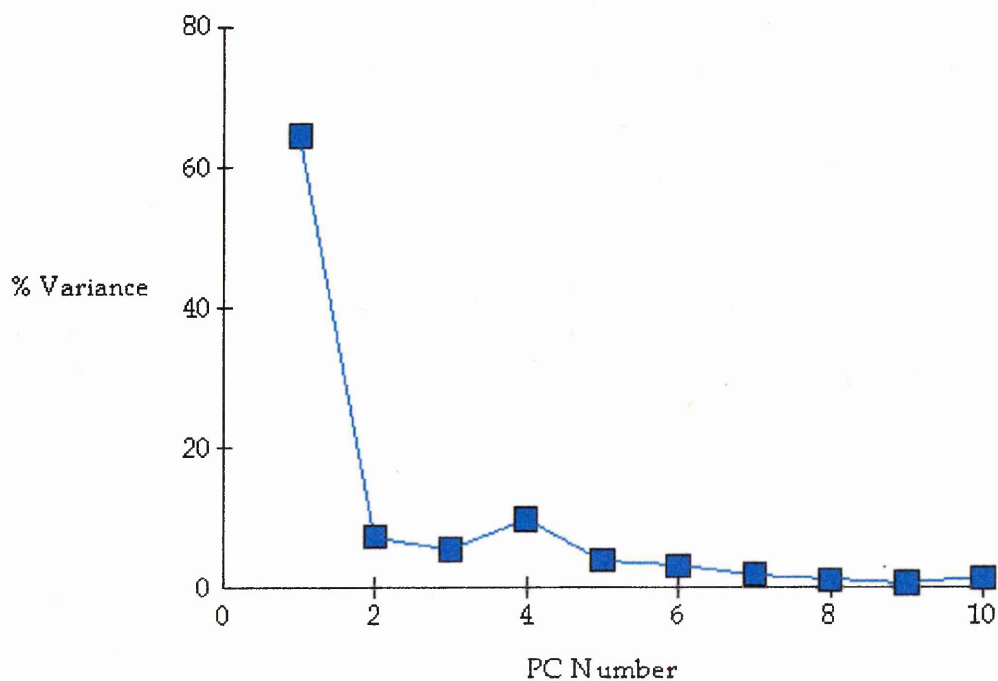


Table 6.36 RT-MS (ion m/z = 18) model③(b) PLS score variance table

PCA Score	Variance	% Variance	Cumulative % variance
1	2.9243E+02	64.55	64.55
2	3.3175E+01	7.32	71.88
3	2.4938E+01	5.51	77.38
4	4.4124E+01	9.74	87.12
5	1.7392E+01	3.84	90.96
6	1.3954E+01	3.08	94.04
7	8.3037E+00	1.83	95.88
8	4.8744E+00	1.08	96.95
9	2.7851E+00	0.61	97.57
10	6.0355E+00	1.33	98.90

Figure 6.53 PLS score plot for RT-MS (ion m/z = 18) model③(b) using score 1 against score 2 (mehalanobis distance)

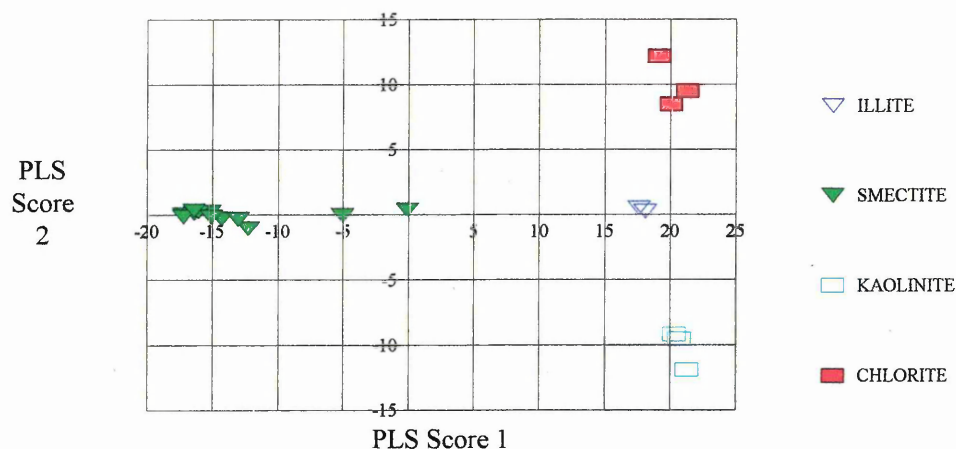


Table 6.37 RT-MS (ion m/z = 18) model③(b) applied to test samples using 2 PLS scores (mehalanobis distance)

Test Observation	Distance From group 1 (Illite)	Distance From group 2 (Smectite)	Distance From group 3 (Kaolinite)	Distance From group 4 (Chlorite)	Actual group	Predicted group
<2umB4 (m/z = 18)	3.44E+00	2.75E+01	1.31E+02	1.27E+02	2	1
<2umB4 (m/z = 73)	2.95E+01	4.36E+00	1.84E+02	1.36E+02	2	2
B4 (Rock) (m/z = 18)	3.19E+00	5.32E+01	1.79E+02	7.83E+01	2	1
B4 (Rock) (m/z = 73)	3.29E+01	4.02E+00	1.30E+02	1.91E+02	2	2
Hollington (m/z = 18)	3.53E-01	5.12E+01	1.49E+02	1.00E+02	1+3	1
Hollington (m/z = 73)	3.21E-01	4.29E+01	1.39E+02	1.10E+02	1+3	1
Std-1 (m/z = 18)	4.10E+00	5.53E+01	1.86E+02	7.39E+01		1
Std-1 (m/z = 73)	5.10E+01	2.07E-01	1.88E+02	1.77E+02		2
Std-2 (m/z = 18)	5.14E+01	1.06E+02	3.52E+02	1.28E+01		4
Std-2 (m/z = 73)	5.51E+01	4.55E-01	1.95E+02	1.79E+02		2
Std-4 (m/z = 18)	1.50E+00	4.82E+01	1.08E+02	1.40E+02		1
Std-4 (m/z = 73)	5.21E+01	3.06E-01	1.91E+02	1.77E+02		2
Std-15 (m/z = 18)	1.80E+01	6.87E+01	5.44E+01	2.19E+02		1
Std-15 (m/z = 73)	4.00E-02	4.85E+01	1.38E+02	1.09E+02		1
Std-20 (m/z = 18)	2.17E+00	4.82E+01	1.03E+02	1.46E+02		1
Std-20 (m/z = 73)	5.56E+01	3.27E-01	1.92E+02	1.83E+02		2
Yorkstone (m/z = 18)	8.06E-01	5.30E+01	1.56E+02	9.43E+01		1
Yorkstone (m/z = 73)	4.45E-01	4.14E+01	1.38E+02	1.12E+02		1

Figure 6.54 RT-MS model③(b) PLS-loading 1

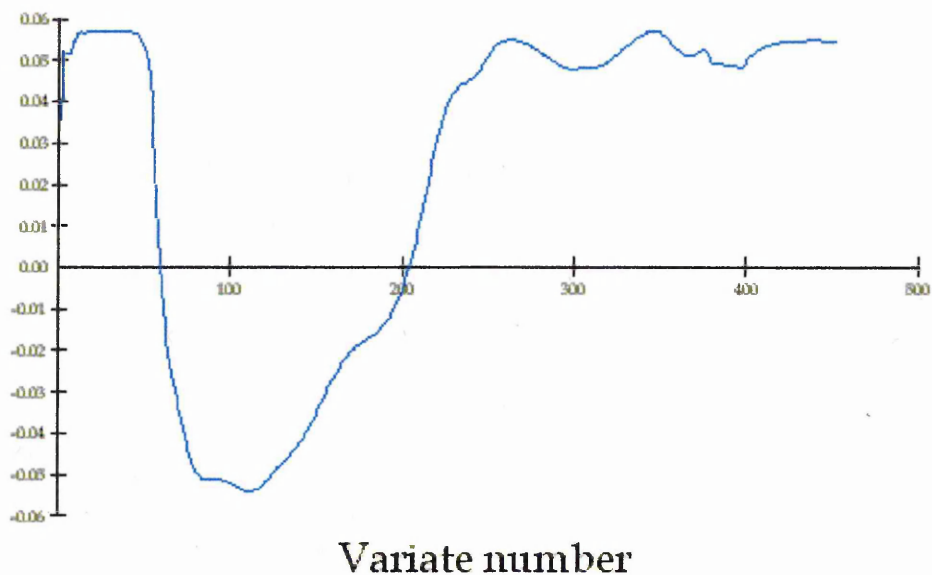
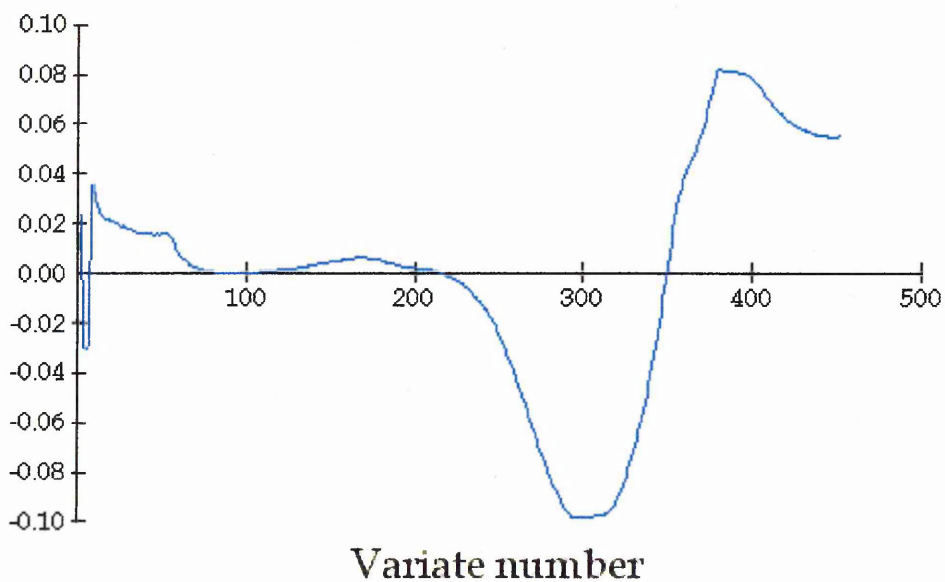
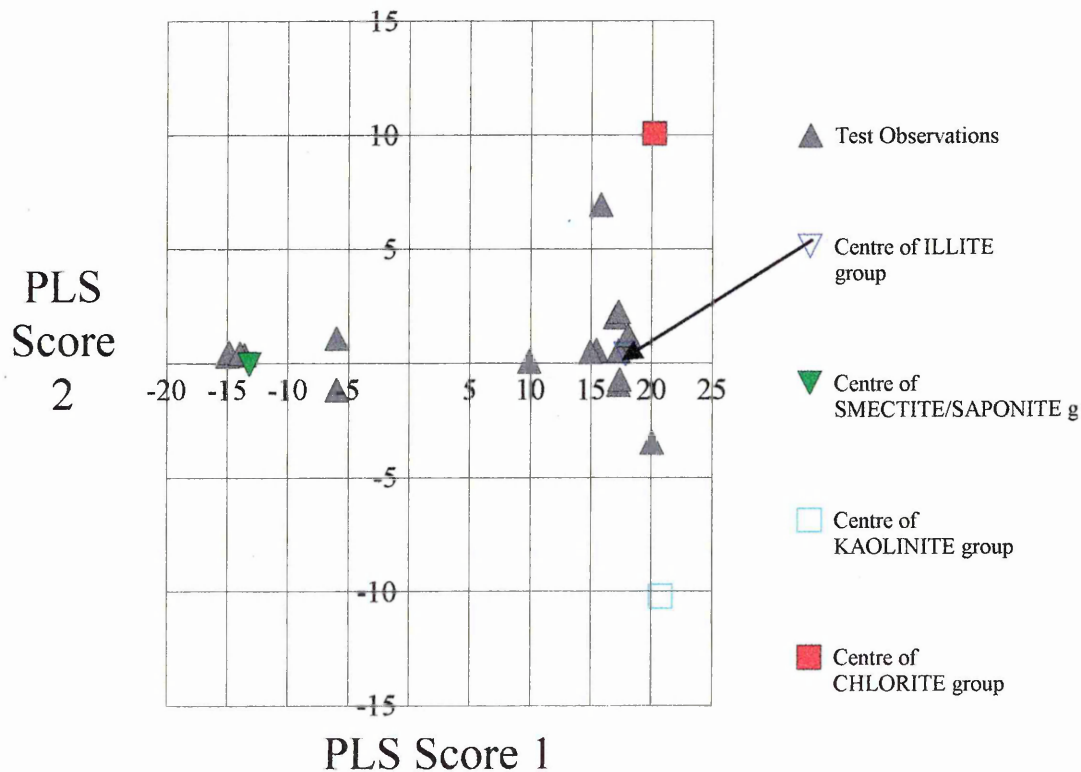


Figure 6.55 RT-MS model③(b) PLS-loading 2



Loadings 1 for model③(b) would seem to represent ion $m/z = 18$ (dehydroxylation) whereas loading 2 would seem to represent ion $m/z = 73$ (DMF).

Figure 6.56 RT-MS (ion $m/z = 18$ and 73) model③(b) applied to Test samples using 2 PLS scores (mehalanobis distance)



6.22 Summary of PLS Model③(b) using RT-MS ions $m/z = 18$ and 73

The use of ions $m/z = 18$ and 73 has shown some promising results. Application of the model to the test samples identified that B4 and its <2 μm extracted phase produced the same results identifying the presence of illite and smectite/saponite. The presence of illite has not been confirmed. However, the model failed to predict the presence of kaolinite in hollington red, which may be due to the low weight percent of kaolinite present. In addition kaolinite was not predicted in Yorkstone, possibly due to its concentration and/or the inability to separate dehydroxylation events. However,

standards 1,2,4,15 and 20 have been successfully identified as containing illite and montmorillonite/saponite. Illite was correctly predicted as the only swelling mineral present in standard 15.

6.23 Conclusion

The feasibility of applying Win-das chemometric analysis to EGA detection profiles has highlighted several important considerations for quantitative analysis of clay minerals.

- (a) In general all training samples were successfully allocated to their respective groups, however more samples would be required to statistically describe the variability within the illite, kaolinite and chlorite groups.
- (b) The clumping observed in M^{n+} exchanged -SWy-2 has shown the closeness of this group and ability to identify individual members from their DMF detection temperatures. For future applications, DMF detection temperatures could aid the choice of a representative montmorillonite for quantitative analysis.
- (c) The detection of non-swelling minerals (kaolinite and chlorite) using dehydroxylation ($m/z = 18$) has highlighted the potential problems due to overlapping dehydroxylation regions and relative concentration of each component, in particular when evaluating the GP-FTIR TIR and RT-MS TIC where the relative contribution from dehydroxylation is small in comparison to DMF. This suggests that the -OH region may benefit from further pre-processing to enhance its features.

(d) The application of the TGA weight loss profile has the ability to successfully discriminate between the four groups chosen, though probably lacks the sensitivity required for quantitative analysis unless more sensitive instrumentation was applied. Preliminary studies (not shown) have investigated the weight loss derivative profiles and have shown that considerable smoothing must be applied with caution to enhance the features therein. It must be noted that the weight loss curves represent all evolved components and in effect is similar to RT-MS TIC. The simplicity of the output is reflected in the fact that most of the variance is contained in the first three scores. Future studies may explore this further.

- (1) GP-FTIR produced reasonable results considering the quality of the profiles obtained, but could in general be subject to fluctuations in detector response rendering it unreliable.
- (2) RT-MS has the potential to be the most sensitive and reliable technique as demonstrated by the quality of the profiles obtained. The selective use of ions 18 and 73 has aided better discrimination and holds the most potential for more sensitive applications. However, the complexity of the output is suggested by the fact that the first three scores only showed 77.38% of the variance within the data which suggests it may show even greater predictive ability in future applications. In view of this RT-MS will be the profile of choice for quantitative chemometric analysis.
- (3) It is important to note that unlike quantitative analysis (Chapter 7), the training sets were pure minerals and

therefore the models were not trained to recognise mixed minerals i.e. Therefore we cannot expect relatively pure clay samples to be a good model for mixed clay mineral samples (standards 1, 2, 4, 15 and 20) diluted by SiO₂. However model③(b) has also highlighted the potential use of selective ion monitoring for particular clay components i.e. m/z = 73 for swelling components (montmorillonite/illite) and m/z = 18 for non-swelling components (kaolinite and chlorite).

Chapter 7 The quantitative characterisation of minerals by chemometric analysis of EGA RT-MS detection profiles

7.0 Introduction

Before constructing any of the experiments herein, all of the components of the mixed mineral standards were evaluated for possible contaminants (i.e. kaolinite in smectite etc.). Because these studies are feasibility studies, it would be neither sensible or practical to use purified minerals for several reasons. Firstly, the time and/or cost constraints would be prohibitive. Secondly, minerals found in rocks are rarely pure and exhibit high physicochemical variance. Therefore it would make more initial sense to use un-purified samples as they would be more representative of that found in nature.

7.1 XRD and DRIFTS evaluation of the components of the mixed mineral standards for quantitative analysis

However, in order to better understand the contribution of each component to a model, it is necessary to examine these constituents by both XRD and DRIFTS spectroscopy, which enables a better understanding of the contribution from each mineral component to the output from a particular standard. This is important in relation to the study of blank samples, which contain no DMF and so provide a starting point from which to observe the effect of DMF on the output of standards. Tables (7.1-7.3) show the characteristic IR bands used for the identification of the individual mineral components.

Table 7.1 Characteristic IR bands for identification of mineral components

Mineral	Characteristic band
Quartz	Overtone/combination region (2000-1400cm ⁻¹) The 800,781 and 695cm ⁻¹ bands
Kaolinite	The four hydroxyl bands between 3696-3620cm ⁻¹ The 916cm ⁻¹ band
Smectite & Illite	Band at 3620cm ⁻¹ or its enhancement in kaolinite is indicative of smectite and/or illite
Smectite	Smectite can be distinguished from illite by the presence of the 1628cm ⁻¹ band
Chlorite	Strong doublet at 3434 & 3565cm ⁻¹ (strong OH stretching from the interlayer hydroxide sheet) enhanced adsorption from 3556 and 3415cm ⁻¹ hydroxyl bands
Feldspar	Wide variation in crystalline order reflected in IR spectra, the enhanced adsorption at 1055cm ⁻¹ could be due to other minerals Albite : quartet of bands between 800-200cm ⁻¹ and a sharp feature at 400cm ⁻¹ , though also seen in Orthoclase
Carbonate	Broad band at 1483cm ⁻¹ and a sharp band at 879cm ⁻¹ ≈

Tables (7.2-7.3) show more specifically the IR bands found in the spectra of layer silicates.

Table 7.2 Specific vibrational frequencies of layer silicates [285]

Specific vibrational mode	Frequency cm^{-1}
OH bending-Al Al OH	nr 915
Al Mg OH	845
Al Fe OH	880
OH stretching (Al rich Montmorillonite)	3626
Si-O-Al	523
Si-O-Si	468
Al-O-Al or Mg (octahedral atoms)	624
Si-O ₂	797

Table 7.3 General vibrational frequencies of layer silicates [120]

General vibrational mode	Frequency cm^{-1}
OH stretching	3700-3500
OH bending	950-800
Si-O stretching	nr 1000
Si-O bending	600-400

Complimentary data from XRD which is diagnostic of the more important clay minerals are shown in table 7.4. XRD can enhance the search for crystalline impurities possibly present in the mixed mineral standard components.

Table 7.4 Diagnostic d-spacings/Å (°2θ) for minerals in this study

Mineral	d-spacing/Å (°2θ)	d-spacing/ Å (°2θ)	d-spacing/Å (°2θ)	d-spacing/ Å (°2θ)	d-spacing/ Å (°2θ)
Chlorite	14.2 (6.22)	7.12 (12.43)	4.75 (18.68)	3.56 (25.01)	
Mica/Illite	9.98 (8.86)	4.97 (17.84)	3.31 (26.93)		
Kaolinite	7.20 (12.29)	3.56 (25.01)			
Montmorillonite	4.48 (19.81)				
Quartz	3.34 (26.67)	4.26 (20.84)			
Orthoclase	3.77 (23.58)	4.22 (21.04)	3.47 (25.66)	3.31 (26.92)	3.29(27.08)
Albite	4.02 (22.10)	3.78 (23.52)	3.63 (24.51)	3.20 (27.86)	3.17 (28.13)

7.2 Results summary of XRD and DRIFTS analysis of the mixed mineral standards components used for quantitative analysis

Greater details of this study can be found in the appendices. Of all the contaminants identified, none were quantified but the intensity of the IR bands and XRD reflections suggest that contaminants are at trace levels. The contaminants identified for each mineral component are summarised in table 7.5.

Table 7.5 Component contaminants identified by XRD and IR

Component	Contaminant
Quartz	- none identified by IR or XRD see MS output for blank samples
SWy-2	-Mica/illite -Quartz and carbonate
KGa-2	- Illite, quartz and carbonate
1-Mt	-Possibly kaolinite and diagenetic NH ₄ ⁺ -illite -Saponite
CCa-1	-Carbonate
Albite	-Possible swelling mineral component (unidentified), quartz, maghemite and orthoclase
Orthoclase	-Quartz

7.3 MS component features of the data output of mixed mineral standards (1-21)

This section reports the detection features seen when the untreated components are subject to EGA. Essentially these experiments are blanks which looked at three different approaches:

(1) untreated (no DMF) individual components

To evaluate the EGA detection of the six individual components

(2) untreated (no DMF) mineral components in a seasand (quartz) feldspar mixture

To evaluate the addition of both quartz and feldspar on the EGA of the clay mineral components

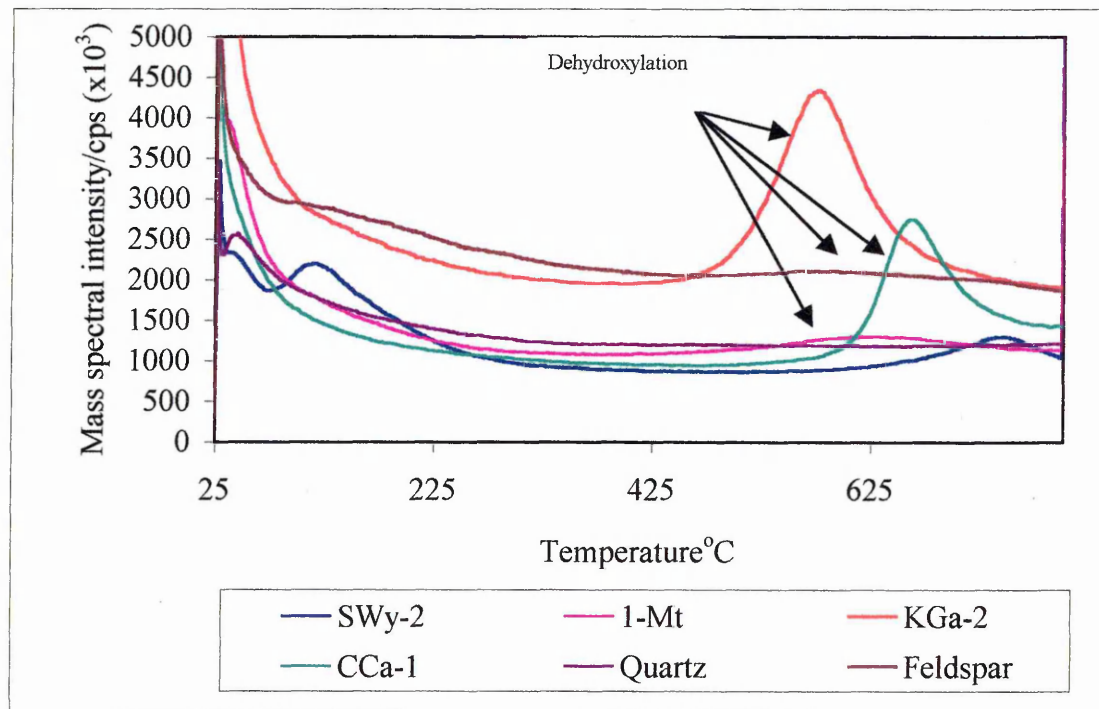
(3) 3 untreated (no DMF) mineral mixtures

To evaluate the combination of all six components

Figure 7.1 demonstrates ion $m/z = 18$ (H_2O) for all standard components. This area highlights the dehydroxylation features which were used during quantitative analysis.

7.4 Untreated (no DMF) individual mineral components

Figure 7.1 RT-MS ($m/z = 18$) for mineral component blanks analysed separately



7.4.1 Summary of RT- MS ion $m/z = 18$

As seen in figure 7.1, the two most promising features, though not resolved, are the dehydroxylation of KGa-2 (kaolinite) and CCa-1 (chlorite). Note, the dehydroxylation of SWy-2 may be masked as a useful feature and will depend on the concentration of KGa-2 and CCa-1 respectively. This does not pose a problem for SWy-2 detection because the DMF parent ion $m/z = 73$ will be shown to be an excellent quantitative detection feature. Unfortunately, illite is also masked within the dehydroxylation region and as discussed in chapter 6, will perhaps provide the greatest challenge because it evolves considerably less DMF and it occurs within the same region as SWy-2. For quartz $m/z = 18$ (detection of water) consists of a slow

1977, Vol. 15, No. 1, pp. 1-12

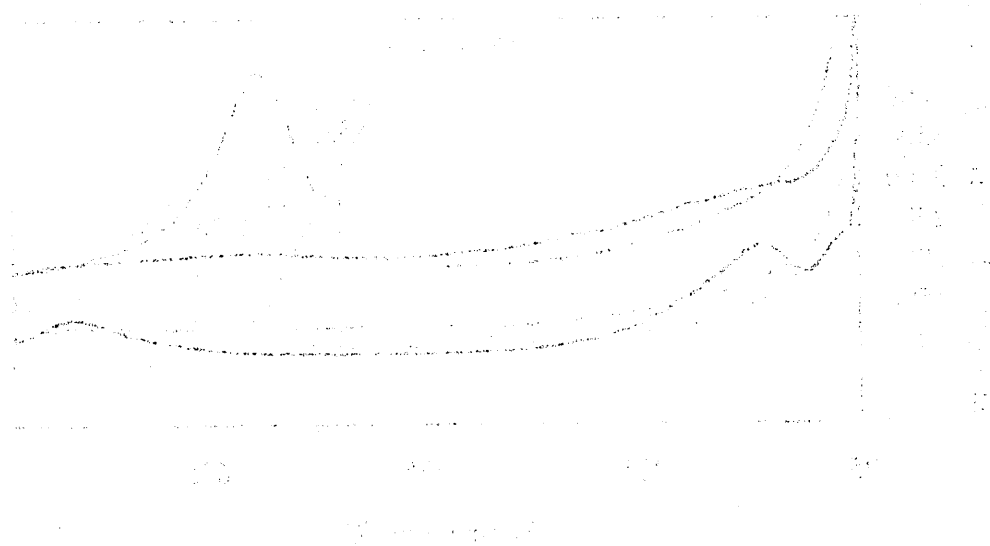


Fig. 1. Dependence of $\log(\eta/\eta_0)$ on temperature for various samples. The curves are labeled: 1) Sample 1; 2) Sample 2; 3) Sample 3; 4) Sample 4.

The curves in Figure 1 show the dependence of the logarithm of the relative viscosity, $\log(\eta/\eta_0)$, on temperature for four different samples. Sample 1 exhibits a sharp peak at approximately 30°C, indicating a significant change in viscosity at this temperature. Sample 2 shows a broader peak around 40°C. Samples 3 and 4 show a more gradual increase in $\log(\eta/\eta_0)$ with temperature, with a slight dip or change in slope around 70-80°C. The y-axis represents $\log(\eta/\eta_0)$ and ranges from 0 to 4. The x-axis represents temperature in degrees Celsius, ranging from 20 to 80.

removal of physisorbed water up to about 330°C. There is no evidence of any clay mineral dehydroxylation. The detection of ion $m/z = 44$ (fig. 7.14) probably correspond to CO_2 trapped in the structure (420°C), traces of organic matter (600°C) and carbonate (calcite) that was naturally mixed with the seasand (700°C). For feldspar $m/z = 18$ consists a slow removal of physisorbed water up to about 450°C. There also appeared to be some evidence of clay mineral dehydroxylation which may correspond to illite dehydroxylation with overlapping peaks at 570° C and 640°C as previously identified (table 7.5). However, if fig 7.2 is observed the intensity range of the $m/z = 18$ ion lies within what may be considered baseline fluctuation when compared to the detection of the most intense maxima for ion $m/z = 44$.

Figure 7.2 RT-MS ($m/z = 18$) for feldspar

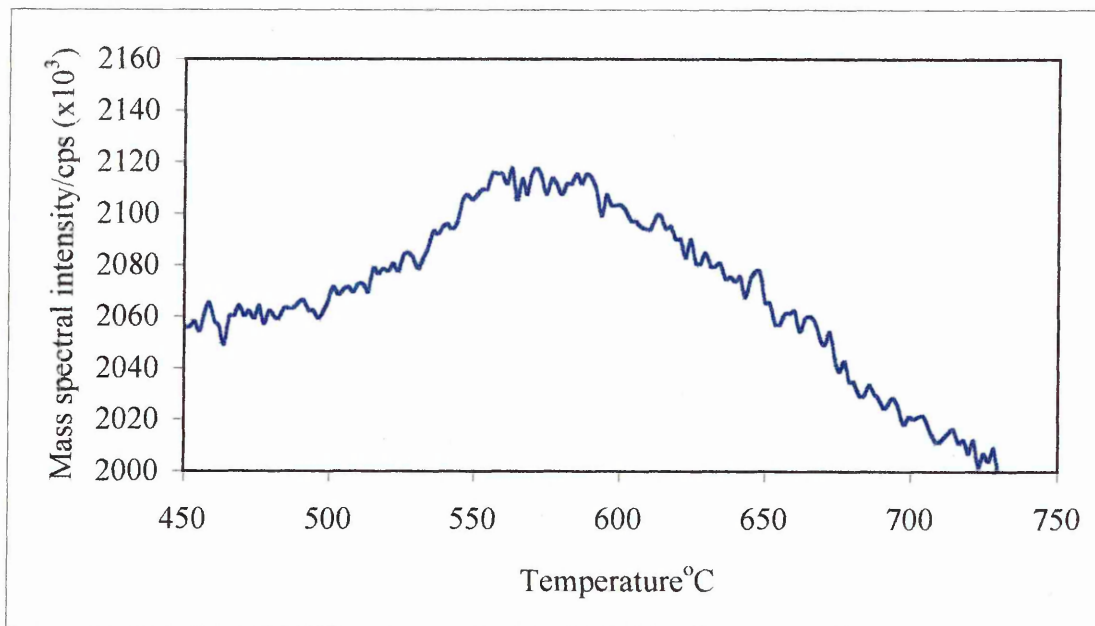
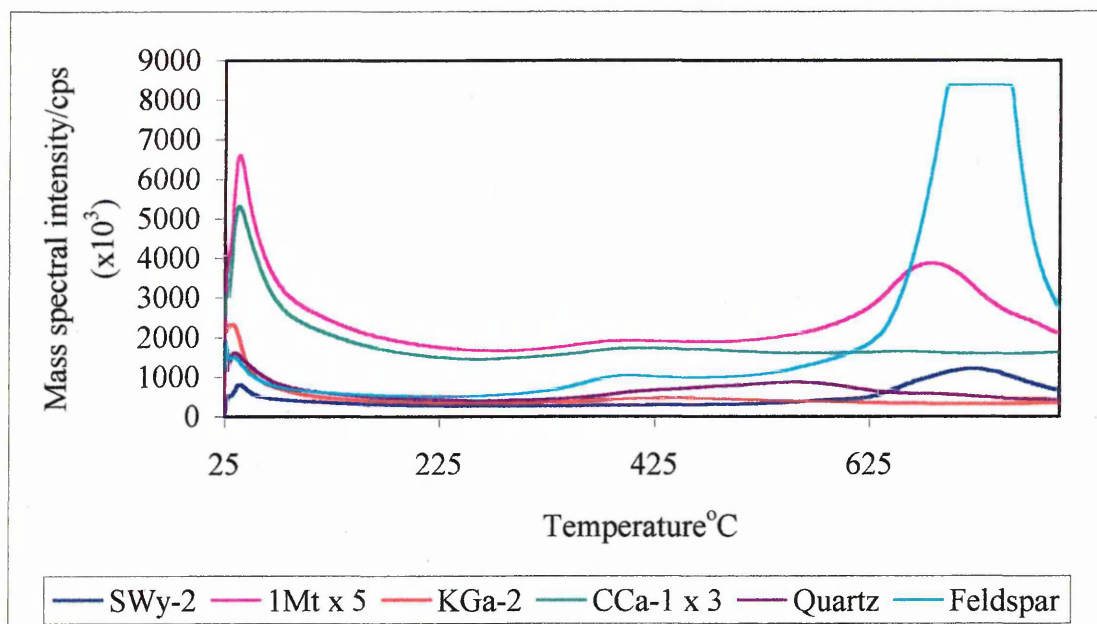


Figure 7.3 RT-MS ion $m/z = 44$ for all mixed mineral component blanks analysed separately (no DMF)



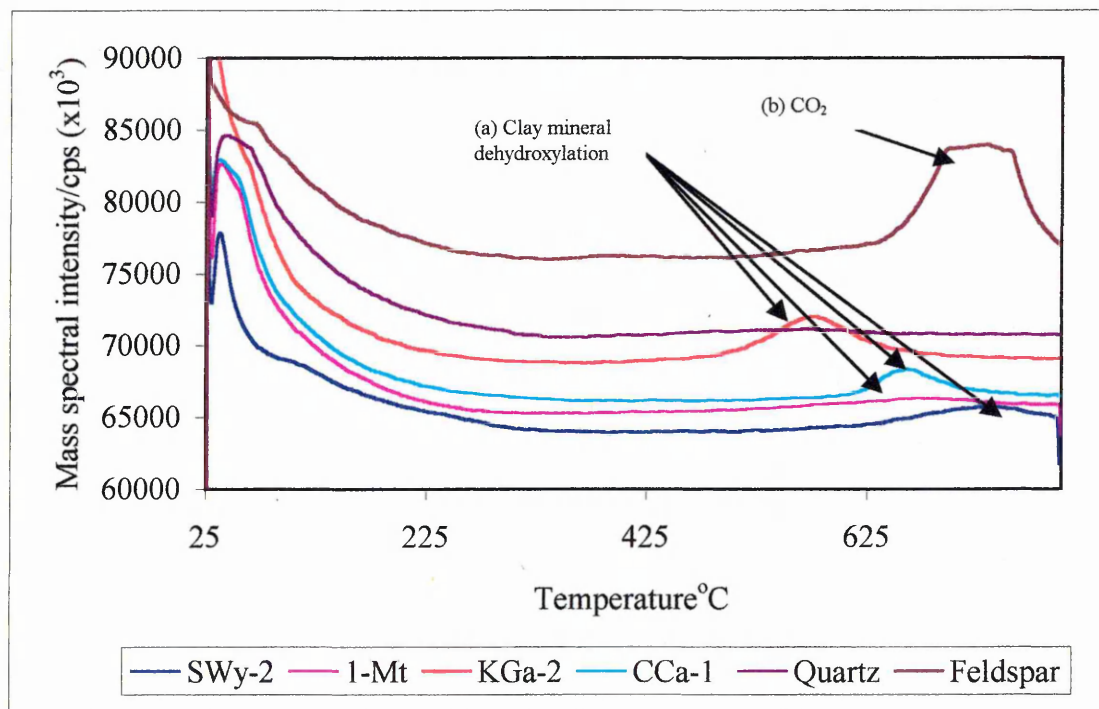
7.4.2 Summary of RT-MS ion $m/z = 44$

(1) For the same sample weight feldspar produces considerably more ion $m/z = 44$ which results in a capped peak indicating detector saturation. Ion $m/z = 44$ used as a characteristic feature could not be relied upon for several reasons:

(2) Firstly the detection events are unresolved

Ion $m/z = 44$ would vary in test samples as the carbonate and organic contents would vary and therefore could not be separated from the DMF fragment ion $m/z = 44$. In addition, vigorous chemical treatment is needed to remove organic matter and carbonates. In turn this would change the pore structure of rock samples leading to loss of clay mineral analyte, changing the surface mineralogy and resulting in un-representative results.

Figure 7.4 RT-MS TIC for all mixed mineral component blanks analysed separately (no DMF)



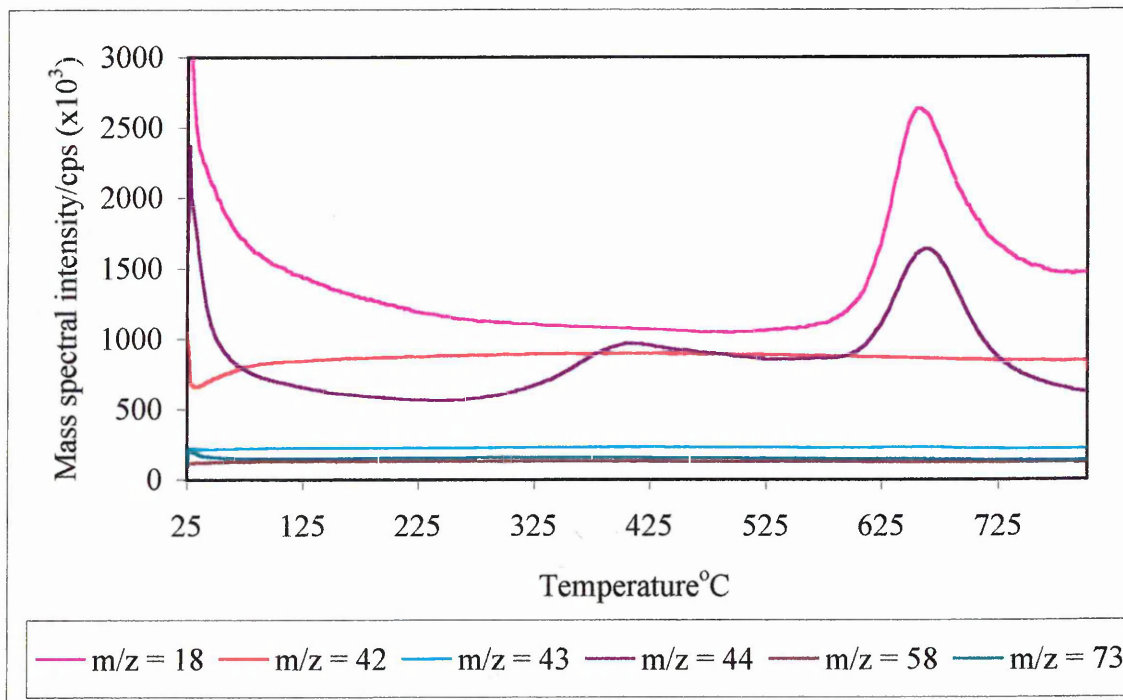
7.4.3 Summary of RT-MS total ion current (TIC) for mixed mineral component blanks analysed separately (no DMF)

For all untreated clay mineral standards dehydroxylation dominates the TIC. Whereas for quartz the TIC is featureless except for the detection of ion $m/z = 18$ (physisorbed H₂O) at low temperature as seen in figure 7.1. In comparison the feldspar mix (albite and orthoclase) show ion $m/z = 44$ to be the most prominent detection feature which will be briefly discussed when the mineral mixtures are examined.

7.5 Examination of untreated components in a quartz feldspar mixture (no DMF) by RT-MS

The individual mineral components were then analysed in a mixture of 10% clay mineral 80% quartz and 10% feldspar to evaluate the combination of each clay component with the non clay minerals (quartz and feldspar) added to the mixed mineral standards.

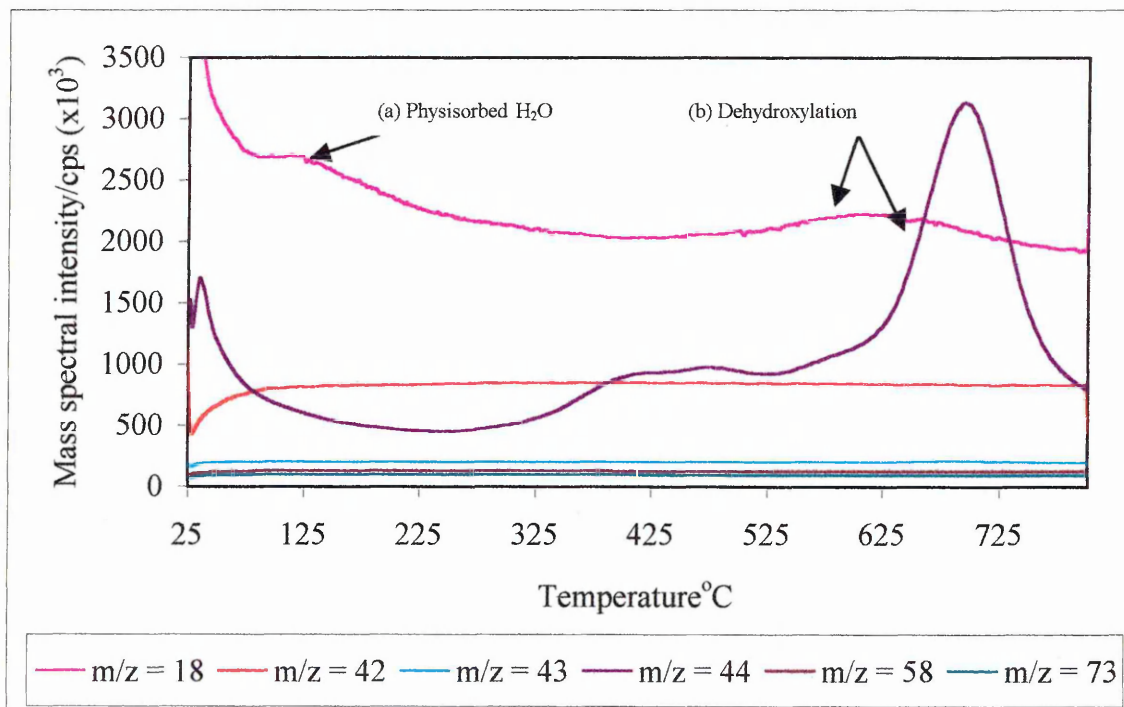
Figure 7.5 RT-MS reconstructed ion chromatograms for 10% Chlorite (CCa-1), 80% Quartz (Seasand), 10% Feldspar (80% Orthoclase, 20% Albite)



7.5.1 Summary of RT-MS reconstructed ion chromatograms for 10% Chlorite (CCa-1), 80% Quartz (Seasand), 10% Feldspar (80% Orthoclase, 20% Albite)

In figure 7.5, the ion $m/z = 18$ (detection of water) consists of one detection maximum. However from the outset of detection there is evidence for a slow removal of physisorbed water. The water maximum which is skewed towards high temperature, begins at 500°C and reaches its maxima at 660°C corresponding to the dehydroxylation of the structural unit. The skewed section to the right of the maximum suggests another unresolved detection maxima which may correspond to the beginning of dehydroxylation of the brucite layer. The detection of ion $m/z = 44$ at approximately 420°C and 670°C probably corresponds to the release of CO₂ trapped within the structure and decomposition of carbonate material (carbonate) that was naturally mixed with the component parts of the (clay/seasand/feldspar) mixture.

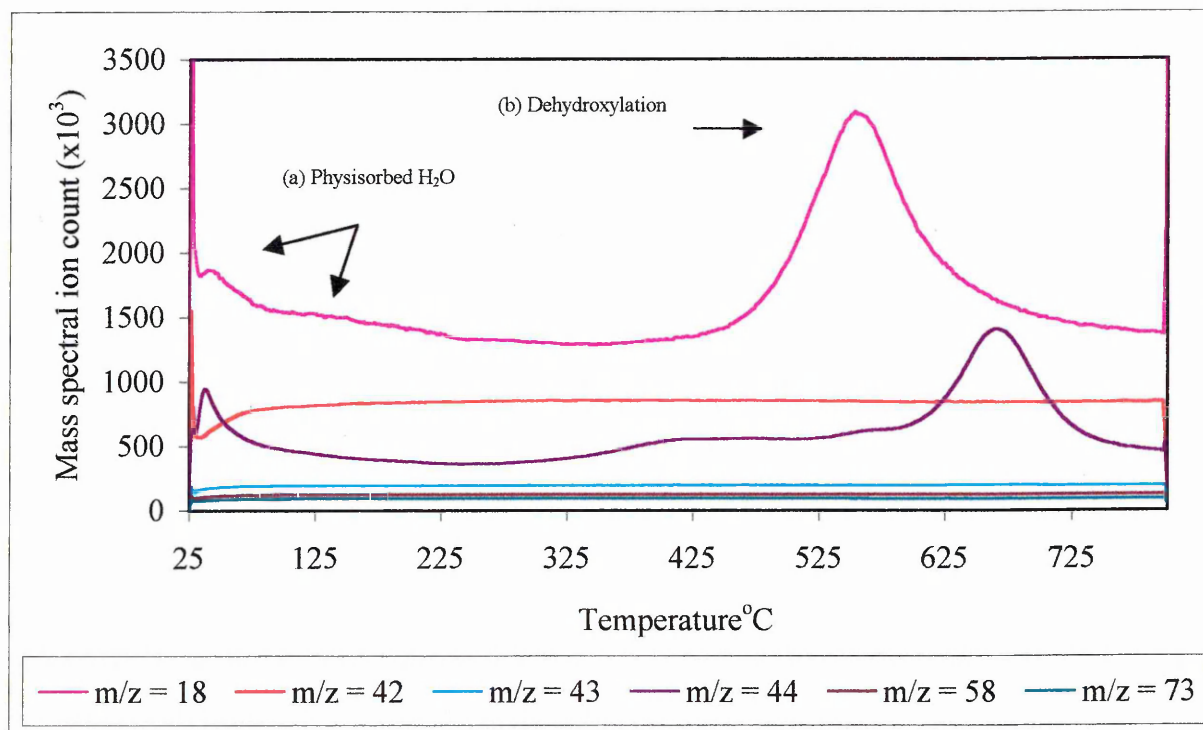
Figure 7.6 RT-MS reconstructed ion chromatograms for 10% Illite (1-Mt), 80% quartz (Seasand), 10% feldspar (80% orthoclase, 20% albite)



7.5.2 Summary of RT-MS reconstructed ion chromatograms for 10% illite (1-Mt), 80% quartz (Seasand), 10% feldspar (80% orthoclase, 20% albite)

Detection of H₂O (m/z = 18) consists of three detection maxima. However from the outset of detection there is evidence for a slow removal of physically adsorbed water showing a maximum at (a) 100 $^{\circ}$ C up to about 350 $^{\circ}$ C. As seen below the second and third maxima are composed of two overlapping peaks at approximately (b) 570 and 640 $^{\circ}$ C corresponding to the dehydroxylation of the structural unit. The detection of ion m/e = 44 at 420 $^{\circ}$ C \approx probably corresponds to CO₂ trapped in the structure and traces of carbonate (calcite) that was naturally mixed with the component parts of the (clay/seasand/feldspar) mixture accounting for the maxima observed at 700 $^{\circ}$ C.

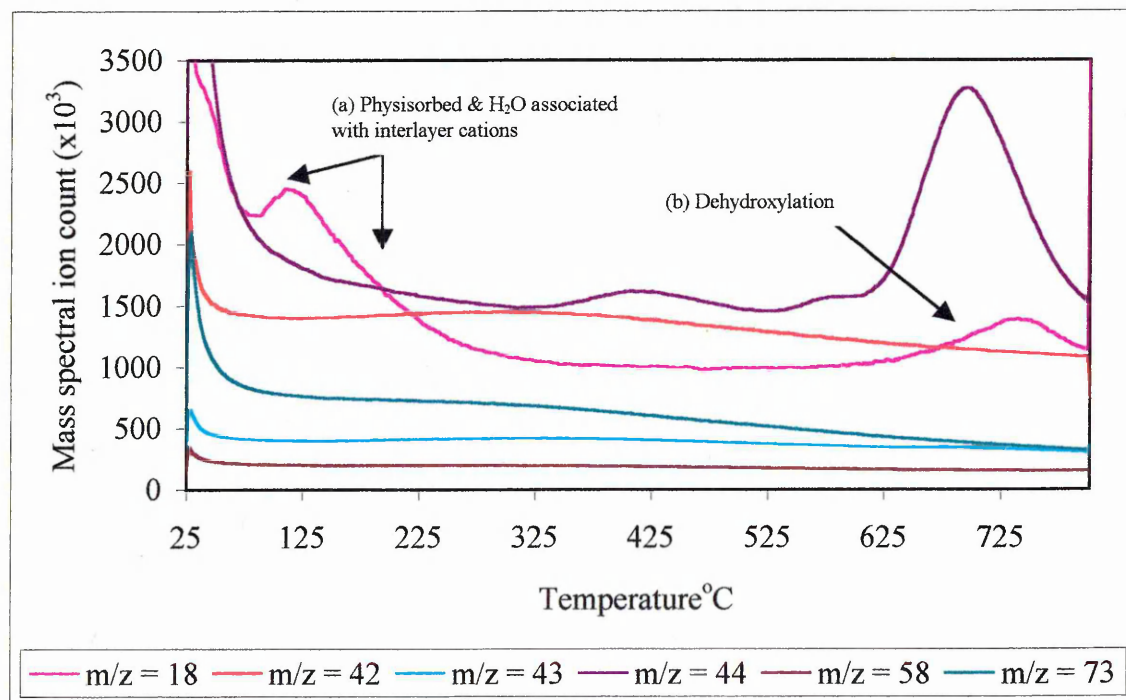
Figure 7.7 RT-MS reconstructed ion chromatograms for 10% kaolinite (KGa-2), 80% quartz (Seasand), 10% feldspar (of which 80% Orthoclase, 20% Albite)



7.5.3 Summary of 10% kaolinite (KGa-2), 80% quartz (Seasand), 10% feldspar (of which 80% Orthoclase, 20% Albite)

The detection of $m/z = 18$ (H_2O) consists of one detection maximum. However, from the outset of detection there is evidence for a slow removal of physisorbed water up to about 250°C. The maximum around 550°C corresponds to the dehydroxylation of the structural unit. The non-symmetry in the dehydroxylation maxima to higher temperature may be caused by the corresponding evolution of CO_2 . The detection of ion $m/z = 44$ at about 420°C, 575-600°C and 670°C probably correspond to decomposition of organic matter/ CO_2 trapped in the structure and carbonate that was naturally mixed with the component parts of the (clay/seasand/feldspar) mixture.

Figure 7.8 RT-MS reconstructed ion chromatograms for 10% montmorillonite (SWy-2), 80% quartz (seasand), 10% feldspar (of which 80% Orthoclase, 20% Albite)



7.5.4 Summary of 10% montmorillonite (SWy-2), 80% quartz (seasand), 10% feldspar (of which 80% Orthoclase, 20% Albite)

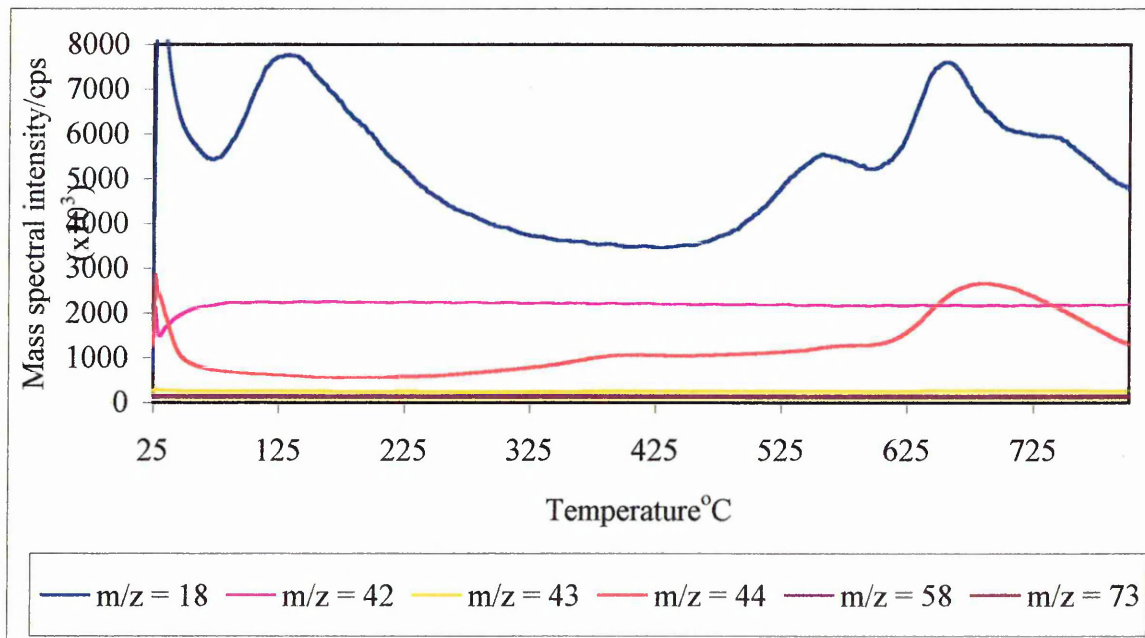
Detection of $m/z = 18$ (H_2O) consists of two detection maxima. The first maxima is centered at about $120^\circ C$ and is skewed to higher temperatures showing a slow removal of physisorbed water which is unresolved from water associated with the interlayer cations to about $370^\circ C$. The maxima around $730^\circ C$ corresponds to the (b) dehydroxylation of the structural unit.

The detection of ion $m/z = 44$ at $420^\circ\text{C} \approx$ probably corresponds to CO_2 trapped in the structure, traces of organic matter 600°C and carbonate(calcite) 700°C that was naturally mixed with the clay.

7.6 Examination of untreated (no DMF) mineral mixtures

It is also useful to examine several blank standards (figs. 7.9-7.11), to give the reader a picture of the overlapping detection profiles of the varying concentrations of montmorillonite, kaolinite and chlorite without DMF i.e. intercomponent interactions.

Figure 7.9 RT-MS of standard 1 (blank-no DMF) 70% Quartz, 10% SWy-2, 4% KGa-2, 4% 1-Mt-Illite, 8% CCa-1, 4% Feldspar



7.6.1 Summary standard 1 (blank-no DMF) 70% Quartz, 10% SWy-2, 4% KGa-2, 4% 1-Mt-Illite, 8% CCa-1, 4% Feldspar

As seen in figure 7.9, without DMF detection, (as seen by the flat detection profiles for DMF fragment ions $m/z = 42, 43, 58$ and 73) $m/z = 18$ (H_2O) dominates the reconstructed chromatogram, the only other detection feature being ion $m/z = 44$.

Figure 7.10 RT-MS of standard 7 (blank-no DMF) 87% Quartz, 0% SWy-2, 10% KGa-2, 2% 1-Mt-Illite, 0% CCa-1, 1% Feldspar

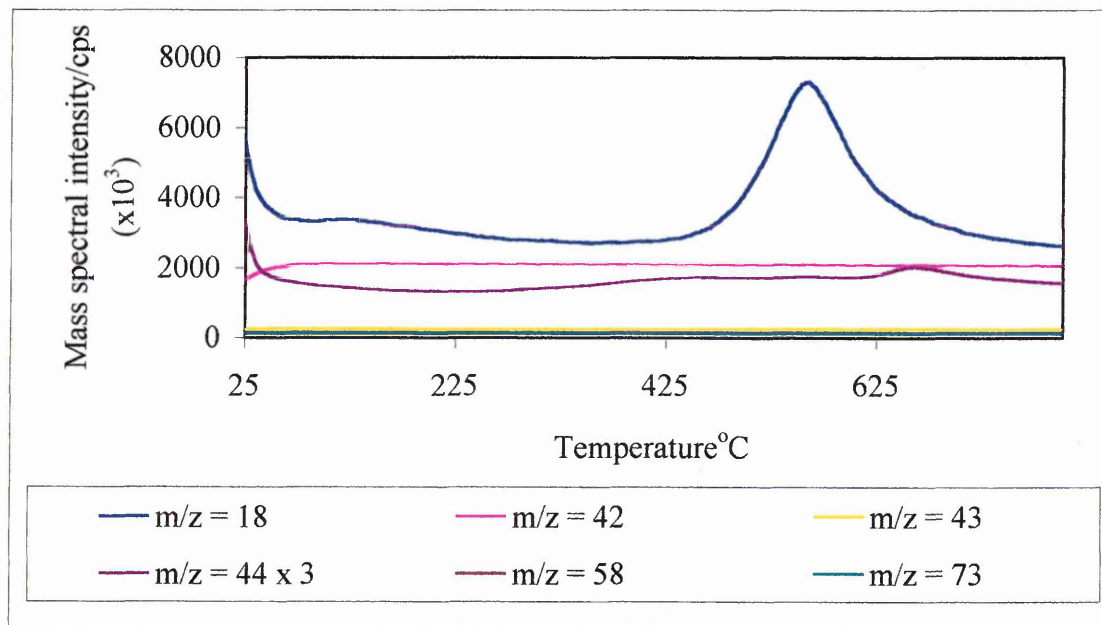


Figure 7.11 RT-MS of standard 16 (blank-no DMF) 74% Quartz, 2% SWy-2, 6% KGa-2, 4% 1-Mt-Illite, 10% CCa-1, 4% Feldspar

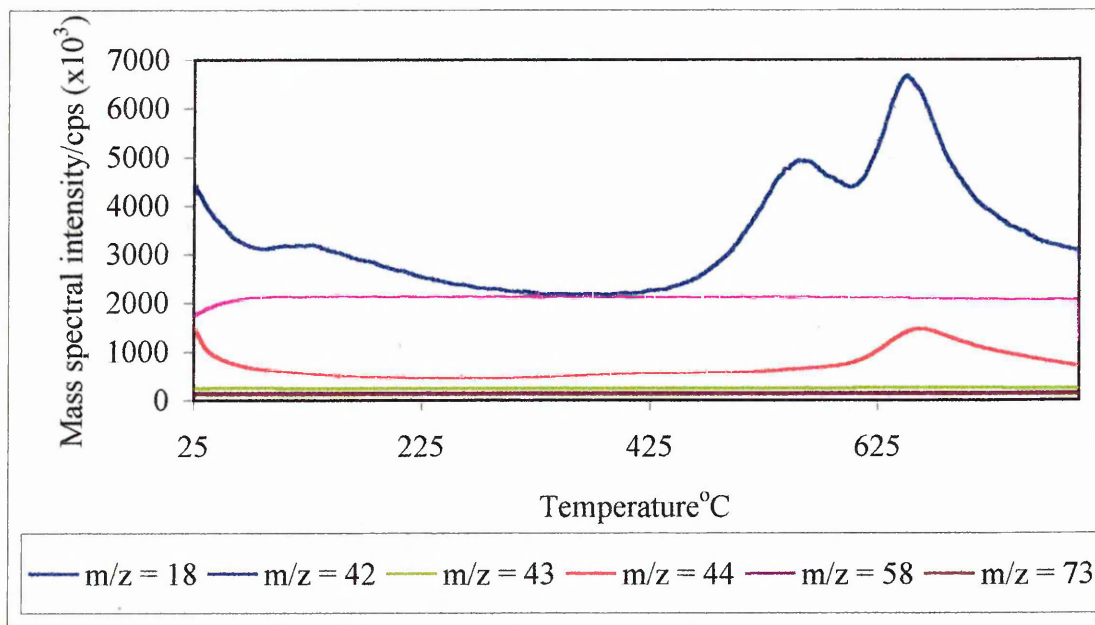


Figure 7.10 shows how KGa-2 dehydroxylation dominates the reconstructed chromatogram. Whereas ion $m/z = 44$ been shown to evolve slightly after dehydroxylation which possibly indicates it is associated with illite, feldspar or quartz as KGa-2 does not detect $m/z = 44$ above 415°C . In comparison, figure 7.11 is dominated by the combined dehydroxylation of kaolinite and chlorite ($m/z = 18$) and $m/z = 44$ at higher temperature.

7.6.2 RT-MS summary (evaluation of source of $m/z = 44$)

For 1-Mt mix (quartz and feldspar) there seems to be 4 peaks for CO_2 415, 480 (unresolved), 600 & 670 but not for 1-Mt (alone), this peak does not seem to be present in either quartz or feldspar. This suggests that this is the result of the overlap

of the beginning of the high temperature feldspar maxima (440°C) and the lower temperature 1Mt maxima (415°C) with some contribution from quartz.

- (1) CCa-1 also suggests it has an extra $m/z = 44$ peak at 480°C in both the mix and alone. This may suggest that feldspar is already present in CCa-1.
- (2) It is obvious from the above figures 7.21-7.23 and other details of the desorption profiles, that feldspar contributes most to the CO₂ evolution at 670°C.
- (3) In SWy-2, both quartz and feldspar contribute to the CO₂ at 415°C as in SWy-2 (alone) there is no evidence for the peak at 400°C.
- (4) The contribution from ion $m/z = 44$ will vary because the contribution from each mineral component varies within mixtures i.e. CO₂, carbonate and organic matter.

7.7 Quantitative characterization of mixed mineral standards by PLS multivariate analysis

7.7.1 Introduction

As previously mentioned during chapter 6 (qualitative studies), RT-MS detection profiles would be used for quantitative characterisation. The studies herein consist of four models constructed within the Grams32-PLS-PLUS IQ software [371].

- (A) Model① which evaluates the RT-MS TIC (derivatised)
- (B) Model② which evaluates RT-MS $m/z = 73$ (DMF parent ion)
- (C) Model③ which evaluates RT-MS $m/z = 18$

7.7.2 Sample Preparation (mixed mineral standards)

Training set standards consisted of 6 components known to be present in sandstone cores i.e. quartz, feldspar, montmorillonite, kaolinite, illite and chlorite. The minerals used to represent each mineral group are shown in table 7.6. Carbonates were not included, though they are known to be present as component constituents.

Table 7.6 Mixed mineral standards components

Group 1 (Quartz)	Group 2 (Montmorillonite)	Group 3 (Kaolinite)	Group 4 Illite	Group 5 Chlorite	Group 6 Feldspar
Seasand	SWy-2	KGa-2	1-Mt-Illite	CCa-1	80% Orthoclase / 20% albite

7.7.3 Collection of RT-MS gas detection profiles

All gas detection profiles were collected using the same EGA experimental parameters used for qualitative analysis (Chapter 6).

7.7.4 Evaluation of the linearity of DMF detection versus increasing montmorillonite concentration

Because montmorillonite is considered to be the most important component, a series of experiments were constructed to assess the linear response of DMF detection (using the integrated ion area of the DMF parent ion $m/z = 73$) with increasing montmorillonite concentration. This consisted of preparing 1-8 % SWy-2 diluted with seasand. The effects of grinding during sample preparation was also investigated as initial sample preparation showed evidence of clay mineral aggregation. This could have an effect on effective mixing (i.e. avoid clumping) and therefore cause problems regarding representative sub sampling from the main batch. This could lead to a reduced uptake of DMF which would effect the quantification of swelling mineral components.

7.7.5 Results of linearity of DMF detection versus increasing montmorillonite concentration

Figure 7.12 Calibration plot for 1-8% Ca-SWy-2/Seasand (ground & mixed)

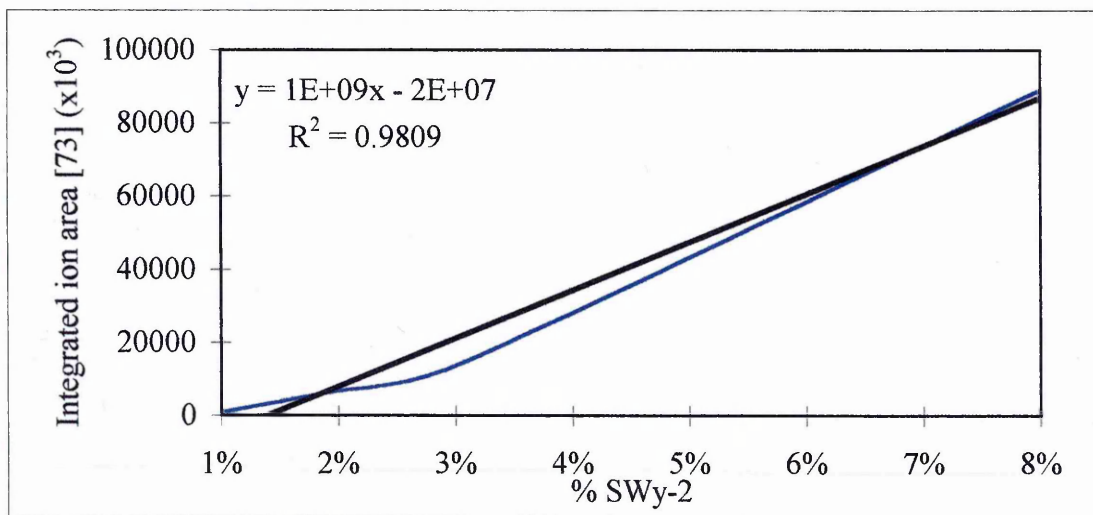
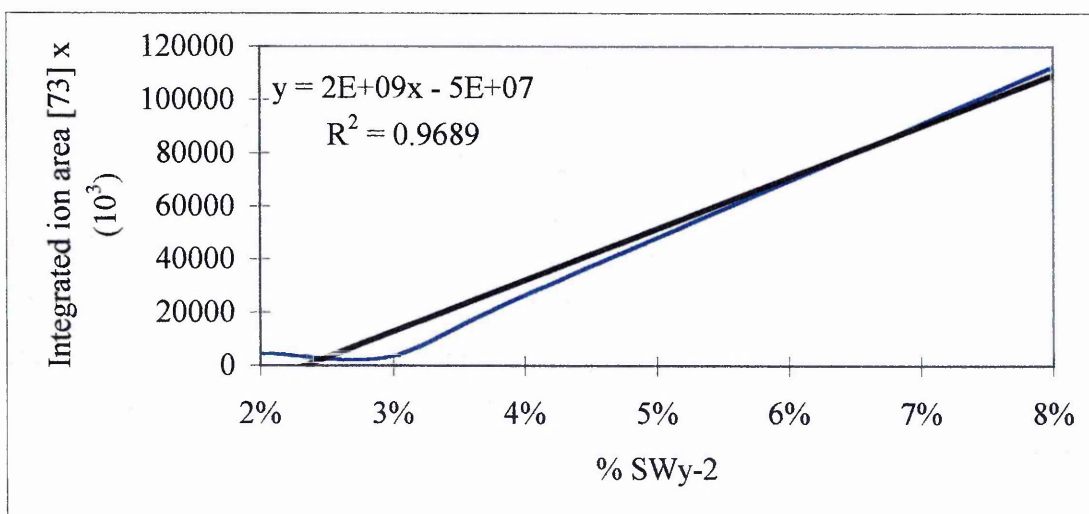


Figure 7.13 Calibration plot for 1-8% Ca-SWy-2/Seasand (un-ground & un-mixed)



7.7.6 Summary of the linearity of DMF detection versus increasing montmorillonite concentration

The results of DMF desorbed from 1-8% SWy-2 (in seasand) shows a good linear response whether the sample has been ground and mixed or un-ground and un-mixed. The ground and mixed sample produced an R^2 value of 0.98 whereas the un-ground sample produced an R^2 value of 0.96. In both cases the reproducibility of the $m/z = 73$ profile was excellent. The lower R^2 value for un-ground and un-mixed samples did show non-linearity between 1-2 % SWy-2 and may be attributed to the sample being less homogenized. However, it must be noted that the un-ground and un-mixed sample showed a steeper slope which is most probably due to the lack of mixing, in turn producing a more rapid desorption response. This may be due to the fact that in un-ground and un-mixed samples, SWy-2 was merely placed on top of the seasand. Therefore it was not coated on the grains as was observed in the ground and mixed samples, and so DMF desorbing from these sample would not have to travel through the seasand bed. In view of these results, all mineral mixture samples for DMF incubation were ground for a period five minutes to aid mixing.

7.7.7 Mixed mineral sample preparation

This study consisted of 21 mixed mineral standards. All standards (batch 5g) were ground for 5 minutes and mixed by rotation for a period of two days. The batch weight was high so as to reduce the weighing error associated with smaller samples. A representative sample (15 mg) of each standard was obtained by coning and quartering the main batch. All standards were then incubated in a DMF saturator for a

period of three weeks. SWy-2 was chosen to represent the montmorillonite group as it is very similar to that found in core samples. Its predominant interlayer cation are of the order $\text{Na} > \text{Ca} > \text{Mg}$. One montmorillonite clay type was chosen, as using a variety of montmorillonites would introduce a concentration and a profile error, caused by the different weight losses and detection temperatures attributed to different interlayer cations (chapter 6). The weight percentage concentration of each mineral component is given in table 7.7.

Table 7.7 Weight percent concentrations of the components in the mixed mineral standards

Std-no	Quartz	Mont.	Kaolinite	Illite	Chlorite	Feldspar
1	70	10	4	4	8	4
2	75	10	0	7	8	0
3	86	0	0	8	1	5
4	75	9	10	0	3	3
5	55	6	3	10	9	17
6	86	0	6	0	2	6
7	87	0	10	2	0	1
8	80	8	5	1	0	6
9	72	6	3	5	6	8
10	80	4	8	4	4	0
11	90	5	0	2	3	0
12	80	10	5	0	0	5
13	86	2	7	3	1	1
14	78	0	0	0	9	13
15	87	0	5	6	0	2
16	74	2	6	4	10	4
17	96	0	0	1	2	1
18	82	0	3	0	5	10
19	83	5	3	5	2	2
20	60	9	10	6	7	8
21	85	0	0	3	3	9

7.7.8 Evaluation of co-linearity between mixed mineral standard components

An important consideration when constructing a series of mixed component standards is minimising co-linearity between component concentrations. Co-linearity may be described as the linear dependence among variables. It is important to remember that the models herein do not calibrate a direct relationship between the component data and spectral response. Instead they try to correlate the change in concentration to some corresponding spectral changes. Therefore when components concentrations are collinear, multivariate models cannot differentiate them and the calibrations will be unstable. To a multivariate model, collinear concentration data will be interpreted as one component [371]. In these eigenvector-based models, only one factor will arise which describes nearly all the variance in the data. The easiest way to monitor this is to plot the sample concentration of one model component against the other components. The co-linearity between the concentration of one mixed mineral component and another is given in table 7.8.

Table 7.8 Results of co-linearity between training set component concentrations

| R² values |
|-----------------------------|-----------------------------|-----------------------------|-----------------------------|-----------------------------|
| Q x M = 0.34 | M x K = 0.02 | K x I = 0.009 | I x C = 0.15 | F x C = 0.24 |
| Q x K = 0.06 | M x I = 0.09 | K x C = 0.04 | I x F = 0.01 | |
| Q x I = 0.34 | M x C = 0.07 | K x F = 0.03 | | |
| Q x C = 0.50 | M x F = 0.009 | | | |
| Q x F = 0.33 | | | | |

Where Q = Quartz M = Montmorillonite K = Kaolinite I = Illite C = Chlorite F = feldspar

7.7.9 Summary of co-linearity between training set component concentrations

Table 7.8 demonstrates that there is little linear relationship between any of the clay minerals under study. However, there is some relationship between quartz and the other components. This is considered to be negligible because of the inert nature of quartz, though the magnitude of this relationship has not been ascertained.

7.8 Model ① using RT-MS TIC (derivatised)

Model① used the whole TIC during training set calibration. The data compression method was PLS-1 and the data was pre-processed using mean centering, variance scaling and Savitzky Golaz 2nd derivative. Mean centering involves calculating the average spectrum of all the spectra in the training set and then subtracting the result from each spectrum. In addition, the mean concentration value for each constituent is calculated and subtracted from the concentrations of every sample. By removing the mean from the data, the differences between the samples are substantially enhanced in terms of both concentration and spectral response. This usually leads to calibration models that give more accurate predictions.

Variance scaling is used to emphasize small variations in the data by giving all values equal weighting. Variance scaling is calculated by dividing the response at each spectral data point by the standard deviation of the responses of all training spectra at that point. The concentration data is scaled likewise for each component. This pre-processing algorithm is most useful when analysing minor (low concentration) constituents that have spectral bands that overlap those of major (higher concentration) constituents i.e. dehydroxylation in the presence of DMF. By

giving all the information in the data equal weighting, the calibration errors in the model should be more consistent across all constituents.

An excellent method of removing baseline effects is to use derivative spectra. The first derivative simply measures the slope of the profile at a given point, whereas the second derivative measures the change of the slope of the curve. This approach ignores both offset and tilt that may exist in the profile and is therefore a very effective method for removing the baseline offset and slope from a spectrum. However, under most conditions the standard point approach of estimating the derivative from between point differences only succeeds in enhancing the noise present in the spectrum. Better algorithms include the Savitsky-Golay method, which use information from localized segments to calculate the derivative at a particular maxima rather than the difference. This avoids noise enhancement and can apply some smoothing to the data. To avoid smoothing out too much or too little of the profile detail, a good general rule is to use sufficient number of points to cover the full width of the at half height of the largest spectral feature.

Cross validation has been applied as it is the most computationally intensive method of optimising a model. In effect, cross-validation attempts to emulate predicting “unknown” samples by using the training set data itself. Cross-validation estimates the performance of the model. Since the predicted samples are not the same as the samples used to build the model, the calculated PRESS value (refer to Ch. 2 for greater detail) is a very good indication of the error in the accuracy of the model when used to predict “unknown” samples in the future. The larger the training set and the smaller the groups of samples left out in each pass (optimally only one sample at a time, but this can be very time consuming), the better this estimate will be. In effect, the model is validated with a large number of “unknown” samples (since each training

sample is left out at least once) without having to measure an entirely new test set of data.

7.8.1 Pre-processing

The TIC for the mixed mineral standards was subject to a variety of experimental pre-processing techniques. The experimental parameters for model ① as shown in table 7.9 produced the training set with the best R^2 values.

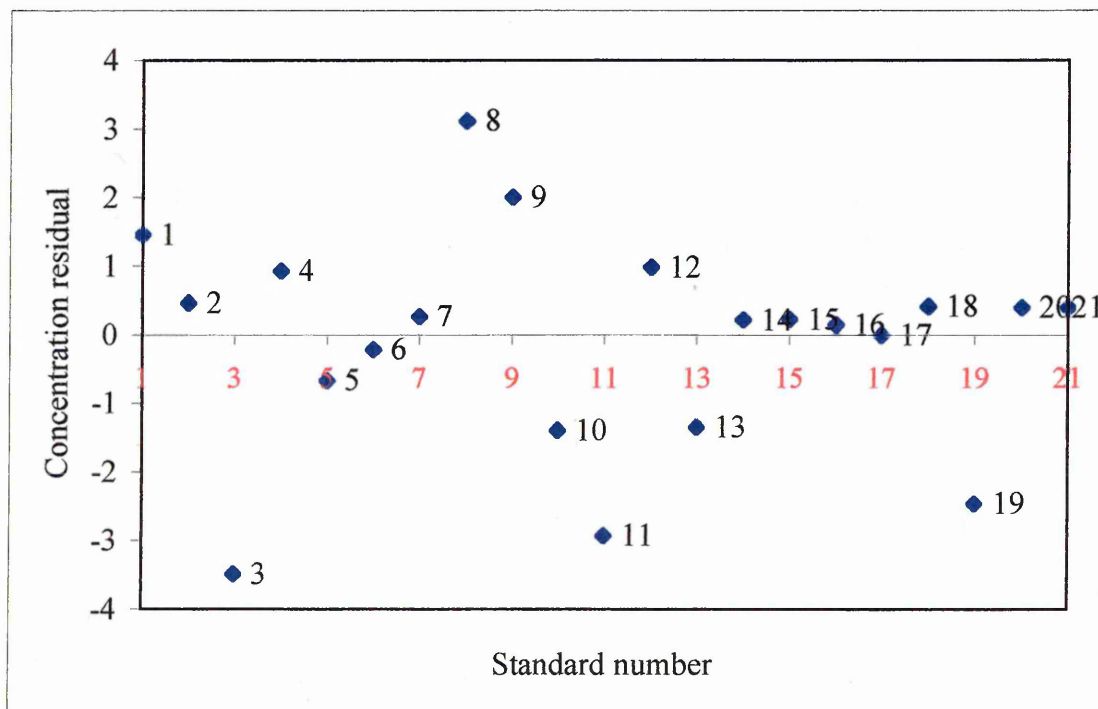
Table 7.9 Chemometric experimental details for TIC model ① training set

Data points	Calibration type	Diagnostic type	Pre-processing
417	PLS-1 (10 factors)	Cross-validation	Mean centre/ Variance scaling/ Auto baseline correction Savitsky-Golay 2 nd derivative-75 points

One powerful tool for outlier detection is the cross-validation procedure used to calculate the PRESS values previously described. When the optimum number of factors for the model has been determined, the predicted concentrations of each training sample from the sample rotation with the selected factor model can be used for outlier detection. The difference between the actual and predicted concentrations for a sample is known as the concentration residual. The model attempts to account for all the variations in the training data when the calibration calculations are performed. Therefore, the prediction error of most of the samples should be approximately the same. Samples that have significantly larger concentration residuals than the rest of the training set are known as concentration outliers. Three

standards were left out of the training set (std: 3, 8, and 9) for montmorillonite and two for kaolinite (std 3, 20) which were highlighted as potential outliers when observing the associated concentration (fig. 7.14). The number of the standard is found to the right of its position.

Figure 7.14 RT-MS TIC model[®] training set concentration residuals for SWy-2



7.8.2 Results of model ① using RT-MS TIC (derivatised)

Figure 7.15 RT-MS TIC model① cross validation PRESS plot for SWy-2

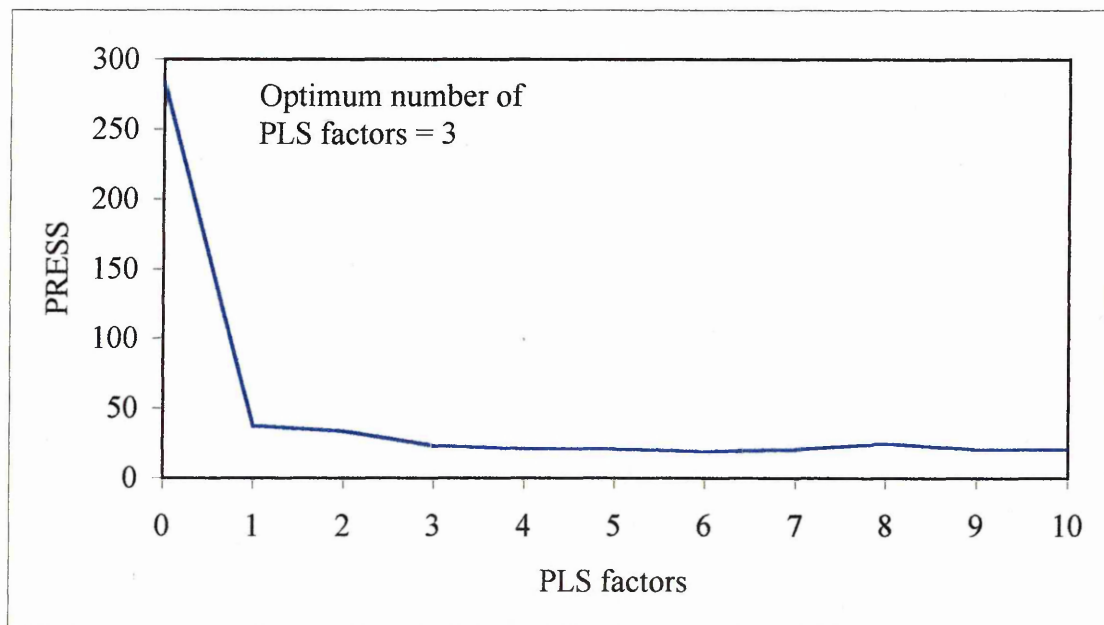


Figure 7.16 RT-MS TIC model① calibration plot for SWy-2 using 3 PLS factors

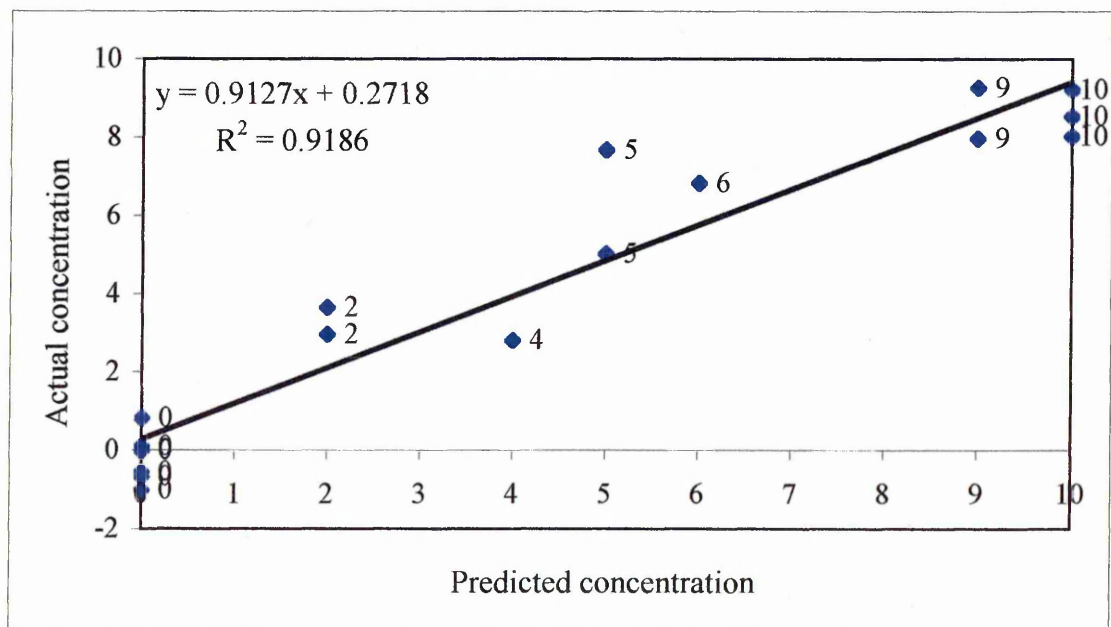


Table 7.10 RT-MS TIC model① actual V predicted concentration for SWy-2

Standard-Actual Concentration%	Predicted Concentration%	Standard-Actual Concentration%	Predicted Concentration%	Standard-Actual Concentration%	Predicted Concentration%
Std 1-10	8.52	Std11-5	7.67	Std18-0	-0.00
Std 2-10	9.20	Std12-10	8.02	Std19-5	5.01
Std 4-9	7.96	Std13-2	3.65	Std 20-10	9.26
Std 5-6	6.83	Std14-0	-0.68	Std-21-0	-0.56
Std 6-0	0.01	Std15-0	0.10		
Std 7-0	0.82	Std 16-2	2.95		
Std10-4	2.81	Std-17-0	-1.02		

Figure 7.17 RT-MS TIC model① cross validation PRESS plot for KGa-2

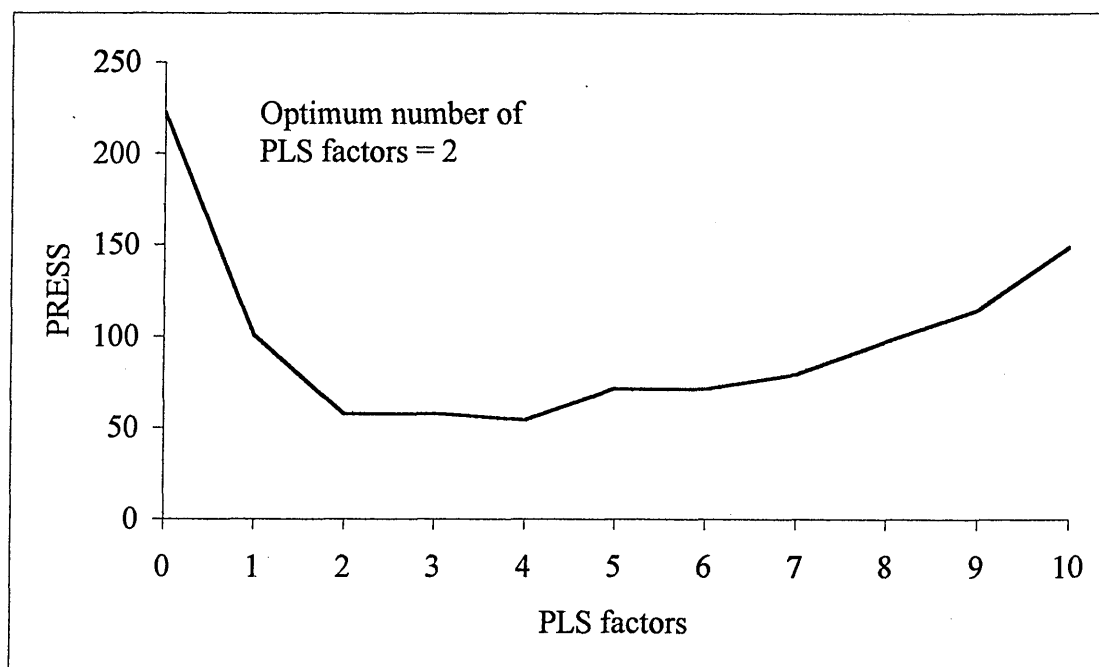


Figure 7.18 RT-MS TIC model ① calibration plot for KGa-2 using 3 PLS factors

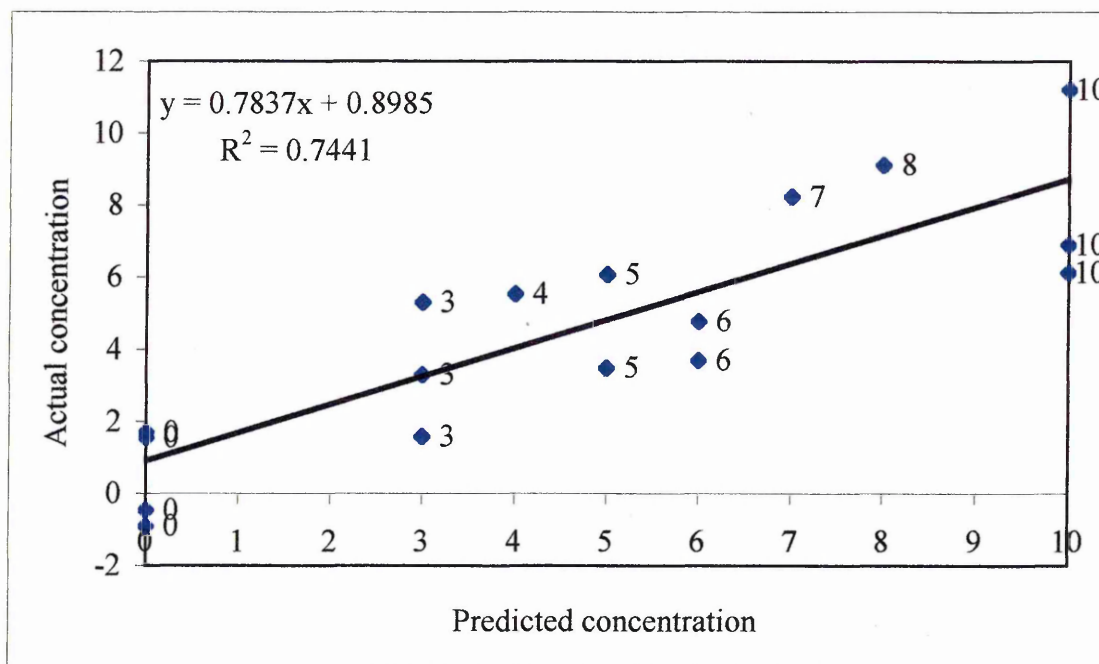
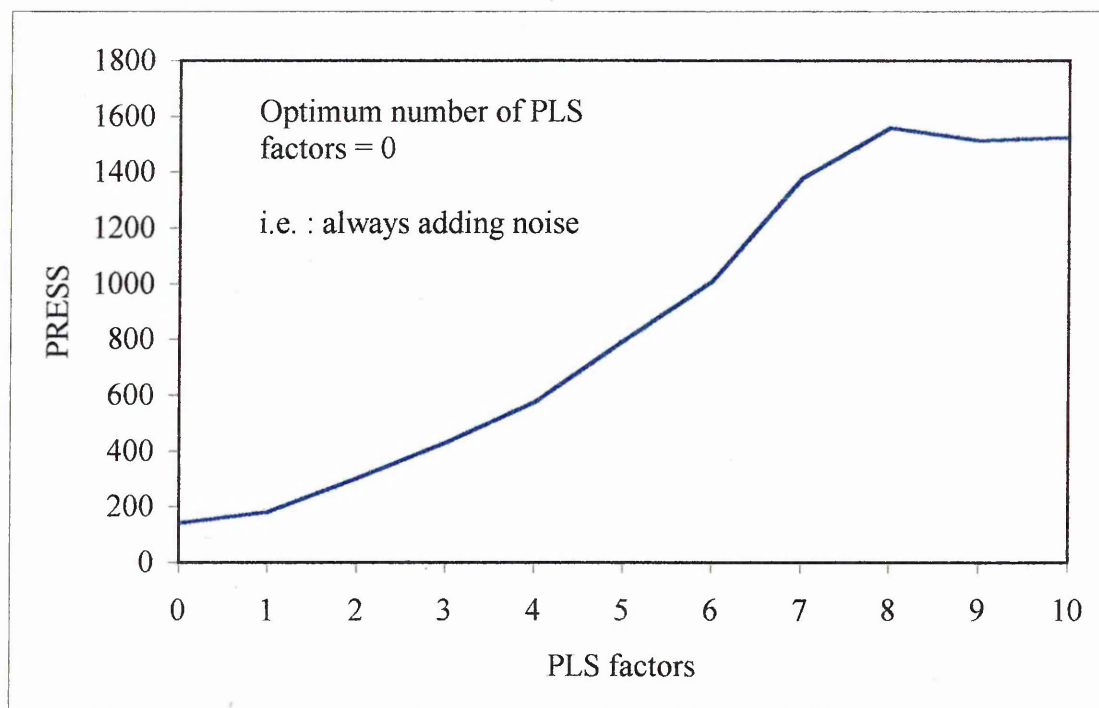


Table 7.11 RT-MS TIC model ① actual V predicted concentration for KGa-2

Standard-Actual Concentration%	Predicted Concentration%	Standard-Actual Concentration%	Predicted Concentration%	Standard-Actual Concentration%	Predicted Concentration%
Std 1-10	5.54	Std11-5	1.70	Std18-0	3.30
Std 2-10	-0.04	Std12-10	3.79	Std19-5	5.3
Std 4-9	11.21	Std13-2	8.23	Std 20-10	6.1
Std 5-6	1.58	Std14-0	-0.90	Std-21-0	1.5
Std 6-0	3.70	Std15-0	6.08		
Std 7-0	6.91	Std 16-2	4.78		
Std10-4	9.12	Std-17-0	1.54		

Figure 7.19 RT-MS TIC model[Ⓢ] cross validation PRESS plot for 1-Mt



Because cross validation was unable to produce any PLS factors which could describe any aspect of 1-Mt (illite) detection a calibration plot is not shown. Applying one PLS factor (which appears mainly as noise) gives an R^2 value of 0.01.

Figure 7.20 RT-MS TIC model[®] cross validation PRESS plot for CCa-1

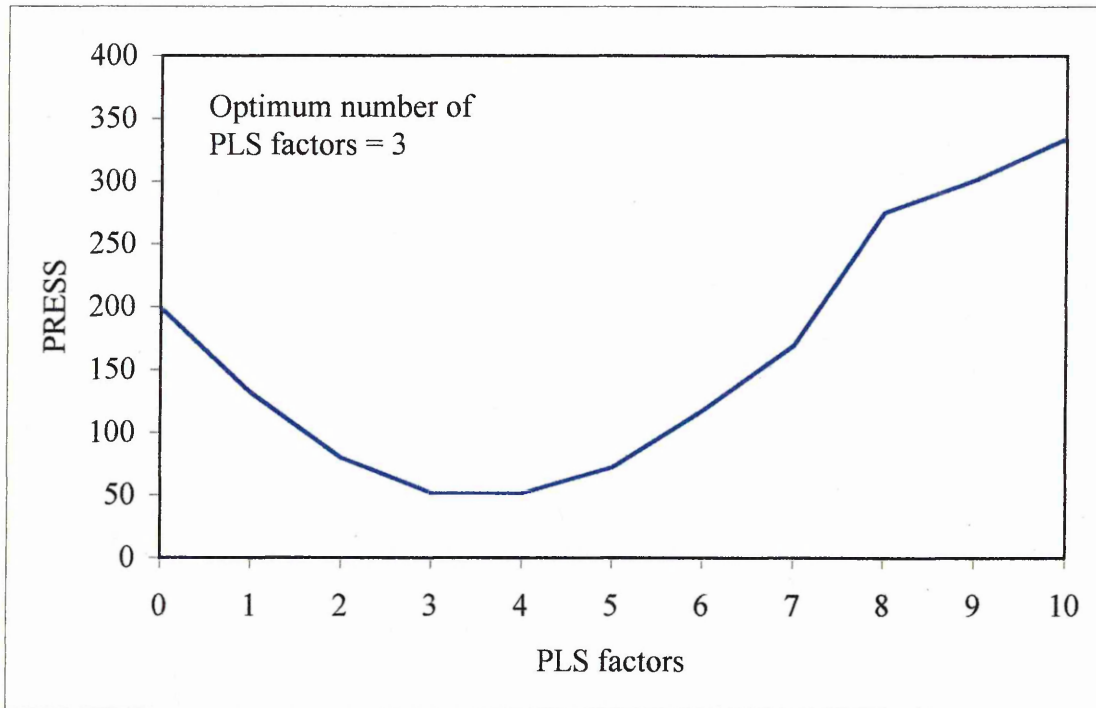


Figure 7.21 RT-MS TIC model[®] calibration plot for CCa-1 using 3 PLS factors

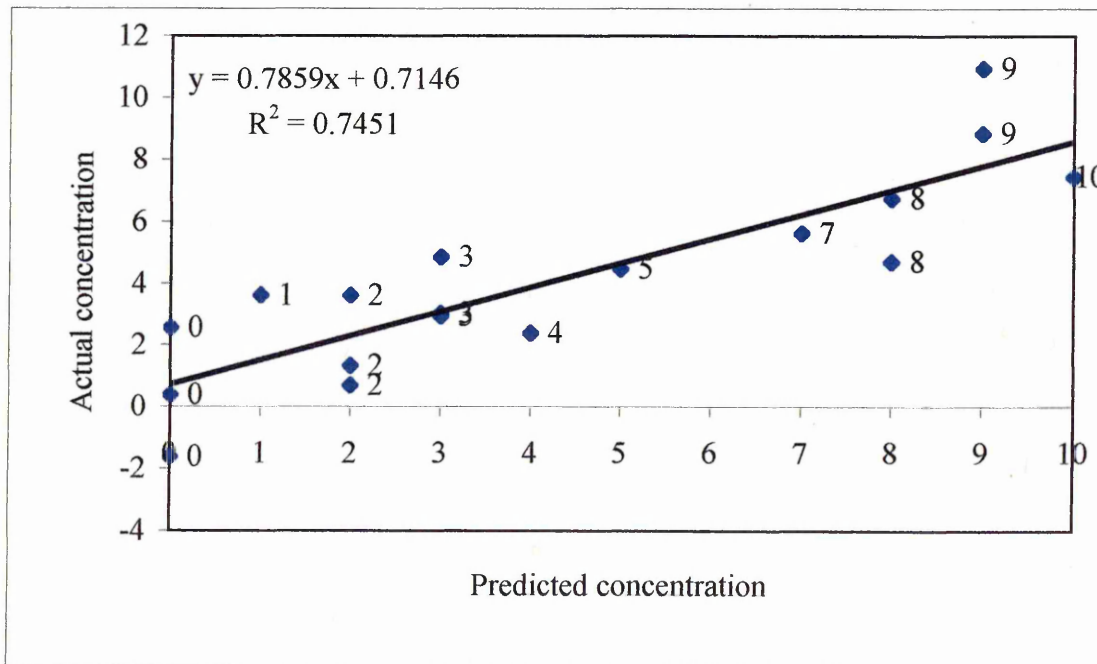


Table 7.12 RT-MS TIC model[Ⓢ] actual V predicted concentration for CCa-1

Standard-Actual Concentration%	Predicted Concentration%	Standard-Actual Concentration%	Predicted Concentration%	Standard-Actual Concentration%	Predicted Concentration%
Std 1-10	4.69	Std11-5	3.02	Std18-0	4.47
Std 2-10	6.70	Std12-10	2.55	Std19-5	0.68
Std 4-9	4.84	Std13-2	3.60	Std 20-10	5.63
Std 5-6	8.83	Std14-0	10.95	Std-21-0	2.94
Std 6-0	3.61	Std15-0	0.38		
Std 7-0	-1.62	Std 16-2	7.44		
Std10-4	2.39	Std-17-0	1.34		

Figure 7.22 RT-MS TIC model[Ⓢ] cross validation PRESS plot for quartz

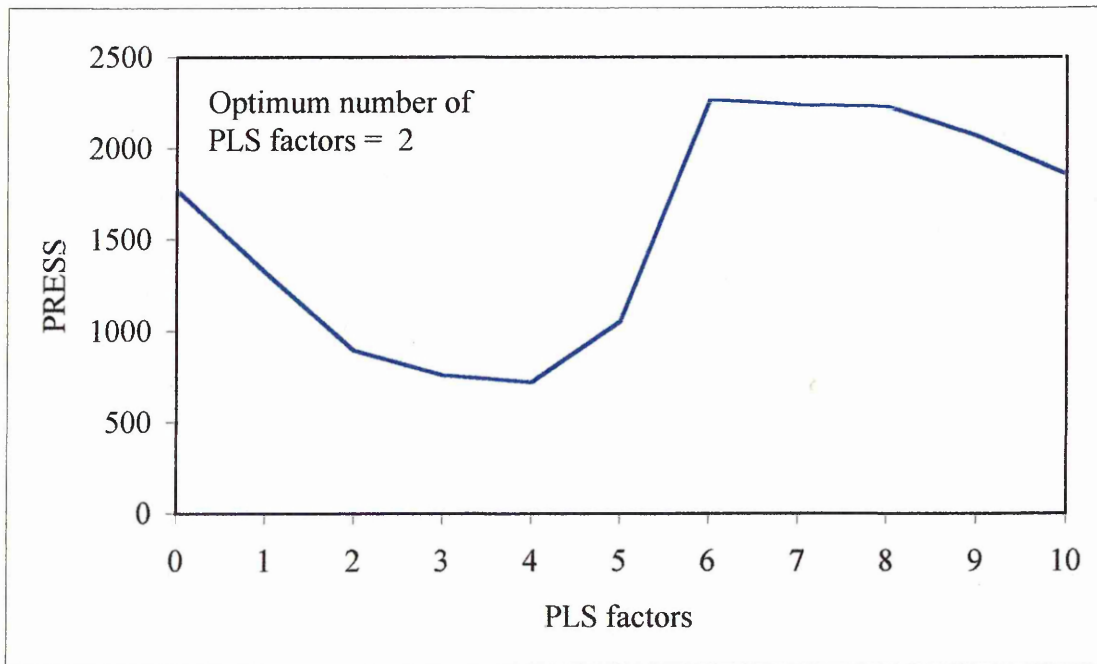


Figure 7.23 RT-MS TIC model calibration plot for quartz using 3 PLS factors

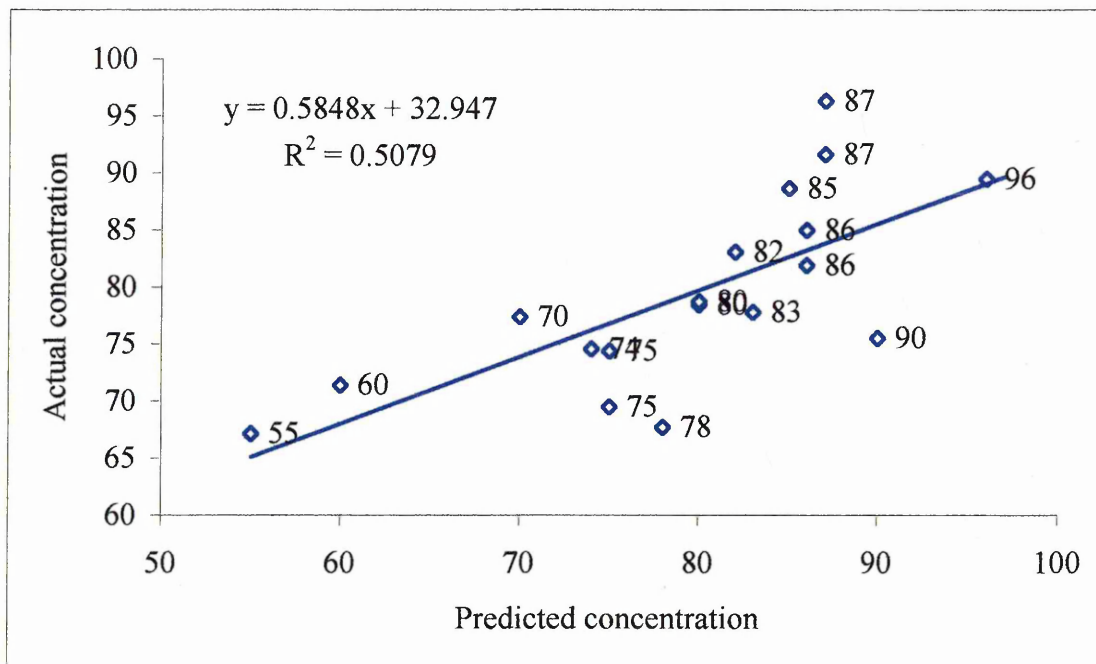


Figure 7.24 RT-MS TIC model cross validation PRESS plot for feldspar

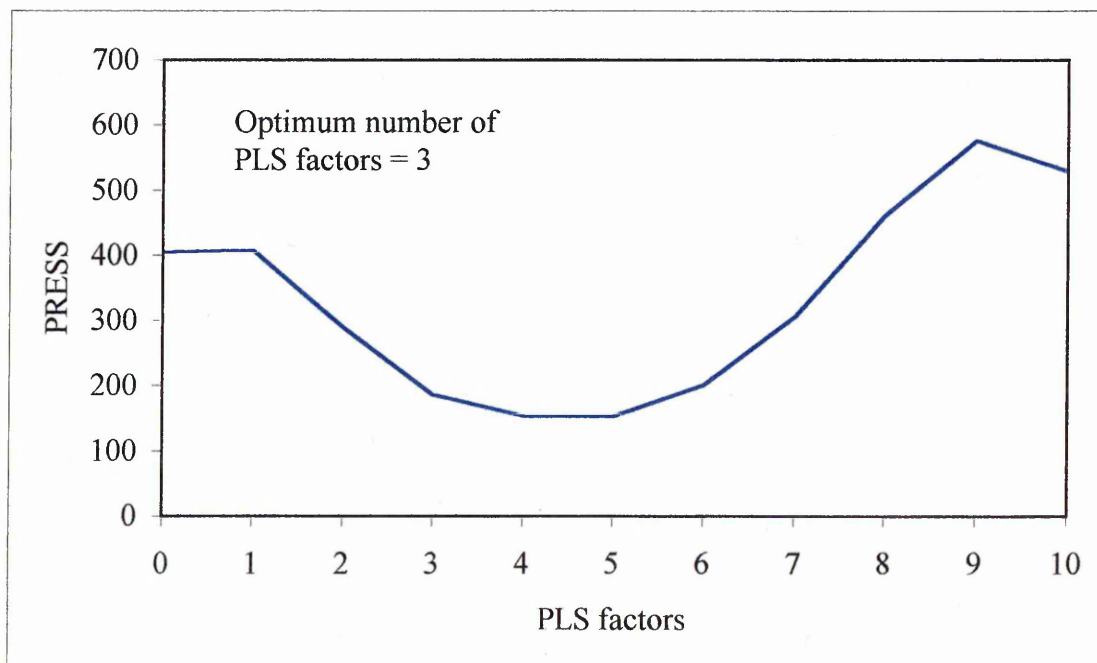
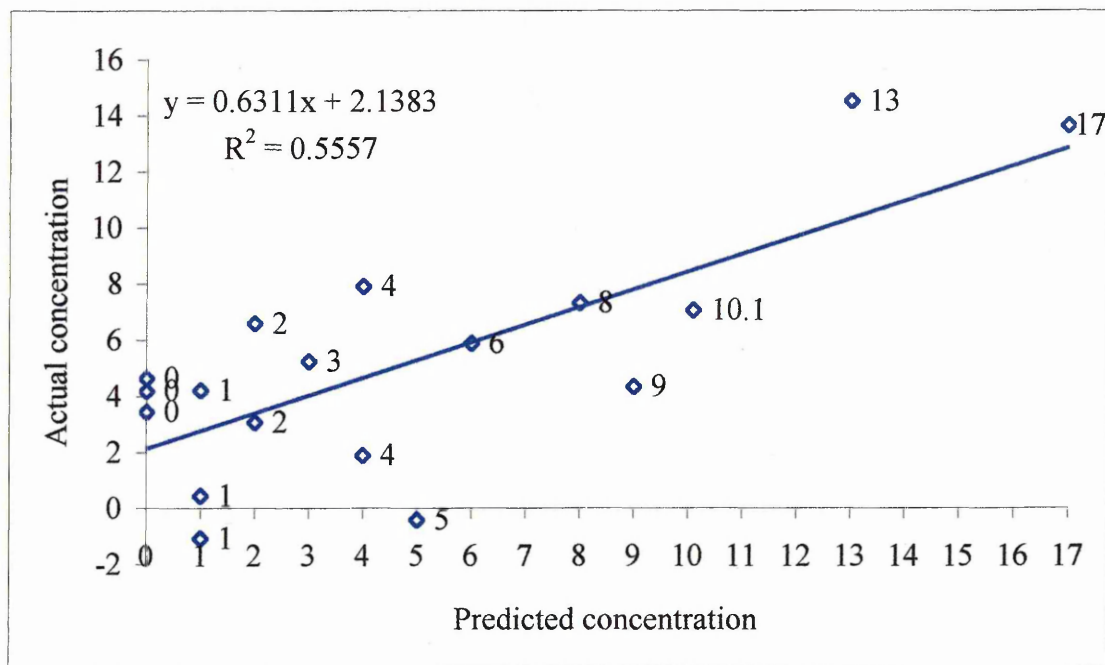


Figure 7.25 RT-MS TIC model[Ⓢ] calibration plot for feldspar using 3 PLS factors



The actual figures for calibration plots of quartz and feldspar are not show due to the fact that they do not enhance the understanding of either plot.

7.8.3 Summary of Model[Ⓢ] RT-MS TIC (derivatised)

Unprocessed TIC models results justify the use of the pre-processing techniques used herein . The best TIC R^2 value for SWy-2 was 0.93 but failed to give an R^2 value above 0.50 for any of the other clay mineral components. Model[Ⓢ] has shown that it is possible to predict SWy-2 successfully ($R^2 = 0.91$) with some potential to predict both KGa-2 and CCa-1. However, as expected the model cannot distinguish between either SWy-2 and 1-Mt because of the considerable overlap of their spectral profiles. Therefore Model[Ⓢ] overestimates the contribution of SWy-2 in some samples due to 1-Mt and probably overestimates for both CCa-1 and KGa-2 in the dehydroxylation

area. The result of DMF dominating the TIC, is that even with considerable pre-processing, contributions from clay mineral dehydroxylation are minimal, producing low R^2 values (0.74) for KGa-2 and CCa-1. If such low spectral resolution can show an R^2 value of 0.74, then the use of ion $m/z = 18$ should show considerable improvement for both of these components. Therefore no test samples were analysed.

7.9 Model[Ⓜ] using the RT-MS $m/z = 73$ (DMF parent ion)

Model[Ⓜ] attempts to further enhance the prediction ability for SWy-2 by using the DMF parent ion in order to reduce the contribution from other minerals as seen in the Model[Ⓛ] i.e. ion $m/z = 18, 44$ etc. Therefore, model[Ⓜ] focuses on SWy-2 by reducing the data area to that of DMF detection which invariably includes 1-Mt detection.

Table 7.13 Chemometric experimental details for ion $m/z = 73$ training set

Data points	Calibration type	Diagnostic type	Pre-processing
225 (reduced spectrum area)	PLS-1 (10 factors)	Cross-validation	-Mean centre -Variance scaling -Auto baseline correction

Figure 7.26 RT-MS $m/z = 73$ Model² cross validation PRESS plot for SWy-2

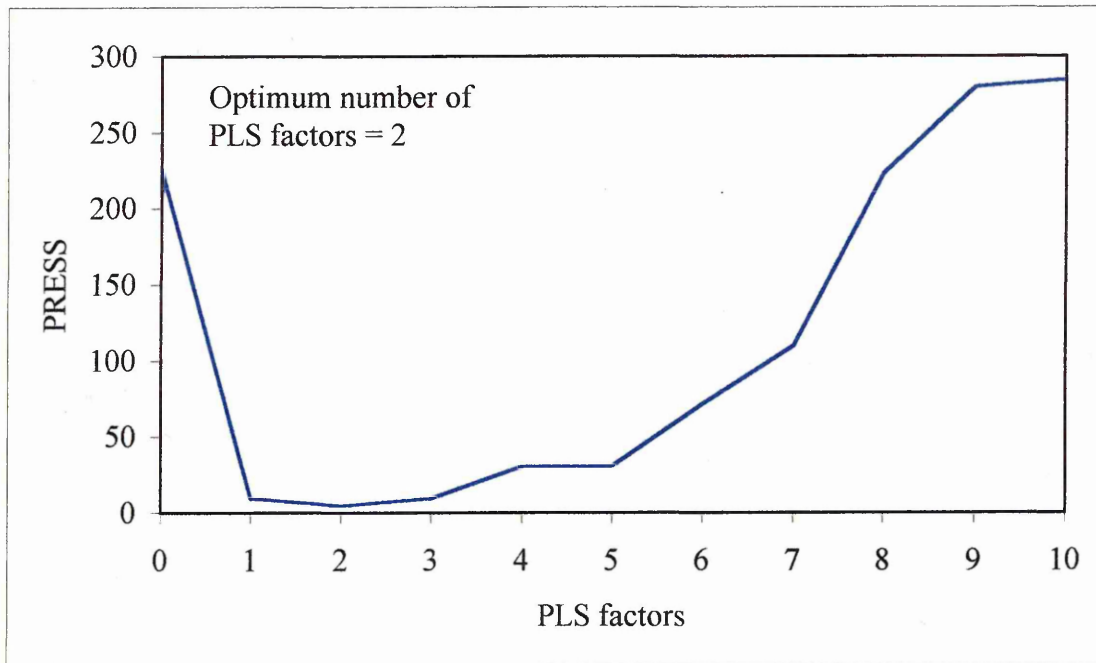
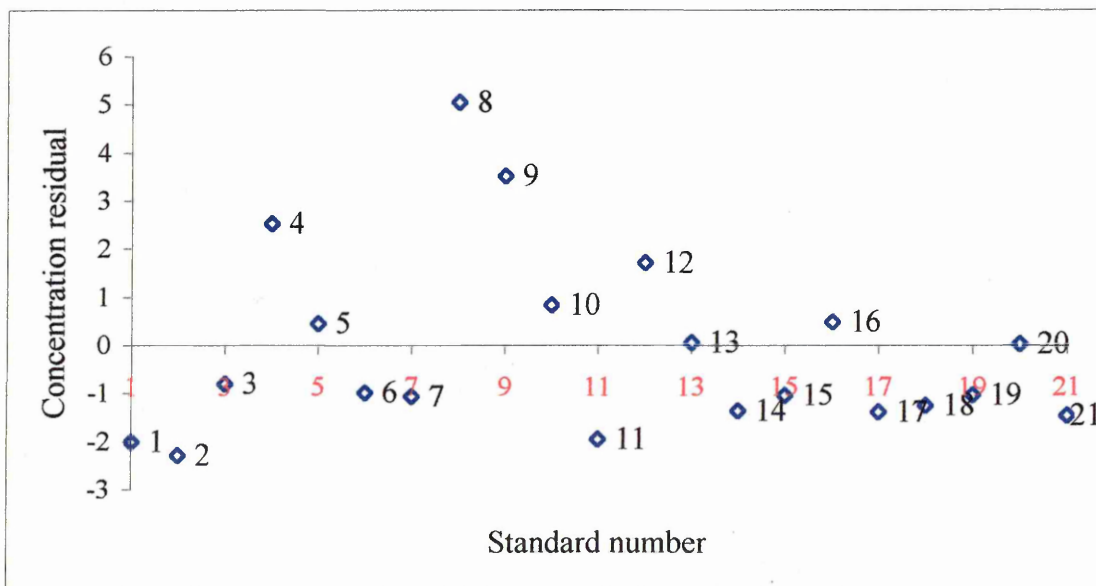


Figure 7.27 RT-MS $m/z = 73$ model² training set concentration residuals for SWy-2



The concentration residuals in figure 7.27 (using the f-statistic with a 99% outlier threshold) highlighted standards 4, 8 and 9 as concentration outliers. In addition observation of corresponding spectral residuals (fig.7.28) highlighted standards 1 and 4 as potential outliers. Therefore standards 1, 4, 8 and 9 were left of the model training set and the model was then re-calculated.

Figure 7.28 RT-MS $m/z = 73$ model training set spectral residuals for SWy-2

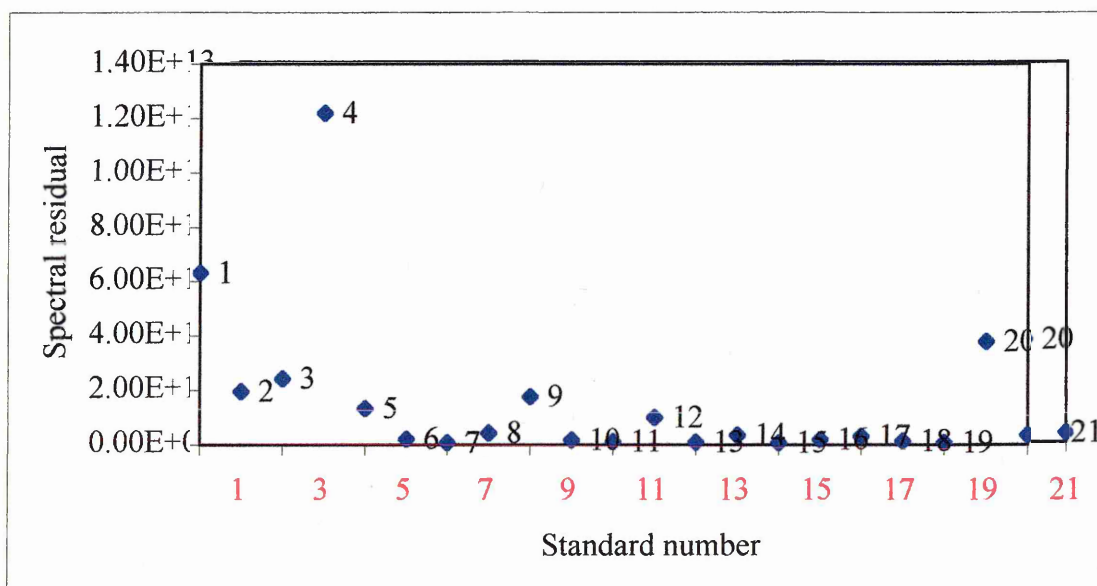


Figure 7.29 RT-MS m/z = 73 model[®] calibration plot for SWy-2 using 2 PLS factors

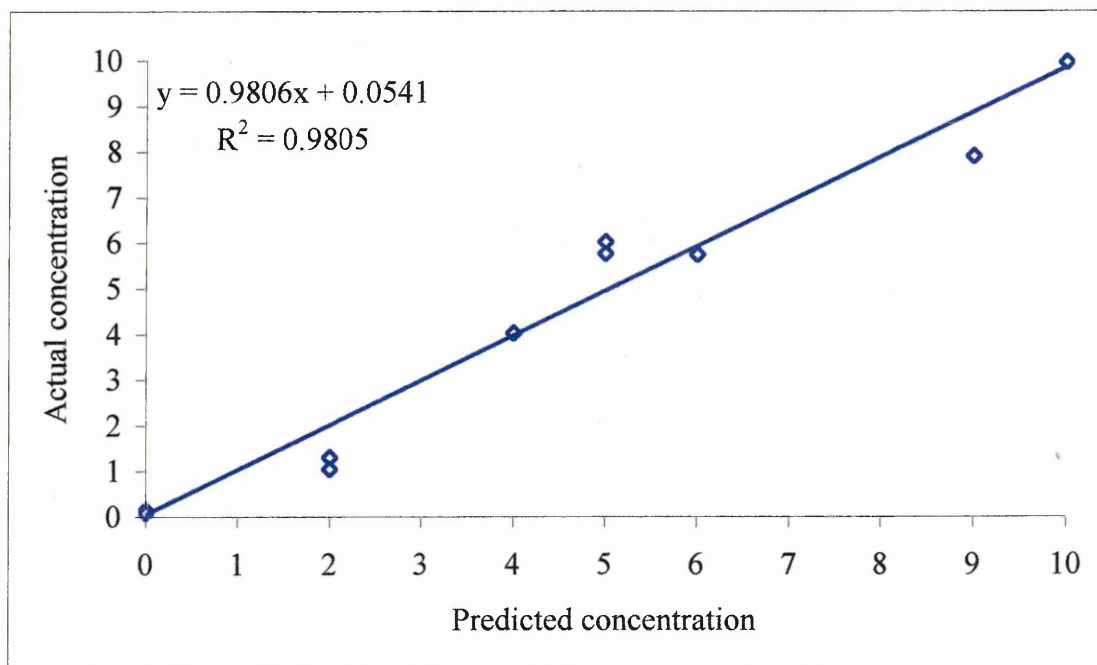


Table 7.14 RT-MS m/z = 73 model[®] actual V predicted concentration for SWy-2

Standard-Actual Concentration%	Predicted Concentration%	Standard-Actual Concentration%	Predicted Concentration%	Standard-Actual Concentration%	Predicted Concentration%
Std 2-10	10.10	Std 12-10	9.96	Std 19-5	6.02
Std 3-0	0.11	Std13-2	1.31	Std 20-9	7.91
Std 5-6	5.7	Std14-0	0.11	Std 21-0	0.09
Std 6-0	0.10	Std15-0	0.14		
Std 7-0	0.15	Std 16-2	1.05		
Std 10-4	4.02	Std17-0	0.12		
Std 11-5	5.77	Std 18-0	0.10		

Table 7.15 RT-MS m/z = 73 model² actual standard concentrations for 1-Mt

Standard-Actual Concentration%	Standard-Actual Concentration%	Standard-Actual Concentration%
Std 2-7	Std 12-0	Std 19-5
Std 3-8	Std13-7	Std 20-6
Std 5-10	Std14-0	Std 21-3
Std 6-0	Std15-6	
Std 7-2	Std 16-4	
Std 10-4	Std17-1	
Std 11-2	Std 18-0	

7.9.1 RT-MS m/z = 73 model² test set

The test samples herein are those used in chapter 6 (qualitative analysis) i.e. B4, Yorkstone and Hollington red sandstones with the addition of two mixed mineral standard left out of the training model. The quantitative analysis of the six components present in these samples is given in table 7.16 (these actual values were obtained from reference [369]). It is also important to note that Hollington red is a banded sandstone and the reported figures are for comparative purposes and are not directly comparable with the Hollington red test sample, which is the extracted 2 um fraction and contains components from both the banded and un-banded sections.

Table 7.16 RT-MS m/z = 73 model[Ⓜ] test set actual V predicted concentrations

(rocks)

Sample Mineral Wt %	B4 rock	(Predicted) B4	(Actual) Yorkstone	(Predicted) Yorkstone	(Actual) Hollington red (between bands/bands)	(Predicted) Hollington red <2um fraction
Smectite	Unknown	1.41	0	0.59	3/< 1	0.43
Illite	Unknown	3.75	7	3.59	6/10	3.59

The highlighted component in table 7.16 is shown for comparison only, as the model did not demonstrate sufficient sensitivity to enable illite prediction.

Table 7.17 RT-MS m/z = 73 model[Ⓜ] test set actual versus predicted concentrations (mixed mineral standards)

Concentration Wt %	Quartz	SWy-2	1-Mt	Feldspar
Test 1 (actual)	70	10	4	4
Test 1 (predicted)	71	7.59	5.41	4.23
Test 2 (actual)	72	6	5	8
Test 2 (predicted)	82	4.68	3.25	4.29

7.9.2 Summary model[Ⓜ] using the RT-MS m/z = 73 (DMF parent ion)

By using the reconstructed chromatogram profile of the DMF parent ion (m/z = 73), Model[Ⓜ] has shown that it is possible to improve upon the R² value of 0.93 and 0.91 seen in the TIC and TIC (derivative) training sets of model[Ⓛ]. Model[Ⓜ] calculated an

excellent R^2 value of 0.98. Repeat runs demonstrated (not shown) good reproducibility, with an R^2 value of between 0.97-0.98. Repeat runs have also shown anomalies in the shape of the $m/z = 73$ profile from particular standards (i.e. standards 10, 13 and 16 i.e. appendices). These particular standards have high concentrations of KGa-2 and/or CCa-1. However, for CCa-1 and KGa-2, there is little or no evidence for contamination from montmorillonite or illite (see XRD and DRIFTS study), nor do they contribute to DMF detection. Normally, the low temperature DMF maxima is more intense than the high temperature maxima. The observed effect was a reversal of the intensity of both low and high temperature maxima (not shown) and may be due to:

- (a) an unusual distribution of interlayer cations (predominance of Ca over Na) in standard samples (10, 13 and 16).
- (b) Intermittent instrumental drift/transfer line problems.

The mixed mineral test set predictions (table 7.17) are variable, but highlight the necessity to determine more accurately the contribution of illite to smectite and vice-versa. More importantly, more mixed mineral test samples are needed which were not included in the original training set, but were prepared in the same fashion.

If the rock test set predictions (table 7.16) are viewed in terms of the figures reported from the SWy-2 calibration plot (fig. 7.29), then the low values reported for both Yorkstone (0.59 wt%) and Hollington red (0.43 wt%) may be within the error of prediction. However, to calculate this error range accurately, would require considerably more samples set at zero % SWy-2. For example, training set values show that when the actual concentration for SWy-2 concentration is zero, the training set calibrations report concentrations which range between 0.09-0.15 wt %. Because the model cannot accurately predict illite, the implication of smectite detection in both

Yorkstone and Hollington red highlights several important points regarding model predictions:

(a) perhaps the most important influence on clay mineral predictions for the rock samples is due to the fact that they may have a different set of components and/or concentrations, which are not like that of the training set. This highlights the need to tailor training sets to the samples under study.

(b) The actual concentrations of the rock samples represent mean bulk concentrations (i.e. the total wt. % found in a powdered rock) of which the standard deviation is not known. In comparison, the model predictions represent surface mineralogy (i.e. those minerals which are exposed within the pore structure). Therefore in order to verify how representative are these predictions would require considerably more samples.

(c) the presence of mixed layer clay minerals (i.e. illite-smectite) may not be represented by the model but are likely to be present in the rock samples.

(d) smectite may be present, but beyond the detection sensitivity of the techniques that were used to determine the actual concentrations of the test samples.

(e) illite is indirectly being detected, as DMF detection for illite occurs in the same temperature region.

7.10 Model^③ using the RT-MS ion $m/z = 18$ (H_2O)

7.10.1 Introduction

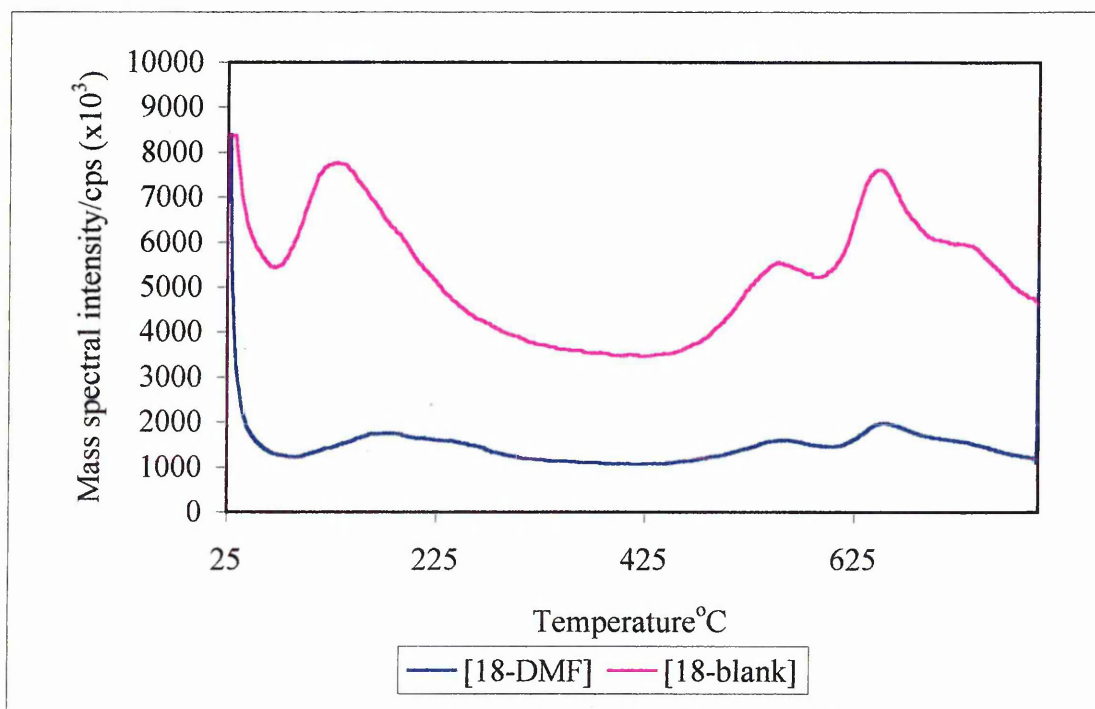
It was envisaged that ion $m/z = 18$ could be used to predict SWy-2, KGA-2 and CCa-1 clay mineral components. This assumption relied on two key observations:

- (a) Firstly, both KGA-2 and CCa-1 gave a strong and reasonably well resolved $m/z = 18$ detection signal at high temperature due to water of dehydroxylation as shown in chapter 6 (qualitative analysis). It was believed that derivative pre-processing could further enhance this region.
- (b) Secondly, evidence from both RT-MS and GP-FTIR suggest that water is somehow bonded with DMF. Previous DRIFTS work has shown [353] that DMF is directly coordinated to the interlayer cations via its carbonyl group. This suggests that the water is associated with DMF via the C-N group through hydrogen with the lone pair electrons of the nitrogen atom. Therefore, as DMF is desorbed, the water associated with the nitrogen atom is desorbed at a different rate (slope of desorption) but across a very similar temperature range. Supporting evidence comes from the comparison of treated and untreated standards (figs. 7.9-7.11). As seen in figure 7.30, the detection maxima for water ($m/z = 18$) in untreated samples (attributed to physisorbed water at low temp (to $100^\circ C \approx$) and water associated with interlayer cations (to higher temperature) consists of one maxima which is skewed to higher temperature. However, for treated samples (fig. 7.31) the shape of the $m/z = 18$ maxima mimics that of $m/z = 73$ seen in model^② and therefore if this

DMF-H₂O relationship was proportional to the concentration of the swelling components, then it could be used to indirectly detect the SWy-2/1-Mt components.

Figure 7.30 Comparison of treated and untreated standard 1 for ion $m/z = 18$

(70% Quartz--10% SWy-2--4% KGa-2--4% Illite--8% CCa-1--4% Feldspar)



By using ion $m/z = 18$, the problems of resolving the TIC dehydroxylation area observed in model① may be overcome. Firstly, the low temperature detection maxima of $m/z = 18$ mimics DMF detection. In addition, using $m/z = 18$ indirectly brings DMF detection into the same intensity range as that of dehydroxylation which would increase the sensitivity and predictive power of the model for both KGa-2 and CCa-1 components with the possibility of separate detection of 1-Mt.

Figure 7.31 Comparison of DMF treated standard 1 for ions $m/z = 18$ (H_2O) and 73 (DMF) (70% Quartz--10% SWy-2--4% KGa-2--4% Illite--8% CCa-1--4% Feldspar)

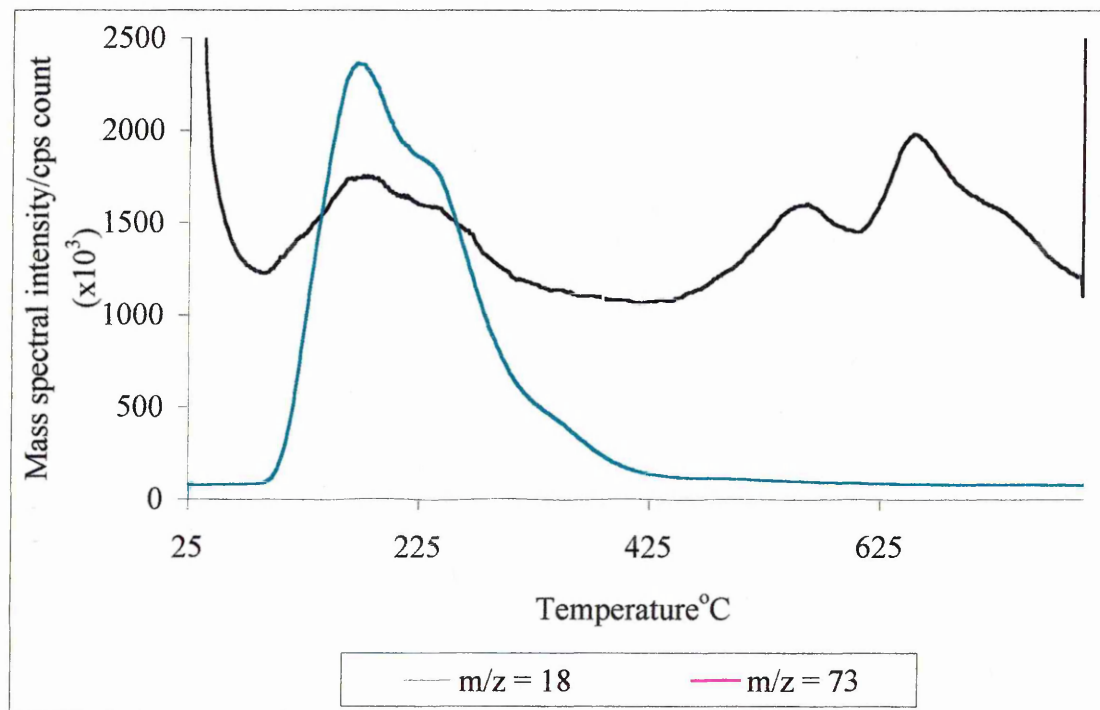
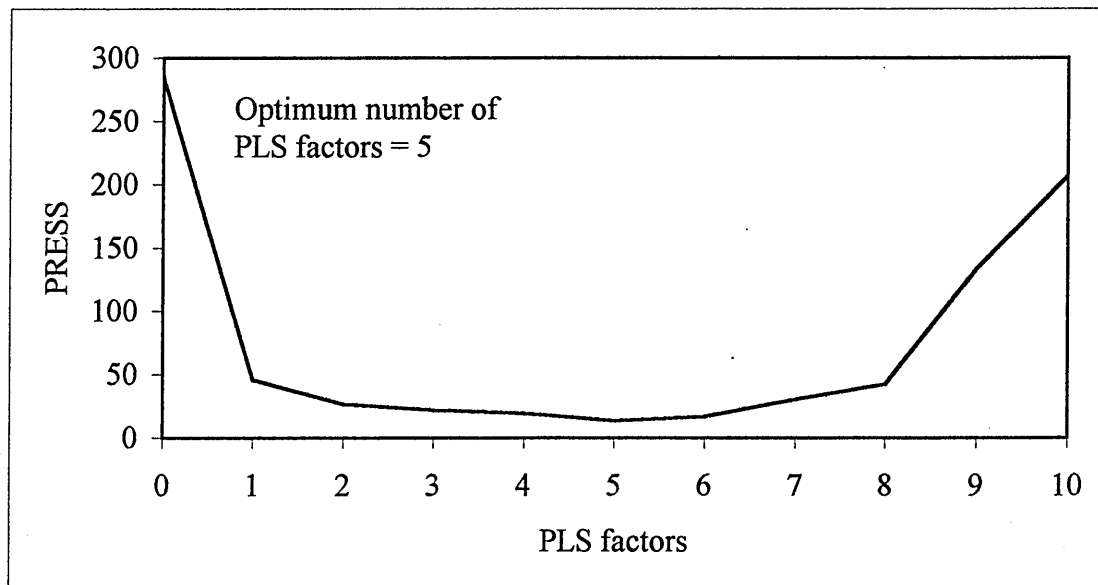


Table 7.18 Chemometric experiment details of $m/z = 18$ model^③ training set

Data points	Calibration type	Diagnostic type	Pre-processing
401 (reduced spectrum area)	PLS-1 (10 factors)	Cross-validation	-Mean centre -Variance scaling -Auto baseline correction -Savitzsky-Golaz 1 st derivative (71 points)

7.10.2 Results of model③ using the RT-MS ion $m/z = 18$ (H_2O)

Figure 7.32 RT-MS $m/z = 18$ model③ cross validation PRESS plot for SWy-2



The initial model for SWy-2 gave an R^2 value of 0.82. After applying the f-test statistic (0.99) to the concentration and spectral residuals three possible outliers were highlighted (standards: 7, 8, and 9). These standards were then left out of the SWy-2 training set and the model re-calculated. The number of the standard is found to the right of its position.

Figure 7.33 RT-MS $m/z = 18$ model³ training set concentration residuals for SWy-2

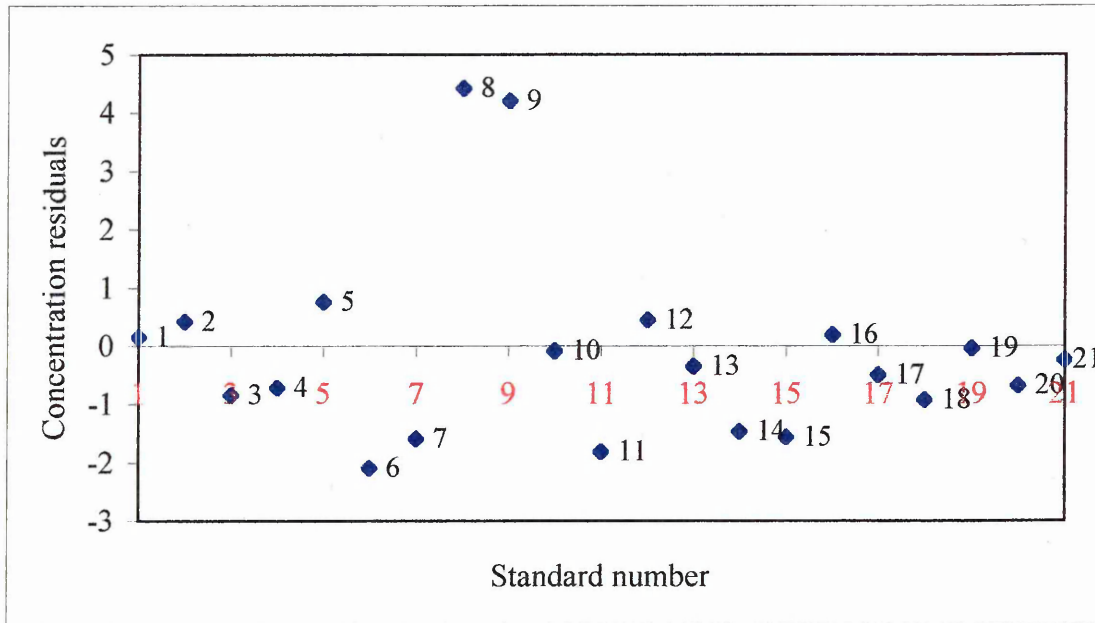


Figure 7.34 RT-MS $m/z = 18$ model³ spectral residuals for SWy-2

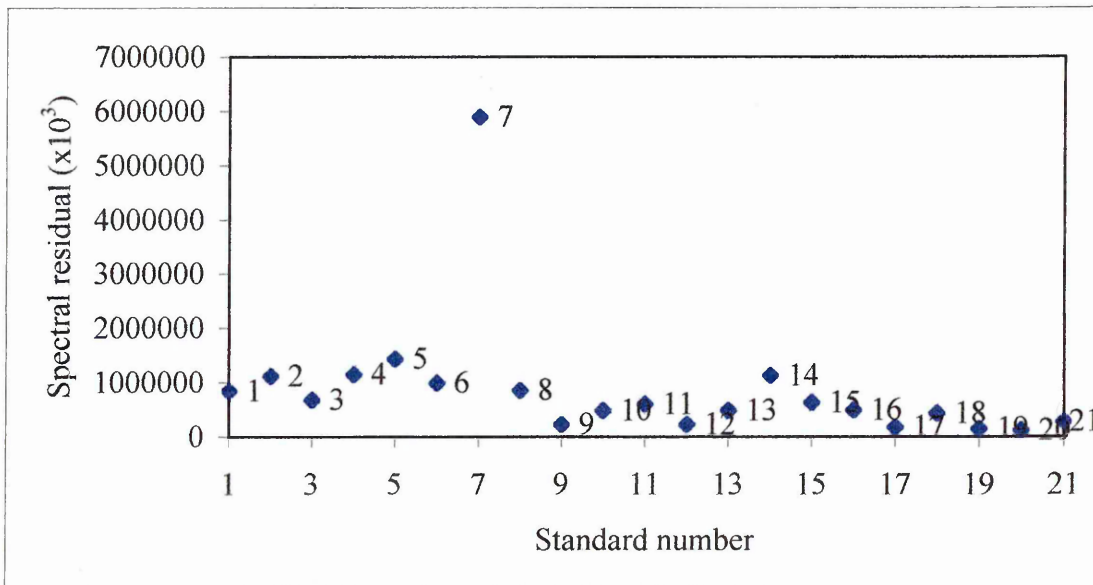


Figure 7.35 RT-MS m/z = 18 model[Ⓢ] calibration plot for SWy-2 using 5 PLS factors

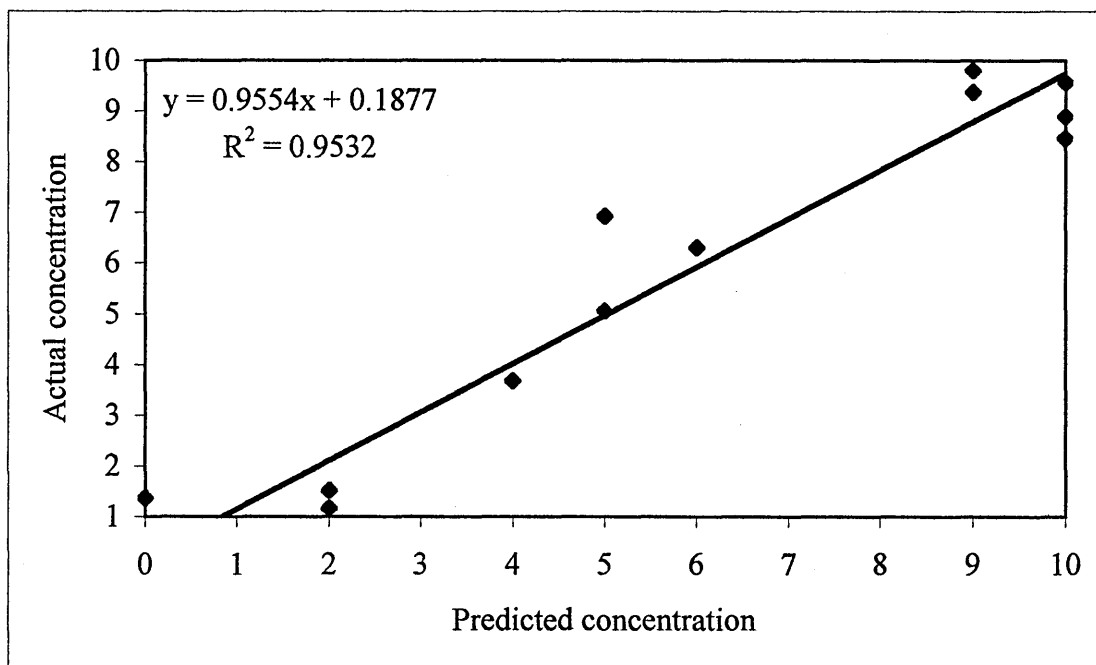


Table 7.19 RT-MS m/z = 18 model[Ⓢ] actual versus predicted concentrations for SWy-2

Standard-Actual Concentration%	Predicted Concentration%	Standard-Actual Concentration%	Predicted Concentration%	Standard-Actual Concentration%	Predicted Concentration%
Std 1-10	8.90	Std 11-5	6.93	Std 18-0	0.32
Std 2-10	9.57	Std 12-10	8.46	Std 19-5	5.05
Std 3-0	0.25	Std13-2	1.17	Std 20-9	9.37
Std 4-9	9.81	Std14-0	0.19	Std 21-0	-1.09
Std 5-6	6.31	Std15-0	0.68		
Std 6-0	1.36	Std 16-2	1.51		
Std 10-4	3.68	Std17-0	-0.36		

Figure 7.36 RT-MS m/z = 18 model③ cross validation PRESS plot for KGa-2

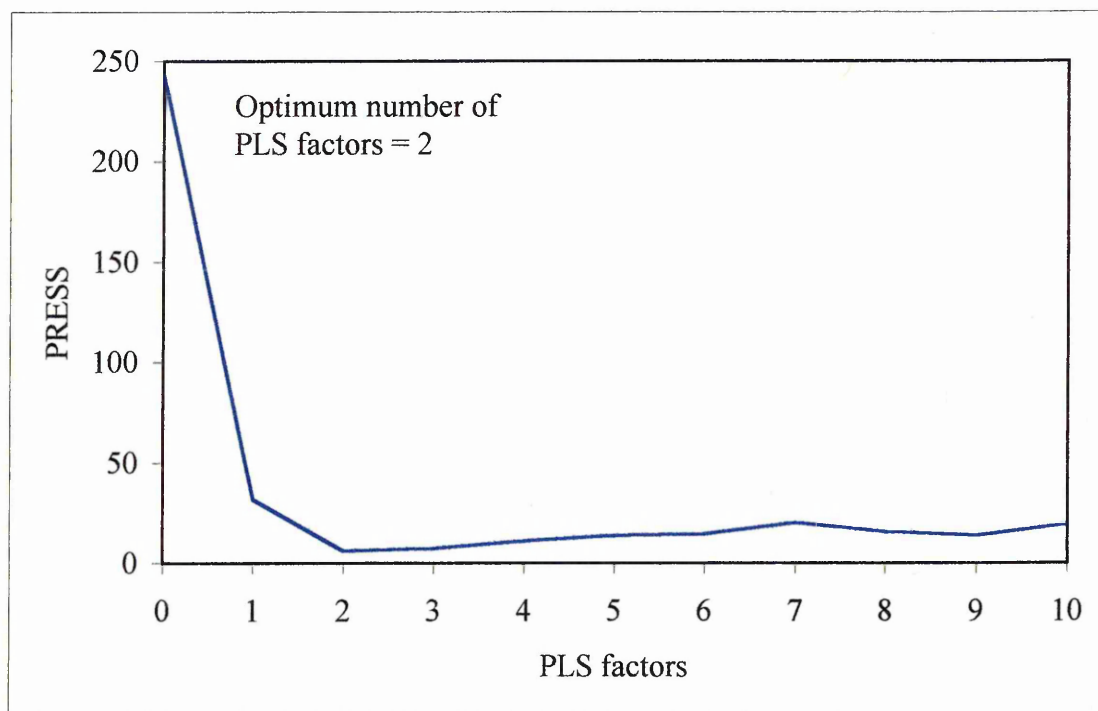


Figure 7.37 RT-MS m/z = 18 model③ calibration plot for KGa-2 using 2 PLS factors

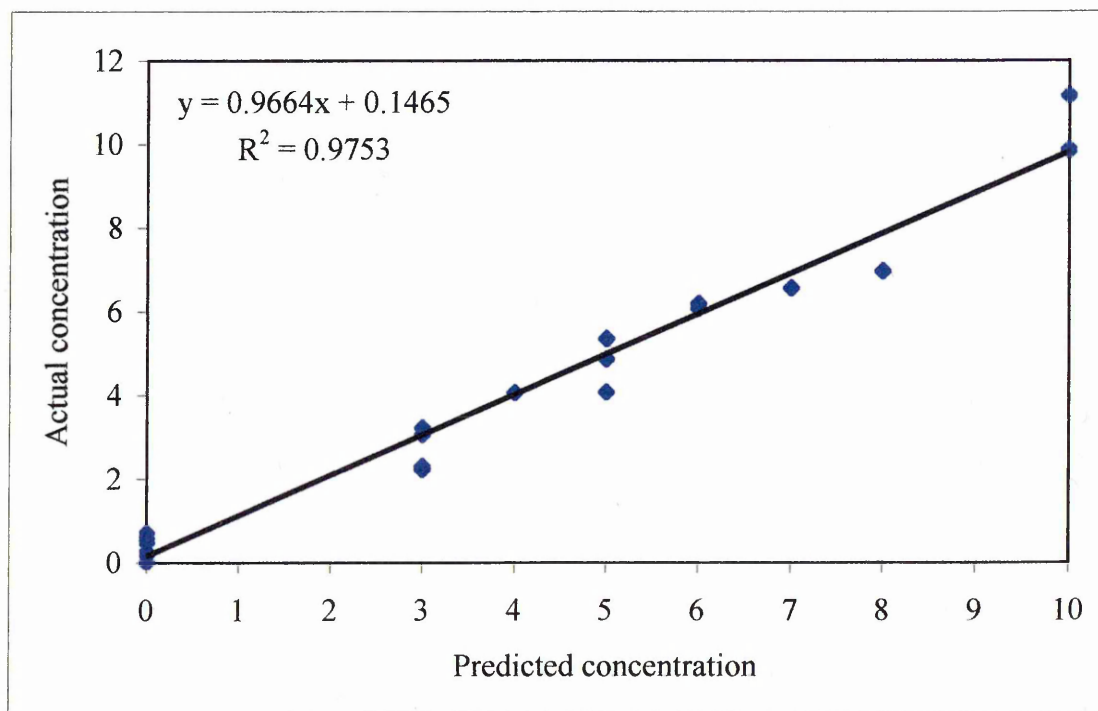


Table 7.20 Model 3 actual versus predicted concentrations for KGa-2

Standard-Actual Concentration%	Predicted Concentration%	Standard-Actual Concentration%	Predicted Concentration%	Standard-Actual Concentration%	Predicted Concentration%
Std 1-4	4.06	Std 8-5	5.35	Std15-5	4.86
Std 2-0	0.00	Std 9-3	2.22	Std 16-6	6.07
Std 3-0	0.71	Std10-8	6.96	Std-17-0	0.48
Std 4-10	11.1	Std11-0	0.26	Std18-3	2.30
Std 5-3	3.22	Std12-5	4.07	Std19-3	3.07
Std 6-6	6.19	Std13-7	6.56	Std 20-10	9.84
Std 7-10	9.87	Std14-0	0.18	Std-21-0	0.51

Figure 7.38 RT-MS m/z = 18 model 3 cross validation PRESS plot for CCa-1

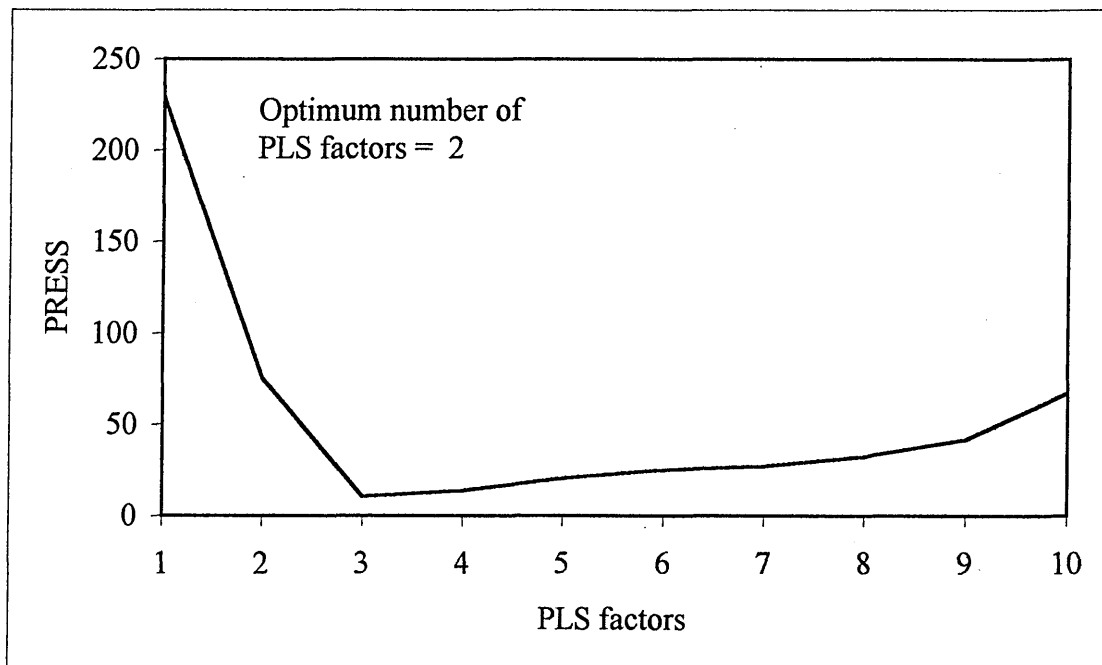


Figure 7.39 RT-MS m/z = 18 model³ calibration plot for CCa-1 using 2 PLS factors

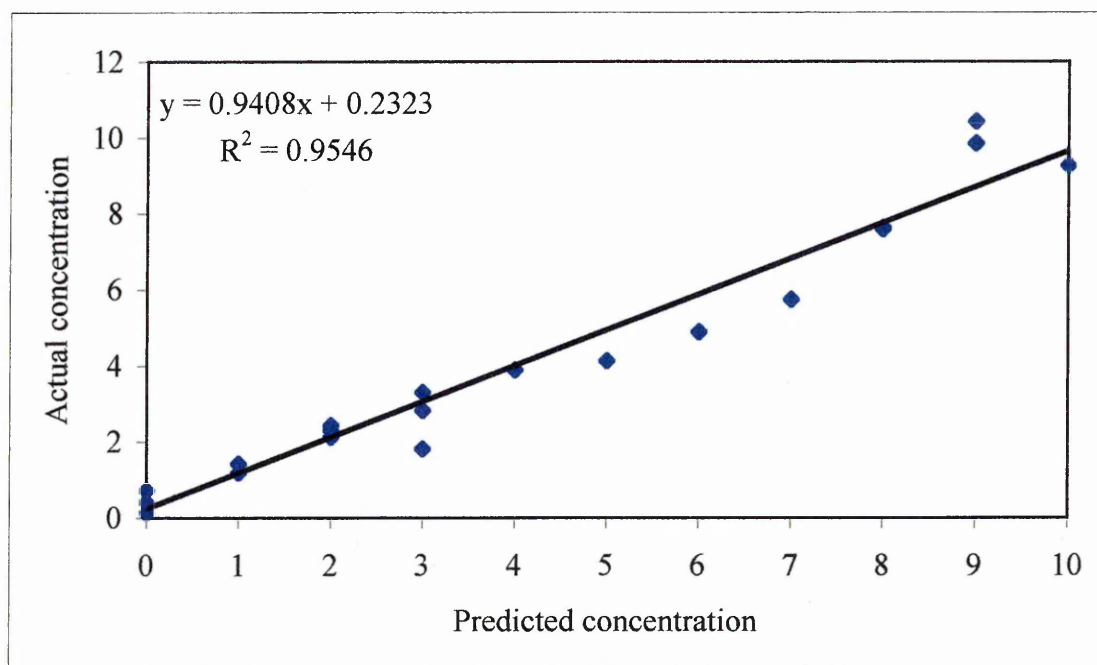


Table 7.21 Model³ actual versus predicted concentrations for CCa-1

Standard-Actual Concentration%	Predicted Concentration%	Standard-Actual Concentration%	Predicted Concentration%	Standard-Actual Concentration%	Predicted Concentration%
Std 1-8	7.60	Std 8-0	0.42	Std15-0	0.73
Std 2-8	7.64	Std 9-6	4.89	Std 16-10	9.26
Std 3-1	1.19	Std10-4	3.90	Std-17-2	2.44
Std 4-3	3.31	Std11-3	2.83	Std18-5	4.14
Std 5-9	10.42	Std12-0	0.73	Std19-2	2.31
Std 6-2	2.12	Std13-1	1.42	Std 20-7	5.75
Std 7-0	0.14	Std14-9	9.85	Std-21-3	1.82

7.10.3 RT-MS m/z = 18 model³ Test set

The test samples herein are those seen in chapter 6 i.e. B4, Yorkstone and Hollington red with the addition of two mixed mineral standard left out of the training model..

The quantitative analysis of the six components present in these samples is given in table 7.22.

Table 7.22 Model³ test samples :actual versus predicted concentrations (rocks)

Sample Mineral Wt %	B4 rock	(Predicted) B4	(Actual) Yorkstone	(Predicted) Yorkstone	(Actual) Hollington red (between bands/bands)	(Predicted) Hollington red <2um fraction
Quartz	Unknown	92.22	72	80.97	74/72	85.93
Smectite	Unknown	2.02	0	0.82	3/< 1	5.13
Kaolinite	Unknown	-0.20	5	-0.75	<1/3	-0.371
Illite	Unknown	3.45	7	4.76	6/10	4.09
Chlorite	Unknown	0.69	0	5.91	0/3	3.08
Feldspar	Unknown	5.10	14	7.74	7	6.12

The highlighted components in table 7.22 are shown for comparison only, as the models did not demonstrate sufficient sensitivity to enable their prediction.

Table 7.23 RT-MS $m/z = 18$ model^③ test set actual versus predicted concentrations (mixed mineral standards)

Test samples	SWy-2	KGa-2	1-Mt	CCa-1
Test 1 (actual)	0	10	2	0
Test 1 (predicted)	-0.40	9.57	1.48	1.32
Test 2 (actual)	9	10	0	3
Test 2 (predicted)	9.81	10.74	4.93	3.26

7.10.4 Summary of model^③ RT-MS ion $m/z = 18$ (H_2O)

As a feasibility study the use of ion $m/z = 18$ has shown great promise for the prediction of clay minerals in rocks. Model^③ has shown that DMF in effect further defines the cation-interlayer water relationship because there is a definite relationship between the amount of DMF defined water and the concentration of SWy-2. The R^2 values for SWy-2 (0.95), KGa-2 (0.97) and CCa-1 (0.95) are excellent. However, the model could not recommend any PLS factors for 1-Mt-illite and could therefore not predict this component.

The rock test samples again highlighted the problems associated with comparing actual and predicted concentrations seen in model^② (i.e. verification of bulk and surface mineralogy). But gave considerably better prediction results than model^② for SWy-2, KGa-2 and CCa-1 for the mixed mineral test samples.

7.10.5 Conclusions

The use of multivariate PLS analysis of EGA detection profiles for the detection of minerals in mixtures and rocks has shown considerable promise for the future. The use of the MS TIC has shown some success but only for SWy-2 ($R^2 = 0.91$) the prediction of which has been further enhanced by the use of the DMF parent ion $m/z = 73$ ($R^2 = 0.98$). Use of ion $m/z = 18$ (H_2O) has perhaps shown most potential, due to its ability to produce training sets with excellent correlation coefficients of 0.95 for SWy-2, 0.97 for KGa-2 and 0.95 for CCa-1. However, because SWy-2 and 1-Mt demonstrate overlapping detection of DMF (where uptake of DMF by 1-Mt is comparatively small), it is impossible to directly separate their relative contributions at the concentration levels under study. In addition, the dehydroxylation of 1-Mt is un-resolved and of low intensity, being spread across a greater temperature range and inseparable from the other components. Considerations for future work may detect 1-Mt by means direct or indirect.

Suggestions may include:

- (a) The necessity to use different carrier gases, as helium is known to broaden the MS signal. An alternative gas may increase resolution of detection maxima. There is also a need to consider altering the gas flow rates in tandem with point (c). In addition, the electron impact (EI-hard ionisation technique) ionisation technique was operated at 70eV and may be reduced to a lower level to improve the signal from the key ions ($m/z = 18$ and 73). Alternatively, a softer ionisation technique such as chemical ionisation (CI) could be used.

(b) The effect of the transfer lines has been discussed in chapters 5 and 6.

Therefore there is a real need to shorten this length to several inches maximum in order to shorten gas transfer time to the MS detector, reduce diffusional broadening and DMF breakdown within the transfer lines.

(c) Detection maxima resolution may also be improved by using controlled rate thermal analysis (CRTA), which could provide greater resolution of detection events.

(d) The models herein, used clay component concentrations of between 1 and 10%. Therefore there is a need to determine the sensitivity limits of the MS. Standards of between 0.1-1% must be constructed. If this is successful in terms of sensitivity and reproducibility. Then the sensitivity of the MS can be enhanced further by selective ion monitoring of ions $m/z = 18$ and 73 , which have already proved to be very successful.

(e) In addition, there is a need to determine the concentration limits of 1-Mt where it becomes undetectable in the presence of SWy-2. For example, standards could be constructed which contain SWy-2 from 0.1 – 0.8 % in the presence of illite in the 1-10% range. This may also be necessary with KGa-2 and CCa-1. As previously mentioned in chapter 6, the maximum DMF detection of the MS detector towards for a given sample size can quite easily be determined in the presence of other components.

(f) High crystallinity kaolinite may also be a consideration for inclusion in future training sets as its higher dehydroxylation maxima ($600^{\circ}\text{C} +$) may interfere with the determination of chlorite.

(g) Carbonates should also be included in future training sets to determine the effects on DMF detection, dehydroxylation and background levels.

- (h) The use of the $m/z = 18$ profile has shown considerable promise. In addition, it was shown that in untreated samples, the intensity of $m/z = 18$ is greater than in treated samples as there are no DMF ions being detected. Future work should also investigate the same standards without DMF as the first detection maxima for $m/z = 18$ could be derivatised (or otherwise) to produce the necessary resolution seen in treated samples. To further enhance this approach, samples could also be pre-conditioned in the nitrogen flow of the system to remove as much physisorbed water as possible.
- (i) Methods of indirect detection of illite may include investigation of DMF fragment ion ratios i.e. 58:73. The reasoning behind this is centered on the premise that DMF detection in illite is known to occur in the same temperature range as SWy-2. Therefore the expected proportions of ion ratio = 58:73 may differ when illite is present.

Chapter 8 Characterization of swelling clay minerals by ESEM-EDX analysis of 2-Bromopyridine (2BPY)

8.0 Introduction

The investigation herein is a feasibility study, which evaluates the potential of ESEM-EDX to detect 2BPY bound to swelling minerals. It was thought that 2BPY would be a potential probe molecule for several reasons:

- (a) Its similarity to the pyridine molecule would facilitate intercalation within the interlayer space of swelling minerals thus highlighting their presence when subject to ESEM-EDX analysis.
- (b) Brominated molecules are known to be scarce in oil well applications and therefore this may enhance the chance of its detection in the presence of other molecular traffic.
- (c) The bromine functional group would provide a signal within the MS and EDX

There is no evidence in the literature for the use of brominated molecules with clay minerals. However, as previously discussed in chapter 6, there is an abundance of literature concerning the interactions of pyridine with clay minerals. The objectives of this study are to:

- (1) Determine whether it is possible to detect 2BPY on the surface of various cation exchanged SWy-2 (ground). For EDX analysis to be successful, the percentage of bromine present must be greater than 1% to be detected by EDX.

(2) To determine whether it is possible to highlight swelling minerals on the surface of a rock using the same method. Ultimately, the goal would be to determine the relationships between bulk and surface mineralogy in rocks, but this is beyond the scope of this study.

The techniques utilised for this work were environmental scanning electron microscope (ESEM) combined with energy dispersive X-ray (EDX). The ability of ESEM to operate at atmospheric pressure allows the application of this technique, which would not be possible with conventional SEM techniques because of the requirement for high vacuum and sample coating. With conventional SEM the 2BPY molecule may be removed under high vacuum or lost under the coating material. Unlike the probes previously examined i.e. DMF and CHA, 2BPY is spectroscopically visible to EDX analysis because of the presence of the bromine functional group. In a sense it will act as a tag to highlight areas rich in swelling clay minerals, the ultimate aim being to quantify the surface mineralogy.

8.1 Experimental schedule

The experimental schedule herein investigates:

- Ni^{2+} and Al^{3+} - exchanged SWy-2 -2BPY by TGA and XRD to determine whether intercalation has been successful. These samples were then investigated by ESEM-EDX analysis to determine whether it is possible to locate the presence of bromine on the clay surface.
- B4 rock and the extracted $2\mu\text{m}$ fraction (previously seen in chapters 6 and 7) are also investigated by ESEM-EDX analysis.

- An artificial tri-partite sample consisting of Al^{3+} -SWy-2, feldspar and quartz was investigated to determine whether 2BPY was associated with quartz or feldspar, common constituents of sandstone rocks.

8.2 Results (thermogravimetric studies)

Samples were exposed to 2BPY vapour for a period of 1 week

Figure 8.1 Derivative thermograms of Al^{3+} - and Ni^{2+} -SWy-2-2BPY

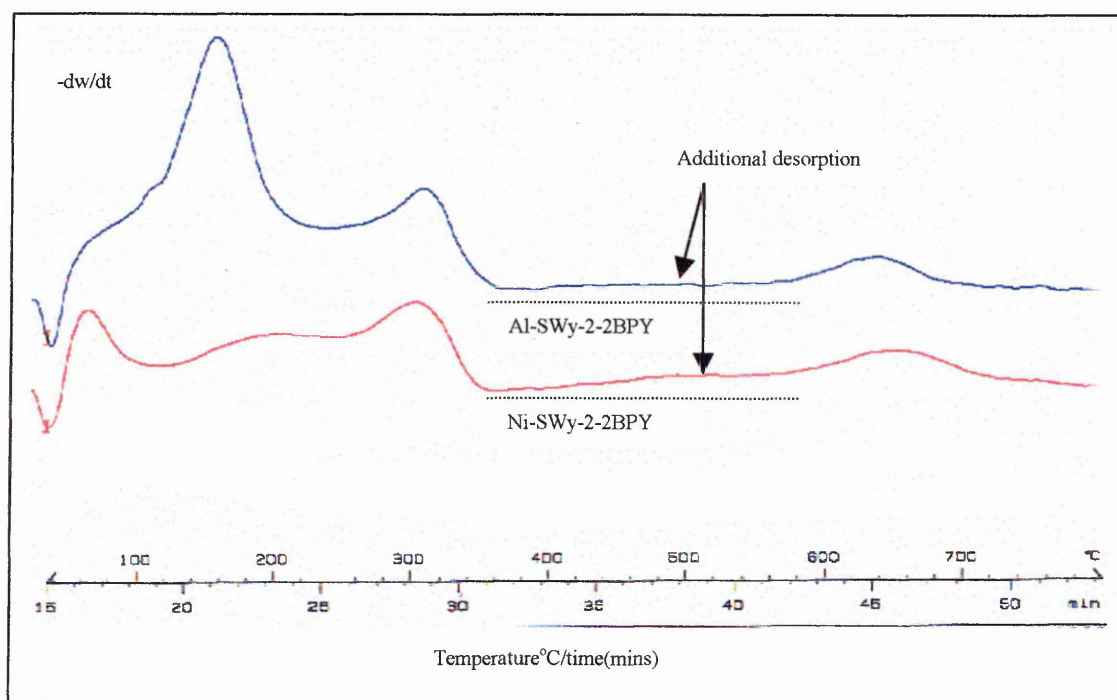


Table 8.1 Thermal desorption summary for Al^{3+} - and Ni^{2+} -SWy-2-2BPY

Sample	1 st / 2 nd weight loss maxima °C	Dehydroxylation maxima °C
Al^{3+} -SWy-2	150/305	650
Ni^{2+} -SWy-2	200/310	640

Figure 8.2 Derivative thermogram of < 2 μ m B4-2BPY

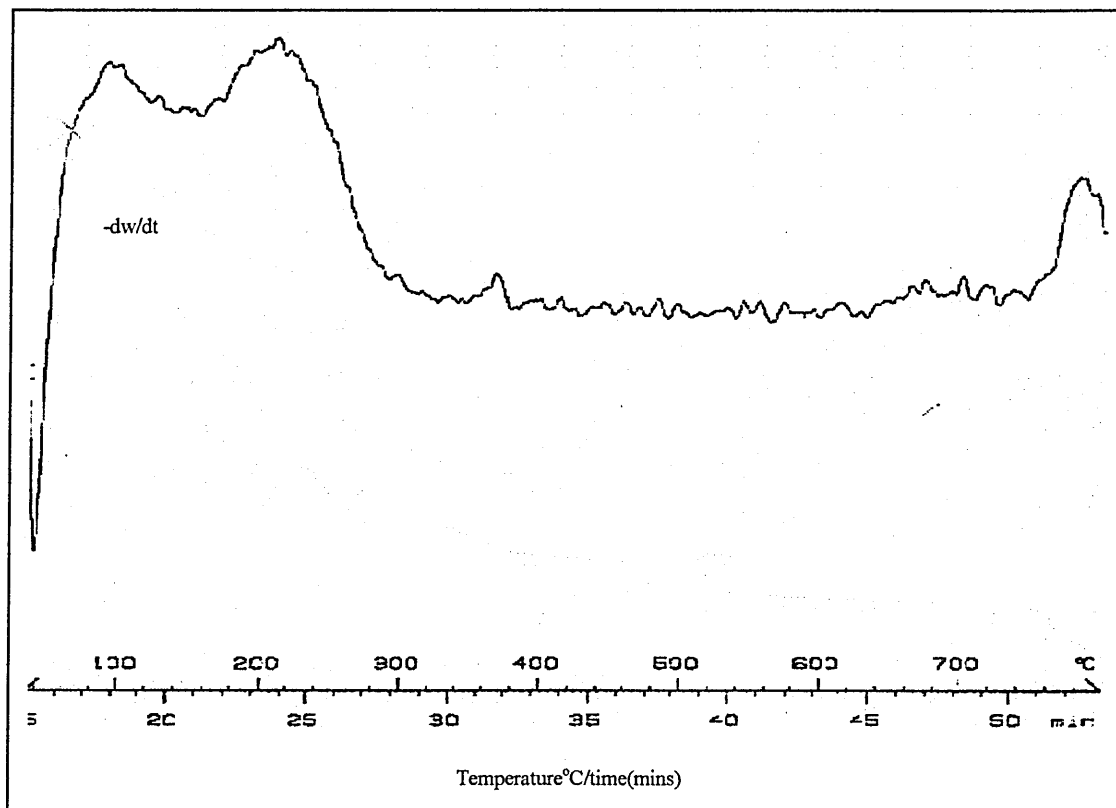


Table 8.2 Thermal desorption summary for < 2 μ m B4-2BPY

Sample	1 st / 2 nd weight loss maxima °C	Dehydroxylation maxima °C
<2 μ m B4 -2BPY	100/210	680/800+

8.3 Summary (thermogravimetric studies)

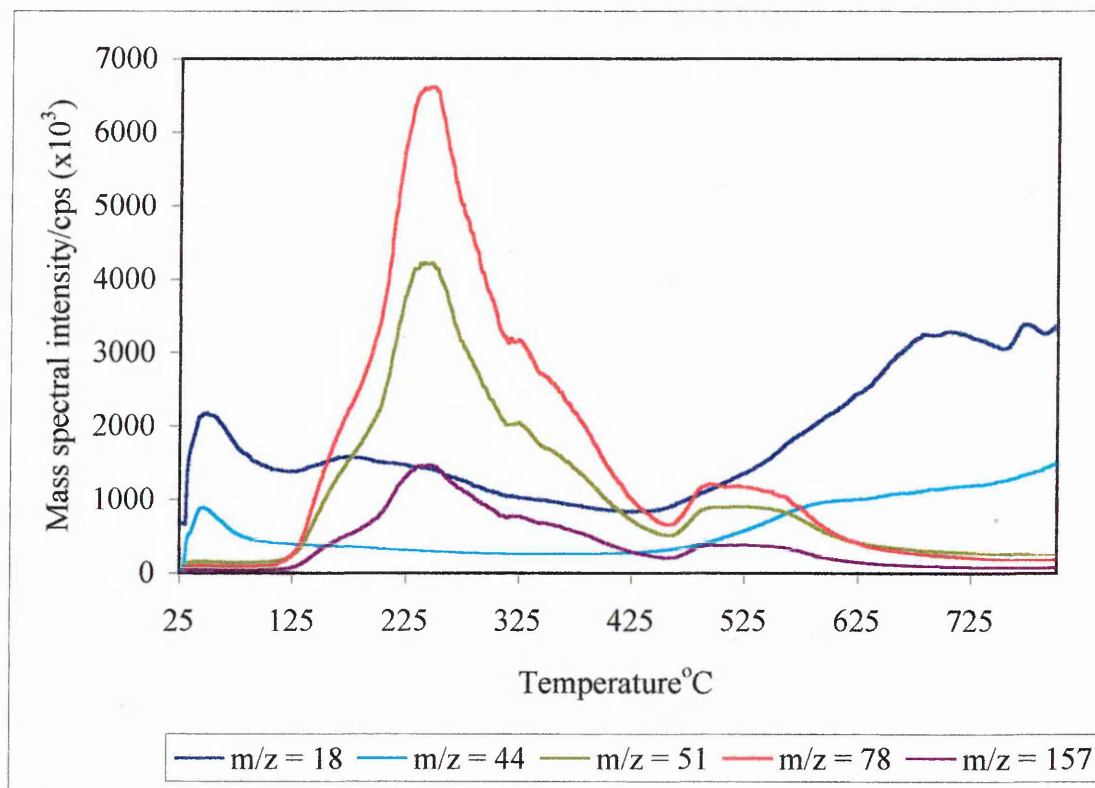
The derivative thermograms for the Ni²⁺- and Al³⁺- exchanged samples are shown in figure 8.1. The desorption maxima at 640 and 650°C has been attributed to structural dehydroxylation. The low temperature desorption maxima of both Ni²⁺(150 and 310°C)- and Al³⁺(200 and 305°C) exchanged SWy-2-2BPY are attributed to 2BPY as

confirmed by RT-MS. In addition figure 8.1 reveals that there is a slow additional weight loss in Ni²⁺-exchanged SWy-2 (but less so in Al³⁺) that occurs from 350°C, being unresolved from the dehydroxylation maxima. The desorption maxima associated with <2um B4-2BPY in figure 8.2 (100/210°C) have been attributed to the desorption of 2BPY. There is evidence for a desorption maxima at 680°C which may be the structural dehydroxylation of a swelling mineral (possible an illite-smectite phase-unconfirmed) and the rising maxima at 800+°C to the dehydroxylation of saponite.

8.4 RT-MS of Al³⁺-SWy-2-2BPY

The RT-MS reconstructed ion chromatograms for Al³⁺-SWy-2-2BPY (fig.8.3) is shown to identify the nature of the additional weight losses (between 350-600°C) observed in the corresponding DTG. Ni²⁺-SWy-2-2BPY and <2um B4 are not shown as the results are very similar. The fragment ions for 2BPY (m/z = 51, 78 and 157 (parent ion)) are shown with ions m/z = 18 (H₂O) and 44.

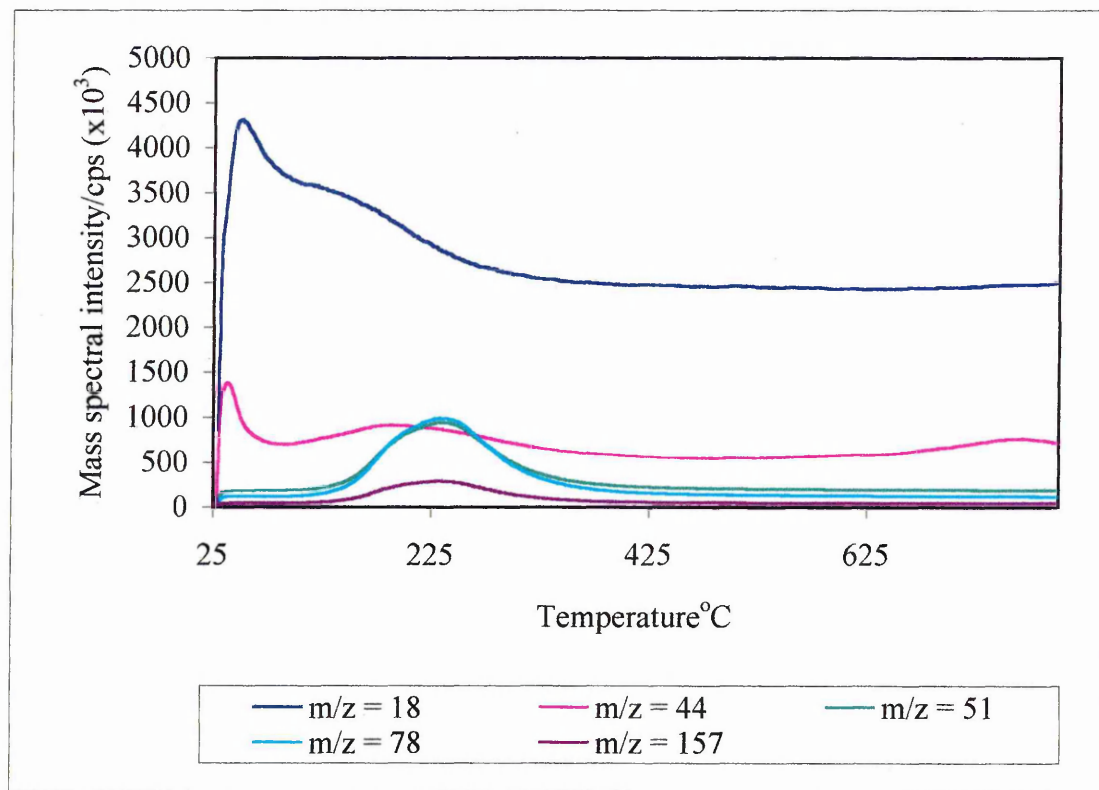
Figure 8.3 RT-MS of Al³⁺-SWy-2-2BPY



8.4.1 Summary RT-MS of Al³⁺-SWy-2-2BPY

RT-MS has confirmed that the additional weight losses (between 350-600°C) in the DTG maxima are due to the combination of water ($m/z = 18$) ion $m/z = 44$ (possibly CO₂ from the breakdown of 2BPY, carbonate material and CO₂ trapped in the structure which is released during dehydroxylation) and 2BPY. The detection of water at low temperature also seems to coincide with the first maxima at 150°C. However, as 2BPY is desorbed at higher temperatures, the detection of water decreases until the beginning of dehydroxylation.

Figure 8.4 RT-MS of <math><2\mu\text{m}</math> B4-2BPY



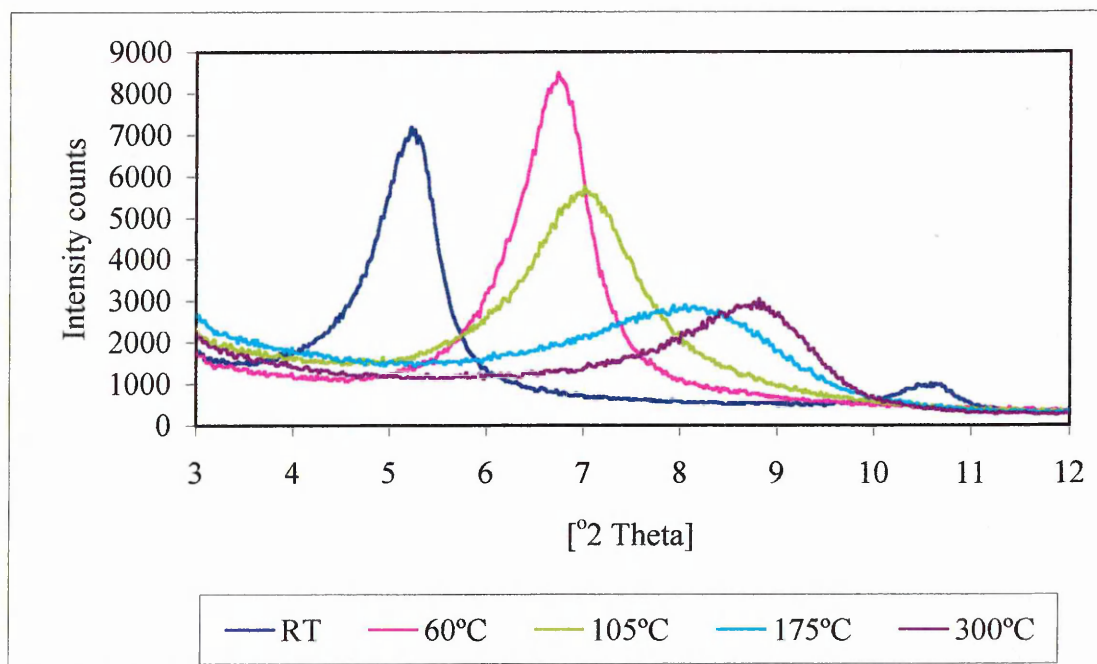
8.4.2 Summary RT-MS of <math><2\mu\text{m}</math> B4-2BPY

RT-MS has confirmed that the primary weight loss observed in the DTG at $200^{\circ}\text{C}+$ is due to $m/z = 18$ (H_2O), $m/z = 44$ (CO_2) and the fragment ions of 2BPY. It would appear that the detection of water from the outset of the run is not directly linked to the detection of 2BPY, as the detection of water is decreasing as the detection of 2BPY is increasing. Therefore the desorption maxima observed at low temperature would appear to consist of two unresolved maxima. RT-MS also reveals the ion $m/z = 44$ at higher temperature which correlates quite well with what was previously thought to be the structural dehydroxylation of a swelling mineral.

8.4.3 Results VT (variable-temperature) XRD

Samples were coated on glass slides and exposed to the probe for a period of 1 week. Diffractograms were recorded at a specific temperature after a 15-minute equilibrium period. Above 300°C (max temperature), the sample was heated in a solvent free oven, then immediately replaced on the heating stage where the XRD trace was recorded. Focusing on the area between 3-12°2 θ , the confirmation and extent of intercalation was measured by noting the intensities and positions of their respective $d_{(001)}$ peaks.

Figure 8.5 VT XRD traces of $d_{(001)}$ spacing of Ni²⁺-SWy-2-2BPY from RT-300°C



* Note 240°C is not shown for Ni²⁺-SWy-2-2BPY so as to aid visualisation

Table 8.3 XRD $d_{(001)}$ spacing for Ni^{2+} -SWy-2-2BPY from RT-300°C

Temperature °C	$d_{(001)}$ spacing/Å	Temperature °C	$d_{(001)}$ spacing/Å
Untreated	14.93	230	11.26
RT	16.80	248	10.72
60	16.39	300	10.63
105	13.02		
175	12.65		

Figure 8.6 VT XRD traces of $d_{(001)}$ spacing of Al^{3+} -SWy-2-2BPY from RT-370°C

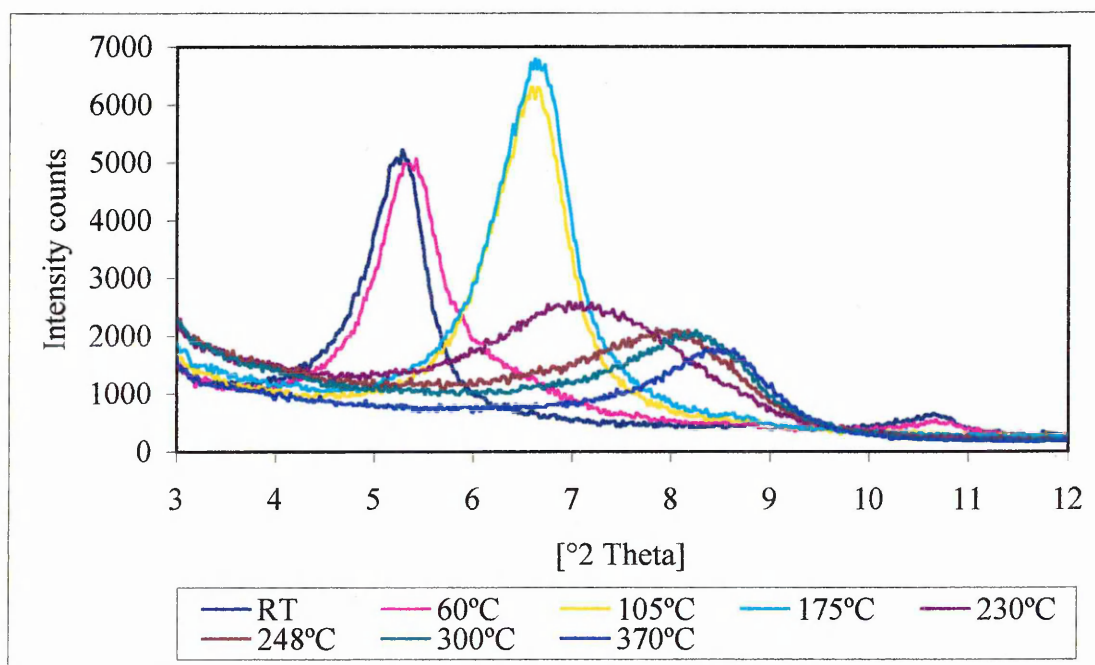


Table 8.4 XRD $d_{(001)}$ spacing for Al^{3+} -SWy-2-2BPY from RT-370°C

Temperature °C	$d_{(001)}$ spacing/Å	Temperature °C	$d_{(001)}$ spacing/Å
Untreated	13.80	230	12.53
RT	16.80	248	11.07
60	16.39	300	10.80
105	13.42	370	10.38
175	13.15		

Figure 8.7 VT XRD traces of $d_{(001)}$ spacing of $<2\mu\text{m}$ B4-2BPY from RT-370°C

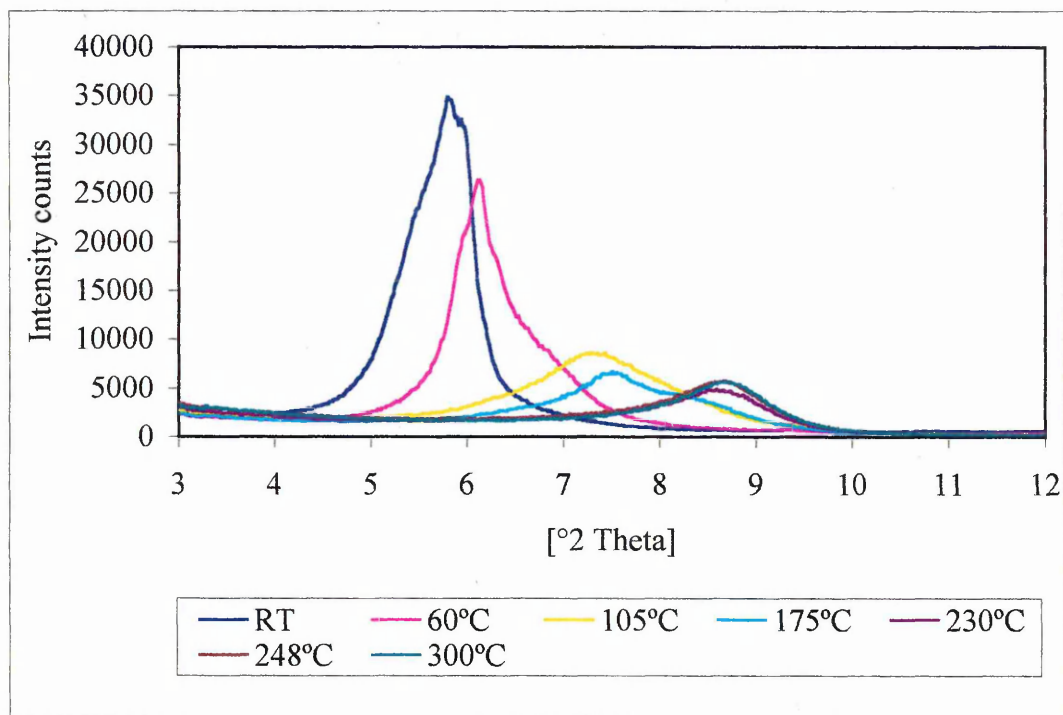


Table 8.5 XRD $d_{(001)}$ spacing for $<2\mu\text{m}$ B4-2BPY from RT-300°C

Temperature °C	$d_{(001)}$ spacing/Å	Temperature °C	$d_{(001)}$ spacing/Å
Untreated	14.90	230	10.31
RT	15.19	248	10.19
60	14.44	300	10.17
105	12.14		
175	11.75		

8.4.4 Summary (XRD)

The d_{001} spacings of both Ni^{2+} - and Al^{3+} -SWy-2 (figs.8.4-8.5) suggest that intercalation of 2BPY has been successful. RT-MS has confirmed the presence of 2BPY to high temperatures (600°C), thus accounting for the un-collapsed interlayer space at 300°C . This suggests that 2BPY is orientated perpendicular to the layer (16.80Å). In comparison the $<2\mu\text{m}$ B4 sample shows very little expansion in the c

direction (15.19Å), the layers being virtually collapsed at 230°C corresponding well with the DTG. This suggests that bonding mechanisms in $2\mu\text{mB4}$ are weaker than those of the cation exchanged SWy-2 and that the orientation of 2BPY is parallel to the layers if intercalation has been successful.

8.4.5 ESEM-EDX analysis of untreated and treated (2BPY) Al^{3+} and Ni^{2+} -SWy-2

8.4.4.1 Experimental

The ESEM was operated in wet mode (using water vapour as the imaging gas) at 20-30kV (accelerating voltage) and pressures of between 1.0-3.1 Torr. The EDX was calibrated using standards supplied by Oxford instruments, the details of which are given in table 8.6 [372]. All samples were ZAF corrected to convert specimen/standard intensity ratios into concentration values.

Table 8.6 EDX standards

Element-($K_{\alpha 1}$ line)	Standard
O-(0.5249)	Quartz
Na-(1.04098)	Albite
Mg-(1.25360)	MgO
Al-(1.48670)	Al_2O_3
Si-(1.73998)	Quartz
S-(2.3074)	FeS_2
K-(3.3138)	MAD-10
Ca-(3.69168)	Wollastonite
Ti-(4.51084)	Titanium
Mn-(5.89875)	Manganese
Fe-(6.40384)	Iron
Cu-(8.04778)	Copper
Br-(11.9242)	KBr

Figure 8.8 ESEM image of untreated Ni²⁺-SWy-2

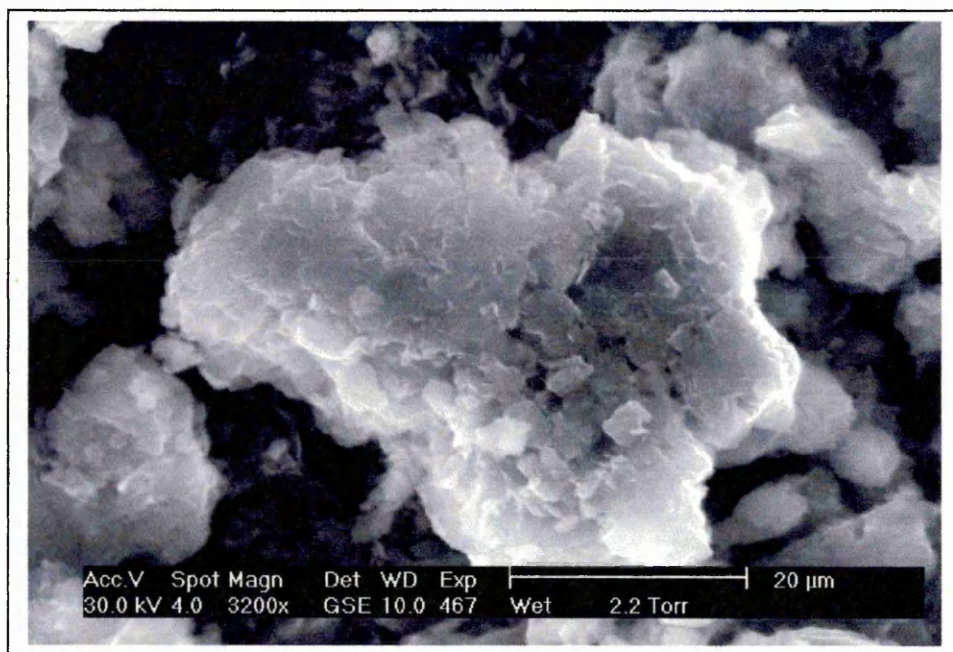


Table 8.7 EDX semi-quantitative analysis of untreated Ni²⁺-SWy-2

Element	Element mass %
O	63.20
Na	0.11
Mg	1.08
Al	9.22
Si	22.75
S	0.07
K	0.45
Ca	0.08
Fe	1.60
Ni	1.47
Br	-0.03

Figure 8.9 ESEM image of Ni²⁺-SWy-2-2BPY

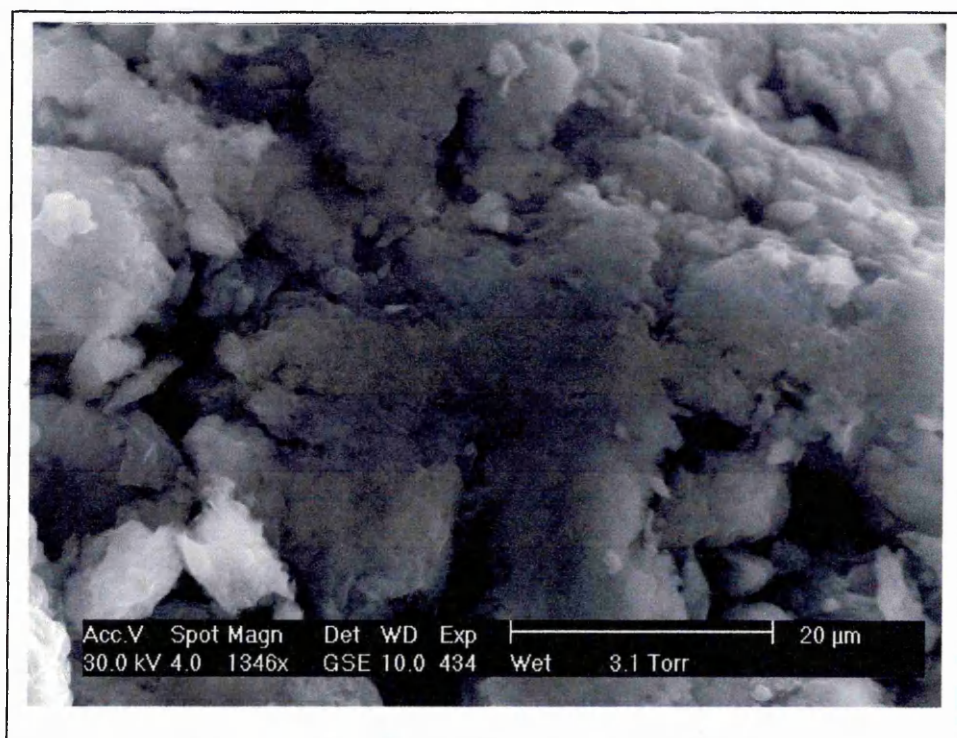


Table 8.8 EDX semi-quantitative analysis of Ni²⁺-SWy-2-2BPY

Element	Element mass %
O	63.05
Na	0.03
Mg	0.99
Al	7.56
Si	23.49
S	0.04
K	0.11
Ca	0.09
Fe	1.45
Ni	3.44
Br	2.34

Figure 8.10 ESEM image of untreated Al³⁺-SWy-2

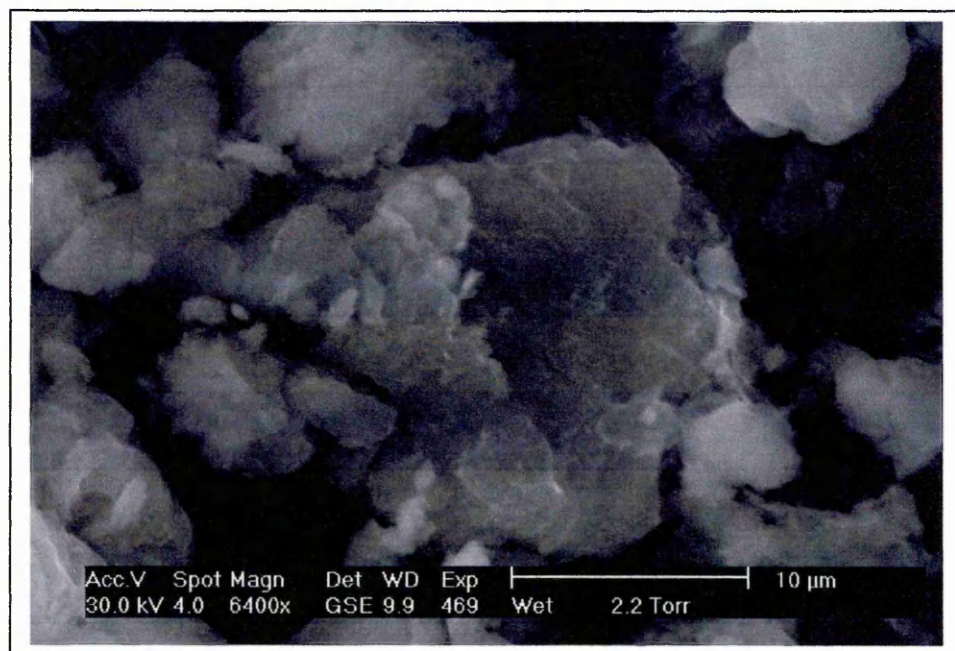


Table 8.9 EDX semi-quantitative analysis of untreated Al³⁺-SWy-2

Element	Element mass %
O	64.63
Na	0.14
Mg	1.18
Al	9.48
Si	22.97
S	-0.01
K	0.09
Ca	0.06
Fe	1.56
Br	-0.10

Figure 8.11 ESEM image of Al^{3+} -SWy-2-2BPY

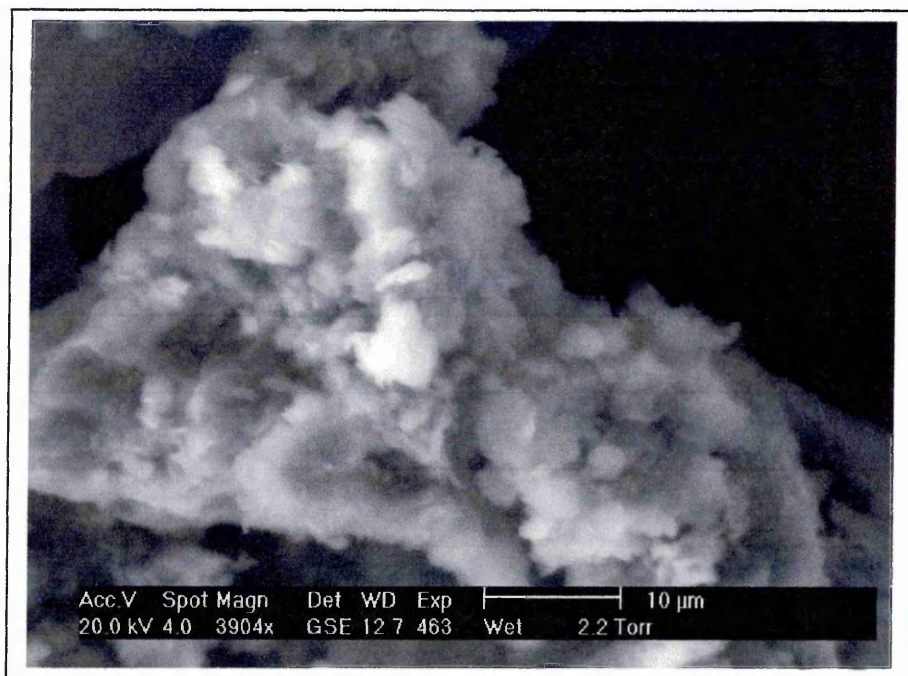


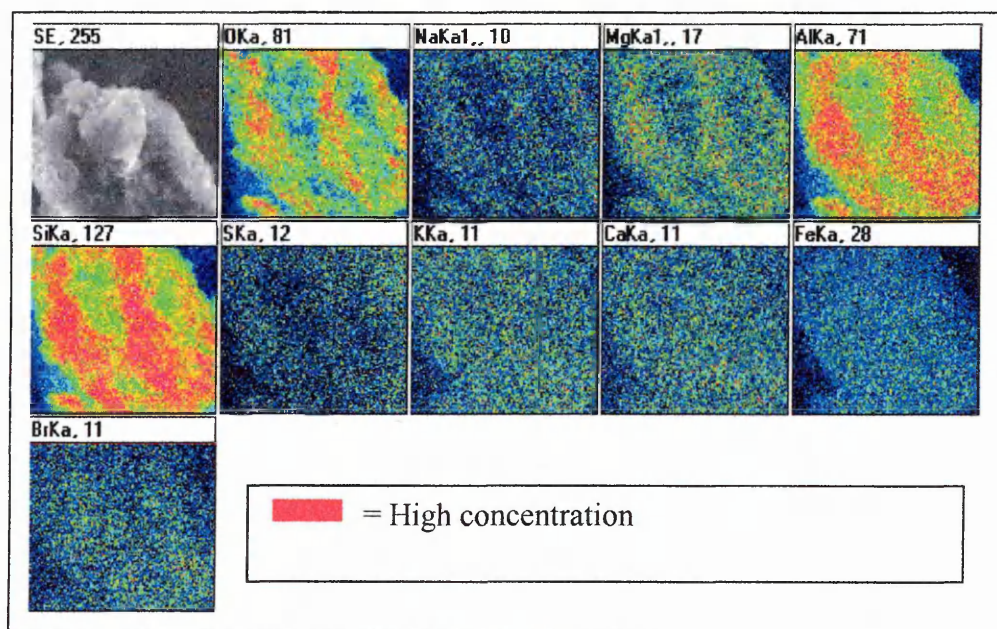
Table 8.10 EDX semi-quantitative analysis of Al^{3+} -SWy-2-2BPY

Element	Element mass %
O	55.54
Na	0.030
Mg	1.06
Al	10.62
Si	26.83
S	-0.002
K	0.12
Ca	0.03
Fe	3.01
Br	2.77

8.4.6 EDX element mapping

An elemental map was constructed (using the K_{α} lines of each element) by focusing the beam on each particular point for a period of 200 seconds in order to visualise the elemental distribution within the sample. The element map of Al^{3+} -SWy-2-2BPY is shown as an example. Ni^{2+} -SWy-2-2BPY is not shown.

Figure 8.12 XDX element map of Al^{3+} -SWy-2-2 BPY



8.4.7 Summary of ESEM-EDX analysis of untreated and treated (2BPY) Al^{3+} and Ni^{2+} -SWy-2

The results of Ni^{2+} - and Al^{3+} - exchanged SWy-2-2BYP by ESEM-EDX has shown that it is possible to:

- show the varying morphologies of cation exchanged SWy-2 with minimal sample preparation
- Identify trace amounts of nickel and bromine in powdered samples at 3.44% and 2.34 % respectively.

The first part of the document discusses the importance of maintaining accurate records of all transactions. It emphasizes that proper record-keeping is essential for the success of any business and for the protection of the interests of all parties involved. The document also highlights the need for transparency and accountability in all financial dealings.

Financial Statement Analysis



The second part of the document discusses the importance of maintaining accurate records of all transactions. It emphasizes that proper record-keeping is essential for the success of any business and for the protection of the interests of all parties involved. The document also highlights the need for transparency and accountability in all financial dealings.

Conclusion

In conclusion, the document emphasizes the importance of maintaining accurate records of all transactions and the need for transparency and accountability in all financial dealings. It also highlights the need for proper record-keeping and the protection of the interests of all parties involved.

The document also highlights the need for transparency and accountability in all financial dealings. It emphasizes that proper record-keeping is essential for the success of any business and for the protection of the interests of all parties involved.

The document also highlights the need for transparency and accountability in all financial dealings. It emphasizes that proper record-keeping is essential for the success of any business and for the protection of the interests of all parties involved.

However, because of the low levels detected the element maps do not highlight any areas of bromine concentration. This may be expected as the sample is virtually pure clay.

8.4.8 ESEM-EDX analysis of B4 rock and <math><2\mu\text{m}</math> B4-2BPY

As previously seen in chapters 6 and 7, B4 is described as a Triassic sandstone containing saponite. The images shown in figures (8.13-8.14) of the untreated rock (whole) show the morphologies of its constituent components.

Figure 8.13 B4-1 (High definition clay particle image)



Figure 8.13 shows evidence of platy clay and fibrous material (illite or amphibole). EDX analysis shows that silicon is the dominant element along with Mg, Al, Ca and Fe. Magnesium is the next dominant phase (approx. 20%), which suggests the presence of saponite. However, at this low vacuum (2.2 Torr) the beam spreads out

causing a skirting effect, the result of which can show the presence of some minor elements (Ca and Fe) up to 100 μ m away for the analysis spot.

Figure 8.14 B4-2 (etched mineral)

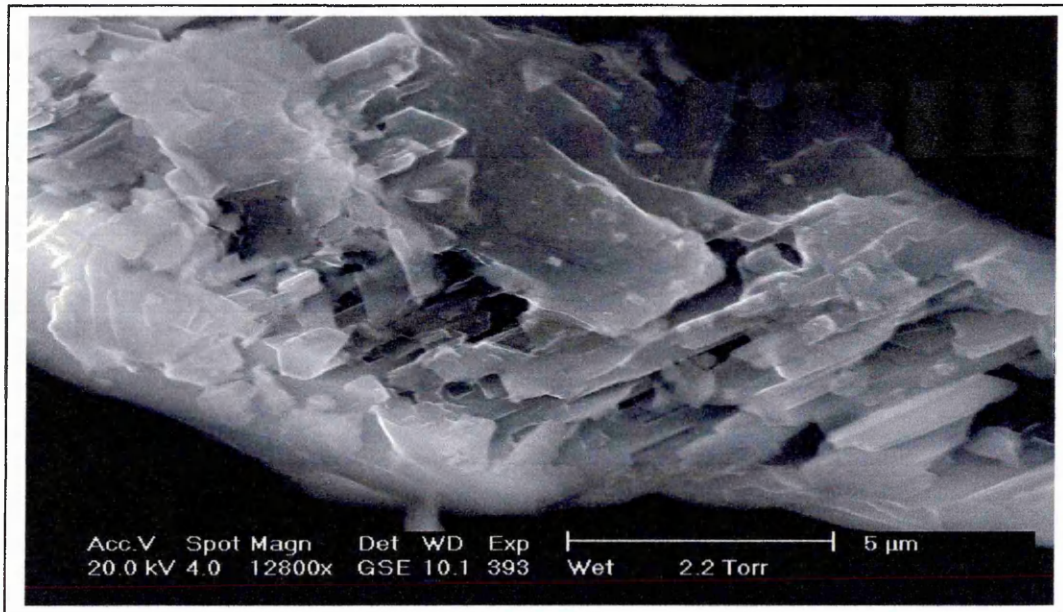


Figure 8.14 shows cylindrical type etching typical of feldspars (possibly albite-due to Na concentration) with some secondary clay particles occupying the etched areas (possibly saponite-high Mg content).

1. The first part of the document is a list of names and addresses.

2. The second part of the document is a list of names and addresses.

3. The third part of the document is a list of names and addresses.

4. The fourth part of the document is a list of names and addresses.

5. The fifth part of the document is a list of names and addresses.

6. The sixth part of the document is a list of names and addresses.

7. The seventh part of the document is a list of names and addresses.

Figure 8.15 B4-3 (composite particle)

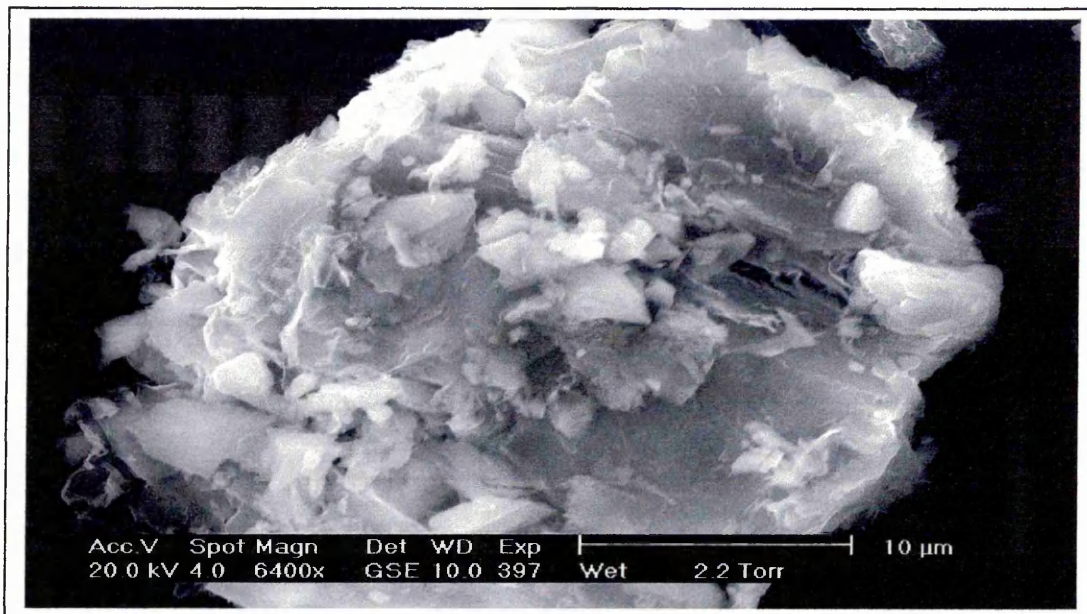


Figure 8.15 shows a composite particle consisting of small crystals wrapped in a clay coating. Table 8.11 shows the EDX results for this particle.

Table 8.11 EDX analysis of B4-3 (composite particle)

Element	Element mass %
O	60.92
Na	1.01
Mg	8.66
Al	4.22
Si	20.56
S	0.19
K	0.01
Ca	0.09
Fe	0.21

Figure 8.16 ESEM image of 2BPY treated B4 rock



Table 8.12 EDX analysis of 2BPY treated B4 rock

Element	Element mass %
O	52.02
Na	1.08
Mg	4.03
Al	0.93
Si	21.13
S	0.03
K	-0.01
Ca	1.76
Fe	12.48
Cu	-0.04
Br	6.29



CHAPTER 10: THE HISTORY OF THE UNITED STATES

The history of the United States is a complex and multifaceted story that spans centuries. It begins with the early Native American civilizations, such as the Mayans, Aztecs, and Incas, who built sophisticated societies in the Americas. The arrival of European explorers in the late 15th century marked the beginning of a new era, as they sought to establish trade routes and colonies. The United States was founded in 1776, and its early years were characterized by a struggle for independence and the development of a unique political system. The American Revolution (1775-1783) was a pivotal moment in the nation's history, leading to the signing of the Declaration of Independence and the establishment of the United States as a sovereign nation. The early 19th century saw westward expansion and the discovery of gold, which fueled the growth of the American economy. The Civil War (1861-1865) was a defining moment in the nation's history, as it resolved the issue of slavery and preserved the Union. The late 19th and early 20th centuries were marked by industrialization, urbanization, and the rise of the Progressive Era. The United States emerged as a global superpower after World War II, and its influence has shaped the modern world. Today, the United States continues to play a leading role in international affairs, and its history remains a source of inspiration and pride for its citizens.

Figure 8.17 ESEM image of <2um B4-2BPY



Table 8.13 EDX semi-quantitative analysis of <2um B4-2BPY

Element	Element mass %
O	59.13
Na	1.90
Mg	7.92
Al	4.0
Si	21.05
S	0.10
K	0.08
Ca	1.41
Ti	0.08
Mn	0.05
Fe	3.87
Cu	0.20
Br	0.20

8.4.9 Summary ESEM-EDX analysis of B4 rock and <2um B4-2BPY

ESEM analysis has been successful in highlighting the variety of mineral morphologies in B4 rock from platy to fibrous material. As previously stated, the high magnesium contents found in the clay particles analysed indicate saponite. The concentration of bromine detected from B4 (6.29%) rock is in contrast to that found in the <2um fraction (0.20%). This immediately highlights the problems associated with



The first part of the study was designed to determine the effect of the treatment on the response of the subjects. The results of the study are presented in the following table. The data show that the treatment had a significant effect on the response of the subjects. The mean response of the subjects in the treatment group was significantly higher than the mean response of the subjects in the control group. This result is consistent with the hypothesis that the treatment would have a positive effect on the response of the subjects.

The second part of the study was designed to determine the effect of the treatment on the response of the subjects. The results of the study are presented in the following table. The data show that the treatment had a significant effect on the response of the subjects. The mean response of the subjects in the treatment group was significantly higher than the mean response of the subjects in the control group. This result is consistent with the hypothesis that the treatment would have a positive effect on the response of the subjects.

representative sampling and the need for more replicate observations and further steps to purify the extracted phase. However, the low desorption maxima (DTG) seen for $<2\mu\text{m}$ may imply that 2BPY is not stable to removal by a small vacuum over long periods.

8.5 ESEM and EDX analysis of a tripartite sample (Al^{3+} -SWy-2, Na-Albite, Quartz (seasand))

The tripartite sample consisted of three materials separated from each other (fig. 8.18) with some slight overlap at the junction of each material. The sample was then placed in an incubator for a period of 1 week and exposed to 2BPY vapour. Analysis of each component occurred about half way across its section.

Figure 8.18 Tripartite sample (Al^{3+} -SWy-2, Na-Albite and Quartz (seasand))

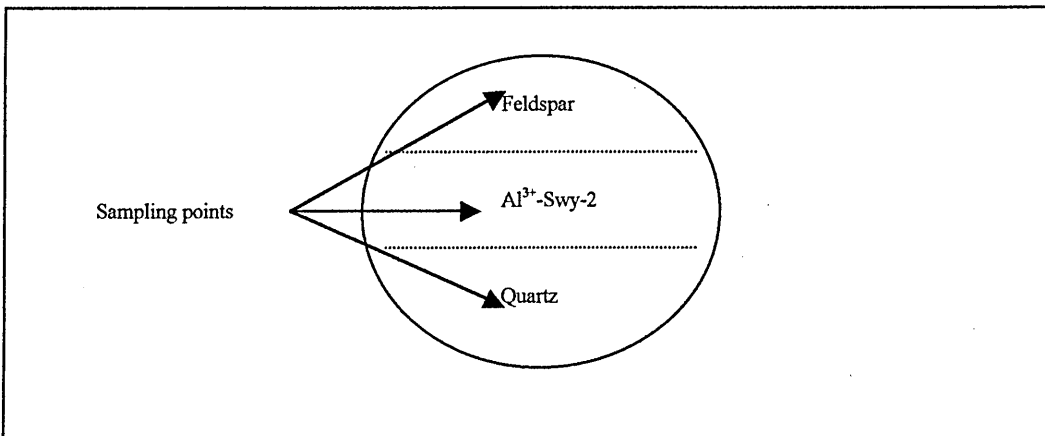


Figure 8.19 ESEM image of Al³⁺-SWy-2-2BPY (tripartite sample)



Figure 8.20 EDX element map of Al³⁺-SWy-2-2BPY (tripartite sample)

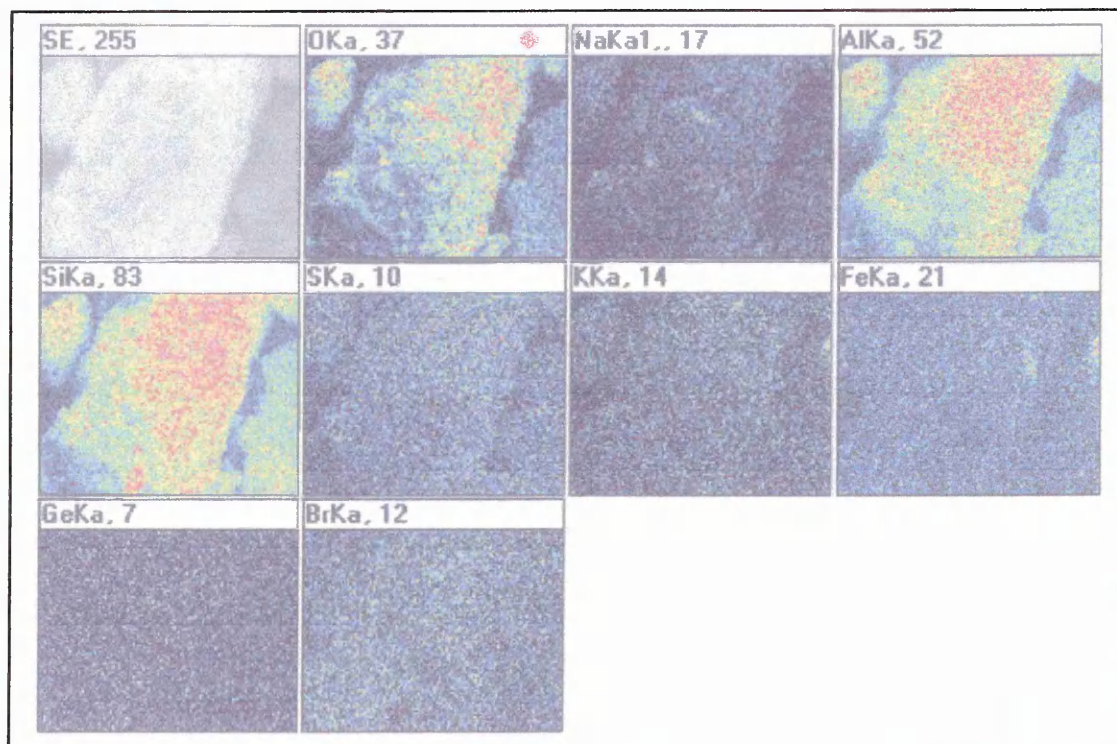


Figure 8.21 ESEM image of Na-feldspar (tripartite sample)

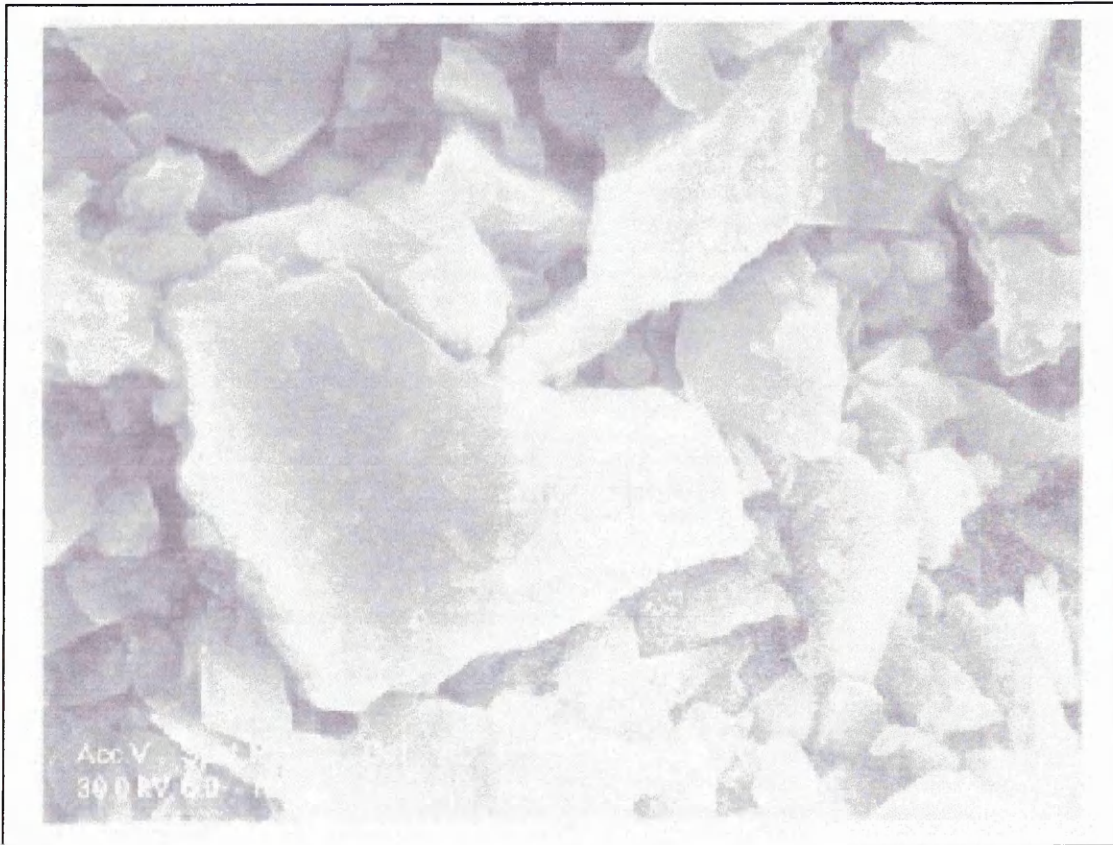


Figure 8.22 EDX element map of Na-feldspar (tripartite sample)

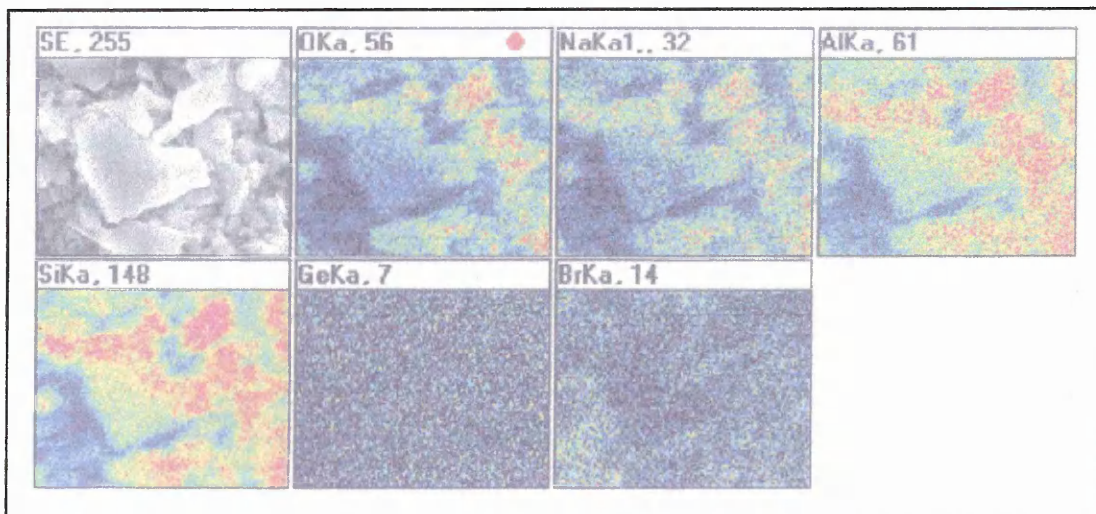


Figure 8.23 ESEM image of Quartz (seasand)(tripartite sample)

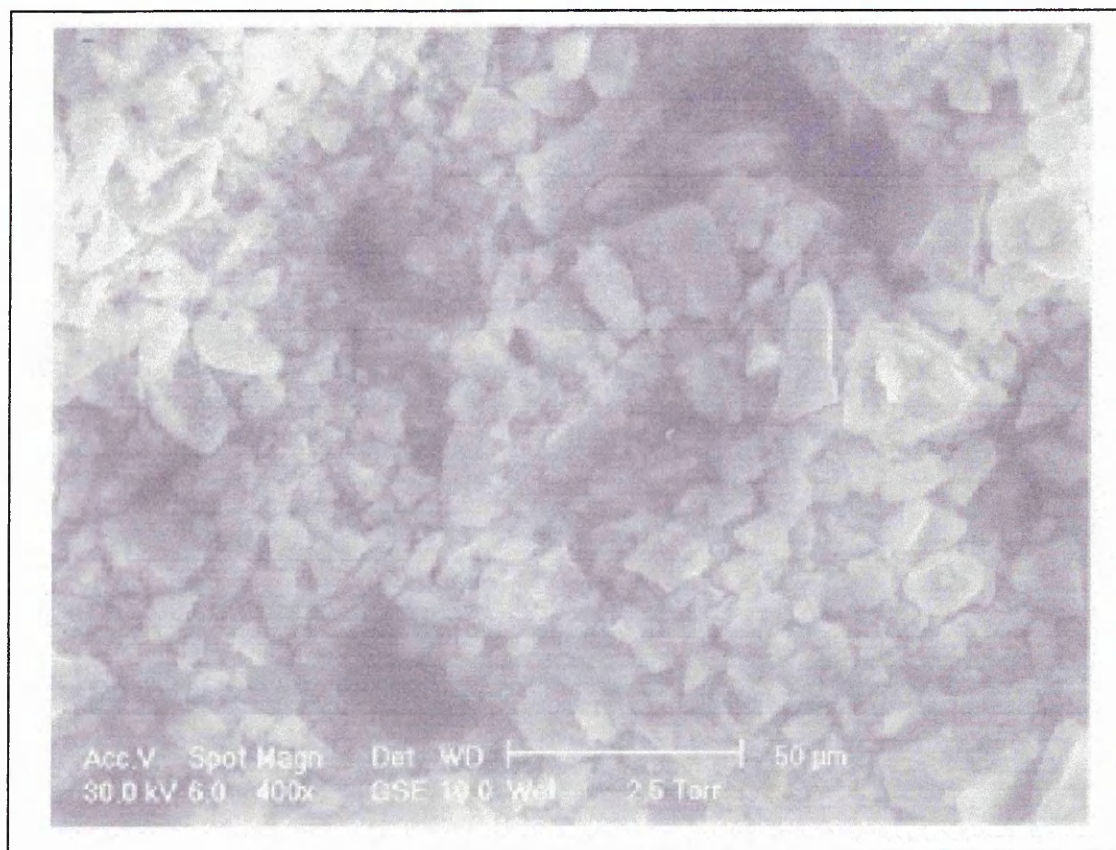
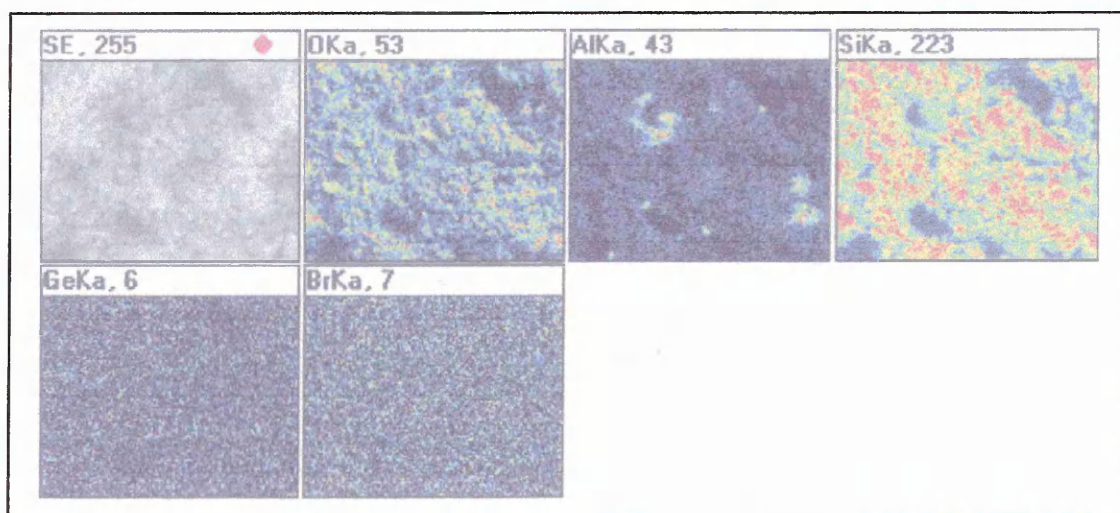


Figure 8.24 EDX element map of Quartz (seasand)-2BPY (tripartite sample)



8.5.1 Summary ESEM and EDX analysis of a tripartite sample (Al³⁺-SWy-2, Na-albite, Quartz-seasand)

The EDX analysis of bromine for each tripartite component is shown in table 8.14

Table 8.14 Tripartite sample EDX bromine results

Al ³⁺ -SWy-2	Na-albite	Quartz (seasand)
4.4-5.7 % Br	1.7-2.0 % Br	0.35-0.71 % Br

The % bromine identified on the Al³⁺-SWy-2 sample is greater than previously observed (table 8.10-2.77%). Na-albite feldspar (a component of the mixed mineral standards shown in chapter 7) shows (fig 8.22) bromine associated with the interstitial phases around the edges of the main particle. This may in part be due to the possible presence of a swelling mineral as identified by the XRD of the feldspar components in chapter 7, or an excess of physisorbed 2BPY. In comparison, quartz showed quite low values for bromine, being only slightly above the background.

8.5.2 Conclusion

The studies herein have been successful in identifying swelling minerals by EDX analysis. However, the detection of bromine on the surface of these minerals has highlighted several important points for future work. The suggestions herein must form part of an integrated methodology.

- There are problems associated with statistically representative sampling areas. A possible solution would be to identify a particle and raster the beam across a specific area whilst collecting X-ray data. Then replicating this approach across a greater area.
- The accelerating beam voltage and analysis spot size needs to be optimised for bromine detection as a lower voltage (i.e. 20kV) may be better for the low energy X-ray emission lines (K_{α} and L lines). * Note there is already overlap from the Al $K_{\alpha 1}$ and the Br $L_{\alpha 1}$ lines.
- In addition, higher voltages (30kV) may burn away 2BYP from the sample surface therefore reducing the accuracy and reproducibility of results.
- At optimum voltage there is a need to determine the stability of 2BYP over time.
- The pressure within the chamber also needs to be optimised so as to reduce beam skirting common at low pressures where interference occurs from analyte outside the main sampling area.
- It would be also advisable to condition each sample in a nitrogen flow (away from the ESEM sample chamber) so as to remove physisorbed 2BYP.
- Though not important at this juncture, there is a need to both qualify and quantify the component constituents present in the untreated samples (i.e.B4) samples so that more accurate relationships can be determined between components and reported bromine concentrations.
- Examination of B4 rock has shown that localised clay concentrations are naturally easier to highlight. A study of a variety of rock types to determine the types and variety of clay distributions may provide valuable information to enhance our understanding of probe desorption.

- Further studies may include real time ESEM-EDX thermal desorption (peltier stage) studies of 2BYP from both powdered and rock samples combined with EGA analysis which would enhance our understanding of the morphological changes occurring during probe desorption and dehydroxylation.

Chapter 9 Conclusions

9.1 Characterisation of swelling minerals using chemical probes

The experimental results in this thesis have shown that characteristic EGA detection profiles can be obtained from the desorption of organic probe molecules from clay minerals. The combination of chemical probe and dehydroxylation profiles has been exploited in order to develop a method of characterising clay minerals contained within sandstones and reservoir rocks. Several potential probe molecules were studied herein.

It has been shown that as a potential probe, CHA (cyclohexylamine) was not considered suitable. EGA has shown that CHA is not a stable probe molecule i.e., the amount of CHA detected is not directly proportional to the amount of swelling mineral present. Instead, detection involved the detection of catalytically altered CHA as evolved products gases, which depended on the interlayer cation and varying amounts of water present.

CHA decomposed along different routes via inter-related mechanisms that were cation dependent. Over Al^{3+} -SWy-2 hydrodenitrogenation via the Hofmann degradation was the predominant route whereas ring dehydrogenation to aniline either directly from CHA or possibly via cyclohexylimine was significant over Ni^{2+} -SWy-2. A proportion of the ammonia produced over Al^{3+} -SWy-2 was retained to temperatures in excess of 500°C . In contrast some ammonia was released from Ni^{2+} -SWy-2 prior to the corresponding alkene which was probably held on the clay surface via the unfilled d-orbitals of the Ni^{2+} -cation. Very little unmodified cyclohexylamine was detected in the evolved gases which means that the desorption of CHA cannot be used as a

quantitative measure of the acidity of cation-exchanged clays. Nonetheless, because all the products which evolve during the diagnostic weight loss are derived from CHA the mass loss does give a semi-quantitative measure of the clay acidity. However, the acidity is likely to be underestimated because ammonia is lost before the diagnostic event in Ni²⁺-SWy-2 and at much higher temperatures from Al³⁺-SWy-2. It appears that this discrepancy may be compensated by the presence of evolved water which contributes to the weight loss under the diagnostic peak. This probably explains why values for the acidity of clays and related oxides derived from 'cyclohexylamine' desorption in the temperature range 250 to 400°C have been linearly related to their catalytic activity. Nonetheless, as a qualitative probe, CHA has the potential to distinguish the difference between Ni²⁺ and Al³⁺-SWy-2 due to the detection maxima of the observed evolved gas patterns.

From a quantitative point of view, the use of CHA highlights several problems. Interference from other co-evolving products makes it difficult to use the CHA parent ion and its detection varies considerably depending on the nature of the interlayer cation. In a mixed cation system, this may inhibit quantitation. The other important feature which may enable the detection of non-swelling minerals is dehydroxylation. The thermal desorption of CHA and its products is known to have an adverse affect on the dehydroxylation region (broadening and lowering its detection range) which would complicate the determination of kaolinite, chlorite and illite by their characteristic dehydroxylation peaks.

The study of 3CYP (3-Cyanopyridine) as a suitable probe has shown highlighted several important points. TGA has shown that temperature programmed desorption (TPD) is capable of distinguishing between the Ni²⁺- and Al³⁺ exchanged forms of SWy-2. Though the unresolved maxima attributed to 3CYP desorption,

indicates that the different adsorption sites had similar desorption energies. However, 3CYP is a solid with a low vapour pressure, which is not ideal for its use as a probe molecule. Therefore the six-day incubation period necessary to produce reasonable weight loss maxima (12-13 %) is expected, but too long in comparison to CHA. However, under conditions of increased temperature and pressure, this incubation period could be reduced to a shorter, more acceptable period. VT DRIFTS indicates that the Al^{3+} -sample protonates 3CYP through the pyridine nitrogen suggesting its acidity is predominantly Brønsted in nature, with some evidence of Lewis acidity at higher temperatures. In relation to the corresponding DTG (derivative thermogram) maxima, this would suggest that the main desorption (240°C -MS) may be attributed to the cyanopyridinium ion and the small shoulder at 340°C attributed to Lewis bound pyridine. There is also evidence to suggest that 3CYP is also coordinated through its nitrile group. The main nitrile band between 100 - 250°C shows a shoulder which changes from 2238 - 2248 cm^{-1} coinciding with increased protonation and alteration to Lewis bound pyridine above 300°C . Moreover, the disappearance of the shoulder at 2248 cm^{-1} and the appearance of one nitrile absorbance at 300°C (2250 cm^{-1}) is very similar to that seen in the Ni^{2+} sample at these temperatures. Contrastingly, the Ni^{2+} -sample shows direct evidence of Lewis bound pyridine and suggests protonation due to a weak band at 1630 cm^{-1} (to 300°C). This corresponds to a weak shoulder on its DTG maxima at 300°C , indicating the possible presence of Brønsted bound pyridine. However, the suggestion of resonance effects makes it difficult to determine whether the nitrile group is involved in bonding in the Ni^{2+} or Al^{3+} sample. However the fact that the Brønsted bound pyridine of the Al^{3+} sample desorbs at 80°C less, suggests that the combination of protonation and nitrile coordination, effects not only coordination, but has the effect of lowering the desorption temperature of the Al^{3+}

sample. Complimentary evidence from VT XRD and TGA has shown that after 6 days incubation, the room temperature trace is representative of two different interlayer orientations (Ni^{2+} -perpendicular-21.45Å/ Al^{3+} -parallel-13.13Å) of 3CYP. Considering one of the probe pre-requisites is the to quickly intercalate, it is not possible to determine whether both samples were fully intercalated. hence studies of this nature were not pursued. However intercalation studies would be necessary for the purpose of publication. Heating from room temperature-105°C quickly reverts the Ni^{2+} - sample to a spacing of 13.88 Å, similar to that of the Al^{3+} -sample at room temperature. The broadness of the changing d_{001} peak between 60-105°C and its sharpening near at 175°C, indicate that 3CYP undergoes rearrangement of its orientation within the interlayer space. The unsuitability of 3CYP as a probe molecule is also highlighted by its ability to condense within the EGA system (Bp 202°C), demonstrated by the detection of 3CYP within the system after a routine post run blank. In particular, contamination occurred within the OTM trap and GC column, taking several days to clean the system.

9.2 The qualitative characterisation of minerals by chemometric analysis of EGA detection profiles

Of the chemical probes studied so far, the one that produced the most potential was DMF (Dimethylformamide). The suitability of DMF as a probe molecule is highlighted by its fast adsorption/intercalation rate, and distinctive maxima seen in the DTG traces for montmorillonite and illite after only 5 and 17 hours respectively. It has also been shown that different exchange cations within montmorillonites could readily be distinguished simply by the temperature at which the DMF molecules

desorbed during TGA studies. However DMF is not without its potential problems and EGA analysis at lower temperatures (145°C) showed it was subject to diffusional broadening which reduces the usefulness of detection features suitable for chemometric analysis. At higher temperatures (250°C) breakdown of DMF within the EGA system occurred. Experimental studies have shown that 190°C and 180°C was the optimum temperatures for both the transfer line and the external heating zone.

The feasibility of applying chemometric analysis to EGA detection profiles (i.e reconstructed chromatograms) has highlighted several important considerations for quantitative analysis of clay minerals. In general all training samples were successfully allocated to their respective groups, however more samples would be required to statistically describe the variability within the illite, kaolinite and chlorite groups. PLS analysis was shown to be the most successful discrimination technique when combined with the mehalanobis distance metric. The clumping observed in M^{n+} exchanged -SWy-2 has shown the closeness of this group and ability to identify individual members from their DMF detection temperatures. The detection of non-swelling minerals (kaolinite and chlorite) using dehydroxylation ($m/z = 18$) has highlighted the potential problems due to overlapping dehydroxylation regions and relative concentration of each component, in particular when evaluating the GP-FTIR TIR and RT-MS TIC where the relative contribution from dehydroxylation is small in comparison to DMF. This suggests that the -OH region may benefit from further pre-processing to enhance its features. The application of the TGA weight loss profile has the ability to successfully discriminate between the four groups chosen, though probably lacks the sensitivity required for quantitative analysis unless more sensitive instrumentation was applied. GP-FTIR produced reasonable results considering the quality of the profiles obtained, but could in general be subject to fluctuations in

detector response rendering it unreliable. RT-MS has the potential to be the most sensitive and reliable technique as demonstrated by the quality and consistency of the profiles obtained. The selective use of ions 18 and 73 has aided better discrimination and holds the most potential for more sensitive applications.

9.3 The quantitative characterisation of minerals by chemometric analysis of EGA RT-MS detection profiles

Quantitative analysis training sets consisted of 6 components known to be present in sandstone cores i.e. quartz, feldspar, montmorillonite, kaolinite, illite and chlorite. It has been shown that grinding and mixing of samples produced the best results for the linearity of DMF detection versus increasing montmorillonite concentration, due to greater sample homogeneity.

The use of data pre-processing techniques (i.e. mean centering, variance scaling and derivatization) have shown improved prediction results. Model① used the TIC profile as a detection feature but produced limited success. The result of DMF dominating the TIC, is that even with considerable pre-processing, contributions from clay mineral dehydroxylation are minimal, producing low R^2 values (0.74) for KGa-2 and CCa-1. By using the reconstructed chromatogram profile of the DMF parent ion ($m/z = 73$), Model② has shown that it is possible to improve upon the R^2 value of 0.93 and 0.91 seen in the TIC (derivative) training sets of model①. Model② calculated a good R^2 value of 0.98 though was unable to predict illite in the presence of montmorillonite because of their overlapping detection profiles (where uptake of DMF by 1-Mt is comparatively small). As a feasibility study the use of ion $m/z = 18$ has shown great promise for the prediction of clay minerals in rocks (model③).

Model③ has shown that DMF in effect further defines the cation-interlayer water relationship because there is a definite relationship between the amount of DMF defined water and the concentration of SWy-2. The R^2 values for SWy-2 (0.95), KGa-2 (0.97) and CCa-1 (0.95) are reasonable. However, the model could not recommend any PLS factors for 1-Mt-illite and could therefore not predict this component.

9.4 Characterization of swelling clay minerals by ESEM-EDX analysis of 2-Bromopyridine (2BPY)

The study of Ni^{2+} - and Al^{3+} - exchanged SWy-2-2BYP (2-Bromopyridine) by ESEM-EDX has shown that it is possible to show the varying morphologies of cation exchanged SWy-2 with minimal sample preparation and identify trace amounts of nickel and bromine in powdered samples. However, there are several issues which demand further study such as representative sampling, optimising beam voltage and the problems associated with beam skirting at low pressures where interference occurs from analytes outside the main sampling area. There is also the possibility that the bromine molecule is possibly being detected in the gas phase. This highlights the need to investigate the stability of the 2BYP over time.

Chapter 10 Postgraduate study, Posters, Publications and References

10.1 Postgraduate study

1. Practical Chemometrics workshop at the Institute of Food Research 2-3 November (1999)

10.2 Posters

Part of the results of this thesis have been presented at the following conferences and meetings.

- (1) Variable temperature Diffuse Reflectance Infrared Fourier Transform Spectroscopy (DRIFTS) and Thermogravimetry-Evolved gas analysis (TGA-EGA) of the desorption of Cyclohexylamine from cation exchanged Montmorillonite by J.Forsyth, C.Breen and J.Yarwood –UK Infrared discussion group (IRDG) (1998).
- (2) Evolved gas analysis (EGA) of DMF desorption from swelling clay minerals in real and synthetic rock mixtures by J.Forsyth, C.Breen. Mineralogical Society, Clay Minerals and Applied Mineralogy Groups. University of Bath, 7-8 September (1998).

10.3 Publications

The following article has been accepted for publication.

1. Thermal desorption-degradation of cyclohexylamine over Ni²⁺- and Al³⁺-exchanged bentonite studied using evolved gas analysis (TG-EGA) and diffuse reflectance spectroscopy (DRIFTS)

C.Breen, J. Forsyth, J. Yarwood and T.Hughes

The Journal of Phys.Chem. Chem Phys., 2000, 2, 3887-3892.

10.4 References

- [1] Neasham, J.W, Soc. Pet Eng. Paper 6858, Presented in Denver, Colorado, Oct 9-12, (1977), 8pp.
- [2] Azari, M and Leimkuhler J, Soc.Pet Eng. Paper 17149, (1988), 61-72.
- [3] Herron, M.M.Clays and Clay Minerals. 34, 2, (1986) 204-213.
- [4] Blatt, H, Middleton G and Murray R. 'Origin of Sedimentary Rocks', Prentice Hall, (New Jersey) (1979).
- [5] Cox, K.G, Price, N.B and Harte D. 'Introduction to the Practical Study of Crystals, Minerals and Rocks, revised first edition, Mc-Graw-Hill (London (1974), 127-134.
- [6] Griffen, D.T. 'Silicate Crystal Chemistry'. Oxford University Press, 2: 37.
- [7] Barth, T.F.W. 'Feldspars', Wiley-Interscience (London (1969).
- [8] Theng, B.K.G. 'The Chemistry of Clay Organic reactions. Adam Hilger (London(1974).
- [9] Adapted from Encyclopedia Britannica (<http://www.Britannica.com>)
- [10] Adapted from Encyclopedia Britannica (<http://www.Britannica.com>)
- [11] Newman, A.C.D. 'Chemistry of Clays and Clay Minerals', Mineralogical Society Monograph N0.6, Longman Scientific and Technical (1987).
- [12] Kirkman, J.H. Clay Minerals 12, (1977), 199-216.
- [13] Tazaki, K. Proc. Int. Clay. Conf. (1981), Italy, 573-584.
- [14] Wada, S.I and Mizota, C. Clays and Clay Minerals.30 (1982), 315-317.

- [15] Marshall, C.E. Layer Lattices and Base-Exchange Clays, *Krist*, 91 (1935) 433-449.
- [16] Hendricks, S.B. *J. Geol.*, 50 (1942) 276-290.
- [17] Hoffmann, U, Endell, K and Wilm. *Z. Krist.*, 86 (1933) 340-348.
- [18] Maegdefrau, E and Hoffman. *Z. Krist.*, 98 (1937) 299-323.
- [19] Hendricks, S.B. *J. Geol.*, 50 (1942) 276-290.
- [20] Marshall, C.E. *Krist*, 91 (1935) 433-449.
- [21] Edelman, C.H and Favejee, Z. *Krist*, A102 (1940) 417-431.
- [22] Figure 9 modified from refs: [17,18,20]
- [23] Brindley, G.W and Brown G. 'Crystal Structures of Clay Minerals and their X-Ray Identification', *Mineralogical Society Monograph N0.5*, (1980) 5.
- [24] Sterne, E.J, Reynolds, R.C and Zantop H. *Clays and Clay Minerals*, 30 (1982) 161-166.
- [25] Hower, J and Mowatt, T.C. *Am. Miner.*, 51 (1966) 825-854.
- [26] Bailey, S.W. *Clay Minerals* 15 (1980) 85-93.
- [27] Johnston, C.T. CMS Workshop Lectures, Vol. 8 'Organic Pollutants in the Environment, Sawhney, B.L., ed. (1966), The Clay Minerals Society, Boulder, CO, USA.
- [28] Mooney, R.W, Keenan, A.G and Wood L.A. *J. AM. Chem. Soc.* 74. (1952), 1367-1371.
- [29] Mooney, R.W, Keenan, A.G and Wood L.A. *J. AM. Chem. Soc.* 74. (1952), 1371-1374.
- [30] Sposito, G. and Prost R. *Chem. Rev.* 82, (1982) 553-573.
- [31] Grandjean, J and Laszlo, P. *J. Mag. Res.* 83 (1989), 128-137.
- [32] Tinet, D. Faugere, A.M. and Prost, R. (1992) *J. Phys. Chem.*
- [33] Bradley, W.F, Grim R.E. *Am. Miner.*, 36 (1951) 182-201.
- [34] Serratos, J.M. *Am. Miner.*, 45, (1960) 1101-1104.
- [35] Johnston, C.T. Sorption of Organic Compounds on Clay Minerals: A Surface Functional Group Approach, 1-44 in: *Organic Pollutants in the Environment*. (Shawney B.L., ed.) (1996) Clay Mineral Society Workshop, Lectures 8, Boulder, CO, USA.
- [36] Johnston, C.T, Sposito, G and Erickson, C. *Vibrational Probe Studies of Water Interactions with Montmorillonite*, *Clays and Clay Minerals*, (1992) 40, 722-730.
- [37] Swoboda, A.R and Kunze, G.W. (1968) *Soil Sci. Soc. Am. Proc.*, 32, 806-811.

- [38] Yariv, S and Heller. (1970) Israel J.Chem, 8, 935-945.
- [39] Griffiths and De Hasser, 'Fourier Transform Infrared Spectroscopy', John Wiley and Sons (New York), 1986.
- [40] Schrader B, Infrared and Raman Spectroscopy. Methods and applications. (Schrader B ed.) VCH, Weinheim, Germany. (1995)
- [41] Chalmers J.M, Dent G, 'Industrial Analysis with Vibrational Spectroscopy', RSC Analytical Monographs, (1997).
- [42] Hollas JM, Modern Spectroscopy (2nd edition), John Wiley and Sons. New York (1992).
- [43] Griffiths P.R, Sloane H.J and Hannah R.W, Applied Spectroscopy, (1977) 31, 6, 485.
- [44] Chenery D.H and Sheppard N, Applied Spectroscopy, (1978) 32, 1, 79.
- [45] Johnston S.F, 'Fourier Transform Infrared: A constantly evolving technology, Ellis Horwood, Chichester, UK (1991).
- [46] Griffiths P.R and de Haseth J.A, 'Fourier Transform Infrared Spectrometry', Wiley-Interscience, New York, USA, (1986).
- [47] Bell R.J, Introductory Fourier Transform Spectroscopy, Academic Press, New York, USA, (1972).
- [48] Mitchell M.B, 'Structure-Property relations in polymers', (1993).
- [49] Griffiths P.R, Fuller M.P, 'Advances in Infrared and Raman Spectroscopy', Vol 9, Edited by Clark R.J.H and Hester R.E, Heyden and Son Ltd (London) (1982).
- [50] Brimmer, P.J , Griffiths P.R., Applied Spectroscopy, 42, 242 (1988).
- [51] (Spectra Tech-TN2) Technical note 2 'DRIFTS spectroscopy (1990).
- [52] Graseby Specac Personal communication regarding the removal of Fresnel reflectance from diffuse reflectance accessory (1998).
- [53] Brimmer, P.J , Griffiths P.R., Applied Spectroscopy, 42, 242 (1988).
- [54] Yang, P.W., Mantsch, H.R, Baudais, F. Applied Spectroscopy 40, 974 (1986).
- [55] Brimmer, P.J , Griffiths P.R., Anal Chem, 58, 2179 (1986).
- [56] Fuller, M.P., Griffiths P.R., Analytical Chemistry, 50, 1906 (1987).
- [57] Martin, K.A., Ferraro, J.R. Journal of Applied Spectroscopy, 41, 45 (1987).
- [58] Fuller, M.P., Griffiths P.R., Analytical Chemistry, 50, 1906 (1978).
- [59] Blitz J.P, Murthy R.S.S and Leyden D.E, Appl. Spectrosc, 40, 829-831 (1986).
- [60] Yang P.W and Casal H.L, Appl. Spectrosc, 40, 1070-1073, (1986).
- [61] Schuster, A. Journal of Astrophysics, 21, 1 (1905).

- [62] Kubelka, P., Munk, F. *Z.Tech Physics*, 12, 593 (1938).
- [63] Bouroumand J.E, Moser and H van der Bergh, *Appl.Spectrosc*, 46 (12) 1874-1886 (1992).
- [64] Yeboah, S.A., Wang, S-H., Griffiths, P.R, (1984) *Applied Spectroscopy* 38, 259.
- [65] Kubelka, P., Munk, F. *Z.Tech Physics*, 12, 593 (1938).
- [66] Hembree, D.M., Smyrl, H.R, (1989) *Applied Spectroscopy* 43, 267.
- [67] Kubelka, P., Munk, F. *Z.Tech Physics*, 12, 593 (1938).
- [68] Krivacsy, Z., Hlavay, J, (1994) *Spectrochim Acta*. 50A, 49.
- [69] Murthy R.S.S, Blitz J.P and Leyden D.E, *Anal.Chem*, 58 3167-3172 (1986).
- [70] White R.L.*Applied Spectroscopy*, 47, 9, (1993)
- [71] White R.L and Nair A, *Chem. Mater*, 2, 742 (1990).
- [72] de Haseth J.A, *Applied Spectroscopy*, 36, 544-552 (1982).
- [73] White R.A, *Anal. Chem*, 64, 2010-2013, (1993).
- [74] Hamadeh I.M, King D and Griffiths J, *J, Catal.* 88, 264-272 (1984).
- [75] Murthy R.S.S and and Leyden D.E, *Anal.Chem*, 58, 1228-1233 (1986).
- [76] Murthy R.S.S, Blitz J.P and Leyden D.E, *Anal.Chem*, 58 3167-3172 (1986).
- [77] Dodd J.W, Tonge K.H, *Thermal methods* (Currell, B.R, ed.) John Wiley & Sons, London, 44, 1987.
- [78] Paama L, Pitkanen and Peramaki P. *Talanta*, 51, 349-357 (2000).
- [79] Thornley D.M, Primmer T.J.*Clay Minerals*, 30, 27-38 (1995).
- [80] Dodd J.W, Tonge K.H, *Analytical Chemistry by Open Learning (ACOL): Thermal methods*, Published on behalf of ACOL by John Wiley & Sons, London (1987).
- [81] Hendricks S.B, Fry W.H. *Soil Science*, 29, 457-478 (1930).
- [82] Kelley W.P, Dore W.H and Brown S.M. *Soil Science*, 31, 25-55 (1931).
- [83] Hendricks S.B, Tellet E. *J.Phys Chem*, 10, 147-167 (1942).
- [84] Berry L.G, Mason B, 'Mineralogy-concepts, descriptions, determinations', W.H Freeman & Company, London, (1959).
- [85] Brindley G.W, Brown G, 'Crystal Structures of Clay Minerals and their X-ray identification', Mineralogical Society, Monograph No: 5, Spottiswoode Ballantyne Ltd, London (1980).
- [86] Cullity B.D, 'Elements of X-ray Diffraction' Addison Wesley, Reading, (1978).
- [87] Moore D.M, Reynolds C (JR), 'X-ray Diffraction and the Identification and Analysis of Clay Minerals', 2nd ed., Oxford University Press, (1997).

- [88] Same ref. As 87, Ch. 2, p58.
- [89] Danilatos G.D, *Adv, Electron, Electron. Phys*, 71, 109, (1988).
- [90] Gerristead W.R, Link L.F, Paciej R.C, Damiani P and Li H, *Microsc.Res.Tech*, 25, 523, (1993).
- [91] Parra R.E, *Microsc. Res.Techn.* 25, 362, (1993).
- [92] Bolon R.B, Robertson C.D, Lifshin E, 'Microbeam Analysis', (P.E Russel, ed), San Francisco Press, San Francisco, 449, (1989).
- [93] Bolon R.B, 'Microbeam Analysis', (D.G Howitt, ed.), San Francisco Press, San Francisco, 199, (1989).
- [94] Anon, *Journal of Petroleum Technology*, 50, 11, (1998).
- [95] Baker J.C, Uwins P.J.R and Mackinnon I.D.R. *Journal of Petroleum Science & Engineering*, 10, 3, 241-247, (1994).
- [96] Huggett, Jennifer M, Uwins, Philippa J.R. *Journal of Petroleum Science & Engineering*, 10, 3, 211-222 (1994).
- [97] Cryo-SEM and ESEM: new techniques to investigate phase interactions within reservoir rocks, *Proceedings-SPE Annual Technical Conference and Exhibition*, 2, 519-525, (1999).
- [98] Adapted from *Environmental Scanning Electron Microscopy: An Introduction to ESEM*, Phillips Electron Optics, Eindhoven, The Netherlands (1990).
- [99] Leroux J, Thinh T, 'Revised Tables of X-ray Mass attenuation Coefficients, Corporation Scientifique Claisse, Inc, Quebec (1977).
- [100] *Energy Dispersive X-ray Microanalysis: An Introduction* (Oxford instruments) (1990) Kevex Corp. (1973).
- [101] Ziebold T.O, " Precision and Sensitivity in Electron Microprobe Analysis", *Anal. Chem* 39, 859, (1967).
- [102] Currie L.A, "Limits for Qualitative Detection and Quantitative Determination", *Anal. Chem* 40(3), 586 (1968).
- [103] Roberts, Dean. *PITCON Proceedings*, Chicago, Illinois. (1994)
- [104] Green, Andrew. *MWTF Minneapolis*, Minnesota (1994).
- [105] Czarnacki J, Thumin D, *Gas Flow Separation :The Sniffer Interface*, NATAS conference proceedings, Toronto, Canada (1995)
- [106] Breen C, Last P.M. *J. Mater. Chem*, 9, 813-818, (1999).

- [107] Pearson K, On lines and Planes of closest fit to systems of points in space. *Phil Mag* 2 (6) 559-572 (1901) in "Introduction to WIN-DAS", Kelmsley K, Wiley (1998).
- [108] Hotelling H. *J Educ. Psychol*, 24 (416-441) (498-520).
- [109] Jolliffe I.T, 'Principal Component Analysis', Springer Verlag, New York, (1986).
- [110] Hudson-Edwards K.A, Schell C, Macklin M.G. *Applied Geochemistry*, 14, 1015-1030 (1999).
- [111] Hillier S. *Clay Minerals*, 29, 665-679 (1994).
- [112] Moore D.M, Reynolds R.C Jr. 'X-ray Diffraction and the Identification and Analysis of Clay Minerals' (2nd edition), Oxford University Press, New York, 28 (1997).
- [113] Klug H.P, Alexander L.E, 'X-ray diffraction Procedures, 2nd Ed, Wiley, New York, 966, (1974).
- [114] Bish D.L, Reynolds R.C Jr. *Reviews in Mineralogy*, 20, Mineralogical Society of America, Washington D.C, 73-74 (1989).
- [115] Churchman G.J, *Clays Clay Minerals*, 38 (6) 591-599 (1990).
- [116] Calvert C.S, *Simplified. Clays and Clay Minerals* 32, 125-30 (1984).
- [117] Bohor B.F, tripplehorn D.M *Tonsteins. special paper* 285, 44. Geological Society of America, Boulder, Colorado (1993).
- [118] Farmer V.C, Russell J.D, *Spectrochim. Acta*, 20 1149-1173 (1964)
- [119] Van der Marel H, Beutelspacher, 'Atlas of Infrared Spectroscopy of Clay Minerals and their Admixtures', Elsevier Science (Amsterdam) (1976)
- [120] Farmer V.C, *Mineralogical Society Monograph* 4, 'The Infrared Spectra of Minerals' Adlard & Son Ltd. Dorking (1974).
- [121] Handke M, Mozgawa W. *Vibrational Spectroscopy*, 5, 75-84 (1993).
- [122] Farmer V.C and (in part) Russell J.D. *Spectrochimica Acta*, 22, 389-398 (1966).
- [123] Hunt J.M Turner D.S. *Anal. Chem*, 25, 1169-1174 (1953).
- [124] Lyon R.J.P Tuddenham W.M and Thompson. *Econ. Geol*, 54, 1047-1055 (1959).
- [125] Lyon R.J.P Burns E.A. *Econ. Geol.* 58, 274-284, (1963).
- [126] Lyon R.P.J, Evaluation of infrared spectrophotometry from compositional analysis of lunar and planetary soils, final report, Stanford Res. Inst. Menlo Park, California (1963).

- [127] Lyon R.P.J, Evaluation of infrared spectrophotometry from compositional analysis of lunar and planetary soils, final report, Stanford Res. Inst. Menlo Park, California (1963).
- [128] Graham J.A, Walker J.M. *Applied Spectroscopy*, 37, 4, (1983).
- [129] Clegg F, PhD thesis 'Thermo-analytical and Spectroscopic Characterisation of Pore lining Minerals in Reservoir Rocks', Sheffield Hallam University (1998).
- [130] Matteson A, Herron M.M, *J. Sediment.Petrol*, 63, 6, 1144-1148 (1993).
- [131] Matteson A, Herron M.M, SDR note: ISD006-90-45, (Dec-1990).
- [132] Kodama H, Oinuma K, *Clays Clay Minerals*, 11, 236-249, (1963).
- [133] Callender C.A, Dahl H.M, Characterisation of petroleum sandstone reservoir rocks by scanning electron microscopy, *Scanning Electron Microscopy*, (IV) 1501-1514 (1984).
- [134] Wilson D, Pittman E.D.J. *Sediment.Petrol*, 47, 1, 3-31, (1977).
- [135] [111] Hillier S. *Clay Minerals*, 29, 665-679 (1994).
- [136] Crocker M.E, Donaldson E.C and Marchin L.M, SPE11973, (1983).
- [137] Clegg F, 'Characterisation of Quarry rocks using scanning electron Microscopy', Internal report , Sheffield Hallam University.
- [138] Baker J.C, Grabowska-Olszewska B and Uwins P.J. *Applied Clay Science*, 9, 465-469 (1995).
- [139] Ali L, Barrufet M.A. *Journal of Petroleum Science and Engineering*, 12, 323-338 (1995).
- [140] Bennett H, Reed R.A, 'Chemical Methods of Silicate Analysis', Academic Press (1971).
- [141] Worrall W.E, 'Clays and Ceramic Raw materials' 2nd Ed, Elsevier Applied Science Publishers, London, (1986).
- [142] Barshad I, Thermal Analysis techniques, in: 'Methods of Soil Analysis', 699-742, American Chemical Society (1965).
- [143] Mackenzie R.C, Basic principles and historical development: in 'Differential Thermal Analysis', Volume 1, Fundamental aspects, Academic Press, London and New York (1970).
- [144] Brindley G.W. *J.Mineral.Soc. Japan* 5, 217-237, (1961).
- [145] Brindley G.W, Milhollen G.L. *Science* 152, 1385-1386, (1966).
- [146] Brindley G.W, Nakahira M. *Z. Kristallogr.* 112, 136-149, (1959)
- [147] Brindley G.W, Sharp J.H, Patterson J.H. *Amer. Mineral.* 52, 201-211.

- [148] El-Akkad T.M, Felix N.S, Guindy N.M, El-Massry and Nashed S. *Thermochim. Acta*, 59, 9-17 (1982).
- [149] El-Barawy K.A, Girgis B.S and Felix N.S. *Thermochim. Acta* 98, 181-189, (1986).
- [150] Koster van Groos A.F, Guggenheim S. *Amer.Mineral.* 69, 872-879 (1984).
- [151] Mackenzie K.J.D, Bowden M.E. *Thermochim. Acta* 64, 83-106 (1983)
- [152] Van Der-Gaast S.J, Frankema T.H.T, Tran and R.L Frost, 8, *International Laboratory News*, Aug, 8 (1996).
- [153] Yariv S. *Thermochimica. Acta.* 88, 49-68, (1985).
- [154] Giese R.F, Precision scanning calorimetry and its applications to mineralogy and the geosciences. In: 'Thermal analysis in clay science', The Clay Minerals Society, Boulder, CO, 9-48 (1990).
- [155] Dubrawski J.V, Differential scanning calorimetry and its applications to mineralogy and the geosciences. Springer, Berlin , 16-59 (1991).
- [156] Lephardt J.O, Fenner R.A, *Applied Spectroscopy*, 34, 2, 174, (1980)
- [157] Lephardt J.O, Fenner R.A, *Applied Spectroscopy*, 35, 1, 95, (1980)
- [158] Lephardt J.O, Fenner R.A, *Applied Spectrosc. Rev.*, 18, 2, 265, (1982/83)
Laboratory News, August (1996).
- [159] Morgan D.J, Warrington S.B and Warne S.St J. *Thermochimica Acta*, 135 207-212 (1988).
- [160] Morgan D.J, *J.Thermal Anal.* 12 245-263 (1977)
- [161] Heiken G, *An atlas of volcanic ash.* Smithsonian Institution Press, Washington, 101 (1974).
- [162] Hampton C.M, Bailey D.K, *J.Non-Crystall.Sol*, 67, 147-168 (1984).
- [163] Keller W.D, *Am. Miner*, 71, 1420-1425 (1986).
- [164] Bloodworth A.J, Hurst A and Morgan D.J, Detection and estimation of low levels of kaolinite by evolved water vapour analysis, *Proceedings of the 9th International Clay Conference, Strasbourg, 1989*, V.C Farmer and Y. tardy (Eds) *Sci. Geol, Mem.* 89, 143-148 (1990)
- [165] Milowdowski A.E, Morgan D.J, Identification and estimation of carbonate minerals at low levels by evolved CO₂ analysis. *Nature*, 286: 248-249 (1980)
- [166] Morgan D.J. *Applied Clay Science*, 8, 81-89 (1993).
- [167] Thornley D.M, Primmer T.J. *Clay Minerals*, 30, 27-38 (1995).
- [168] Cai G. *Journal of Thermal Analysis*, 45, 167-176 (1995).

- [169] Heide K, Gerth K, Büchel G and Hartmann E. *Journal of Thermal Analysis*, 48, 73-81 (1997).
- [170] Holdiness M.R, *Thermochimica Acta*, 75, 361-399 (1984).
- [171] Gibson E.K (J.r), Johnson S.M, *Thermochimica Acta*, 42, 49 (1972).
- [172] Gibson E.K (J.r), *Thermochimica Acta*, 5, 243-255 (1973).
- [173] Muller-Vonmoos M, Khar G, Rub A, *Thermochimica Acta*, 20, 387 (1977).
- [174] Chisem I.C, Cosgrove S.D and Jones W. *Journal of Thermal Analysis*, 50, 757-766 (1997).
- [175] Lindberg W.J, Persson and Wold S, *Anal. Chem.* 55, 643 (1983).
- [176] Peuchant E, Salles C and Jensen R, *Anal.Chem*, 59,1816 (1987).
- [177] Dubois P, Martinez J.R and Levillian P, *Analyst* 112, 1675 (1987).
- [178] Bjorsvik H.R, Bye E, *Appl. Spectrosc*, 45, 5, 771-778 (1991)
- [179] Moudgil B.M, Mathur S and Behl S, *Colloids Surf.*, 92 181-188 (1994).
- [180] Johnston L.J, Chu C.H and Hussey G.A. *Clays and Clay Minerals*, 33, 2, 107-117 (1985).
- [181] Hughes T.L, Methven C.M, Jones T.G.J, Pelham S.E, Fletcher P and Hall C. *Advanced Cement Based Materials*, 2, 91-104, (1995).
- [182] Luinge H.J, Van der Maas J.H, Visser T. *Chemometrics and Intelligent Lab Systems*, 28, 129-138 (1995).
- [183] Pottel H. *Fire and Materials*, Vol 19, 221-231 (1995).
- [184] Wilson R.H, Goodfellow B.J, *Mid-infrared spectroscopy*. In *Spectroscopic Techniques for Food Analysis*, ed. R.H Wilson, VCH, New York, 59-85 (1994).
- [185] Defernez M, Kelmsley E.K and Wilson R.H. *Journal of Agricultural and Food Chemistry*, 43, 109-113 (1995).
- [186] Defernez M, Wilson R.H. *Journal of Agricultural and Food Chemistry*, 67, 461-467 (1995).
- [187] Yoke Wah L, Kelmsley E.K and Wilson R.H. *Journal of Agricultural and Food Chemistry*, 42, 1154-1159 (1994).
- [188] Briandet R, Kemsley E.K and Wilson R.H. *Journal of Agricultural and Food Chemistry*, 44, 170-174 (1996).
- [189] Osama Al-Jowder, Defernez M, Kemsley E.K and Wilson R.H. *Journal of Agricultural and Food and Food Chemistry*, 47, 8, 3210-3218 (1999).
- [190] Nordmark U. *Journal of Analytical and Applied Pyrolysis*, 55, 93-103, (2000).
- [191] Gardner W.R. *Sensors and Actuators*, VB4, N-12, (1991).

- [192] Héberger K, Görgé M. *Journal of Chromatography A*, 845, 21-31 (1999).
- [193] Wesolowski M, Czerwonka M and Koniecznyński P. *Thermochimica Acta*, 323, 159-168 (1999).
- [194] Elomaa M, Kaljurand M, Koel M and Kudrjashova M. *Thermochimica Acta*, 336, 73-83 (1999).
- [195] Essington M.E. *Catalysis Today*, 41, 53-71 (1998).
- [197] Sastry N.V, Sequaris J.M. *J. Colloid Interface Sci*, 171, 224-233 (1995)
- [198] Lee J.F, Mortland M.M, Chiou C.T, Kile D.E and Boyd S.A. *Clays and Clay Minerals*, 38, 113-120 (1990).
- [199] Mortland M.M. *Clays and Clay Minerals*, 34, 581-585 (1986)
- [200] Sawhney B.L (Ed.) *CMS Workshop Lectures Vol. 8, Organic pollutants in the environment*, The Clay Minerals Society, Boulder, IO, USA.
- [201] Farmer V.C, Mortland M.M. *J.Chem.Soc. A*, 344-351 (1966).
- [202] Bradley W.F. *Journal of the American Chemical Society*, 67, 975-981 (1945)
- [203] MacEwan D.M.C. *Trans. Faraday Soc.*, 44, 349-368 (1948).
- [204] Farmer V.C, Mortland M.M. *J.Chem.Soc. A*, 344-351 (1966).
- [205] Yariv S, Wettability of clay minerals. In : *Modern approaches to wettability*, Schrader M.E and Loeb G.I, Eds, Plenum Press, New York, 279-326 (1992)
- [206] Yariv S. *Intern.Rev.Phys.Chem*, 11, 345-375 (1992).
- [207] Farmer V.C, Mortland M.M. *J.Chem.Soc. A*, 344-351 (1966).
- [208] Farmer V.C, Mortland M.M. *J.Chem.Soc. A*, 344-351 (1966).
- [209] Serratosa J.M, Rausell-Colom J.A and Sanz J. *Journal of Molecular Catalysis*, 27, 225-234 (1984).
- [210] Barzetti T, Selli, Moscotti and L Forni, *J.Chem. Soc, Faraday Trans. 92,8*, 1401-1407 (1996).
- [211] Serratosa J.M, *Clays and Clay Minerals*,14,385-391 (1966).
- [212] Breen C. *Clay Minerals*, 26, 487-496 (1991).
- [213] Haderlein S.B and Schwarzenbach R.P, In: *Transport and reactive processes in aquifers* (Eds. Dracos T.H and Stauffer F), Balkema (Rotterdam) 67-72 (1994).
- [214] Knozinger H, *Infrared spectroscopy as a probe of surface acidity In: Elementary reaction steps in heterogeneous catalysis*, 267-285, Kluwer Academic Press (1993)

- [215] Shimazu S, Ishii K and Uhematsu T, Intercalation behaviour of pyridine derivatives in clays, *New Developments in ion exchange, Proc. Intern. Conf. Ion Exchange*. Tokyo 219-224 (1991).
- [216] Gonzalez F, Pesquera C, Blanco C, Benito I and Mendioroz S. *Inorg. Chem*, 31, 727-731 (1992).
- [217] Barrer R.M. *Clays and Clay Minerals*, 37, 5, 385-395 (1989).
- [218] Lagaly G, Beneke K. *Colloid Polymer Science*, 269, 1198-1211 (1991).
- [219] Jones W, Thomas J.M, Tilak D, Tennakoon B, Schlogl and Diddams P. *Amer. Chem.Soc.* 40, 472-484 (1985).
- [220] Wali A, Unnikrishnan, Muthukumara Pillai, Kaushik and Satish S. *J. Catalysis*, 173, 84-94 (1998).
- [221] Nishihama S, Yamada H and Nakazawa H. *Clay Minerals*, 32, 645-651 (1997).
- [222] Lacher M, Lahav and Yariv S, *J. Thermal Anal*, 40, 41-57 (1993)
- [223] Lahav N, Lacher M and Yariv S, *J. Thermal Anal*, 39, 1233-1254 (1993)
- [224] Yariv S, Lahav N and Lacher M, *J. Thermal Anal*, 42, 13-3- (1994)
- [225] Lorprayoon V, Condrate R.A (S.r), *Clays Clay Miner*, 29, 1, 71 (1981).
- [226] Bosetto M, Arfaioli P and Fusi P, *Soil Sci*, 155, 2, 105-113.
- [227] Laird D.A, Barriuso E, Dowdy R.H and Koskinen W.C, *Soil Sci. Soc.Am.J*, 158, 3, 181-188 (1994)
- [228] Theng B.K.G, *The Chemistry of Clay Organic Reactions*. Adam Hilger (1974).
- [229] Harper M, Purnell C.J, *Environ. Sci. Technol*, 24, 1, 55-62 (1990).
- [230] Peker S, Yapar S and Besun N, *Colloids Surf.* 104, 249 (1995)
- [231] Frost R.L, Lack D.A, Paroz G.N and Tran T.H.T, *Clays Clay Minerals*, 47, 297, (1999).
- [232] Olejnik S, Posner A.M and Quirk J.P, *Clays Clay Minerals*, 19, 83, (1971).
- [233] Reis A.S (Jr), Simoni J de A and Chagas A.P, *J. Colloid Interface Sci*, 177, 1 (1996).
- [234] Dash man T, Stotzky G, *Soil Biol. Biochem*, 14, 447-456 (1982).
- [235] Weiss A, Thielepape W and Orth H, in *proceedings of the International Clay Conference, Jerusalem, Vol 1, 277, Israel University Press, Jerusalem, (1966)*.
- [236] Lagaly G, *Clay organic interactions. Phil. Trans. R. Soc. Lond*, A311, 315-332.
- [237] Olejnik S, Posner A.M and Quirk J.P, *The intercalation of Polar Organic compounds into kaolinite, Clay Minerals*, 8, 421-434 (1970).

- [238] Olejnik S, Aylmore L.A.G, Posner A.M and Quirk J.P, *J.Phys.Chem*, 72, 241 (1968).
- [239] Breen C , Lynch S. *Clays and Clay Minerals*, 36, 1, 19-24 (1988).
- [240] Olejnik S, Aylmore L.A.G, Posner A.M and Quirk J.P, *J.Phys.Chem*, 72, 241 (1968).
- [241] Benesi H.A, *J.Catal*, 28, 176 (1973).
- [242] Lapidés I, Lahav N, Michaelian K.H, Yariv S, *J.Therm.Anal*, 49,1423 (1997).
- [243] Lahav N, *Clays and Clay Minerals*, 38, 219 (1990).
- [244] Breen C , Lynch S. *Clays and Clay Minerals*, 36, 1, 19-24 (1988).
- [245] Johnston CT, Stone D.A. *Clays and Clay Minerals*, 38, 2, 121-128 (1990).
- [246] Frost R.L, Kristof J, Horvath E and Klopogge J.T. *Thermochimica Acta*, 327, 155-166 (1999).
- [247] Sugahara Y, Satokawa S, Yoshioka K , Kuroda K and Kato C. *Clays and Clay Minerals*, 37, 2, 143-150 (1989).
- [248] Ledoux R.L, White J ,Infrared studies of hydrogen bonding of organic compounds on oxygen and hydroxyl surfaces of layer lattice silicates. *Proceedings of the International Conference, Jerusalem, Israel, Vol 1, (Theng Ed.) 361-374 (1966).*
- [249] Srodon J, Eberl , Illite: In Bailey, S.W (Ed.) *Micas, Vol 13, in reviews in Mineralogy, Mineralogical society of America, Washington D.C, 495-544 (1984).*
- [250] Frissel M.J, Bolt G.H, *Soil Sci*, 94, 284-291 (1962).
- [251] Pinck L.A, Holton W.H and Allison F.E, *Soils Sci*, 91, 22-28 (1961)
- [252] Tomlinson T.E, Knight B.A.G, Bastow A.W and Heaver A.A, In: *Physico-chemical and Biophysical factors affecting the activity of pesticides, Monograph 29, Soc. Chem. Indus. London, 317-329 (1969).*
- [253] Grim R.E, Allaway W.H and Cuthbert F.L, *J. Am. Ceram. Soc.* 30, 137-142 (1947).
- [254] Faure P, Landais P, *Fuel*, 79, 1751-1756, (2000)
- [255] Theng B.K.G, 'The chemistry of clay organic interactions', Adam Hilgier Ltd, London, 211-238 (1974).
- [256] Sannino F, Filazzola M.T, Violante A and Gianfreda L, *Env. Sci. Tech.* 33, 23, 4221-4225 (1999)
- [257] Gagnon C, Arnao M, Brindle J-R, *Water Research*, 26, 8, 1067-1072 (1992).
- [258] Sokoll R, Hobert H and Schmuck I, *J.Chem.Soc., Faraday Trans. 1*, 82, 3391-3399 (1986).

- [259] Paukshtis E.A; Yurchenko E.N, Russ. Chem. Rev.52, 42, (1983)
- [260] Boem H.-P, Knozinger H, in : Catalysis-Science and Technology, Anderson J.R and Boudart (Eds.), Springer, Berlin, Heidelberg and New York, Vol 4, 39 (1983).
- [261] Titova T.I, Kosheleva L.S, Colloids Surf, 63, 97-101 (1992).
- [262] Zhandanov S.P, Kosheleva L.S and Titova T.I, Langmuir, 3, 960-967 (1987).
- [263] Koretsky C.M, Sverjensky D.A, Salisbury J.W and D'Aria D.M, Geochim. Cosmochim. Acta. 61, 11, 2193-2210 (1997).
- [264] Dodd J.W, Tong K.H, in: Thermal Methods, John Wiley & Sons, 1, (1987).
- [265] Mitchell B.D, Birnie A.C in: 'Differential Thermal Analysis', Academic Press, London, 611, (1970).
- [266] Morillo E, Perez-Rodriguez J.L, Real C and Sanchez-Soto P.J, J. Thermal Analysis. 44, 313-327 (1995).
- [267] Yariv S, Thermochimica Acta, 88, 49-68 (1985).
- [268] Dollimore D, Gamlen G.A and Taylor T.J, Thermochim Acta, 75, 59, (1984).
- [269] Redfern J.P, Polym.Int. 26, 51 (1991); J. Appl. Polym. Sci. Applied Polymer Symposium, 55, 65 (1994).
- [270] Friedman H.L, Thermochimica Acta, 1, 199, (1970).
- [271] Holdiness M.R, Thermochimica Acta, 75, 361-399, (1984).
- [272] Roche R.S, Saloman D.R and Levinson A.A, Applied Geochemistry. 1, 619-626 (1986).
- [273] Shepherd T.J et al. British Geological Survey report {contract no: MAIM-0027-UK} Nottingham, 109, (1990).
- [274] Morgan D.J, Journal of Thermal Analysis, 12, 245-263 (1977).
- [275] Yariv S, Journal of Thermal Analysis, 36, 1953-1961 (1990).
- [276] Inglethorpe S, Morgan D.J, Journal of Thermal Analysis, 40, 29-40 (1993).
- [277] Morgan D.J, Warrington S.B and Warne S St, Thermochimica Acta, 135, 207-212 (1988).
- [278] Mullens J, Yperman J, Carleer R, Franco D, Van Poucke L.C and Van der Bist J, Applied Clay Science, 8, 91-99 (1993).
- [279] Bloodworth AJ, Hurst A and Morgan D.J, Proceedings of the 9th International Clay Conference Strasbourg, 1989, V.C farmer and Y.Tardy (Eds.) Sci. Geol. Mem., 89, 143-148 (1990).
- [280] Morgan D.J, Milodowski, Thermal analysis proceedings of the Seventh International Conference, 624-629 (1982).

- [281] Thornley D.M, primmer T.J, Clay Minerals, 30, 27-38 (1995).
- [282] Heide K, Gerth, K, Buchel G and Hartmann E, Journal of Thermal Analysis, 48, 73-81 (1997).
- [283] Parker R.W, Frost R.L, 357-360, (1)
- [284] Breen C, Clegg F, Hughes T.L and Yarwood J, Thermal and spectroscopic characterisation of Dimethylformamide/Ca, Mg and Na Exchanged Montmorillonite Intercalates. (submitted for publication Phys. Chem. Chem. Phys 2001).
- [285] Petit S, Righi D, Madejova J and Decarreau A, Clay Minerals, 34, 543-549 (1999)
- [286] Johnson C.T, Tipton T, Trabue S.L, Erickson C and Stone D.A, Environ. Sci. Technol. 26, 382-290 (1992).
- [287] White R.L, Journal of Analytical and Applied Pyrolysis, 18, 325-329 (1991).
- [288] Davies D.D, Kilduff J.E, Koontz S.L, Spectrochimica Acta, 47A, 2, 299-308 (1991).
- [289] Chalmers J.M, Mackenzie M.W, Applied Spectroscopy, 39, 634, (1985).
- [290] Martin K.A, Zabransky R.F, Applied Spectroscopy, 45, 68, (1991).
- [291] Frost R.L, Tran T.H, Rintoul L, Kristof J, Analyst, 123, 611-616 (1998)
- [292] Cenens J, Schoonheydt, Clays Clay Minerals, 36, 214-224 (1988).
- [293] Harris D. J, Bonagamba T. J, Schmidt-Rohr K. Macromolecules, 32, 20, 6718-6724 (2000).
- [294] Breen C, Applied Clay Science, 15,1, 187-219 (1999).
- [295] Boek E.S, Covney P.V, Skipper N.T, J. Am. Chem. Soc, 117, 12608-12617 (1995).
- [296] Teppen B.J, Ching-Hsing Yu, Miller D.M, Schafer L, Journal of Computational chemistry, 19, 2, 144-153 (1998).
- [297] Lipsicas M, Raythatha R, Giese R.F (Jr.), Costanzo P.M, Clays Clay Minerals, 34, 635-644 (1986).
- [298] Hayashi S, J. Phys. Chem, 99, 7120-7129 (1995).
- [299] Dumestre A, McBride M, Baveye P, Environmental Science and Technology, 34, 7, 1259-1264 (2000).
- [300] Yariv S, Heller, Israel J. Chem, 8 935-945 (1970).
- [301] Haderlein S.B, Schwarzenbach R.P in: Transport and Reactive Processes in Aquifers, (Editors-T.H. Dracos and F Stauffer), Balkema, Rotterdam, 67-72 (1994).
- [302] Adams J.M, App. Clay Sci. 2, 309, (1987).

- [303] Ballantine J.A. The reactions in clays and pillared clays. Pp197-212 in: *Chemical Reactions in Organic and Inorganic Constrained Systems* (R. Button, editor). Reidel, Dordrecht, (1986).
- [304] Thomas J.M, Sheet silicate intercalates: New agents for unusual chemical conversions.Pp 56-97 in: *Intercalation Chemistry* (M.S. Whittington & A.J. Jacobson, editros). Academic Press, New York, (1982).
- [305] Vaccari A. *Appl. Clay Sci.*, 14, 161, (1999).
- [306] Jacobs P.A. & Uytterhoeven J.B, *J. Catal.* 26, 175 (1972).
- [307] Ghosh A.K, *J. Catal*, 96, 288 (1985).
- [308] Brown D.R. & Rhodes C.N, *Thermochim. Acta* 294, 33 (1997).
- [309] Yiu H.H.P., Brown D.R. & Barnes P.A, *Catal. Lett.* 59, 201 (1999).
- [310] Breen C, *Clay Miner.* 26, 487 (1991a).
- [311] Breen C., Deane A.T & Flynn J.J, *Clay Miner.* 22, 169, (1987).
- [312] Breen C. *Clay Miner.* 26, 473 (1991b).
- [313] Breen C. & Moranta A.J, *J. Phys. Chem. B.*, 103, 5675 (1999).
- [314] Breen C., Madejova J. & Komadel P, *J. Mater. Chem.* 5, 469 (1995a).
- [315] Breen C., Madejova J. & Komadel P, *Appl. Clay Sci.* 10, 219 (1995b).
- [316] Koolif. & Jones W, *Clay Miner.* 32, 633 (1997).
- [317] Mokaya R. & Jones W, *J. Catal.*, 153, 76 (1995).
- [318] Ballantine J.A., Graham P, Patel I, Purnell J.H, Williams K, Thomas J.M, *Proc. Int. Clay Conf. Denver*, 311 (1987).
- [319] Moronta A.J. PhD Thesis Sheffield Hallam University, 1999.
- [320] Yariv S, Heller L, *Israel J. Chemistry* 8, 935 (1970).
- [321] Billingham J., Breen C. & Yarwood J, *Clay Miner.* 31, 513 (1996).
- [322] Brown D.R., Rhodes C.N, *Catal. Lett.*, 45, 35 (1997).
- [323] Velghe F, Schoonheydt R.A. & Uytterhoeven J.B, *Clays Clay Miner*, 25, 375 (1977).
- [324] Calvet R. & Prost R, *Clays Clay Miner.*,19, 175 (1971).
- [325] Hofmann V, Klemen R Z. *Anorg. Allg. Chem.* 262, 95 (1950).
- [326] Shuali U, Steinberg M, Yariv S, Muller-Vonmoos M, Kahr G, Rub A, *Clay Miner.*, 25, 107 (1990).
- [327] Huang S.X, Gland J.L, *J. Phys. Chem.* 100, 2206 (1996).
- [328] Huang S.X., Fisher D.A.,Gland J.L, *J. Phys. Chem.* 100, 13629 (1996).
- [329] Sokoll R, Hobert H, Schmuck I, *J. Catal.* 125, 276 (1990).

- [330] Webb M., Last P.M, Breen C, *Thermochim. Acta* 326, 151 (1999).
- [331] Meijers S. & Ponc V, *J. Catal.*, 149, 307 (1994).
- [332] Chisem I.C, Cosgrove S.D, Jones W, *J. Thermal Anal.*, 50, 757 (1997).
- [333] Durand B., Pelet R, Fripiat J.J. *Clays Clay Miner.*, 20, 21 (1972).
- [334] Sokoll R., Hobert H, Schmuck I, *J. Chem. Soc. Faraday Trans. I.* 82, 3391 (1986).
- [335] Ledoux M.J, Serati M. J. *Catal.* 83, 229 (1983).
- [336] Lycourghiotis A., Katsanos N.A, Vattis D, *J. Chem. Soc. Faraday Trans. I.* ,75, 2481 (1979).
- [337] Breen C, *Clay Miner.* 26, 487 (1991a).
- [338] Walton R.A, *J. Inorg. Nucl. Chem.* 28, 2229, (1966)
- [339] El-Sayed L, Ragsdale R.O, *J. Inorg. Nucl. Chem.* 30, 651, (1968)
- [340] Greenwood N.N, Wade K, *J.Chem.Soc.* 1130 (1960).
- [341] Coerver H.J, Curran C, *J.Am, Chem. Soc.*, 80, 3522, (1958).
- [342] Kubota M, Schulze S.R, *Inorg, Chem*, 3, 853 (1964).
- [343] Gill N.S, Nuttall R.H, Scaife D.E and Sharp D.W.A, *J. Inorg. Nucl. Chem*, 18, 79 (1961).
- [344] Tarasevich Yu, I, Telichkun V.P, Ovcharenko F.D, *Dokl. Akad. Nauk, S.S.S.R*, 182, 141-143 (1968)
- [345] Serratos J.M, *Clays Clay Minerals*, 53, 1281-1286 (1968).
- [346] Weizong X, Johnston C.T, Parker P, Agnew S.T, *Clays and Clay Minerals*, 48, 1, 120-131 (2000).
- [347] Nelson et al. *Inorg.Phys.Theor.*, 1597 (1969).
- [348] Kohout J, Hvastijova M, Koehler H, Omelka L, *Collect. Czech.Chem. Commun*, 55 (1990).
- [349] Ocelli M.L, Lester J.E, *Eng. Chem. Res. And Dev*, 24, 27-32 (1984).
- [350] Brindley G.W, Hoffmann R.W, *Clays Clay Minerals*, 9, 546-556 (1962).
- [351] Serratos J.M, *Am. Mineralogist*, 53, 1244-1251.
- [352] van Olphen H , Deeds C.T, *Nature*, 194, 176-177 (1961).
- [353] Clegg F, *Thermo-Analytical and Spectroscopic Characterisation of Pore lining Materials in Reservoir rocks*, PhD thesis, Sheffield Hallam University (1998).
- [354] Olejnik S, Posner A.M, J.P Quirk, *Clays Clay Miner.*, 22, 361-365 (1974).
- [355] Olejnik S, Posner A.M, J.P Quirk, *Clays Miner.*, 8, 421-434 (1970).
- [356] Churchman G.J, Theng B.K.J, *Clay Miner.*, 19, 161-175 (1984).

- [357] Rouquerol J, *Thermochim. Acta* 100, 23 (1986).
- [358] Paulik F, Paulik J, *Anal. Chim. Acta* 56, 328 (1971).
- [359] Raemaekers K.G.H, Bart J.C.J, *Thermochim. Acta.* 295, 1-58 (1997).
- [360] Kaisersberger E, Post E, *Thermochim. Acta* 295 73-93 (1997).
- [361] Parkes G.M.B, Barnes P.A, Charsley E.L, Reading M, Abrahams I, *Thermochim. Acta.* 354, 39-43 (2000).
- [362] Kelmsley K, Win-das™, Wiley Scientific (1998).
- [363] Frost R.L, Vasallo A.M, *Clays and Clay Miner*, 44, 5, 635-651 (1996).
- [364] El-Shabiny A.M, Hammad S.M, Ibrahim, Ismail, *J. Therm. Anal*, 46, 1421-1435 (1996).
- [365] Worrall W.E, 'Clays and Ceramic Raw Materials', 2nd Edition, Elsevier Applied Science Publishers (London) (1986).
- [366] Van der Gaast,, Frankema W, Tran T.H.T, Frost R.L, *International Laboratory News*, August, p8 (1996).
- [367] Keller W.D, Pickett E.E, Reesman A.L, *Proc.Int.Clay.Conf*, Jerusalem, 1, 75-85 (1966).
- [368] Mackenzie R.C, 'The Differential Thermal Investigations of Clays', Mineralogical Society (London) (1957).
- [369] Kemsley E.K, *Chemom. Intell. Lab. Syst.*, 33, 47 (1996)
- [370] Doff D, (personal communication) Trinity College(Department of Geology), Dublin, Republic of Ireland.
- [371] Grams32-PLS-PLUS IQ software and chemometric manuals, Galactic Industries Corp. 395 Main street, Salem, NHO 3079, USA.
- [372] Bearden J.A, 'X-Ray Wavelengths', *Review of Modern Physics*, 88-99 (1967).

10.5 Appendices

Appendix 1 (Transfer line experiments)

The DMF C-H 2937 cm^{-1} and C=O 1720 cm^{-1} as a function of temperature are shown in figures A1.1 and A1.2.

Figure A1.1 GP-FTIR absorbance intensity for DMF (C-H stretch) at 2937 cm^{-1}

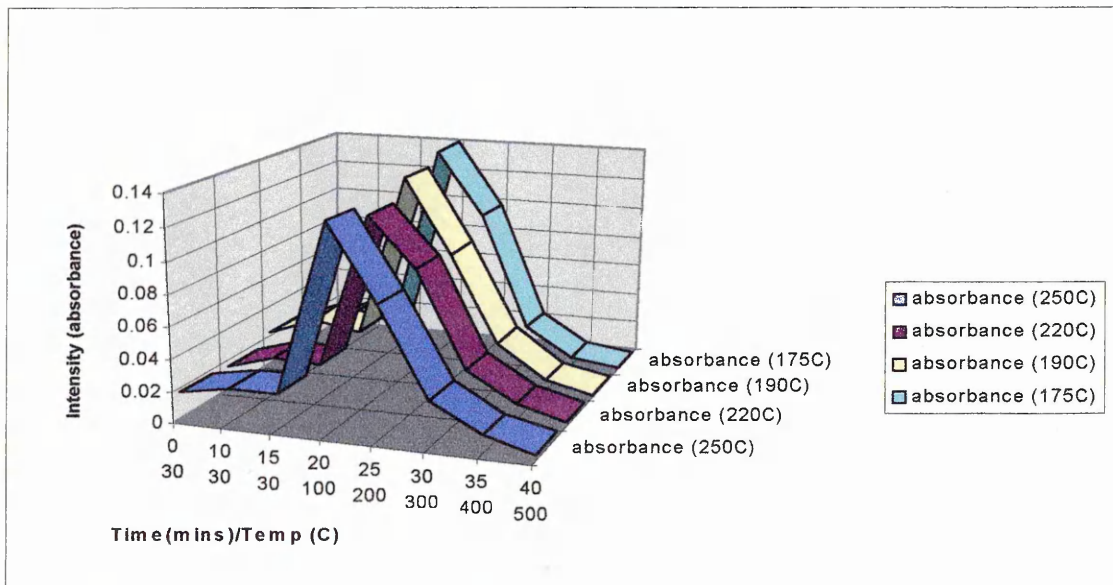
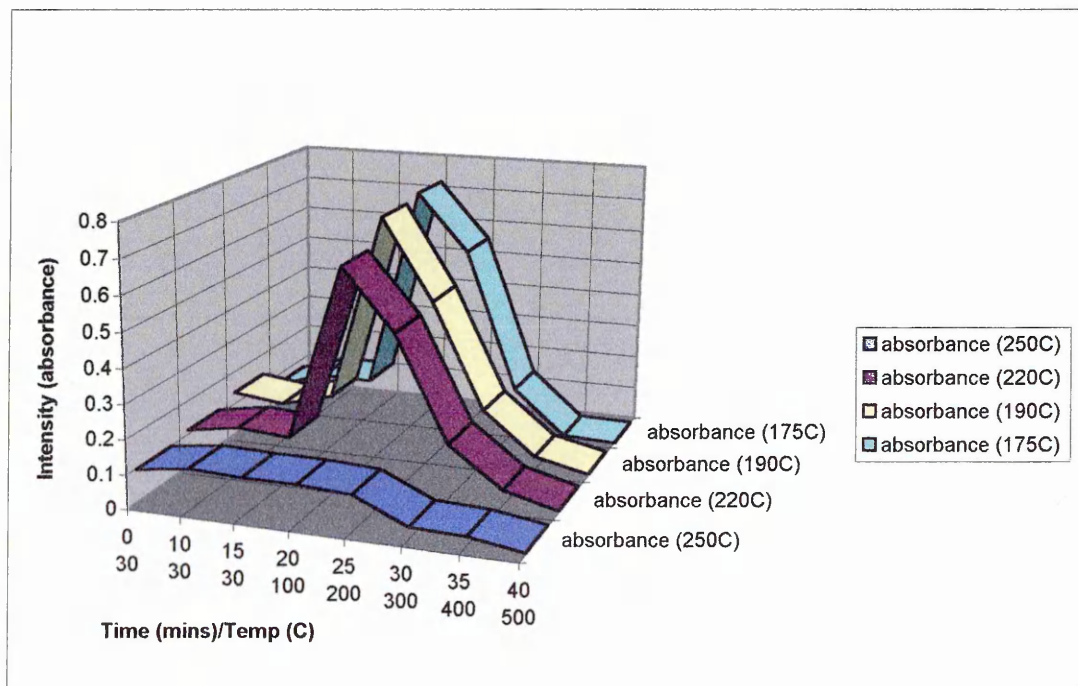


Figure A1.2 GP-FTIR absorbance intensity for DMF (C=O) at 1720 cm^{-1}



The intensity of both bands as shown in figures (A1.1-2) generally indicate that intensity for both bands increases with decreasing temperature, which implies that a lower transfer line temperature limits DMF degradation. The chosen operational temperature was 190°C so as to strike a balance between DMF degradation (a slight increase on 175°C) and diffusional broadening. In comparison, at 250°C the carbonyl band intensity is very low which indicates high DMF degradation, making 250°C an unsuitable temperature. The ratio of these bands (2937:1720 cm) indicates the proportion of DMF degradation. A graphic representation of these ratios is shown in figure A1.3.

Figure A1.3 GP-FTIR intensity ratios of DMF (CH:C=O)

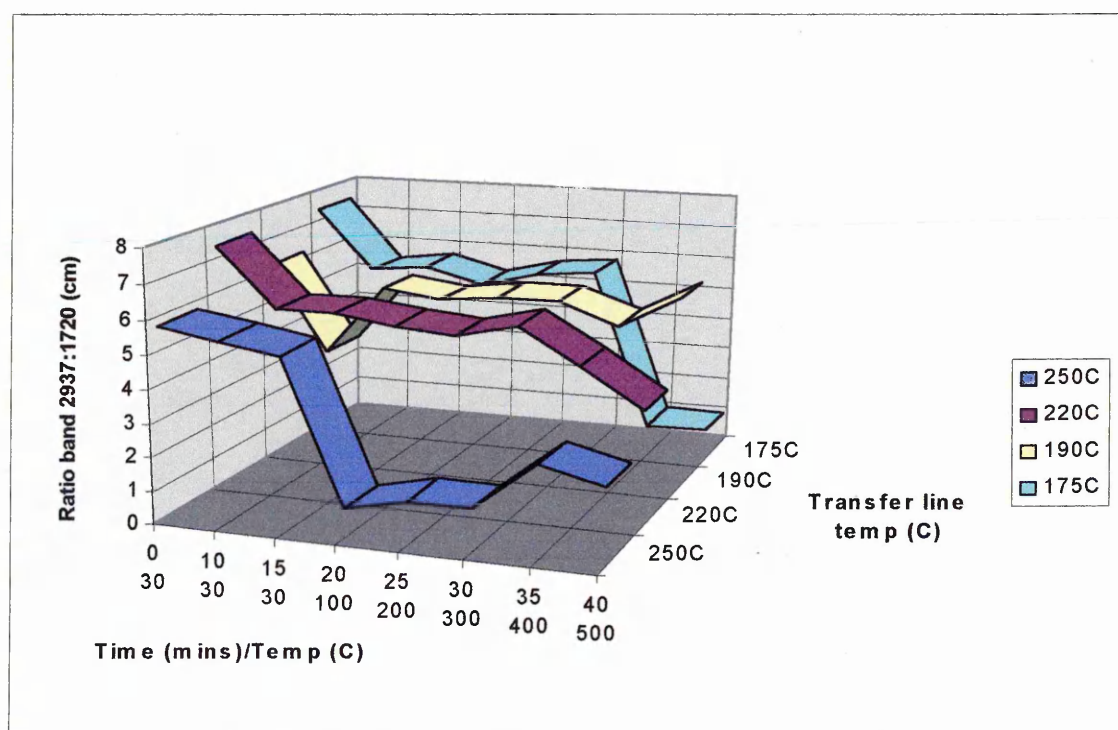


Figure A1.3 highlights several important points. Firstly, the temperatures of the TG crucible and transfer lines are important in determining the shape of these curves in terms of the susceptibility of various parts of the molecule to bond breakage whilst

subject to a fixed temperature transfer line and a changing ramp rate. Therefore it is also plausible that the temperature ramp rate is having an effect on the thermal stability of the DMF molecule, though the results are inconsistent. Previous work has shown that MS detects DMF in two stages (previous experiments used greater sample weights in order to highlight differences [353]). Yet the detection of two DMF stages in the MS is not as defined with smaller samples. This may be due to the fact that DMF was in excess in, the first detection maxima being attributed to DMF leaving the crucible and the second maxima due to residual DMF still present in the transfer lines.

Results Real time MS (RT-MS)

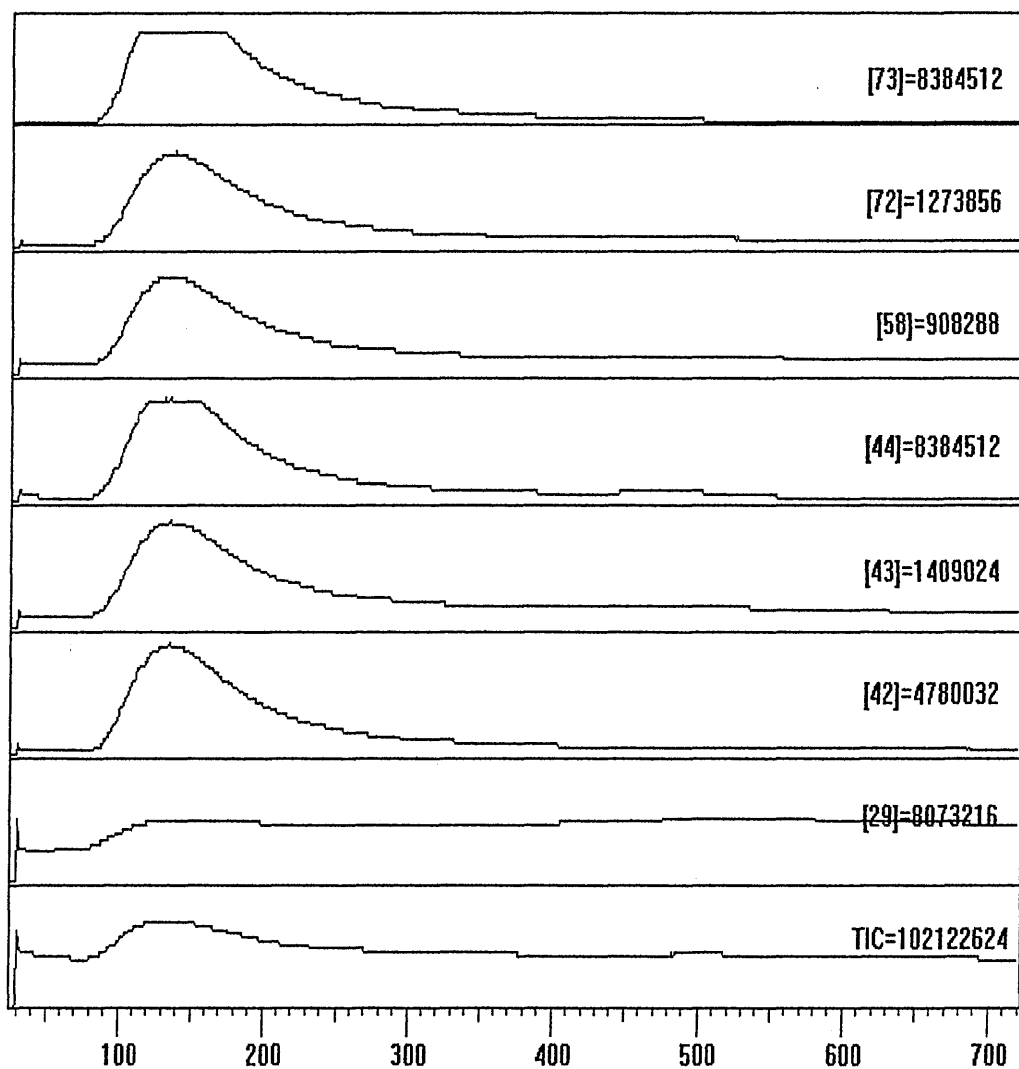
MS analysis at these transfer line temperatures has highlighted several important points. Firstly the objective of these experiments was to determine the optimum transfer line temperature that would produce the most intense signal for DMF in the MS. This would mean the minimum disturbance to the MS ion ratios (seen in chapter 6) and therefore indicate less DMF breakdown. The ions used to indicate degradation in this study were 73 (DMF-parent ion), 58 (DMF-secondary ion), and 44 (DMF fragment and/or CO₂). The presence of high proportions of the fragment ions 58 and 44 is indicative of DMF breakdown and reduced amounts of parent ion 73 indicates DMF breakdown.

Results External heat zone experiments

It has been shown that between 100-160°C, the detection of the DMF parent ion has saturated the detector (figure A1.4) demonstrated by the capping of the parent ion

peak at $m/z = 73$. This was also the case for ion $m/z = 44$ (CO_2 and DMF fragment) whereas $m/z = 58$ was not capped, because under normal ionisation conditions its relative intensity is only 4.8% of the parent ion (100%).

Figure A1.4 RT-MS reconstructed ion chromatograms for DMF with transfer lines at 190°C and the EHZ at 100°C



It is not possible when the peaks are capped to compare the relative amounts of DMF reaching the detectors. The contribution at each temperature is calculated by

integrating the area of $m/z = 73$. However, detection of DMF between 180-200°C revealed uncapped peaks for $m/z = 73$, which suggested 180°C (24901198-integrated ion area) to be the optimum temperature (figure A1.5) and 200°C (557328-integrated ion area) showing greater DMF breakdown (figure A1.6).

Figure A1.5 RT-MS reconstructed ion chromatograms for DMF with transfer lines at 190°C and the EHZ at 180°C

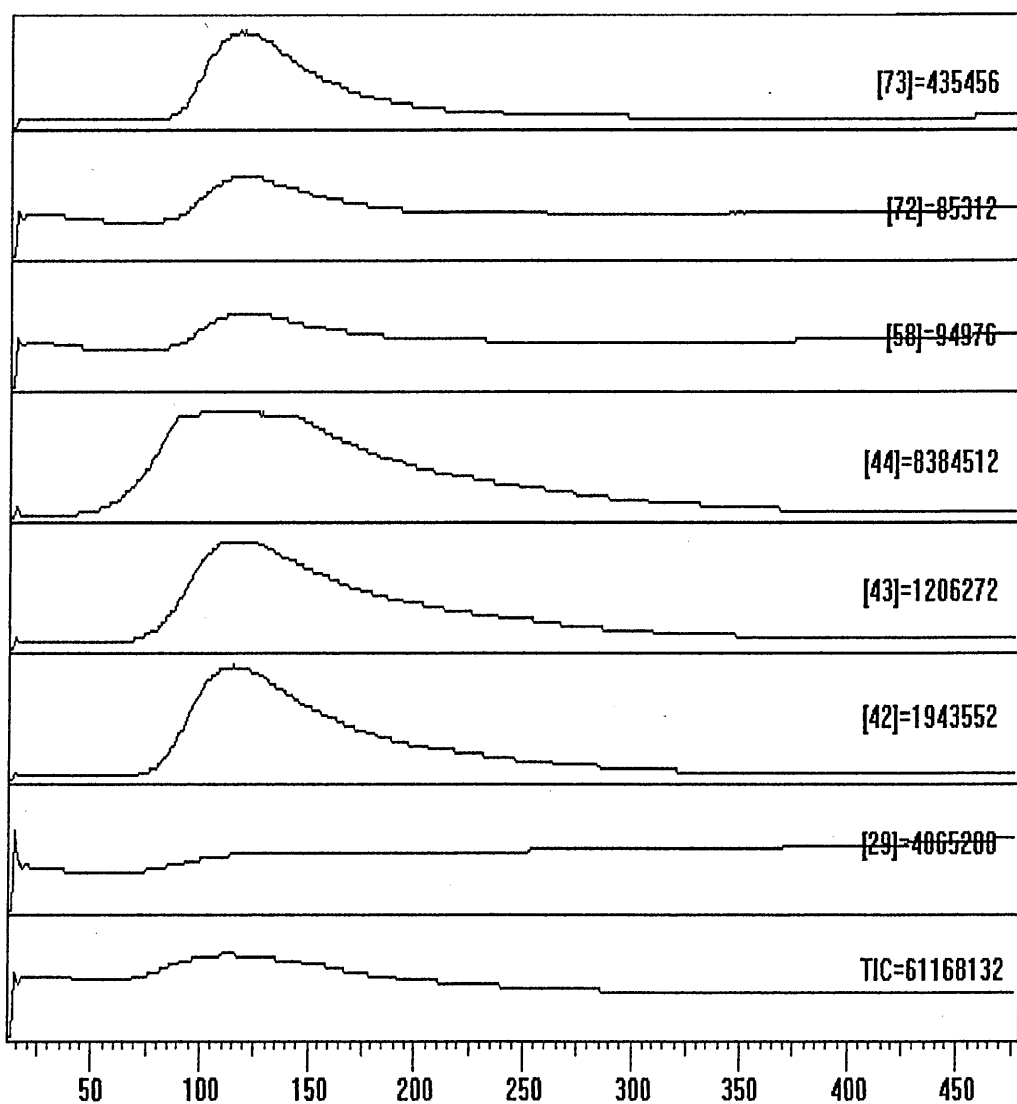
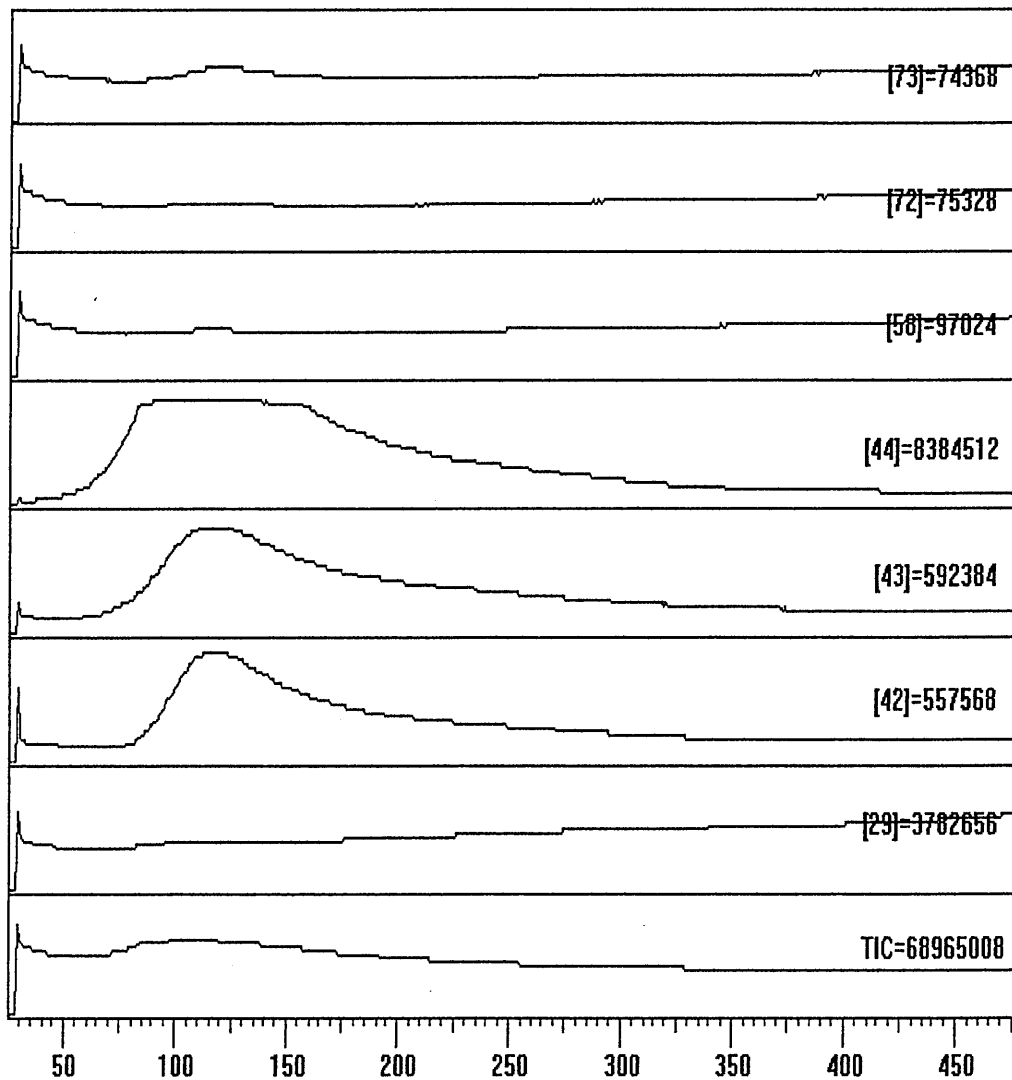


Figure A1.6 RT-MS reconstructed ion chromatograms for DMF with transfer lines at 190°C and the EHZ at 200°C



As previously mentioned, the presence of high proportions of the fragment ions 58 and 44 is indicative of DMF breakdown. It is obvious from figure A2.6, that at 200°C a greater amount of ion $m/z = 44$ is detected. Also if the integrated ion areas of $m/z = 73$ and 58 are compared, then the relative proportions can be ascertained (table A1.1).

Table A1.1 Ion ratios of $m/z = 73:58$ at EHZ temperatures 180 and 200°C

Integrated ion area	EHZ 180°C	EHZ 200°C
($m/z = 73$)	24901198	557328
($m/z = 58$)	2818176	129408
% $m/z = 73/58$	11.31%	23.21%
($m/z = 44$)	Slightly capped	capped

Table A1.1 shows that the relative ion ratio ($m/z = 73/58$) is lower at 200°C(EHZ) when the transfer lines are held at 190°C. Therefore the optimum temperature of the EHZ when the transfer lines are at 190°C was 180°C. These temperatures were used for all the DMF related work herein.

Appendix 2 (XRD and DRIFTS study of mixed mineral standard components)

Figure A2.1 Room temperature XRD trace of SWy-2 (montmorillonite)

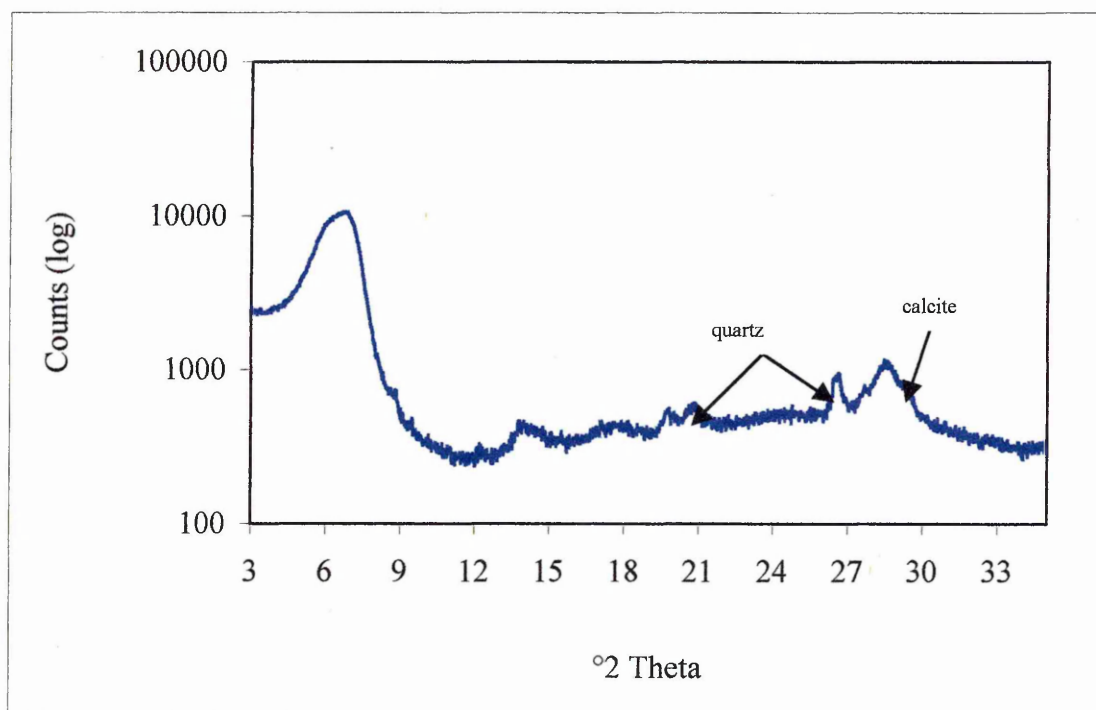


Table A2.1 RT-XRD trace peak assignments for SWy-2 impurities

d value Å	Angle °2θ	Potential impurities
10.0008	8.835	Mica/Illite
4.9762	17.81	Mica/Illite
4.2621	20.825	Quartz
3.3466	26.615	Quartz
3.0346	29.410	Calcite

The XRD trace of SWy-2 (fig. A2.1) is dominated by a reflection at 6.75°2θ due to the dominance of the montmorillonite swelling mineral component. Further evidence for this component is seen at 19.75°2θ. The presence of a mica/illite mineral is suggested by reflections at 8.83 and 17.81°2θ. In the corresponding DRIFTS

spectrum (fig A2.2), the presence of smectite is confirmed by a band at 1628cm^{-1} , but the diagnostic bands of illite at 750 and 825cm^{-1} are not visible because they may be masked by the broad and intense quartz doublet located at 781 and 800cm^{-1} . XRD evidence for quartz in SWy-2 is confirmed by reflections at 20.82 and $26.61^\circ 2\theta$. XRD evidence for kaolinite is suggested by a weak reflection at $12.22^\circ 2\theta$, though corroborative DRIFTS evidence shows that diagnostic kaolinite bands are absent ($2696\text{-}3620\text{cm}^{-1}$ & 916cm^{-1}). This may be due to a concentration effect and the typical broadness of the IR bands of dioctahedral smectite. In both XRD and DRIFTS there is no visible evidence for the presence of chlorite. The presence of a carbonate mineral is suggested in XRD by a weak reflection at $29.41^\circ 2\theta$. Corroborative evidence in DRIFTS shows the occurrence of weak calcite (CaCO_3) bands at 1407 and 712cm^{-1} and a strong (MgCO_3) band at 1436cm^{-1} suggesting this is the dominant carbonate mineral.

Figure A2.2 Room temperature DRIFTS spectra of SWy-2

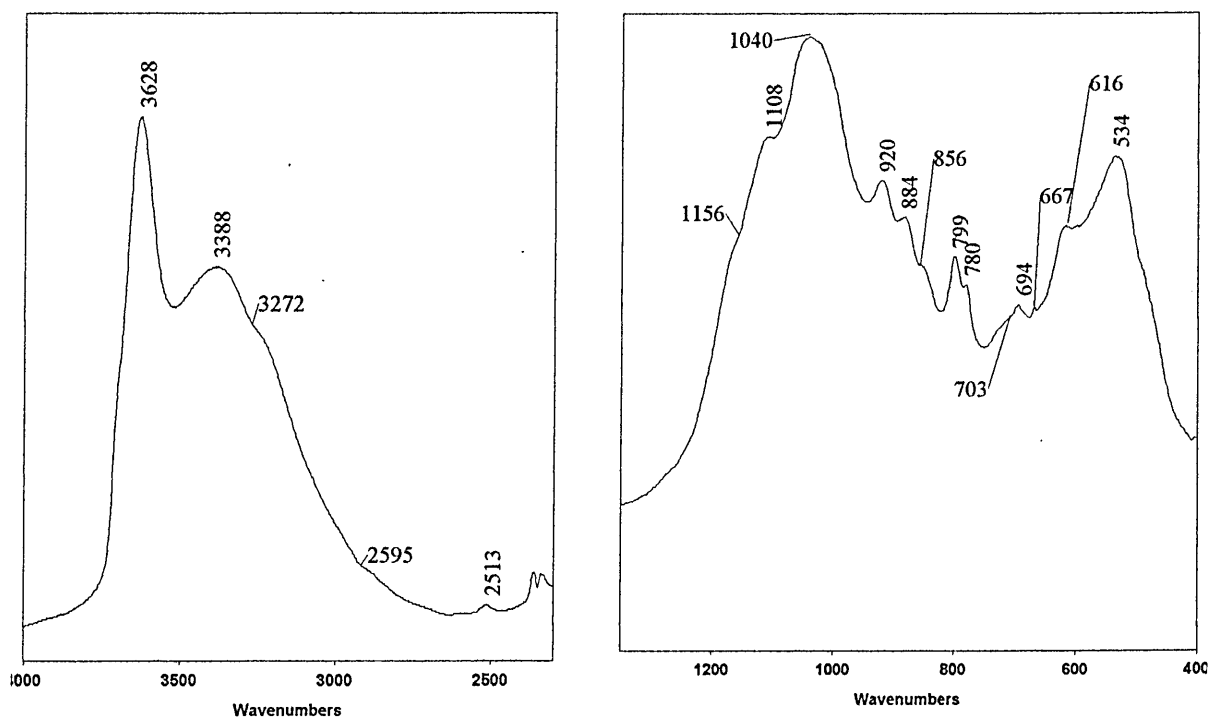
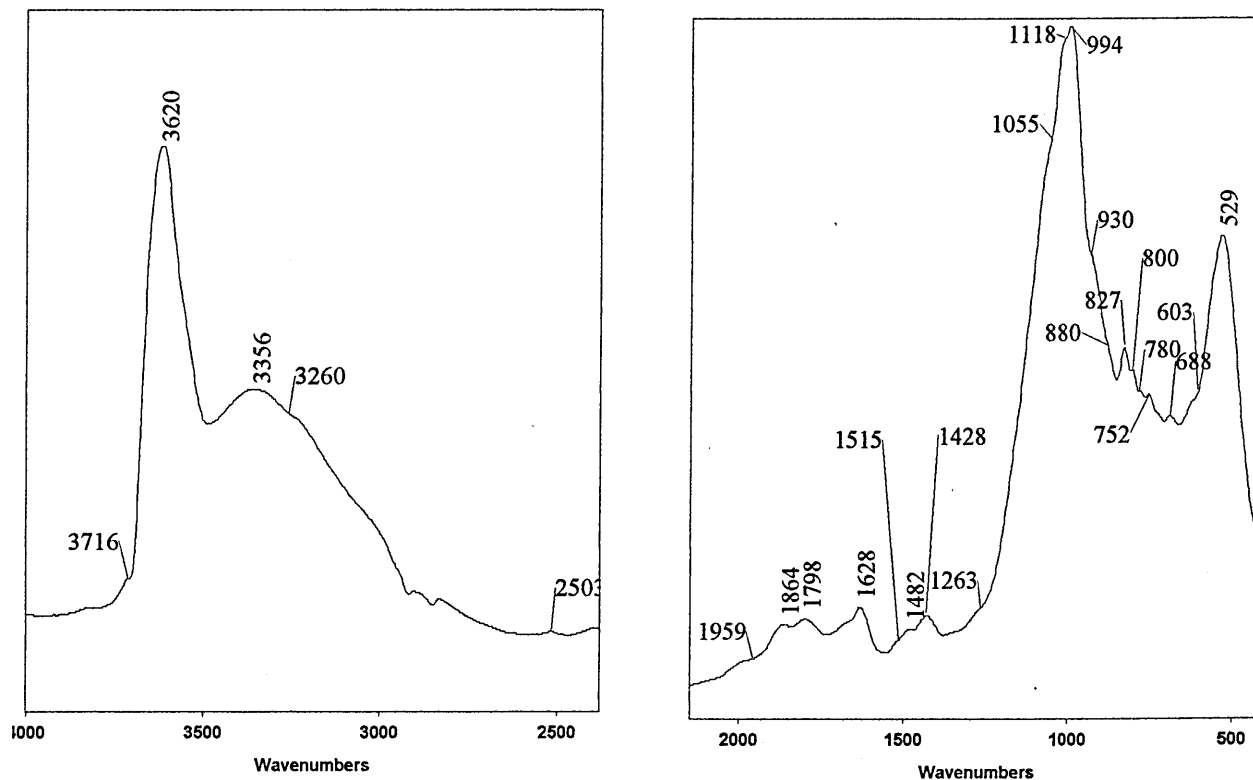


Table A2.2 Room temperature XRD trace peak assignments for 1-Mt (illite)

d value Å	Angle 2θ	Possible impurities
7.1960	12.290	Kaolinite
4.2520	20.875	Quartz
2.9782	29.980	Tridymite SiO ₂

The XRD trace of 1Mt-illite(not shown) is dominated by mica/illite reflections at 8.78 (10.06 Å), 17.70 (5.0 Å) and 26.80 (3.33 Å) °2θ. Corroborative evidence from DRIFTS is demonstrated by a broad band at 3620cm⁻¹ coupled with the 827, 750cm⁻¹ doublet. In DRIFTS there is also evidence of a shoulder at 3260cm⁻¹ and a band at 1428cm⁻¹, which is indicative of diagenetic illite containing interlayer NH₄⁺ ions. However the 1428cm⁻¹ band coupled with a shoulder at 880cm⁻¹ is also diagnostic of the presence of carbonates. Evidence for the presence of a smectite/illite mineral is provided by an XRD reflection at 19.74 (4.49 Å) and a DRIFTS band at 1628cm⁻¹. Further evidence points more specifically to saponite (tri-octahedral), due to a band at 3716cm⁻¹ coupled with a strong band at 529cm⁻¹.

Figure A2.3 DRIFTS spectra of 1Mt-illite



There is evidence for phengite (high Mg content) illite at 527cm^{-1} . However this is not certain as the position of the OH stretch for $\text{Mg}_3(\text{OH})$ grouping in micas varies from 3704 to 3712cm^{-1} . The broadness of the 3620cm^{-1} band may suggest the presence of saponite 3633cm^{-1} band ($\text{MgFe}^{2+}\text{Fe}^{2+}\text{OH}$ stretch). Evidence for the presence of kaolinite in illite is suggested in XRD by a reflection at $12.29^\circ 2\theta$ (7.20 \AA) but no corroborative evidence if available from DRIFTS as the four diagnostic bands between (3696 - 3620cm^{-1} -OH stretching vibrations) and a band at 916cm^{-1} are not visible. There is no XRD or DRIFTS evidence for the presence of chlorite in 1Mt-illite. Evidence for the presence of Quartz by XRD reveals reflections at 26.69 (3.34 \AA) and 20.845 (4.26) $^\circ 2\theta$.

Figure A2.4 Room temperature XRD trace of KGa-2 (kaolinite)

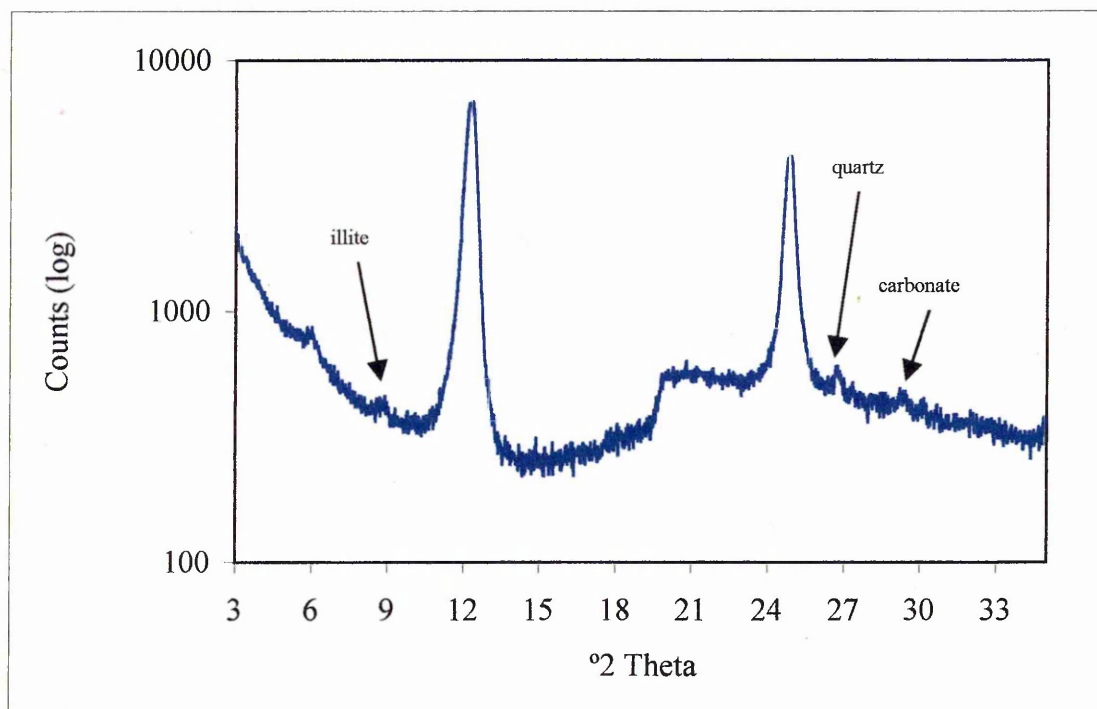
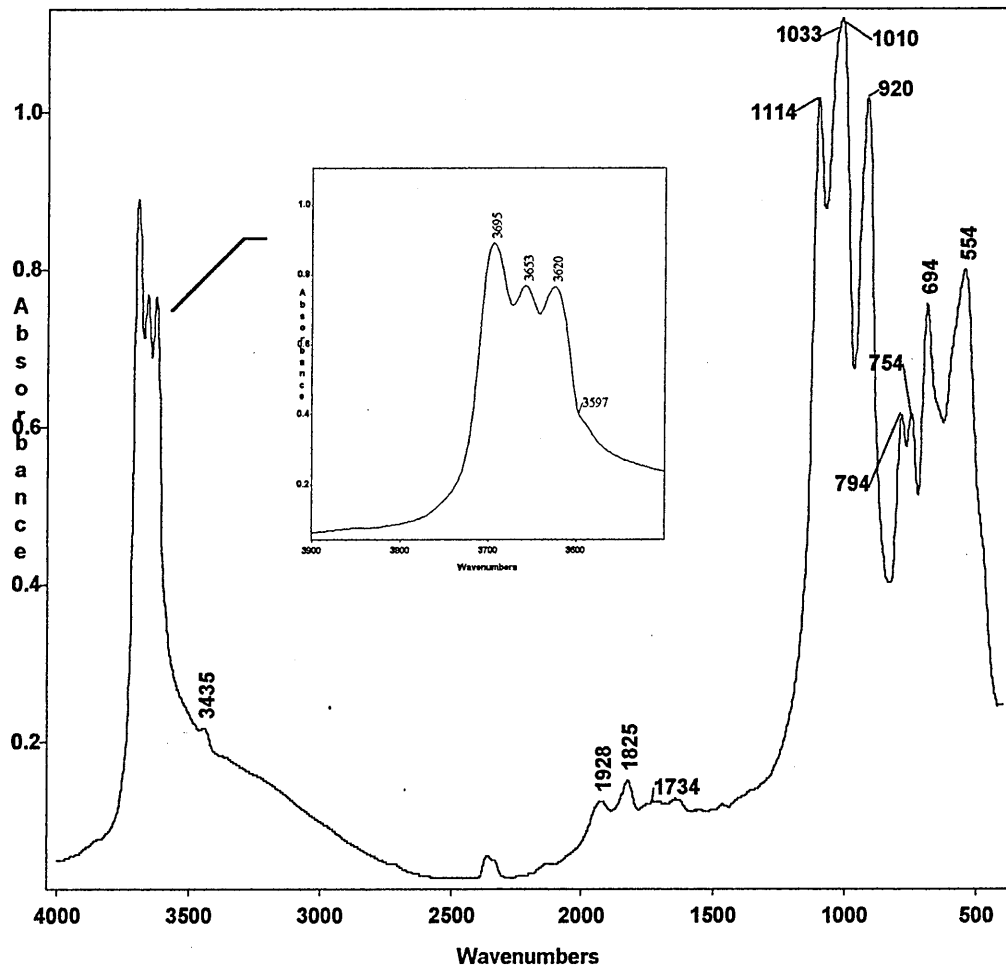


Table A2.3 Room temperature XRD trace peak assignments for KGa-2 impurities

d value Å	Angle 2θ	Impurities
4.2580	20.845	Quartz
3.0371	29.385	Calcite

Figure A2.5 Room temperature DRIFTS spectrum of Kaolinite (KGa-2)



The XRD trace of KGa-2 shown in figure A2.4 is dominated by 001 and 002 reflections of kaolinite at 12.26 and $24.91^{\circ}2\theta$. There is some evidence that illite is present in KGa-2. Though the illite 001 reflection ($8.86^{\circ}2\theta$) is not present, there is the suggestion of a reflection at $8.75^{\circ}2\theta$, which is lost within a sloping background. There is weak evidence for the presence of the illite 002 and 003 reflections (weak) at 17.84 and $26.93^{\circ}2\theta$ respectively. The corresponding DRIFTS spectrum (fig.A2.5) shows no enhancement of the 3620cm^{-1} band attributed to illite or montmorillonite. This broad OH-stretching band near 3620cm^{-1} which is often coupled with a doublet at 825 (missing)- 750cm^{-1} is not present. Also the diagnostic band at 1628cm^{-1} of

montmorillonite is not present. The IR spectral region used to identify kaolinite in the presence of halloysite focuses on two weak bands found at 795 and 758 cm^{-1} respectively. If halloysite were present, the 795 cm^{-1} band would be reduced to a weak inflection. However, these bands are of equal intensity which suggests only kaolinite is present. There is no evidence for chlorite in either XRD or DRIFTS.

Evidence for the presence of Quartz in the XRD trace of KGa-2 reveals 001 and 002 reflections at 26.67 and 20.845 $^{\circ}2\theta$. The broadness of this area suggests interference from other minerals such as feldspar. Examination of the DRIFTS spectra for the bands representative of Quartz (1162, 1112, 800, 781 and 696 cm^{-1}) reveal the presence of bands at 694 and 1112, but the 800,781 cm^{-1} doublet is not present. However, there is a strong band at 792 cm^{-1} which is indicative of tridymite a polymorph of quartz.

There is no conclusive evidence for the presence of feldspar in the XRD trace of KGa-2 as the area between 16 and 24 $^{\circ}2\theta$ is both broad and diffuse. However there are some suggestions that reflections at 21.04 and 23.58 $^{\circ}2\theta$ may be present. Though this is more likely to be quartz due to the complimentary bands observed in the DRIFTS spectra, which demonstrate no evidence of feldspar, in particular the absence of the 1055 cm^{-1} band.

For CCa-1 (chlorite), the only evidence for impurities was a very weak XRD reflection at 3.05 29.52 $^{\circ}2\theta$ which could be attributable to calcite (not shown).

Figure A2.6 Room temperature XRD trace of albite (feldspar)

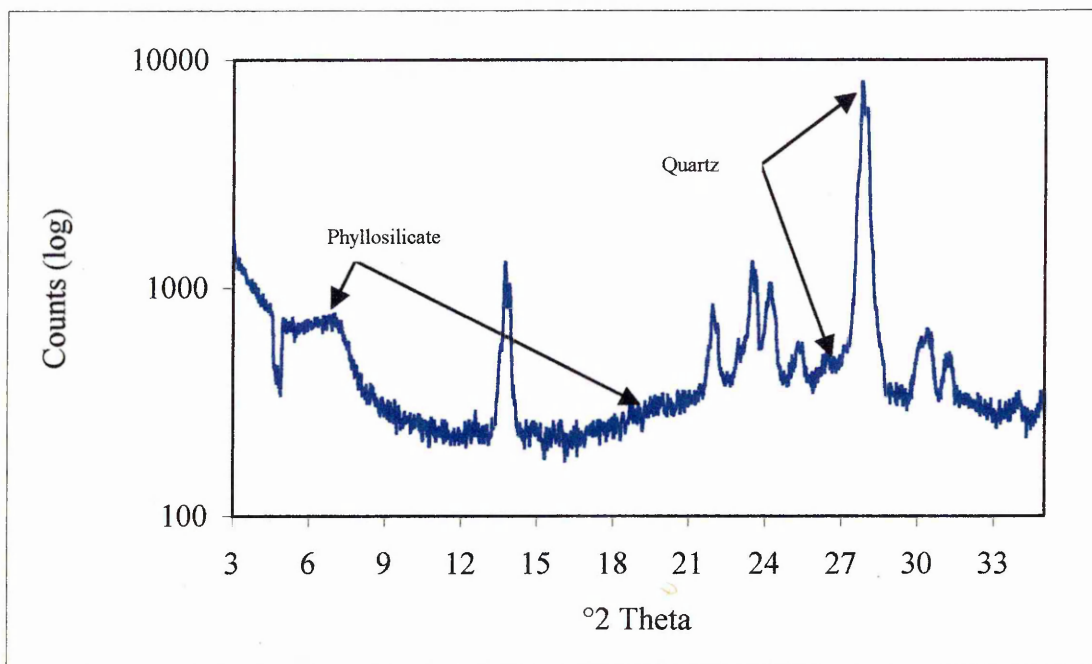


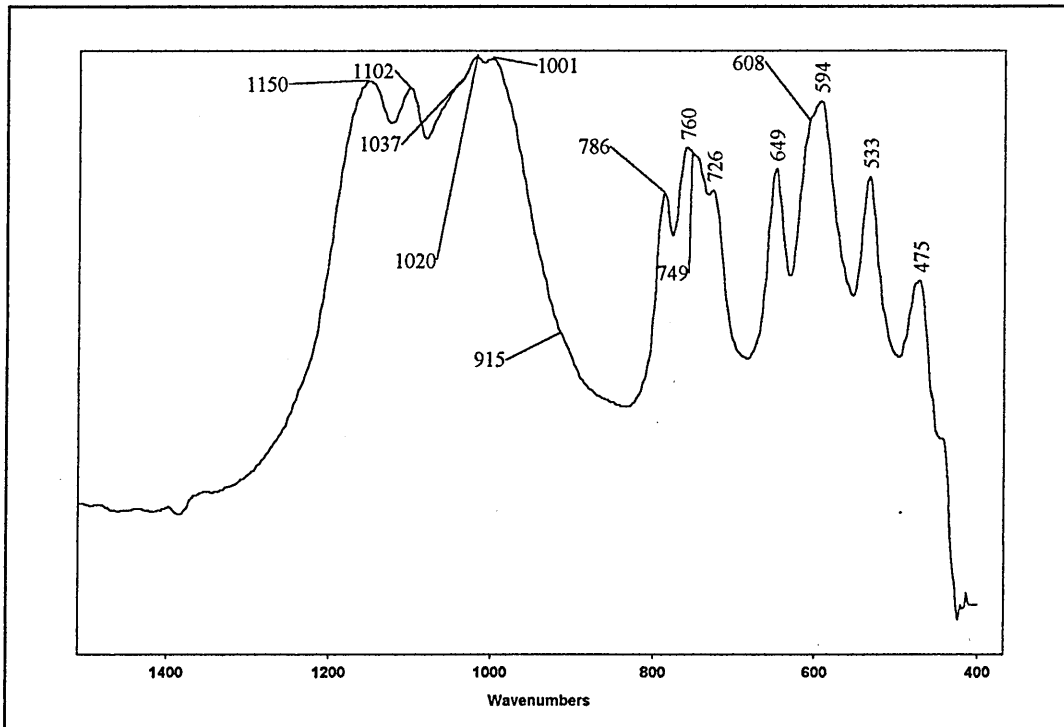
Table A2.4 Room temperature XRD trace peak assignments for albite (feldspar)

d value Å	Angle °2θ	6.2 Potential impurities
12.8190	6.890	Phyllosilicate
4.4803	19.800	Phyllosilicate
3.3658	26.460	Quartz
3.2293	27.600	Quartz
2.9723	30.040	Magnetite
2.9229	30.560	Orthoclase

XRD evidence for Albite (fig.A2.6) is provided by peaks at 22.096 and 23.45°2θ. Its main peak at 27.86°2θ has several un-resolved shoulders at 27.59 and 27.72°2θ suggesting the presence of diopside ($\text{CaMg}(\text{SiO}_3)_2$) and orthoclase. In the corresponding DRIFTS spectrum, a quartet of bands between 700-800 cm^{-1} are present

(786, 760, 748 & 726 cm^{-1}) are characteristic of both albite and orthoclase, but a sharp band at 400 cm^{-1} to highlight albite is absent due to the limits of the mid-infrared scan. Because the DRIFTS spectrum for orthoclase is very similar to albite, further evidence for its presence is indicated by an XRD peak at 23.58 $^{\circ}2\theta$. There is no visible evidence for the presence of quartz or its polymorphs, as XRD peaks at 26.67 and 20.84 $^{\circ}2\theta$ are missing and the DRIFTS doublet at 800,781 cm^{-1} characteristic of quartz is absent. XRD may provide evidence for the presence of iron minerals due to weak reflections at 30.29 (maghemite) and 30.07 (magnetite) $^{\circ}2\theta$. However corroborative DRIFTS evidence is not available, due to the low abundances of these oxides in clays and their spectral overlap with the silicate structure at low wavenumbers.

Figure A2.7 Room temperature DRIFTS spectra of albite (feldspar)



Both XRD and DRIFTS analysis of albite show no evidence for the presence of kaolinite or chlorite. However, a band at 3621cm^{-1} without the presence of a band at 1628cm^{-1} (montmorillonite) suggests the presence of illite. However, there is the presence of a band at 1620cm^{-1} . XRD analysis also highlights the possibility of a swelling component due to the presence of a peak at $6.98^\circ 2\theta$ (12.65). Examination of orthoclase by XRD and DRIFTS showed no evidence for the presence of clay mineral components. The other component present was quartz.

Appendix 3 EGA (RT-MS) reconstructed chromatograms of DMF and H₂O fragment ions detected from mixed mineral standards (25-800°C).

Figure A3.1 Standard 1: 70% Quartz, 10% Montmorillonite, 4% Kaolinite, 4% Illite, 8% Chlorite, 4% Feldspar

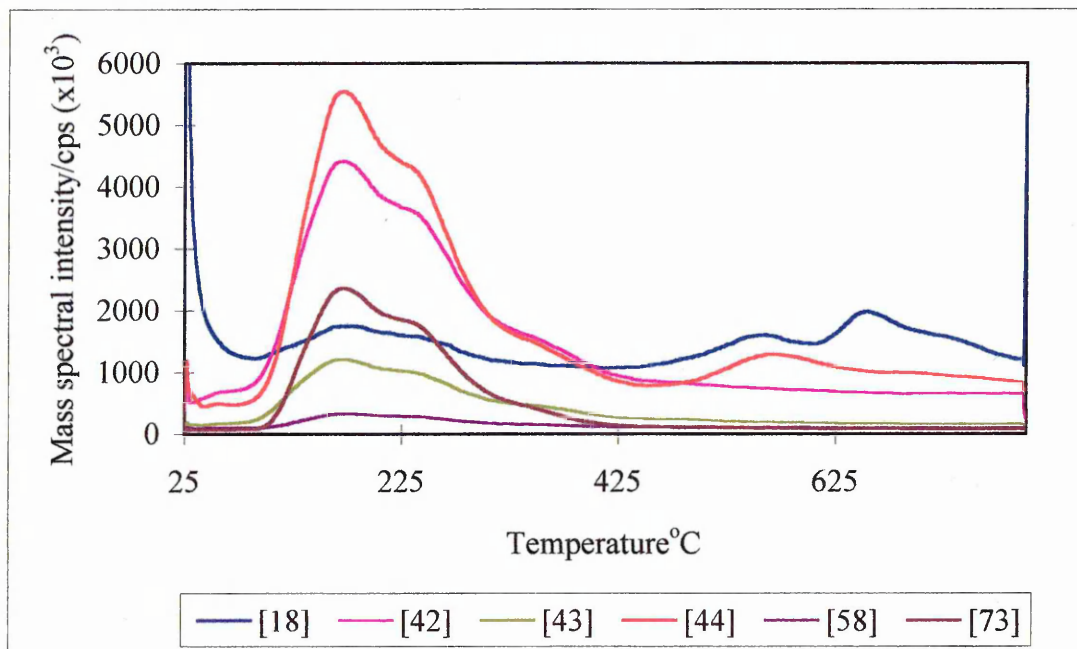


Figure A3.2 Standard 2: 75% Quartz, 10% Montmorillonite, 0% Kaolinite, 7% illite, 8% Chlorite, 4% Feldspar

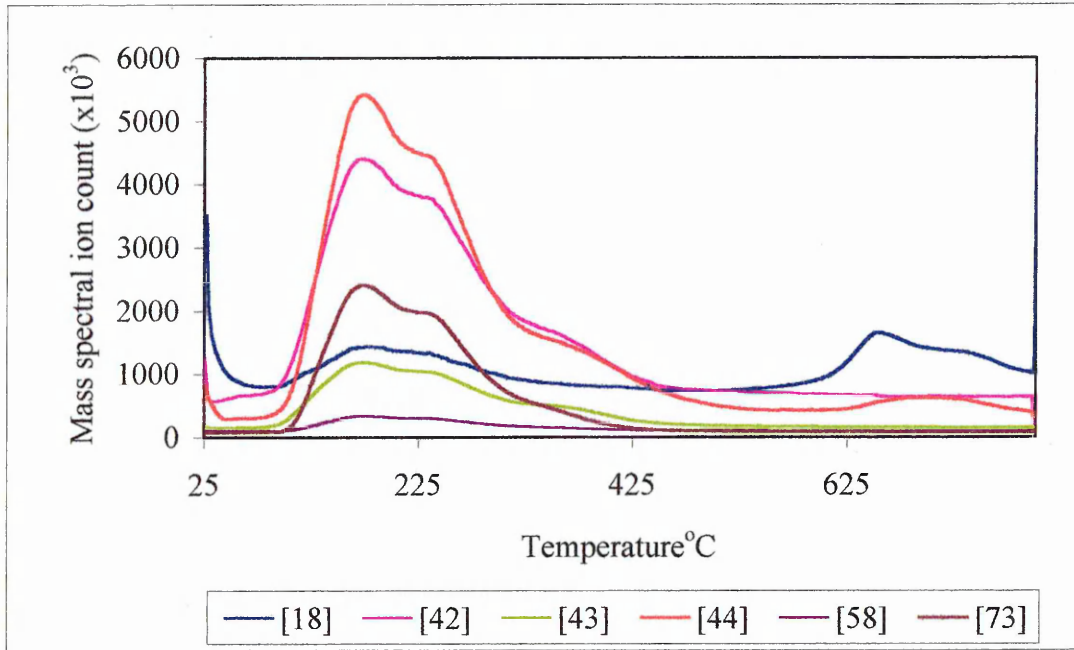


Figure A3.3 Standard 3: 86% Quartz, 0% Swy-2, 0% Kaolinite, 8% Illite, 1% Chlorite, 5% Feldspar

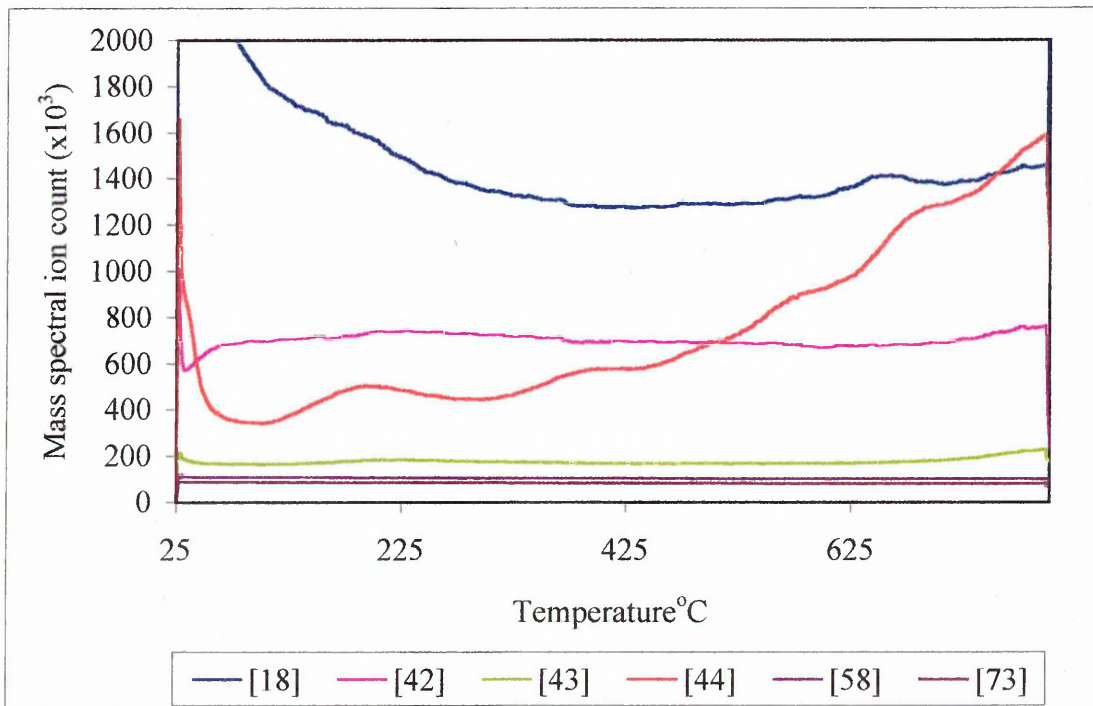


Figure 1: Comparison of the experimental results with the theoretical predictions for the first two modes of vibration.

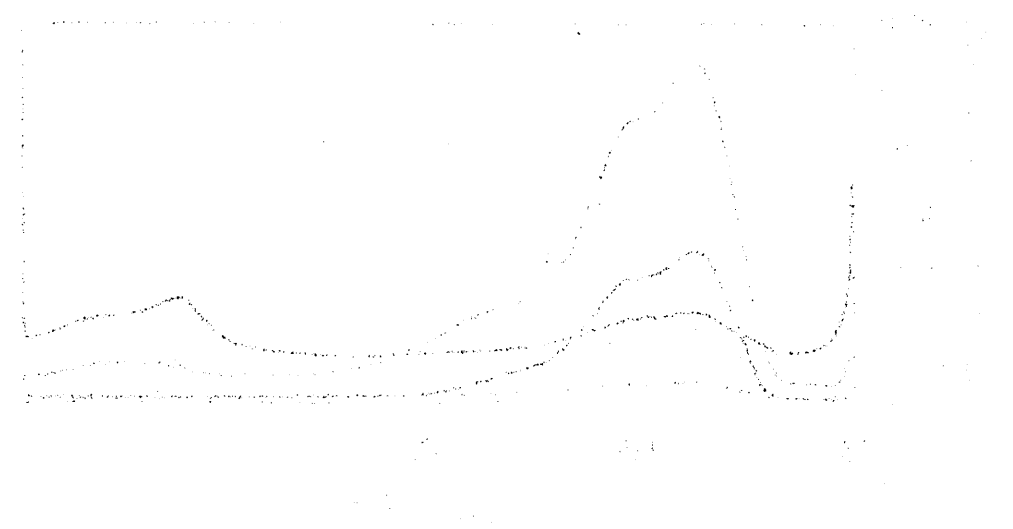


Figure 2: Comparison of the experimental results with the theoretical predictions for the third mode of vibration.

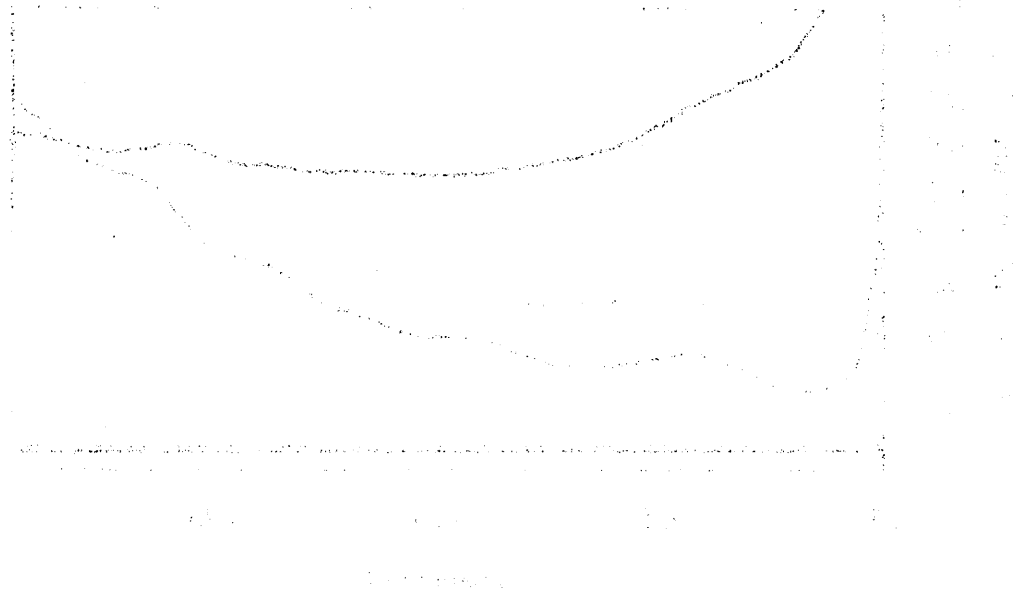


Figure 3: Comparison of the experimental results with the theoretical predictions for the fourth mode of vibration.

Figure A3.4 Standard 4: 75% Quartz, 9% Montmorillonite, 10% Kaolinite, 0% Illite, 3% Chlorite, 3% Feldspar

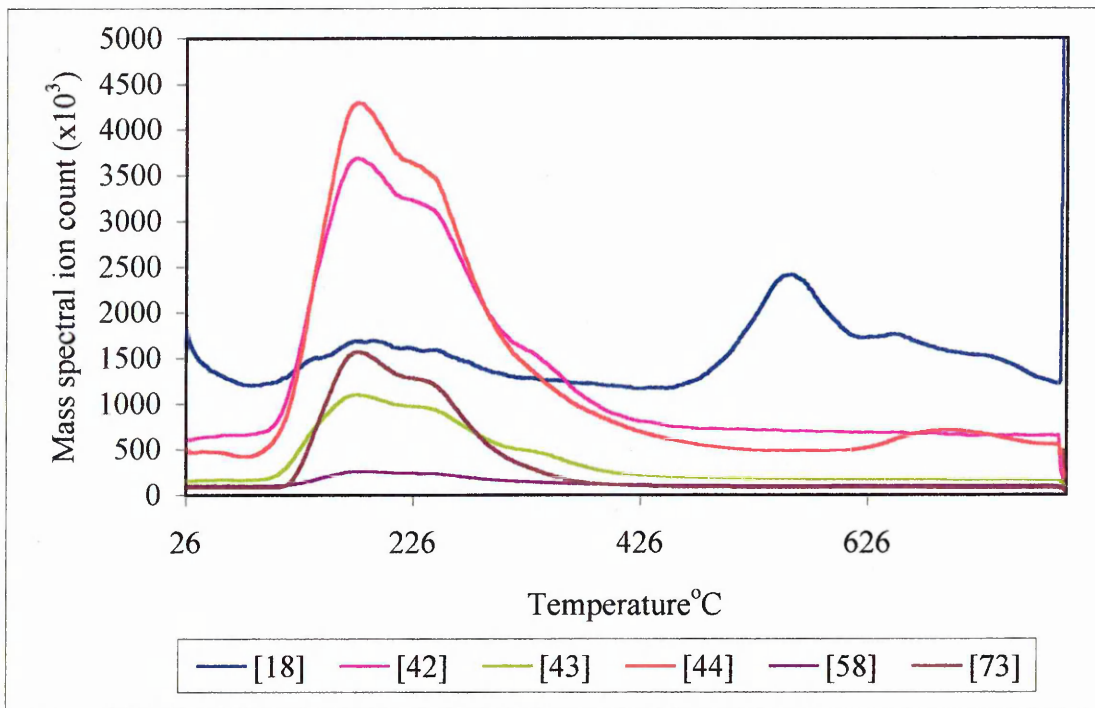


Figure A3.5 Standard 5: 55% Quartz, 6% Montmorillonite, 3% Kaolinite, 10% Illite, 9% Chlorite, 17% Feldspar

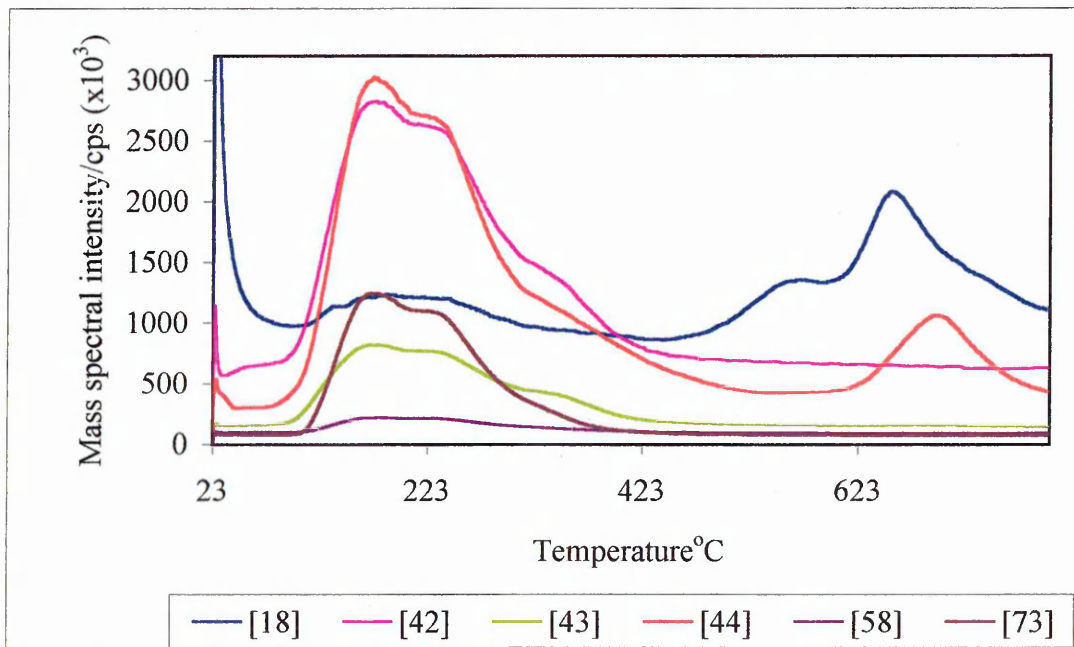


Figure A3.6 Standard 6: 55% Quartz, 6% SWy-2, 3% Kaolinite, 10% Illite, 9% Chlorite, 17% Feldspar

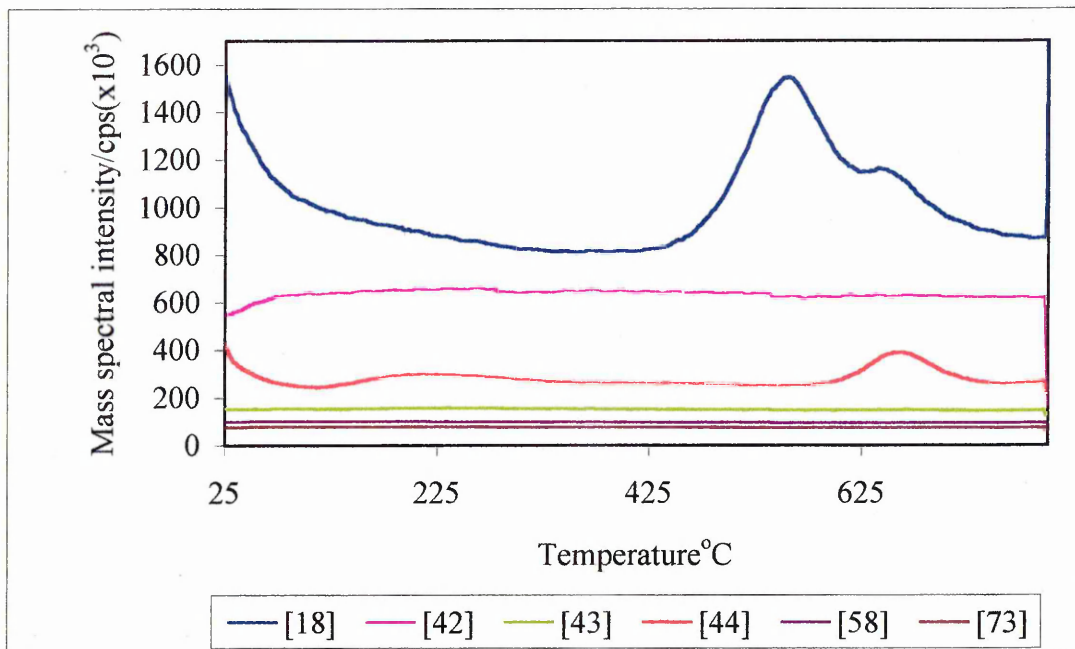


Figure A3.7 Standard 7: 87% Quartz, 0% SWy-2, 10% Kaolinite, 2% illite, 0% Chlorite, 1% Feldspar

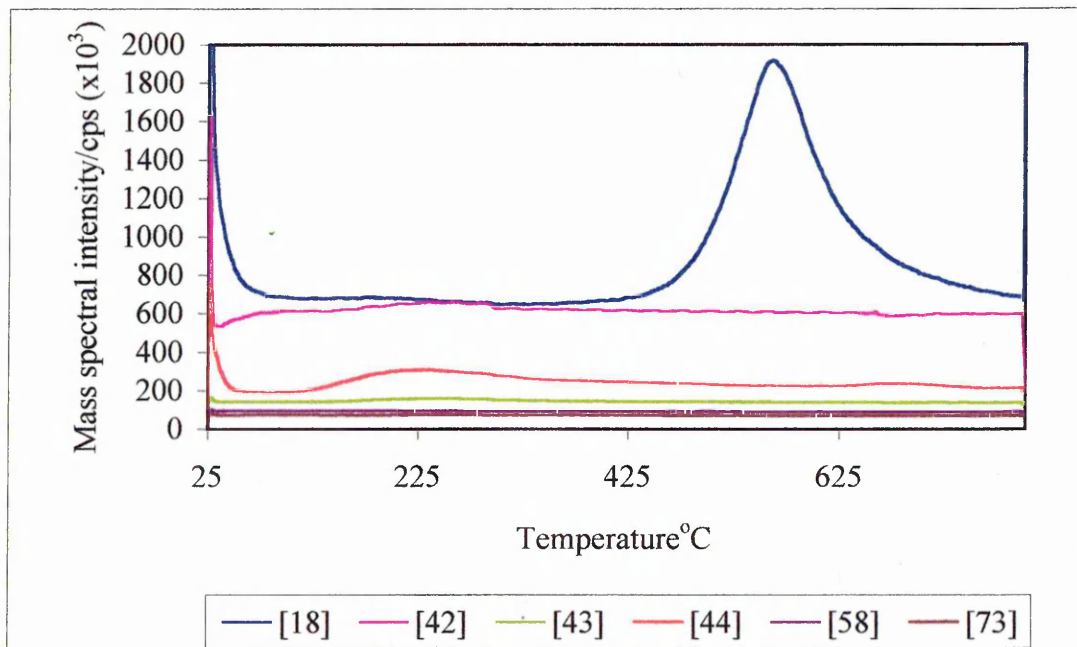


Figure A3.8 Standard 8: 80% quartz, 8% SWy-2, 5% Kaolinite, 1% Illite, 0% Chlorite, 6% Feldspar

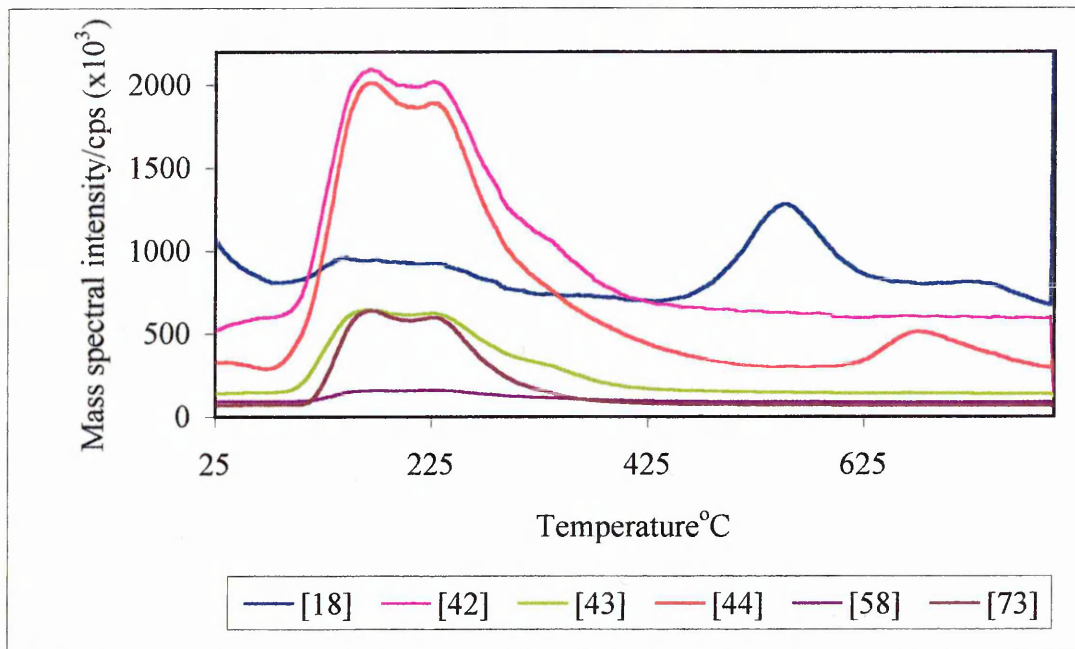


Figure A3.9 Standard 9: 72% Quartz, 6% SWy-2, 3% Kaolinite, 5% Illite, 6% Chlorite, 8% Feldspar

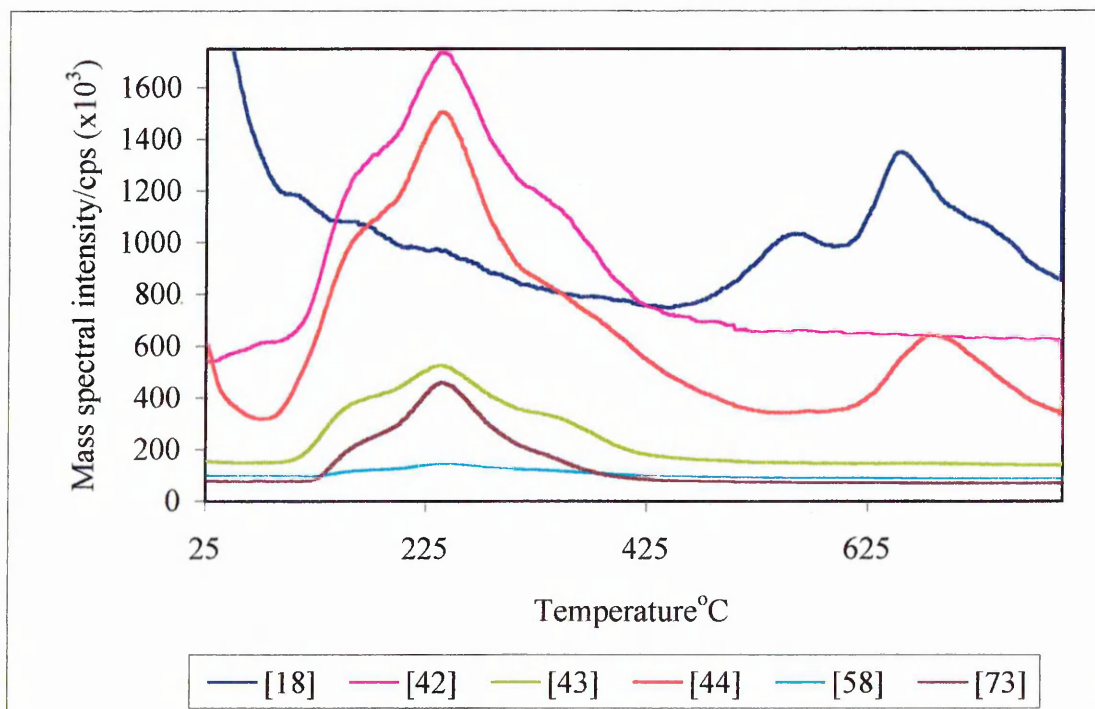


Figure A3.10 Standard 10: 80% Quartz, 4% SWy-2, 8% Kaolinite, 4% Illite, 4% Chlorite, 0% Feldspar

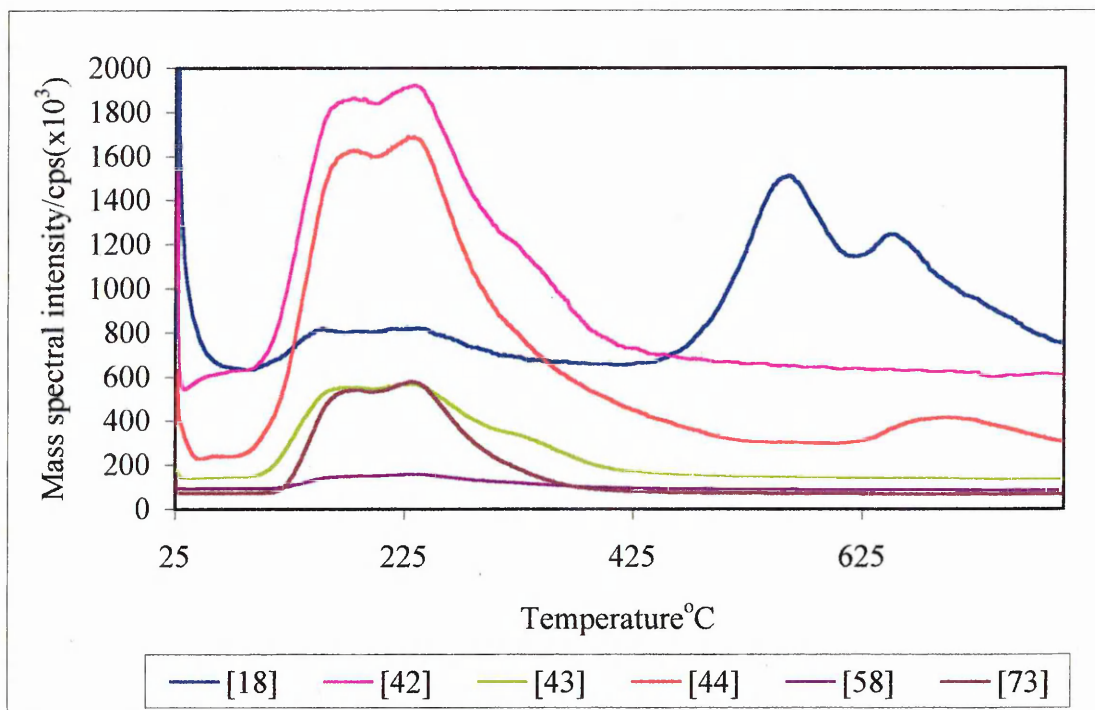


Figure A3.11 Standard 11: 90% Quartz, 5%, Montmorillonite, 0% Kaolinite, 2% Illite, 3% Chlorite, 0% Feldspar

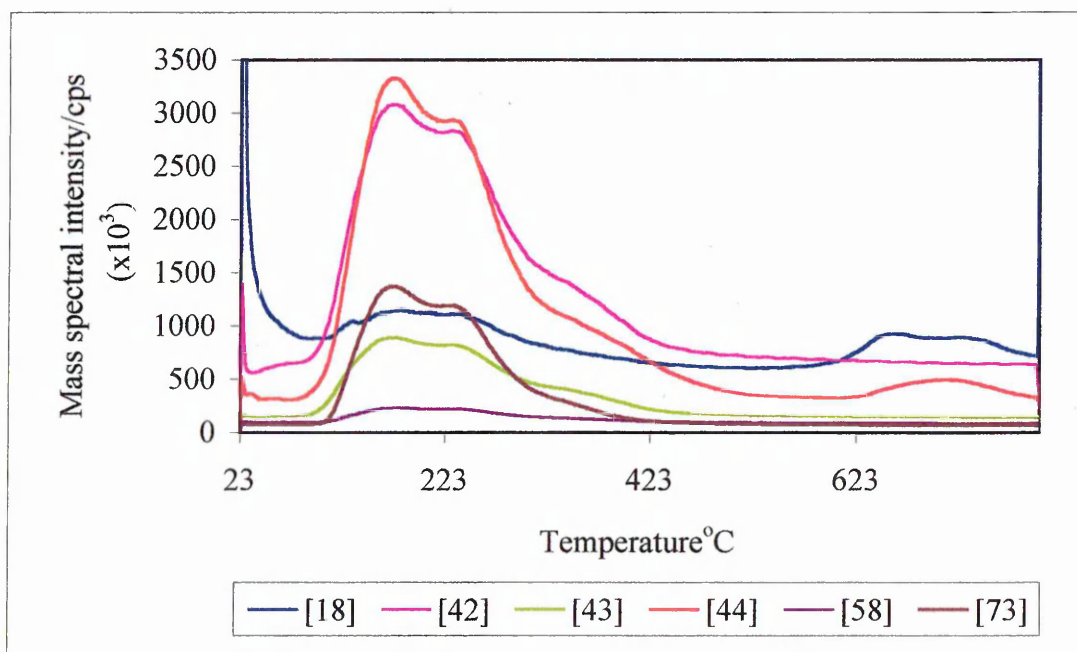


Figure A3.12 Standard 12: 80% Quartz, 10% Montmorillonite, 5% Kaolinite, 0% Illite, 0% Chlorite, 5% Feldspar

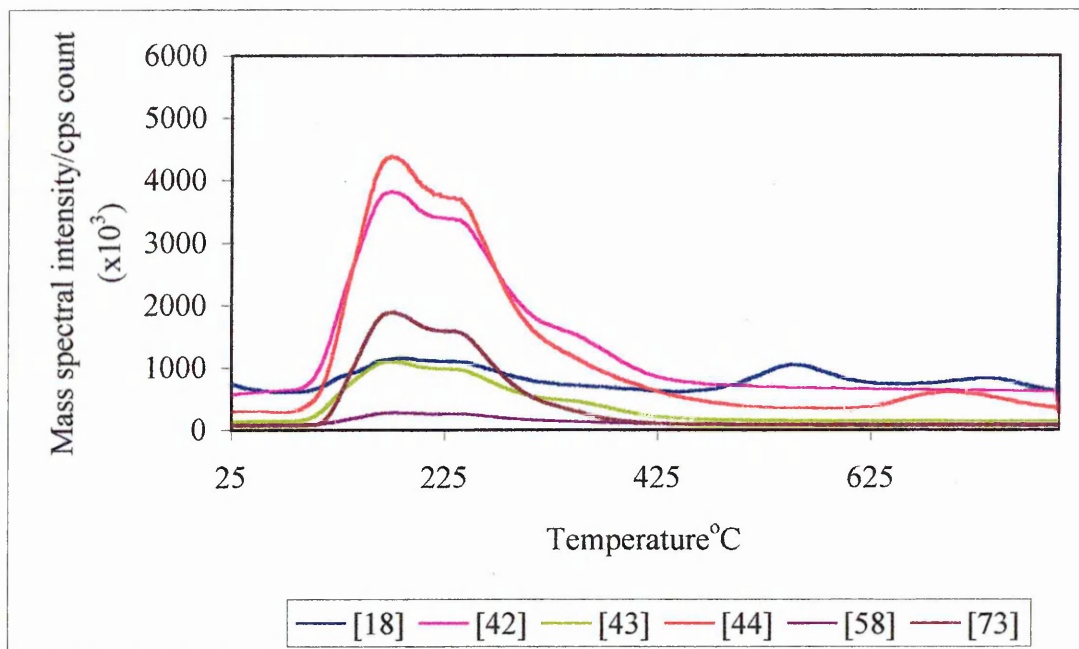


Figure A3.13 Standard 13: 86% Quartz, 2% Montmorillonite, 7% Kaolinite, 3% Illite, 1% Chlorite, 1% Feldspar

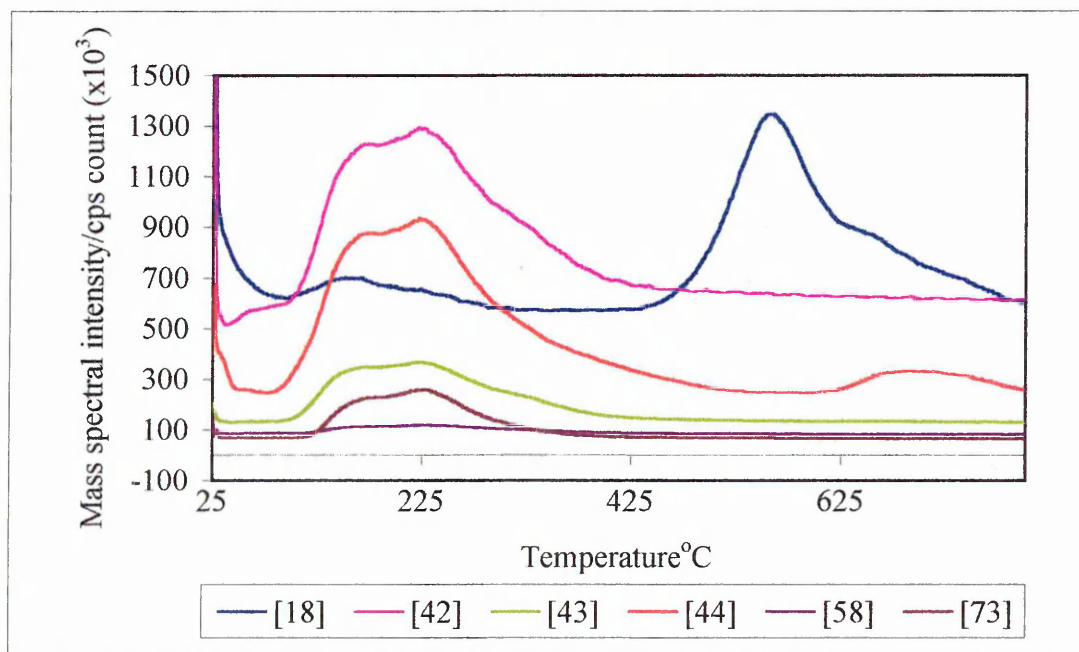


Figure 10: The effect of the parameter α on the solution of the problem. The plot shows the solution $u(x, t)$ versus x for $t = 0.5$ and $t = 1.0$ for $\alpha = 0.1, 0.2, 0.3, 0.4, 0.5$. The solution is shown for $x \in [0, 1]$ and $t \in [0, 1]$. The plot shows that the solution is highly sensitive to the parameter α , with the peak height increasing significantly as α increases.

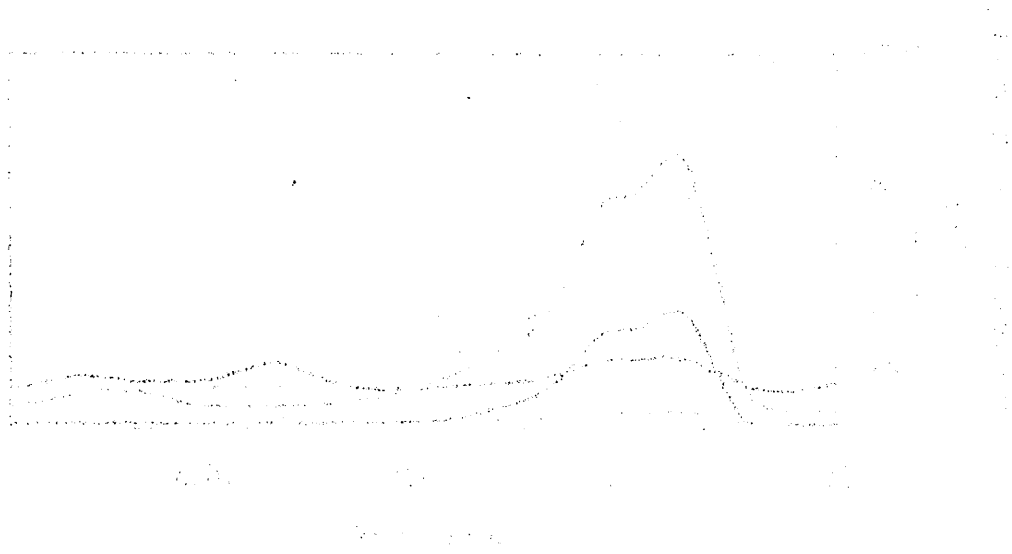


Figure 10: The effect of the parameter α on the solution of the problem.

Figure 11: The effect of the parameter α on the solution of the problem. The plot shows the solution $u(x, t)$ versus x for $t = 0.5$ and $t = 1.0$ for $\alpha = 0.1, 0.2, 0.3, 0.4, 0.5$. The solution is shown for $x \in [0, 1]$ and $t \in [0, 1]$. The plot shows that the solution is highly sensitive to the parameter α , with the peak height increasing significantly as α increases.

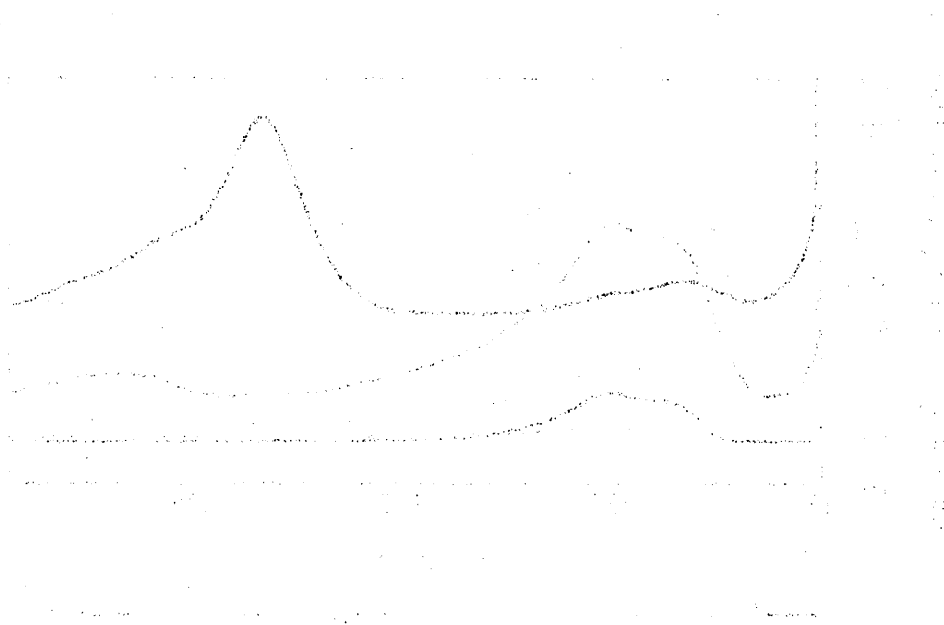


Figure 11: The effect of the parameter α on the solution of the problem.

Figure A3.14 Standard 14: 78% Quartz, 0% Montmorillonite, 0% Kaolinite, 0% Illite, 9% Chlorite, 13% Feldspar

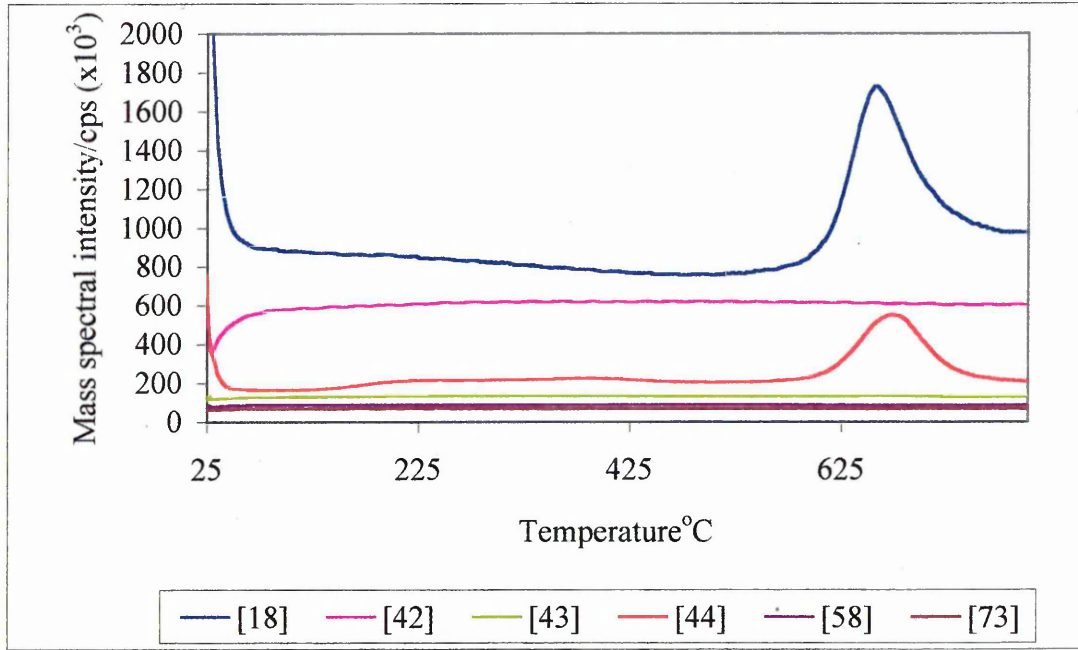


Figure A3.15 Standard 15: 87% Quartz, 0% Montmorillonite, 5% Kaolinite, 6% Illite, 0% Chlorite, 2% Feldspar

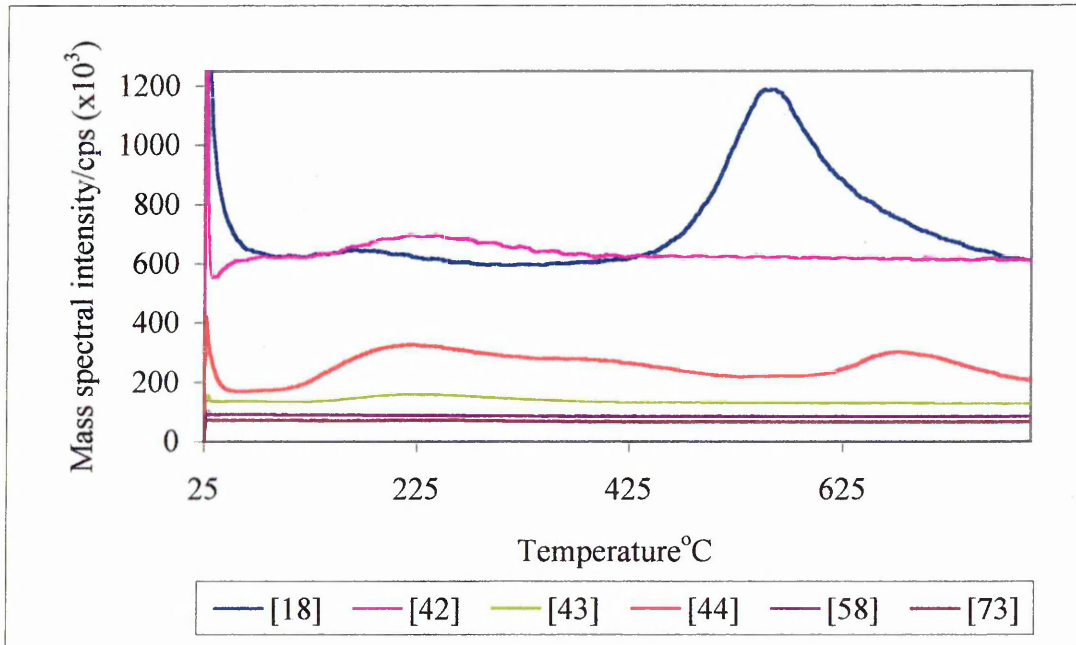


Figure A3.16 Standard 16: 74% Quartz, 2% Montmorillonite, 6% Kaolinite, 4% Illite 10% Chlorite, 4% Feldspar

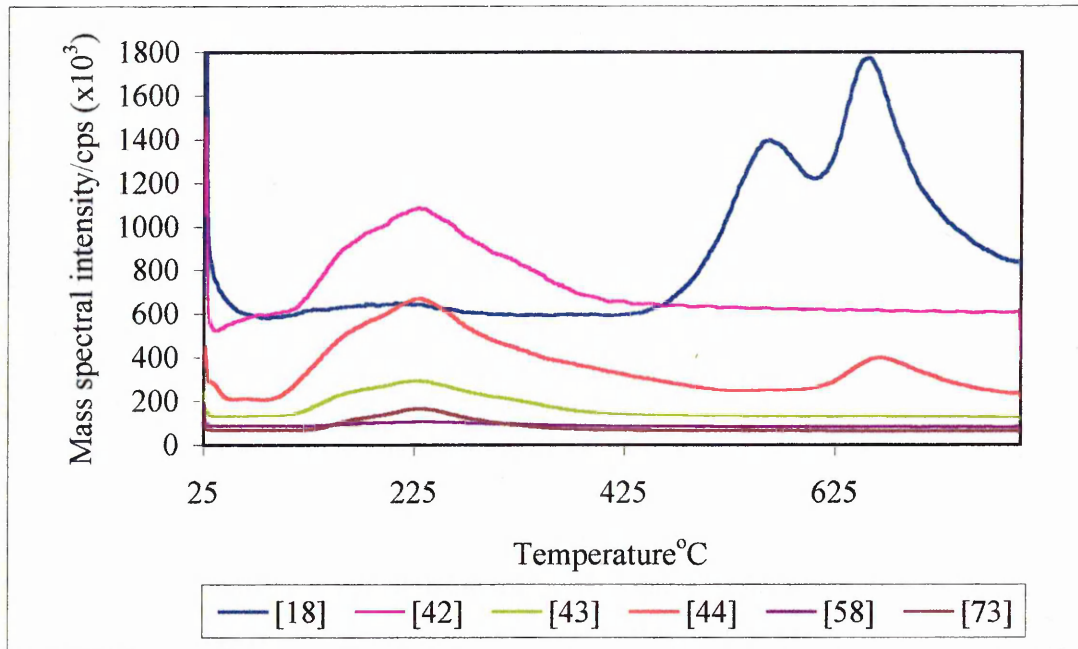


Figure A3.17 Standard 17: 96% Quartz, 0% SWy-2, 0% Kaolinite, 1% Illite, 2% Chlorite, 1% Feldspar

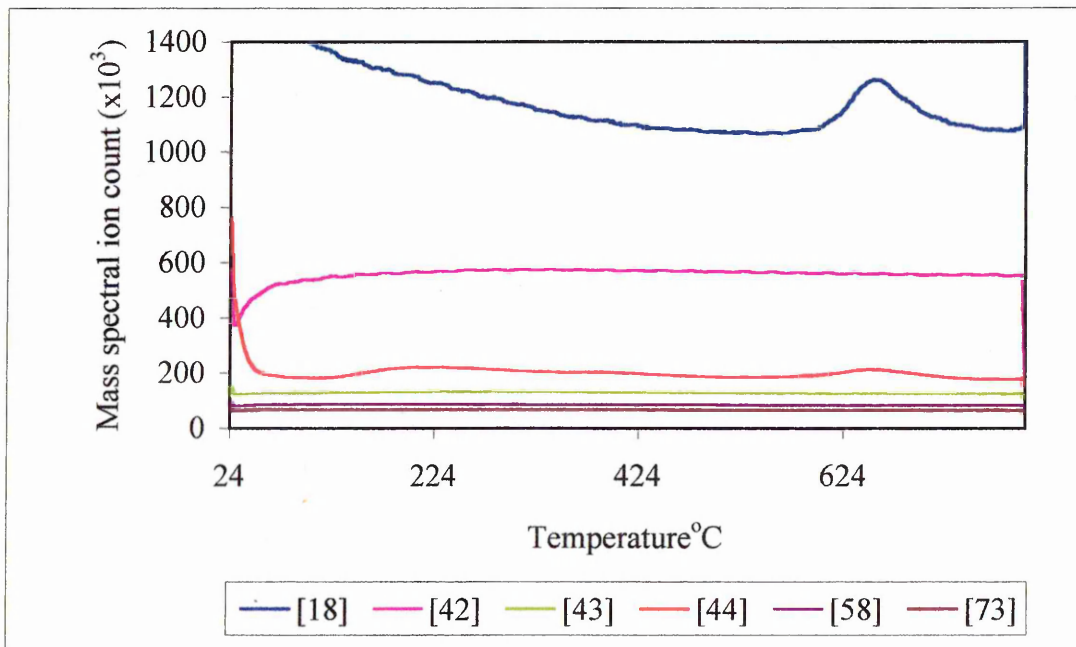


Figure A3.18 Standard 18: 82% Quartz, 0% SWy-2, 3% Kaolinite, 0% Illite, 5% Chlorite, 10% Feldspar

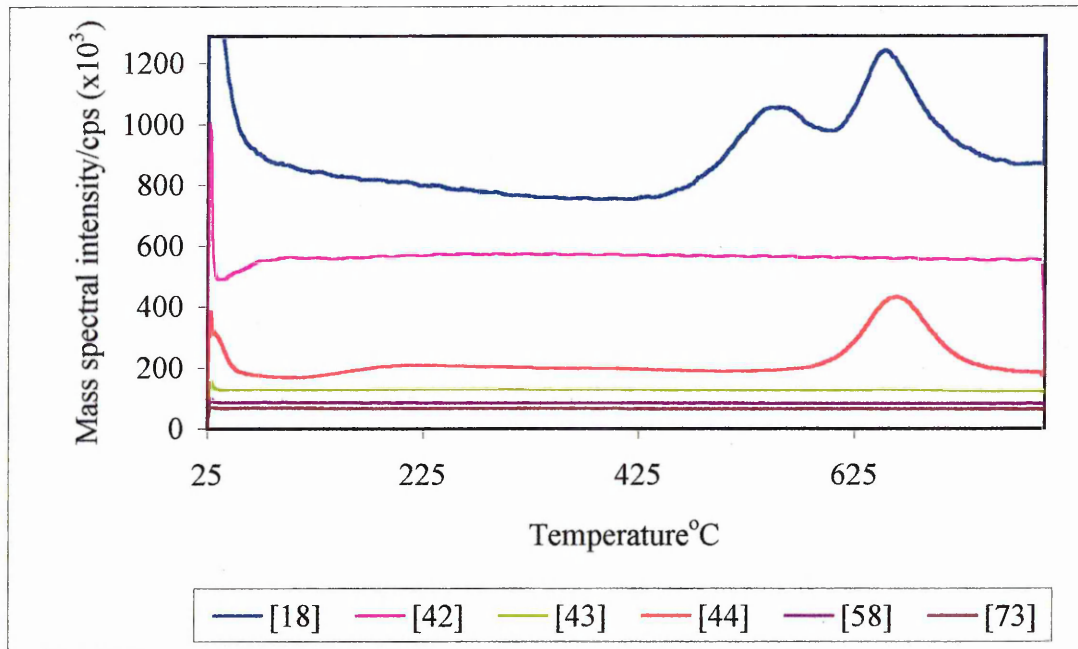


Figure A3.19 Standard 19: 83% Quartz, 5% Montmorillonite, 3% Kaolinite, 5% Illite, 2% Chlorite, 2% Feldspar

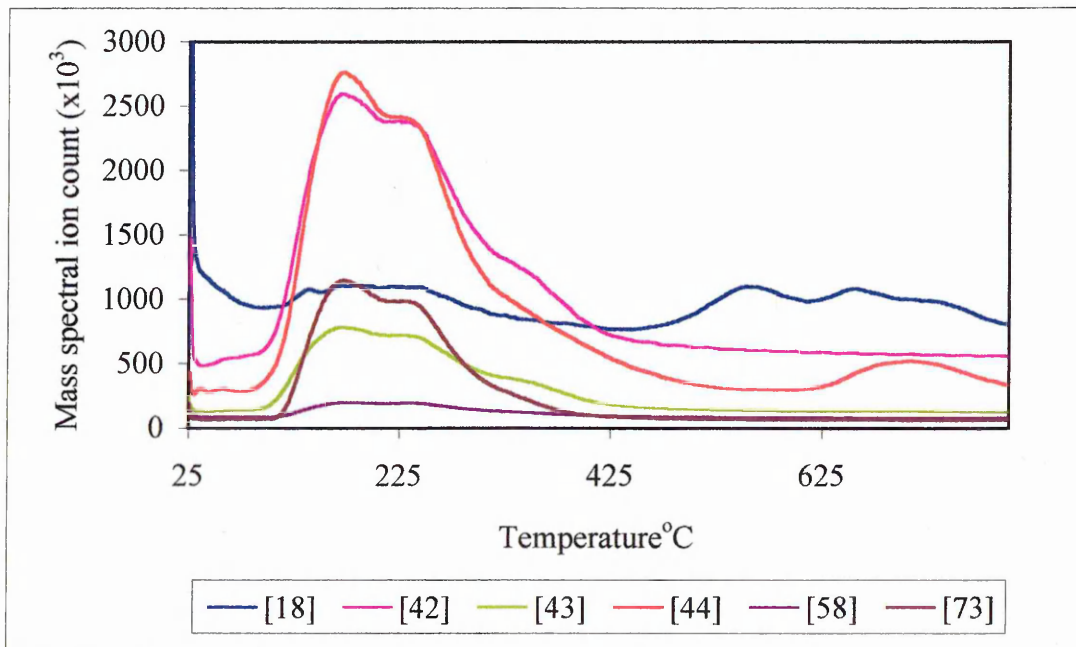


Figure A3.20 Standard 20: Quartz 60%, 9% Montmorillonite, 10% Kaolinite, 6% Illite, 7% Chlorite, 8% Feldspar

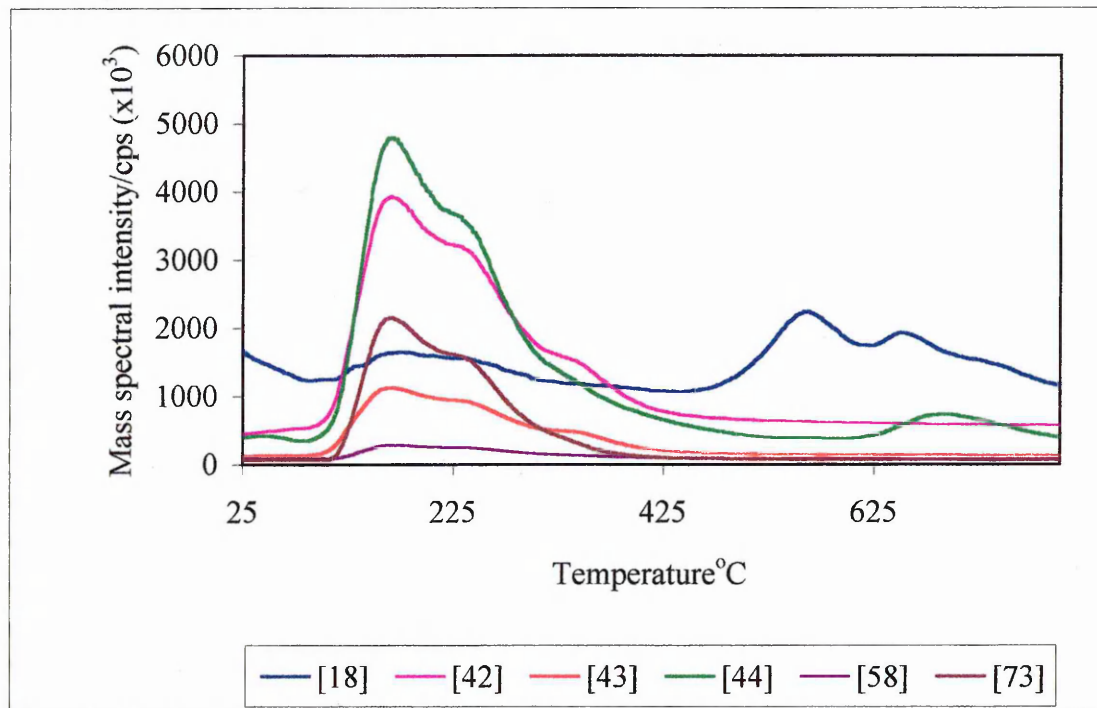


Figure A3.21 Standard 21: 0% Quartz, Montmorillonite 0%, 3% Illite, 3% Chlorite, 9% Feldspar

